High Energy Density Laboratory Astrophysics

Edited by
George A. Kyrala

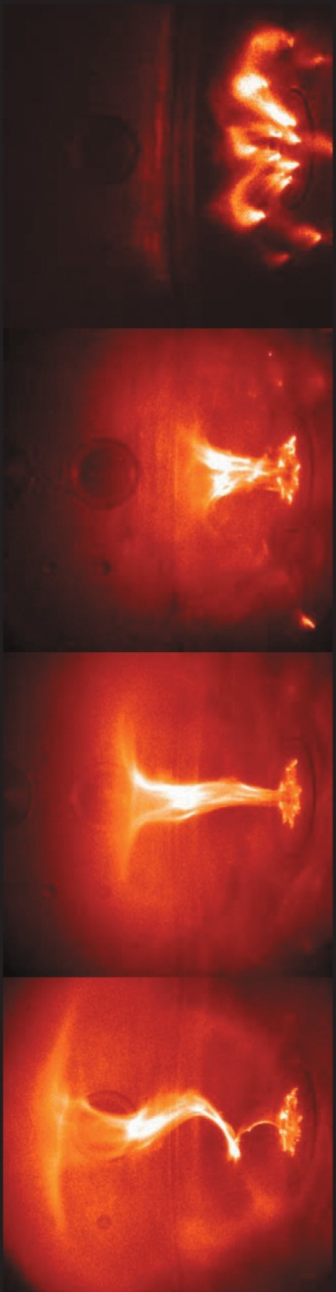

Springer

HIGH ENERGY DENSITY LABORATORY ASTROPHYSICS

Edited by:

G.A. KYRALA

Reprinted from *Astrophysics and Space Science*
Volume 298, Nos. 1–2, 2005

Springer

Library of Congress Cataloging-in-Publication Data is available

ISBN 1-4020-3483-0

2003055495

Published by Springer,
P.O. Box 17, 3300 AA Dordrecht, The Netherlands.

Printed on acid-free paper

Printed in the Netherlands

TABLE OF CONTENTS

PREFACE

The 5th International conference on High Energy Density Laboratory Astrophysics was held on March 10–13, 2004 in Tucson, Arizona. This is a continuation of the very successful previous workshops, held in 1996 at Pleasanton, California, in 1998 at Tucson, Arizona, in 2000 at Houston, Texas, and in 2002 at Ann Arbor, Michigan. During the past several years, research teams around the world have developed astrophysics-relevant research utilizing high energy-density facilities such as intense lasers and z-pinches. Research is underway in many areas, such as compressible hydrodynamic mixing, strong shock phenomena, radiation flow, radiative shocks and jets, complex opacities, equations of state, and relativistic plasmas. Beyond this current research and the papers it is producing, plans are being made for the application, to astrophysics-relevant research, at the 2 MJ National Ignition Facility (NIF) laser at Lawrence Livermore National Laboratory; the 60 kJ Ligne d'Integration Laser (LIL) and the 2 MJ Laser Megajoule (LMJ) in Bordeaux, France; petawatt-range lasers now under construction around the world; and current and future Z pinches. The goal of this conference and these proceedings is to continue focusing attention on this emerging research area. The conference brought together different scientists interested in this emerging new field, with topics covering:

Hydrodynamic instabilities in astrophysics,
Supernovae and supernova remnant evolution,
Astrophysical shocks, blast waves, and jets
Stellar opacities
Radiation and thermal transport
Dense plasma atomic physics and EOS
X-ray photoionized plasmas
Ultrastrong magnetic field generation.

These proceedings cover many of the invited and contributed talks presented at the conference, and refereed by at least three referees. Each invited paper was allowed six pages, and each contributed poster paper was given 4 pages in these proceedings. Of 100 papers that were presented, we have 50 that were submitted for this publication.

The conference was organized by:

Adam Frank, Laboratory for Laser Energetics, University of Rochester, NY
Bruce Remington, L-021, LLNL, Livermore, CA 94550
David Arnett, University of Arizona, Tucson, AZ

Astrophysics and Space Science **298:** 1–2, 2005.

Paul Drake, University of Michigan, Ann Arbor, MI
Alexei Khokhlov, The University of Chicago, Chicago, IL
Sergey V. Lebedev, The Blackett Laboratory, Imperial College, London, UK
Hideaki Takabe, Institute of Laser Engineering, Osaka University, Osaka, Japan
George Kyrala, MS E-526, LANL, Los Alamos, NM 87545

The organizers would like to thank Carmen Ortiz-Henley for the conference administration, as well as the sponsor and endorsing organizations:

Theoretical Astrophysics Program and Steward Observatory,
University of Arizona, Tucson, AZ
Lawrence Livermore National Laboratory, High Energy Density Program
DOE ASCI FLASH Center, The University of Chicago, Chicago, IL
Laboratory for Laser Energetics of the University of Rochester, Rochester, NY
Los Alamos National Laboratory, Physics Division
APS Division of Plasma Physics
APS Topical Group for Plasma Astrophysics
DOE – NNSA

Finally, the editor would like to thank all the authors, editors at Los Alamos, and the referees. They spent a significant amount of their time to help produce this tome, which embodies a significant fraction of the latest in this work. The editor wished that other authors contributed to this effort as well, and hopes they would contribute to proceedings of forthcoming conferences.

GEORGE KYRALA
Guest Editor
Los Alamos, 2004

ASYMMETRIC SUPERNOVAE: YES, ROTATION AND MAGNETIC FIELDS ARE IMPORTANT

J.C. WHEELER, S. AKIYAMA and P.T. WILLIAMS
Department of Astronomy, 1 University Station C1400, Austin, TX, U.S.A.;
E-mails: wheel@astro.as.utexas.edu, shizuka@astro.as.utexas.edu, ptw@lanl.gov

(Received 18 May 2004; accepted 6 July 2004)

Abstract. Spectropolarimetry of core collapse supernovae has shown that they are asymmetric and often bi-polar. This raises the issue of whether some jet-like phenomena are at work involving rotation and magnetic fields. We summarize the importance of the magnetorotational instability for the core collapse problem and sketch some of the effects that large magnetic fields, $\sim 10^{15}$ G, may have on the physics of the supernova explosion.

Keywords: supernovae, jets, lasers

1. Introduction

New vistas have recently opened in the long quest to understand how stellar core collapse is reversed to produce spectacular explosions. There have been two parallel, occasionally overlapping, perhaps converging paths of development. One of these has been the study of asymmetries in supernovae. Campaigns to obtain spectropolarimetry of supernovae continue to show that all core collapse supernovae (those associated with young populations; Type II, Type Ib/c) are polarized and hence substantially asymmetric (Wang et al., 1996, 2001, 2002, 2003a,b; Leonard et al., 2000–2002; Leonard and Filippenko, 2001). Similar bi-polar, jet-like patterns have long been known in Cas A (Fesen, 2001 and references therein) and reinforced by recent work with CXO (Laming and Hwang, 2003 and references therein) and can be seen in HST images of the ejecta of SN 1987A (Wang et al., 2002). The other new vista is the growing connection between supernovae and GRBs that was dramatically confirmed when SN 2003dh was revealed in the afterglow of GRB 030329 (Stanek et al., 2003).

Jets of sufficient strength can explode the star and produce these asymmetries (Khokhlov et al., 1999; Khokhlov and Höflich, 2001; Höflich et al., 2001), but the origin of any such jets remains a mystery. Rotation alone can induce asymmetric neutrino fluxes (Shimizu et al., 1994; Fryer and Heger, 2000), but rotation will inevitably lead to magnetic field amplification that can both produce MHD effects, including possibly jets (Wheeler et al., 2000, 2002; Akiyama et al., 2003), and

Astrophysics and Space Science **298:** 3–8, 2005.

affect neutrino transport (Lai and Qian, 1998; Bhattacharya and Pal, 2003; Ando, 2003). Asymmetries will also affect nucleosynthesis (Maeda et al., 2002; Nagataki et al., 2003).

The ultimate problem of core collapse is one of three dimensions, magnetic field, and neutrino transport. We have known that all along, but the polarization of supernovae and jets from GRBs demand new attention to these issues.

2. The Magneto-Rotational Instability and Core Collapse

Akiyama et al. (2003) have presented a proof-of-principle calculation that the physics of the magneto-rotational instability (MRI: Balbus and Hawley, 1991, 1998) is inevitable in the context of the differentially-rotating environment of proto-neutron stars. The magnetic fields can in turn affect the neutrino transport.

The great power of the MRI to generate magnetic field is that while it works on the rotation time scale of Ω^{-1} (as does simple field-line wrapping), the strength of the field grows exponentially. This means that from a plausible seed field of 10^{10} to 10^{12} G that might result from field compression during collapse, only $\sim$7–12 e-folds are necessary to grow to a field of 10^{15} G.

Core collapse will lead to strong differential rotation near the surface of the proto-neutron star even for initial solid-body rotation of the iron core. For sub-Keplerian post-collapse rotation, Akiyama et al., found that fields can be expected to grow to 10^{15} to 10^{16} G in a few tens of milliseconds. The resulting characteristic MHD luminosity (cf. Blandford and Payne, 1982) is:

$$L_{\rm MHD} \sim \frac{B^2 r^3 \Omega}{2} \sim 3 \times 10^{52}\,\mathrm{erg\ s^{-1}}\ B_{16}^2 R_{\rm NS.6}^3 \left(\frac{P_{\rm NS}}{10\,\mathrm{ms}}\right)^{-1} \tag{1}$$

If this power can last for a significant fraction of a second, a supernova could result. The energy of rotation is approximately

$$E_{\rm rot} \sim \frac{1}{2 I_{\rm NS} \Omega_{\rm NS}^2} \sim 1.6 \times 10^{50}\,\mathrm{erg}\ M_{\rm NS}\ R_{\rm NS.6}^2 \left(\frac{P_{\rm NS}}{10\,\mathrm{ms}}\right)^{-2} \tag{2}$$

A sufficiently fast rotation of the original iron core is needed to provide ample rotation energy. This will also promote a strong MHD luminosity.

The implication of the work of Akiyama et al. (2003) is that the MRI is unavoidable in the core collapse ambience, as pertains to either supernovae or GRBs. The field generated by the MRI must be included in any self-consistent calculation. These implications need to be explored in much greater depth, but there is at least some possibility that the MRI may lead to strong MHD jets by the magneto-rotational (Meier et al., 2001) or other mechanisms. A key point is that the relevant dynamics will be dictated by large, predominantly toroidal fields that are generated internally, not the product of twisting of external field lines that is the basis for so much work on MHD jet and wind mechanisms. Understanding the role of these internal toroidal fields in producing jets (Williams, 2001; Hawley and Balbus, 2002), in providing the ultimate dipole field strength for both ordinary pulsars and magnetars (Duncan and Thompson, 1992), in setting the "initial" pulsar spin rate after the supernova dissipates (that is, the "final" spin rate from the supernova dynamicists point of view), and any connection to GRBs is in its infancy (Proga et al., 2003).

There are a large number of important open issues. Chief among them are whether or not the rotation and magnetic fields associated with core collapse lead to sufficiently strong MHD jets or other flow patterns to explode supernovae. This issue touches on many others.

– Magnetic effects in the rotating progenitor star.
– Dynamos and saturation field strengths.
– Affect of large fields on the equation of state.
– Affect of large fields on the neutrino cross sections and transport.
– Affect of large fields on structure and evolution of the neutron star.
– Affect of large fields on jet formation.
– Relevance of MRI and field generation to GRBs and "hypernovae."

2.1. The poleward slip instability

Akiyama et al. (2003) found that the acceleration implied by the hoop stress they derived was competitive with, and could even exceed, the net acceleration of the pressure gradient and gravity. The large scale toroidal field is thus likely to affect the dynamics by accelerating matter inward along cylindrical radii. The flow, thus compressed, is likely to be channeled up the rotation axes to begin the bi-polar flow that will be further accelerated by hoop and torsional stresses from the field, the "spring and fling" outlined in Wheeler et al. (2002).

In this context, another interesting element of MHD physics that may pertain to core collapse is the poleward slip instability. This is analogous to wrapping a rubber band around the equator of a ball and then sliding it upward. We are especially interested in the non-linear behavior, an aspect that is virtually unexplored in the literature. In the example just given, the rubber band is expelled at the pole in a dramatic way. Can the analogous physics applied to magnetic fields affect the formation of jets in core collapse?

The linear stability of toroidal magnetic fields in stars has been investigated by, among others, Tayler (1973) and Pitts and Taylor (1985) often neglecting rotation or including it only in the simplified context of constant rotation. A general solution for the *stability* in response to an axisymmetric ($m = 0$) perturbation to the equations of motion of a gravitating plasma permeated by a toroidal magnetic field is given by Chanmugam (1979). Such a toroidal field is absolutely unstable in the absence of rotation (Spruit and van Ballegooijen, 1982). The actual situation in core collapse is expected to be complex with strong differential rotation, on-going collapse of outer matter, convection, strong neutrino fluxes, and significant time dependence.

Most of the analyses of the poleward slip instability and related instabilities in the literature assume that the field is continuously distributed both in angle and in distance from the center or axis. In practice, the field will have a complex nature. In addition, for most dynamos to work, there must be a turbulent element to twist the field so that shear can stretch it. For the MRI, the turbulence is self-generated by the instability. Not only does the field have a substantial turbulent component in this case, but the field reverses sign in simulations on a timescale comparable to Ω^{-1}. Brandenburg et al. (1995) find the field to reverse globally on a timescale of order $30\,\Omega^{-1}$.

The question thus arises of whether or not these complications affect or even eliminate the poleward slip instability. We argue that they do not. At a basic level, the hoop stress, the key component that drives field contraction is a local quantity. It will have a finite value whenever the field has a local curvature. In the geometries we are considering that have the field wrapped around the axis, this curvature must exist. More formally, Ogilvie (2001) and Williams (2001, 2003) have shown that a plasma permeated by a field acts like a viscoelastic fluid with associated non-local, hysteresis effects. Williams has argued that even for completely turbulent conditions where the mean field vanishes $\langle B \rangle = 0$, but the rms field is finite $\langle B^2 \rangle^{1/2} \neq 0$, the field will exert a hoop stress as long as the field has a mean curvature. We thus conclude that the field will be unstable to the poleward slip instability even if the structure is substantially turbulent and subject to field reversal. We note that a turbulent field will be subject to a full range of non-axisymmetric perturbations and these may be far more unstable than to purely axisymmetric perturbations.

One of our primary interests is the non-linear response of the field to this poleward slip instability. As a crude way of examining this, let us assume that the pressure gradient balances gravity to first order and look at the acceleration resulting from the hoop stress and centrifugal potential, assuming conservation of angular momentum of the matter associated with a flux tube. The result is

$$a \sim -\frac{v_{\mathrm{a}}^2}{r} + \frac{R^4 \Omega_{\mathrm{eq}}^2}{r^3}, \tag{3}$$

where r is the cylindrical radius, R the value on the equator, and Ω_{eq} the value of the angular velocity on the equator. For the case of interest, the saturation field condition is that $v_{\mathrm{a}} < R\,\Omega_{\mathrm{eq}}$, so that the centrifugal term dominates and the field cannot slip along the neutron star surface. Rather, we conjecture that the hoop stresses drive circulation flow inward along the equator in analogy to a viscoelastic fluid and then upward parallel to the spin axis. The issue is then whether or not this sort of flow pattern can contribute to the formation of a bi-polar flow, perhaps by affecting or being affected by the resulting asymmetric neutrino deposition. Since in this picture the field does not necessarily contact nor follow along with the neutron star surface, this general behavior should apply to both neutron stars and for black holes. This is the opposite of the preliminary conclusion expressed in Wheeler (2004).

A very interesting question in the context of this meeting is whether some of these ideas could be tested in a magnetized laser experiment.

Acknowledgments

This work was supported in part by NASA Grant NAG5-10766.

References

Ando, S.: 2003, *Phys. Rev. D* **68**, 63002.
Akiyama, S., Wheeler, J.C., Meier, D. and Lichtenstadt, I.: 2003, *ApJ* **584**, 954.
Balbus, S.A. and Hawley, J.F.: 1991, *ApJ* **376**, 214.
Balbus, S.A. and Hawley, J.F.: 1998, *Rev. Modern Phys.* **70**, 1.
Bhattacharya, K. and Pal, P.B.: 2003, hep-ph/0209053.
Blandford, R.D. and Payne, D.G.: 1982, *MNRAS* **199**, 833.
Brandenburg, A., Nordlund, A., Stein, R.F. and Torkelsson, U.: 1995, *ApJ* **446**, 741.
Chanmugam, G.: 1979, *MNRAS* **187**, 769.
Duncan, R.C. and Thompson, C.: 1992, *ApJ* **392**, L9.
Fesen, R.A.: 2001, *ApjS* **133**, 161.
Fryer, C.L. and Heger, A.: 2000, *ApJ* **541**, 1033.
Höflich, P., Khokhlov, A. and Wang, L.: 2001, in: J.C. Wheeler and H. Martel (eds.), *Proceedings of the 20th Texas Symposium on Relativistic Astrophysics*, AIP, New York, p. 459.
Khokhlov, A. and Höflich, P.: 2001, in: H.-Y., Chang, C.-H. Lee and M. Rho (eds.), *Explosive Phenomena in Astrophysical Compact Objects*, AIP Conference Proceedings No. 556, New York: AIP, p. 301.
Khokhlov, A.M., Hoflich, P.A., Oran, E.S., Wheeler, J.C., Wang, L. and Chtchelkanova, A.Yu.: 1999, *ApJ* **524**, L107.
Lai, D. and Qian, Y.-Z.: 1998, *ApJ* **505**, 844.
Laming, J.M. and Hwang, U.: 2003, *ApJ* **597**, 347.
Leonard, D.C., Filippenko, A.V., Earth, A.J. and Matheson, T.: 2000, *ApJ* **536**, 239.
Leonard, D.C. and Filippenko, A.V.: 2001, *PASP* **113**, 920.
Leonard, D.C., Filippenko, A.V., Ardila, D.R. and Brotherton, M.S.: 2001, *ApJ* **553**, 861.
Leonard, D.C., Filippenko, A.V., Chornock, R. and Foley, R.J.: 2002, *PASP* **114**, 1333.
Maeda, K., Nakamura, T., Nomoto, K., Mazzali, P., Patat, F. and Hachisu, I.: 2002, *ApJ* **565**, 405.
Meier, D.L., Koide, S. and Uchida, Y.: 2001, *Science* **291**, 84.
Nagataki, S., Mizuta, A., Yamada, H., Takabe, H. and Sato, K.: 2003, *ApJ* **596**, 401.
Ogilvie, G.I.: 2001, *MNRAS* **325**, 231.
Pitts, E. and Tayler, R.J.: 1985, *MNRAS* **216**, 139.
Proga, D., MacFayden, A.I., Armitage, P.J. and Begelman, M.C.: 2003, *ApJ* **599**, L5.
Shimizu, T., Yamada, S. and Sato, K.: 1994, *ApJ Lett.* **432**, L119.
Spruit, H.C. and van Ballegooijen, A.A.: 1982, *A&A* **106**, 58.
Stanek, K.Z. et al.: 2003, *ApJ* **591**, L17.
Tayler, R.J.: 1973, *MNRAS* **161**, 365.

Wang, L., Howell, D.A., Höflich, P. and Wheeler, J.C.: 2001, *ApJ* **550**, 1030.
Wang, L., Wheeler, J.C., Li, Z. and Clocchiatti, A.: 1996, *ApJ* **467**, 435.
Wang, L. et al.: 2002, *ApJ* **579**, 671.
Wang, L. et al.: 2003a, *ApJ* **591**, 1110.
Wang, L. et al.: 2003b, *ApJ* **592**, 457.
Wheeler, J.C.: 2004, in: P. Höflich, P. Kumar and J.C. Wheeler (eds.), *Cosmic Explosions in Three Dimensions: Asymmetries in Supernovae and Gamma-Ray Bursts*, Cambridge University Press, Cambridge, astro-ph/0401323.
Wheeler, J.C., Meier, D.L. and Wilson, J.R.: 2002, *ApJ* **568**, 807.
Wheeler, J.C., Yi, L, Höflich, P. and Wang, L.: 2000, *ApJ* **537**, 810.
Williams, P.T.: 2001, astro-ph/0111603.
Williams, P.T.: 2003, in: J.M. De Buizer (ed.), *IAOC Workshop "Galactic Star Formation Across the Stellar Mass Spectrum," ASP Conference Series*, in press (astro-ph/0206230).

PROGRESS TOWARD THE STUDY OF LABORATORY SCALE, ASTROPHYSICALLY RELEVANT, TURBULENT PLASMAS

C.C. KURANZ[1], R.P. DRAKE[1], D.R. LEIBRANDT[1], E.C. HARDING[1], H.F. ROBEY[2], A.R. MILES[2], B.E. BLUE[2], J.F. HANSEN[2], H. LOUIS[2], M. BONO[2], J. KNAUER[3], D. ARNETT[4] and C.A. MEAKIN[4]

[1]*University of Michigan*
[2]*Lawrence Livermore National Laboratory*
[3]*Laboratory for Laser Energetics*
[4]*University of Arizona*

(Accepted July 2004)

Abstract. Recent results from an ongoing series of Rayleigh-Taylor instability experiments being conducted on the Omega Laser are described. The goal of these experiments is to study, in a controlled laboratory setting, the mixing that occurs at an unstable interface subjected to an acceleration history similar to the explosion phase of a core-collapse supernova. In a supernova, the Reynolds number characterizing this mixing is extremely large ($\mathrm{Re} > 10^{10}$) and is more than sufficient to produce a turbulent flow at the interface. In the laboratory experiment, by contrast, the spatial scales are much smaller, but are still sufficiently large ($\mathrm{Re} > 10^{5}$) to support a turbulent flow and therefore recreate the conditions relevant to the supernova problem. The data from these experiments will be used to validate astrophysical codes as well as to better understand the transition to turbulence in such high energy density systems. The experimental results to date using two-dimensional initial perturbations demonstrate a clear visual transition from a well-ordered perturbation structure consisting of only a few modes to one with considerable modal content. Analysis of these results, however, indicates that while a turbulent spectrum visually appears to be forming, the layer has not yet reached the asymptotic growth rate characteristic of a fully turbulent layer. Recent advances in both target fabrication and diagnostic techniques are discussed as well. These advances will allow for the study of well-controlled 3D perturbations, increasing our ability to recreate the conditions occurring in the supernova.

1. Introduction

Laboratory astrophysics provides a link between astrophysical observations and models. These hydrodynamics experiments support the effort to model astrophysical systems. They are also compared to observations made in astrophysics. Intense lasers can create large energy densities in targets of mm-scale volume. These targets are well scaled to a supernova explosion so that the two will have similar hydrodynamic evolution (Ryutov et al., 1999).

The rapid collapse of the Fe core of a supernova causes a shockwave to move outward through the star. When the dense core is accelerated by a blast wave into the less dense outer layers, the Richtmeyer-Meshchov (Richtmyer, 1960; Meshkov, 1969) instability and the Rayleigh-Taylor (Rayleigh, 1900; Taylor, 1950) instability

Astrophysics and Space Science **298:** 9–16, 2005.

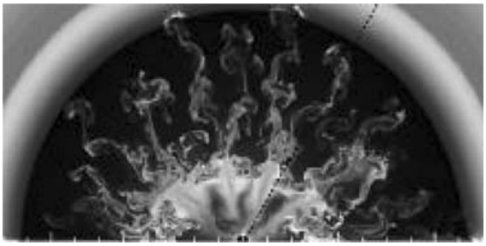

Figure 1. Simulation of supernova explosion.

occur. Structures evolve as the dense layer is decelerated by the less dense outer layer. Simulations of a supernova show spikes of heavier elements move outward into the less dense hydrogen layer, while bubbles of hydrogen penetrate inward. Kifondis et al. (2000) simulated the explosion with perturbations produced by neutrino-driven convection but did not include a perturbation at the outer surface. It is shown in Figure 1. These simulations under-predict the observed radial extent of material mixing in supernova. In SNe, the Rayleigh-Taylor instability generates outwardly propagating spikes of Fe group elements. The radial velocity of these spikes in simulations is lower than the observed value by a factor of approximately 2. In part the spikes are slowed when they encounter the dense material at the He/H interface (Kifonidis et al., 2000). Fryxell, Müller, and Arnett had another 2D model that not include neutrino-driven convection, but did have a random perturbation on the entire volume. There was penetration of heavy elements, but not at velocities high enough to explain observations (Fryxell et al., 1991).

Laboratory experiments are being used to investigate two possible explanations for this mixing discrepancy. The Reynolds number characterizing mixing in supernova explosions is estimated to be of order 10^{10} (Ryutov et al., 1999). By comparison with classical flows, this should result in turbulent flow. None of the simulations done to date, however, appear to be turbulent. A transition to turbulence will provide an increase in the radial transport of material. Also, the initial conditions in the progenitor might give rise to an asymmetrical explosion, which would again result in enhanced radial transport of a fraction of the core material. Both numerical simulations and observations suggest the possibility of asymmetrical explosions. Laboratory experiments can be valuable in providing data on the transition to turbulence in similar instability-driven, high-Reynolds-number systems.

2. 2D, 2-Mode Coupling Target Design and Experiment

The experiments are conducted in mm-scale shock-tubes that create similar interfacial acceleration history to that of supernova. This acceleration history can be seen in Figure 2. Figure 3 shows the target design for the experiment. The target is

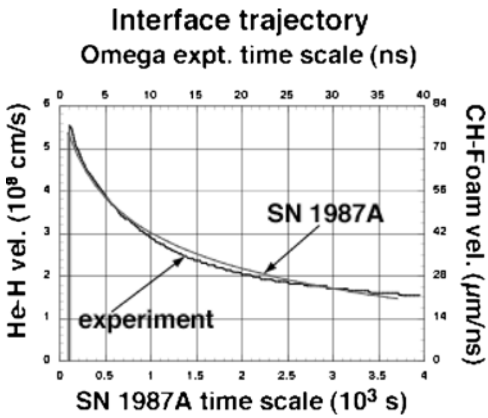

Figure 2. Acceleration history of SN1987A and experiment.

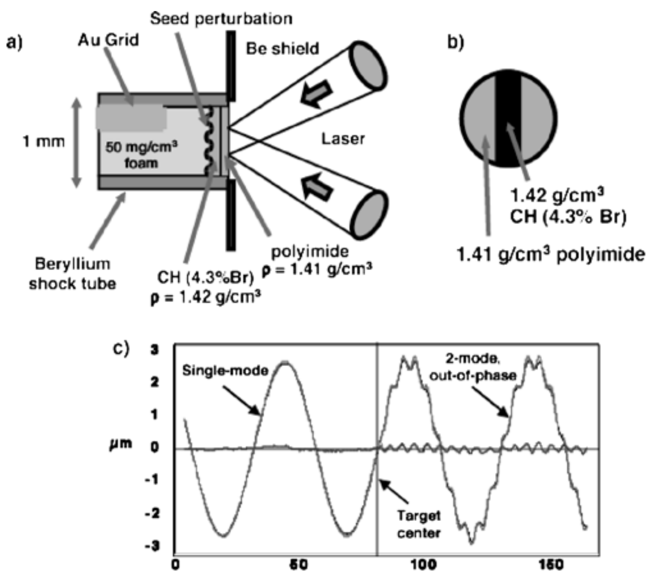

Figure 3. (a) Target schematic. (b) A face-on view of the rear surface of the polyimide with the doped CH strip in place. (c) Plot of single-mode perturbation and 2-mode perturbation with out of phase variation.

800 μm in diameter with a front surface of polyimide. Ten Omega (Boehly et al., 1995) laser beams with a 1 ns flat-topped pulse irradiate the polyimide surface with an intensity of approximately 10^{15} W/cm^2. The laser has a wavelength of 0.35 μm and a spot size of 820 μm FWHM. The ablated polyimide surface is 150 μm thick with a density of 1.41 g/cm^3. The rear surface of the polyimide has a 200 μm, 75 μm deep μm opening and a strip of material glued into it that is CH doped with 4.3 at.% of bromine or 3 at.% iodine. A face-on view of the rear surface of the polyimide is

shown in Figure 3b. The strip is density matched to the surrounding material and is also low Z so that the two materials will have similar hydrodynamic responses to extreme pressure. X-rays are used to make a radiograph during the experiment. Since doped CH strongly absorbs the X-rays one can better observe the structure formed during the experiment. A 2 dimensional perturbation is machined onto the rear surface of the polyimide/doped CH package. The amplitude of this perturbation is $a_0 \sin(k_x x)$, where $a_0 = 2.5\,\mu\text{m}$ and the wave number $k_x = 2\pi/(50\,\mu\text{m})$. On top of the initial perturbation this experiment included a second perturbation with a variation in phase. The target was split between a single mode perturbation and a 2-mode perturbation. A plot of this amplitude can be seen in Figure 3c. Behind the polyimide/doped CH package is approximately 2.4 mm thick carbonized resorcinol formaldehyde (CrF) foam. The foam has a density of 50 mg/cm^3. This package is held together by a Be shock tube 1100 μm in outer diameter and the front end of the target has a 2.5 mm Be shield to prevent interference with the diagnostics. A gold grid is placed on the target facing the diagnostic for location and magnification calibration.

The primary diagnostic in these experiments is X-ray radiography. These experiments used a point projection backlighting technique to increase resolution and contrast. A Ti foil was irradiated with several Omega laser beams, creating X-rays. The X-rays were focused through a 10 μm pinhole in Ta through the target and to a single-strip framing camera.

3. 2D, 2-Mode Simulations

The experimental setup for the 2-dimensional mode coupling experiment was simulated using the CALE code. CALE is a 2D Arbitrary Eulerian Lagrangian radiation hydrodynamics code. These simulations can be seen in Figures 4a–4d. Each figure is at a different time in the simulations and compares the single mode, 2-mode in-phase and 2-mode out-of-phase. The simulations are at 7 ns, 16 ns, 26 ns, and 38 ns. The simulations of this experiment show clear difference resulting from the initial phase of the two modes. The out-of-phase initial condition clearly produces a mixed layer of greater complexity.

4. Experimental Results for 2D, 2-Mode Coupling Experiment

Figures 5a–5c are the radiographs from the 2D mode coupling experiment at times of 13 ns, 25 ns, and 37 ns respectively. These radiographs show a clear transition toward a more complicated modal structure, with clear difference from the supernova simulation as seen in Figure 1. By taking a horizontal lineout measurement of the spike and bubble one is able to calculate the amplitude of the mixing layer. Figure 6 is a plot of the average amplitude of the mixed layer vs. time. The solid lines are predictions from simulations and the different plot values represent single-mode,

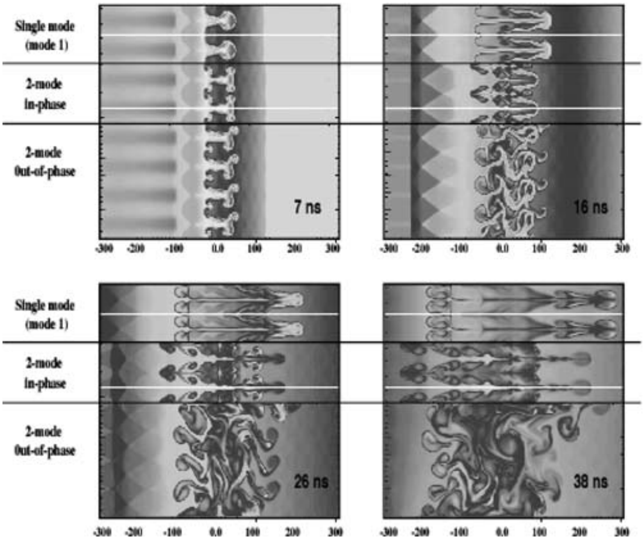

Figure 4. 2D CALE simulations single mode, 2-mode out-of-phase, and 2-mode in-phase perturbations at $t = 7$ ns, $t = 16$ ns, $t = 25$ ns, $t = 38$ ns.

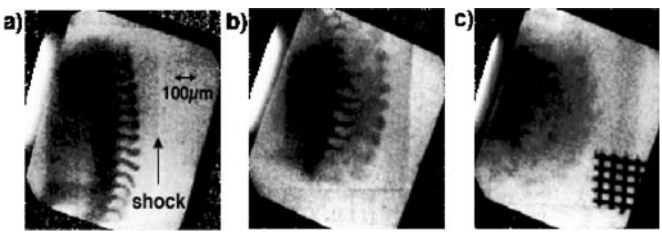

Figure 5. X-ray radiograph of 2D mode coupling experiment, (a) $t = 13$ ns, (b) $t = 25$ ns, (c) $t = 38$ ns.

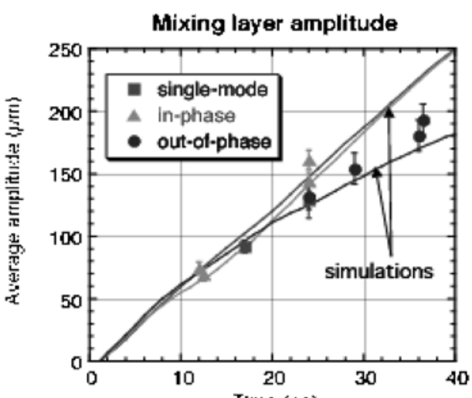

Figure 6. Plot of amplitude vs. time for 2D mode coupling experiment for single-mode, in-phase, and out-of-phase.

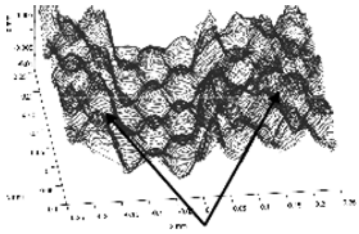

Figure 7. Mean elevation of the doped CH tracer strip is lower by 5 μm compared to polyimide.

2-mode in-phase, and 2-mode out-of-phase experiments. This plot shows that even though the interface is increasing in modal complexity there is no increased in the overall layer growth rate has been observed. Some experimental issues limit the observational time, such as the edge effects from the shock tube walls. Also, the blast-wave strength decays with time, which impedes late-time growth. The upcoming National Ignition Facility will eventually allow for greater length scales and much longer evolution times.

5. 3D Perturbation Experiments

Experiments were also performed with a 3D surface perturbation. An "egg-crate" perturbation was machined onto the rear surface of the polyimide/doped CH package. The amplitude of this perturbation is $a_0 \sin(k_x x)\sin(k_y y)$, where $a_0 = 2.5$ μm and the wave numbers $k_x = k_y = 2\pi/(71\ \mu\text{m})$. These experiments have resulted in significantly increased spike growth. After the experiment was performed it was realized that the method used to machine the polyimide/doped CH surface introduced short-scale roughness in the doped CH strip. In addition, the interface had an unintentional large-scale (low-mode number) 2D perturbation that can be seen in the mean elevation of the tracer strip in Figure 7. Therefore, the initial surface perturbation has both shorter and longer components than the fundamental 3D mode.

The 3D experiments used an area backlighter as opposed to a pinhole backlighter that was used in the 2D mode coupling experiment. A thin Sc foil was placed approximately 4 mm from the target and irradiated on either side with additional laser beams. These beams were delayed 10 to 30 ns relative to the drive beams to monitor the evolution of the interface over time. The result is several radiographs at different times.

6. 3D Experimental Results

X-ray radiographs of the 3D experiments can be seen in Figure 8. The top row of radiographs used a 3D perturbation and the second row had a planar interface used

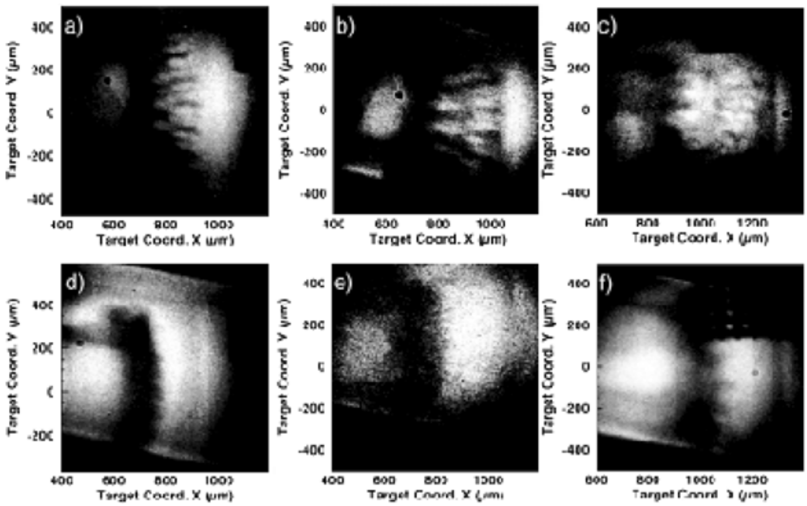

Figure 8. X-ray radiographic data for a three-dimensional perturbed interface and a planar interface in the top and bottom row, respectively.

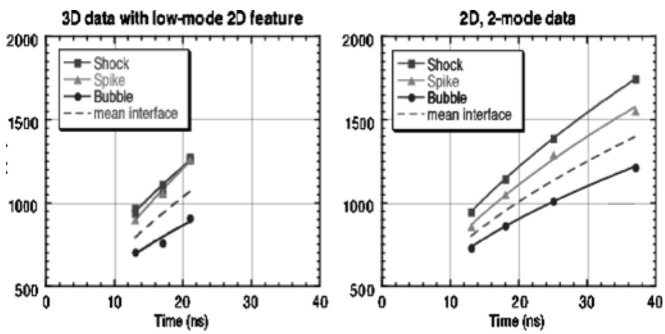

Figure 9. A comparison of the 3D perturbation experiment and 2D mode coupling perturbation experiment.

as a reference for the initial growth. At 17 ns the spikes are at the shock front and at 21 ns the spike structure is poorly resolved. The 2D and 3D data are compared in Figure 9. The plots show the position vs. time of the shock, spike and bubble. It is clear the spikes in the 3D perturbation have reached the shock while the spikes in the multi-mode 2D experiment are falling away from the shock front. This suggests the possibility that the superposition of a low-mode perturbation could significantly affect the extent of mixing in supernova.

To explore the increased spike penetration phenomenon a target with a recessed tracer perturbation was simulated in 2D with CALE. The target schematic used in this simulation can be seen in Figure 10a. The recessed tracer perturbation generates a jet-like flow enhancing the spike penetration. The CALE simulation at 17 ns can be

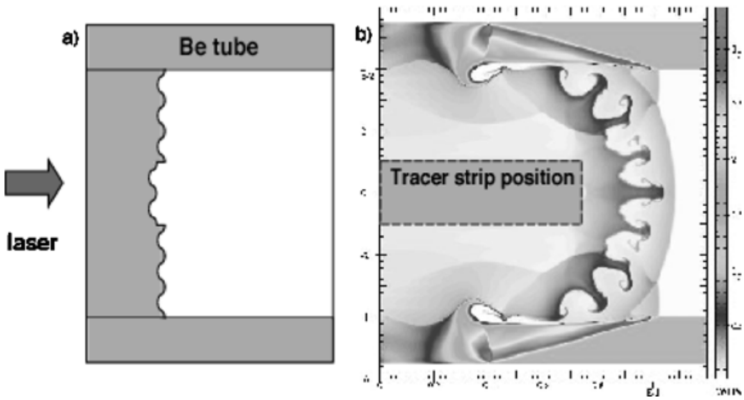

Figure 10. a) Target schematic with recessed tracer strip b) CALE simulation with recessed tracer strip.

seen in Figure 10b. From the diagnostic view, the spikes are essentially at the shock location. The enhanced spike penetration results primarily from a superposition of a jet-like flow as opposed to mode coupling.

7. Conclusions

Experiments have been performed on the Omega laser to study two possible mechanisms for enhanced radial transport in SN explosions. Significant improvements have been made in the target fabrication process, resulting in 3D surfaces of great precision. Future experiments in this series can now be more directly coupled to recent results from 3D stellar evolution models to address the issue of the effect of initial conditions on SN mixing.

Acknowledgments

This work is supported by the U.S. Department of Energy under grants DE-FG03–99DP00284 and DE-FG03-00SF22021.

References

Boehly, T.R., Craxton, R.S. et al.: 1995, *Rev. Sci. Intsr.* **66**(1), 508.
Fryxell, B., Muller, E. et al.: 1991, *ApJ* **367**, 619.
Kifonidis, K., Plewa, T. et al.: 2000, *ApJ Lett.* **531**(2), L123.
Meshkov, E.E.: 1969, *Fluid Dyn.* **4**, 101.
Rayleigh, L.: 1900, *Scientific Papers II*. Cambridge, England.
Richtmyer, D.H.: 1960, *Commun. Pure. Appl. Math* **13**, 297.
Ryutov, D.D., Drake, R.P. et al.: 1999, *ApJ* **518**(2), 821.
Taylor, S.G.: 1950, *Proc. R. Soc.* **A201**, 192.

EFFECTS OF INITIAL CONDITIONS ON COMPRESSIBLE MIXING IN SUPERNOVA-RELEVANT LABORATORY EXPERIMENTS

A.R. MILES[1,2], M.J. EDWARDS[1] and J.A. GREENOUGH[1]

[1]*Lawrence Livermore National Laboratory, Livermore, CA, USA*

[2]*University of Maryland, MD, USA; E-mail: miles_15@llnl.gov*

(Received 3 May 2004; accepted 14 July 2004)

Abstract. In core-collapse supernovae, strong blast waves drive interfaces susceptible to Rayleigh–Taylor (RT), Richtmyer–Meshkov (RM), and Kelvin–Helmholtz (KH) instabilities. In addition, perturbation growth can result from material expansion in large-scale velocity gradients behind the shock front. Laser-driven experiments are designed to produce a strongly shocked interface whose evolution is a scaled version of the unstable hydrogen–helium interface in core-collapse supernovae such as SN 1987A. The ultimate goal of this research is to develop an understanding of the effect of hydrodynamic instabilities and the resulting transition to turbulence on supernovae observables that remain as yet unexplained.

This paper represents a summary of recent results from a computational study of unstable systems driven by high Mach number shock and blast waves. For planar multimode systems, compressibility effects preclude the emergence of a regime of self-similar instability growth independent of the initial conditions (ICs) by allowing for memory of the initial conditions to be retained in the mix-width at all times. With higher-dimensional blast waves, divergence restores the properties necessary for establishment of the self-similar state, but achieving it requires very high initial characteristic mode number and high Mach number for the incident blast wave. Initial conditions predicted by some recent stellar calculations are incompatible with self-similarity.

1. Introduction

The appearance of Supernova 1987A in the Large Magellanic Cloud marked the beginning of a change in the way people think about the violent endpoint of massive stars. Although it had been known for some time that the layered structure of the progenitor should be hydrodynamically unstable during the explosion (Falk and Arnett, 1973; Chevalier, 1976), the assumption of spherical symmetry was almost always incorporated into models and otherwise reflected in the paradigm of core-collapse supernovae. This was due in large part to the practical limitations of multidimensional numerical calculations. But when heavy elements originating from the core of SN 1987A appeared at the photosphere 6 months earlier than predicted by one-dimensional explosion models, it became clear that something significant was being neglected (Tueller et al., 1990). Since then, the evidence that asymmetry is the rule in core-collapse supernovae has continued to accumulate (Wang et al., 2003; Hughes et al., 2000), and multidimensional computer codes

Astrophysics and Space Science **298:** 17–24, 2005.

have been developed and applied to the problem in an effort to understand the proposed asymmetry mechanisms.

One such mechanism is based on the hydrodynamic instability of perturbed interfaces when subjected to a reversal of pressure and density gradients. Due to processes such as convective stirring and localized thermonuclear burn, boundaries between layers of different materials within the star are unlikely to be perfectly smooth. Even if the shock wave produced as the core rebounds against neutron degeneracy pressure is initially spherical, it can drive the amplification of any such preexisting perturbations via the Rayleigh–Taylor (RT) (Rayleigh, 1899; Taylor, 1950) and Richtmyer–Meshkov (RM) (Richtmyer, 1960; Meshkov, 1969) instabilities. After passage of the shock front, this interface evolves into a complicated structure of outward-growing spikes of heavier material and infalling “bubbles” of lighter elements (Arnett et al., 1989). Late in time, these spikes can move far ahead of what a 1D model would predict as the interface position and might explain the anomalously early appearance heavy elements at the photosphere.

In ongoing experiments aimed at studying instability-driven mixing under supernova-relevant conditions, laser energy is used to drive high Mach number planar shock and blast waves into one end of millimeter-scale cylindrical targets (Drake et al., 2002; Miles, 2004). A typical target consists of a more dense plastic section and a less dense foam section, with a prescribed perturbation machined into the plastic at the plastic/foam interface. After the passage of the shock, the interface is unstable and evolves under the combined influence of RT, RM, and Kelvin–Helmholtz (KH) instabilities. Additional laser beams directed on high-Z backlighter foils yield X-rays that pass through the target and are used to image the developing instability.

2. Self-Similar RT Growth and Transition to Turbulence

For classical RT systems comprised of incompressible fluids under constant acceleration, it is widely believed that memory of the initial conditions is lost at late times after the establishment of a self-similar regime (Youngs, 1984). This idea ultimately is based on the simple fact that larger bubbles rise faster than smaller bubbles, and can be explained in terms of bubble competition and merger (Sharp, 1984; Glimm and Li, 1988; Oron et al., 2001). As a larger bubble rises above its smaller neighbor, it is free to expand laterally, eventually filling the space previously occupied by its neighbor. Material flowing around the larger bubble and into the spikes below sweeps the smaller bubble downstream. This process leads to the continual generation of larger, faster moving objects and an acceleration of the bubble and spike fronts. Eventually, the interface is dominated by structures resulting from many successive generations of bubble merger rather than from the unstable growth of preexisting perturbations. Loss of memory of the initial conditions means that the statistical properties observed in the late-time interface could have arisen from a wide range of initial perturbation spectra. If the initial conditions are forgotten, the height of the bubble front as well as the dominant transverse scale must grow in proportion to gt^2, where g is the acceleration and t is time, as this is the only length scale remaining in the problem. The interface can be described in a statistical sense by a bubble-size distribution function. In the self-similar or scale-invariant regime, this function does not change in time except for a scale factor proportional to the characteristic bubble size.

Although the idea of self-similar RT growth is well motivated, it has yet to be demonstrated conclusively. If the self-similar regime does exist, then it is certainly difficult to reach in simulations and diagnosable experiments. The gt^2 scaling is observed, but there is a great deal of disagreement and debate about the constant of proportionality α (Dimonte and Schneider, 2000). Despite limited understanding of nonlinear instability evolution in classical RT systems, the ideas of self-similar growth are sometimes invoked in discussions of blast-wave-driven instabilities in core-collapse supernovae. Even if valid in the classical case, one should question to what extent these ideas would apply in the more complicated blast-wave-driven case, where RM is present, the acceleration is time-dependent, and the flow is compressible.

Whether or not there is a true self-similar regime, hydrodynamically unstable systems certainly can undergo a transition from an early time, more ordered structure to a late time structure that is disordered and appears random. If the Reynolds number is sufficiently high and sufficient time is allotted, this late-time structure will be turbulent. Many unanswered questions remain about the requirements for transition and its relationship to loss of memory of initial conditions. In particular, the effect of the initial conditions on the transition is not well understood. In addition, it is also important to understand what effect the transition has on the instability growth rate. For 3D systems, it has been noted that there will be a competition between the continual generation of larger, faster growing structures and the tendency of increased turbulent dissipation to inhibit the growth (Youngs, 1994). To date, 2D simulations of mixing in Type II supernovae produce spike velocities about a factor of two smaller than the observed velocities of heavy core elements beyond the photosphere (Kifonidis et al., 2003). It remains unclear whether or not this discrepancy can be resolved once 3D effects, including the transition to turbulence, are included in high-resolution calculations.

3. Summary of Results from Models and Simulations

We have developed a model that describes the evolution of a blast-wave-driven multimode interface in terms of bubble competition and merger (Miles, 2004). Our model goes beyond previous work by including the effects of material decompression and stretching behind the shock front for both planar and divergent systems.

On the basis of this model, we are able to show that self-similarity and loss of initial conditions might be possible in divergent systems such as supernovae but are not realizable in planar systems such as most laser-driven experiments intended to study mixing in supernovae. The difference arises because modes in divergent systems undergo transverse in addition to radial stretching. Because the time dependence of the stretching is the same in both directions, the ratio of transverse to parallel scales is preserved.

For planar systems, we predict a quasi-self-similar regime during which the instability evolution is approximately self-similar over a limited period of time. During this regime, the ratio of characteristic wavelength to perturbation amplitude decreases slowly in time rather than approaching a constant asymptotic value. Even in the divergent case, loss of initial conditions is possible only for systems with very small-scale initial conditions driven by very high Mach number blast waves. Recent stellar calculations (Kifonidis et al., 2003; Meakin and Arnett, in preparation) predict significant amplitudes for modes as low as 24–48 due to convection. If these predictions are correct, the late-time interface structure observed in supernova remnants likely depends strongly on the initial conditions present within the star at the time of explosion.

Finally, the model predicts that the finite duration of the blast-wave drive sets a maximum scale that can be generated on a given interface. For planar systems, we call this scale the "effective box size". For divergent systems, this corresponds to a minimum mode number that depends weakly on the incident Mach number and initial mode number as long as both are sufficiently high (see Figure 1).

Model predictions for planar systems have been tested against 2D and 3D Raptor (Howell and Greenough, 2003) simulations with broadbanded multimode interfaces under drive conditions to be attainable at the National Ignition Facility (NIF). The

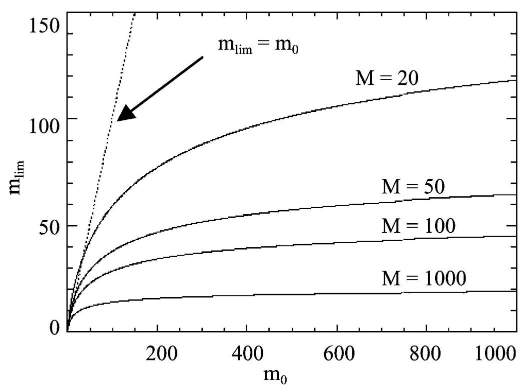

Figure 1. Model-predicted minimum mode number that can be generated by a spherical blast wave as a function of the initial mode number. Drive decay imposes a limiting mode number for divergent systems. The asymptotic modal structure depends weakly on the initial conditions and the drive strength if the incident shock Mach number and the initial mode number are both high.

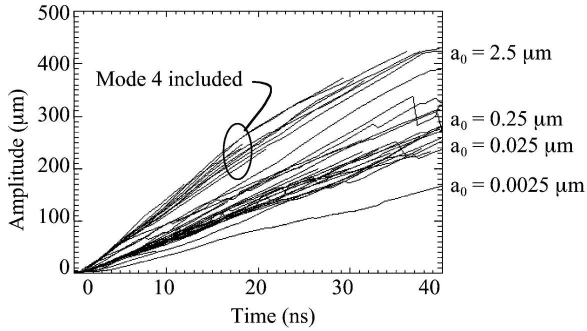

Figure 2. Amplitude histories from 52 2D simulations of planar laser-driven systems under NIF-like drive conditions. Memory of the initial conditions is retained in the parallel scales at late times.

calculation set includes over 70 high-resolution (at least 512 cells in the transverse direction) 2D simulations and five 3D simulations (with 256 cells in each transverse direction). In agreement with our model, the perturbation growth shows no apparent approach to a self-similar regime independent of the initial conditions (see Figure 2). We also observe the effective box size due to drive decay, which sets a maximum transverse scale that can be generated, and the quasi-self-similar regime. This regime is found to exist after the generation of scales larger than the initial conditions but before the effective box size is reached.

The existence of the quasi-self-similar state and the drive-imposed effective box size make the blast-wave-driven case distinct from classical RT. However, transition to the quasi-self-similar state is very similar to its classical counterpart. In both cases, it is marked by an increase in the degree of small-scale mixing (see Figure 3), a decrease in the spike velocity, and often an increase in the bubble velocity.

Significantly, the apparently random variations observed in late-time amplitudes (in Figure 2) and growth rates are not well correlated with initial spectral shape. Only the average spectral properties are important, such as the initial rms amplitude and characteristic wavenumber. This bodes well for simulations of similarly strongly driven systems that leave a portion of the short-wavelength end of the spectrum unresolved. As long as the system contains some fast-growing and interacting modes that can be resolved computationally or reproduced experimentally (and has the correct initial rms amplitude), the late-time instability evolution will likely closely resemble the fully resolved or complete system. This reaffirms the hope that laser-driven experiments can serve as useful and relevant platforms for studying compressible mixing in supernovae despite their drastically more limited available range of scales. Similarly, carefully designed numerical simulations need not necessarily reproduce the full range of spectral details present in their physical counterparts in order to reasonably reproduce the late-time large-scale interface structure. These conclusions apply in particular to systems with

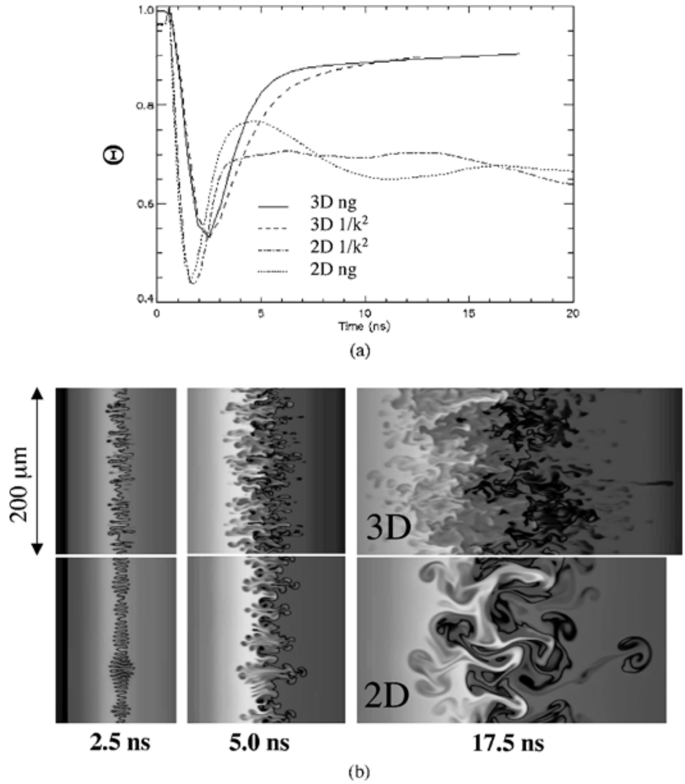

Figure 3. (a) Mixing parameter from 2D and 3D calculations with narrow gaussian (ng) and $1/k^2$ initial perturbation spectra and (b) log density plots for the narrow gaussian case. The mixing parameter is equal to zero when there is no mixing in the interface region and one if the interface material is completely mixed.

long-wavelength modes large enough in amplitude to reach the nonlinear phase early on.

In agreement with 3D classical RT calculations performed by others, we find more fine-scale mixing and small-scale structure in 3D than in 2D after transition to the turbulent-like state (see Figure 3). The process of transition, however, is very similar in both cases. Transition is triggered by spike interaction and breakdown that is complete when the perturbation amplitude is 5–6 times the characteristic wavelength in the initial spectrum.

Due to enhanced mixing, the post-transition bubble growth is reduced relative to that observed in the 2D calculations. The spike growth, however, does not appear to be inhibited and might even be enhanced. This is particularly significant in light of the fact that 2D supernova calculations that invoke instability-driven mixing to explain enhanced transport of heavy core elements consistently underpredict the late-time spike velocities by about a factor of 2.

4. Future Work

We plan to continue this research along several parallel directions directly applicable to both supernovae and ICF applications. We would like to further investigate the effect of spike interactions on their velocity distribution in order to determine the extent to which spike material can be accelerated towards the shock front.

With the greater energy, temporal, and spatial scales afforded by the NIF laser, experiments will potentially be capable of unambiguously demonstrating transition to 3D turbulence, the generation of larger scales through multiple generations of bubble merger, and the late-time freeze-out stage. Through collaboration with astrophysicists studying supernova progenitors, we will attempt to incorporate realistic initial spectra into the experiments.

Planar experiments are particularly valuable because of their improved diagnosability relative to spherical systems and their ability to better maintain high energy density in the absence of divergence. However, our buoyancy-drag model has suggested that the absence of divergence changes the nature of the instability evolution by ensuring that memory of the initial conditions is retained in the perturbation amplitudes at all times. Consequently, we are working to develop a divergent platform for supernova-relevant compressible mixing experiments. Finally, we note that current ICF diagnostics in general and X-ray radiography in particular are not optimized for detailed studies of 3D turbulence in laser-drive targets. The long-term success of this program will ultimately depend on the development of innovative new experimental techniques.

Acknowledgments

This work was performed under the auspices of the U.S. Department of Energy by the University of California, Lawrence Livermore National Laboratory under Contract W-7405-Eng-48.

References

Chevalier, R.: 1976, *ApJ* **207**, 872.

Dimonte, G., Youngs, D. L., Dimits, A., Weber, S., Marinak, M., et al.: 2002, *Phys. Fluids* **16**(5), 1668.

Drake, R.P., Robey, H.F., Hurricane, O.A., Zhang, Y., Remington, B.A. et al.: 2002, *AJ* **564**, 896.

Falk, S.W. and Arnett, W.D.: 1973, *ApJ Lett.* **180**, L65.

Glimm, J. and Li, X.L.: 1988, *Phys. Fluids* **31**(8), 2077.

Howell, L.H. and Greenough, J.A.: 2003, *J. Comput. Phys.* **184**, 53.

Hughes, J.P., Rakowski, C.E., Burrows, D.N. and Slane, P.O.: 2000, *ApJ* **528**, L109.

Kifonidis, K., Plewa, T., Janka, H.-Th. and Muller, E.: 2003, *A&A* **408**, 621.

Meakin, C.A. and Arnett, W.D.: in preparation.

Meshkov, E.E.: 1969, *Izv. AN SSSR Mekhanika Zhidkosti I Gaza* **4**(5), 151.

Miles, A.R.: "Bubble merger model for the nonlinear Rayleigh–Taylor instability driven by a strong blast wave", to appear in Phys. Plasmas.

Oron, D., Arazi, L., Kartoon, D., Rikanati, A., Alon, U. and Shvarts, D.: 2001, *Phys. Plasmas* **8**(6), 2883.

Rayleigh, J.W.S.: 1899, *Scientific Papers*, Cambridge University press, Cambridge.

Richtmyer, R.D.: 1960, *Commun. Pure Appl. Math.* **13**, 297.

Sharp, K.I.: 1984, *Physica D* **12**, 3.

Taylor, G.I.: 1950, *Proc. R. Soc. Lond. Ser. A* **201**, 192.

Tueller, J., Barthelmy, S., Gehrels, N., Teegarden, B.J., Leventhal, M. and MacCallum, C.J.: 1990, *ApJ* **351**, L41.

Wang, L., Baade, D., Höflich, P., Khokhlov, A., Wheeler, J.C. et al.: 2003, *ApJ* **591**, 1110.

Youngs, D.L.: 1984, *Physica D* **12**, 32.

Youngs, D.L.: 1994, *Laser Part. Beams* **12**(4), 725.

LABORATORY ASTROPHYSICS EXPERIMENTS FOR SIMULATION CODE VALIDATION: A CASE STUDY

A.C. CALDER[1,2]
[1]*Department of Astronomy and Astrophysics, The University of Chicago, 5640 S. Ellis, Chicago, IL, USA*
[2]*The Center for Astrophysical Thermonuclear Flashes, The University of Chicago, 5640 S. Ellis, Chicago, IL, USA; E-mail: calder@flash.uchicago.edu*

(Received 4 May 2004; accepted 7 July 2004)

Abstract. The growing field of Laboratory Astrophysics seeks to study the extreme environments found in many astrophysical events in the controlled setting of a laboratory. In addition to the opportunity to perform basic research into the nature and properties of materials in astrophysical environments, laboratory astrophysics experiments serve beautifully for validating calculations performed by simulation codes designed to model astrophysical phenomena. I present results from our ongoing validation effort for FLASH, a parallel adaptive-mesh hydrodynamics code for the compressible, reactive flows of astrophysical environments. The first test case is a laser-driven shock propagating though a multilayer target introducing Rayleigh–Taylor and Richtmyer–Meshkov fluid instabilities at the material interfaces. The second is an accelerating fluid interface that is subject to the Rayleigh–Taylor instability. We found good agreement between simulations and experiment for the multilayer target case, but disagreement between experiment and simulation in the Rayleigh–Taylor case. I discuss our findings and possible reasons for the disagreement.

Keywords: methods, numerical hydrodynamics instabilities

Introduction

The growing field of high-energy density Laboratory Astrophysics seeks to understand the physics of astrophysical environments by studying similar conditions in the laboratory. Contemporary research utilizes modern facilities such as intense lasers to probe the physics of turbulent compressible flow and mixing, shock phenomena, radiation flow, jet phenomena, and to study the opacities and equations of state of materials in conditions far from those encountered in our normal terrestrial environment. These experiments, in addition to advancing our basic understanding, provide unique opportunities for the validation of theory, numerical models, and simulations of astrophysical phenomena.

Verification and validation are essential testing steps of computational science with the goal of assessing credibility and building confidence in numerical modeling and simulation. With advances in computing and numerical methods leading to the increased acceptance of numerical modeling in science and engineering, verification

Astrophysics and Space Science **298:** 25–32, 2005.

and validation methodology has emerged as a discipline (AIAA, 1998; Roach, 1998a, b). Verification is testing to ensure that a numerical model or simulation accurately represents the conceptual model, and verification testing consists of comparing the results of simulations to known solutions of simple problems with the emphasis on quantifying error in the simulation. For finite-difference, finite-volume, and finite element methods, the approach is typically a systematic study of mesh and time step refinement (AIAA, 1998). Validation is determining the degree to which a numerical model or simulation meaningfully describes nature. In validation tests, the results of simulations are compared to actual experimental data with the goal of assessing the applicability and credibility of the governing model equations and their numerical implementation. While the scope of validation is larger than verification, the tests are performed in similar ways to quantify error. Validation testing requires assessing error and uncertainty in the experimental results as well as in the models and simulations, which requires a detailed understanding of both the experimental diagnostics and the simulations. Accordingly, the process of validation is greatly enhanced by close interaction between experimentalists and theorists.

The simulation code that is the subject of verification and validation is the FLASH code developed at the Center for Astrophysical Thermonuclear Flashes at The University of Chicago. FLASH is a parallel, adaptive-mesh simulation code for studying the multidimensional compressible reactive flows found in many astrophysical environments. FLASH utilizes a block-structured adaptive grid, adding resolution elements where needed to resolve flow features. The hydrodynamics module assumes that the flow is described by the Euler equations for compressible, inviscid flow and solves these equations by an explicit, directionally split version of the Piecewise Parabolic Method. FLASH also carries a separate advection equation for the partial densities as is required for reactive flows. FLASH is designed for minimal effort to swap or add physics modules, so testing FLASH requires testing each module as well as the framework integrating the modules. This work presented in this contribution describes two validation tests of the hydrodynamics method. Details of regression testing, verification tests, and additional details of these validation tests may be found in (Calder et al., 2002), and results from recent validation tests may be found in Weirs et al. (2005). Details about FLASH may be found in Fryxell et al. (2002).

The Three-Layer Target Experiment

A strong shock driven through a multilayer target produces Richtmyer–Meshkov (Richtmyer, 1960) and Rayleigh–Taylor (Chandrasekhar, 1981) instabilities at the fluid interfaces. Experiments of this kind are of interest in astrophysics because a similar situation is thought to occur during a core-collapse supernova. The proposed scenario is that a shock born deep in the collapsing core passes through the outer layer of a massive star. The outer layers have a shell-like structure with different chemical compositions of decreasing density, and the idea is that fluid instabilities and the resulting mixing of material can explain certain features observed in the spectra of these events (see Kifonidis et al., 2000, and references therein).

Three-layer target experiments probing these fluid instabilities were performed at the Omega laser facility at the University of Rochester. The targets consist of three materials, copper, polyimide plastic, and carbonized resorcinol formaldehyde (CRF) foam (densities 8.93, 1.41, and 0.1 g/cm^3) inside a cylindrical beryllium shock tube of inner diameter 0.08 cm. The laser illuminates ablating material on the copper, which produces a strong shock that propagates through the materials in the direction of decreasing density. The laser drive consisted of 10 beams delivering 420 J/beam in 1 ns at a peak intensity of 7.2×10^{14} W/cm^2, and diagnostics came from additional beams hitting an iron backlighter foil producing x-rays for radiography. Complete details about the experiment may be found in Kane et al. (2001).

The targets were manufactured with a sinusoidal perturbation of wavelength 0.02 cm and amplitude 0.0015 cm between the copper and polyimide plastic. As the shock propagates through this interface it is perturbed, and as the perturbed shock propagates through the second interface it imprints this perturbation on the interface. The result is the formation of instability growth seen as spikes of copper and bubbles of foam growing into the intermediate plastic material. We chose the length of the copper spikes as the metric of comparison between the experiments and simulations. In both the experimental data and the simulation results, testing demonstrated this was a reasonably robust measurement.

The two-dimensional simulations were performed on a 0.1 cm $\times$ 0.188 cm domain with outflow boundary conditions in the directions along the direction of shock propagation and periodic boundary conditions in the transverse directions. The three materials were modeled as ideal gasses because of the inherent inaccuracy found in realistic, tabular material equations of state. The domain had a 0.0242 cm region of copper, a 0.0150 cm region of polyimide plastic, and a 0.149 cm region of CRF foam, and the interface between the copper and plastic had the same sinusoidal perturbation as the experiment. The initial conditions for the shock came from a simulation performed by a one-dimensional radiation hydrodynamics code that modeled the radiation deposition and development of the shock. At $t = 2.1$ ns (after radiation effects are no longer important to the evolution), the density and pressure profiles from the one-dimensional simulation were mapped to the two-dimensional domain as initial conditions for the two-dimensional simulations.

Figure 1 shows an image of density from a simulation at 13 ns. The image shows qualitative agreement with the experiment. By this point in the evolution, the shock has passed through both interfaces and imprinted the perturbation on the second interface. The figure shows the initial development of the copper spikes (the dense regions about $x = 0.04$ cm) and foam bubbles (the lower density regions about $x = 0.06$ cm). The bubbles and spikes are growing in opposing directions (toward

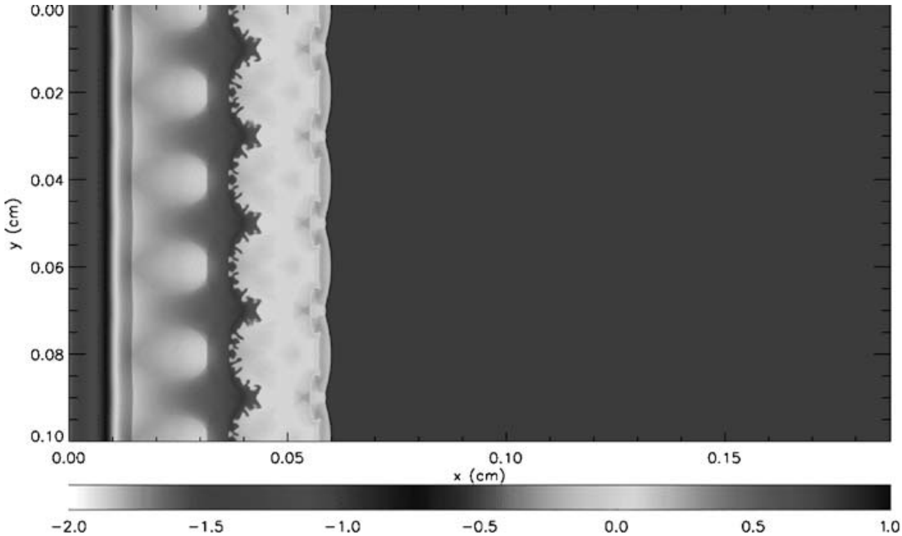

Figure 1. Density image from a simulation of the laser-driven, three-layer target experiment at an intermediate time, $t = 13$ ns. The simulation had an effective resolution of 1024×512. The shock propagated from the left. The growing copper spikes are the dark, dense regions near $x = 0.04$ cm, and the bubbles of foam are just to the left of the perturbed shock at $x = 0.06$ cm. Figure 2 shows the length of the spikes during the course of the simulation.

each other), and though it is not pictured, the shock oscillations observed earlier demonstrated agreement with theoretical predictions.

Figure 2 shows a plot of the copper spike length from two simulations of the three-layer target experiment. The simulations were performed at effective resolutions typical of a two-dimensional production simulation. The copper region shows initial compression followed by instability growth. Experimental results at 39.9 and 66.0 ns are also shown on the plot. The vertical error bars indicate the spatial uncertainty and the width of the symbols indicates the temporal uncertainty. The results of the simulation fall within the spatial error bars at both times, indicating good agreement between simulation and experiment.

The Rayleigh–Taylor Instability Experiment

The Rayleigh–Taylor instability occurs at an interface between fluids when a light fluid accelerates or applies a force to a dense fluid. The classic scenario is a light fluid supporting a dense fluid in a gravitational field. In the case of a multimode perturbation of the interface between the fluids, merging bubbles and spikes are thought to lead to instability growth governed by a t^2 scaling law,

$$h_{\mathrm{b,s}} = \alpha_{\mathrm{b,s}} g A t^2,$$

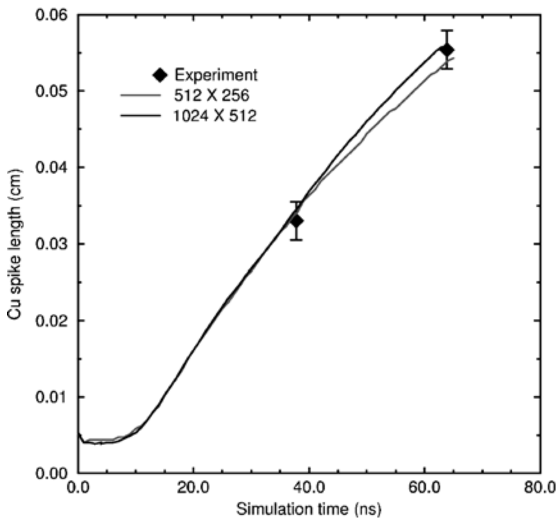

Figure 2. Plot of spike amplitude vs. time at two typical effective resolutions, 512 × 256 and 1024 × 512, from simulations of the laser-driven, three-layer target experiment. Also shown are the experimental results. The error bars indicate spatial uncertainty of $\pm 2.5 \times 10^{-5}$ cm, and the width of the symbol represents the timing uncertainty.

where $h_{b,s}$ is the height of a bubble or spike, g is the acceleration due to gravity, t is the time, and $A = (\rho_2 - \rho_1)/(\rho_2 + \rho_1)$ is the Atwood number (Youngs, 1994). $\rho_{1(2)}$ is the density of the light (dense) fluid. The coefficient α is a measure of the efficiency of potential energy release. This nonlinear expression for the instability growth allows for the quantitative comparison between simulations and experiments by comparing αs obtained from each.

The initial conditions for the for the three-dimensional simulation of the multimode Rayleigh–Taylor instability came from a standard set distributed to the Alpha Group, a consortium of researchers investigating the t^2 scaling law (Dimonte et al., 2004). The experimental results came from an investigation of the multimode Rayleigh–Taylor instability over a range of Atwood numbers and acceleration histories (Dimonte and Schneider, 2004). The initial conditions for the simulation consisted of a configuration with $A = 0.5$, $g = 2$ cm/s^2, and a 10 cm × 20 cm × 10 cm simulation domain. The pressure at the interface (500 dyn/cm^2) was chosen so that the maximum density variation with height was $<6\%$, and the initial velocity perturbation consisted of modes 32–64. The initial conditions for the simulation do not describe an experimental configuration, which typically involves a much smaller capsule, but both experiment and simulation are in the limit dominated by mode-coupling in which case the coefficient α is thought to be insensitive to the initial conditions (Dimonte et al., 2004).

The metric for comparison between simulation and experiment was the coefficient α. Figure 3 shows plots of $h_{b,s}$ vs. gAt^2 for the simulation (left panel) and the experiment (right panel). The slope of a straight line fit through the curves gives

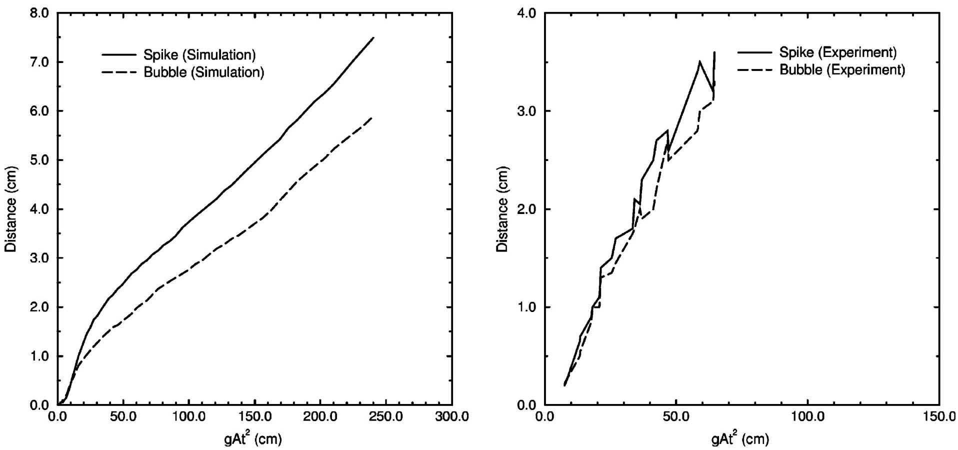

Figure 3. Plots of bubble and spike amplitude vs. gAt^2 for the Rayleigh–Taylor simulation (left panel) and the experiment (right panel). While the scales of the two plots differ, the aspect ratio is the same. α is given by the slope obtained from fitting a straight line to each curve. For the experiment, a fit gives $\alpha_{\text{bubble}} = 0.052$ and $\alpha_{\text{spike}} = 0.058$. For the simulation, a fit to the data after 5 s ($gAT^2 = 25$ cm), which neglects the rapidly changing region, gives $\alpha_{\text{bubble}} = 0.021$ and $\alpha_{\text{spike}} = 0.026$.

$\alpha_{\text{bubble}} = 0.052$ and $\alpha_{\text{spike}} = 0.058$ for the experiment and $\alpha_{\text{bubble}} = 0.021$ and $\alpha_{\text{spike}} = 0.026$ for the simulation. Note that in fitting a straight line to the simulation results, we neglected the growth before $t = 5$ s ($gAt^2 = 25$ cm) to eliminate this region of rapid change in slope.

Figure 4 shows cross-sections of density from the simulation at 75% of the maximum bubble height. The left panel is a cross-section at a relatively early time

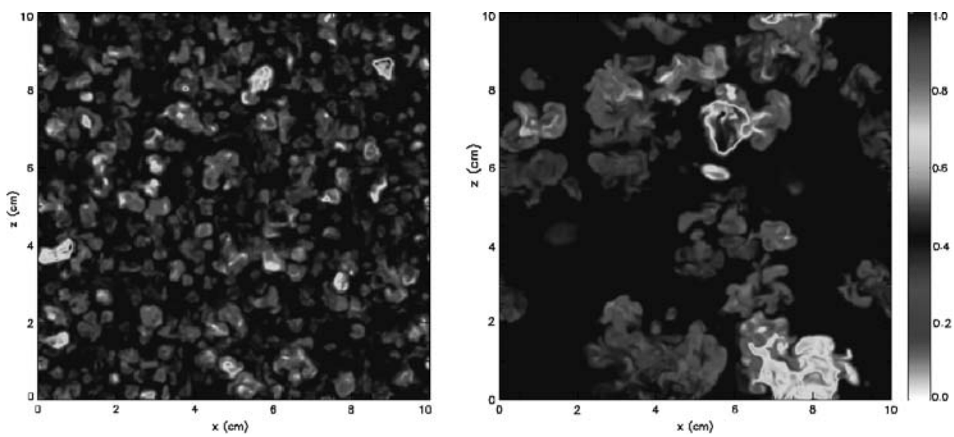

Figure 4. Images of density from the three-dimensional Rayleigh–Taylor simulation. Shown are cross-sections of the simulation domain at 75% of the maximum bubble height at an early time (left panel) and a late time (right panel). Comparison of the diameters of the bubbles illustrates the inverse cascade from small scales to large.

in the simulation, and it shows the presence of many small bubbles. The right panel is a cross-section at a relatively late time in the simulation, and it shows fewer, but larger, bubbles. The figure illustrates the expected inverse cascade in the bubble size, demonstrating that generations of bubble mergers have occurred as is expected. Note that the figure also provides qualitative information about the amount of small-scale or "atomic" mixing that has occurred. In both panels, the bubbles are not composed of constant-density "pure" fluid.

Discussion and Conclusions

The results of these validation tests are mixed. The simulations of the multilayer target experiment agreed well with the experimental results. We observed the expected instabilities at the fluid interfaces and showed quantitative agreement with the experimental copper spike lengths. We conclude that we are capturing the morphological properties of the flow reasonably well, but note that we cannot conclude that we have thoroughly validated the simulations for many reasons. First, the simulations were two-dimensional. While the experimental configuration produced an essentially two-dimensional result, the experiment is a three-dimensional event and correctly capturing the fluid instabilities may require full three-dimensional simulations. Next, the models were incomplete. The materials were modeled as ideal gasses, which is a questionable assumption, and the simulations used periodic boundary conditions instead of modeling the shock tube. Part of validation is also an attempt at quantification of the importance of the missing or omitted physics (e.g., a physically motivated equation of state), and we did not perform such a study. The comparison is also limited by the experimental diagnostics. The radiographs produced in the experiment are shadows and may not adequately capture small-scale structure.

The simulation of the multimode Rayleigh–Taylor experiment did not agree well with the experimental result. The simulation qualitatively agreed with bulk properties of the flow and demonstrated the expected inverse cascade to larger bubbles and spikes, but the values for $\alpha_{\mathrm{b,s}}$ from the simulation were approximately half of the values from the experiment. Proposed reasons for this disagreement include problems with both the simulation and the experiment. The initial conditions of the experiment are difficult to characterize. Long wavelength noise in the initial conditions of the experiment could "short circuit" the multimode growth leading to premature development of the dominant mode. In the simulations, the primary concern is resolution. The results of a similar Rayleigh–Taylor simulation at lower resolution did not agree with the results of the simulation presented here, indicating poor convergence with resolution. Furthermore, resolution studies of the Rayleigh–Taylor instability with a single-mode perturbation did not demonstrate convergence at the limiting resolutions attained (Calder et al., 2002). This result suggests we are far from adequately resolving the multimode case.

Although the results of these validation tests were mixed and did not allow us to conclude that we had successfully validated the simulations and models, the process of a formal ongoing verification and validation effort is extremely valuable. The experience gained with these two validation tests better prepares us for modeling astrophysical events and serves to increase confidence in our simulations. The unanswered questions such as the required resolution for simulating Rayleigh–Taylor instability also serve to improve simulations by alerting us to issues we otherwise might not have noticed in astrophysical simulations.

In closing, a point mentioned above warrants emphasis. This work, with its detailed comparison between the results of experiments and simulations, would not have been possible without a close collaboration between the experimentalists and theorists. The determination of the metric for comparison and the measurement of experimental results (particularly the copper spike case) required the expertise of the experimentalists. Without that expertise, the modelers would have had little chance at making a meaningful comparison with the experimental results.

Acknowledgments

The author gratefully acknowledges the contributions of many people at the Flash Center, the National Labs, and other institutions who were part of this work. The author also thanks the organizers of the 5th International Conference on High Energy Density Laboratory Astrophysics for putting together a wonderful conference and giving the author the opportunity to speak on this work. This work was supported in part by the U.S. Department of Energy under grant B341495 to the Center for Astrophysical Thermonuclear Flashes at The University of Chicago.

References

AIAA: 1998, Validation of Computational Fluid Dynamics Simulations, Report G-077-1998, American Institute of Aeronautics and Astronautics, Reston.

Calder, A.C. et al.: 2002, *ApJSS* **143**, 201.

Chandrasekhar, S.: 1981, *Hydrodynamic and Hydromagnetic Stability*, Dover, New York, p. 428.

Dimonte, G. et al.: 2004, *Phys. Fluids* **16**, 1668.

Dimonte, G. and Schneider, M.: 2000, *Phys. Fluids* **12**, 304.

Fryxell, B. et al.: 2002, *ApJSS* **131**, 273.

Kane, J.O. et al.: 2001, *Phys. Rev. E* **63**, 055401.

Kifonidis, K., Plewa, T., Janka, H.-Th. and Müller, E.: 2000, *ApJ Lett.* **531**, 126.

Richtmyer, R.D.: 1960, *Commun. Pure Appl. Math.* **13**, 297.

Roach, P.J.: 1998a, *Fundamentals of Computational Fluid Dynamics*, Hermosa, Albuquerque.

Roach, P.J.: 1998b, *Verification and Validation in Computational Science and Engineering*, Hermosa, Albuquerque.

Weirs, G., Dwarkadas, V., Plewa, T., Tomkins, C. and Mark, M.-L.: 2005, *Ap&SS* **298**, 341.

Youngs, D.L.: 1994, *Laser Part. Beams* **12**, 725.

HOW DID CASSIOPEIA A EXPLODE? A CHANDRA VLP

J. MARTIN LAMING and UNA HWANG
Naval Research Laboratory/Goddard Space Flight Center; E-mail: laming@nrl.navy.mil

(Received 30 April 2004; accepted 8 July 2004)

Abstract. The Cassiopeia A supernova remnant will be observed by Chandra for 1 Ms this spring. We discuss our motivations and plans for acquiring and analyzing these data.

Keywords: supernova remnants, element abundances

Core-collapse supernovae represent an area of astrophysics that perhaps more than any other cries out for firm observational results with which to compare the multitude of theoretical models that have been developed over the years. With this idea in mind, two recent papers (Laming and Hwang, 2003; Hwang and Laming, 2003) explored new analysis methods for the youngest known galactic supernova remnant, Cassiopeia A (Cas A), that by virtue of various fortuitous sets of circumstances appears to offer the best chance of making progress in this area.

Cas A is approximately 330 years old (the possible observation of the supernova by Flamsteed in August 1680 is now largely discredited by modern scholarship (Stephenson and Green, 2003). It is observed in all wavebands from the radio, where it was first detected, to TeV γ rays, with the exception of the extreme ultraviolet. It has an accurately known distance, radius and forward shock speed (Delaney and Rudnick, 2003), and this dynamical information combined with its age allows us to make considerable simplifications in the analysis in specifying an explosion energy, ejecta mass and circumstellar medium density.

A significant fraction of the ejecta of Cas A are observed in X-rays to be in knots or clumps (see Figures 1 and 2 for examples of O-rich and Fe-rich knots and sample spectra). Some of these are located very close to the forward shock position, inviting the somewhat naive assumption that they are significantly overdense compared to their surroundings. If overdense knots did indeed undergo reverse shock passage early in the evolution of Cas A, then an important question arises as to how they survived to be observed as knots by Chandra/ACIS. A number of authors (Klein et al., 1994, 2003; Poludnenko et al., 2001, 2004) have modelled cloud-shock or knot-shock interactions. Upon entering a higher (lower) density medium, the shock decelerates (accelerates). The different acceleration with respect to the ambient medium experienced by the cloud or knot gives rise to hydrodynamic instabilities

Astrophysics and Space Science **298:** 33–37, 2005.

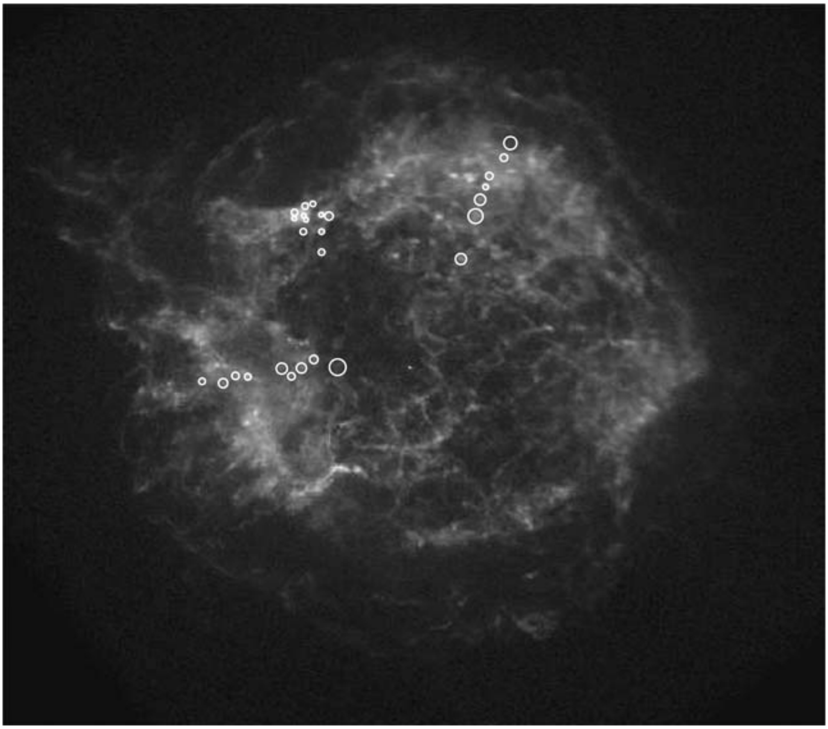

Figure 1. Locations of O-rich knots analyzed in Laming and Hwang (2003). Two radial series in the NNW and the E directions show lower temperatures than the cluster at the "jet-base" in the NE. The forward shock is delineated by the outer rim in the left panel. The reverse shock is at about 0.55–0.67 times the forward shock radius (see Gotthelf et al., 2001). The "jet" is seen protruding ahead of the forward shock in the NE.

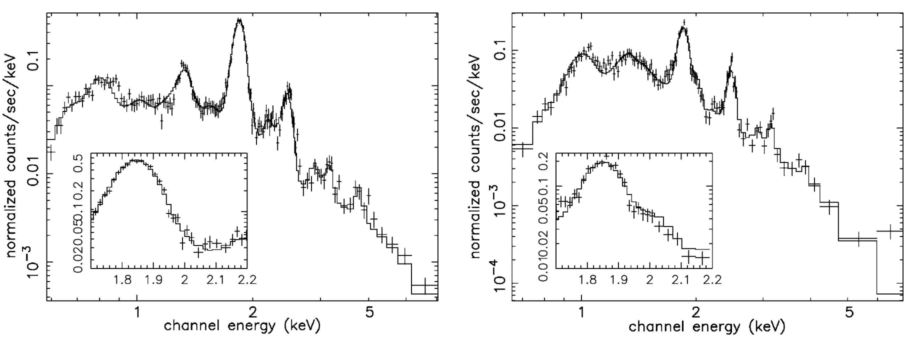

Figure 2. Sample spectra extracted from the knot locations illustrated in Figure 1. The feature close to 2 keV energy is He- and H-like Si. At the temperature determined from the thermal bremsstrahlung continuum, Si would be ionized to the H-like or bare charge states in ionization equilibrium. The presence of the He-like charge state indicates that the plasma is not in ionization equilibrium, and this departure from equilibrium gives us a "timing" signature allowing the inference of ejecta mass coordinates. The spectrum on the right showing more H-like Si than on the left is clearly at a more advanced state of ionization ("ionization age" defined as the integral of electron density over time).

with the net result of the destruction of the cloud or knot on a timescale of a few shock crossing times. For knots 1″ across in Cas A (5×10^{16} cm) the shock crossing time is 15–30 years for a 500–1000 km s^{-1} reverse shock. The knot destruction time of $\sim$50 years is consistent with observed lifetimes of the optical fast moving knots and quasi-stationary flocculi (Thorstensen et al., 2001). However the X-ray knots of interest here are of similar temperature to their surroundings (i.e. they have not cooled to optically emitting temperatures), and their apparent survival for $\sim$200–300 years places an upper limit on their density with respect to the surrounding plasma of around a factor of 3 (see Table I of Klein et al., 1994). We believe the X-ray knots underwent reverse shock passage, and perhaps interacted with secondary shocks, some time early in the evolution of Cas A and are now expanding with the rest of the remnant plasma, as in fact appears to be the case (Delaney and Rudnick, 2003).

Accordingly we extract spectra of individual knots and on the assumption that each knot was shocked "instantaneously" on the evolution timescale of Cas A, fit single electron temperatures and ionization ages (the product of electron density and time which parameterizes the non-ionization equilibrium aspect of the spectrum) to compare with models. We use an analytic representation of the SNR hydrodynamics to follow a Lagrangian plasma element through the forward or reverse shock, integrating equations for the ionization balance and electron and ion temperatures, assuming Coulomb equilibration between the species and energy losses due to radiation, ionization and adiabatic expansion. We assume a circumstellar density profile $\rho \propto 1/r^2$ appropriate to a remnant presupernova stellar wind and ejecta density profiles represented by a uniform density core with a power law outer envelope $\rho \propto 1/r^n$ with $5.5 < n < 12$. We plot the locus of electron temperature against ionization age that result from Lagrangian plasma elements encountering the reverse shock at different time following explosion, and repeat this exercise for various different elemental abundance sets (Figure 4).

In Figure 3 we show the curves that result for pure O and a mixture of Fe and Si that best represent the various spectra observed. Overlaid on these plots are data points resulting from our fits. The left hand panel of Figure 3 shows results from the O-rich knots illustrated in Figure 1. Knots from the radial series indicate various ejecta envelope power laws between 7 and 12, while those from the "jet base" region (but not actually in the jet itself) indicate $n = 5.5$. Physically, the lower n indicates that the explosion energy is distributed much more evenly through the ejecta, and requires higher explosion energy to give the same blast wave radius and velocity as observed (Laming and Hwang, 2003). The inference of $n = 5.5$ at the jet base compared with higher values elsewhere (see Figure 1) suggests approximately a factor of two more explosion energy going in this direction compared with that at other latitudes. Such asymmetry is consistent with, but at the low end of, energy asymmetries coming from models of explosions from rotating progenitors (Khokhlov et al., 1999; Akiyama et al., 2003; Fryer and Warren, 2004), and also with the asymmetry in the velocities of fast moving optical knots (Fesen, 2001).

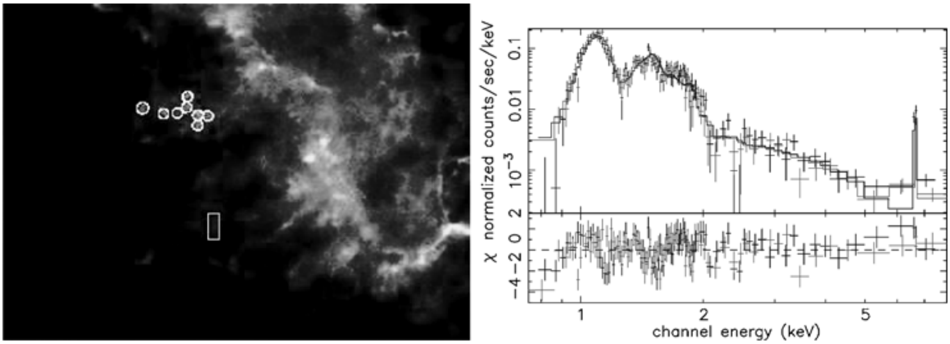

Figure 3. Locations of Fe-rich knots on the east limb analyzed in Hwang and Laming (2003) (*left*). The spectrum on the right is from the rectangular region and it particularly interesting in that it shows emission from essentially pure Fe. Such complete Si burning, either as α-rich freezeout or in higher density plasma, indicates an origin close to the center of the explosion. The precise amount of such plasma is sensitive to such details of the explosion as the mass cut and natal pulsar kick.

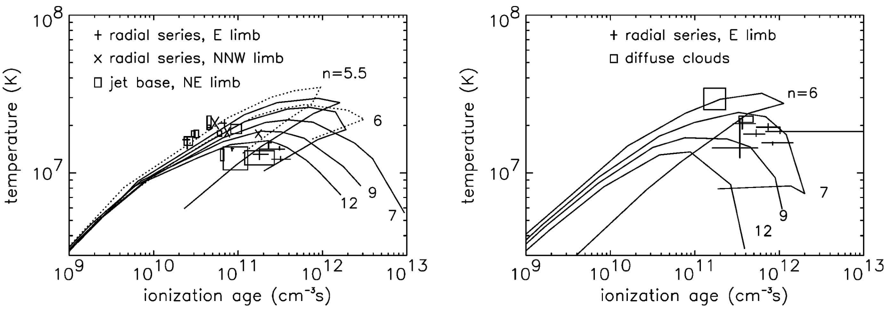

Figure 4. Loci of electron temperature against ionization age for oxygen dominated composition (*left*) and iron-silicon plasma (*right*). The point at the highest ionization age for $n = 5.5$, 6 and 7 (*left*) corresponds to ejecta at the core-envelope boundary. For higher values of n for O-rich composition and for all values for Fe-Si, this region becomes thermally unstable. Overlaid on these plots are data points coming from our spectral fits. See text for details.

The results for Fe-rich knots in Figure 3 indicate that we see Fe as mixed as far out into the ejecta as the thermal stability requirements allow. Fe clumps that were mixed further out and consequently encountered the reverse shock earlier in their evolution would have undergone thermal instability before now and cooled out of the X-ray emitting temperature range.

According to hydrodynamical models (Laming and Hwang, 2003), the reverse shock is currently at an ejecta mass coordinate $q = 0.1$–0.14 for $n = 9$–7 models respectively. Hence the inner 10% of ejecta, i.e., the inner 0.2 solar masses (for a 2 solar mass ejecta model), has yet to encounter the reverse shock. Cas A is highly unlikely to have ejected more than 0.05–0.1 solar masses of ^{56}Ni (which β decays to ^{56}Fe), so the reverse-shocked ^{56}Fe that we do see must have been mixed out into the envelope by Rayleigh–Taylor instabilities shortly after explosion. The estimated knot masses (Hwang and Laming, 2003) probably amount to a few percent of the total mass ejected, which is similar to the mass of ^{56}Ni inferred to have been mixed out into the envelope of SN 1987A (Pinto and Woosley, 1988).

The one million second Chandra observation will allow us to extract spectra with sufficient signal to noise for spectral fitting from *each pixel of the ACIS CCD* allowing us to fully exploit the unprecedented spatial resolution of the Chandra mirrors. This will allow us to characterize much more of the Fe emission with temperatures and ionization ages. Many of the knots currently visible cannot so far be fit with single electron temperatures and ionization ages, since a relatively large spatial extraction region is required. Other topics for study include the proper motions and X-ray explosion center, cosmic ray acceleration, searching for signatures of radioactivity in the ejecta, as well as the first quantitative study of nucleosynthesis in core-collapse supernova.

Acknowledgments

Work supported by basic research funds of the Office of Naval Research and by the Chandra GI Program.

References

Akiyama, S., Wheeler, J.C., Meier, D.L. and Lichenstadt, I.: 2003, *Astrophys. J.* **584**, 954.

Delaney, T.A. and Rudnick, L.: 2003, *Astrophys. J.* **589**, 818.

Fesen, R.A.: 2001, *Astrophys. J. Suppl.* **133**, 161.

Fryer, C.L. and Warren, M.S.: 2004, *Astrophys. J.* **601**, 391.

Gotthelf, E.V., Koralesky, B., Rudnick, L., Jones, T.W., Hwang, U. and Petre, R.: 2001, *Astrophys. J.* **552**, L39.

Hwang, U. and Laming, J.M.: 2003, *Astrophys. J.* **597**, 362.

Khokhlov, A.M., Höflich, P.A., Oran, E.S., Wheeler, J.C., Wang, L. and Chtchelkanova, A.Yu.: 1999, *Astrophys. J. Lett.* **525**, 107.

Klein, R.I., McKee, C.F. and Colella, P.: 1994, *Astrophys. J.* **420**, 213.

Klein, R.I., Budil, K.S., Perry, T.S. and Bach, D.R.: 2003, *Astrophys. J.* **583**, 245.

Laming, J.M. and Hwang, U.: 2003, *Astrophys. J.* **597**, 346.

Pinto, P.A. and Woosley, S.E.: 1988, *Nature* **333**, 534.

Poludnenko, A.Y., Frank, A. and Blackman, E.G.: 2001, *Astrophys. J.* **576**, 832.

Poludnenko, A.Y., Dannenberg, K.K., Drake, R.P., Frank, A., Knauer, J., Meyer-hofer, D.D., Furnish, M., Asay. J.R. and Mitran, S.A.: 2004, *Astrophys. J.* **604**, 213,

Stephenson, F. and Green, D.: 2003, *The Historical Supernova Remnants*, Cambridge University Press, Cambridge UK.

Thorstensen, J.R., Fesen, R.A. and van den Bergh, S.: 2001, *Astron. J.* **122**, 297.

STUDIES OF LASER-DRIVEN RADIATIVE BLAST WAVES

A.D. EDENS[1], T. DITMIRE[1], J.F. HANSEN[2], M.J. EDWARDS[2], R.G. ADAMS[3], P. RAMBO[3], L. RUGGLES[3], I.C. SMITH[3] and J.L. PORTER[3]

[1]*Department of Physics, University of Texas at Austin, Austin, TX, USA;*
E-mail: aedens@mail.utexas.edu
[2]*Lawrence Livermore National Laboratory, Livermore, CA, USA*
[3]*Sandia National Laboratories, Albuquerque, NM, USA*

(Received 30 April 2004; accepted 12 July 2004)

Abstract. We have performed two sets of experiments looking at laser-driven radiating blast waves. In the first set of experiments the effect of a drive laser's passage through a background gas on the hydrodynamical evolution of blast waves was examined. The laser's passage heated a channel in the gas, creating a region where a portion of the blast wave front had an increased velocity, leading to the formation of a bump-like protrusion on the blast wave. The second set of experiments involved the use of regularly spaced wire arrays used to induce perturbations on a blast wave surface. The decay of these perturbations as a function of time was measured for various wave number perturbations and found to be in good agreement with theoretical predictions.

Keywords: laser produced blast waves, laboratory astrophysics, Vishniac overstability

Introduction

Physicists and astronomers have long been studying the stability of shock waves (Erpenbeck, 1962; Isenberg, 1977; Ryu and Vishniac, 1987; Elmegreen and Elmegreen, 1978). In particular, there are several instabilities of interest associated with the formation and evolution of shock waves produced by supernovae, i.e. supernova remnants (SNRs) (Isenberg, 1977; Ostriker and Mckee, 1988; Welter, 1982). One important hydrodynamic feature associated with some radiative SNRs, an overstability proposed by Vishniac et al. about 20 years ago (Ryu and Vishniac, 1987; Vishniac, 1983; Ryu and Vishniac, 1991), arises from a mismatch between the ram and thermal pressures at the surface of a blast wave, which can cause a growing, oscillating ripple on that surface. Radiative SNR shocks are cooler and more compressible than non-radiative SNR shocks, leading to a thinner blast front which is susceptible to this Vishniac overstability (Liang and Keilty, 2000). The Vishniac overstability may be responsible for the large-scale structure seen in some radiative SNRs and may also play a role in the formation of stars (Elmegreen and Elmegreen, 1978; Welter and Schmidburgk, 1981).

Vishniac et al. (Ryu and Vishniac, 1991) made quantitative predictions for the temporal evolution of small perturbations on a blast wave front and derived the growth rate of the overstability as a function of the effective adiabatic index of the shocked material and wave number of the oscillation. There have since been several attempts to confirm these growth rates both through simulation and experiment. The appearance of the Vishniac overstability in both one- and two-dimensional astrophysical simulations was seen by Blondin et al. (1998), who observed perturbations on the order of 10% of the blast wave radius growing from a 1% density perturbation seed using the numerical hydrodynamics code VH-1. MacLow and Norman ran simulations (MacLow and Norman, 1993) using the numerical gas dynamics code ZEUS-2D which confirmed the theoretical growth rates of Vishniac et al. (Ryu and Vishniac, 1991) assuming the amplitude of the ripple was small compared to the radius of the blast wave.

Most experimental attempts to see the Vishniac overstability have used laser irradiation of a target to create a blast wave in a background gas (Ditmire et al., 2000; Shigemori et al., 2000; Edwards et al., 2001; Grun et al., 1991). These experiments take advantage of a laser's ability to deliver a large amount of energy to a small focal spot in a time span that is short compared to the evolution of the resulting explosion. There are several complications associated with these experiments that make it difficult to measure the growth rate of the overstability. The first complication for laser experiments in spherical geometry (Grun et al., 1991), as opposed to cylindrical geometry (Ditmire et al., 2000; Shigemori et al., 2000; Edwards et al., 2001), is the effect of the laser's passage on the background gas, which can pre-ionize the gas. A second complication to experimental observation is that if the overstability grows from noise it is difficult to achieve large growth in the limited lifetime of the experiments. In this paper we describe experiments where we have looked at both of these issues and explored the evolution of perturbations by inducing ripples on a blast wave using regularly spaced wire arrays.

Experimental Setup and Data

Some of the data described here was acquired on the Z-Beamlet (Rambo et al., 2002) laser at Sandia National Laboratories, which fired 500 J–1000 J, 1 ns pulses of 527 nm wavelength. The remainder of the data was taken on the Janus laser (Glaze et al., 1976) at Lawrence Livermore National Laboratory, which fired 10 J–150 J, 1 ns laser pulses at 1054 nm wavelength. These pulses illuminated 500-μm-diam cylindrical solid targets immersed in 5–10 Torr of nitrogen or xenon gas. The resulting explosions created the blast waves that we studied. The setup used is diagramed in Figure 1. The inset in Figure 1 shows the main diagnostic employed: a dark-field telescope. This diagnostic is used with a probe laser and is sensitive to density gradients, such as those that occur at the edge of a blast wave. The probe laser used with Z-Beamlet fired ~80-mJ, 150-ps pulses at 1064 nm. The probe laser used with Janus fired ~10-mJ, 2-ns pulses at 527 nm. These lasers could be fired at a variable interval after the drive laser allowing us to examine the evolution of our

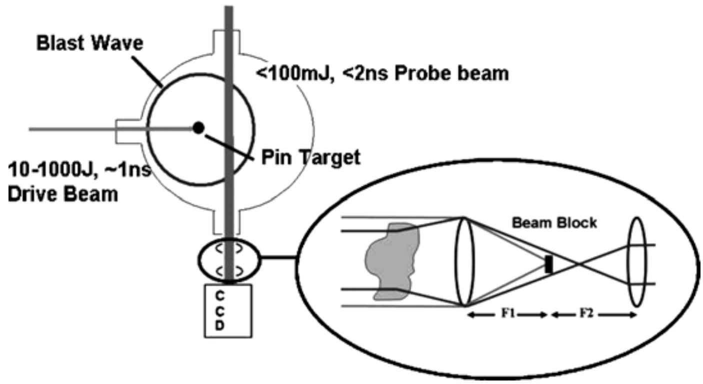

Figure 1. Experimental setup for laser-produced blast wave experiments. The 10–1000-J, 1 ns drive beam enters one side of the chamber, illuminating a 0.5 mm solid target and creating a blast wave. At a variable time later a probe laser is fired and comes in perpendicular to the drive beam, imaging the blast wave. The inset shows a diagram of a dark field telescope. Light that goes through the experiment undeflected gets blocked by a beam block at the focus of the imaging telescope. Deflected light shows up as a bright area on the CCD.

blast wave over several microseconds. For part of the experiments, regularly spaced wire arrays were used to induce single-frequency perturbations on blast waves. The wire array contained a square of open space approximately 3 cm on a side through which 30-gauge tin-copper wire was strung. The wires were spaced 2, 4, or 6 mm apart, corresponding to induced perturbations with spherical ℓ numbers of $\sim$28, 14, and 9 given the size of the blast wave at the time it intersected the array.

The first experiments were performed without the wire array and looked at the evolution of the radius of the blast wave as a function of time. The position of any feature of a blast wave, such as the blast wave front, will evolve as $R(t) = \beta t^{\alpha}$. Blast waves that do not lose or gain a significant fraction of their initial energy during their evolution, i.e., those where radiation does not play an important role in the hydrodynamics, follow the Taylor–Sedov solution, where $\alpha = 0.4$ (Taylor, 1950; Sedov, 1946). In blast waves where radiation is important, a solution with a lower α will be followed, as the energy loss via radiation causes these blast waves to slow down more quickly. Therefore, the trajectory of a blast wave can show the importance of radiation on its hydrodynamics.

Images of blast waves produced by 1000-J laser pulses at various times along with a measured trajectory are shown in Figure 2 with 10 Torr of nitrogen as the background gas and in Figure 3 with 10 Torr of xenon as the background gas. The trajectory in nitrogen follows a $t^{0.4}$ trajectory to a high degree of accuracy over its entire history. In contrast, while xenon at late times ($>$400 ns) may expand as $t^{0.4}$, at earlier times the trajectory appears to exhibit a lower α. This lower exponent most likely arises from the fact that energy losses via radiation have an effect on the hydrodynamics of the blast wave. Another indication that radiation plays a much

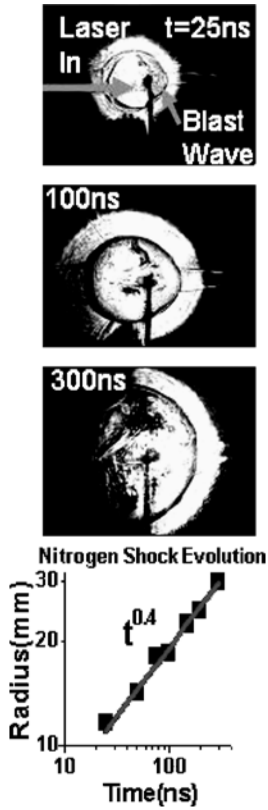

Figure 2. Images of blast waves in nitrogen at 25 ns, 100 ns, and 300 ns after a 1000-J drive beam has hit a 0.5-mm nylon target. The bottom panel is a graph of the radius of the blast waves as a function of time. It shows that the blast waves follow a $t^{0.4}$ trajectory, indicating that radiation losses do not play an important role in the hydrodynamics of the blast waves.

larger role for blast waves in xenon than in those travelling through nitrogen is the radiative precursor. When a blast wave radiates, some of the energy is absorbed by the background gas, creating a heated, ionized region in front of the blast wave. This ionized region shows up as a bright area on the dark field images. In Figure 2, although there is a noticeable glow surrounding the blast waves, it is localized to the region immediately surrounding the blast wave, never extending more than 7 mm away from the edge of the blast wave. This can be contrasted with Figure 3, where the precursor region extends off the field of view, at least several cm, demonstrating a significantly greater amount of radiation emitted from blast waves in xenon.

Another feature of note from these images is the presence of a "bump" feature on the laser side of the blast waves, especially those in xenon gas. A closer look at an example of this feature can be seen in Figure 4. A qualitatively similar feature occurs for blast waves in xenon at all drive laser energies from 10 J to 1000 J; this feature always occurs along the path of the laser focal cone and arises from the interaction

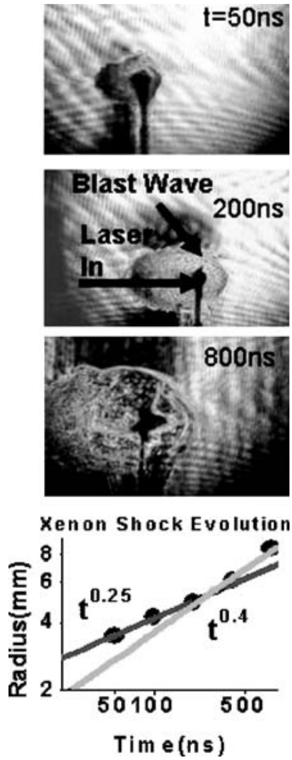

Figure 3. Images of blast waves in xenon at 50 ns, 200 ns, and 800 ns after a 1000-J drive beam has hit a 0.5-mm nylon target. The bottom panel is a graph of the radius of the blast waves as a function of time. It shows that the blast waves follow a trajectory slower than $t^{0.4}$ before $\sim$400 ns, indicating significant energy losses due to radiation.

Figure 4. Zoomed in view of bump feature on blast wave 400 ns after 1000-J laser pulse illuminated a 0.5-mm nylon target. This feature is caused by a portion of the blast wave front moving faster in the region heated by the drive laser’s passage.

of the laser with the background gas. As the laser passes through the background gas, it heats and ionizes the gas it passes through. This creates a warm, lower-density channel of gas where the blast wave will travel faster than in other regions, which results in the bump-like feature seen in the data. Simulations of this phenomenon

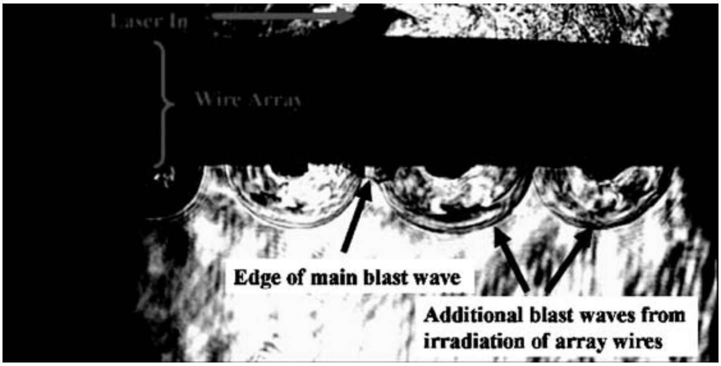

Figure 5. The 9-mm spaced wire array in xenon gas 700 ns after a 1000-J laser pulse illuminated the 0.5-mm nylon target. The main blast wave is just passing the wire array. Additional blast waves created by radiation from the main blast wave have already formed around each wire in the array and are moving outward.

were performed using CALE, the Lawrence Livermore National Laboratory two-dimensional arbitrary Lagrangian Eulerian (ALE) code with a tabular equation of state (EOS) and interface tracking (*CALE Users Manual*, 1991). They indicate that for a 100-J drive laser pulse, the laser channel region is heated to up to 12 eV, comparable to what we expect the temperature of the shock-heated gas to be.

For the next set of experiments, we placed wire arrays in the path of blast waves produced by 1000-J laser pulses in order to induce perturbations. When we did this for blast waves travelling through xenon, the radiation from the blast wave ablated the wire array, creating secondary blast waves that interfered with our main blast wave until they were outside our field of view. The formation of these secondary blast waves is illustrated in Figure 5. For blast waves traveling through nitrogen, we expected that the induced perturbations would decay over time. Because radiation does not appear to play an important role in the energy dynamics of these blast waves, their blast fronts should be too thick for growth of the Vishniac overstability to occur. However, the radiative precursor around the nitrogen blast wave images in Figure 2 indicates that some radiation is emitted, which could lower the effective adiabatic index somewhat, resulting in slightly thinner blast waves. The adiabatic index for a perfect monatomic gas is 1.66 and we would expect that our adiabatic index would be somewhere between this value and 1.2, the value where growth begins to occur for the Vishniac overstability. Some images corresponding to each of our wire arrays are shown in Figure 6. In each case, the induced perturbations clearly damp out, matching our intuition.

In order to measure the rate of this decay, we traced out the edge of the blast waves in polar coordinates. We Fourier-transformed this curve to select the frequency corresponding to our wire-array wave number. An example of the results of this procedure is shown in Figure 7. After we determined the amplitude of the frequency component of interest to us, we plotted this amplitude relative to the radius of the

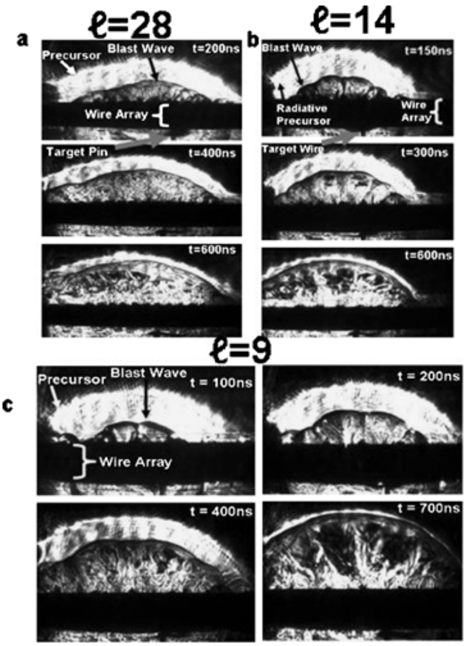

Figure 6. Evolution of perturbations on blast waves produced by (a) 2-mm-, (b) 4-mm-, and (c) 6-mm-spaced wire arrays. The perturbations damp out with time due to the high effective adiabatic index of the nitrogen gas.

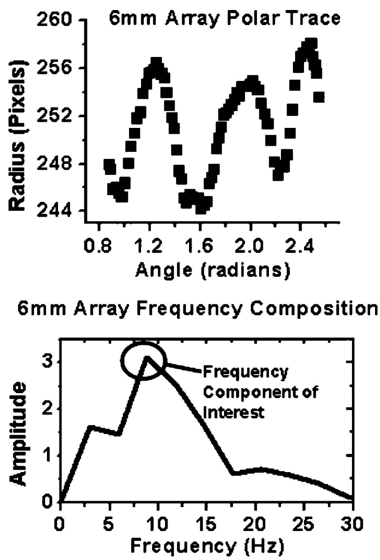

Figure 7. Top panel is the coordinates of the edge of a blast wave moving past a 6-mm spaced wire array in polar coordinates. The bottom panel is the Fourier transform of the same shot. Highlighted is a peak at a wave number of $\sim$9, which corresponds to the wave number of the induced perturbation of the wire array.

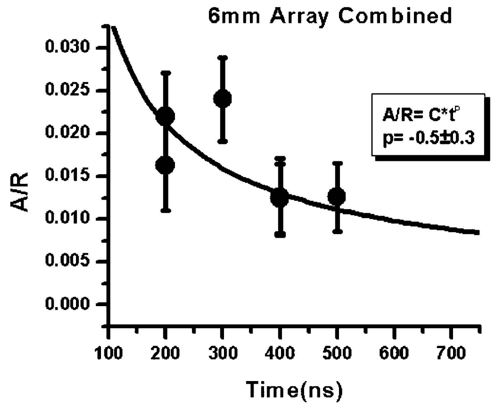

Figure 8. Amplitude of perturbations induced by a 6-mm spaced wire array on a blast wave traveling through nitrogen as a function of time. The measured decay rate can be compared to theoretical predictions.

blast wave as a function of time and fit these data with a function of the form $R/A = C^*t^p$. The results of this for the 6-mm array are shown in Figure 8. We compared these results to theoretical predictions for p as a function of spherical wave number l from Vishniac et al. (Ryu and Vishniac, 1991). This comparison is illustrated in Figure 9. Here we see the experimental data compared to theoretical predictions for various adiabatic indices. The best agreement occurs for an effective adiabatic index of 1.4–1.5. This agrees well with our intuition for the nitrogen gas in our experiment. In order to better determine the adiabatic index of our gas, we are currently performing simulations using the Hyades code (*HYADES*, 2004), a one-dimensional Lagrangian hydrodynamics code with tabular EOS.

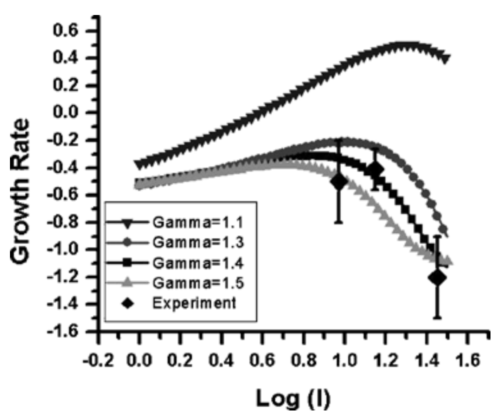

Figure 9. Comparison of experimental results to theoretical predictions for decay rates as a function of wave number of perturbations for blast waves traveling through nitrogen. The experimental results match well to theoretical predictions for a gas with an adiabatic index of 1.4–1.5.

Conclusion

We have performed experiments designed to look at two complications that arise in laser-produced blast wave studies of the Vishniac overstability. The first is the effect of the laser passage on the background gas in the experiment. We find that the passage of the drive laser beam in these experiments can create a warm, low-density channel of gas that creates a region where the blast-wave moves faster relative to the rest of the blast wave surface, creating an artificial bump-like feature. The second set of experiments have induced perturbations on blast waves and measured the resulting decay rate. We have compared this result to theoretical predictions relevant to the Vishniac overstability (Ryu and Vishniac, 1991) and found good agreement. These results suggest that there is a wealth of physical processes occurring in laser-driven blast wave experiments. These processes can have unanticipated consequences, as illustrated by the formation of secondary blast waves on our wire array, produced by radiation from the primary blast wave in xenon.

References

Blondin, J.M., Wright, E.B. and Borkowski, K.J.: 1998, *Astrophys. J.* **500**(1), 342.
CALE Users Manual: 1991. (Lawrence Livermore National Laboratory, Livermore, CA).
Ditmire, T., Shigemori, K. and Remington, B.A.: 2000, *Astrophys. J. Suppl. Ser.* **127**(2), 299.
Edwards, M.J., MacKinnon, A.J. and Zweiback J.: 2001, *Phys. Rev. Lett.* **87**(8) art. no.-85004.
Elmegreen, B.G. and Elmegreen, D.M.: 1978, *Astrophys. J.* **220**(3), 1051.
Erpenbeck, J.J.: 1962, *Phys. Fluids* **5**(10), 1181.
Glaze, J.A., Simmons, W.W. and Hagen, W.F.: 1976, *Status of Large Neodymium Glass Lasers*, Soc. Photo-Optical Instrumentation Engrs, Palos Verdes Estates, CA, Reston, VA).
Grun, J., Stamper, J. and Manka, C.: 1991, *Phys. Rev. Lett.* **66**(21), 2738.
Inc. Cascade Applied Sciences: 2004, *HYADES User's Guide*, Cascade Applied Sciences, Boulder, Co).
Isenberg, P.A.: 1977, *Astrophys. J.* **217**(2), 597.
Liang, E. and Keilty, K.: 2000, *Astrophys. J.* **533**(2), 890.
MacLow, M.M. and Norman, M.L.: 1993, *Astrophys. J.* **407**(1), 207.
Ostriker, J.P. and Mckee, C.F.: 1988, *Rev. Mod. Phys.* **60**(1), 1.
Rambo, J.L., Rambo, P.K., Jr., Bennett, G.R., Smith, I.C., Erlandson, A.C., Murray, J.E. and Caird, J.: 2002, *OSA Trends in Optics and Photonocs, Conference on Lasers and Electro-Optics* **73**, 362.
Ryu, D. and Vishniac, E.T.: 1987, *Astrophys. J.* **313**(2), 820.
Ryu, D. and Vishniac, E.T.: 1991, *Astrophys. J.* **368**(2), 411.
Sedov, L.: 1946, *Prikl. Mat. Mekh.* **10**(2), 241.
Shigemori, K., Ditmire, T. and Remington, B.A.: 2000, *Astrophys. J.* **533**(2), L159.
Taylor, S.G.: 1950, *Proc. R. Soc. A* **201**(A), 159.
Vishniac, E.T.: 1983, *Astrophys. J.* **274**(1), 152.
Welter, G. and Schmidburgk, J.: 1981, *Astrophys. J.* **245**(3), 927.
Welter, G.L.: 1982, *Astron. Astrophys.* **105**(2), 237.

RADIATIVE SHOCKS IN ASTROPHYSICS AND THE LABORATORY

R. PAUL DRAKE
Atmospheric Oceanic and Space Sciences, University of Michigan, Ann Arbor, MI, USA;
E-mail: rpdrake@umich.edu

(Received 28 April 2004; accepted 25 May 2004)

Abstract. This paper explores the variations in radiative shock behavior originating from the properties of the system containing the shock. Specifically, the optical depth of the upstream region and the downstream region both affect the behavior of radiative shocks. Optically thick systems such as stellar interiors or supernovae permit only limited shock-induced increases in density. At the other limit, the radiation and shock dynamics in optically thin systems permits the post-shock density to reach arbitrarily large values. The theory of the shock structure is summarized for systems in which the upstream region is optically thin, common to some astrophysical systems and a number of experiments.

Keywords: shock waves, radiative shock waves, laboratory astrophysics

1. Introduction

A radiative shock is one in which the structure of the density and temperature is affected by radiation from the shock-heated matter. Here we explore the properties of such shocks in a large context – that of all (nonrelativistic) laboratory experiments and astrophysical systems. In order for a shock to be radiative in any medium, it must at minimum be fast enough that the radiative fluxes, which scale as the fourth power of the temperature, exceed the material energy fluxes, which scale as the three-halves power of temperature. In the nonradiative regime, the immediate post-shock temperature T_i is given by

$$k_B T_i = \frac{2(\gamma - 1)}{(\gamma + 1)^2} \frac{A m_p}{(Z + 1)} u_s^2, \tag{1}$$

in which k_B is the Boltzmann constant, γ is the usual ratio of specific heats, A is the average atomic weight, m_p is the proton mass, and u_s is the shock velocity. The average number of electrons that share energy with each ion is Z, which can be a source of difficulty in two senses.

First, the shock heats the ions and then the electrons and ions equilibrate, so that in sufficiently low-density matter Z might be zero immediately following the density jump. Thus, in general, one may need to allow separate temperatures for ions and electrons. It is the electrons, though, that couple significantly to the radiation. Here for simplicity we assume immediate equilibration of ions and electrons. In practice, this means that the region just behind the shock (the jump in density and ion temperature) where ions and electrons equilibrate is ignored. The radiation from this equilibration zone increases as the fourth power of the electron temperature, so that most of the equilibration zone is not a significant contributor to the radiation dynamics.

Second, Z may be temperature-dependent if the medium is not fully ionized. This is particularly true for Xenon, a common material in laboratory radiative shock experiments. Here we use for Xenon the approximation $Z = 20\sqrt{T_i}$, with the initial post-shock electron (and ion) temperature T_i in keV. This can be derived from the Saha equation and thus assumes equilibrium (Drake, 2005). It converts Eq. (1) to a cubic equation relating temperature and shock velocity, easily dealt with in today's era of computational algebra.

One can then ask when radiative fluxes or pressure matter in shock-heated systems. This ultimately can be a complicated problem, as Eq. (1) breaks down when radiation pressures begin to become significant, and as the importance of radiative effects depends on the structure and opacity of the system. To obtain a preliminary assessment, we assume that Eq. (1) applies throughout, and consider optically thick conditions so that radiation temperatures equal material temperatures. This second assumption is valid for some astrophysical systems and some laboratory experiments, but not others. We explore this further in later sections. Under these assumptions, one can ask when the radiative flux, $F_R = \sigma T_i^4$, equals the material flux, $F_m = \rho_o c_v T_i u_s$, in which the upstream density is ρ_o, the heat capacity at constant volume is c_v, and the Stefan–Boltzmann constant is σ. One can also ask when the radiation pressure, $P_R = 4\sigma T_i^4/(3c)$ equals the material pressure, p.

One finds the results shown in Figure 1. Curves are shown for xenon and for CH as labeled. In the space to the right of each curve, the radiation parameter (F_R or p_R) exceeds the corresponding material parameter for the given material. One sees that there is roughly an order of magnitude in shock velocity over which radiation fluxes dominate the energy transport but radiation pressures are unimportant. As radiative conditions have been difficult to reach in experiments, this regime has been the most common one to date. In general, one sees that in optically thick systems shock velocities of tens to hundreds of km/s are required to reach radiative regimes.

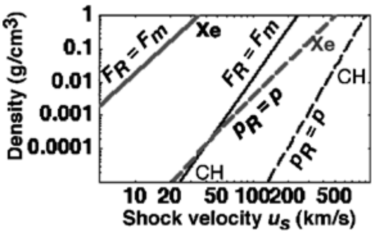

Figure 1. Regimes of radiative effects for optically thick media. The lines show boundaries, with stronger radiative effects to the right.

The shock velocities required to reach radiative regimes are larger in optically thin systems. The radiative flux from an optically thin system, for thermal emission, equals $\varepsilon F_{\mathrm{R}}$, where ε is the optical depth of the system. However, many optically thin systems, especially in astrophysics, produce primarily line emission, in which case ε would be an appropriate average over the spectral variation of the optical depth and thermal spectrum. Indeed, astrophysicists more often work with a "cooling function" to characterize the power radiated, and in optically thin astrophysical systems the optical depth decreases so rapidly with increasing temperature that the radiation tends to decrease as electron temperature T_{e} increases up to T_{e} of order 1 keV. Curiously, the shock velocity required for radiation fluxes to be significant is increased by finite optical depth into the range of >100 km/s, which is just where it is for laboratory experiments with foams or dense gas. Similarly, the radiation pressure in an optically thin system is $\varepsilon p_{\mathrm{R}}$, This makes the radiation-dominated regime genuinely difficult to reach in experiments. From Figure 1, one might seek to reach this regime at lower shock velocity by using low-density xenon gas. However, the size of the experiment must increase as some (regime-dependent) power of the decrease in density to hold the optical depth fixed. Claims that specific regimes have been reached in experiments with gas must be carefully justified.

2. Radiative Precursors and the Definition of the Shock Transition

We showed in Section 1 that a steady shock must reach some velocity if radiative energy fluxes are to exceed material energy fluxes, with the exact value dependent on conditions. By the time this occurs, the radiation is affecting the medium upstream of the region across which the rapid density increase takes place. There are two ways to think about this development. On the one hand, if one views the medium as infinite (measured in optical depths), then one may take the point of view that the radiation alters the structure of the shock transition, extending it in space over a (potentially large) number of radiation mean free paths. In this case one will speak of the "shock" as the entire region between a distant, undisturbed upstream region and a distant, steady-state downstream region.

On the other hand, it may be that the optical depth from the shock to "infinity" is small, as is the case in certain classes of astrophysical shocks. What is meant here is that the sum of radiation from distant sources and radiation returning to the shock from any upstream, shock-heated matter is negligible. Beyond this, the downstream region might not be optically thick, as is the case for example in the shocks driven by supernova remnants and in some short-lived experiments. Whenever the entire region affected by radiation from the shock is not well isolated from other influences, it seems more natural to speak of the "shock" as the region across which the rapid density increase takes place, often referred to as the viscous shock transition or viscous density jump. This use of "shock" is more common in discussions of optically thin astrophysical shocks. In this case, the interactions of the radiation and the surrounding medium affect both the upstream and the downstream conditions.

In either case, it is useful to discuss the development of radiative effects ahead of the shock, or of a radiative precursor, with three levels of sophistication. On the first level, one can say that a radiative precursor will be present when the flux of ionizing photons radiated ahead of the shock equals the flux of ionized neutral atoms incident on the shock (Keiter et al., 2002). This point of view is that one will certainly see heating of the upstream medium when all (or most) of the incoming atoms are ionized. This balance can be expressed by

$$2.3 \times 10^{23} \varepsilon_{\mathrm{u}} \varepsilon_{\mathrm{d}} \eta T_{\mathrm{i}}^{3} > \frac{\rho_o u_{\mathrm{s}}}{(A m_{\mathrm{p}})}, \tag{2}$$

where T_{i} is in eV, ρ_o is the mass density in g/cm^3, and η is the fraction of the photons that are ionizing. The emissivity (or the optical depth for small optical depth) of the downstream region is ε_{d} and the emissivity (equal to the absorptivity) of the upstream region is ε_{u}. The downstream emissivity determines what fraction of blackbody emission is actually produced and the upstream emissivity determines what fraction of these photons is absorbed. The corresponding threshold for a radiative precursor, using Eq. (1) for T_{i}, is $u_{\mathrm{s}} > 270\ [\rho_o/(\varepsilon_{\mathrm{d}}\varepsilon_{\mathrm{u}}\eta)]^{1/5}$ km/s. For shock velocities above 50 km/s, relevant to many laboratory experiments, nearly all the photons are ionizing. In laboratory experiments with dense gases or foams, both emissivities may be of order unity as well. For low-density astrophysical systems, with ρ_o of order 10^{-24} g/cm^3, obtaining a radiative precursor will require first of all that the post-shock temperature be high enough to obtain a sufficient fraction of ionizing photons and beyond that on the optical depth of the system.

On a second level, one can treat the precursor as a nonlinear radiation diffusion wave. Since such waves have a length-dependent velocity, one can argue that, in steady state, the precursor length ahead of a shock must be such that the diffusion wave velocity equals the shock velocity.(Mihalas and Weibel-Mihalas, 1999). A diffusion wave from a constant-temperature source has a length L that scales with time t as $L = K\sqrt{t}$, in which the coefficient K depends on the scaling of the material opacity with density and temperature, and thus does depend on the shock velocity. From the velocity matching argument just given one finds $L = K^2/(2u_{\mathrm{s}})$. One finds for example that in experiments with xenon the precursor becomes very large as the velocity increases above 10 km/s. However, the timescale required for the precursor to reach its steady state, found from the above to be $t = K^2/(4u_{\mathrm{s}}^2)$, also increases as the precursor length increases. The consequence is that real experiments, and even some astrophysical systems, may not establish a steady state precursor during their lifetime.

On a third level, one can consider finer details. An important issue in some contexts will be that many such shocks, in astrophysics and in experiments with low-density gases, are not planar. Spherical and even cylindrical models would be useful tools for these cases. For a specific experiment, one might consider the actual time dependence of the shock velocity and the consequent radiation source, as Fleury et al. have done (Fleury et al., 2002). Details beyond those treated by diffusion models can also be considered. Zel'dovich and Razier (1966), for example, argue that the leading edge of such a diffusion wave cannot be in equilibrium, with the result that there is a low-radiation-temperature foot ahead of the diffusion wave. However, this foot is decoupled from the material, and so is not a precursor in the sense that the state of the upstream medium is affected.

3. Regimes of Radiative Shocks

The category of radiative shocks includes a wide range of behavior. For example, in some regimes the density increase across the viscous transition and subsequent radiative cooling layer (if any) can be limited to values less than 10, while in other regimes it can be formally unbounded so long as the plasma is not radiation-dominated. (The γ of radiation is 4/3, so the density jump in any radiation-dominated plasma is 7.) One way to identify types of radiative shocks, and to classify their behavior, is to plot them in a space defined by the optical depth of the upstream and downstream regions. Figure 2 shows a qualitative depiction of this space. We next briefly discuss each of the four labeled regions.

3.1. Thick–thick shocks

In regime A, both the downstream and the upstream region are optically thick. This is the realm in which it makes the most sense to treat the viscous density increase and all the radiative effects as part of a single, extended, shock structure, and in which many of the features of this structure can be found from a theory that assumes the medium to be in LTE everywhere. This is also the realm that is treated at length

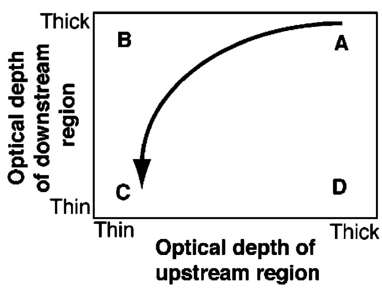

Figure 2. The types of radiative shocks can be identified in a space based on optical depth. The four regimes corresponding to the corners of this plot are discussed in the text. The curve shows the qualitative trajectory of a supernova blast wave.

in books that discuss radiation hydrodynamics, such as those by Zel'dovich and Razier (1966) and Mihalas and Weibel-Mihalas (1999) and discussed as well in some recent theory papers (Boireau et al., 2004; Bouquet et al., 2000). There is a definite limit on the density ratio of such shocks. For typical ideal gases with $\gamma \sim 5/3$, the density ratio never exceeds 7. (In some complex atoms at low temperatures, the ratio can be somewhat larger (Boireau et al., 2004).) In addition, in some regimes the density transition is continuous, with no localized jump. Astrophysical environments in which such shocks exist are necessarily both hot and dense. Shocks in stellar interiors are of this type, as are the blast waves within the exploding star in supernovae. Such shocks may also exist within some compact objects, but their treatment would have to be relativistic. It is difficult, however, to imagine laboratory experiments in this regime other than transiently and in special cases. One difficulty is that the precursor length increases so strongly with shock velocity that one could not produce a measurable precursor of finite length over any variation of experimental parameters. One ought to obtain a slower scaling of length with velocity in spherical geometry, but at the low densities where such experiments are straightforward the downstream region is far from being optically thick. (Note that a finite precursor is not necessarily optically thick in the sense that matters here; an optically thick precursor would have many optical depths between the density jump and the heat front.)

3.2. Thick–thin shocks

In regime B the downstream region is optically thick but the upstream region is thin. We discuss the theory of this regime in the next section. There is a cooling layer downstream of the viscous shock transition, followed by a steady downstream final state. This regime is common in experiments (Bouquet et al., 2004; Bozier et al., 1986; Fleury et al., 2002; Keiter et al., 2002; Koenig et al., 2001; Reighard et al., 2004), in which an optically thick piston (and in some cases optically thick shocked material) drives a radiative shock into a medium whose depth is small compared to the steady-state precursor length. The upstream medium is then quickly heated so that it becomes optically thin. Astrophysical examples of such systems include the blast wave in a supernova as it emerges from the star (Ensman and Burrows, 1992) and the accretion shocks produced during star formation (Calvet and Gullbring, 1998; Hujeirat and Papaloizou, 1998; Lamzin, 1999).

3.3. Thin–thin shocks

In regime C both downstream and upstream regions are optically thin. Such shocks are the most commonly observed in astrophysics, in part because they are easy to see (as the radiation escapes). Supernova remnant (SNR) shocks in dense enough environments are of this type – it is thought that Type II supernovae from red supergiants produce such conditions (Chevalier, 1997). Many shock–cloud interactions including some of those driven by SNR shocks are also of this type. Shocks that propagate up jets (or are driven by clumps propagating up jets) may be of this type (Hartigan, 2003). In such shocks, the entire downstream region is a radiative cooling layer, and it ends (in large enough systems) when the downstream temperature reaches a value determined by local sources and losses of energy rather than by the shock. The density increase associated with such shocks is formally unbounded in the sense that it is limited only by external factors, such as the compression of an initially negligible magnetic field or the presence of a limiting temperature due to other energy sources. These shocks have much in common with the radiative phase of old supernova remnants (Blondin et al., 1998), which occurs when an SNR shock cools enough that the slope of the radiative flux (astrophysicists would say the cooling function) with temperature changes from positive to negative, enabling the entire shocked region to rapidly radiate away its energy and the density to increase by orders of magnitude. Some experiments, with shocks in sufficiently low-density gases, may produce these conditions (see, for example (Grun et al., 1991)), but this question deserves more detailed examination than we can provide here. We discuss the theory of these shocks briefly in the next section. It is also discussed by Shu (1992).

3.4. Thin–thick shocks

Regime D is difficult to access, and perhaps is only seen in a transient sense. If the upstream region is optically thick, then the downstream, shocked material is likely to become optically thick as it accumulates and radiatively cools. Ignoring the increase in optical depth, such a system could produce a very dense shocked layer as it continued to lose energy in the downstream direction. Two transient examples are certain shock–cloud collisions and certain experiments. A shock–cloud collision in which the cloud was dense enough and large enough to be optically thick for some time would be of this type. The collision of SNR 1987A with its inner “ring” may be of this type (Borkowski et al., 1997), especially if the ring turns out to be a disk. An experiment might be in this regime while a hot, thin layer of gas drives a shock through a much larger volume of gas, as seems to be the case in some experiments done with xenon gas at low densities. (See for example the papers by F. Hansen and by T. Ditmire in this issue.) All these cases seem likely to transition to the thin–thin regime if driven harder or longer, and they may never develop a thick upstream region in the sense discussed above.

4. Structure of the Radiative Cooling Layer

In shocks with an optically thin upstream region, the structure of the radiative cooling layer behind the shock is of interest. One would like to understand its size,

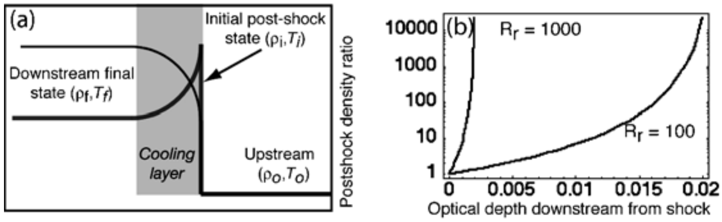

Figure 3. (a) Structure of the radiative cooling layer. (b) Density profiles for a thin–thin shock.

its shape, and the maximum density that is reached. For this purpose, one can work with a fluid theory including radiation transport. However, for the radiation one cannot assume LTE because the material temperature turns out to change on scales much smaller than a radiation mean-free-path.

Under these assumptions, the structure of the cooling layer is shown in Figure 3(a). There is some upstream density, pressure and temperature. The upstream region has perhaps been heated by the precursor but is not evolving further in the optically thin limit, and contributes a negligible radiation heat flux. At the viscous shock, there is a density jump and an increase in temperature, with the immediate post-shock (and post-electron–ion-equilibration) temperature given by Eq. (1). Downstream from this is the cooling layer, whose behavior we wish to calculate. The cooling layer ends when the temperature and density reach their final values, T_f and ρ_f, respectively. If the final temperature is nonzero, then the downstream radiation from the cooling layer must balance the upstream radiation from the steady downstream layer, which is σT_f^4. This upstream radiation flux must also equal half the loss of downstream material energy flux between the shock and the final downstream state, as this is the only source of energy for the radiation from the cooling layer (which radiates both upstream and downstream). This flux balance condition can be used to determine the final post-shock density and temperature.

The equations that describe the evolution of the cooling layer are as follows. The fluid energy equation, in steady state, is

$$\nabla \cdot \left[\rho \mathbf{u}\left(\varepsilon + \frac{u^2}{2}\right) + p\mathbf{u}\right] = -\nabla \cdot \mathbf{F}_R, \tag{3}$$

in which the velocity is $\mathbf{u}$, the density is ρ, the pressure is p, and the internal energy ε will be taken to equal $p/(\gamma - 1)$. The radiation flux is $\mathbf{F}_R$. Using the momentum and continuity equations, one can express the equation of state for some location, relative to the immediate post-shock density ρ_i and temperature T_i, as

$$\frac{T}{T_i} = \frac{\gamma + 1}{2}\frac{\rho_i}{\rho}\left[1 - \frac{\gamma - 1}{\gamma + 1}\frac{\rho_i}{\rho}\right]. \tag{4}$$

We express the radiation loss in the "transport" approximation corresponding to isotropic scattering, taking $-\nabla \cdot \mathbf{F}_{\mathrm{R}} = 4\pi\kappa(B - J_{\mathrm{R}})$, in which κ is a frequency-averaged absorption coefficient, approximately equal to the Planck mean opacity, B is the intensity of radiation within a black body at the local electron temperature, and J_{R} is the angularly averaged radiation intensity. From these relations one can obtain

$$\left[1 - \frac{(\gamma - 1)}{\gamma}\frac{\rho_{\mathrm{i}}}{\rho}\right]\frac{\partial}{\partial \tau}\left(\frac{\rho_{\mathrm{i}}}{\rho}\right) = -R_r\left(\left(\frac{T}{T_{\mathrm{i}}}\right)^{4-n} - \left(\frac{\pi J_{\mathrm{R}}}{\sigma T_{\mathrm{i}}^4}\right)\left(\frac{T}{T_{\mathrm{i}}}\right)^{-n}\right)\left(\frac{\rho_i}{\rho}\right)^m \tag{5}$$

in which the optical depth variable $\tau = z\kappa_{\mathrm{i}}$, with κ_{i} being the value of the opacity at T_{i} and ρ_{i}. The opacity is taken to vary as powers of $1/T$ and ρ, with exponents n and m, respectively. The parameter that characterizes the importance of the radiation is R_r, given by

$$R_r = \frac{4(\gamma + 1)}{\gamma}\frac{\sigma T_{\mathrm{i}}^4}{\rho_o u_{\mathrm{s}}^3} \tag{6}$$

and approximately equal to the ratio of upstream energy flux produced by a black-body at temperature T_{i} to the energy flux of heated material downstream from the shock. When this exceeds roughly unity, there evidently must be significant cooling. The quantity J_{R} in Eq. (5) is the radiation intensity within the final downstream layer, and equals $\sigma T_{\mathrm{f}}^4/\pi$. This quantity is constant through the cooling layer, as it is unaffected by changes in the direction of the radiation from the cooling layer. Using Eq. (4), one can integrate Eq. (5) for the profile of the density, from which other quantities can be calculated.

Figure 3(b) shows results of this calculation for the thin–thin case. Here $n = 4/3$ and $m = 2$, which is the correct density dependence and a plausible temperature dependence for experiments with gas, though too weak for astrophysical cases. There is no minimum downstream temperature here, and so the temperature would decrease to zero and the density to infinity. The density ratio shown is the post-shock density increase. The total density increase is larger by the factor produced at the viscous jump, which is 7 here as $\gamma = 4/3$ was used. (This value of γ, or something near it, is not only the radiation-dominated value but is also a good estimate for an ionizing plasma.)

In a system for which enough material accumulates downstream to produce a steady final state, the properties of this state are determined from the overall energy flux balance, as is discussed above. The final state becomes only a function of R_r (and γ), and has the dependence shown in Figure 4. As in the optically thin case of Figure 3(b), the scale of the density increase with optical depth depends inversely on R_r. The shape of the cooling layer, in this simple model, depends on the power of density assumed in the opacity. If the opacity is taken to be independent of density, as can occur in some dense materials, then the shape of the curve becomes convex [as opposed to the concave behavior seen in Figure 3(b)]. In simulations

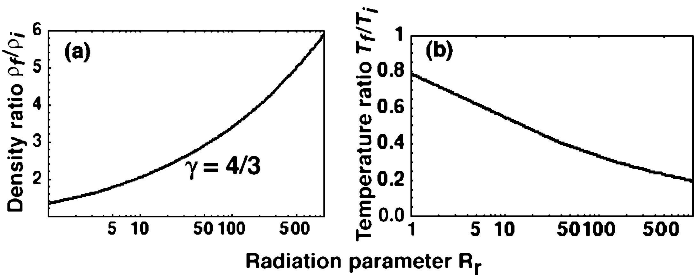

Figure 4. Post shock compression and cooling for an optically thick downstream layer. Results are shown for $\gamma = 4/3$.

of experiments, we see various shapes, sometimes evolving in time. We do not yet understand all the controlling factors for this.

5. Conclusion

We have shown that the detailed properties of radiative shocks depend upon the regime within which they develop, and that this regime can be conveniently characterized in terms of the optical depth of the upstream and downstream regions. At present one might say that shocks with thick upstream and thick downstream regions have been the most explored theoretically, that shocks with thin upstream and thick downstream regions have been the most observed experimentally, and that shocks with thin upstream and thin downstream regions have been the most observed in astrophysics. Yet one can do theory for all the regions and astrophysical examples exist for all regions. So the challenge for various experiments is to access these different regimes and to gain a clear understanding, and clear evidence, regarding the regime studied in any specific experiment.

Acknowledgments

The author acknowledges useful conversations on this subject with S. Bouquet, D. Ryutov, and M. Hermann. This research was sponsored by the National Nuclear Security Administration under the Stewardship Science Academic Alliances program through DOE Research Grant DE-FG03–99DP00284 and other grants and contracts.

References

Blondin, J.M., Wright, E.B., Borkowski, K.J. and Reynolds, S.P.: 1998, *ApJ* **500**, 342.

Boireau, L., Clique, C. and Bouquet, S.: 2004, Radiative Shocks in Low-Pressure Gases, Inertial Fusion Science and Applications, Monterey, CA, American Nuclear Society.

Borkowski, K.J., Blondin, J.M. and McCray, R.: 1997, *ApJ* **477**, 281.
Bouquet, S. et al.: 2004, *Phys. Rev. Lett.* **92**, 22500/1.
Bouquet, S., Teyssier, R. and Chieze, J.P.: 2000, *ApJS* **127**, 245.
Bozier, J.C., Thiell, G., Le-Breton, J.P., Azra, S., Decroisette, M. and Schirmann, D.: 1986, *Phys. Rev. Lett.* **57**, 1304.
Calvet, N. and Gullbring, E.: 1998, *ApJ* **509**, 802.
Chevalier, R.A.: 1997, *Science* **276**, 1374.
Drake, R.P.: 2005, *Phys. Plasmas*, in preparation.
Ensman, L. and Burrows, A.: 1992, *ApJ* **393**, 742.
Fleury, X. et al.: 2002, *Laser Part. Beams* **20**, 263.
Grun, J., Stamper, J., Manka, C., Resnick, J., Burris, R., Crawford, J. and Ripin, B.H.: 1991, *Phys. Rev. Lett.* **66**, 2738.
Hartigan, P.: 2003, *Ap&SS* **287**, 111.
Hujeirat, A. and Papaloizou, J.C.B.: 1998, A&A **340**, 593.
Keiter, P.A., Drake, R.P., Perry, T.S., Robey, H.F., Remington, B.A., Iglesias, C.A., Wallace, R.J. and Knauer, J.: 2002, *Phys. Rev. Lett.* **89**, 165003/1.
Koenig, M. et al.: 2001, Radiative shock experiment using high power laser, *Shock Compression of Condensed Matter 2001*, American Institute of Physics **620**, pt2, 1367.
Lamzin, S.A.: 1999, *A&SS* **261**, 137.
Mihalas, D. and Weibel-Mihalas, B.: 1999, *Foundations of Radiation Hydrodynamics*, Dover, Mineola.
Reighard, A.B. et al.: 2004, *Inertial Fusion and Science Applications*, Monterey CA, American Nuclear Society.
Shu, F.H.: 1992, *The Physics of Astrophysics: Gas Dynamics*, Vol. II, University Science Books, Mill Valley, CA.
Zeldovich, Y.B. and Razier, Y.P.: 1966, *Physics of Shock Waves and High-Temperature Hydrodynamic Phenomena*, Vol. 1, Academic Press, New York.

LABORATORY SIMULATIONS OF SUPERNOVA SHOCKWAVE PROPAGATION

J.F. HANSEN[1], M.J. EDWARDS[1], D. FROULA[1], G. GREGORI[1], A. EDENS[2] and T. DITMIRE[2]

[1]*Lawrence Livermore National Laboratory, Livermore, CA, USA; E-mail: hansen46@llnl.gov*
[2]*University of Texas at Austin, Austin, TX, USA*

(Received 7 April 2004; accepted 22 July 2004)

Abstract. Supernovae launch spherical shocks into the circumstellar medium (CSM). These shocks have high Mach numbers and may be radiative. We have created similar shocks in the laboratory by focusing laser pulses onto the tip of a solid pin surrounded by ambient gas; ablated material from the pin rapidly expands and launches a shock through the surrounding gas. Laser pulses were typically 5 ns in duration with ablative energies ranging from 1–150 J. Shocks in ambient gas pressures of $\sim$1 kPa were observed at spatial scales of up to 5 cm using optical cameras with schlieren. Emission spectroscopy data were obtained to infer electron temperatures ($<$10 eV).

In this experiment we have observed a new phenomena; at the edge of the radiatively heated gas ahead of the shock, a second shock forms. The two expanding shocks are simultaneously visible for a time, until the original shock stalls from running into the heated gas. The second shock remains visible and continues to expand. A minimum condition for the formation of the second shock is that the original shock is super-critical, i.e., the temperature distribution ahead of the original shock has an inflexion point. In a non-radiative control experiment the second shock does not form. We hypothesize that a second shock could form in the astrophysical case, possibly in radiative supernova remnants such as SN1993J, or in shock-CSM interaction.

Keywords: shock, radiative, super critical, interstellar matter, xenon, Taylor, Sedov, Barenblatt, Mach

1. Introduction

Interstellar space consists of a tenuous plasma capable of propagating shocks over great distances. Shocks originate in supernova (SN) explosions (Müller et al., 1991; Reed et al., 1995; Sonneborn et al., 1998; Remington et al., 1999; Bartel et al., 2000) and other astrophysical phenomena (e.g., T Tauri stars and stellar winds) and are important to understand as they mix up interstellar matter and thus affect mass-loading, stellar formation (McKee and Drain, 1991; Allen and Burton, 1993; Klein and Woods, 1998) and the history of the Milky Way and other galaxies. The shocks have high Mach numbers and can be strongly radiative (Blondin, 1998). Until recently, these properties have not been easily attainable in laboratories, but using high-power lasers, similar shocks can be now created and studied experimentally (Remington et al., 1999; Bozier et al., 1986; Grun et al., 1991; Ryutov et al.,

Astrophysics and Space Science **298:** 61–67, 2005.

1999; Shigemori et al., 2000; Robey et al., 2001; Fleury et al., 2002; Keiter et al., 2002).

An SN shock expanding through interstellar space sweeps up interstellar material, most of which ends up in a shell just behind the shock. Once more mass has been swept up by the shock than what was initially present, the shock could be regarded as without characteristic length or time scales, and so one would expect the well-known self-similar motion of a Taylor–Sedov blast wave, $r_s \propto t^{2/5}$, where r_s is shock radius and t is time (Taylor, 1950; Sedov, 1959; Zeldovich and Raizer, 1966). If radiation removes energy from the shock in an optically thin environment – and SN shocks can be strongly radiative – analytical and numerical studies predict a slower shock expansion, such as $r_s \propto t^{2/7}$ ("pressure driven snow-plow") and $r_s \propto t^{1/4}$ ("momentum driven snow-plow"; the shock is simply coasting) (Blondin et al., 1998; McKee and Ostriker, 1977). Furthermore, a radiative shock is expected to "stall" (vanish) sooner than a non-radiative shock, as its energy is lost.

We have conducted experiments at the Janus laser at the Lawrence Livermore National Laboratory in California, comparing the shock expansion for non-radiative and radiative shocks, and we report here on our findings, including a new phenomena that has not previously been observed.

2. Experimental Set-Up

We create spherically expanding blast waves in the following fashion: a high-power infrared pulsed laser (1064 nm wavelength) is focused onto the tip of a solid (stainless steel) pin surrounded by an ambient gas typically at a pressure of $\sim$1 kPa. The laser pulse (5 ns duration and energy ranging from 1 to 150 J) ablates the pin and rapid expansion of ablated material shocks the ambient gas. The initial shock travels radially outward from the pin, collecting ambient gas in a shell immediately behind the shock front. The blast wave velocity drops as more and more of the ambient gas is accumulated and set in motion by the passing shock.

3. Diagnostics

We obtain image and spectrometer data of the shocks to deduce blast wave radius as a function of time and temperature profiles across the shock. To image a blast wave on spatial scales up to $\sim$5 cm, we use two lenses in a telescope configuration and a gated, single-frame, high-speed CCD camera (2 ns gate), along with a low energy, green laser pulse ($\lambda = 532$ nm wavelength) as a backlighter. Blast wave radius as a function of time is obtained from schlieren images. A spectrometer is used to infer electron temperatures ahead of and behind the blast wave.

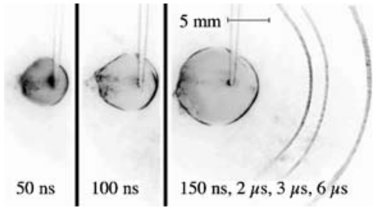

Figure 1. Blast wave expansion through nitrogen gas (1.3 kPa) at times $t = 150$ ns to 6 μs after an ablative laser pulse (energy $E = 10$ J, duration 5 ns) is focused on a solid pin (visible in images, pointed down). The laser pulse was incident from the left. The shock grows as a Taylor–Sedov blast wave. The image to the right ($t = 150$ ns to 6 μs) is a composite of four images (with overlapping pin locations).

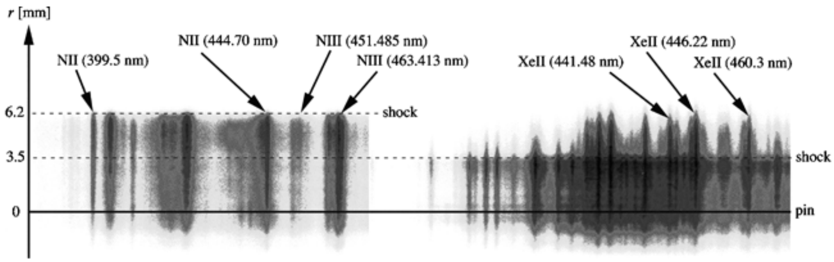

Figure 2. Spectra for nitrogen (left) and xenon (right) at $t = 150$ ns. The location of the pin is marked with a solid line. The shock locations, as obtained from schlieren images, are indicated by dashed lines at radii $r = 6.2$ mm for nitrogen and $r = 3.5$ mm for xenon.

4. Results with Nitrogen as the Ambient Gas

Schlieren images were obtained from 5 ns up to 35 μs after the initial laser pulse. Examples of images using nitrogen as the ambient gas can be seen in Figure 1. In each image, the laser is incident from the left. The pin is clearly visible, as is the expanding blast wave. After an initial, brief, non-self similar phase, the shock expansion settles into the Taylor–Sedov relationship for a blast wave, $r_s \propto (\frac{E}{\rho_0})^{\frac{1}{5}} t^{\frac{2}{5}}$, where r_s is the shock radius, t is time, E is the ablative laser energy, and ρ_0 is the density of the ambient gas.

Emission spectroscopy data in the near ultraviolet range was readily obtained at and behind the blast wave in nitrogen, but no readings discernible from noise were possible ahead of the shock. Figure 2 shows spectra taken at a time $t = 150$ ns after the initial laser pulse ($E = 10$ J), with electron temperatures in the range 4–7 eV at and behind the shock.

5. Results with Xenon as the Ambient Gas

With its higher atomic mass number, xenon radiates more strongly than nitrogen. Therefore, we expected to see a slower shock expansion in xenon, and also to

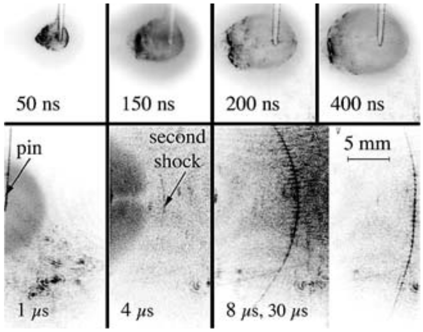

Figure 3. Blast wave expansion through ambient Xe gas (1.3 kPa) at times $t = 50$ ns to 30 μ s after an ablative laser pulse (energy $E = 10$ J, duration 5 ns) is focused on a solid pin (visible in images, pointed down; pin location in bottom row of images is at the left edge of each image). The laser pulse was incident from the left. The initial shock is strongly radiative (super-critical) and preheats the ambient gas. At $t = 150$ ns both the initial shock and the preheated gas ahead of it are clearly visible. At $t \approx 1$ μs the initial shock begins to stall, and the shock front is no longer sharp. At $t \approx 4$ μs a second shock pops out (located at tip of arrow), ahead of the initial shock. The initial shock stalls, while the second shock expands like a Taylor–Sedov blast wave. The final image ($t = 8$ μs, 30 μs) is a composite of two images (with overlapping pin locations).

observe the shock stalling. Examples of images obtained with xenon as the ambient gas are shown Figure 3.

There are several notable differences compared to the images of shocks in nitrogen, all pointing to the radiative nature of the shocks in xenon: (a) plasma emission from pre-heated gas, that is gas heated by the radiation from the shock, is clearly visible as a glow surrounding the shock at early times ($t \lesssim 400$ ns). Spectroscopy data (see Figure 2) confirm that the temperature immediately ahead of the shock is roughly the same as behind the shock. A few millimeters in front of the shock the temperature then drops sharply (to noise levels). (For comparison to the nitrogen case, at $t = 150$ ns and a laser energy of $E = 10$ J the temperatures in xenon ranged from 2 to 5 eV.) (b) As expected, the shock rapidly becomes diffuse and stalls, as seen in images from $t \approx 1$ to 4 μs. (c) Another shock forms ahead of the initial shock. This second shock is a new phenomena that has not previously been discussed in literature. It is not surrounded by a glow of pre-heated gas, and it continues to propagate long after the initial shock has vanished.

Measurements of shock radii versus time, reproduced in Figure 4, surprisingly revealed that the (initial) shock in xenon follows a Taylor–Sedov-like time dependence, despite being radiative. The second shock also grows Taylor–Sedov like.

6. Discussion

In xenon, the creation of a second shock ahead of the initial shock is a direct consequence of the initial shock being radiative. Figure 5 (computed by the LASNEX

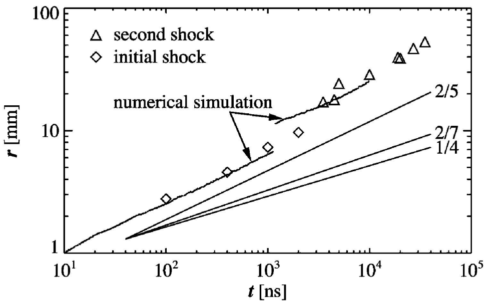

Figure 4. Plot of shock radius as a function of time as measured in the experiment, compared to a numerical simulation and to analytical estimates of shock propagation. The 1D numerical simulation by the LASNEX code shows the largest radius at which the compression $\eta > 1.25$. The analytical estimates are represented by the three (displaced) lines with slopes $p = \frac{2}{5}, \frac{2}{7}$, and $\frac{1}{4}$.

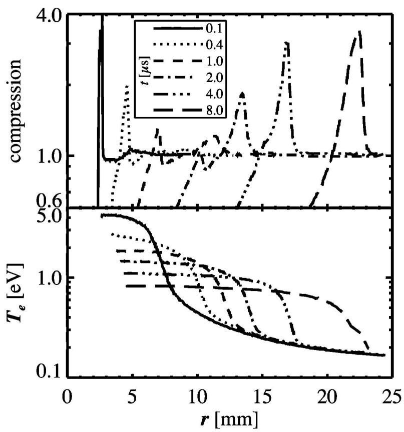

Figure 5. Numerical simulation showing compression η (upper graph) and electron temperature (lower graph) as a function of radius for six different times. At $t = 100$ ns the initial shock has $\eta \approx 6$. Note the initial shock dissipating and the second shock being born at the radiative heat wave front.

code (Zimmerman and Kruer, 1975) in 1D) shows a plot of compression versus radius in which both shocks are clearly identifiable. The initial shock weakens over time; the second shock grows stronger. In the plot of electron temperature versus radius, the temperature distribution is that of a supercritical shock, with a radiative heat wave moving toward larger radii. The high temperature ahead of the initial shock makes the shock Mach number quite low, resulting in a rapid weakening and shock stall, as can be seen in the compression plot. A vertical comparison of the two plots in Figure 5 shows that the second shock is born at the sharp front of the radiative heat wave. This is confirmed in a second LASNEX calculation where we set up a temperature distribution identical to that in Figure 5, but excluded the initial shock; with time a shock essentially identical to the second shock in Figure 5 forms. A third LASNEX calculation with a piston instead of the laser as the initial energy source develops the same temperature distribution and the same second shock, confirming details of initial conditions are not important.

Mathematically, we can make an estimate for where the second shock forms by considering equations for conservation of mass $\rho_1 u_1 = \rho_2 u_2$ and momentum $p_1 + \rho_1 u_1^2 = p_2 + \rho_2 u_2^2$ in the lab frame of the radiative heat wave front, where subscript 1 denotes the region ahead of the front, and subscript 2 denotes the region behind it. Combining the equations assuming $p_1 \approx 0$ and $p_2 = \rho_2 c_2^2$, where c_2 is the sound speed, we find that a real solution of the compression $\eta \equiv \rho_2/\rho_1$ requires the mixed Mach number $M = u_1/c_2 \geq 2$, so we would expect that the second shock should form at the radiative heat wave front when the velocity of the front drops below Mach 2 (analogous to when a blast wave forms ahead of a fireball (Zeldovich and Raizer, 1966; Mihalas and Mihalas, 1984)).

To make a numerical comparison to the experiment, we thus need to know the velocity of the radiative heat wave front and the sound speed (or temperature) immediately behind the front. Assuming that we can write the radiative conductivity of the ambient gas as $\chi = \chi_0 \rho^{\mathrm{a}} T^{\mathrm{b}}$, then the temperature $T(r, t)$ and the location $r_h(t)$ of the radiative heat wave front is given by Barenblatt's solution (Barenblatt, 1979; Reinicke and Vehn, 1991). Using values for our experiment in xenon, $E = 10$ J, $\rho_0 = 78$ g/m^3, $\gamma = 1.2$, and $\chi = 10^{-44}\rho^{-2.2}T^{-10}$ in SI-units, we find that the Mach number at the heat front $M(r_h, t) = \frac{dr_h(t)}{dt}\sqrt{\frac{m_0}{RT(r_h,t)}}$ drops to Mach 2 when $r_h \approx 10$ mm, consistent with what was actually observed ($\approx$12 mm).

Despite its radiative nature, for reasons that are not fully understood, the shock in xenon still follows the Taylor–Sedov relationship, $r_{\mathrm{s}} \propto t^p$ with $p = \frac{2}{5}$. This may be because most of the radiative losses occurred very early in time (at $t \lesssim 50$ ns), or it may be that the radiative effects (causing $p \to \frac{2}{7}$, or $p \to \frac{1}{4}$) and the effect of the shock stalling (causing $p \to 1$) balance each other so that $p \approx \frac{2}{5}$ by a fortuitous circumstance.

7. Conclusion

We have conducted experiments with blast waves traveling through ambient gas, intended to simulate supernova-like shocks. In nitrogen, radiative effects are minimal and the shock expands as a Taylor–Sedov blast wave. In xenon, the shock is strongly radiative, heating the ambient gas ahead of the (supercritical) shock. The loss of energy through radiation and a comparatively low Mach number cause the shock to stall much sooner than the shock in nitrogen. We also report on the first experimental observation of a second shock forming ahead of the initial shock. We show by numerical simulation that the second shock is created at and from the temperature gradient at the front of the slowing radiative heat wave ahead of the initial shock. The second shock is formed at a location that agrees reasonably well with an analytic estimate.

Acknowledgments

We thank Dwight Price and the staff at the Janus facility for their valuable assistance.

This work was performed under the auspices of the U. S. Department of Energy by the University of California, Lawrence Livermore National Laboratory under Contract No. W-7405-Eng-48.

References

Müller, E., Fryxell, B. and Arnett, D.: 1991, *A&A* **251**, 505.

Reed, J.I., Hester, J.J., Fabian, A.C. and Winkler, P.F.: 1995, *ApJ* **440**, 706.

Sonneborn, G., Pun, C.S.J., Kimble, R.A., Gull, T.R., Lundqvist, P., McCray, R., Plait, P., Boggess, A., Bowers, C.W., Danks, A.C. et al.: 1998, *ApJ Lett.* **492**, L139.

Remington, B.A., Arnett, D., Drake, R.P. and Takabe, H.: 1999, *Science* **284**, 1488.

Bartel, N., Bietenholz, M.F., Rupen, M.P., Beasley, A.J., Graham, D.A., Altunin, V.I., Venturi, T., Umana, G., Cannon, W.H. and Conway, J.E.: 2000, *Science* **287**, 112.

McKee, C.F. and Draine, B.T.: 1991, *Science* **252**, 397.

Allen, D.A. and Burton, M.G.: 1993, *Nature* **363**, 54.

Klein, R.I. and Woods, D.T.: 1998, *ApJ* **497**, 777.

Blondin, J.M., Wright, E.B., Borkowski, K.J. and Reynolds, S.P.: 1998, *ApJ* **500**, 342.

Bozier, J.C., Thiell, G., LeBreton, J.P., Azra, S., Decroisette, M. and Schirmann, D.: 1986, *Phys. Rev. Lett.* **57**, 1304.

Grun, J., Stamper, J., Manka, C., Resnick, J., Burris, R., Crawford, J. and Ripin, B.H.: 1991, *Phys. Rev. Lett.* **66**, 2738.

Ryutov, D., Drake, R.P., Kane, J., Liang, E., Remington, B.A. and Wood-Vasey, W.M.: 1999, *ApJ* **518**, 821.

Shigemori, K., Ditmire, T., Remington, B.A., Yanovksy, V., Ryutov, D., Estabrook, K.G., Edwards, M.J., MacKinnon, A.J., Rubenchik, A.M., Keilty, K.A. and Liang, E.: 2000, *ApJ* **533**, 159.

Robey, H.F., Kane, J.O., Remington, B.A., Drake, R.P., Hurricane, O.A., Louis, H., Wallace, R.J., Knauer, J., Keiter, P., Arnett, D. and Ryutov, D.D.: 2001, *Phys. Plasmas* **8**, 2446.

Fleury, X., Bouquet, S., Stehle, C., Koenig, M., Batani, D., Benuzzi-Mounaix, A., Chieze, J.-P., Grandjouan, N., Grenier, J., Hall, T. et al.: 2002, *Laser Part. Beams* **20**, 263.

Keiter, P.A., Drake, R.P., Perry, T.S., Robey, H.F., Remington, B.A., Iglesias, C.A., Wallace, R.J. and Knauer, J.: 2002, *Phys. Rev. Lett.* **89**, 165003.

Taylor, G.I.: 1950, *Proc. R. Soc. London A* **201**, 159.

Sedov, L.I.: 1959, *Similarity and Dimensional Methods in Mechanics*, Academic Press, New York.

Zeldovich, Y.B. and Raizer, Y.P.: 1966, *Physics of Shock Waves and High-Temperature Hydrodynamic Phenomena*, Academic Press, New York.

McKee, C.F. and Ostriker, J.P.: 1977, *ApJ* **218**, 148.

Zimmerman, G.B. and Kruer, W.L.: 1975, *Comments Plasma Phys. Controlled Fusion* **2**, 51.

Mihalas, D. and Mihalas, B.W.: 1984, *Foundations of Radiation Hydrodynamics*, Oxford University Press, Oxford.

Barenblatt, G.I.: 1979, *Similarity, Self-Similarity and Intermediate Asymptotics*, Consultants Bureau, New York.

Reinicke, P. and Meyer-ter-Vehn, J.: 1991, *Phys. Fluids A* **3**, 1807.

RADIATIVE SHOCK EXPERIMENTS AT LULI

M. KOENIG[1], T. VINCI[1], A. BENUZZI-MOUNAIX[1], S. LEPAPE[1], N. OZAKI[1,7], S. BOUQUET[2], L. BOIREAU[2,3], S. LEYGNAC[3], C. MICHAUT[3], C. STEHLE[3], J.-P. CHIÈZE[4], D. BATANI[5], T. HALL[6], K. TANAKA[7] and M. YOSHIDA[8]

[1]*Laboratoire pour l'Utilisation des Lasers Intenses, CNRS-CEA-Université Paris VI-Ecole Polytechnique, Palaiseau, France*

[2]*Département de Physique Théorique et Appliquée, CEA-DIF, BP 12, Bruyères-le-Châtel, France*

[3]*Laboratoire de l'Univers et de ses Théories, Observatoire de Paris, Meudon, France*

[4]*CEA – Saclay, DSM/DAPNIA and DSM/DRECAM, Gif-sur-Yvette Cedex, France*

[5]*Dipartimento di Fisica 'G. Occhialini', Università di Milano-Bicocca and INFM, Piazza della Scienza 3, Milano, Italy*

[6]*University of Essex, Colchester CO4 3SQ, United Kingdom*

[7]*Institute of Laser Engineering and the Graduate School of Engineering, Osaka University, Osaka, Japan*

[8]*National Institute of Advanced Science and Technology (AIST), Tsukuba, Japan*

(Received 21 April 2004; accepted 6 June 2004)

Abstract. We present the set-up and the results of a supercritical radiative shock experiment performed with the LULI nanosecond laser facility. Using specific designed targets filled with xenon gaz at low pressure, the propagation of a strong shock with a radiative precursor is evidenced. The main measured quantities related to the shock (electronic density, propagation velocities, temperature, radial dimension) are presented and compared with various numerical simulations.

Keywords: radiative shocks, laser plasmas

Radiative hydrodynamic processes (Mihalas and Mihalas, 1984; Zeldovich and Raizer, 1967) are very important in several physics areas such as ICF (Lindl, 1995) and astrophysics (Drake et al., 2002). Recently, several experiments have been performed to simulate radiative hydrodynamic flows of astrophysical interest like jets or blast waves (Edwards et al., 2001; Grun et al., 1991; Lebedev et al., 2002) and radiative shocks (Bouquet et al., 2004; Bozier et al., 1986; Keiter et al., 2002). In most astrophysical environments, a radiative shock (RS) is essentially characterized by: 1) a hot ionized precursor in the upstream material, heated by radiation coming from the high temperature shocked gas, 2) a shock front followed by a short extension region where relaxation between ions, electrons and photons takes place, and 3) a recombination zone in the downstream flow. In the vicinity of the shock and, provided its velocity is sufficiently high, $D_{\rm cr}$, the precursor is heated up to a temperature $T_{\rm cr}$ equal to that of the shocked material. Shocks satisfying $D > D_{\rm cr}$ are often called "supercritical" (Zeldovich and Raizer, 1967). The understanding of the properties and structures of these shocks are very sensitive to the treatment of radiation transport and to its coupling with hydrodynamics. Consequently, laboratory experiments are relevant benchmarks for modeling as well as for validating theoretical predictions.

In order to be in the radiative regime, we first designed our target characteristics according to semi-analytical models such as the supercritical shock (Zeldovich and Raizer, 1967) or the steady radiative shock (Boireau et al., 2003; Bouquet et al., 2000). The critical velocity, D_{cr} , above which a radiative shock enters the supercritical regime is given by power laws $D_{\mathrm{cr}} \approx \rho^a/A^b$ where ρ and A are mass density and atomic number respectively.

To strengthen radiative effects against thermal ones, a low-density material, with high atomic mass, is suitable to achieve radiative regime. Previous experiments, have shown that shock velocities about 50 km/s in a low density medium are achievable with the LULI nanosecond laser facility (Koenig et al., 1999). According to the power laws mentioned above it is, therefore, quite appropriate to generate supercritical shocks in low density xenon gas (0.1 and 0.2 bar). The quantitative design of the whole experiment has been carried out with radiation hydro-codes. An optimized three layer-pusher drives the shock into the xenon gas cell. This pusher is made of a 2 μm CH ablator, a 3 μm Ti X-rays screen and a 25 μm CH foam accelerator.

Our main goals regarding the experimental diagnostics were to focus on the time-dependent properties of the radiative shock and precursor. It concerns namely piston and shock velocities (U_{p}, U_{s}), precursor velocity (V_{p}), electron density in the precursor (N_{e}), their radial extension (R) and the electron temperature (T_{e}). In order to fulfilled these goals, we implemented several diagnostics as shown in Figure 1. The self-emission diagnostic records time evolution of the emitted light from the rear surface of the target and gives the temperature (T_{e}). Two VISAR (Celliers et al., 1998), with different sensitivities measure the shock velocity in the foam and/or the foam-xenon interface velocity (U_{p}). Finally, a Mach-Zehnder interferometer is

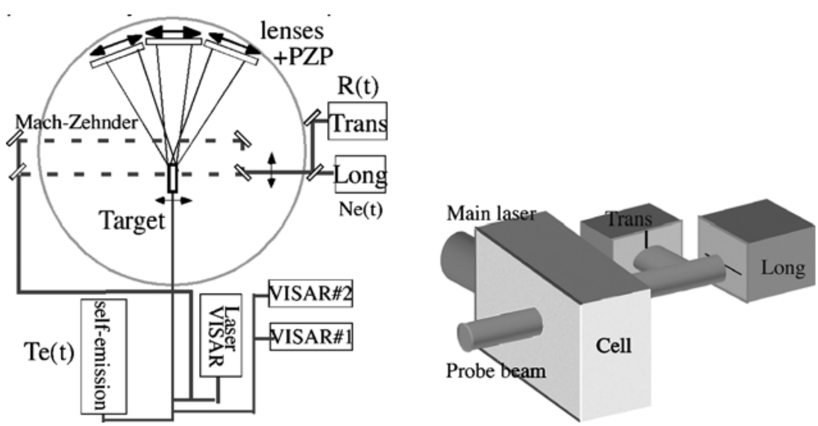

Figure 1. Experimental set-up, gaz cell and diagnostics.

implemented to determine U_s, V_p and N_e. Two streak cameras are used, one looking at the fringes longitudinally (LONG), the other one providing a transverse image at a given position in the gas (TRANS) leading to the determination of the radius R (Figure 1b). Electronic densities ranging from 10^{18} to 10^{20} cm^{-3} in the precursor can be inferred from the interferometer. With the VISAR, we measured on some shots the piston velocity U_p (foam/gas interface), which drives the shock in the xenon as pointed out in recent papers (Bouquet et al., 2004).

From measured U_p, using SESAME EOS tables (1992) we deduced the shock velocity U_s which mean value was roughly 67 km/s with modulations at the shock breakout during 1 ns (due to a reflection on the pusher interfaces) and a smooth decaying shock after (Figure 2). The computed velocities are in good agreement with this experimental value.

From the Mach-Zehnder interferometer pattern (Figure 3a), one may distinguish two different perturbations propagating in the gas. The first one (dashed curve) separates the region where the electronic density is high enough to reflect or absorb

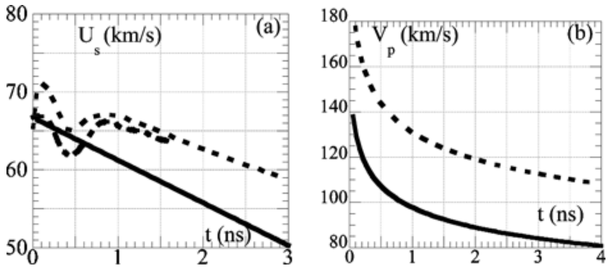

Figure 2. (a) Shock velocities: experimental results obtained with VISAR (— ·) and longitudinal interferometer (——), · · · corresponds to 1D hydro simulation. (b) precursor velocities: experimental results obtained with longitudinal interferometer (——). · · · 1D hydro simulation.

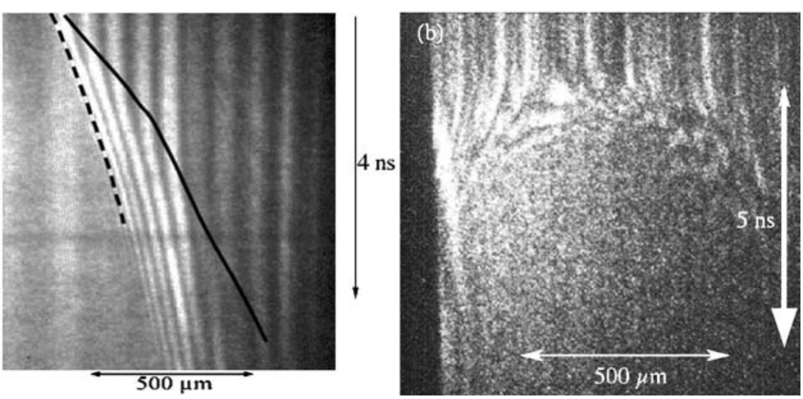

Figure 3. (a) Longitudinal interferometry along the direction of the shock propagation. Dashed and solid lines define the shock and precursor front trajectories, respectively. (b) Transverse diagnostic gives the radial extension $R(t)$.

the probe beam, its frequency being greater than the plasma frequency (overcritical) from the zone in the front part of the cell. It corresponds to the shock front and provides its velocity. When compared to the VISAR data and 1D simulations (Figure 2a) we find a fairly good agreement with these values. During the first 0.4 ns, the value is 68 km/s and decays down to 60 km/s when averaged over the first 3 ns. This value is very close to the VISAR result (67 km/s). After those 3 ns, it slows down. This is mainly due to the laser pulse duration that is shorter than the time scale evolution of the shock. In addition, on Figure 3a, we also observe clearly fringe shifts, ahead the shock front, due to a change in the electron density. We associate the region located in between the two lines with the radiative precursor and the full curve represents the position of its front. At the beginning, its velocity is close to 140 km/s and decreases with time due to the piston deceleration. Indeed we do measure precursor velocity which is quite in a rather good agreement with the simulations (Figure 2b). The fringe shift gives the electron density change through the relation: $N_e = \frac{\lambda N_c \Delta\Phi}{\pi d}$ where $\Delta\phi$ is the phase change related to the fringe shift, λ the probe beam laser wavelength, N_c the critical density above which the laser probe beam cannot penetrate, d the radial size of the shock/precursor. The latter have been assessed by the transverse diagnostic (TRANS). Indeed, looking at a given longitudinal position in the cell ($\approx$100–200 μm away from the foam interface), we get a picture of the shape of the shock-front in the transverse direction (departure from the plane geometry).

According to the transverse imaging system, a 300 μm wide plasma is created by the precursor so that one can deduce the variation of $N_e(t)$ (Figure 4).

Here we did take into account the increase in $R(t)$ as deduced from Figure 3b and the temperature measurement (Vinci et al., 2004). Using these data, we can therefore deduce N_e and compare it to numerical simulations. In Figure 4, we show the variation of N_e along the cell at a given time (4.5 ns after the laser maximum). We clearly observe that the precursor has a few hundreds microns extension in a good agreement with the code.

The last parameter we measured was the shock temperature. Among the methods existing for its determination (Collins et al., 2001; Hall et al., 1997), we adopted

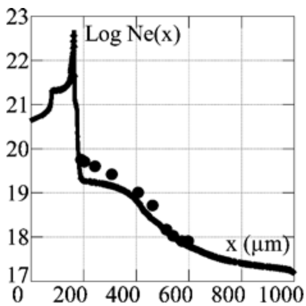

Figure 4. Electron density versus position in the cell 4.5 ns after the maximum of the laser.

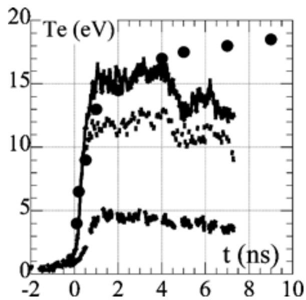

Figure 5. Deduced temperatures: (——) 0.1 bar 70J, (· · ·) 0.2 bar, 70 J (—-) 0.2 bar 50 J and (●●●) 1D hydro simulation for the first case.

an absolute photon counting technique. This implied a precise measurement of the total transmission efficiency of the rear side imaging system and the response of the detector (streak + CCD) at a given wavelength. Therefore we can associate to the counts on the CCD to a brightness temperature. However, we have to extract the temperature T_e by fitting intensity I(λ) to a grey body Planck spectrum. In Figure 5, we show various T_e measurements with different initial conditions. As expected, increasing laser intensity or decreasing initial Xe pressure lead to higher temperatures. Also our results are in quite good agreement with simulations.

Finally, with the new LULI Facility (LULI2000) we shall be able to drive shocks in Xenon at much higher velocities typically ranging from 120–250 km/s depending on the adopted target scheme. Due to the much higher intensity on target (2–4×10^{14} W/cm^2), one has to pay attention to preheating effects. For that purpose, the flyer plate technique as developed many years ago at LULI and more recently at ILE (Tanaka et al., 2000) seems to be a promising alternative. This technique consists (Figure 6 (left)) to accelerate a multilayer foil which impinge a second one, generating a very high pressure. In a recent experiment, performed on the Hyper facility at ILE, we were able to accelerate a multilayer foil (350 μm foam -10 μm tantalum) to a 70 km/s velocity. In Figure 6 (right), we observe the shock trajectory in the foam and the Ta free surface using a transverse x-ray radiography coupled to a streak camera. Such a velocity could produce, when impacting a 10 μm aluminum foil embedded in Xe gaz, a piston velocity up to 120 km/s.

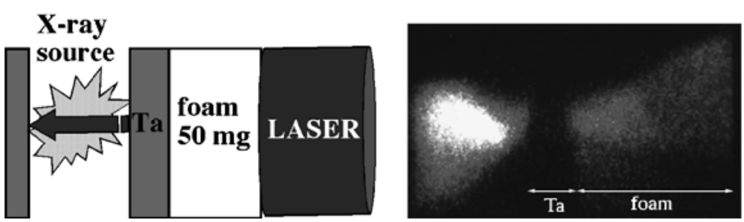

Figure 6. Target scheme (left). Experimental shock trajectory in foam and Ta free surface velocity (right).

As a conclusion, we have observed the development of a radiative precursor ahead a strong supercritical shock wave, in a xenon gas cell at low pressure. Our experimental results are in good agreement with numerical simulations either regarding hydrodynamical (U_s, V_p) or plasma parameters (N_e, T_e). In the next future, the upgraded laser facility at LULI will allow to explore a further step into the study of the radiating shock to the full radiative regime where E_{rad} and P_{rad} begin to play a significant role.

References

SESAME: 1992, *The LANL Equation of State Database. Rep. LA-UR-92-3407*, Los Alamos National Laboratory.
Boireau, L. et al: 2003, *Proc. of IFSA (Monterey, CA, USA)*.
Bouquet, S. et al.: 2000, *Astroph. J. Supp.* **127**, 245.
Bouquet, S. et al.: 2004, *Phys. Rev. Lett.* **92**, 225001.
Bozier, J.C. et al.: 1986, *Phys. Rev. Lett.* **57**, 1304.
Celliers, P.M. et al.: 1998, *Applied Phys. Lett.* **73**, 1320.
Collins, G.W. et al.: 2001, *Phys. Rev. Lett.* **87**.
Drake, P. et al.: 2002, *Astroph. J.* **564**, 896.
Edwards, M.J. et al.: 2001, *Phys. Rev. Lett.* **87**, 085004.
Grun, J. et al.: 1991, *Phys. Rev. Lett.* **66**, 2738.
Hall, T. et al.: 1997, *Phys. Rev. E* **55**, R6356.
Keiter, P.A. et al.: 2002, *Phys. Rev. Lett.* **89**, 165003.
Koenig, M. et al.: 1999, *Phys.Plasmas* **6**, 3296.
Lebedev, S. et al.: 2002, *Astrophys. J.* **564**, 113.
Lindl, J.: 1995, *Phys. Plasmas* **2**, 3933.
Mihalas, D., Mihalas, B.W.: 1984, *Foundations of Radiation Hdrodynamics*, Oxford University Press.
Tanaka, K.A. et al.: 2000, *Phys. of Plasmas* **7**, 676.
Vinci, T. et al.: 2004, Proc. of HEDLA (Tucson, AZ, USA).
Zeldovich, Y.B. and Raizer, Y.P. 1967, *Physics of Shock Waves and High Temperature Hydrodynamic Phenomena*, Academic Press, New York.

ANALYTICAL STUDY OF SUPERNOVA REMNANT NON-STATIONARY EXPANSIONS

X. RIBEYRE[1], V.T. TIKHONCHUK[1] and S. BOUQUET[2]

[1]*Centre Lasers Intenses et Applications, UMR 5107, CNRS – Université Bordeaux 1 – CEA, Université Bordeaux 1, 351, cours de la libération, Talence, France; E-mail: ribeyre@celia.u-bordeaux1.fr*

[2]*Commissariat à l'Energie Atomique, DIF/Département de Physique Théorique et Appliquée, Bruyères-le-Châtel, France*

(Received 27 April 2004; accepted 22 July 2004)

Abstract. We study analytically the Rayleigh–Taylor instability in expanding supernova gas shell. The instability appears at the inner shell surface accelerated by blowing pulsar wind. The most dangerous perturbations correspond to wavelengths comparable to the shell thickness. We analyze the fragility of the supernova remnant shell in function of the initial perturbation amplitude and the shell thickness.

Keywords: hydrodynamics, instabilities, supernova remnant, pulsar: general

1. Introduction

The Rayleigh–Taylor (hereafter R–T) instability plays an important role in several astronomical objects: pulsar nebulae (Jun, 1998), supernovae (Fryxell et al., 1991), supernova remnants (Gull, 1975; Chevalier et al., 1992). For a massive star, once the core has collapsed, the pulsar wind blows up the outer parts of the star, and the inner surface of the expanding shell becomes R–T unstable. This instability seems to lead to the filamentary structure observed in the Crab Nebula (Hester et al., 1996). In type II supernovae explosions, this instability might be responsible for the mixing of the metallic layers Ni, Co with the He, H layers (SN 1987A for instance), and that provides a better interpretation of the light curve (Arnett and Fryxell, 1989). This process differs from the one, which arises later in the supernova remnant (SNR) expansion, when the ejecta of the supernova (SN) swept the interstellar medium. In this deceleration phase, the ejecta might become R–T unstable and lead to a non-spherical structure (Velázquez et al., 1998) for type Ia SN (Tycho), and bow-shock features in type II SN (Cassiopeia A) (Gotthelf et al., 2001; Jun et al., 1996).

In this paper, we are interested in the R–T instability that develops at the early stage of pulsar nebula evolution. In this phase the pulsar wind accelerates the ejecta shell: the pulsar radiation is absorbed at the inner surface of the ejecta dense shell and this configuration is R–T unstable (see Figure 1). We develop an analytical

Astrophysics and Space Science **298:** 75–80, 2005.

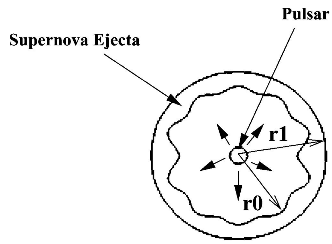

Figure 1. Schematic representation of the classical type II supernova remnant (SNR) model. The figure shows the central pulsar blowing the expanding SNR, where r_0 (resp. r_1) is the inner (resp. outer) shell radius.

model which takes into account the non-stationary shell evolution. Moreover, we analyze the linear evolution of the perturbations for wavelengths comparable to the shell thickness. Since they are dangerous for the shell integrity, we estimate its fragility.

2. Pulsar Wind Nebula and Supernova Remnant Model

Figure 1 shows schematically the interaction between the pulsar wind nebula (PWN) and the SNR ejecta (shell). The pulsar wind blows the supernova ejecta and accelerates their expansion. The expanding shell is called "plerion," which constitutes a class of SNR similar to the Crab nebula (Lequeux, 2002). The "plerion" evolution is a non-stationary problem because the pulsar wind pressure decreases with time, due to slowing down rotation (Reynolds and Chevalier, 1984; Blondin et al., 2001) of the pulsar. The shell evolution can be studied with the Euler's hydrodynamic equations, if we neglect all dissipative processes and the gravitational field:

$$\frac{\partial \rho}{\partial t} + \frac{1}{r^2}\frac{\partial (r^2 \rho v)}{\partial r} = 0, \qquad \frac{\partial v}{\partial t} + v\frac{\partial v}{\partial r} = -\frac{1}{\rho}\frac{\partial p}{\partial r}, \qquad p = K\rho^\gamma. \tag{1}$$

In first approximation we assume a spherical symmetry and $\rho(r, t)$, $p(r, t)$, $v(r, t)$ are respectively the density, the pressure and the velocity of the flow. The quantities K and γ are respectively a constant and the polytropic coefficient of the gas. This system of equations is difficult to solve because of the non-stationary character of the evolution. In order to make possible an analytical study of the shell stability, we would like to obtain a solution for the radial shell expansion. This is achieved by using a special coordinate transformation into the non-stationary co-moving frame (Bouquet et al., 1985) where the flow becomes stationary.

Once the solution is found in the co-moving frame, one can use the inverse transformation to return in the initial space. The transformation between the two frames is defined by the rescaling functions $A(t)$, $B(t)$, $C(t)$ and $D(t)$ according to:

$$r = C(t)\hat{r}, \quad dt = A(t)^2 d\hat{t}, \quad \hat{v} = \frac{d\hat{r}}{d\hat{t}}, \tag{2a}$$

$$p(r,t) = B(t)\hat{p}(\hat{r},\hat{t}), \quad \rho(r,t) = D(t)\hat{\rho}(\hat{r},\hat{t}). \tag{2b}$$

Any physical quantity $q(=r, t, v, \rho, p)$ from the initial space (r, t) will be labeled with a hat '$\wedge$', i.e., $q(=\hat{r}, \hat{t}, \hat{v}, \hat{\rho}, \hat{p})$ in the new space $(\hat{r}, \hat{t})$. The two spaces coincide at $t = 0$ and consequently, $A(0) = B(0) = C(0) = D(0) = 1$. The Euler's equations in the new frame read:

$$\frac{\partial\hat{\rho}}{\partial\hat{t}} + \frac{1}{\hat{r}^2}\frac{\partial(\hat{r}^2\hat{\rho}\hat{v})}{\partial\hat{r}} = -\frac{A^2}{D}\left(\frac{3\dot{C}}{C} + \frac{\dot{D}}{D}\right)\hat{\rho}, \tag{3a}$$

$$\frac{\partial\hat{v}}{\partial\hat{t}} + \hat{v}\frac{\partial\hat{v}}{\partial\hat{r}} = -\left(\frac{BA^4}{C^2D}\right)\frac{1}{\hat{\rho}}\frac{\partial\hat{p}}{\partial\hat{r}} - 2A^2\left(\frac{\dot{C}}{C} - \frac{\dot{A}}{A}\right)\hat{v} - \frac{\ddot{C}A^4}{C}\hat{r}, \tag{3b}$$

$$\hat{p} = K\left(\frac{D^\gamma}{B}\right)\hat{\rho}^\gamma, \tag{3c}$$

where the dot stands for *d/dt*. The rescaling functions can be found from invariance considerations and conservation laws. In order to have a mass conservation in the $(\hat{r}, \hat{t})$ space and to keep the continuity Eq. (3a) identical to Eq. (1), the R.H.S of (3a) should vanish: $3\dot{C}/C + \dot{D}/D = 0$, i.e. $D = C^{-3}$. Moreover, in momentum Eq. (3b), two new forces appear, one is a friction proportional to $\hat{v}$ and another is a radial force proportional to $\hat{r}$ (see below).

First, we remove the time-dependent coefficients in the pressure gradient term in (3b) and in the polytropic Eq. (3c). This provides $BA^4/(C^2D) = D^\gamma/B = 1$ and since $D = C^{-3}$, we obtain $B = C^{-3\gamma}$ and $A = C^{(3\gamma-1)/4}$. At this stage, we have derived the scaling functions $A(t)$, $B(t)$ and $D(t)$ in terms of $C(t)$, which is the function governing the relation between the spatial coordinates r and $\hat{r}$. Under these conditions the friction and the radial force in (3b) become respectively $-(3\gamma - 5)\dot{C}C^{3(\gamma-1)/2}\hat{v}/2$ and $-\ddot{C}C^{3\gamma-2}\hat{r}$. The friction vanishes for $\gamma = 5/3$ (mono-atomic ideal gas) and the radial force reduces to $-\hat{r}/\tau^2$ provided $C(t) = [1 + (t/\tau)^2]^{1/2}$, where τ is a constant representing the characteristic time of the expansion. The scaling function C gives the time evolution of the radius of the pulsar bubble and for $t \gg \tau$ the shell is in ballistic expansion (see Figure 2a). Having all these conditions fulfilled, one can look for a static solution, $\hat{v}(\hat{r}, \hat{t}) = 0$, in the rescaled space $(\hat{r}, \hat{t})$. Eq. (3a) is identically satisfied since $\partial/\partial\hat{t} \equiv 0$ and the equation of motion reduces to the static equation $(1/\hat{\rho})(d\hat{p}/d\hat{r}) = -\hat{r}/\tau^2$. Using (3c), the density profile is $\hat{\rho}(\hat{r}) = [(\hat{r}_1^2 - \hat{r}^2)/(5K\tau^2)]^{3/2}$ where $\hat{r}_1$ is an arbitrary constant (outer surface of the configuration). The density profile $\hat{\rho}(\hat{r})$ is given in Figure 2b. Using the coordinate transformation (2a) the density profile $\rho(r, t)$ in the initial (r, t)-space is $\rho_0(r, t) = I(t)\{1 - [r/r_1(t)]^2\}^{3/2}$ where $r_1(t)$ is defined by $r_1(t) \equiv C(t)\hat{r}_1$, $I(t) \equiv \{5K\tau^2[C(t)]^4/[r_1(t)]^2\}^{-3/2}$ and where the subscript "0" stands for the unperturbed

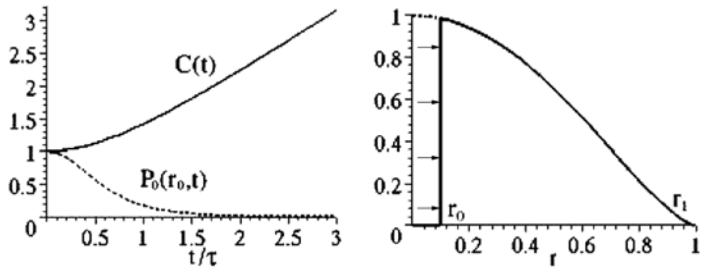

Figure 2. (a) Scaling function $C(t)$ (solid line), $P_0(r_0, t)$, pressure evolution at the inner surface of the SNR shell (doted line), (b) Normalized density profile $\hat{\rho}(\hat{r})$ (doted line) and density profile of the SNR shell $\rho_0(r, t = 0)$ at $t = 0$ (solid line).

non-stationary flow. The corresponding non-perturbed time-dependent velocity is $v_0(r, t) = r\dot{C}(t)/C(t) = (rt/\tau^2)\{1/[1 + (t/\tau)^2]\}$.

The SNR shell is obtained from the hollow sphere where matter is removed ($\hat{\rho} = 0$) in the range $0 \le \hat{r} \le \hat{r}_0$ (see the density jump on Figure 2b). In the (r, t)-space, the shell thickness is $\Delta(t) = \Delta_0 C(t)$ where $\Delta_0 = \hat{r}_1 - \hat{r}_0$ is the thickness at $t = 0$. The unperturbed density profile in the shell is given by $\rho_0(r, t)$ where r moves in the range $r_0(t) \equiv \hat{r}_0 C(t) \le r \le r_1(t)$. The pressure acting (pulsar wind) on the shell inner surface ($r = r_0$) is obtained from $p = K\rho^{5/3}$, i.e., $p_0(r_0, t) = K[C(t)]^{-5}(5K\tau^2/\hat{r}_1^2)^{-5/2}\{1 - [r_0(t)/r_1(t)]^2\}^{5/2}$. Since the ratio $r_0(t)/r_1(t) = \hat{r}_0/\hat{r}_1$ is constant, we conclude that the pulsar pressure decreases according to C^{-5} (see Figure 2a).

3. Stability Study of the SNR Shell

Since the inner surface of the shell is accelerated, it is unstable. Its analysis in the laboratory frame is complicated because the pressure and the density vary with time. The stability analysis of a small perturbation is more simple in the co-moving frame. We define any perturbed physical quantity $\hat{q}$ as $\hat{q}(\hat{r}, \theta, \phi, \hat{t}) = \hat{q}_0(\hat{r}) + \delta\hat{q}(\hat{r}, \theta, \phi, \hat{t})$, with $\hat{\theta} = \theta$, $\hat{\phi} = \phi$ being the polar and azimuthal angles. The perturbed position of the inner interface is $\delta\hat{r}_0 = \hat{\eta}(\theta, \phi, \hat{t}) = \hat{a}Y_{lm}(\theta, \phi)e^{\omega\hat{t}}$, where ω is the growth rate, $Y_{lm}(\theta, \phi)$ is the spherical harmonic function. Rewriting the perturbed Euler's Eqs. (3a–3c) in $(\hat{r}, \hat{t})$, the equation for the spatial part $S(\hat{r})$ of the density perturbation: $\delta\hat{\rho}(\hat{r}, \theta, \phi, t)/\hat{\rho}_0(\hat{r}) = S(\hat{r})Y_{lm}(\theta, \phi)e^{\omega\hat{t}}$ reads:

$$C_{s0}^2 S'' + C_{s0}^2\left(\frac{2}{\hat{r}} - \frac{7}{3R}\right)S' + \left(C_{s0}^2\frac{2}{3R^2} - C_{s0}^2\frac{l(l+1)}{\hat{r}^2} - \omega^2 - \frac{2}{\tau^2}\right)S$$
$$- C_{s0}^2\frac{l(l+1)}{R\hat{r}^2}a - \frac{\omega^2}{R}a = 0, \tag{4a}$$

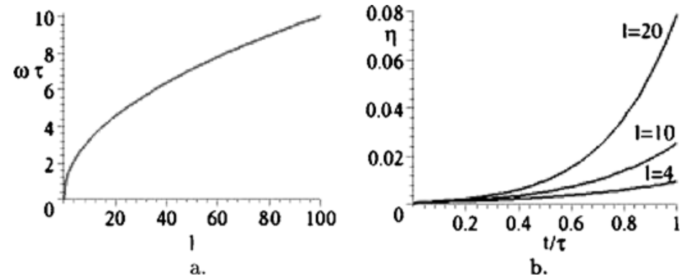

Figure 3. (a) Dispersion relation $\omega = f(l)$, (b) Evolution $\eta(t)$ for three mode numbers for $\hat{a} = 0.0016\hat{r}_0$.

where $R = \tau^2 C_{s0}^2/\hat{r}$ and $C_{s0}^2 = 5K[\hat{\rho}(\hat{r})]^{2/3}/3$ is the static sound velocity. We assume here that the density perturbation is located near the inner surface, for $\hat{r} \to \hat{r}_0$. Then the coefficients in the Eq. (4) become constant and by matching the boundary conditions for the pressure and density one can obtain the dispersion relation $\omega = f(l)$ between ω and the mode number l (see Figure 3a).

Since $A = C$ and $dt = A(t)^2 d\hat{t}$, the relation between $\hat{t}$ and t is $\hat{t} = \arctan(t/\tau)$ and the amplitude of the perturbation in (r, t)-space reads $\eta(t) = \hat{a}C(t)\exp[\omega\tau \arctan(t/\tau)]$. Instead of a usual exponential evolution in the (r, t)-space, we obtain a time power which is more general than a self-similar solution (Chevalier et al., 1992).

4. Discussions

From the dispersion relation, it is found that the R–T growth rate depends on the SNR shell thickness Δ and it allows to estimate the initial perturbation that would disrupt the shell. The most unstable wavelength λ_c is of order of Δ and it may tear up the shell. Moreover, $\eta(t)$ allows to find the initial perturbation amplitude a_c for which the shell will disrupt at $t = \tau$. The importance of the non-stationary treatment of the R–T instability for SNR can be shown for the example considered by Blondin et al. (2001): $r_0 = 4 \times 10^{18}$ cm, $r_1 = 2r_0$, $\Delta = r_1 - r_0 = r_0$ and $\rho_0(r_0, 0) = 2 \times 10^{-23}$ g/cm^3. The shell mass $M_s = 4.2M_\odot$ and for $\lambda_c \simeq \Delta$ one gets $l_c = 6$ while the dispersion relation provides $\omega_c\tau = 5/2$. We find therefore that for $a_c = r_0/7$, the shell will break for $t = \tau$. This example shows that a perturbation about 14% might be enough to disrupt the SNR shell.

In conclusion, this study allows to calculate the R–T growth rate for a non-stationary flow. It predicts the conditions for the shell disruption which may lead to further Crab-like filamentary structures. Further studies are needed to study the perturbation propagation toward the outer shell surface (Eq. (4)) and its non-linear evolution.

References

Arnett, D. and Fryxell, B.: 1989, *ApJ* **341**, L63.
Blondin, J.M., Chevalier, R.A. and Frierson, D.M.: 2001, *ApJ* **563**, 806.
Bouquet, S., Feix, M., Fijalkov, E. and Munier, A.: 1985, *ApJ* **293**, 494.
Chevalier, R.A., Blondin, J.M. and Emmering, R.T.: 1992, *ApJ* **392**, 118.
Fryxell, B., Müller, E. and Arnett, D.: 1991, *ApJ* **367**, 619.
Gotthelf, E. et al.: 2001, *ApJ* **552**, L39.
Gull, S.F.: 1975, *MNRAS* **171**, 263.
Hester, J.J. et al.: 1996, *ApJ* **456**, 225.
Jun, B.-I.: 1998, *ApJ* **499**, 282.
Jun, B.-I. et al.: 1996, *ApJ* **468**, L59.
Lequeux, J.: 2002, Le *milieu interstellaire*. CNRS editions.
Reynolds, S.P. and Chevalier, R.: 1984, *ApJ* **278**, 630.
Velázquez, P.F., Gómez, D.O., Dubner, G.M., Gimenez de Castro, G. and Costa, A.: 1998, *A&A* **334**, 1060.

HYPERNOVAE AND GAMMA-RAY BURSTS

KEN'ICHI NOMOTO[1,2], KEIICHI MAEDA[1,3], NOZOMU TOMINAGA[1], TAKUYA OHKUBO[1], JINSONG DENG[1] and PAOLO A. MAZZALI[2,4]

[1]*Department of Astronomy, School of Science, University of Tokyo, Tokyo, Japan;*
E-mail: nomoto@astron.s.u-tokyo.ac.jp
[2]*Research Center for the Early Universe, School of Science, University of Tokyo, Tokyo, Japan*
[3]*Department of Earth Science and Astronomy, College of Arts and Sciences, University of Tokyo, Tokyo, Japan*
[4]*INAF-Osservatorio Astronomico, Via Tiepolo, Trieste, Italy*

(Received 21 May 2004; accepted 22 July 2004)

Abstract. The nature of very energetic supernovae (hypernovae) is discussed. They are the explosive death of stars more massive than $\sim$20–25$M_{\odot}$, probably linked to the enigmatic Gamma-Ray Bursts. The optical properties of hypernovae indicate that they are significantly aspherical. Synthetic light curves and late-phase spectra of aspherical supernova/hypernova models are presented. These models can account for the optical observations of SNe 1998bw and 2002ap. The abundance patterns of hypernovae are characterized by large ratios (Zn, Co)/Fe and small ratios (Mn, Cr)/Fe, indicating a significant contribution of hypernovae to the early Galactic chemical evolution.

Keywords: Gamma-Ray Bursts, supernovae, nucleosynthesis, extremely metal-poor stars

1. Introduction

One of the most exciting developments in recent studies of supernovae (SNe) is the discovery of very energetic SNe (Hypernovae), whose (isotropic) kinetic energy (KE) exceeds 10^{52} erg, about 10 times the KE of normal core-collapse SNe (hereafter $E_{51} = E/10^{51}$ erg), and their association with Gamma-Ray Bursts (GRBs).

A SN/GRB connection has been suggested for SN 1998bw/GRB980425 (Galama et al., 1998; Iwamoto et al., 1998), SN 2003dh/GRB030329 (Stanek et al., 2003; Hjorth et al., 2003; Kawabata et al., 2003), and SN 2002lt/GRB021211 (Della Valle et al., 2003) on the basis of their optical spectra. Recently, another case has been observed, SN2003lw/GRB031203 (Gal-Yam et al., 2004; Thomsen et al., 2004). By fitting early-phase ($\lesssim$50 day) optical light curves and spectra of supernovae, the KE and the main-sequence mass $M_{\rm ms}$ of the progenitor star can be derived (Figure 1: Nomoto et al., 2003a,b). At least SNe 1998bw and 2003dh are classified as hypernovae (Figure 1: Iwamoto et al., 1998; Mazzali et al., 2003). Other possible SNe in GRBs have been reported, but in these cases the evidence was limited to the detection of 'bumps' in GRB afterglows (e.g., Bloom et al., 2002; Garnavich et al., 2003).

Astrophysics and Space Science **298:** 81–86, 2005.

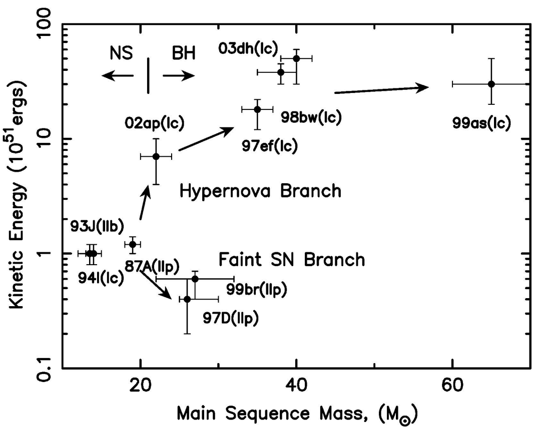

Figure 1. Explosion energies as a function of the main-sequence mass M_{ms} of the progenitor star for core-collapse supernovae/hypernovae.

The link to GRBs is a strong hint that hypernovae could be significantly aspherical, as is widely believed for GRBs (e.g., Frail et al., 2001). This speculation received further support from detailed investigations of the optical properties of hypernovae. Furthermore, problems have arisen for spherically symmetric explosion models. Such models do not reproduce the light curves consistently from early phases to late phases (Nakamura et al., 2001; Maeda et al., 2003a), nor the late-phase nebular spectra (Mazzali et al., 2001; Maeda et al., 2002). These features might indicate asphericity in SN ejecta, as anticipated by most of the explosion scenarios of hypernovae/GRBs (e.g., MacFadyen and Woosley, 1999; Wheeler et al., 2000).

In this paper, optical light curves and late-phase nebular spectra of aspherical explosion models are presented. By comparing them with those of SNe 1998bw and 2002ap, we identify some properties of the hypernovae, e.g., asphericity and energies, which are essential to understand the nature of GRBs. We also briefly discuss the possible contribution of hypernovae to early Galactic chemical evolution.

2. Aspherical Natures of SNe 1998bw and 2002ap

In this section, the optical properties of aspherical supernovae/hypernovae are presented, and are compared with observations. First, a series of aspherical explosion models is constructed using a two-dimensional hydrodynamic code and a nuclear reaction network code (Maeda et al., 2002; Maeda and Nomoto, 2003b; Maeda, 2004). Two progenitor models, i.e., $M_{\mathrm{ms}} = 40M_\odot$ and $25M_\odot$, are considered. The model parameters cover a range of explosion energies ($E_{51} = 1$–30) and of degree of asphericity (from a spherical model to a highly-aspherical jet-induced model). Synthetic light curves and late-phase nebular spectra are then computed for these

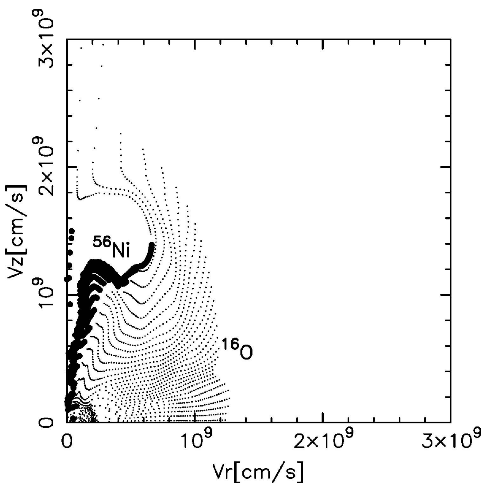

Figure 2. The distribution of Fe (points) and O (dots).

two-dimensional explosion models, using a Monte Carlo two-dimensional radiation transport code (Maeda, 2004).

Figure 2 shows the typical distribution of elements in the ejected materials in an aspherical explosion model. In the model in Figure 2, the energy injected by the central collapsing core is assumed to be a factor of 4 larger on the z-axis than on the r-axis. ^{56}Ni is synthesized preferentially along the polar axis, where the shock is stronger, while a lot of unburned material, dominated by O, is left at low velocity in the equatorial region, where burning is much less efficient.

Figure 3 shows examples of synthetic light curves and nebular spectra of the aspherical explosion models. Strictly speaking, the shape of the light curve of the aspherical model of course depends on orientation. Here we present an 'angle-averaged' light curve for the sake of simplicity. The viewing angle effect on the light curve is actually not significantly large (Maeda, 2004). The spherical model fails to reproduce the observed late-time luminosity of SN 1998bw, while the aspherical models can well account for the observed light curve.

The nebular spectrum is also consistent with the aspherical models. The spherical hyper-energetic model results in too wide [MgI] 4571Å and [OI] 6300 + 6363Å, while the aspherical model produces a spectrum reasonably similar to the observed one. Because elements newly synthesized at the explosion such as iron are distributed in a very aspherical way (Figure 2), profiles of emission lines of these elements are sensitive to the orientation toward the observer. These lines are broader if the angle between the observer's direction and the jet axis is smaller. We find the best match (especially [FeII] around 5200Å) to the observed spectrum if the explosion is viewed within 30 degrees of the polar direction.

Comparing the light curve and late-phase nebular spectra with the observed ones, and using the column density along a fixed line of sight (compared with that

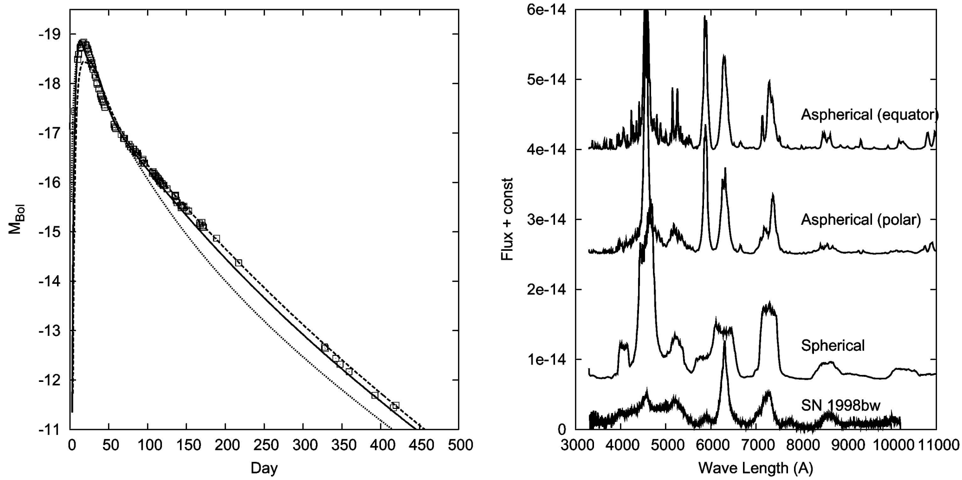

Figure 3. Left: Synthetic light curves of the aspherical models with $E_{51} = 25$ (solid line) and $E_{51} = 6$ (dashed line), and that of the spherical model with $E_{51} = 25$ (dotted line). Also shown are the bolometric light curve of SN 1998bw (squares). Right: Synthetic spectra of the aspherical model ($E_{51} = 6$) at day 200, for two orientations (viewed at the polar and the equator). That of the spherical model ($E_{51} = 25$) is also shown. They are compared with the observed spectrum of SN 1998bw at day 216 (bottom). The progenitor model is the $16M_{\odot}$ He star ($M_{\rm ms} = 40M_{\odot}$).

derived from spectra close to maximum light), we constrain the asphericity, mass, energy, and the viewing angle of SNe 1998bw and 2002ap. The values we derived are as follows. For SN 1998bw, $E_{51} \sim 10$, $M_{\rm ms} \sim 40M_{\odot}$, viewing angle $\lesssim 30°$. For SN 2002ap, $E_{51} = 2$–5, $M_{\rm ms} = 25$–$30M_{\odot}$. (The range corresponds to the uncertainty in the viewing angle.) These aspherical models account satisfactorily for all the observational features mentioned above (see Figure 3).

For both SNe, the progenitor masses are not very different from the estimate of spherically symmetric models. On the other hand, the estimated energies are different. For SN 1998bw, our revised value ($E_{51} \sim 10$) is smaller than the previous estimate ($E_{51} = 30$–50) by a factor of 3–5, because we interpret that the SN was viewed from near the polar direction where most of the energy is concentrated. It is worth stressing that the explosion energy, derived after taking into account the effect of asymmetry, is still well above that of normal supernovae. Therefore, the explosion mechanism of hypernovae is very likely different from that of normal supernovae.

3. Nucleosynthesis

It is interesting to investigate the possible influence of hypernovae to the earliest phases of Galactic chemical evolution. Observational studies of metal-poor halo stars have shown that there exist interesting trends in the abundances of iron peak

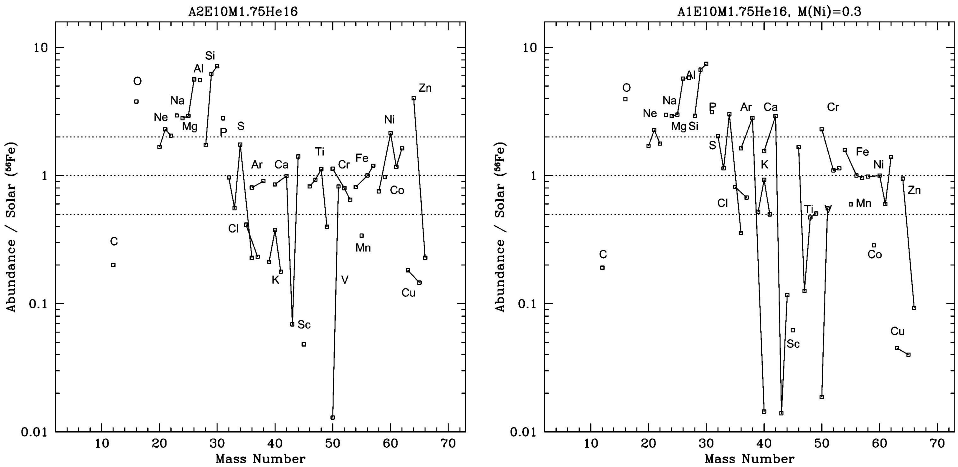

Figure 4. Isotropic yields of an aspherical model (left) and a spherical model (right). The explosion characteristics are as follows: $E_{51} = 10$ and $M_{\rm ms} = 40M_\odot$.

elements for [Fe/H] $\lesssim -2.5$ (McWilliam et al., 1995; Ryan et al., 1996; Primas et al., 2000; Blake et al., 2001). Both [Cr/Fe] and [Mn/Fe] decrease toward smaller [Fe/H], while [Co/Fe] and [Zn/Fe] increase to reach ~0.3–0.5 at [Fe/H] ~ -3. Also [(O, Mg)/Fe] are as large as ~0.5 for [Fe/H] $\lesssim -2.5$, indicating that the amount of Fe was not excessively large in the ejecta of supernovae which were responsible for forming those stars.

Figure 4 compares the abundance patterns of one of the aspherical models and of a spherical model with the same kinetic energy and $M_{\rm ms}$. We note the larger (Zn, Co)/Fe and the smaller (Mn, Cr)/Fe in the aspherical model. As is mentioned above, the same trend can be seen in abundances in extremely metal-poor stars (EMPSs). Indeed, we find that the abundances of these elements predicted by the aspherical model are consistent with those seen in EMPSs. This might indicate a significant contribution of hypernovae to the early Galactic chemical evolution.

4. Concluding Remarks

We have performed the first systematic calculations of explosions, light curves, and nebular spectra of aspherical supernovae/hypernovae. We find that the aspherical models give reasonably good fits to the optical properties of SNe 1998bw and 2002ap. The explosion characteristics of these SNe are revised in the context of the aspherical model. The revised estimates of the progenitor masses are not very different from the previous spherically symmetric estimates, but the energies are different by a factor of 3–5, depending on the viewing angle. The main conclusion of the previous studies is, however, unchanged even if the asymmetry effects are taken into account – they are hyper-energetic explosions of very massive stars.

There is now almost no doubt that relativistic jets (a GRB) coexist with a Newtonian (aspherical) explosion (a SN or a hypernova) in the observed SN/GRB events. However, how a SN and a GRB are physically connected is still an open question. How the jets are formed, propagated through the envelope to induce a hypernova, could be the important subject of 'Experimental Astrophysics'.

References

Blake, L.A.J. et al.: 2001, *Nucl. Phys. A* **688**, 502.
Bloom, J.S. et al.: 2002, *ApJ* **572**, L45.
Della Valle, M. et al.: 2003, *A&A* **406**, L33.
Frail, D.A. et al.: 2001, **562**, L55.
Galama, T. et al.: 1998, *Nature* **395**, 670.
Gal-Yam, A. et al.: 2004, *ApJL* **609**, L59.
Garnavich, P.M. et al.: 2003, *ApJ* **582**, 924.
Hjorth, J. et al.: 2003, *Nature* **423**, 847.
Iwamoto, K., Mazzali, P.A., Nomoto, K. et al.: 1998, *Nature* **395**, 672.
Kawabata, K., Mazzali, P.A., Deng, J., Nomoto, K. et al.: 2003, *ApJ* **593**, 931.
MacFadyen, A.I. and Woosley, S.E.: 1999, *ApJ* **524**, 262.
Maeda, K., Mazzali, P.A., Deng, J., Nomoto, K. et al.: 2003a, *ApJ* **593**, 931.
Maeda, K., Nakamura, T., Nomoto, K. et al.: 2002, *ApJ* **565**, 405.
Maeda, K. and Nomoto, K.: 2003b, *ApJ* **598**, 1163.
Maeda, K.: 2004, Ph.D. Thesis, University of Tokyo, Tokyo.
Mazzali, P.A., Deng, J., Tominaga, N., Maeda, K. et al.: 2003, *ApJ* **599**, L95.
Mazzali, P.A., Nomoto, K., Patat, F. and Maeda, K.: 2001, *ApJ* **559**, 1047.
McWilliam, A., Preston, G.W., Sneden, C. and Searle, L.: 1995, *AJ* **109**, 2757.
Nakamura, T., Mazzali, P.A., Nomoto, K. and Iwamoto, K.: 2001, *ApJ* **550**, 991.
Nomoto, K. et al.: 2003a, in: V.D. Hucht, A. Herrero and C. Esteban (eds.), *A massive Star Odyssey, from Main Sequence to Supernova*, ASP, San Francisco, 395 (astro-ph/0209064).
Nomoto, K., Maeda, K., Mazzali, P.A. et al.: 2003b, in: C.L. Fryer (ed.), *Stellar Collapse*, *A&SS* Springer **277**, (astro-ph/0308136).
Primas, F. et al.: 2000, in: A. Weiss et al. (eds.), *The First Stars*, Springer, Berlin, p. 51.
Ryan, S.G., Norris, J.E. and Beers, T.C.: 1996, *ApJ* **471**, 254.
Stanek, K.Z. et al.: 2003, *ApJ* **591**, L17.
Thomsen, B. et al.: 2004, *A&A* **419**, L21.
Wheeler, J.C., Yi, L., Höflich, P. and Wang, L.: 2000, *ApJ* **537**, 810.

RADIATION HYDRODYNAMICS IN SUPERNOVAE

PETER HÖFLICH

Department of Astronomy, University of Texas, Austin, TX , USA;
E-mail: pah@astro.as.utexas.edu

(Received 29 April 2004; accepted 4 June 2004)

Abstract. We discuss the current status of our hydrodynamical radiation (HYDRA) code for rapidly expanding, low-density envelopes commonly found in core collapse and thermonuclear supernovae. In supernovae, one of the main issues is the coupling between a radiation field and properties of the matter. Due to the low densities, nonthermal excitation by high-energy photons from radioactive decays and the time dependence of the problem, significant departures from local thermodynamical equilibrium (LTE) are common throughout the envelope even at large optical depths. This effect must be taken into account to simulate the evolution of spectra and light curves which are the basic tools to link between explosion physics and observations.

The large velocity fields and the non-LTE problem result in a coupling of spatial, frequency space and the level population. This physical system can be described by a large system of coupled integro-differential equations for which the spatial and energy discretization (and its errors) are coupled. For the numerical solution, we use variable separation, analytic solutions and approximations, and iterative schemes. The need for adaptive mesh refinement (AMR) is demonstrated. As example, we show detailed spectra and light curves for the thermonuclear Supernova *SN99by*.

Keywords: radiation transport, hydrodynamics, supernova

1. Introduction

There is a profound difference between experiments and physics and astrophysics. In physics, the experiments are conducted in a well-defined environment to measure a physical effect. In astronomy, both the general setup and the physics of interest must be extracted to constrain the possible scenarios, to identify the relevant physics involved, and to test and verify our understanding of physical processes. In general, this raises the question on the uniqueness of an interpretation/model but allows us to study interesting objects and physics under extreme conditions. As a goal, we have to maximize the information going into an analysis. Observations are one of the sources for information. They provide the time-evolution of flux and polarization spectra of specific object, statistical properties within the same class of objects, and integrated quantities such as abundance patterns of elements seen in our galaxy. Physical laws and relations taken into account are the other source of information.

For supernova (SN) explosions, the last decade has witnessed an explosive growth of high-quality data both from ground and space observatories. Combined

Astrophysics and Space Science **298:** 87–92, 2005.

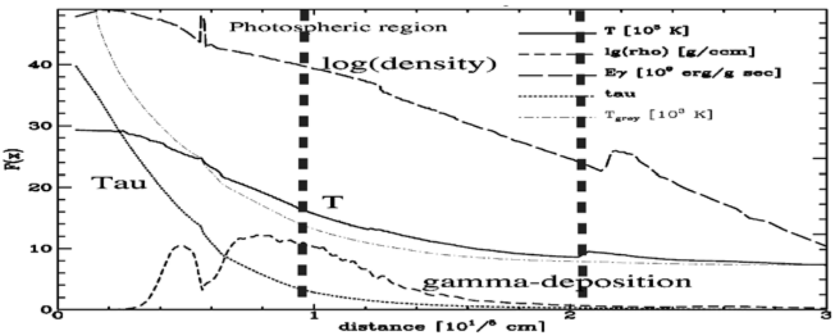

Figure 1. Temperature T, energy deposition due to radioactive decay E_γ, Rosse-land optical depth *Tau* (left scale) and density $\log(\rho)$ (right scale) are given as a function of distance (in 10^{15} cm) for a typical SNe Ia at 15 days after the explosion. For comparison, we give the temperature T_{grey} for the grey extended atmosphere. The light curves and spectra of Type Ia Supernovae are powered by energy release due to radioactive decay of ^{56}Ni $\rightarrow$ ^{56}Co $\rightarrow$ ^{56}Fe. The two dotted, vertical lines indicate the region of spectra formation. SN models go well beyond classical, stellar atmospheres: density structures require detailed hydrodynamics, low densities cause strong non-LTE effects throughout the envelopes, chemical profiles are depth dependent, energy source and sink terms due to hydrodynamical effects and radioactive decays may dominate throughout the photon decoupling region, and all physical properties are time-dependent (Höflich, 1995).

with the progress in computational and experimental physics, these advances led to spectacular results that constrain physical models and the progenitor systems, and open new perspectives for cosmology and high-energy physics. Hydrodynamical radiation calculations provide the link between the observables, such as light curves and spectra, and the underlying physics of the objects under study (Figure 1).

2. Numerical Tools and Methods

The computational tools summarized below were used to carry out many of the analyses of SNIa and Core Collapse Supernovae (Höflich, 1988, 1995; Höflich et al., 1993; Howell et al., 2001) . All components of the codes have been written or adopted in a modular form with well-defined interfaces. This structure allows for an easy coupling (see Figures 2 and 3) and code verification by exchanging modules while keeping the remaining setup identical (e.g. Figure 4). The modules consist of physical units to provide a solution for the nuclear networks, the statistical equations to determine the atomic level population, equation of states (EOS), the opacities, and the hydro (Fryxell et al., 1991) or the radiation transport problem. The individual modules are coupled explicitly. Consistency between the solutions is achieved iteratively by linear perturbation methods (Scharmer, 1984; Olson et al., 1986; Hillier, 1990; Höflich, 1990; Hubeny and Lanz, 1992) with higher-order coupling terms included directly into the radiation transport (Athay, 1972; Cannon, 1973). For more details, see Höflich (2003, and references therein).

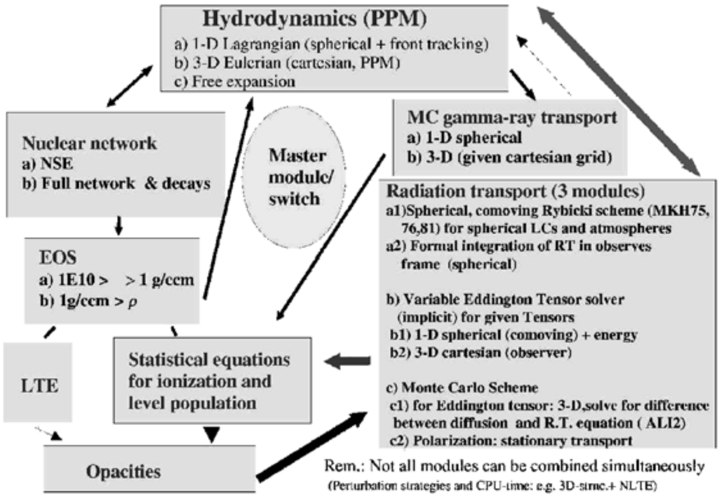

Figure 2. Block diagram of our numerical scheme to solve radiation hydrodynamical problems including detailed equation of state, and nuclear (Thielemann et al., 1994) and atomic networks (Höflich, 1990; Kurucz, 1991, 1995). For specific problems, a subset of the modules is employed (Figures 4 and 5). The hydro modules use the explicit Piecewise Parabolic Method by Colella and Woodward (1984) in 1-D Lagrangian or 3-D Eulerian mode. We use variable separation (e.g. Figure 3), analytic solutions and approximations, and iterative schemes to couple the various modules. To improve the stability and convergence rate/control we use several methods, including the accelerated Λ iteration, the concept of leading elements, the use of net rates, level locking, reconstruction of global photon-redistribution functions, equivalent-2-level approach, and predictive corrector methods. For appropriate conditions, the solution of the time-dependent rate equations can be reduced to the time-independent problem plus the (analytic) solution of an ordinary differential equation (Höflich, 1990). For the 3-D problem, we solve the radiation transport via the moment equations. To construct the Eddington tensor elements similar to Stone et al. (1992), we use a Monte Carlo scheme to determine the deviation of the solution for the radiation transport (RT) equation from the diffusion approximation.

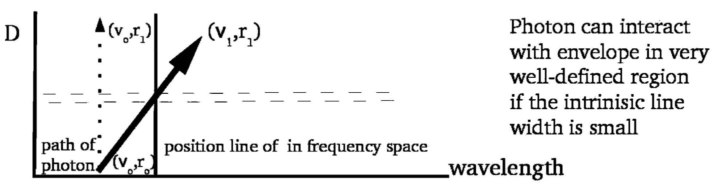

Figure 3. In expanding envelopes, a photon travels both in the spatial and wavelength space from (r_0, ν_0) to (r_1, ν_1) (*red arrow*). Consequently, any line transition (blue line) $\in[\nu_0, \nu_1]$ will effect the absorption probability of the photon whereas, in the static case, only lines will influence the absorption probability if $|\nu_{\text{line}} - \nu_0|$ is smaller than the internal line width $\Delta\nu_{\text{line}}$. For large velocities, a photon can be absorbed by a given line in a small region with almost constant physical properties. This allows for an operator splitting in the radiation transport between frequency and spatial coordinates.

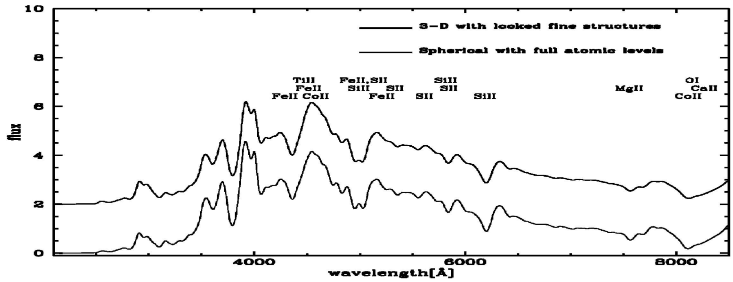

Figure 4. Comparison between theoretical spectra for the SNe Ia 1999by at about maximum light assuming spherical symmetry. The spectra are based on our spherical (blue) and full 3-D radiation transport scheme, using 90 depth points, 20,000 frequency points and 520 non-LTE-levels and 67/67/67 depth points, 2000 frequency points and non-LTE-super-levels, respectively. Differences are up to 20%. They can be understood due to the lower resolution in the 3-D calculations. As an application, see the study of asphericity effects in SN99by (see Figure 5, Howell et al., 2001).

2.1. Current Status

Not all modules can be combined simultaneously because not all iteration schemes have been implemented and because of requirements on CPU time:

(a) For full non-LTE-spectra with large model atoms and a high-frequency resolution, we are restricted to the time-independent case based on a given hydrodynamical structure (Figure 5) and, for 3-D models, reduced atomic models with super-levels have to be used (Figure 4).

(b) Radiation hydrodynamics to calculate light curves is restricted to reduced frequency resolutions with reduced atomic levels (level-merging) and spherical geometry (see Figure 5). In case of multidimensional radiation hydrodynamics, CPU-time requirements restrict applications even further. Currently, we can use a few frequencies to represent the fluxes e.g. in the Lyman and ‘Balmer and higher continua’, and 3-level atoms plus spherically symmetric velocity fields for the radiation transport (RT) (Höflich et al., 2002a,b), or to the grey case for arbitrary field. In the remainder of this section, we want to describe the various modules. For more details, see (Höflich, 2003), and references therein.

2.2. Automatic Mesh Refinement for Radiation Transport by a Monte Carlo Torch

AMR, a well-established procedure in hydrodynamics, makes adjustments to the required resolution for the radiation transport. In stellar atmospheres, a logarithmic spacing of the optical depth τ is adopted to guarantee an appropriate resolution. In dynamical problems, for example in extended atmospheres/envelopes with arbitrary morphologies, the problem is to determine the region of last scattering of photons.

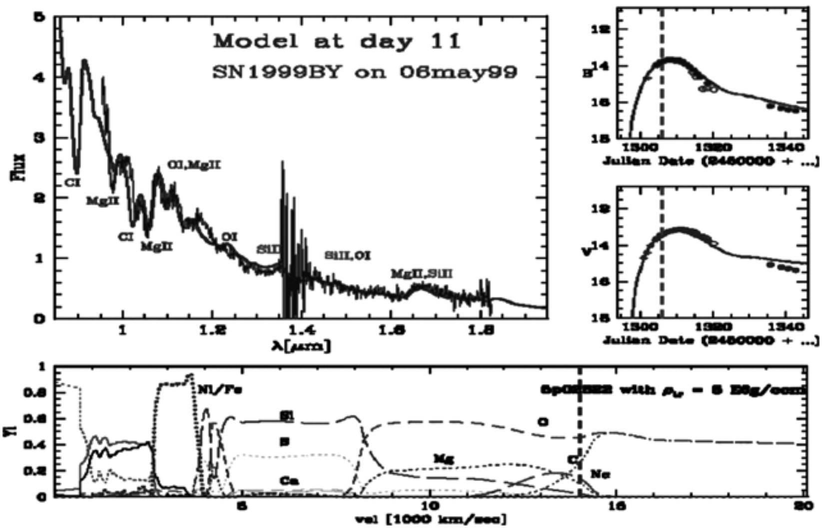

Figure 5. Comparison of an explosion model with the SNe Ia 1999by. We show spectra at day 11 (upper left), the the B and V light curves (right plots), and the chemical structure (lower panel). The explosion and evolution of the spectra are calculated self-consistently with the only free parameters being the initial structure of the exploding White Dwarf, and a parameterized description of the nuclear burning front. The explosion is calculated by a spherical hydro-modules using 912 depth points including a nuclear network with 218 isotopes. After about 10 s, only radioactive decays are taken into account but we solve the time-dependent, full non-LTE, radiation hydro. The light curves are based on several thousand non-LTE-spectra utilizing 912 depth, 2000 frequency points, and atoms with a total of 50 super-levels. For several moments of time, 1, detailed non-LTE spectra have been constructed using 90 depth and ≈30,000 frequency points with ≈500 non-LTE levels (from Höflich et al., 2002).

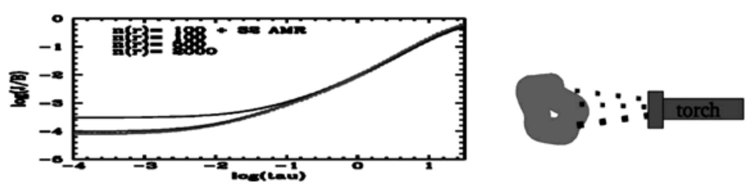

Figure 6. AMR for radiation hydro problem at the example of a isothermal, scattering-dominated, spherical atmosphere with a scattering/absorption fraction of 1000 and a total optical depth of 30. We show the ratio between mean radiation field J and the Planck function B. The numerical resolution in mass coordinates ΔM is given for various numbers n of grid points. Errors remain small for large optical depth because the solution is given by the local diffusion, but becomes large at $\tau \approx 1$, the photosphere. At the photosphere, the radiation field changes from isotropic to non-isotropic. Placing additional grid points at the photosphere improves the resolution dramatically. In time-dependent situation, we need AMR because the location of the photosphere changes with time. For 3-D geometries, we use a MC-torch to localize the decoupling region using the symmetry of the problem, i.e. photons decouple in the same region as those coming from outside are absorbed.

To determine its morphology, we make use of the fact that the the regions are identical at which photons decouple when coming from inside and to which photons penetrate when coming from outside (Figure 6).

Acknowledgments

This research is supported in part by NASA Grant LSTA-98-022.

References

Athay, R.: 1972, *Radiation Transport in Spectral Lines*. Reidel, Dordrecht.
Cannon, C.J.: 1973, *JQSRT* **13**, 627.
Colella, P. and Woodward, P.R.: 1984, *J. Comput. Phys.* **54**, 174.
Fryxell, B., Arnett, D. and Müller, E.: 1991, *ApJ* **367**, 619.
Hillier, D.J.: 1990, *A&A* **231**, 116.
Höflich, P.: 2003, in: Hubney et al. (eds.) *Stellar Atmospheres*, ASP 288, 185 & 371.
Höflich, P., Gerardy, C.L., Fesen, R.A. and Sakai, S.: 2002a, *ApJ* **568**, 791.
Höflich, P., Khokhlov, A.M. and Wang, L.: 2002b, in: *20th Texas Converence on Relativistic Astrophysics*, *AIP Conference Proceedings* 586, p. 459.
Höflich, P.: 1995, *ApJ* **443**, 89.
Höflich, P., Mueller, E. and Khokhlov, A.: 1993, *A&A* **268**, 570.
Höflich, P.: 1990, *A quantitative analysis of type II supernovae atmospheres*. Thesis submitted for the degree of Dr.rer.nat.habil., U München, MPA 563.
Höflich, P.: 1988, *PASP* **7**, 434.
Howell, D.A., Höflich, P., Wang, L. and Wheeler, J.C.: 2001, *ApJ* **556**, 302.
Hubeny, L. and Lanz, T.: 1992, *A&A* **262**, 501.
Kurucz, R.L.: 1995, *CD-23, Center for Astrophysics*. Cambridge MA.
Kurucz, R.L.: 1991, *CD-1, Center for Astrophysics*. Cambridge MA.
Olson, G.L., Auer, L.H. and Buchler, J.R.: 1986, *JQSRT* **35**, 431.
Scharmer, G.B.: 1984, in: Kalkofen (ed.), *Methods of Radiative Transfer*, Cambridge University Press, London.
Stone, J.M., Mihalas, D. and Norman, M.L.: 1992, *ApJ* **80**, 819.
Thielemann, F.-K., Nomoto, K. and Hashimoto, M.: 1994, in: S. Bludman et al. (eds.) *Supernovae, Les Houcheseds*, Elsevier, Amsterdam, p. 629.

EXPERIMENT ON COLLISIONLESS PLASMA INTERACTION WITH APPLICATIONS TO SUPERNOVA REMNANT PHYSICS

C. COURTOIS[1], R.A.D. GRUNDY[1], A.D. ASH[1], D.M. CHAMBERS[1,3], R.O. DENDY[2], K.G. MCCLEMENTS[2] and N.C. WOOLSEY[1]

[1]*Department of Physics, University of York, York, YO10 5DD, UK; E-mail: ncw2@york.ac.uk*
[2]*UKAEA Culham Division, Culham Science Centre, Abingdon, OX14 3DB, UK*
[3]*Present address: AWE, Aldermaston, Reading, RG7 4PR, UK*

(Received 30 April 2004; accepted 27 May 2004)

Abstract. Results from a scaled, collision-free, laser-plasma experiment designed to address aspects of collisionless plasma interaction in a high-plasma β supernova remnant (SNR) are discussed. Ideal magneto-hydrodynamic scaling indicates that the experimental plasma matches the SNR plasma at 500 ps. Experimental data show that the magnetic field can alter the plasma density profile when two similar plasmas interact in a colliding geometry. These results are not explained by magnetic-field pressure; they do, however, suggest magnetic field penetration that localizes the plasma particles to the Larmor radius, which appears smaller than the size of the experiment and the particle mean-free paths and may thus increase the *effective* collisionality of the interacting plasma system.

Keywords: supernova remnant, collisionless shocks, laboratory experiments

1. Introduction

High-power laser-plasma experiments have been used extensively in the emerging field of laser-laboratory astrophysics to simulate aspects of astrophysical phenomena (Remington et al., 2000). The relevance of many of these comparative studies relies on a scaling analysis between the experiment and the astrophysical object of interest. Assuming both systems are described by the same fluid or magneto-hydrodynamics models and using invariant properties of these models, plasma systems will behave similarly if a series of dimensionless parameters governing microscopic and macroscopic physical properties are matched (Ryutov et al., 2001).

An interesting astrophysical problem is the formation of collisionless shocks in supernova remnants (SNRs) and, in general, wave-particle processes. These shocks occur in magnetized SNR plasmas as the ejected matter of an exploding star interacts at high speed with the low-density interstellar medium (ISM). Wave-particle processes at these shocks are believed to be the origin of high-energy cosmic rays of energies up to 10^{15} eV, and these processes contribute in the heating of the ISM (Enomoto et al., 2002).

In a previous publication (Woolsey et al., 2001), we presented scaling analysis between a 100-year-old SNR reverse shock and a laser-plasma experiment. These

Astrophysics and Space Science **298:** 93–98, 2005.

experiments attempted to form a collisionless shock through the interaction of two supersonic counter-propagating plasmas immersed in an external magnetic field. The supersonic plasmas were formed by explosive expansion of laser-irradiated thin plastic foils. The experiment is scaled to match SNR conditions approximately 500 ps after laser irradiation. As in SNR, the role of the magnetic field is to introduce new short scale lengths in a collision-free system, namely the ion and electron Larmor radii. The plasma can be described as a magnetized fluid by ensuring that the Larmor radii are much shorter than the particle collisional mean-free path (MFP), as well as sufficiently short in comparison to the scale of the system. This is a consequence of the Larmor radii *effectively* increasing the collisionality of the system.

2. Scaling

Table I shows a set of parameters describing the plasma characteristics for a young SNR (Decourchelle et al., 2000); these are compared to a set of parameters derived for our experiment (Courtois et al., 2004). The four dimensionless parameters relevant to ideal magneto-hydrodynamic (MHD) scaling are shown in the left-hand side of Table I and illustrate this scaling is a reasonable description of an SNR plasma.

An SNR plasma is binary collision free as indicated by the collisionality parameter ζ, which is defined as the ion collisional MFP normalized to the size of the system, L. The ζ must be much larger than 1, which needs to be reproduced in an experiment. The ideal MHD (fluid) similarity between the SNR and the experiment requires conservation of the Euler number, Eu, and the plasma beta parameter, β. An SNR plasma is typified by a large β, indicating that the magnetic field does not dominate the global fluid motion yet is sufficiently strong to localize charged particles on scales $\ll L$. The ion localization parameter r_{Li}/L, defined as the ion Larmor radius r_{Li} normalized to the size of the system L, must be smaller than 1 (Ryutov et al., 1999). In this situation, the magnetic field is believed to increase the *effective* collisionality of a plasma and result in fluid-like dynamics. The experimental

TABLE I

Comparison of the scaling parameters for the reverse shock in a young SNR (Decourchelle et al., 2000) and the experimentally derived values measured at 500 ps

Parameters	SNR: 100 years	Exp: 500 ps	Parameters	SNR: 100 years	Exp: 500 ps
ζ	2×10^6	3×10^2	M_{A}	3×10^2	20
Plasma β	$\beta = 5 \times 10^2$	$\beta^* = 4 \times 10^2$	r_{Li}/L	10^{-9}	10^{-1}
Eu	18	21	R_{e}	10^{13}	10^7
M	16	12	P_{e}	10^{11}	10^{10}

plasma β, β^* is defined as the plasma ram pressure normalized to the magnetic-field pressure. Parameters identified with an asterisk are inferred from the flow kinetic energy rather than the thermal kinetic energy. Strong shock formation requires the sonic Mach number, *M,* and the Alfvénic Mach number, M_A, to be greater than unity. The description of plasma dynamics with ideal MHD equations assumes that the plasma behaves like an ideal fluid and that dissipative effects, such as thermal conductivity and viscosity, are negligible if the Péclet and Reynolds numbers are very large.

3. Experimental Results

Details of the experimental setup and results can be found elsewhere (Courtois et al., 2004; Gregory et al., 2005). Experimental results from a single exploded foil, 500 ps after laser irradiation, indicate that the plasma expansion is supersonic and that it is not affected by a 7.5 T magnetic field transverse to the plasma flow.

Results from opposing plasma experiments, with foils initially separated by 1 mm and 500 ps after laser irradiation in a magnetic-field-free case, suggest that the plasma interaction is collision-free and that counter-propagating plasmas interpenetrate. Yet the plasma interaction is altered when a magnetic field is applied. In these experiments a density plateau, 300 μm wide, is observed in the collision area. This only occurs when the magnetic field is present.

4. Discussion

The experimental scaling parameters are compared to simulated temporal and spatial variation of these parameters in Figures 1 and 2. Experimental results are shown by the dot, and simulation is shown by the solid line. Dotted lines indicate

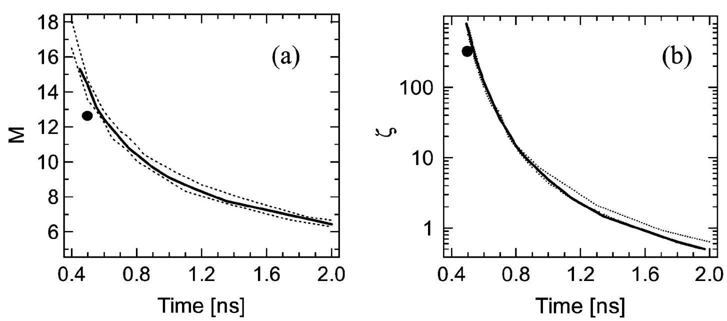

Figure 1. (a) The experimental Mach number, M, (solid dot) at 0.5 mm and 500 ps delay compared to simulated M (thick solid line) at 0.5 mm from foil target surface as a function of time. (b) The experimental (solid dot) collisionality parameter, ζ, at 500 ps delay and 0.5 mm from foil surface compared with simulated (thick solid line) as a function of time.

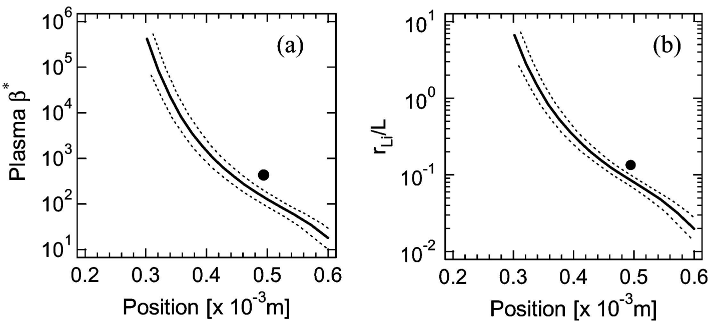

Figure 2. (a) The experimental (solid dot) plasma beta, β^*, at 0.5 mm and 500-ps delay compared to the simulated β^* (thick solid line) versus distance from the foil target surface. (b) The experimental ion localization parameter, r_{Li}/L, (solid dot) at 0.5 mm and 500 ps (delay?), compared with the simulated r_{Li}/L (thick solid line) as a function of distance from the foil target surface.

the influence of varying the laser energy and foil thickness by $\pm 10\%$ in an attempt to account for experimental uncertainty. The numerical results were obtained using the one-dimensional hydrodynamic model Med103 (Djaoui et al., 1992).

Figure 1a shows the Mach number, M, of one exploded foil 500 μm from the foil surface as a function of time. Time 0 corresponds to the peak of the 80-ps-duration laser pulse. The experimental Mach number at 500 ps after laser irradiation of 12 approaches the regime necessary for the formation of a strong shock. Numerical results indicate the plasma expansion remains supersonic for at least 2 ns.

Figure 1b illustrates how the collisionality parameter, ζ, of two opposing plasmas without a magnetic field varies with time. The experimental point and simulation indicate that the ζ at 500 ps at the midpoint between the foils (500 μm from each foil surface) is 300. Numerical results suggesting that ζ decreases quickly with time and that it falls to unity at 1.4 ns indicate that plasma interaction at around 500-ps delay is collision-free. Without a magnetic field, plasma interpenetration should occur, this is observed in the experimental electron density profiles.

Figures 2a and 2b show the dimensionless parameters most relevant to the role of the magnetic field in the experiment. The results are based on a model of magnetic-field penetration that is discussed in more detail by Courtois et al. (2004). Figure 2a shows the experimental parameter β^* at 500-ps delay for a single plasma as a function of position in the plasma. Position 0 corresponds to the initial foil position; the laser beam approaches from the left to the right. The experimental β^*, 500 μm from the foil surface, is equal to 400. Simulation suggests that the increase in β^* towards the initial target surface results from the attenuation of the magnetic field inside the plasma. This inferred large value of β^* indicates why the magnetic field does not affect the expansion of an exploding single foil. The magnetic field has no effect on plasma expansion up to 750 ps after laser irradiation and for propagation distances of 1 mm.

Figure 2b illustrates how the ion localization parameter, r_{Li}/L, at 500-ps delay varies as a function of position in the plasma. The r_{Li}/L is calculated using the thermal kinetic energy of the ion. The experimentally derived r_{Li}/L, located at a distance 500 μm from the foil surface, is equal to 0.1. Simulation suggests that r_{Li}/L increases toward the initial foil location and approaches unity at around 150 μm from the position 0.5 mm. The ion-flow kinetic energy can be used to estimate a $(r_{Li}/L)^*$; the $(r_{Li}/L)^*$ is around unity, which is still smaller than the MFP, but not localized. However, the electrons with r_{Le}/L and $(r_{Le}/L)^*$ around 10^{-3} are localized at all times, where r_{Le} is the electron Larmor radius. Electrostatic fields caused by charge separation are then expected to keep the ions localized.

Measurements show that applying a 7.5-T magnetic field affects the counter-propagation of the two exploding plasmas. These results indicate that a distinct change in the density profiles occurs with steeper density gradients and a density plateau that is approximately 300 μm wide. The electron density profile within this plateau region shows small density increases; these are not observed in the field free experiments. Numerical simulations suggest that the plasma density profile is sensitive to experimental conditions; as 10% variation in the foil thickness, the foil separation, or the laser intensity on target will alter the plasma density in the collision region. Currently, it is not possible to use absolute electron density measurements to determine how the magnetic field effects the plasma interaction. These results must be viewed as qualitative; nevertheless the formation of a plateau and the small plasma density increases in the collision region are qualitatively different to the field free measurements. Since β^* is large, these results are difficult to explain in terms of direct magnetic-field pressure on plasma flow. We also believe field compression between the leading edges of the two plasmas does not occur. We infer that the shape of the density profile may be related to the role of a magnetic field that has penetrated these plasmas. If the magnetic field penetrates, then the field will introduce new scale lengths, the Larmor radius to the plasma. If the magnetic field is sufficiently strong so that the shortest scale length is the Larmor radius, as it is in our experiment, then this is the scale at which fluid-like behaviour may occur in a collision-free system. Figure 2b illustrates that ion localization occurs when a 7.5-T strong magnetic field penetrates the plasma and with localization, $r_{Li}/L < 1$, to approximately 150 μm from the expanding edge of the plasmas. These scales are similar to the observed 300-μm-wide plateau in the interaction area, and such features only appear when counter-propagating plasma interact with a magnetic field.

The scaling parameters for an SNR are compared to the experimentally inferred values in Table I and are reported in more detail by Courtois et al. (2004). These indicate that the scaling between a laser-plasma experiment, and a collisionless SNR plasma is achievable. Nevertheless, we note that no evidence of a collisionless shock has been observed. A possible explanation is that the plasma scale lengths are not short enough and that the parameter, r_{Li}/L, must be reduced to below 10^{-2}.

5. Conclusion

We have experimentally investigated the dynamics of single laser-exploded foil targets and the interaction of two counter-propagated laser-exploded foil target with and without an applied magnetic field. Dimensionless parameters governing plasma evolution of a collisionless SNR have been compared to those inferred from these experiments and from numerical simulation. These results show that the experimental parameters obtained 500 ps after laser irradiation match those of a reverse shock in a young SNR and that the laboratory simulation of collisionless phenomena relevant to an SNR is possible. A magnetic field has been observed to affect a collision-free plasma interaction through the formation of an extended density plateau with a small electron density features centered on the collision area. Experiment indicates that the magnetic field is not sufficiently strong to affect the plasma expansion dynamics directly. However, analysis indicates that the magnetic field may penetrate these plasmas; the relevant scale lengths are reduced from the particle MFP to the particle Larmor radii. The electrons and the ions are magnetized and weakly magnetized, respectively. The magnetic-field penetration length is consistent with the width of the experimental observed plateau. Shock formation was not observed, this is probably due to the relatively large value of r_{Li}/L.

Acknowledgments

We express our thanks to Dr. Karl Krushelnick and Imperial College of the loan of the electromagnet, to B. Lings, K. Rosol'anková, University of Oxford, and to Dr. Per Helander for discussions, and to the Central Laser Facility staff. This work was funded by the United Kingdom Engineering and Physical Sciences Research Council.

References

Courtois, C., et al.: 2004, *Phys. Plasmas* **11**, 3386.
Djaoui, A. and Rose, S.J.: 1992, *J. Phys. B* **25**, 2745.
Decourchelle, A., Ellison, D.C. and Ballet, J.: 2000, *ApJ* **543**, L57.
Drake, R.P.: 2002, *Phys. Plasmas* **9**, 727.
Enomoto, R., et al: 2002, *Nature* **416**, 823.
Gregory, C.D., et al.: 2005, *Ap&SS* **298**, 389.
Remington, B.A., et al.: 2000, *Phys. Plasma* **7**, 1641.
Ryutov, D., et al.: 1999, *ApJ* **518**, 821.
Ryutov, D.D., Remington, B.A., Robey, H.F. and Drake, R.P.: 2001, *Phys. Plasmas* **8**, 1804.
Woolsey, N.C., et al.: 2001, *Phys. Plasmas* **8**, 2439.
Woolsey, N.C., et al.: 2002, *Phys. Plasmas* **9**, 729.

LABORATORY EXPERIMENTS OF STELLAR JETS FROM THE PERSPECTIVE OF AN OBSERVER

PATRICK HARTIGAN

Department of Physics and Astronomy, Rice University, Houston, Texas, USA;
E-mail: hartigan@sparky.rice.edu

(Received 30 April 2004; accepted 19 July 2004)

Abstract. It has been two decades since astronomers first discovered that accretion disks around young stars drive highly collimated supersonic jets. Thanks to concerted efforts to understand emission line ratios from jets, we know that velocity variations dominate the heating within these flows, and motions in stellar jets, now observed in real time, are primarily radial. The fluid dynamics of the cooling zones can be complex, with interacting shocks, clumps, and instabilities that could benefit from insights into the physics that only experiments can provide. Recent laboratory experiments have reproduced jets with velocities and Mach numbers similar to those within stellar jets, and the field seems poised to make significant advances by connecting observations and theories with experiments. This article points out several aspects of stellar jets that might be clarified by such experiments.

Keywords: ISM: jets and outflows, ISM: kinematics and dynamics, shock waves

1. Introduction

A main focus of the HEDLA conferences has been to identify areas of possible overlap between astronomical observations and theory with laboratory experiments. Stellar jets are one promising possibility, because the physics that governs stellar jets is that of supersonic MHD flows, which is in principle amenable to experiment. We know a great deal about stellar jets because they radiate emission lines which reveal the densities, temperatures, velocities, and locations of shocks in the flow, and recent images of jets from HST show observable motions on the sky within a few years.

Space limitations prevent any overview of the field for this article. We refer the reader to Reipurth and Bally (2001) for a general review of stellar jets, and Hartigan (2003) for a summary of jet motions, magnetic properties, and techniques used to estimate mass loss. Eislöffel et al. (2000) and Hartigan et al. (2000) cover observations and interpretations of shocks in outflows, while Draine and McKee (1993) give a broad overview of shock waves in the interstellar medium, including processes related to supernova remnants, blast waves, and C-shocks.

Laboratory simulations have contributed little to our understanding of stellar jets to this point, though that situation is likely to change soon. Lebedev et al. (2002) have

Astrophysics and Space Science **298:** 99–105, 2005.

succeeded in creating a jet by vaporizing an array of wires and driving the plasma through a collimation shock similar to that envisioned by Canto and Rodriguez (1980). By running this jet into a crosswind, Ciardi et al. (2004) were able to reproduce a bent jet, like those observed when stellar jets emerge from a dense disk and encounter a large scale flow from another source (Lim and Raga, 1998). Being able to study the strength and stability of the deflection shock in the jet provides a unique insight into the physics of this process that is difficult to constrain observationally because the deflection shock may not heat the gas enough to become visible.

In what follows I point out areas like the one above where laboratory experiments could help observers and theoreticians make sense of the complexities within stellar jets. These examples focus on the fluid dynamics rather than on emission line ratios or line profiles, the latter probably impossible to simulate in the lab.

2. Variable Velocity Flows

Fluctuations in the jet velocity that exceed the local sound speed produce shocks when faster material overtakes slower material in the flow, and *this mechanism dominates the heating within stellar jets*. Evidence for variable velocity flows existed for decades in the emission line ratios, which indicate low shock velocities of $\sim$30 km s^{-1} despite the fact that the jet moves at $\sim$300 km s^{-1}. With new HST images of flows in the plane of the sky, one can measure the proper motions of individual knots with high precision, and differential motions within the jet are indeed $\sim$30 km s^{-1}, as expected (Hartigan et al., 2001).

A natural consequence of a flow that varies in velocity is that individual bow shocks in the jet will occasionally collide. Figure 1 shows the aftermath of just such an event in HH 111, where two bow shocks lie in close proximity. The outer bow shock has a higher proper motion than the inner one; the motions imply that the shocks coincided about 80 years ago.

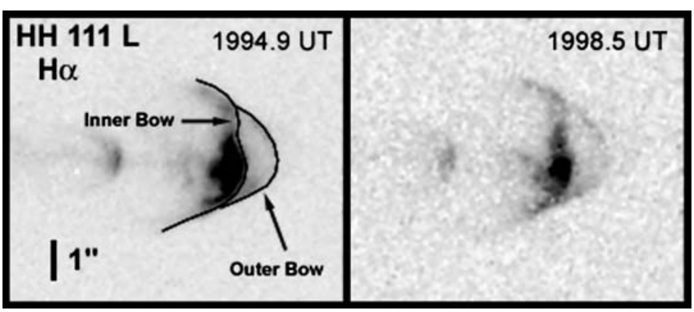

Figure 1. These images resolve the knot HH 111 L into two bow shocks. The faster bow shock, on the right, widened and faded between the two epochs. The two shocks coincided about 80 years ago. The scale bar is one arcsec, or 6.9 × 10^{15} cm for all of the figures.

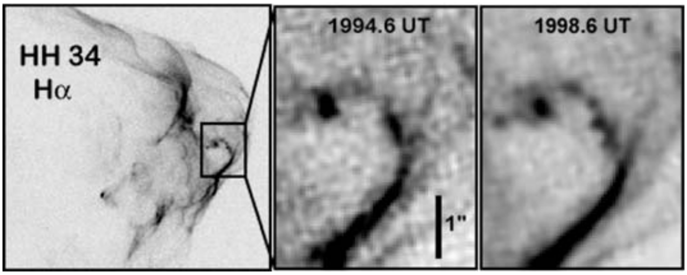

Figure 2. The boxed filament in the large bow shock of HH 34 marked in the figure either fragments, or encounters four distinct clumps between the two epochs.

Colliding shocks like HH 111 L suggest a range of laboratory experiments relevant to astrophysical flows. An obvious experiment is to observe how working surfaces of the bow shocks evolve with time during the collision of the shocks, and to see if the collision generates any fragmentation. Because we know the velocity in jets like HH 111 at each point in the flow, if an experimenter could set up this velocity law in a laboratory jet then it would be possible to watch the jet evolve, with shocks and rarefaction waves developing and dissipating as they will hundreds of years in the future in the actual jet. The ability to create specified velocity law with time would open up other interesting possibilities. For example, jets that vary rapidly with time should form shocks close to the source, and then bunch up into distinct bullets at larger distances. Each shock tends to splatter material laterally, so the observed opening angle of the jet increases because of this process. Experiments should be able to quantify these ideas for real flows.

3. Interface Instabilities

Figure 2 shows that the HH 34 bow shock breaks up into four evenly-spaced clumps which lag behind the main shock (Reipurth et al., 2002), a morphology which resembles that of a R-T instability (observed in real time!). A more prosaic explanation is that the preshock medium is clumpy, and the bow shock has overtaken clumps. Dynamical instabilities in shocks should be possible to study in the lab. Some issues to address include learning the conditions under which jets fragment, and when they do, if there is a characteristic fragmentation length. Identifying the physical process responsible for a preferred fragmentation scale is a key to understanding the flow dynamics.

4. Clumpy Flows

When a collimated jet strikes material ahead of it (in jets from young stars, typically previously ejected gas), a bow shock accelerates the ambient gas and a shock called the Mach disk decelerates the jet. Numerical simulations show that the ‘working

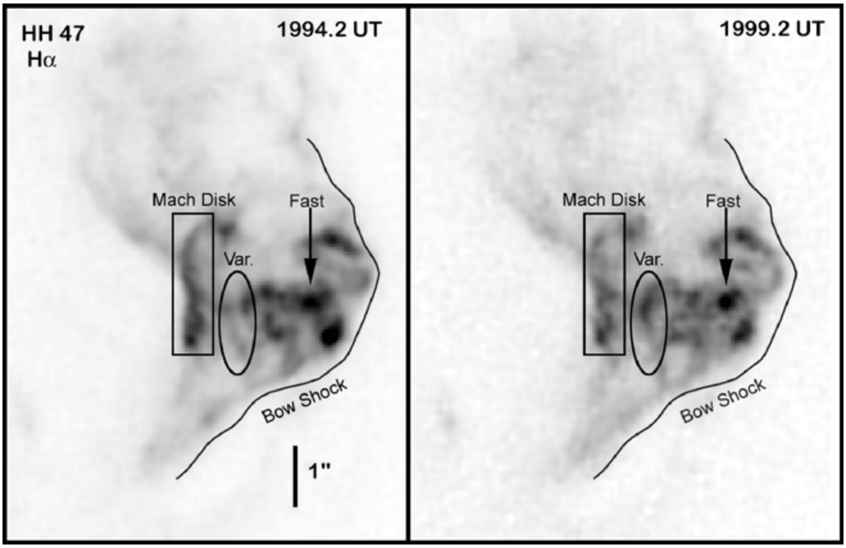

Figure 3. The working surface of HH 47A is the textbook example of a Mach Disk/bow shock pair. The system of shocks, which moves to the right in the figure, appears to be developing instabilities or has small clumps which plow through the Mach disk. The bright condensation labeled as 'fast' moves ahead of the other emission in the flow. The area marked 'Var' denotes a region where shocks appear to be forming.

surface' region between these two shocks can be quite complex, and may host a variety of fluid and cooling instabilities (Frank et al., 2000; Blondin et al., 1990). Images of HH 47 (Figure 3) reveal yet another complication – the jet itself appears to be clumpy both along the jet and laterally to the jet. Between 1994 and 1999, the Mach disk began to break up, as if several denser clumps were passing through it. A very dense knot is now moving through the working surface, and should be emerging from the bow shock within a decade or so.

There are several aspects of the dynamics within the working surface of HH 47 that could be clarified by experiments. Experiments could quantify the density contrast required to allow jet clumps to penetrate through the entire bow shock, and follow how the working surface changes with time. Determining how clumps affect the morphology of the Mach disk, and observing whether or not clumps fragment when they encounter shocks would be a substantial contribution to the subject.

5. Entrainment

Entrainment occurs within stellar jets as faster material overtakes slower material, and along the edges of bow shocks where shear exists (discussed in the next section). Along the jet we sometimes observe a slow clump being accelerated by a fast wind (Figure 4; Reipurth et al., 2002). These slow clumps then show 'reverse' bow

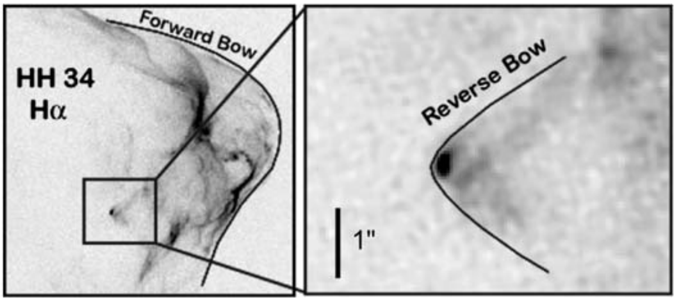

Figure 4. The knot indicated in the figure lies within the large bow shock of HH 34, but the small bow that forms around the knot is oriented as if it being entrained by faster material. The proper motion of this knot is slower than the rest of the flow, and material flows past it to the right.

shocks where the apex of the bow points in the direction of the exciting source (e.g. Schwartz, 1978).

As clumps are accelerated by a supersonic wind, Kelvin–Helmholtz instabilities along the shock should begin to destroy the clump. Lab experiments could quantify this process, determining clump lifetimes for various density contrasts of the clump and the wind, clump sizes, wind velocities, magnetic field configurations, and so on.

6. Supersonic Shear and Wakes

Images and movies of HH 1 show a remarkable zone of strong shear along the top portion of the large bow shock (Figure 5; Bally et al., 2002). The morphology of the flow in that region lacks the smooth arcs of the bow shocks along the axis of

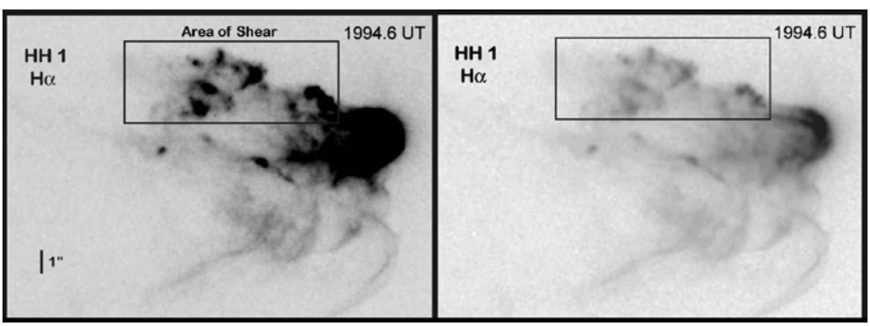

Figure 5. The boxed region of these Hα images of the HH 1 bow shock moves much more slowly, and appears clumpier than the arc-shaped shocks at the bottom of the images. This zone of shear is an excellent place to study fluid instabilities. The exciting source lies outside the images to the left. The two images are identical except for greyscale levels.

the flow, and instead shows a clumpier morphology. The images suggest turbulent motions, or perhaps even vortices, in this region, which appears to be a real example of a supersonic mixing layer. Shear also appears to be tearing a piece of knot F from the HH 34 jet (Reipurth et al., 2002).

Although variations in the flow velocity dominate the heating within the majority of stellar jets, the HH 110 flow appears to result from a glancing collision of a jet and a dense molecular cloud. Images and proper motions of this object show the flow begins as a typical collimated jet, but suddenly fans out into a diffuse flow at an angle of about 45 degrees to the direction of the initial jet (Reipurth et al., 1996). The velocity structure within the wake is unusual for a jet, as it lacks any ordered structure (Riera et al., 2003).

Laboratory experiments can help us interpret images like HH 1 by determining the types of structures, such as shocks, clumps, and vortices, that occur in mixing layers with different amounts of supersonic shear, The HH 110 flow is an obvious target for the lab, where one could explore the velocity structure and morphologies of supersonic wakes of flows deflected by various angles with a range of velocities.

7. Concluding Remarks

Laboratory experiments have begun to make substantial contributions to our understanding of the dynamics of shocked astrophysical flows. Including variable velocities and clumps will be the biggest steps experimenters can make toward modeling the dynamics present in real astrophysical flows.

All the experiments outlined in this article would be greatly enhanced by including magnetic fields of various strengths and orientations within the flows. Modeling MHD flows is notoriously difficult when including non-LTE atomic cooling, and fields are also challenging to constrain observationally. Laboratory experiments may also be able to shed some light on how easily dust is heated and destroyed in shocks of various velocities, densities, and field strengths, and assess the extent to which dust is charged behind shocks. Another possibility would be to create a C-shock in the lab, which forms when the flow is supersonic but sub-Alvenic. In a C-shock, ions and neutrals act as separate fluids in the postshock gas, and friction between these fluids produces a spatially extended heating zone that is difficult to model theoretically and not easily resolved with current observations. C-shocks play a critical role in accelerating molecular outflows from young stars by transferring momentum and energy from stellar jets to the ambient molecular cloud.

References

Blondin, J., Fryxell, B. and Konigl, A.: 1990, *ApJ* **360**, 370.
Canto, J. and Rodriguez, L.F.: 1980, *ApJ* **239**, 982.

Ciardi, A., et al.: 2004, *5th International Conference on High Energy Density Laboratory Astrophysics*, Tucson, AZ, poster paper.
Draine, B. and McKee, C.: 1993 *Ann. Rev. Astr. Ap.* **31**, 373.
Eislöffel, J., Mundt, R., Ray, T.P. and Rodriguez, L.F.: 2000, in: Mannings, V., Boss, A. and Russell, S. (eds.), *Protostars and Planets IV*, University of Arizona Press, Tucson, p. 815.
Frank, A., Lery, T., Gardiner, T., Jones, T. and Ryu, D.: 2000, *ApJ* **540**, 342.
Hartigan, P.: 2003, *Ap. Sp. Sci.* **287**, 111.
Hartigan, P., Bally, J., Reipurth, B. and Morse, J.: 2000, in: V. Mannings, A. Boss and S. Russell (eds.), *Protostars and Planets IV*, University of Arizona Press, Tucson, p. 841.
Hartigan, P., Morse, J., Reipurth, B., Heathcote, S. and Bally, J.: 2001, *ApJ* **559**, L157.
Lebedev, S., et al.: 2002, *ApJ* **564**, 113.
Lim, A.J. and Raga, A.C.: 1998, *MNRAS* **298**, 871.
Reipurth, B. and Bally, J.: 2001, *Ann. Rev. Astr. Ap.* **39**, 403.
Reipurth, B., Heathcote, S., Morse, J., Hartigan, P. and Bally, J.: 2002, *AJ* **123**, 362.
Reipurth, B., Raga, A. and Heathcote, S.: 1996, *A&A* **311**, 989.
Riera, A., Raga, A.C., Reipurth, B., Amram, P., Boulesteix, J., Canto, J. and Toledano, O.: 2003, *AJ* **126**, 327.

A HED LABORATORY ASTROPHYSICS TESTBED COMES OF AGE: JET DEFLECTION VIA CROSS WINDS

A. FRANK[2,3], E.G. BLACKMAN[2,3], A. CUNNINGHAM[2,3], S.V. LEBEDEV[1], D. AMPLEFORD[1], A. CIARDI[1], S.N. BLAND[1], J.P. CHITTENDEN[1] and M.G. HAINES[1]

[1]*The Blackett Laboratory, Imperial College, London, UK*
[2]*Department of Physics and Astronomy, University of Rochester, Rochester NY; E-mail: afrank@pas.rochester.edu*
[3]*Laboratory for Laser Energetics, University of Rochester, Rochester, NY*

(Received 13 May 2004; accepted 20 June 2004)

Abstract. We present new data from High-Energy Density (HED) laboratory experiments designed to explore the interaction of a heavy hypersonic radiative jet with a cross wind. The jets are generated with the MAGPIE pulsed power machine where converging conical plasma flows are produced from a cylindrically symmetric array of inclined wires. Radiative hypersonic jets emerge from the convergence point. The cross wind is generated by ablation of a plastic foil via soft-X-rays from the plasma convergence region. Our experiments show that the jets are deflected by the action of the cross wind with the angle of deflection dependent on the proximity of the foil. Shocks within the jet beam are apparent in the data. Analysis of the data shows that the interaction of the jet and cross wind is collisional and therefore in the hydrodynamic regime. We consider the astrophysical relevance of these experiments applying published models of jet deflection developed for AGN and YSOs. We also present results of 3-D numerical simulations of jet deflection using a new astrophysical Adaptive Mesh Refinement code. These simulations show highly structured shocks occurring within the beam similar to what was observed in the experiments.

Keywords: hydrodynamics, methods: laboratory, ISM: Herbig–Haro objects, stars: winds, outflows

1. Introduction

Collimated plasma beams also known as “jets” are ubiquitous in astrophysics occurring in wide variety of environments, most notably those associated with young stars (Young Stellar Objects, YSOs, Bally and Reipurth, 2001a) and Active Galactic Nuclei (AGN, Balsara and Norman, 1992). In both environments a subset of observed bipolar jets shows a characteristic **C**-shaped symmetry. Bally and Riepurth (2001b) have reported observations of a number of YSO jet systems which showed bending along either a single jet in a bipolar jet system or the **C**-shaped morphological pattern for both jets.

A number of authors have studied the cause of jet deflection and their conclusions tend to support the hypothesis that bending occurs due to the ram pressure of a “cross wind” (Begelman et al., 1979; Canto and Raga, 1995). In the context of AGN the crosswind can be provided by the motion of the host galaxy through the IGM. For the case of YSO outflows the cross wind may be produced by ionization or a wind from nearby massive star or by motion of the jet source.

Analytical models of jet deflection by a cross wind *neglecting the presence of shocks* have been carried out by a Begelman et al. (1979) and Canto and Raga (1995). Numerical simulations of the process have been performed by a number of authors including Balasra and Norman (1992) for the extragalactic case and Lim and Raga (1998) for the YSO case. These simulations demonstrated good agreement with existing analytical models.

Although the physics of jet deflection appears well understood in terms of simulations and analysis, what are missing are direct experimental tests in a controlled setting. The advent of high-energy devices used for Inertial Confinement Fusion (High-Power Lasers, Fast Z Pinches) allows for direct experimental studies of astrophysical hypersonic flow problems. High-Mach number jets have played an integral part in defining this new field (Raga et al., 2001; Farley et al., 1999; Shigemori et al., 2000). In Lebedev et al. (2002), the results of pulsed power machine studies were presented in which a conical array of 16 wires was used to generate highly collimated radiative jets. These studies were noteworthy in that they not only confirmed the utility of the pulsed power testbed for creating scalable astrophysically relevant jets, they also were also able to confirm predictions of the Canto et al. (1988) theory of collimation via converging conical flows and address previously unresolved issues of the stability of this collimation mechanism (Frank et al., 1996). In this contribution, we present further results using the astrophysical jet testbed on the MAGPIE pulsed power device. Here we study the deflection of hypersonic jets via a cross wind produced by ablation of an irradiated target.

2. Experiment and Results

2.1. Configuration

Details of our experiment can be found in (Lebedev et al., 2004). A supersonic, radiatively cooled plasma jet is produced using a conical array of fine metallic wires (Lebedev et al., 2002), driven by a fast rising current (IMA, 250 ns). The resistive heating of the wires rapidly converts some fraction of the wire material into hot coronal plasma, which is then accelerated towards the array axis by the net $\boldsymbol{J} \times \boldsymbol{B}$ force. When the plasma driven off the wires reaches the array axis, a conical standing shock is formed. Such shocks are effective in redirecting the plasma flow into an axial directed flow, i.e. a jet. The high rate of radiative cooling behind this shock allows the jet to become highly collimated (Canto et al., 1988). The plasma jet formed in this configuration is hypersonic (velocity $\sim$200 km/s, internal Mach number $\sim$30), radiative and, most importantly, has dimensionless parameters similar to those of astrophysical (stellar) jets (Lebedev et al., 2002).

The jet is driven from the wire array region into vacuum and then passes through a region with a transverse flow of plasma (the cross wind). The cross wind is produced as a result of radiative ablation of a thin plastic foil installed parallel to the axis of the jet. The foil is exposed to the XUV and soft X-ray radiation from the standing conical shock (the region of the jet formation) and from the wires. The ablation rate of the foil is increasing with time, due to an increase of the radiation flux allowing some degree of control over the parameters of the cross wind by simply changing the position of the foil with respect to the jet axis.

2.2. RESULTS

Figures 1a and b shows typical results of laser probing (interferometry) diagnostics of the jet propagating through the region with a cross wind. Both images show the jet remains well collimated after passing next to the foil, but is deflected away from it. The deflection depends on the position of the foil and is stronger when the foil is placed closer to the jet axis. In Figure 1a the foil is situated 4.6 mm from the axis and the jet is deflected by $\sim 4^\circ$. In Figure 1b the foil is only 1.8 mm from the axis and the deflection angle is $\sim 27^\circ$. The difference in foil positions leads to a difference in the ram pressure of the plasma wind impacting the jet, and therefore, to the difference in the degree of beam deflection. We note here that the difference in the ram pressure is mainly due to the temporal variation of the plasma flow. The decrease of the ram pressure due to divergence of the flow is relatively small, at most a factor of ~ 2, because the dimensions of the foil are larger or comparable to the distance between the foil and jet.

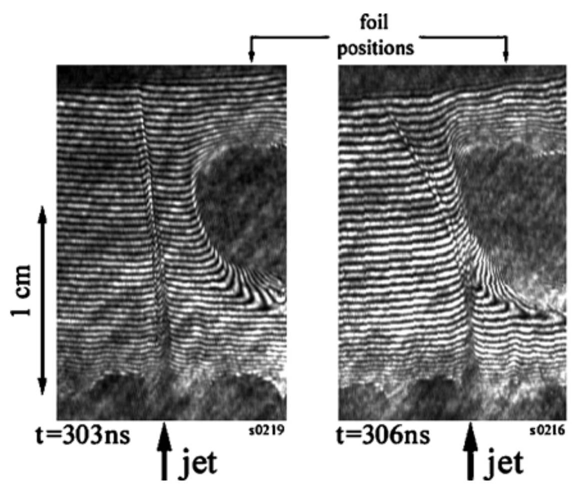

Figure 1. (a,b) Interferometric image shows well-collimated plasma jet with deflection for two experiments with different ram pressure in the cross wind. Ram pressure variation was achieved by variation of position of the ablated foil.

The impact of the wind on the jet affects the internal structure of the jet. Interferometric analysis shows appearance of asymmetries in the transverse density profiles, and a localised increase of the density gradient in the region where the jet bends. These sharp density gradients are significant in that they could be interpreted as internal shocks in the jet formed by the action of the plasma flow. In the process of deflection the diameter of the jet becomes smaller than that in the free-propagating jet, and reaches its minimum value of $\sim$0.3 mm at the position of the sharpest change of the jet's direction.

2.3. Localisation criteria (collisionality)

The interaction of the plasma flow with the jet in our experiment is collisional, i.e. it is similar to the hydrodynamic interaction in the astrophysical system. The condition for collisionallity is that the ratio of the particle mean free path (λ) to the jet radius be much less than unity ($\lambda/R_j \ll 1$, Ryutov et al., 1999). We note that for typical YSO jet parameters ($T_j \sim .1$ eV, $n_j \sim 10^4\,\mathrm{cm}^{-3}$, $R_j \sim 100$ AU) the collisionality condition is achieved. For the experiment we must ensure that both the jet and the wind are collisional with respect to themselves, i.e. that the mean free paths of the ions are significantly smaller than the characteristic spatial scales of the jet and cross wind. In addition we must also ensure that the interaction between the cross wind and jet is collisional in that ion collision distances are smaller that the spatial scale of the interaction region.

Despite the highly directed velocity of the jet, the temperature of both the ions and the electrons in the jet is relatively low. Estimates based on comparison with the precursor in cylindrical wire arrays and results of computer simulations indicate a temperature of $T < 50$ eV. Assuming that tungsten has $Z \sim 5$–10 at this temperature the upper estimate of the ion mean free path, for the typical electron densities in the jet of $n_e > 10^{18}\,\mathrm{cm}^{-3}$, is $\lambda_j \sim 10^{-4}$–10^{-5} cm; this is significantly smaller than the jet radius ($r_j \sim 0.05$ cm). Thus the dimensionless parameter $\delta_j = \lambda_j/r_j \ll 1$ and the jet is collisional with itself on the spatial scale corresponding to the wind–jet interaction.

The cross wind is also highly collisional, even if we assume that the electron temperature is as high as 50 eV. The mean free path, for electron densities in the wind $n_e \sim 10^{18}\,\mathrm{cm}^{-3}$ and $Z \sim 2$, is $\lambda_w \sim 10^{-3}$ cm, which is a factor of 50 smaller than the jet radius.

The character of the impact of the side wind on the jet is determined by the m.f.p. of the wind ions interacting with the jet. For an electron density in the jet of $n_e > 5 \times 10^{18}\,\mathrm{cm}^{-3}$ and an ionic charge $Z > 5$, one finds $\lambda_{wj} < 2 \times 10^{-3}$ cm. Thus $\delta_{jw} = \lambda_{wj}/r_j \sim 0.04 \ll 1$ and the ions in the plasma wind will lose their momentum in collisions with the jet, therefore providing the pressure acting to deflect the jet. We conclude that the interaction of the plasma wind with the jet in our experiments can be described hydrodynamically.

3. Astrophysical Relevance

3.1. Analytic models

Canto and Raga (1995) presented an analysis of jet deflection via a cross wind for both adiabatic and isothermal jet/wind interactions. Although these authors found that if the jet were to travel enough scale lengths it would, eventually be turned to flow parallel to the wind, a solution close to the initial point of jet/wind contact could be written as a quadratic in the distance x along the original jet propagation direction. When the jet is initially flowing perpendicular to the direction of the wind the solution takes the form.

$$r = \left(\frac{1}{2d}\right)(z - z_s)^2, \quad d = \sqrt{\frac{\dot{M}_j v_j^3}{\pi c^2 \rho_w v_w^2}} = \left(\frac{v_j^2}{c v_w}\right)\sqrt{\frac{\rho_j}{\rho_w}} r_j \tag{1}$$

where z_s is the initial position at which the jet encounters the crosswind and r is the direction perpendicular to the initial flow. In the above d, is the principle parameter determining the deflected jet trajectory with c being the sound speed in the shocked jet. The utility of these expressions comes when we combine them with the actual jet trajectories to extract internal characteristics of the jets.

Focusing on extracting values of the jet Mach number, we fit the data from the experiment with quadratics on the basis of the Eqs. (2) and (3). From these we find limits on the Mach number in the shocked jet to be, $6 < M < 26$. This is consistent with the values of the jet Mach number, $M > 15$–20, taken from experiments in which the beam is undisturbed (Lebedev et al., 2002). Such consistency not only strengthens the argument for the hydrodynamic nature of the behaviour observed in the experiments, it also demonstrates the ability of experiments to make contact with existing astrophysical theory.

3.2. Astrophysical simulations

In Figures 2a, b we show results of 3-D simulations of jet wind interactions. These simulations were carried out using AstroBEAR, a new adaptive mesh refinement code for astrophysical fluid dynamics (Poludnenko et al., 2004; Varniere et al., 2004) These simulations were designed to track the structure of a jet interacting with a localized cross wind (i.e. one with limited spatial extent as occurs in the experiments). We note that all published astrophysical simulations of this problem utilize a continuous cross wind which fills the computational grid. A continuous cross wind is appropriate only in cases where the jet propagation scale is smaller than the scale of any inhomogeneities in the surrounding environment which contains the cross wind. When the cross wind forms due to motion of the source this assumption may not be valid especially when the jet propagates over large distances which may

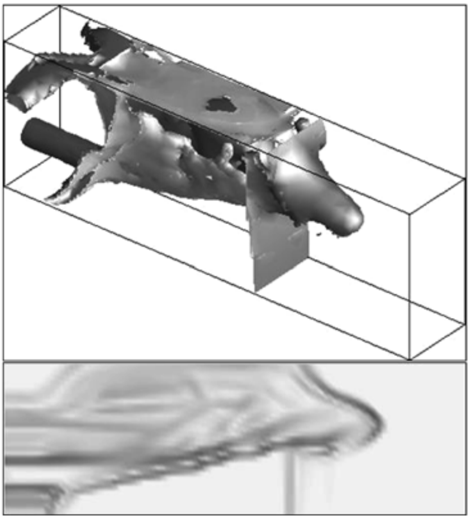

Figure 2. (a,b) Images of density in 3-D simulations of a jet interacting with a cross wind of limited extent at time $t = 106.6$ yr. The jet propagates in the z direction and the crosswind propagates in the x direction. Top image shows 2 iso-density surfaces. The bottom image shows a greyscale schlieren map of the density at a cross-cut in the x–z plane at mid-position in y.

take it out of its natal environment. Our simulations were performed using a three level adaptive mesh with a maximum resolution $384 \times 128 \times 64$. Our simulations allowed for radiative losses using a standard cooling curve.

Figure 2 shows a 3-D visualization of a simulation initialized such that both the jet and the cross wind begin propagation at the start of the simulation. The most interesting aspect of these simulations is the clearly defined initiation of the jet bending at the location where the cross wind impinges on the jet beam. In Figure 2a one can make out the relatively "naked" jet beam emanating from the injection point and being deflected downstream. Figure 2b shows a Schlieren map of the cross-cut along the x–z plane which highlights shock waves. Near the injection point the Schlierien map shows the cocoon and bow shock surrounding the beam. Once the cross wind strikes the cocoon a shock forms which deflects the cross wind. As this shock propagates diagonally, an internal shock in the jet also becomes apparent and as these two shocks cross the beam, the jet begins its deflected trajectory. As the jet crosses out of the region of the cross wind we find that the shock strengths decrease. We note that in the continuous wind simulations the shocks remain of constant strength. This simulation demonstrates that shocks within the beam result from the jet/cross-wind interaction and that these shocks are a key part of the deflection process. It is noteworthy the high-density features (interpreted as shocks) in the experiments only appear after the jet reaches the approximate location of the plastic foil, just as we would predict from the simulations.

4. Conclusions

We conclude that our experiments provide a new window in the nature of jet deflection relevant to astrophysics. While our ability to recover reasonable flow parameters from the deflections using an astrophysical model gives us confidence that our experiments are reaching relevant astrophysical behaviours, there remain uncertainties. In particular, while the structures seen in the jet in the experiments appear linked to shocks we do not see evidence for the strongest oblique shock in the wind material, which the 2-D simulations indicate, drives the initial deflection. However, we do see a strong internal shock in the jet and the narrowing of the jet after this shock. Thus the real situation may be more complex than can be recovered in either the higher resolution 2-D simulations or lower resolution 3-D simulations. This point should receive more attention in future studies.

We note that recent studies of star formation in cluster environments show that many stars may be born with significant proper motions (Bonnel et al., 2004). For example, recent studies of PV Ceph indicate it is travelling across its molecular cloud environment at speeds of order $10\,\mathrm{km\,s^{-1}}$ (Goodman and Arce, 2004) and that its molecular outflow shows evidence for deflection. If a scenario in which high-proper motions are common then it is likely that jet or molecular outflow deflection may be more common than previously expected and in many cases the signatures of deflection are difficult to see due to confusion with different sources. Thus further experimental studies which can articulate the nature of deflection for different outflow properties (such as degree of collimation) are warranted.

Acknowledgments

This research was sponsored by the NNSA under DOE Cooperative Agreement DE-F03-02NA00057. Support to AF was also provided at the University of Rochester by NSF grant AST-9702484 and AST-0098442, NASA grant NAG5-8428, and the Laboratory Astrophysics program at the Laboratory for Laser Energetics.

References

Bally, J., Devine, D. and Alten, V.: 1996, *ApJ* **473**, 921.
Bally, J. and Reipurth, B.: 2001a, *ApJ* **546**, 299.
Bally, J. and Reipurth, B.: 2001b, *ARAA*.
Balsara, D. and Norman, M.: 1992, *ApJ* **393**, 631.
Begelman, M.C., Rees, M.J. and Blandford, R.D.: 1979, *Nature* **279**, 770.
Bonnell, I.A., Bate, M.R. and Vine, S.: 2003, *MNRAS* **343**, 413.
Canto, J. and Raga, A.: 1995, *MNRAS* **277**, 1120.
Canto, J., Tenorio-Tagle, G. and R'ozyczka, M.: 1988, *A&A* **192**, 287.
Farley, D.R. et al.: 1999, *Phys. Rev. Lett.* **83**,1982.

Frank, A., Balick, B. and Livio, M.: 1996, *ApJ* **471**, 53.

Lebedev, S.V., Chittenden, J.P., Beg, F.N., Bland, S.N., Ciardi, A., Ampleford, D., Hughes, S., Haines, M.G., Frank, A., Blackman, E.G. and Gardiner, T.A.: 2002, *ApJ* **564**,113.

Lim, A.J. and Raga, A.C.: 1998, *MNRAS* **298**, 871.

Logory, L., Miller, P., and Story, P.: 2000, *ApJS* **127**, 421.

Poludnenko, A., Varniere, P., Frank, A. and Mitran, S.: 2004, Springer's Lecture Notes in Computational Sciences and Engineering (LNCSE) series (to appear).

Raga, A., Sobral, H., Villagrán-Muniz, M., Navarro-González, R. and Masciadri, E.: 2001, *MNRAS* **324**, 206.

Varniere, P., Poludnenko, A., Cunningham, A., Frank, A. and Mitran, S.: 2004, Springer's Lecture Notes in Computational Sciences and Engineering (LNCSE) series (to appear).

Shigemori, K.: 2000, *Phys. Rev. E.* **62**, 8838.

RELATIVISTIC JETS FROM ACCRETION DISKS

R.V.E. LOVELACE, P.R. GANDHI and M.M. ROMANOVA
Cornell University, Ithaca, NY, USA; E-mail: RVL1@cornell.edu

(Received 27 April 2004; accepted 25 May 2004)

Abstract. The jets observed to emanate from many compact accreting objects may arise from the twisting of a magnetic field threading a differentially rotating accretion disk which acts to magnetically extract angular momentum and energy from the disk. Two main regimes have been discussed, hydromagnetic jets, which have a significant mass flux and have energy and angular momentum carried by both matter and electromagnetic field and, Poynting jets, where the mass flux is small and energy and angular momentum are carried predominantly by the electromagnetic field. Here, we describe recent theoretical work on the formation of relativistic Poynting jets from magnetized accretion disks. Further, we describe new relativistic, fully electromagnetic, particle-in-cell (PIC) simulations of the formation of jets from accretion disks. Analog Z-pinch experiments may help to understand the origin of astrophysical jets.

Keywords: jets, accretion disks, magnetic fields, MHD, AGN

1. Introduction

Powerful, highly collimated, oppositely directed jets are observed in active galaxies and quasars (see for example Bridle and Eilek, 1984), and in old compact stars in binaries – the "microquasars" (Mirabel and Rodriguez, 1994; Eikenberry et al., 1998). Further, highly collimated emission line jets are seen in young stellar objects (Bührke et al., 1988). Different models have been put forward to explain astrophysical jets (Bisnovatyi–Kogan and Lovelace, 2001). Recent observational and theoretical work favors models where twisting of an ordered magnetic field threading an accretion disk acts to magnetically accelerate the jets. Here, we discuss the origin of the relativistic jets observed in active galaxies and quasars and in microquasars. We first discuss a theoretical model (Section 1), and then new results from relativistic PIC simulations (Section 2).

2. Poynting Jets

The powerful jets observed from active galaxies and quasars are probably not hydromagnetic outflows but rather Poynting flux dominated jets. The motions of these jets measured by very long baseline interferometry correspond to bulk Lorentz factors of $\Gamma = \mathcal{O}(10)$ which is much larger than the Lorentz factor of the Keplerian

Astrophysics and Space Science **298:** 115–120, 2005.

disk velocity predicted for hydromagnetic outflows. Furthermore, the low Faraday rotation measures observed for these jets at distances < kpc from the central object implies a very low plasma densities. Similar arguments indicate that the jets of microquasars are not hydromagnetic outflows but rather Poynting jets. Poynting jets have also been proposed to be the driving mechanism for gamma ray burst sources (Katz, 1997). Theoretical studies have developed models for Poynting jets from accretion disks (Lovelace et al., 1987; Lynden-Bell, 1996; Romanova and Lovelace, 1997; Levinson, 1998; Li et al., 2001; Lovelace et al., 2002; Lovelace and Romanova, 2003). Stationary nonrelativistic Poynting flux dominated outflows were found by Romanova et al. (1998) and Ustyugova et al. (2000) in axisymmetric magnetohydrodynamic (MHD) simulations of the opening of magnetic loops threading a Keplerian disk. Here, we summmarize a model for the formation of relativistic Poynting jets from a disk (Lovelace and Romanova, 2003).

Consider a dipole-like coronal magnetic field – such as that shown in the lower part of Figure 1a – threading a differentially rotating Keplerian accretion disk. The disk is perfectly conducting, high-density, and has a small accretion speed ($\ll$ Keplerian speed). The field may be generated in the disk by a dynamo action and released. Outside of the disk there is assumed to be a "coronal" or "force-free" plasma ($\rho_e\mathbf{E} + \mathbf{J} \times \mathbf{B}/c \approx 0$, Gold and Hoyle, 1960). We use cylindrical (r, ϕ, z) coordinates and consider axisymmetric field configurations. Thus the magnetic field has the form $\mathbf{B} = \mathbf{B}_p + B_\phi\hat{\boldsymbol{\phi}}$, with $\mathbf{B}_p = B_r\hat{\mathbf{r}} + B_z\hat{\mathbf{z}}$. We have $B_r = -(1/r)\partial\Psi/\partial z$ and $B_z = (1/r)\partial\Psi/\partial r$, where $\Psi(r, z) \equiv rA_\phi(r, z)$ is the flux function.

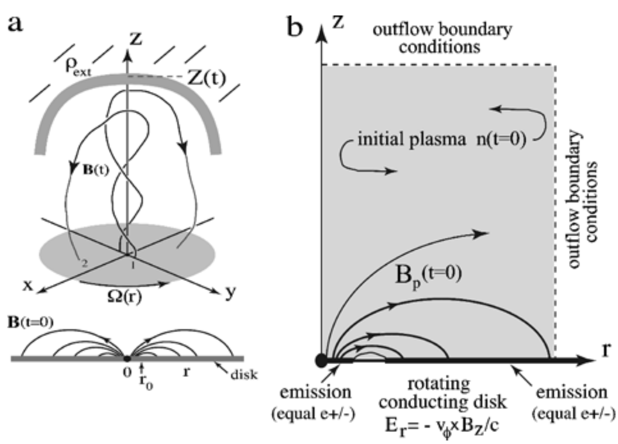

Figure 1. (a) Sketch of the magnetic field configuration of a Poynting jet from Lovelace and Romanova (2003). The bottom part of (a) shows the initial dipole-like magnetic field threading the disk which rotates at the angular rate $\Omega(r)$. The top part shows the jet at some time later when the head of the jet is at a distance $Z(t)$. At the head of the jet there is force balance between electromagnetic stress of the jet and the ram pressure of the ambient medium of density ρ_{ext}. (b) Sketch of the initial conditions for the relativistic PIC simulations of jet formation from an accretion disk.

Most of the azimuthal twist $\Delta\phi$ of a field line of the Poynting jet occurs along the jet from $z = 0$ to $Z(t)$ as sketched in Figure 1a, where $Z(t)$ is the axial location of the "head" of the jet. Along most of the distance $z = 0$ to Z, the radius of the jet is a constant and $\Psi = \Psi(r)$ for $Z \gg r_0$, where r_0 is the radius of the O-point of the magnetic field in the disk. Note that the function $\Psi(r)$ is different from $\Psi(r, 0)$ which is the flux function profile on the disk surface. Hence $r^2 d\phi/dz = r B_\phi(r, z)/B_z(r, z)$. We take for simplicity $V_z = dZ/dt = \text{const}$. We determine V_z subsequently. In this case $H(\Psi) = [r^2\Omega(\Psi)/V_z]B_z$ can be written as a function of Ψ and $d\Psi/dr$. With H known, the relativistic Grad–Shafranov equation,

$$\left[1 - \left(\frac{r\Omega}{c}\right)^2\right]\Delta^*\Psi - \frac{\nabla\Psi}{2r^2}\nabla\left(\frac{r^4\Omega^2}{c^2}\right) = -H(\Psi)\frac{dH(\Psi)}{d\Psi}, \tag{1}$$

can be solved (Lovelace and Romanova, 2003).

The quantity not determined by Eq. (1) is the velocity V_z, or Lorentz factor $\Gamma = 1/(1 - V_z^2/c^2)^{1/2}$. This is determined by taking into account the balance of axial forces at the head of the jet: the electromagnetic pressure within the jet is balanced against the dynamic pressure of the external medium which is assumed uniform with density ρ_{ext}. This gives $(\Gamma^2 - 1)^3 = B_0^2/(8\pi\mathcal{R}^2\rho_{\text{ext}}c^2)$, or for $\Gamma \gg 1$,

$$\Gamma \approx 8\left(\frac{10}{\mathcal{R}}\right)^{1/3}\left(\frac{B_0}{10^3 G}\right)^{1/3}\left(\frac{1/\text{cm}^3}{n_{\text{ext}}}\right)^{1/6}, \tag{2}$$

where $\mathcal{R} = r_0/r_g \gg 1$ and $r_g \equiv GM/c^2$, and B_0 the magnetic field strength at the center of the disk. A necessary condition for the validity of this equation is that the axial speed of the counter-propagating fast magnetosonic wave (in the lab frame) be larger than V_z so that the jet is effectively 'subsonic.' This value of Γ is of the order of the Lorentz factors of the expansion of parsec-scale extragalactic radio jets observed with very-long-baseline-interferometry (see, e.g., Zensus et al., 1998). This interpretation assumes that the radiating electrons (and/or positrons) are accelerated to high Lorentz factors ($\gamma \sim 10^3$) at the jet front and move with a bulk Lorentz factor Γ relative to the observer. The luminosity of the $+z$ Poynting jet is $\dot{E}_j = c\int_0^{r_0} r\,dr E_r B_\phi/2 = cB_0^2\mathcal{R}r_g^2/3 \sim 2.2 \times 10^{45}(B_0/10^3G)^2(\mathcal{R}/10)(M/10^9M_\odot)^2$ erg/sec, where M is the mass of the black hole.

For long time-scales, the Poynting jet is time-dependent due to the angular momentum it extracts from the inner disk ($r < r_0$) which in turn causes r_0 to decrease with time (Lovelace et al., 2002). This loss of angular momentum leads to a "global magnetic instability" and collapse of the inner disk (Lovelace et al., 1994, 1997, 2002) and a corresponding outburst of energy in the jets from the two sides of the disk. Such outbursts may explain the flares of active galactic nuclei blazar sources (Romanova and Lovelace, 1997; Levinson, 1998) and the one-time outbursts of gamma ray burst sources (Katz, 1997).

3. Relativistic Electromagnetic PIC Simulations

We performed relativistic, fully electromagnetic, PIC simulations of the formation of jets from an accretion disk initially threaded by a dipole-like magnetic field. This was done using the code XOOPIC developed by Verboncoeur et al. (1995). Earlier, Gisler et al. (1989) studied jet formation for a monopole type field using the relativistic PIC code ISIS. The geometry of the initial configuration is shown in Figure 1b. The computational region is a cylindrical "can," $r = 0 - R_m$ and $z = 0 - Z_m$, with outflow boundary conditions on the outer boundaries, and the potential and particle emission specified on the disk surface $r = 0 - R_m$, $z = 0$. Equal fluxes of electrons and positrons are emitted so that the net emission is effectively space-charge-limited. About 10^5 particles were used in the simulations reported here. The behavior of the lower half-space ($z < 0$) is expected to be a mirror image of the upper half-space.

Figure 2 shows the formation of a relativistic jet. The gray scale indicates the logarithm of the density of electrons or positrons with 20 levels between the lightest (10^{12}) and darkest ($4 \times 10^{15}/\mathrm{m}^3$). The lines are poloidal magnetic field lines $\mathbf{B}_p$. The total $\mathbf{B}$-field is shown in Figure 3. The computational region has $(R_m, Z_m) =$

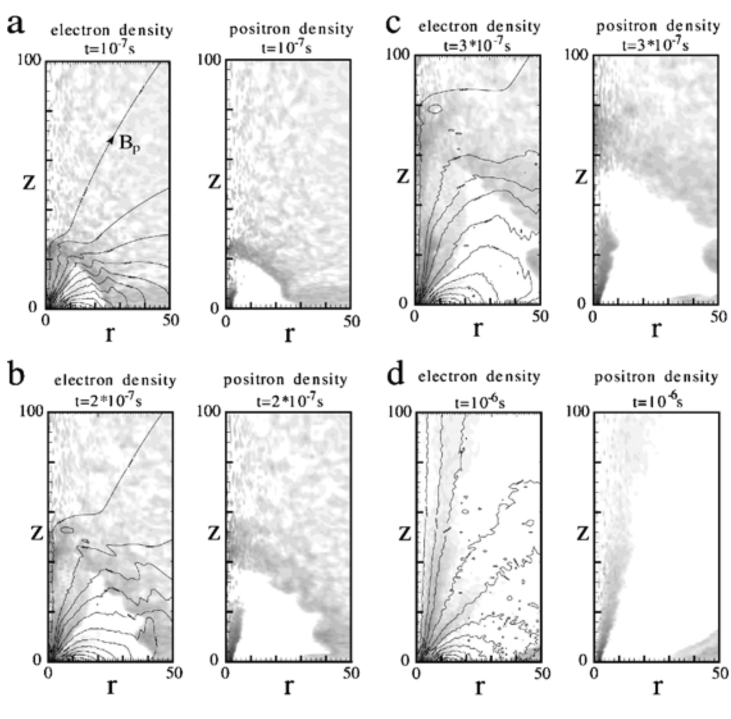

Figure 2. Relativistic PIC simulations of the formation of a jet from a rotating disk, (a)–(c) give snapshots at times $(1, 2, 3) \times 10^{-7}$ sec, and (d) is at $t = 10^{-6}$ sec.

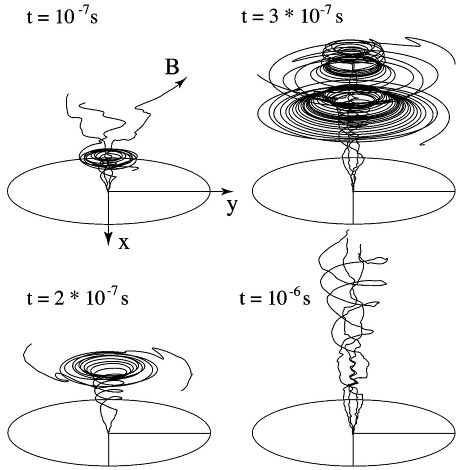

Figure 3. Three-dimensional magnetic field lines originating from the disk at $r = 1, 2$ m for the same case as Figure 2.

(50, 100) m, the initial **B**-field is dipole-like with $B_z(0, 0) \equiv B_0 = 28.3$ G and an O-point at $(r, z) = (10, 0)$ m, and the electric potential at the center of the disk is $\Phi_0 = -10^7$ V relative to the outer region of the disk. Initially, the computational region was filled with a distribution of equal densities of electrons and positrons with $n_\pm(0, 0) = 3 \times 10^{13}/\mathrm{m}^3$. Electrons and positrons are emitted with equal currents $I_\pm = 3 \times 10^5$ A from both the inner and the outer portions of the disk as indicated in Figure 1b with an axial speed much less than c. For a Keplerian disk with $r_0 \gg r_g$, the scalings are $\Phi_0 \propto I \propto B_0\sqrt{r_0}$ and the jet power is $\propto B_0^2 r_0$. The calculations were done on a grid stretched in both the r and z directions so as to give much higher spatial resolution at small r and small z. These simulations show the formation of a quasi-stationary, collimated current-carrying jet. The Poynting flux power of the jet is $\dot{E}_j \approx 7 \times 10^{11}$ W and the particle kinetic energy power is $\approx 4.7 \times 10^{10}$ W. The charge density of the electron flow is partially neutralized by the positron flow. Simulations are planned with the positrons replaced by ions. Scaled Z-pinch experiments configured as shown in Figure 1b can allow further study of astrophysical jet formation.

Acknowledgments

We thank C. Birdsall, S. Colgate, H. Li, J. Verboncoeur, I. Wasserman, J. Wick, and T. Womack for valuable assistance and discussions. This work was supported in part by NASA grants NAG5-13060 and NAG5-13220, by NSF grant AST-0307817, and by DOE cooperative agreement DE-FC03 02NA00057.

References

Bisnovatyi-Kogan, G.S. and Lovelace, R.V.E.: 2001, *New Astron. Rev.* **45**, 663.
Bridle, A.H. and Eilek, J.A. (eds.): 1984, in *Physics of Energy Transport in Extragalactic Radio Sources*, Greenbank, NRAO.
Bührke, T., Mundt, R. and Ray, T.P.: 1988, *A&A* **200**, 99.
Eikenberry, S., Matthews, K., Morgan, E.H., Remillard, R.A. and Nelson, R.W.: 1998, *ApJ* **494**, L61.
Gisler, G., Lovelace, R.V.E. and Norman, M.L.: 1989, *ApJ* **342**, 135.
Gold, T. and Hoyle, F.: 1960, *MNRAS* **120**, 89.
Katz, J.I.: 1997, *ApJ* **490**, 633.
Levinson, A.: 1998, *ApJ* **S07**, 145.
Li, H., Lovelace, R.V.E., Finn, J.M. and Colgate, S.A.: 2001, *ApJ* **561**, 915.
Lovelace, R.V.E., Li, H., Koldoba, A.V., Ustyugova, G.V. and Romanova, M.M.: 2002, *ApJ* **572**, 445.
Lovelace, R.V.E., Newman, W.I. and Romanova, M.M.: 1997, *ApJ* **484**, 628.
Lovelace, R.V.E. and Romanova, M.M.: 2003, *ApJ* **596**, L159.
Lovelace, R.V.E., Romanova, M.M. and Newman, W.I.: 1994, *ApJ* **437**, 136.
Lovelace, R.V.E., Wang, J.C.L. and Sulkanen, M.E.: 1987, *ApJ* **315**, 504.
Lynden-Bell, D.: 1996, *MNRAS* **279**, 389.
Mirabel, I.F. and Rodriguez, L.F.: 1994 *Nature* **371**, 46.
Romanova M.M. and Lovelace, R.V.E.: 1997, *ApJ* **475**, 97.
Romanova, M.M., Ustyugova, G.V., Koldoba, A.V., Chechetkin, V.M. and Lovelace, R.V.E.: 1998, *ApJ* **500**, 703.
Ustyugova, G.V., Lovelace, R.V.E., Romanova, M.M., Li, E.L. and Colgate, S.A.: 2000, *ApJ* **541**, L21.
Verboncoeur, J.P., Langdon, A.B. and Gladd, N.T.: 1995, *Comput. Phys. Commun.* **87**, 199.
Zensus, J.A., Taylor, G.B. and Wrobel, J.M. (eds.): 1998, in: Radio Emission from Galactic and Extragalactic Compact Sources, IAU Colloquium 164 (Astronomical Society of the Pacific).

RECENT EXPERIMENTAL RESULTS AND MODELLING OF HIGH-MACH-NUMBER JETS AND THE TRANSITION TO TURBULENCE

P.A. ROSEN[1], B.H. WILDE[2], R.J.R. WILLIAMS[1], J.M. FOSTER[1], P.A. KEITER[2], R.F. COKER[2], T.S. PERRY[3], M.J. TAYLOR[1], A.M. KHOKHLOV[4], R.P. DRAKE[5], G.R. BENNETT[6], D.B. SINARS[6] and R.B. CAMPBELL[6]

[1]*AWE, Aldermaston, UK; E-mail: paula.rosen@awe.co.uk*
[2]*Los Alamos National Laboratory, USA*
[3]*Lawrence Livermore National Laboratory, USA*
[4]*University of Chicago, USA*
[5]*University of Michigan, USA*
[6]*Sandia National Laboratories, Albuquerque, USA*

(Received 21 April 2004; accepted 31 May 2005)

Abstract. In recent years, we have carried out experiments at the University of Rochester's Omega laser in which supersonic, dense-plasma jets are formed by the interaction of strong shocks in a complex target assembly (Foster et al., *Phys. Plasmas* **9** (2002) 2251). We describe recent, significant extensions to this work, in which we consider scaling of the experiment, the transition to turbulence, and astrophysical analogues. In new work at the Omega laser, we are developing an experiment in which a jet is formed by laser ablation of a titanium foil mounted over a titanium washer with a central, cylindrical hole. Some of the resulting shocked titanium expands, cools, and accelerates through the vacuum region (the hole in the washer) and then enters a cylinder of low-density foam as a jet. We discuss the design of this new experiment and present preliminary experimental data and results of simulations using AWE hydrocodes. In each case, the high Reynolds number of the jet suggests that turbulence should develop, although this behaviour cannot be reliably modelled by present, resolution-limited simulations (because of their low-numerical Reynolds number).

Keywords: jets, turbulence, laboratory astrophysics, supernovae

1. Introduction

Jet-like features are observed in many different kinds of astrophysical objects such as young stellar objects, active galactic nebulae and planetary nebulae. Recent theories and calculations (Khokhlov et al., 1999) imply that jets might also play a principal role in the explosion of core collapse supernovae. Recent observations of core collapse supernovae provide evidence that the explosion is intrinsically asymmetric. For example, jet-like features have been observed in the remnants of supernovae, such as the radio image of SNR W50 and in X-ray images of the Vela pulsar. Khokhlov has developed an explosion model which assumes that bi-polar, non-relativistic jets form via a magneto-rotational mechanism during a core collapse, and this results in the production of a highly asymmetric supernova envelope.

There are many facets of jets which are not yet fully understood, in particular the processes by which the strongly collimated flows are driven. Of particular interest is the question of whether and when these jets become turbulent. This has important implications for the range of jets and the manner in which their material and energy content is deposited, as well as for the entrainment and acceleration of material in their envelopes. Reynolds numbers in supernovae are predicted to be astronomical ($\sim 10^{10}$), but, to date, none of the simulations has gone turbulent (Kifonidis et al., 2000). It is suspected that the reason for this is that the numerical Reynolds number in these simulations is too low; i.e. the problem cannot be resolved finely enough to calculate mixing at the required scale lengths over which instability growth and turbulent dissipation occur. Many hydrocodes codes are therefore developing sub-grid-scale mix models to capture these effects.

An experimental platform using the Omega laser (Soures et al., 1996) to generate astrophysically relevant jets is being developed to validate these models, and to better understand the physics of jets. We have built upon our success at studying hydrodynamic jets at early time ($t < 15$ ns) (Foster et al., 2002), and modified our platform to study the jet at late time. Our earlier experiments used a laser-heated hollow cylindrical gold hohlraum (Kauffman et al., 1994; Lindl, 1995) to radiatively drive the targets. However, axial plasma stagnation within the hohlraum generates additional pressure at the target which perturbs the hydrodynamics of the jet. It is for this reason that our current experiments use direct laser drive.

In addition to our experiments at Omega, we are also developing large field-of-view imaging at the Z pulsed-power facility (SNLA) using a monochromatic curved crystal imager at 6.151 keV (Sinars et al., 2003). This experimental configuration offers the exciting potential of increased effective spatial resolution, but this work will not be discussed further in this paper, due to limitation of space.

2. Experiment Design

A diagram of the target is shown in Figure 1. We use between three and seven beams of the Omega laser to irradiate a 125-μm thickness titanium foil in direct contact with a 700-μm thickness titanium washer with a central, 300-μm diameter cylindrical hole. A 2-μm thickness layer of solid ($1.0\,\mathrm{g\,cm^{-3}}$) plastic (Parylene-N) is placed on the driven side of the titanium to constrain the expansion of hot titanium coronal plasma (for diagnostic reasons). Laser ablation of the surface launches a shock that penetrates through the titanium, some of which expands, cools, and accelerates through the vacuum region. Lateral shocks emanating from the sides of the cylindrical hole act to collimate the accelerating titanium and it penetrates the 6-mm-length, low-density, resorcinol-formaldehyde (RF), aerogel foam as a high-Mach-number jet. The density of the RF foam is $0.1\,\mathrm{g\,cm^{-3}}$, its

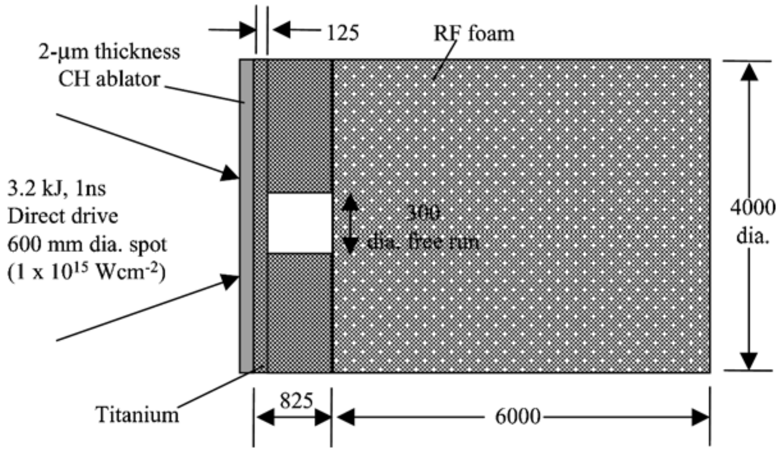

Figure 1. The experimental package for the titanium jet experiment comprises a titanium foil mounted on to a titanium washer. The washer has a central cylindrical hole. Adjacent to the washer is a cylindrical hydrocarbon-foam block. A plastic ablator covers the driven face of the target. Dimensions are in microns.

chemical composition is $C_{15}H_{12}O_4$, and it has a cell size of less than 0.1 μm. The exterior diameter of all components is 4 mm. We use between 1.5 and 3.2 kJ of laser energy in a 1-ns-length square pulse of 0.35 μm wavelength. Super-Gaussian phase plates are used to smooth the incident laser intensity profile; these give a 600-μm diameter spot at the 50% intensity point (825-μm diameter at the 5% intensity point).

As our images are relatively large (several mm in size) we diagnose the jet using pinhole-apertured, point-projection X-ray backlighting. (Our earlier experiments studied smaller jets and used wide-area backlighting.) We use vanadium as the backlighter material to provide good contrast with the titanium jet. (The He-like resonance line of vanadium (at 5.205 keV) lies just above the K-absorption edge of titanium). The vanadium backlighter foil is illuminated with two laser beams ($\sim$450 J per beam) in a 1-ns duration laser pulse (0.35 μm wavelength).

A major challenge for this experiment has been the provision of adequate shielding for this target assembly, and early experimental campaigns were devoted to understanding the source of background radiation.

3. Simulations

The experiment is being modelled using the RAGE (Gittings, 1992), LASNEX (Zimmerman and Kruer, 1975) and ALLA (Khokhlov, 1998) hydrocodes, as well as the AWE hydrocodes NYM (Roberts et al., 1980), PETRA (Youngs, 1982, 1984) and TURMOIL3D (Youngs, 1994). Due to limitation of space, only the AWE calculations will be described in detail in this paper.

NYM is a 2D Lagrangian hydrocode which includes laser ray trace and laser energy deposition packages, and non-local-thermodynamic equilibrium (NLTE) physics. The laser light is input as a 600-μm diameter spot on the axis of the calculation. Laser energy absorption is modelled as inverse bremsstrahlung in the coronal plasma, with a 30% deposition of energy at the critical surface. Radiation transport is treated by Monte Carlo photonics (Fleck and Cummings, 1971). NLTE physics in the laser absorption region is treated by the ZEUS package, which provides in-line time-dependent NLTE modelling by solutions of rate equations for average ion populations in the screened hydrogenic approximation. This NLTE treatment is applied in selected cells of the simulation, including and bordering the region of laser transport and energy deposition; elsewhere, tabular LTE opacities are used, calculated off-line using the IMP (Rose, 1992) opacity code. Equation of state is also input in tabular form, using the SESAME (Lyon and Johnson, 1992) database.

The NYM calculation proceeds until approximately 2 ns after the beginning of the laser pulse. After this time, the calculational timestep becomes impracticably small, and we transfer the simulation to the AWE 2D Eulerian hydrocode PETRA. In this phase of the calculation, no further energy is input from an external source and the code tracks the further evolution of the jet. Radiation transfer is treated by single-group (grey) diffusion. Ion, electron and radiation temperatures are assumed equal (1-T model). Square, 5 μm zones are used in the central part of the Eulerian problem (up to a radius of 500 μm), then the size of the radial zones increases geometrically, with an increase in size of 10% per cell.

Finally, we post-process the simulation to produce a synthetic radiograph for comparison with the experimental data.

Figure 2 shows plots of log density, titanium volume fraction and a simulated radiograph at $t = 300$ ns from a NYM-PETRA simulation. Coarseness of the

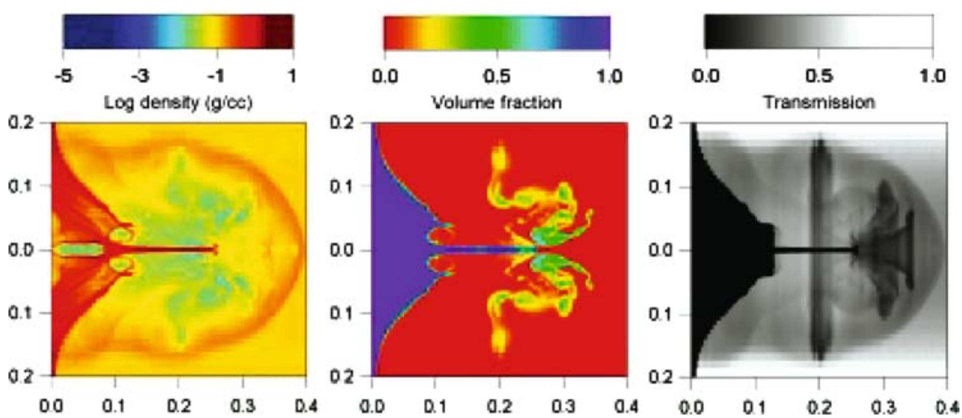

Figure 2. Log density (left), titanium volume fraction and simulated radiograph (right) from a NYM-PETRA calculation at $t = 300$ ns. Dimensions are in centimetres.

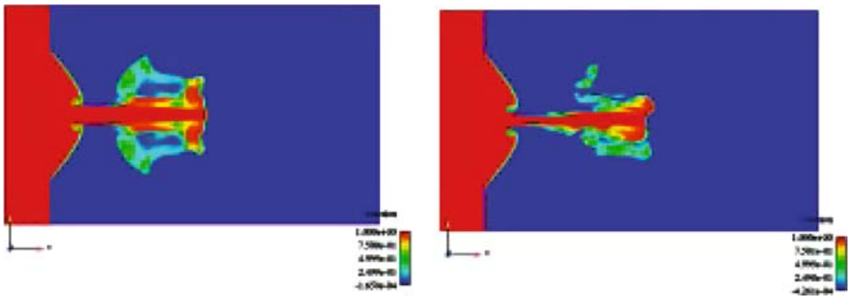

Figure 3. Titanium mass fraction from TURMOIL3D simulations. The left-hand image is from an unperturbed simulation and the right-hand image is from a simulation in which a 20 μm random roughness was introduced on the inner surface of the hole in the titanium washer.

calculational mesh is evident at larger radii. The jet exhibits large-scale structures but does not have sufficient resolution to look "turbulent."

These experiments are also being modelled using a three-dimensional Eulerian code, TURMOIL3D, which treats the flow of polytropic gases using perfect-gas equations of state. The code uses a finite-difference staggered-grid Lagrangian-remap algorithm, extended from the two-dimensional method used in PETRA (but without interface reconstruction). The remap phase uses the third-order monotonic method of Van Leer (1977) to maintain sharp contact discontinuities without producing negative densities. The code includes the facility to advect the mass fractions of two distinct species, including the variation in the adiabatic index as a function of the composition. Figure 3 shows plots of titanium mass fraction from two TURMOIL3D calculations: an unperturbed simulation and one where 20-μm random perturbations have been introduced on the inner surface of the hole in the titanium washer.

4. Scaling the Jet

The morphology of the jets created in our experiment shows many points of similarity with numerical models of astrophysical supersonic jets, and the question arises of the extent to which the experiment can be scaled to systems of vastly different physical size. Such scaling has been studied in detail by Ryutov et al. (1999, 2001) and Ryutov and Remington (2002) who show that if dissipative processes are negligible, then scaling transformations exist that enable the hydrodynamic evolution of the laboratory system to be mapped onto that of another system at different physical size, providing that certain dimensionless scaling parameters are common to both systems.

From the NYM-PETRA simulation shown in Figure 2, we examine the collimated part of the jet and the region of Kelvin–Helmholtz roll-up. Table I includes values for typical conditions within these parts of the problem together with the

TABLE I

Representative physical conditions, and corresponding dimensionless scaling numbers, in the fully-developed jet at $t = 300$ ns, and at the He–H interface of SN1987a at $t = 2000$ s

Quantity	Symbol	Value in collimated stem of jet	Value in roll-up at head of jet	Value in SN1987a
Temperature	T	0.3	3	900 eV
Density	ρ	4	0.1	$0.0075\ \mathrm{g\,cm^{-3}}$
Pressure	P	1×10^{11}	1.5×10^{10}	$3.5 \times 10^{13}\ \mathrm{dyn\,cm^{-2}}$
Mean ionisation	Z	3	1.4	2.0
Fluid velocity	u	1×10^{6}	1×10^{6}	$2 \times 10^{7}\ \mathrm{cm\,s^{-1}}$
Length scale	r	4×10^{-3}	4×10^{-3}	9×10^{10} cm
Sound speed	$c_s = \sqrt{\frac{(Z+1)kT}{m_i}}$	1.6×10^{5}	3.8×10^{5}	$2.6 \times 10^{7}\ \mathrm{cm\,s^{-1}}$
Internal Mach number	$M = u/c_s$	6.2	2.6	0.8
Kinematic viscosity[a]	υ	1.7×10^{-8}	4.5×10^{-3}	$7.0 \times 10^{7}\ \mathrm{cm^2\,s^{-1}}$
Reynolds number	$Re = ur/\upsilon$	2.4×10^{11}	1×10^{6}	2.6×10^{10}
Euler number	$Eu = u\sqrt{\frac{\rho}{P}}$	6.3	2.6	0.29

[a]Spitzer–Braginskii ion viscosity (Spitzer, 1962).

Reynolds, (internal) Mach and Euler numbers. For purposes of comparison, Table I also includes corresponding data at the (Rayleigh–Taylor unstable) He–H interface of SN1987a at 2000 s (Ryutov et al., 1999).

These values of Re are above the threshold for the transition to turbulence (Dimotakis, 2000), and thus we would expect to see turbulence develop in this experiment, after sufficient elapse of time.

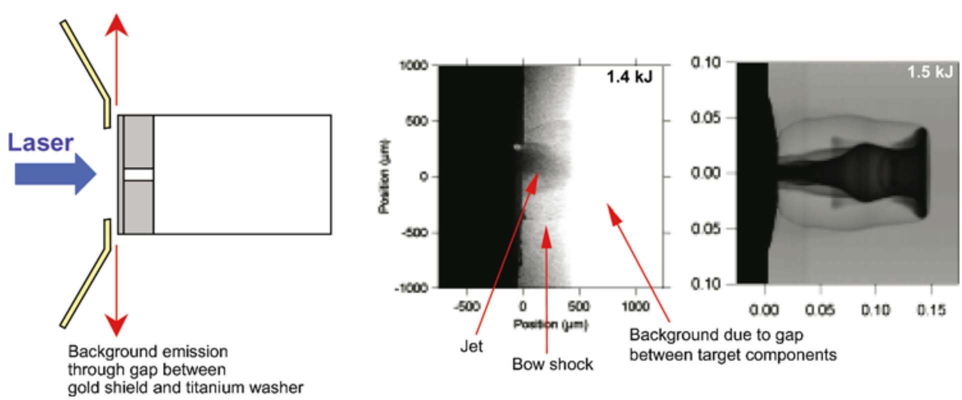

Figure 4. Preliminary experimental data from the titanium jet experiment at $t = 100$ ns. Parts of the jet and bow shock are visible. The over-exposed part of the image is due to leakage of radiation through a gap between the washer and shield. A simulated radiograph from a NYM-PETRA calculation is qualitatively similar to the data.

5. Comparison of Preliminary Experimental Results with Simulation

Figure 4 shows preliminary experimental data at $t = 100\,\text{ns}$ with a simulated radiograph from NYM-PETRA. The experimental data clearly show evidence of a jet and bow shock, but the data are compromised by background X-ray emission which has leaked through a gap between the titanium washer and a gold target shield used as part of the experimental assembly. Several modifications to the target and backlighter configuration have been identified which should eliminate the problem of background radiation, and these will be implemented in future experiments.

6. Summary

We are developing a platform to study astrophysically relevant jets at late time (up to several hundred ns). Preliminary experimental results are encouraging and we are optimistic that the next experiment (March 2004) will return high-quality data.

Many different hydrocodes employing different calculation schemes are being used to calculate this experiment. None of the simulations to date shows the transition to turbulence, and it is believed that this is because the numerical Reynolds number is too low (i.e. the finest resolution achievable on today's computers is not high enough to resolve turbulent length scales) or perhaps that there is insufficient time for the transition to turbulence at the numerical Reynolds numbers obtained (Zhou et al., 2003a,b).

These experiments will provide data to test subgrid-scale dynamic mix models in our codes.

Acknowledgements

The authors would like to thank Jim Knauer (LLE) for helpful discussions on point projection imaging, Chuck Source (LLNL) for diagnostic support, the Omega laser operations team and target fabrication groups at AWE and LLNL. Finally, we are indebted to Bruce Remington and Adam Frank for their motivation, encouragement and support in the pursuit of laboratory analogues of astrophysical jets.

References

Dimotakis, P.E.: 2000, *J. Fluid Mech.* **409**, 69.

Fleck, J.A. and Cummings, J.D.: 1971, *J. Comput. Phys.* **8**, 313.

Foster, J.M. Wilde, B.H., Rosen, P.A., Perry, T.S., Fell, M., Edwards, M.J., Lasinski, B.F., Turner, R.E. and Gittings, M.L.: 2002, *Phys. Plasmas* **9**, 2251.

Gittings, M.L.: 1992, Numerical Methods Symposium, April 28–30. Copies may be ordered from the Defence Nuclear Agency, 56801 Telegraph Road, Alexandria, VA 22310-3398.
Khokhlov, A.M.: 1998, *J. Comput. Phys.* **143**, 519.
Khokhlov, A.M., Hoflich, P.A., Oran, E.S., Wheeler, J.C., Wang, L. and Chtchelkanova, A.Yu.: 1999, *ApJ* **524**, 107.
Kauffman, R.L., Suter, L.J., Darrow, C.B., Kilkenny, J.D., Kornblum, H.N., Montgomery, D.S., Phillion, D.W., Rosen, M.D., Theissen, A.R., Wallace, R.J. and Ze, F.: 1994, *Phys. Rev. Lett.* **73**, 2320.
Kifonidis, K., Plewa, T., Janka, H.-T.H. and Muller, E.: 2000, *ApJ* **531**, 123.
Lindl, J.: 1995, *Phys. Plasmas* **2**, 3933.
Lyon, S.P. and Johnson, J.D.: 1992, "Sesame: The Los Alamos National Laboratory Equation of State Database", Los Alamos National Laboratory, Los Alamos, NM, LA-UR-92-3407.
Roberts, P.D., Rose, S.J., Thompson, P.C. and Wright, R.J.: 1980, *J. Phys.* D **13**, 1957.
Rose, S.J.: 1992, *J. Phys.* B **25**, 1667.
Ryutov, D.D., Drake, R.P., Kane, J., Liang, E., Remington, B.A. and Wood-Vesey, W.M.: 1999, *ApJ* **518**, 821.
Ryutov, D.D., Remington, B.A., Robey, H.F. and Drake, R.P.: 2001, *Phys. Plasmas* **8**, 1804.
Ryutov, D.D. and Remington, B.A.: 2002, *Plasma Phys. Controlled Fusion* **44**, B407.
Sinars, D.B., Cuneo, M.E., Bennett, G.R., Wenger, et al.: 2003, *Rev. Sci. Instrum.* **74**, 2202.
Sinars, D.B., Cuneo, M.E. Bennett, G.R., Wenger, Cuneo, M.E. and Porter, J.L.: 2003, *Appl. Opt.* **42**, 4059.
Soures, J., McCrory, R.L. Verdon, C.P., et al.: 1996, *Phys. Plasmas* **3**, 2108.
Spitzer, L.: 1962, *The Physics of Fully Ionised Gases*, 2nd edn., Wiley, New York, pp. 143.
Van Leer, B.: 1977, *J. Comput. Phys.* **23**, 276.
Youngs, D.L.: 1982, Time-dependent multi-material flow with large fluid distortion, in: K. W. Morton and M. J. Baines (eds.), *Numerical Methods for Fluid Mechanics*.
Youngs, D. L.: 1984, *Physica* **12D**, 32.
Youngs, D.L.: 1994, Laser and particle beams, **12**, 725.
Zhou, Y., Remington, B.A., Robey, H.F., et al.: 2003a, *Phys. Plasmas* **10**, 1883.
Zhou, Y., Robey, H.F. and Buckingham, A.C.: 2003b, *Phys. Rev. E* **67**, 056305-1-11.
Zimmerman, G. and Kruer, W.: 1975, *Comments Plasma Phys. Controlled Fusion* **11**, 51.

HYDROGEN EOS AT MEGABAR PRESSURES AND THE SEARCH FOR JUPITER'S CORE

WILLIAM B. HUBBARD

Lunar and Planetary Laboratory, The University of Arizona, Tucson, AZ, USA;
E-mail: hubbard@lpl.arizona.edu

(Received 28 April 2004; accepted 27 May 2004)

Abstract. The interior structure of Jupiter serves as a benchmark for an entire astrophysical class of liquid–metallic hydrogen-rich objects with masses ranging from $\sim 0.1 M_J$ to $\sim 80 M_J$ ($1 M_J$ = Jupiter mass = $1.9e30$ g), comprising hydrogen-rich giant planets (mass $< 13 M_J$) and brown dwarfs (mass $> 13 M_J$ but $\sim < 80 M_J$), the so-called substellar objects (SSOs). Formation of giant planets may involve nucleated collapse of nebular gas onto a solid, dense core of mass $\sim 0.04 M_J$ rather than a stellar-like gravitational instability. Thus, detection of a primordial core in Jupiter is a prime objective for understanding the mode of origin of extrasolar giant planets and other SSOs. A basic method for core detection makes use of direct modeling of Jupiter's external gravitational potential terms in response to rotational and tidal perturbations, and is highly sensitive to the thermodynamics of hydrogen at multi-megabar pressures. The present-day core masses of Jupiter and Saturn may be larger than their primordial core masses due to sedimentation of elements heavier than hydrogen. We show that there is a significant contribution of such sedimented mass to Saturn's core mass. The sedimentation contribution to Jupiter's core mass will be smaller and could be zero.

Keywords: Jupiter, Saturn, extrasolar planets

1. Introduction

Precise determination of Jupiter's core mass $M_{C,J}$ has remained elusive; $M_{C,J}$ is estimated to lie in the range $0 < M_{C,J} < 12 M_E$, where M_E = Earth's mass (Guillot et al., 1997). On the other hand, Saturn possesses a substantial core comprising $M_{C,S} \sim 20 M_E$ (Hubbard and Stevenson, 1984). If both Jupiter and Saturn had formed from nucleated collapse onto a primordial solid core composed of rock and ices (such as, in largest proportion, H_2O), and if solar abundances were preserved in both planets, the core mass would comprise $\sim$1.5% in both planets, or respectively $M_{C,J} \sim 5 M_E$ and $M_{C,S} \sim 1.4 M_E$. In reality, these values should be lower limits to the actual core masses, since the standard nucleation theory for the origin of hydrogen-rich giant planets predicts that a core mass $M_C \sim$ 10–15 M_E is required to induce gas collapse (Mizuno, 1980).

The reason that a primordial nucleation core of $M_C \sim$ 10–15 M_E will be more readily detectable in Saturn than in Jupiter is because it would comprise $\sim$14–20% of the total mass in the former, but only $\sim$4–5% in the latter. The equation of state

Astrophysics and Space Science **298:** 129–134, 2005.

(EOS) of hydrogen is probably known to better than $\sim$15% over the relevant pressure range, but probably not to within $\sim$5%. In this paper, we show that, consistent with the stated uncertainties, a consistent scenario can be constructed for the formation of both Jupiter and Saturn initiated by nucleated collapse onto cores of similar mass, $\sim 15M_{\mathrm{E}}$.

2. Evolution of Jupiter and Saturn

The theory for the evolution of giant planets has been presented in a series of papers (Hubbard, 1977; Hubbard et al., 2002; Fortney and Hubbard, 2003, 2004). As is well-known, the present age and intrinsic luminosity of Jupiter are in good accord with the theory for evolution of a homogeneous hydrogen–helium sphere, but the same theory applied to Saturn results in a model that is significantly underluminous at present, compared with data (Stevenson and Salpeter, 1977a,b). As discussed by Hubbard and Stevenson (1984), gravitational energy release in Saturn in the course of sedimentation of a dense component, adding mass to a primordial core, could add to Saturn's luminosity by the requisite amount. However, a quantitative theory for this process has only become available recently, following development of an improved grid of model atmospheres. In the 2003 and 2004 papers by Fortney and Hubbard, theory for H–He binary mixtures proposed by Stevenson (1975) and by Hubbard and DeWitt (1985) is investigated and shown to be inapplicable to the evolution of Saturn. This theory (HDW/S) is plotted in Figure 1.

A more recent calculation of H–He phase separation by Pfaffenzeller et al. (1995) is also shown in Figure 1 (Pfaff.). As is evident, Saturn does not cool sufficiently for this phase diagram to come into play. However, Fortney and Hubbard (2003) consider adjustments to either the HDW/S theory or to the Pfaff. theory that would cause Saturn's age/luminosity to come into agreement with observation. The adjustment is carried out by fitting a standard equation to the saturation helium number concentration x in metallic hydrogen, as a function of temperature T:

$$x = \exp\left(B - \frac{A}{T}\right), \tag{1}$$

where B is dimensionless and at high pressures expected to be smaller than one in absolute value; the constant A and the temperature T are both expressed in eV. In the HDW/S theory, A is a decreasing function of pressure, while in the Pfaffenzeller theory it increases with pressure (see Figure 1). Figure 2 shows results of calibrating the HDW/S and Pfaff. theories to Saturn's evolution, via the constants A and B.

Once the phase-separation model is calibrated to Saturn, one can apply the same model to Jupiter, and to a suite of extrasolar giant planets (Fortney and Hubbard, 2004). The results indicate that Jupiter should *not* have undergone He phase separation in the age of the solar system, whereas the process is well advanced in Saturn. However, the Galileo entry probe result for Jupiter's atmospheric helium

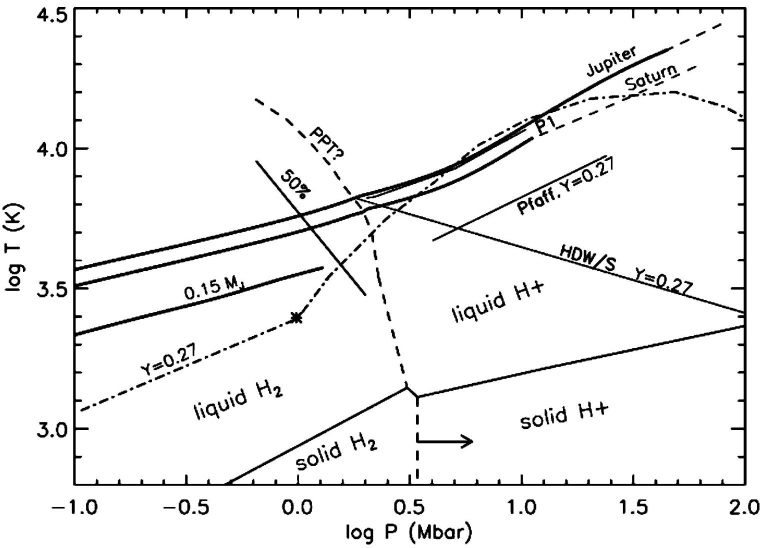

Figure 1. Phase diagram of hydrogen (temperature T vs. pressure P), adapted from J. Fortney's Ph.D. dissertation (2004). Heavy solid lines show interior T vs. P for present Jupiter and Saturn. The dashed "PPT" line shows the proposed "plasma phase transition" of Saumon et al. (1995), while the solid "50%" line shows Ross' (1998) estimate of 50% pressure-dissociation of H_2 molecules. The solid line marked "HDW/S" shows the maximum temperature for uniform mixing of metallic hydrogen with 0.27 mass fraction of He, according to the theories of Hubbard and DeWitt (1985) and Stevenson (1975). The solid line marked "Pfaff." shows results of the same calculation by Pfaffenzeller et al. (1995). The dot-dashed line labeled with "$Y = 0.27$" shows the maximum-temperature line proposed by Fortney and Hubbard (2003, 2004).

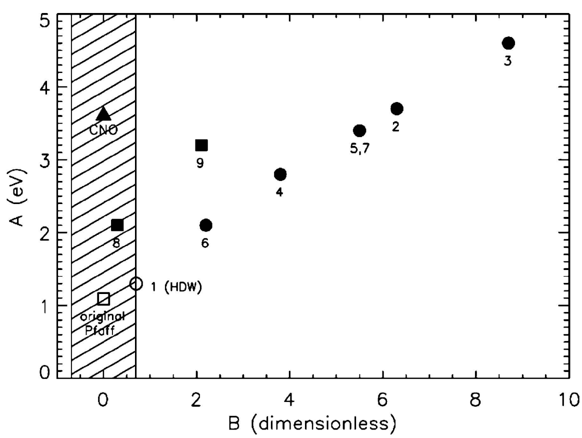

Figure 2. Calibration of solubility parameters, at a pressure of 5 Mbar, to the evolution of Saturn; see Fortney and Hubbard (2003). Squares are for Pfaff. phase diagram and circles are for HDW/S phase diagram. Solid symbols show successful models and open symbols show models that do not provide enough gravitational energy. Under the constraint that $|B| < 1.5$, model 8 is the only acceptable one. Triangle shows an alternative model in which the "ice" component becomes immiscible and forms a core.

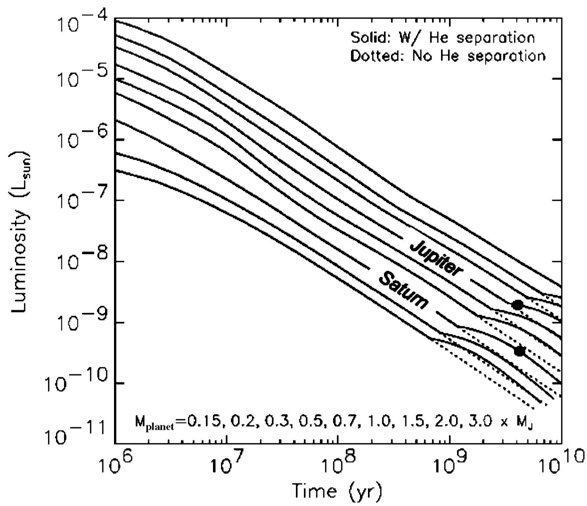

Figure 3. Luminosity vs. time for isolated (non-irradiated) giant planets, ranging from 0.15 Jupiter masses to 3 Jupiter masses. Dots show luminosity of an isolated Jupiter and Saturn at an age of 4.5 gigayears.

mass fraction, $Y = 0.231 \pm 0.006$ (Von Zahn and Hunten, 1996) suggests that some He separation has occurred, as it is less than the primordial solar value, $Y = 0.27$.

We suspect that there is not a true inconsistency between Jupiter and Saturn. Most likely, the reason that our models do not find an intersection between the present jovian interior isentrope and the Saturn-calibrated critical mixing line for $Y = 0.27$ is connected to an inadequate treatment of the modification of the atmospheric surface condition due to solar irradiation. To illustrate this point, we present Figure 3, which shows the evolution of a suite of *isolated* giant planets, including an isolated Jupiter and Saturn.

As Figure 3 shows, helium separation maintains the luminosity of giant planets when they drop below $\sim 10^{-8}$–10^{-9} solar luminosity. Our theory predicts that Jupiter would just enter a helium-separation phase at its present age, if irradiation were neglected. This result suggests that a more careful treatment of irradiation effects may resolve the discrepancy. Moreover, a proper treatment of irradiation is particularly important for the evolution of highly irradiated extrasolar giant planets such as HD 209458B. Such improved calculations are in progress.

3. Core Masses for Jupiter and Saturn

Helium is not the only candidate for an immiscible component in Jupiter and Saturn. Both planets appear to contain $\sim$30–40M_{E} of non-hydrogen–helium material in their interiors, including but not limited to a dense core (Guillot et al., 1997).

Assuming that the preponderance of such material contains the atoms C, N, and O, one can construct a self-consistent scenario for extending Saturn's luminosity via separation of such material by appropriately adjusting the constant A in Eq. (1); see Figure 2. Again, with our present treatment of irradiation, we do not find any such separation in Jupiter.

However, an important byproduct of our Saturn calculation is that we can predict two quantities that are (in principle) observable. First, the atmospheric depletion in Saturn of the sedimented component is predicted. Second, the mass added to Saturn's core via sedimentation is predicted.

If helium is the separating component in Saturn, we predict that Saturn's present atmospheric helium abundance should be reduced to $Y = 0.185$. The depleted helium, amounting to $7M_{\mathrm{E}}$, would then have been added to Saturn's core, increasing its primordial core mass of $16M_{\mathrm{E}}$ to a present core mass of $23M_{\mathrm{E}}$. If "ice" (i.e., the CNO component) is the separating component in Saturn, we predict that Saturn's present atmospheric helium abundance should still be primordial, but that the "ice" mass fraction in its outer layers would be reduced from a primordial value $Z = 0.145$ to a present-day value of $Z = 0.045$. About $8M_{\mathrm{E}}$ of this component would be deposited on the core, increasing its primordial core mass ($13M_{\mathrm{E}}$ for the "ice"-depletion model) to a present core mass of $21M_{\mathrm{E}}$. Thus, the He-depletion and "ice"-depletion models give similar results: the primordial Saturn core mass was about $15M_{\mathrm{E}}$.

4. Summary

We conclude that the standard model for formation of the giant planets Jupiter and Saturn, via a nucleated instability in a hydrogen–helium nebula, could still be correct. Once we have allowed for the sedimentation in Saturn of a major dense component, energy-balance calculations suggest that Saturn's primordial core mass was not anomalously large, but was instead very close to the value suggested by models.

Although the He-depletion and "ice"-depletion models for Saturn give similar results, the latter requires a primordial value of Z which is almost ten times the solar value. In one scenario for the origin of Jupiter, oxygen (a proxy for most of the elements comprising Z) could be enhanced by about a factor of eight (Gautier et al., 2001); this might also be the case for Saturn. In either scenario for extending Saturn's evolution, the results suggest that a Jupiter core of $\sim 15M_{\mathrm{E}}$ may ultimately be detected. However, progress toward this goal depends critically on improvements in the hydrogen–helium EOS.

Acknowledgments

This work was supported by NASA Grants NAG5-13775 and NAG5-10760.

References

Fortney, J.J. and Hubbard, W.B.: 2003, *Icarus* **164**, 228.
Fortney, J.J. and Hubbard, W.B.: 2004, *ApJ* **608**, 1039.
Gautier, D., Hersant, F., Mousis, O. and Lunine, J.I.: 2001, *ApJ* **550**, L227; Erratum **559**, L183.
Guillot, T., Gautier, D. and Hubbard, W.B.: 1997, *Icarus* **130**, 534.
Hubbard, W.B.: 1977, *Icarus* **30**, 305.
Hubbard, W.B. and Stevenson, D.J.: 1984, in: T. Gehrels and M. Matthews (eds.), *Saturn*, University of Arizona Press, Arizona, p. 47.
Hubbard, W.B. and DeWitt, H.E.: 1985, *ApJ* **290**, 388.
Hubbard, W.B., Burrows, A. and Lunine, J.I.: 2002, *Annu. Rev. Astronom. Astrophys.* **40**, 103
Mizuno, H.: 1980, *Prog. Theor. Phys.* **64**, 544.
Pfaffenzeller, O., Hohl, D. and Ballone, P.: 1995, *Phys. Rev. Lett.* **74**, 2599.
Ross, M.: 1998, *Phys. Rev. B* **58**, 669.
Saumon, D., Chabrier, G. and van Horn, H.M.: 1995, *ApJS* **99**, 713.
Stevenson, D.J. and Salpeter, E.E.: 1977a, *ApJS* **35**, 221.
Stevenson, D.J. and Salpeter, E.E.: 1977b, *ApJS* **35**, 239.
Stevenson, D.J.: 1975, *Phys. Rev. B* **12**, 3999.
Von Zahn, U. and Hunten, D.M.: 1996, *Science* **272**, 849.

ASTROPHYSICAL IMPLICATIONS OF THE RECENT SHOCKED DEUTERIUM EXPERIMENTS

D. SAUMON[1] and T. GUILLOT[2]

[1]*Applied Physics Division, Los Alamos National Laboratory, MS F699, Los Alamos, NM 87545, USA; E-mail: dsaumon@lanl.gov*

[2]*Observatoire de la Côte d'Azur, BP 4229, 06304 Nice, Cedex 04, France; E-mail: guillot@obs-nice.fr*

(Received 30 April 2004; accepted 25 May 2004)

Abstract. In the last few years, deuterium has been the focus of a high level of laboratory activity that was sparked by a disagreement on the experimental value of the maximum compression along the Hugoniot.

Astrophysically, the uncertainty in the EOS of hydrogen is most consequential in models of the interiors of Jupiter and Saturn since a significant fraction of their mass falls in the region where the EOS uncertainty is largest. We present a study of the range of interior structures allowed by the shock-compression experiments on deuterium and constrained by astrophysical observations of the two planets. We find that the EOS uncertainty must be reduced to less than 3% along the planet's isentrope to get good interior models of Jupiter.

These models provide values for the mass of a core of heavy elements (other than H and He) and the total mass of heavy elements in these planets. The amount and distribution of heavy elements are quite sensitive to the EOS of hydrogen and constitute important clues to their formation process.

Keywords: equation of state, hydrogen, deuterium, Jupiter, Saturn

1. Introduction

Typically, the equation of state (EOS) of simple fluids is least understood in the regime of pressure ionization, where the temperature is low compared to the ionization energy and the density is high enough for the wavefunctions of bound electrons of neighboring particles to overlap significantly. Electrons become unbound upon further increasing the density. For hydrogen, this regime corresponds to $T \lesssim 10^5$ K and $P \sim 0.5$–50 Mbar and is found in the planets Jupiter and Saturn, in nearly all extrasolar giant planets discovered to date, and in all brown dwarfs.

Giant gaseous planets like Jupiter, Saturn, and the extrasolar giant planets have compositions similar to that of the Sun, or about ∼70% hydrogen by mass, the rest being mostly helium with a small admixture of heavy elements (anything but H and He). For objects with masses up to a few Jupiter masses (M_J), most of the mass lies in the region of the phase diagram of hydrogen with the largest uncertainty. We can expect that improvements in the EOS of hydrogen will have a significant impact on their interior structures.

Recent advances in shock compression techniques have permitted measurements of the deuterium EOS at pressures of $\sim$1 Mbar and above (Da Silva et al., 1997; Collins et al., 1998; Knudson et al., 2001; Belov et al., 2002; Boriskov et al., 2003; Knudson et al., 2003; Nellis, 2005) along the single shock Hugoniot, i.e. within the regime of pressure ionization. These experiments provide very valuable constraints on the EOS of hydrogen in the regime of interest for giant gaseous planets and for the first time, allow an estimation of the uncertainty on the EOS in that regime.

In view of these new EOS measurements, we have performed extensive modeling of the interiors of Jupiter and Saturn by considering a range of hydrogen EOS allowed by the current data and uncertainties (Saumon and Guillot, 2004). Of great astrophysical interest are the mass of their putative cores of heavy elements and the mass of heavy elements distributed in their outer envelopes. The total amount of heavy elements and their distribution inside Jupiter and Saturn provide essential constraints on their poorly understood formation process by the accretion of both gaseous (H and He) and solid material from the protoplanetary nebula (Pollack et al., 1996; Boss, 2000).

2. EOS's for Hydrogen

The interiors of giant planets follow adiabats in the EOS for a mixture of H, He, and heavy elements with a specific entropy determined by observations of the surface. On the other hand, shock-compression experiments follow Hugoniots that are typically much hotter than the Jupiter adiabat for the pressures of interest. For example, at 1 Mbar the temperature inside Jupiter is $\sim$6000 K, while the principal Hugoniot reaches $\sim$ 20000 K. The gas-gun reshock experiments overlap Jupiter's adiabat up to 0.8 Mbar, however (Nellis et al., 1983).

Since the adiabat and the Hugoniot overlap minimally, two EOS's that predict nearly identical Hugoniots may produce different adiabats. For the purposes of this study, we computed interior models of Jupiter using seven different hydrogen EOS's. These have been chosen to reproduce selected subsets of shock data, realistically bracket the actual EOS of hydrogen, and are based on a variety of EOS models to map the experimental Hugoniot data on the jovian adiabats.

Six of the seven hydrogen EOS's are described in detail in Saumon and Guillot (2004) and will only be discussed briefly here. We have computed four different EOS's based on the linear mixing model (Ross, 1998a,b; Ross and Yang, 2001). The linear mixing model interpolates linearly in composition between a molecular fluid and a metallic fluid. An entropy term is introduced in the metallic EOS and adjusted to fit the data. This model is well known for its ability to reproduce the high compressibility observed in the NOVA experiment (Da Silva et al., 1997; Collins

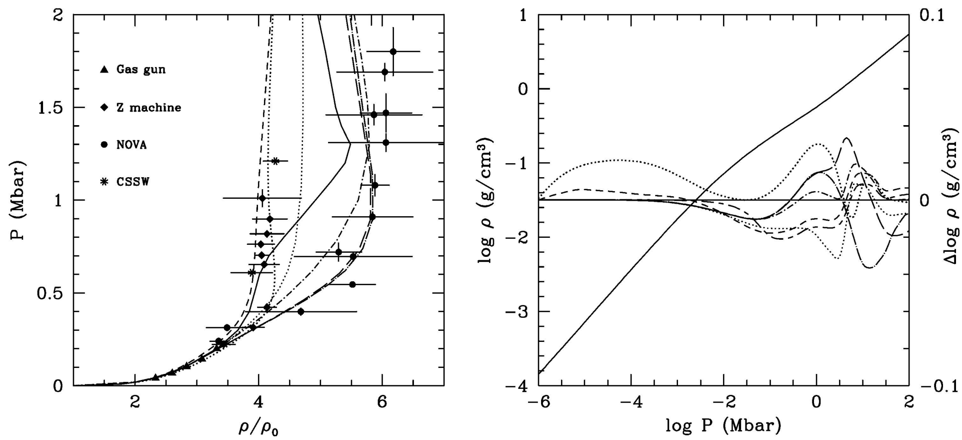

Figure 1. Left panel: Principal Hugoniots of deuterium compared to experimental data. ρ_0 is the density of the initial (unshocked) state. The Hugoniots are computed from the following EOS: SESAME (dashed), Kerley04 (heavy dotted) line, LM-SOCP (dotted), SCVH-I (solid), LM-H4 (short dash-dot), LM-A (long dash), and LM-B (long dash-dot). The LM-A and LM-B Hugoniots are nearly identical. Experimental data are taken from Nellis et al. (1983), Da Silva et al. (1997), Collins et al. (1998), Knudson et al. (2001, 2003), Belov et al. (2002) and Boriskov et al. (2003). *Right panel:* Jupiter hydrogen adiabat (diagonal solid curve, left-hand scale). The differences between the adiabats computed from the various EOS and the SCVH-I adiabat are also shown (right-hand scale).

et al., 1998). It has the advantage of being relatively simple and easily modified to reproduce different data sets or to introduce different levels of sophistication in the underlying physical model. We label those four linear mixing EOS's **LM-A**, **LM-B**, **LM-SOCP**, and **LM-H4**.

In addition, we have used three tabular EOS's. The **SESAME** EOS 5251 for hydrogen is a density scaling of the SESAME deuterium EOS 5263 (Kerley, 1972). The **SCVH-I** EOS of (Saumon et al., 1995), which has been used extensively in modeling the interiors of giant planets (Guillot (1999) and references therein), and the **Kerley04** hydrogen EOS (Kerley, 2003). The latter is the most recent hydrogen EOS and it reproduces a large set of experimental data and *ab inito* EOS simulations.

A comparison of deuterium Hugoniots computed with all seven EOS's with the single shock pressure data is shown in Figure 1. Additional comparisons with other shock data can be found in Saumon and Guillot (2004). The corresponding Jupiter hydrogen adiabats are also shown in Figure 1. The uncertainty on the density along the adiabat is largest between 0.1 and 100 Mbar with a maximum of $\pm 8\%$ at $P \sim 7$ Mbar.

3. Interior Models

The interior is represented by a 3-layer model with a core, an inner envelope, and an outer envelope (Guillot et al., 1994). The core is assumed to be predominantly composed of heavy elements, while the envelope is dominated by hydrogen and helium, with a small admixture of heavy elements. For a given EOS and input parameters, a rotating, fluid, hydrostatic 3-layer structure is computed and its response to the rotational perturbation is compared to the observed gravitational moments, which are moments of the density profile of the planet (Zharkov and Trubitsyn, 1978).

The free parameters of this model are the mass of the core and the mass of heavy elements homogeneously mixed in the H/He envelope. Many other sources of uncertainty in modeling of the interior are taken into account, such as the mix of heavy elements, the interior rotation of the planet, residual uncertainties in the EOS, etc. The range of these uncertainties constitutes our parameter space. For a given H EOS, a very large number of models is computed to fully explore the parameter space. Models that do not fit the observed constraints within the 2σ error bars are rejected (Guillot, 1999).

3.1. Jupiter

The solutions for Jupiter are summarized in Figure 2. For each EOS considered, a range of core masses ($M_{\rm core}$) and masses of heavy elements in the envelope (M_Z) is obtained after varying the other parameters. The domain of acceptable models for a given hydrogen EOS is enclosed in a box.

The total range of solutions for all EOS's considered is much larger than the allowed range for any given EOS. This means that the current uncertainties on the hydrogen EOS remains the largest source of uncertainty in interior models of Jupiter. All EOS's lead to models that are enriched in heavy elements ($M_{\rm core} + M_Z = 6$–$42\,M_\oplus$, where $M_\oplus$ is the mass of the Earth) compared to solar abundances (which

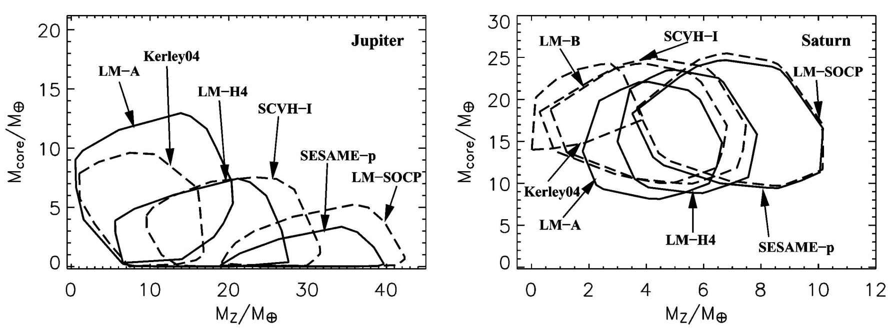

Figure 2. Core mass and mass of heavy elements in the envelope of Jupiter (*left panel*) and Saturn (*right panel*) in units of the Earth's mass ($M_\oplus$). Each box represents the ensemble of solution that fits the observational constraints for a given H EOS. Note that it is not possible to model Jupiter with the LM-B EOS. The total masses of Jupiter and Saturn are 317.83 $M_\oplus$ and 95.147 $M_\oplus$, respectively. The two panels are plotted on different scales.

would give $\sim$6 $M_\oplus$). The core mass of Jupiter is between 0 and 12 $M_\oplus$ and the mass of heavy elements in the envelope is between 0 and 42 $M_\oplus$. All EOS's allow solutions with no core at all! While the LM-A and LM-B EOS produce identical Hugoniots, the corresponding adiabats are sufficiently different that no Jupiter model can be found with the LM-B EOS. Interestingly, the Kerley04 EOS and the LM-A EOS correspond to the extremes in shock compression along the principal Hugoniot (Figure 1) and yet give very similar solutions for $M_{\rm core}$ and M_Z. This indicates that the calculation of adiabats for Jupiter is strongly model-dependent and that the current data do not constrain the adiabat well enough. Most formation models of Jupiter require an initial core mass of 10–20 $M_\oplus$ (Pollack et al., 1996). The small core masses we find would imply significant mixing of the core and the envelope *after* the bulk of the planet had formed (Guillot et al., 2004). Alternatively, Jupiter may have formed without a core by a direct instability of the gas (Boss, 2000), but it is then difficult to explain its large enrichment in heavy elements.

3.2. Saturn

For Saturn, we find that there is much more overlap between the solutions for the different EOS than is the case for Jupiter and that $9 \lesssim M_{\rm core} \lesssim 22\, M_\oplus$ and $1 \lesssim M_Z \lesssim 8\ M_\oplus$ (Figure 2). The total mass of heavy elements is between 13 and 28 $M_\oplus$. The EOS is an important source of uncertainty in modeling Saturn's interior but it is not as dominant as in Jupiter. In contrast with Jupiter, the LM-B EOS gives acceptable models of Saturn. The amount of heavy elements in the envelope is rather modest but globally Saturn has a 6–14-fold enrichment compared to the solar value. The choice of EOS has no discernible effect on $M_{\rm core}$. The distribution and the amount of heavy elements in Saturn is in very good agreement with the core accretion formation model.

4. Conclusions

Our work confirms that the interior of Jupiter is qualitatively different from that of Saturn. Taken at face value, this suggests that the two planets formed with different processes. Unfortunately, the uncertainties on $M_{\rm core}$ and M_Z remain large and provide only loose boundary conditions on the formation processes.

Models of the interiors of Jupiter and Saturn would greatly benefit from improved measurements of their gravitational moments and refinements of other astrophysical uncertainties. This can be accomplished with proposed space missions to Jupiter and with the Cassini spacecraft currently orbiting Saturn. This would reduce the dimensions of the boxes in Figure 2.

Our extensive study reveals the full possible range of interior models for these two planets. We also find that the recent shock compression experiments in the Mbar range do not constrain the EOS along the Jupiter and Saturn adiabats sufficiently and that the interior models still depend rather strongly on the choice of EOS model. It is highly desirable to have EOS measurements that are closer to the Jupiter adiabat to remove this dependence on the EOS model.

Acknowledgements

This work was supported in part by NASA Planetary Geology & Geophysics grant NAG5-8906, by the United States Department of Energy under contract W-7405-ENG-36, and by the *Programme National de Planétologie* (France).

References

Belov, S.I., et al.: 2002, *JETP Lett.* **76**, 433.
Boriskov, G.V., et al.: 2003, *Dokladi Phys.* **48**, 553.
Boss, A.P.: 2000, *Astrophys. J. Lett.* **536**, L101.
Collins, G.W., et al.: 1998, *Science* **281**, 1178.
Da Silva, L.B., et al.: 1997 *Phys. Rev. Lett.* **78**, 483.
Guillot, T.: 1999, *Plan. Space Sci.* **47**, 1183.
Guillot, T., Chabrier, G., Morel, P. and Gautier, D.: 1994, *Icarus* **112**, 354.
Guillot, T., Stevenson, D.J., Hubbard, W.B. and Saumon, D.: 2004, *Jupiter. The Planet, Satellites and Magnetosphere*, F. Bagenal, T.E. Dowling and W.B. McKinnon (eds.), Cambridge University Press, Cambridge **35**.
Kerley, G.I.: 1972, Los Alamos Scientific Laboratory, Technical Report LA-4776, p. 1.
Kerley, G.I.: 2003, Sandia National Laboratory, Sandia Report SAND2003-3616, p. 1.
Knudson, M.D., Hanson, D.L., Bailey, J.E., Hall, C.A. and Asay, J.R.: 2001, *Phys. Rev. Lett.* **87**, 225501/1–4.
Knudson, M.D., Hanson, D.L., Bailey, J.E., Hall, C.A. and Asay, J.R.: 2003, *Phys. Rev. Lett.* **90**, 035505/1–4.
Nellis, W.J.: 2005, *Ap&SS* **298**, 141.
Nellis, W.J., Mitchell, A.C., van Thiel, M., Devine, G.J. and Trainor, R.J.: 1983, *J. Chem. Phys.* **79**, 1480.
Pollack, J.B., Hubickyj, O., Bodenheimer, P., Lissauer, J.J., Podolak, M. and Greenzweig, Y.: 1996, *Icarus* **124**, 62.
Ross, M.: 1998, *Phys. Rev. B* **58**, 669.
Ross, M.: 1998, *Phys. Rev. B* **60**, 6923.
Ross, M. and Yang, L.H.: 2001, *Phys. Rev. B* **64**, 134210/1–8
Saumon, D., Chabrier, G. and van Horn, H.M.: 1995, *Astrophys. J. Suppl.* **99**, 713.
Saumon, D. and Guillot, T.: 2004, *Astrophys. J.* **609**, 1170.
Zharkov, V.N. and Trubitsyn, V.P.: 1978, *Physics of Planetary Interiors*, Pachart, Tucson.

DEUTERIUM HUGONIOT UP TO 120 GPa (1.2 Mbar)

W.J. NELLIS*
Lawrence Livermore National Laboratory, Livermore, California 94550, USA
**Present address: Department of Physics, Harvard University, Cambridge, Massachusetts 02138, USA*

(Received 10 May 2004; accepted 27 May 2005)

Abstract. The shock compression curve (Hugoniot) of D_2 has been controversial because the two data sets measured previously with a laser (L) and with pulsed currents (PC) differ substantially. Recently, Hugoniot points of D_2 have been measured at shock pressures of 123, 109, 61, 54, and 28 GPa using hemispherically converging, explosively-driven systems (CS). The CS results are in good agreement with the PC data and the error bars of the CS-PC data are less than half those of the L data. The limiting compression obtained from the best fit to the CS-PC data is 4.30 ± 0.10 at 100 GPa. The CS-PC data are in good agreement with PIMC and DFT calculations, which is expected to be the case at higher shock temperatures and pressures, as well.

Keywords: deuterium, Hugoniot

1. Introduction

The equation of state (EOS) of dense fluid hydrogen and its isotopes is needed to model the interiors of giant hydrogeneous planets in this and other solar systems, to design ICF (Inertial Confinement Fusion) targets, and to understand the physics of dense matter as it transitions from a degenerate to a nondegenerate state with increasing temperature (warm dense matter). Pressures of 100s of GPa, compressions of 2–12 times liquid deuterium density at 20 K, and temperatures up to a few 10,000 K can be reached by dynamic compressions ranging from the Hugoniot to the isentrope.

The Hugoniot of deuterium up to 100 GPa (1 Mbar) pressures has been controversial because limiting shock compression close to ~6-fold of initial liquid density has been reported using a high-intensity laser (L) (Da Silva et al., 1997) and limiting compression close to ~4-fold has been reported using large pulsed currents (PC) (Knudson et al., 2001, 2004). The systematics of Hugoniots of diatomic liquids suggests that the PC data are correct (Nellis, 2002). To resolve this issue, independent measurements have been made from 28 to 121 GPa by Belov et al. (2002) and by Boriskov et al. (2003, 2005) using hemispherical convergence driven by explosives (CS).

2. Experiments

The CS experiments used the shock-impedance match method (Altshuler et al., 1958); the error analysis is described by Nellis and Mitchell (1980). Samples were

Astrophysics and Space Science **298:** 141–145, 2005.

liquid or solid D_2. Hugoniot points were measured in $u_s - u_p$ space, where u_s is shock velocity and u_p is mass velocity. The Hugoniot equations were used to calculate P and ρ from u_s and u_p, where P is shock pressure and ρ is shock-compressed density. Since $u_s - u_p$ data are related systematically, least-squares fits to the $u_s - u_p$ data were obtained first. Experimental results were compared to those obtained with a two-stage gun (GG) at lower pressures (Nellis et al., 1983). The CS and PC data above $u_p = 15$ km/s, the controversial region, and GG data below $u_p = 9$ km/s have a linear relationship. The $u_s - u_p$ data obtained by all three methods are plotted in Figure 1.

The fit to the GG data is $u_{s1} = C_1 + S_1 u_p$ with $S_1 = 1.21 \pm 0.04$ and $C_1 = 2.04 \pm 0.21$ km/s. The fit to the CS-PC data in the range $15 < u_p < 22$ km/s is $u_{s3} = C_3 + S_3 u_p$ with $S_3 = 1.22 \pm 0.08$ and $C_3 = 1.70 \pm 1.50$ km/s. Uncertainties in shock velocity calculated from the best $u_s - u_p$ fit are used to calculate uncertainties

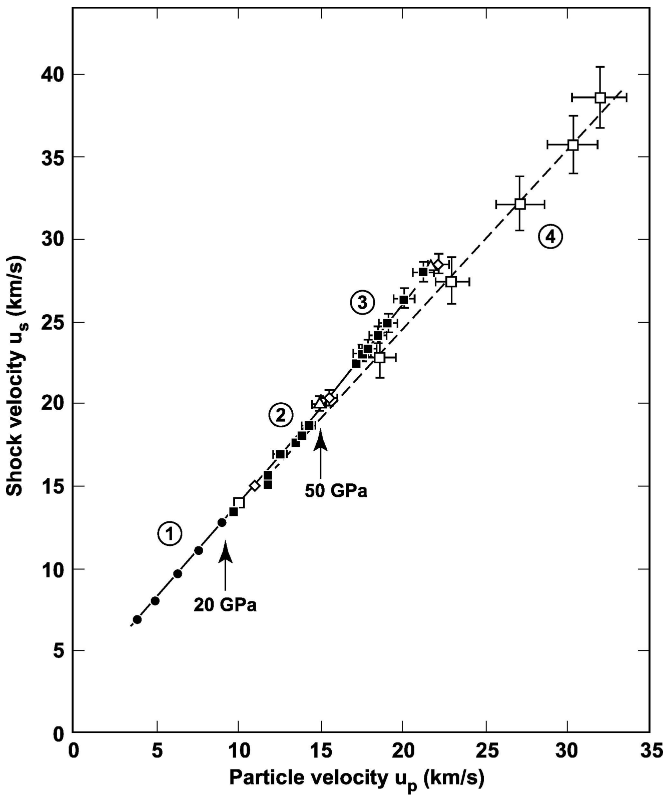

Figure 1. Shock velocity u_s versus mass velocity u_p for deuterium: open diamonds (Boriskov et al., 2005), open triangles (Belov et al., 2002; Boriskov et al., 2003), solid squares (Knudson et al., 2004), solid circles (Nellis et al., 1983), open squares (Da Silva et al., 1997). Solid curve is least-squares fits in region 1–3; dashed curve in region 4 is linear fit to Da Silva et al. (1997).

in the P–ρ curve derived from that fit. The *standard deviation* in u_{s3} as a function u_p is given by

$$\sigma(u_s(u_p)) = \left[\sum_j (\delta C_j + u_p \delta S_j)^2\right]^{1/2} \tag{1}$$

where $\delta C_j = C_j - C$, $\delta S_j = S_j - S$, C and S are obtained from the best fit, and C_j and S_j are the values of C and S obtained by varying the jth value of u_{s3} by its experimental uncertainty (Beers, 1957). This *standard deviation* is relatively small because δC_j and δS_j have opposite signs. For the 19 CS-PC points in the range $15 < u_p < 22$ km/s, this *standard deviation* is $\sigma(u_s(u_p)) = (3.216 - 0.3301u_p + 0.008487u_p^2)^{1/2}$. The relative *standard deviation* $\sigma(u_s(u_p))/u_s(u_p)$ has a minimum of 0.4% at $u_p = 19.5$ km/s and 85 GPa, which is precisely the regime in which high accuracies are needed.

In the region, $9 < u_p < 15$ km/s, the combined CS-PC data have a small curvature. The shock pressures corresponding to these velocities are 20 and 50 GPa, respectively. This is the same shock pressure range in which optical reflectivity experiments indicate that deuterium undergoes a transition from a diatomic insulator below 20 GPa to a monatomic, strong-scattering metal above 50 GPa (Celliers et al., 2000). This reflectivity data justifies treating the small curvature in this region as physical in nature. Thus, in the region $9 < u_p < 17$ km/s a cubic polynomial was used to fit 15 PC-CS points. This expression represents an initial softening in u_{s2} (~3%) caused by dissociation, followed at higher u_p by a stiffening in u_{s2} caused by completion of the temperature-driven nonmetal-metal transition from Maxwell-Boltzmann statistics for the diatomic insulator to Fermi-Dirac statistics for the monatomic metal (Nellis, 2003).

The laser data (L) are linear ($u_{sL} = C_L + S_L u_p$) in the range $18 < u_p < 32$ km/s. The CS experimental results are in good agreement with the PC data and the error bars of the CS and PC data sets are less than half those of the L data. The CS-PC and the L data agree only at the extremes of the error bars of the respective $u_s - u_p$ data. Thus, in a general scientific sense all the data sets agree when error bars are taken into account. However, the CS-PC data should be used for comparison of experiment with theory.

The $u_s - u_p$ fits to the CS-PC, L, and GG data were transformed to P versus compression (ρ/ρ_0), where ρ_0 is initial liquid density. The results are shown in Figure 2 as the solid and dashed curves, respectively.

The solid curve is composed of fits in three regions described above. The error bars of compression for the solid and dashed curves in the range 50 to 110 GP are their *standard deviations* calculated from the uncertainties in measured shock velocities. No effort was made to obtain a smooth join in P-(ρ/ρ_0) space for the three regions of the solid curve. The best fit to the CS-PC data is in good agreement with Path Integral Monte Carlo calculations (Militzer and Ceperley, 2000) and with

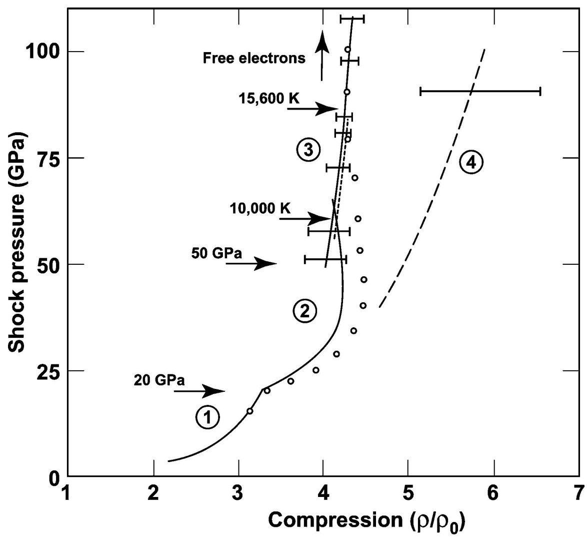

Figure 2. Shock pressure versus compression (ρ/ρ_0) calculated with Hugoniot equations and $u_s - u_p$ fits. Solid curve is CS-PC result and dashed curve is L result. Error bars of fits are *standard deviations* calculated from uncertainties in shock velocity measurements. Dotted curve and indicated temperatures were calculated with PIMC by Militzer and Ceperley (2000). Open circles were calculated with DFT by Desjarlais (2003).

Density Functional Theory (Desjarlais, 2003), also shown in Figure 2 as the dotted curve and open circles, respectively.

3. Conclusions

Several conclusions can be drawn from these results:

(i) When error bars are taken into account, all three $u_s - u_p$ data sets are in agreement.
(ii) The CS-PC $u_s - u_p$ data are in excellent mutual agreement and their error bars are less than half those of the L data. Thus, to compare experiment to theory, the $u_s - u_p$ fits to the combined CS-PC data should be transformed to P–ρ space.
(iii) $u_s(u_p)$ is weakly sensitive to dissociation.
(iv) Limiting compression of the best fit to the CS-PC experimental data is 4.30 ± 0.10 at 100 GPa. Limiting compression of an initially degenerate free-electron gas is 4.0. Thus, D_2 Hugoniot data at 100 GPa pressures can barely resolve the presence of interactions.
(v) Thus, kinetic thermal energy dominates potential energy at 100 GPa shock pressures.

(vi) Because interparticle potential energies become even smaller relative to thermal kinetic energies at higher shock pressures, it is expected that the deuterium Hugoniot will not have a compression higher than 4.3 at higher shock temperatures and pressures.

Acknowledgments

Work at Lawrence Livermore National Laboratory was performed under the auspices of the U.S. Department of Energy by the University of California under contract No. W-7405-Eng-48. We want to acknowledge M. D. Knudson for providing his experimental data and M. P. Desjarlais for providing his calculational results.

References

Altshuler, L.V., Krupnikov, K.K., Ledenev, B.N., Zhuchikhin, V.I. and Brazhnik, M.I.: 1958, *Sov. Phys. JETP* **7**, 606.

Beers, Y.: 1957, *Introduction to the Theory of Errors*, Addison Wesley, 41.

Belov, S.I., Boriskov, G.V., Bykov, A.I., Ilkaev, R.I., Luk'yanov, N.B., Matveev, A. Ya., Mikhailova, O.L., Selemir, V.D., Simakov, G.V., Trunin, R.F., Trusov, I.P., Urlin, V.D., Fortov, V.E. and Shuikin, A.N.: 2002, *JETP Lett.* **76**, 433.

Boriskov, G.V., Bykov, A.I., Ilkaev, R.I., Selemir, V.D., Simakov, G.V., Trunin, R.F., Urlin, V.D., Fortov, V.E. and Shuikin, A.N.: 2003, *Dokl. Phys.* **48**, 553.

Boriskov, G.V., Bykov, A.I., Ilkaev, R.I., Selemir, V.D., Simakov, G.V., Trunin, R.F., Urlin, V.D., Shuikin, A.N. and Nellis, W.J.: 2005, *Phys. Rev. B* **71**, 092104.

Celliers, P.M., Collins, G.W., Da Silva, L.B., Gold, D.M., Cauble, R., Wallace, R.J., Foord, M.E. and Hammel, B.A.: 2000, *Phys. Rev. Lett.* **84**, 5564.

Da Silva, L.B., Celliers, P., Collins, G.W., Budil, K.S., Holmes, N.C., Barbee Jr., T.W., Hammel, B.A., Kilkenny, J.D., Wallace, R.J., Ross, M. and Cauble, R.: 1997, *Phys. Rev. Lett.* **78**, 483.

Desjarlais, M.P.: 2003, *Phys. Rev. B* **68**, 064204-1 to 064204-8.

Knudson, M.D., Hanson, D.L., Bailey, J.E., Hall, C.A., Asay, J.R. and Anderson, W.W.: 2001, *Phys. Rev. Lett*. **87**, 225501-1 to 225501-4.

Knudson, M.D., Hanson, D.L., Bailey, J.E., Hall, C.A., Asay, J.R., and Deeney, C.: 2004, *Phys. Rev. B*. **69**, 144209.

Militzer B. and Ceperley, D.M.: 2000, *Phys. Rev. Lett*. **85**, 1890.

Nellis, W.J. and Mitchell, A.C.: 1980, *J. Chem. Phys*. **73**, 6137.

Nellis, W.J., Mitchell, A.C., van Thiel, M., Devine, G.J., Trainor, R.J. and Brown, N.: 1983, *J. Chem. Phys*. **79**, 1480.

Nellis, W.J.: 2002, *Phys. Rev. Lett*. **89**, 165502-1.

Nellis, W.J.: 2003, *J. Appl. Phys*. **94**, 272.

MODELING X-RAY PHOTOIONIZED PLASMAS PRODUCED AT THE SANDIA Z-FACILITY

P.A.M. VAN HOOF[1], M.E. FOORD[2], R.F. HEETER[2], J.E. BAILEY[3], H.-K. CHUNG[2], M.E. CUNEO[3], W.H. GOLDSTEIN[2], V. JONAUSKAS[1], F.P. KEENAN[1], R. KISIELIUS[1], D.A. LIEDAHL[2], C. RAMSBOTTOM[1], S.J. ROSE[4], P.T. SPRINGER[2] and R.S. THOE[2]

[1]*APS Division, Physics Department, Queen's University, Belfast BT7 INN, Northern Ireland; E-mail: p.van-hoof@qub.ac.uk*

[2]*University of California, Lawrence Livermore National Laboratory, Livermore, CA 94551, USA*

[3]*Sandia National Laboratory, Albuquerque, NM 37185, USA*

[4]*Department of Physics, Clarendon Laboratory, Parks Road, Oxford OX1 3PU, United Kingdom*

(Received 14 May 2004; accepted 31 May 2004)

Abstract. In experiments at the high-power Z-facility at Sandia National Laboratory in Albuquerque, New Mexico, we have been able to produce a low density photoionized laboratory plasma of Fe mixed with NaF. The conditions in the experiment allow a meaningful comparison with X-ray emission from astrophysical sources. The charge state distributions of Fe, Na and F are determined in this plasma using high resolution X-ray spectroscopy. Independent measurements of the density and radiation flux indicate unprecedented values for the ionization parameter $\xi = 20$–$25\,\mathrm{erg\,cm\,s^{-1}}$ under nearly steady-state conditions. First comparisons of the measured charge state distributions with X-ray photoionization models show reasonable agreement, although many questions remain.

Keywords: photoionization, X-ray, spectroscopy

1. Introduction

With the recent launch of the X-ray observatories *Chandra* and *XMM-Newton*, high resolution spectra from numerous photoionized X-ray sources such as X-ray binaries and active galactic nuclei are being obtained. With these instruments we are able for the first time to resolve individual lines in these spectra, and they often contain prominent lines from iron which can be used as diagnostics for the physical conditions in the plasma. However, the analysis of these lines is hampered, amongst other things, by a lack of high quality atomic data and uncertainties in the treatment of the energy balance in optically thick plasmas. As a consequence, we do not know how accurate the results from our modeling codes are. To address this problem, we have set up an experiment to create a near steady-state laboratory X-ray photoionized plasma with observationally constrained physical conditions that are astrophysically relevant.We have produced a low-density plasma of Fe mixed with NaF, and observed absorption and emission spectra of this plasma which will be used to benchmark existing astrophysical and laboratory modeling codes. These experiments are being combined with an effort to calculate high quality atomic data of relevant iron ions. In Section 2 we briefly describe the experiment and the determination of the physical parameters, while in Section 3 we describe the current status of our modeling effort. Finally, in Section 4 we briefly outline the current status of our atomic data calculations.

2. The Experiment

In experiments at the high-power Z-facility at Sandia National Laboratory in Albuquerque, New Mexico, we have been aiming to produce a low density photoionized laboratory plasma of Fe mixed with NaF. The radiation from the z-pinch is generated by inductively coupling a 20 MA, 100 ns rise time current pulse into a 2 cm diameter wire array, consisting of 300 tightly strung 11.5 μm tungsten wires. The electromagnetic forces drive the wires radially inward onto the central axis, creating a 8 ns FWHM, 120 TW peak power, 165 eV near-blackbody radiation source. The emission from the z-pinch was directly observed by several spectrometers, which allowed us to determine the time-resolved history of the absolute spectral flux of the pinch. The spectrum at peak emission is shown in Figure 1.

Free standing thin (500–750 Å) rectangular foils were suspended in frames and positioned parallel to the z-axis of the pinch at a distance of 1.5–1.6 cm. The foils consisted of a 1.35:1 molar ratio of Fe/NaF and were overcoated on each side with 1000 Å of lexan $(C_{16}H_{14}O_3)_n$ to help maintain uniform conditions during heating and expansion. The radiation generated during the 100 ns run-in phase preheats and expands the foil to about 1.5–2 mm. When the wires collide on axis, the resulting

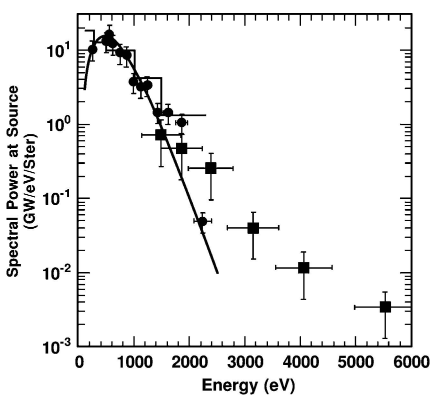

Figure 1. Z-pinch X-ray spectral emission measured at peak power with an XRD array (histogram), a transmission grating spectrometer (dots), and a PCD array (squares). The peak-normalized 165 eV blackbody fit is also shown.

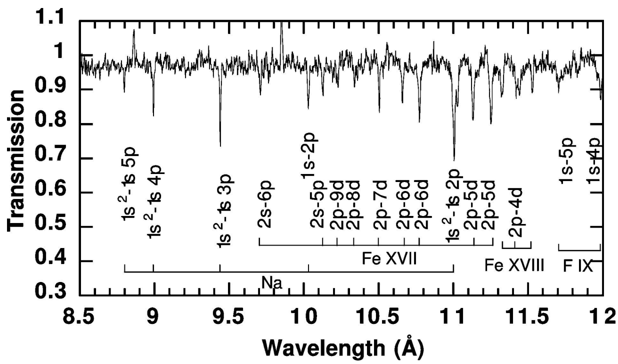

Figure 2. Time-integrated absorption spectrum of L-shell Fe and K-shell Na and F lines.

X-ray pulse quickly photoionizes the low density expanded foil. Two spectrometers were used to record the time-integrated absorption and emission spectrum of the plasma. For the absorption spectrum, the z-pinch emission was used as a backlighter. The instrumental resolution was $E/\Delta E = 500$–800 in the range 8.5–17 Å. A section of the absorption spectrum is shown in Figure 2. This is weighted by the time evolution of the pinch emission, and therefore reflects conditions near the peak of the emission. To account for the estimated few ns required to reach steady-state equilibrium, the values of the absolute spectral flux and the electron density used in the calculations were taken at $+3$ ns after the peak of the radiation pulse, thus justifying the use of steady-state modeling codes.

2.1. The charge state distribution

To determine the relative populations of each of the charge states in the plasma, we used a curve of growth analysis which gives a relation between the equivalent width of an absorption line (this is the integrated depth of the normalized absorption line) and the abundance of a given ion. We adapted the theory to account for the expansion of the plasma in the foil. Details can be found in Foord et al. (2004). The analysis was applied to the Na and F absorption spectrum shown in Figure 2. The resulting ratio of Na^{10+}:Na^{9+} ground state ions was 1:4.5. Similar analysis of F absorption lines indicated a ratio of 6.0:1 for F^{8+}:F^{7+}. The reversed ratio for F relative to Na is due to its lower photoionization threshold. For the Fe ions a somewhat different method was used because many of the observed lines were blended. Line positions and oscillator strengths for many thousands of Fe lines were calculated using the HULLAC suite of codes (Klapisch et al., 1977). The charge state distribution was then determined by varying each Fe charge state concentration to best fit the absorption line strengths. The resulting Fe charge state distribution is shown in Figure 3.

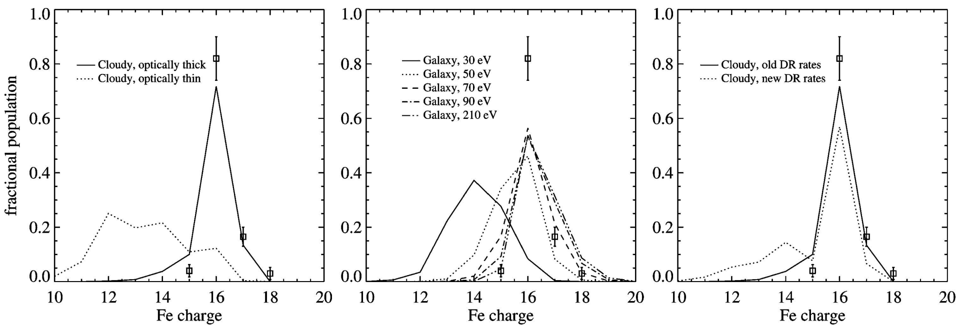

Figure 3. The experimental charge state distribution of Fe (open squares) compared to various models of the experiment.

2.2. The density determination

To determine the density of the plasma, a time-gated filtered X-ray pinhole camera was used that imaged the Fe/NaF emission region nearly edge-on. This allowed us to determine the thickness of the plasma as a function of time. Combined with the areal density of the material in the foil (supplied by the manufacturer), we could determine the volume density of each of the elements that were present in the plasma. The tamping effect of the lexan coating of the foil helped to maintain uniform conditions in the plasma, thus justifying this approximation. Combining this information with the charge state distribution we derived above, allowed us to determine the number density of each ionic state and finally the electron density (n_e). The resulting value is $n_e = 2.0 \pm 0.7 \times 10^{19}\,\mathrm{cm}^{-3}$ at $+3$ ns after the peak. When we combine the absolute flux calibration derived in the previous section with this value of the electron density, we find that we reach peak values of the ionization parameter $\xi = 16\pi^2 J/n_e = 20$–$25\,\mathrm{erg\,cm\,s}^{-1}$, where J is the mean intensity in $\mathrm{erg\,cm}^{-2}\,\mathrm{s}^{-1}$ integrated from 13.6 eV to infinity. We believe these are the highest values reached in laboratory experiments to date, and are approaching the astrophysically relevant domain.

2.3. The temperature determination

We have not yet been able to identify a reliable means of obtaining the electron temperature (T_e) from the observations. Hence to obtain an estimate for the temperature, we used the astrophysical modeling code CLOUDY (Ferland et al., 1998). This code calculates T_e by a detailed energy accounting of all relevant heating and cooling processes in the plasma. Our first model calculation included a restricted set of Fe emission lines that effectively treated the Fe resonance lines as optically thick. This assumption is consistent with the measured saturation of the strongest Fe lines. The model yielded $T_e \approx 150$ eV and an average charge state $\langle Z \rangle \simeq 16.0$ (see Figure 3, left panel), in reasonable agreement with both the measured distribution width and the average ionization state. To test the sensitivity to optical depth effects, a second model was constructed which treated all lines as optically thin. This yielded a much lower temperature (38 eV), due to enhanced cooling from line emission, and a distribution that peaked at Fe^{12+}. The latter model is clearly inconsistent with the observations, but does set a lower limit for T_e. We will adopt $T_e = 150\,\text{eV}$ as our current best estimate, but we do intend to obtain independent measurements of the electron temperature in future work, e.g. through Thomson scattering. We also aim to improve the treatment of optical depth effects in the cooling lines using escape probabilities in order to obtain better estimates of T_e from our modeling codes.

3. The Modeling

The charge state distributions for Fe, Na, and F were calculated with the collisional-radiative code GALAXY (Rose, 1998). For a given density, temperature, and incident radiation field, GALAXY calculates the steady-state ionization balance within the plasma. Collisional and radiative excitation and ionization, as well as autoionization and all reverse processes are included. A rate matrix is constructed that couples the initial and final levels using simple scaled-hydrogenic expressions. Accurate Hartree-Dirac-Slater photoionization cross sections are used where possible, and Kramers cross sections are used otherwise. The GALAXY code employs an average-of-configuration approximation for electronic states with a principal quantum number $n \leq 5$ and averages over all the configurations with the same principal quantum number for higher n.

To account for the estimated few ns required to reach steady-state equilibrium, the values of the absolute spectral flux and sample density ($n_e = 2.0 \pm 0.7 \times 10^{19}\,\text{cm}^{-3}$) used in the calculations were taken at +3 ns after the peak of the radiation pulse. We estimate that the decrease in ξ from 25 to $20\,\text{erg cm s}^{-1}$ during this time has a very small effect on the ionization balance. Using these values, the charge state distribution for Fe was calculated for various temperatures between 30 and 210 eV (see Figure 3, middle panel). Above 70 eV, the distributions peak near Fe^{16+} and are quite insensitive to T_e. In this temperature regime (90–210 eV) calculations indicate that photoionization of Fe L-shell ions dominates over collisional ionization processes by more than a factor of ten. The weak temperature dependence of the charge state distribution therefore is likely due to the thermal electrons having insufficient energy to ionize the L-shell ions in this regime. Below 50 eV, the contribution from three-body recombination begins to dominate, reducing the degree of ionization substantially. This indicates that we succeeded in creating a photoionization dominated plasma.

The average charge state predicted by GALAXY in the 90 to 210 eV temperature range is $\langle Z \rangle \simeq 16.4 \pm 0.2$ (see Figure 3). The uncertainty in $\langle Z \rangle$ is determined from folding in the sensitivities to the uncertainties in the absolute flux ($\pm 20\%$) and density (±35%) measurements. The calculated distribution is slightly more ionized than measured. This may be due, in part, to the fact that the measured time-integrated absorption spectrum is weighted by the time-history of the backlighter intensity, which peaks a few nanoseconds before the sample reaches steady-state equilibrium, resulting in a slightly lower average charge. GALAXY calculations of H to He-like ratios for F and Na yielded ratios of 6.7:1 and 1:1.4, respectively at $T_e = 150$ eV. The F ratio agrees well with the observations, while the Na observations indicate a lower degree of ionization than the model.

Recently two papers have been published that defended the need for an update in the dielectronic recombination (DR) rates of Fe (Netzer, 2004; Kraemer et al., 2004), claiming that the new rates produce a better fit to *Chandra* and *XMM-Newton* data. To test this hypothesis, we made a CLOUDY model using the new rates but without any further modifications (Figure 3, right panel). Taken at face value, this model indicates that the new DR rates give a worse fit to our observations by overpopulating the M-shell stages. We intend to investigate this discrepancy further.

4. The Atomic Data Calculations

We are currently undertaking a comprehensive effort to calculate high quality atomic data for all the transitions that are relevant in this experiment. The current status of this effort is as follows:

IFeXII–XIV: We have calculated energy levels and El transition probabilities for L-shell photo-excitation using the Breit-Pauli approximation implemented in the CIV3 code (Kisielius et al., in preparation).

FeXV–XVI: We have calculated energy levels and El transition probabilities for L-shell photo-excitation using the Breit-Pauli approximation implemented in the CIV3 code (Kisielius et al., 2003).

FeXVII: We have calculated energy levels and transition probabilities (El, Ml, E2, M2) upto $n = 5$ using the fully relativistic GRASP code. (Aggarwal et al., 2004). Calculations of the collision strengths using the relativistic DARC code are in progress (Kisielius et al., in preparation).

FeXVIII: We have calculated energy levels and transition probabilities (El, Ml, E2) using the GRASP code (Jonauskas et al., 2004a). Calculations of the collision strengths are in progress.

FeXIX: We have calculated energy levels and transition probabilities (El, Ml, E2) using the GRASP code (Jonauskas et al., 2004b).

Acknowledgements

FPK and SJR are grateful to AWE Aldermaston for the award of William Penney Fellowships. This work was supported by EPSRC and PPARC, and also by NATO

Collaborative Linkage Grant CLG.979443. We are also grateful to the Defense Science and Technology Laboratory (dstl) for support under the Joint Grants Scheme. The photoionization code CLOUDY, written by Gary J. Ferland and obtained from http://www.nublado.org, was used.

References

Aggarwal, K.M., Keenan, F.P. and Kisielius, R.: 2004, *A&A* **420**, 783.
Ferland, G.J. et al.: 1998, *PASP* **110**, 761.
Foord, M.E. et al.: 2004, *Phys. Rev. Letters* **93**, 055002.
Jonauskas, V. et al.: 2004a, *A&A*, **416**, 383.
Jonauskas, V. et al.: 2004b, *A&A* **424**, 363.
Kisielius, R. et al.: 2003, *MNRAS*, **344**, 696.
Klapisch, M. et al.: 1997, *J. Opt. Soc. Am.* **67**, 148.
Kraemer, S.B., Ferland, G.J. and Gabel, J.R.: 2004, *ApJ* **604**, 556.
Netzer, H.: 2004, *ApJ* **604**, 551.
Rose, S.J.: 1998, *J. Phys. B* **31**, 2129.

RADIATION PROPERTIES OF HIGH-ENERGY ASTROPHYSICAL PLASMAS

KUNIAKI MASAI

Department of Physics, Tokyo Metropolitan University, Hachioji, Tokyo 192-0397, Japan; E-mail: masai@phys.metro-u.ac.jp

(Received 30 April 2004; accepted 1 July 2004)

Abstract. We discuss radiation properties of plasmas in high-energy astrophysics with a keyword *nonequilibrium:* non-LTE level populations, nonequilibrium ionization, and non-Maxwellian distribution function, beginning with radiative transfer. We focus particularly on supernova remnants interacting with the circumstellar/interstellar matter, and also mention line emission processes in accretion gas onto a neutron star or black hole, and in the X-ray afterglow of γ-ray bursts.

Keywords: radiation mechanisms, X-rays, supernova remnants

1. Introduction

K-lines of highly ionized atoms of heavy elements have been observed from hot or energetic astrophysical plasmas, such as supernova remnants, intracluster gas of galaxy clusters, accretion gas onto a neutron star or black hole, and possibly afterglow of gamma-ray bursts. The plasmas are collisionally ionized or photoionized, and the relevant energy of particles or photons must be of order of $\sim$ keV to be responsible for such high ionization states. We discuss radiation properties of the plasmas in high-energy astrophysics with a keyword *non-equilibrium*.

– Non-LTE level population: To establish LTE level populations, collisional excitation/de-excitation must balance with each other. Since competitive spontaneous emission rates increase with the atomic number Z as Z^q with $q = 4$ for E1 and $q > 4$ for non-E1 transitions, high densities would be required for heavy elements.
– Nonequilibrium ionization: Young supernova remnants are ionizing plasmas, because collisional ionization cannot immediately follow rapid heating by shocks in the low-density interstellar medium. In contrast, in accretion-powered sources the accretion gas is photoionized to be a recombining plasma.
– Non-Maxwellian distribution function: Acceleration, e.g. due to fluctuations of magnetic field, of thermal electrons forms a quasi-thermal component. Unlike nonthermal electrons which are almost collisionless, even a small fraction of quasi-thermal electrons significantly affects radiation processes in the plasma.

Astrophysics and Space Science **298:** 155–162, 2005.

When LTE, kinetic energies of particles are given by the Maxwellian distribution, level populations by the Boltzmann's, ionization by the Saha's, and the radiation by the Planck's, as a function of local temperature T (for both matter and radiation) which is a unique parameter in LTE. Such a monochromatic world may be attained, for instance, in the interior of a star, and then the black/grey-body radiation emerges out of the surface.

In high-energy astrophysics, LTE may be the case for the *standard* accretion disk that is optically thick and geometrically thin, but level populations of highly-ionized heavy elements are far from their LTE values. In the present paper, as requested, we focus on supernova remnants (SNRs) interacting with the ambient matter. Actually, this is a good example to consider above non-equilibria. We begin with radiative transfer for level populations in Section 2, discuss ionization states in Section 3, and mention distribution functions of electrons in Section 4.

2. Radiation Transfer

Radiation transfer of a line with frequency ν in the direction $\mathbf{\Omega}$ (unit vector) is written as

$$\mathbf{\Omega}\nabla\Delta I_\nu = \frac{dI_\nu}{dx} = -\kappa\phi_\nu I_\nu + j\phi_\nu \tag{1}$$

where I_ν is the intensity, κ and j are the opacity and volume emissivity, respectively, and ϕ_ν is the line profile with $\int \phi_\nu d\nu = 1$. For formulation in more details, see Masai and Ishida (2004). With n_1 and n_2 being the ion densities in the ground state and excited state, respectively, the balance of transitions between the two-levels of the ion is written as

$$\frac{n_2}{n_1} = \frac{n_e C_{12} + B_{12}cU_\nu}{n_e C_{21} + A_{21} + B_{21}cU_\nu}, \tag{2}$$

where n_e is the electron density, $A_{nn'}$ and $B_{nn'}$ are the Einstein coefficients, $C_{nn'}$ the collisional excitation/de-excitation rate coefficients, and U_ν is the energy density of the radiation field.

The transfer problem becomes simple in the two extreme cases: optically thick and thin, or LTE and coronal regimes (see also Masai, 1994a). In LTE, $n_e \gg A_{21}/C_{nn'}$ for the density and $\kappa\phi_\nu x \gg 1$ for the optical thickness. Then, with g_n being the statistical weight, the level populations are given by the Boltzmann distribution

$$\frac{n_2}{n_1} \simeq \frac{C_{12}}{C_{21}} = \frac{B_{12}cU_\nu}{A_{21} + B_{21}cU_\nu} = \frac{g_2}{g_1}e^{-h\nu/kT}. \tag{3}$$

This means nothing but detailed balancing in LTE. The density to establish LTE scales as Z^7 for the H-like resonance line (Masai and Ishida, 2004) and is of order of $10^{18}\,\mathrm{cm}^{-3}$ for iron (Masai, 1994a).

In the opposite, $n_e \ll A_{21}/C_{nn'}$ for the density and $\kappa\phi_\nu x \ll 1$ for the optical thickness, we have the coronal distribution

$$\frac{n_2}{n_1} \simeq \frac{n_e C_{12}}{n_e C_{21} + A_{21}} \simeq \frac{n_e C_{12}}{A_{21}} \quad (\ll 1). \tag{4}$$

Since $j = (1/4\pi)h\nu n_2 A_{21}$, the intensity is obtained as

$$I_\nu(x) \simeq I_\nu(0) + j\phi_\nu x \simeq I_\nu(0) + \frac{1}{4\pi} h\nu n_e n_1 C_{12}\phi_\nu x. \tag{5}$$

This is a well known result for optically thin emission from a tenuous plasma. Accordingly, non-E1 transitions with small A_{21} like forbidden line can be as intense as E1 transitions. The optically thin and coronal limit is the case for hot gas of SNRs.

3. Ionization State

When an ionization state is maintained by the thermal pool of electrons, the kinetic energy must be comparable to the ionization energy. Therefore, if we represent the ionization degree by T_z in units of temperature, T_z should be close to the electron temperature T_e. Figure 1 shows the relation of T_z and T_e with the ionization state. Deviation from equilibrium ionization, ionizing or recombining, is not simply the issue of the ion abundances, but significantly affects the emission processes in the plasma. The right panels of Figure 1 show the contribution of each emission process to iron Kα line on the T_z–T_e diagram, where we calculate $n = 1$–2 transitions of all the ionic states, including satellite lines due to innershell ionization/excitation and dielectronic recombination (see also Masai, 1994b). One can see that the dominant emission process depends strongly on the relation between T_z and T_e.

When a plasma is in collisional ionization equilibrium ($T_z \sim T_e$), the ionization rate balances with the recombination rate, as $n_e S \sim n_e \alpha$. Here $S(T_e) = \langle\sigma_{\mathrm{ion}} v_e\rangle = \int \sigma_{\mathrm{ion}} v_e f(v_e) dv_e$ and $\alpha(T_e) = \langle\sigma_{\mathrm{rec}} v_e\rangle$ are the collisional rate coefficients of ionization and recombination, respectively, for the cross sections σ_{ion} and σ_{rec} and the electron distribution function $f(v_e)$ with $\int f(v_e) dv_e = 1$. For the hot gas in galaxy clusters, $T_z \sim T_e$ is attained because time of order of 10 Gyr ($\sim H_0^{-1}$, Hubble time) goes by since clusters are formed and virialized.

Otherwise, if the ionization state is maintained by photons, the degree of ionization is higher than expected for the thermal pool of electrons on account of photoionization: the ionization balance is written as $\beta + n_e S \sim n_e \alpha$ and then $S < \alpha$, where β is the photoionization rate. Accordingly, the ionization temperature must be higher than the electron temperature as $T_z > T_e$ for photoionized

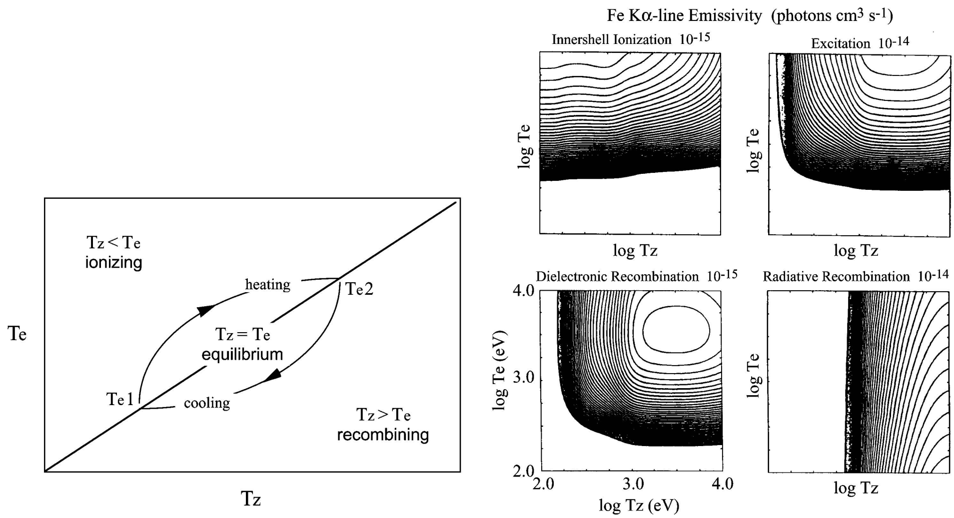

Figure 1. Left panel: Schematic diagram to show the regimes of ionizing ($T_z < T_e$) and recombining ($T_z > T_e$). The diagonal line ($T_z = T_e$) represents equilibrium ionization. When a plasma is heated from T_e1 to T_e2 slowly enough to establish ionization equilibrium at local T_e, the plasma traces the diagonal line. When a plasma is heated/cooled rapidly compared to the time scale of ionization/recombination, the plasma deviates from the equilibrium line into the ionizing/recombining regimes. Photoionized gas is naturally in the recombining regime on account of $T_z > T_e$. Right panels: Emissivity of iron Kα lines including satellites is expressed by contours on the T_z–T_e diagram for each emission process. The number attached to each process represents the maximum level of the contours. Fluorescence lines following innershell ionization and cascade lines following radiative recombination dominate in the ionizing ($T_z < T_e$) and recombining ($T_z > T_e$) regimes, respectively, while lines following excitation and dielectronic recombination are dominant in equilibrium, i.e. around the diagonal line ($T_z = T_e$).

plasmas. Note that for $T_z > T_e$ the plasma is recombining ($S < \alpha$) in view of atomic collisions for radiation processes, though the ionization balance holds in cooperation with photoionization.

Figure 2 shows a spectrum of X-ray photoionized gas, where $\xi = L/nR^2$ is the ionization parameter for photoionization with n and R being the gas density and the distance from the source of the luminosity L, respectively (Tarter et al., 1969). In a photoionized recombining plasma, radiative recombination plays a key role for level populations. Capture of electrons into excited levels is enhanced because of $T_z > T_e$ (see Nakayama and Masai, 2001), and followed by line emissions through cascades to the lower levels, while recombination radiation during the capture produces a narrow continuum. A typical example of photoionized/recombining plasmas is the accretion gas onto a neutron star or black hole. The gas is irradiated by UV/X-ray photons from the central compact object or the inner accretion disk.

Now we consider transient ionization states after rapid heating or cooling (see Figure 1). Since collision time of electrons with each other is much shorter than that with ions, T_z does not follow T_e but is left behind; cooling in this case must

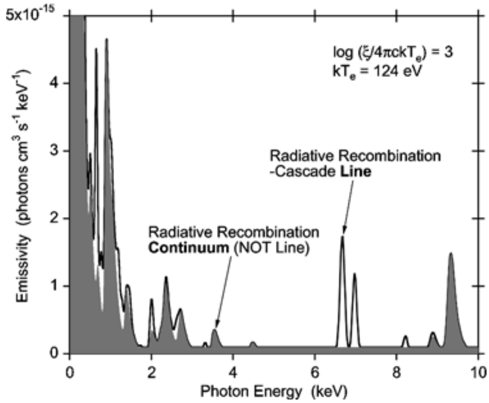

Figure 2. Radiation spectrum of a photoionized recombining plasma. The hatched area represents continuum emission which is dominated almost by recombination radiation. Since a photon of energy $I_{Z,z,n} + (1/2)m_e v_e^2$ is emitted in recombination, where $I_{Z,z,n}$ is the ionization potential and $(1/2)m_e v_e^2$ is the kinetic energy of the free electron being captured, the narrow recombination continua in the spectrum tell that $T_e \sim (m_e/3k)\langle v_e^2 \rangle$ is quite low compared to T_z, i.e. ionization degree.

be a process other than radiation due to atomic collisions, of which time scale is comparable with the recombination time scale. The rate equation of ionization-recombination is written in the form

$$\frac{d\boldsymbol{n}}{d(n_e t)} = F\boldsymbol{n}, \tag{6}$$

where matrix F is the ionization operator and vector $\boldsymbol{n}$ represents the ionization state, i.e. fractional ion abundances with $\sum n_z = 1$. For the solution, see Masai (1984, 1994b). Here we focus on the time scale for ionization to be equilibrium. In SNR plasmas, the population of excited states is negligibly small compared to that of the ground state (Eq. (4)), and therefore one has only to consider transitions from/to the ground states for the collisional ionization process. Then, without Auger transitions, the ionization matrix is tri-diagonal.

Equation (6) has an equilibrium solution given by det $F = 0$, and F has a zero eigenvalue and Z negative eigenvalues. The time scale t_{eqI} for equilibrium ionization is given by the harmonic mean of the negative eigenvalues or approximately of the diagonal elements. Thus, t_{eqI} has no systematic dependence either on the elements, ionic state, or the electron temperature, but is of order given by

$$n_e t_{\mathrm{eqI}} \sim \sum_z (S_z + \alpha_z)^{-1} \sim 10^{12}\,\mathrm{cm}^{-3}\,\mathrm{s}. \tag{7}$$

For discussion in more details, see Masai (1994b). For SNRs, i.e., for densities of order of $1\,\mathrm{cm}^{-3}$ of the interstellar medium, this time scale is 10^4 yr or longer and comparable to the age during which the SNR evolution is nearly adiabatic.

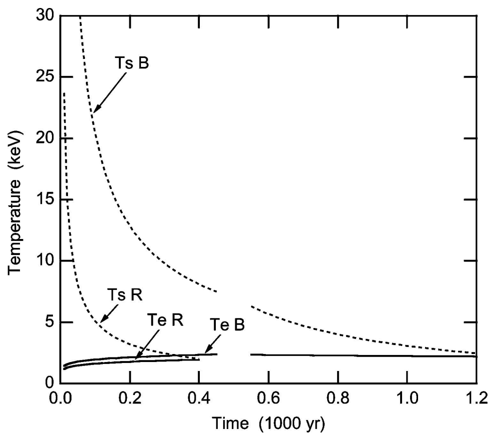

Figure 3. Time evolutions of the shock temperature T_s and electron temperature T_e for SN explosion into uniform ISM of density $1\,\mathrm{cm}^{-3}$ with the kinetic energy 0.5×10^{51} erg of explosion. The letters 'B' and 'R' attached represent the outward shock (blast wave) and reverse shock, respectively.

Time for energy equipartition between ions and electrons is $\sim 10^4$ yr comparable to t_{eqI}, and F varies with time as a function of T_e through S_z and α_z. However, through Coulomb collisions with ions in the post shock region, the temperature of electrons becomes $\sim$ keV in the age of interest, and does not vary very much through the adiabatic phase, i.e. free-expansion phase and following Sedov/Taylor phase, as shown in Figure 3. In the Sedov/Taylor phase, while the shock temperature varies as $T_s \propto t^{-6/5}$, well known as the Sedov solution, the electron temperature varies as $T_e \propto t^{-2/25}$ (Masai, 1994b). Therefore, assuming F to be constant with time can be a valid approximation for SNRs.

SNR plasmas are ionizing almost through the adiabatic phase of evolution, during which SNRs are bright at X-ray wavelengths. In the equilibrium case, line emission dominates at temperatures below 2 keV, while bremsstrahlung dominates above 2 keV. In ionizing plasmas, emission lines of heavy elements becomes prominent compared to equilibrium plasmas on account of impact excitation by relatively high-energy electrons ($T_e > T_z$). This is true of young SNRs or supernova (SN) explosion in the interstellar medium (ISM). However, when SN explosion occurs in its progenitor's stellar wind remnant, the SN ejecta collide with the circumstellar matter (CSM). This may be the case for a massive progenitor that emits a considerable amount of stellar wind before explosion.

When the blast wave breaks out of the dense CSM into rarefied ISM, the plasma that is once shocked undergoes rapid cooling by adiabatic expansion and turns to be strongly recombining (Itoh and Masai, 1989). The overall intensity of the radiation drops rapidly by orders of magnitude and the spectrum becomes dominated by radiative recombination into excited levels that is followed by cascade lines. The spectrum of such a strongly cooled recombining plasma is similar to those of photoionized recombining plasmas, shown in Figure 2.

Possible emission of K-line and/or recombination edge has been reported for the afterglow of some γ-ray bursts. Thermal lines like those in SNR spectra seem unlikely, because, if electron-impact excitation were responsible for the line emission, bremsstrahlung would dominate over the synchrotron emission which is commonly observed in the afterglow. Nevertheless, if the γ-ray bursts are related with explosion of massive stars, e.g. Wolf–Rayet stars, the interaction of the ejecta with the ambient matter may be understood on the analogy of SNRs.

If the relativistic blast wave breaks out of the dense CSM or ejecta envelope which does not obey the uniform expansion law $v \propto r$, rapid rarefaction would occur to produce a recombining plasma. Then, iron K-line and/or recombination edge are prominent, yet bremsstrahlung is strongly suppressed (see Figure 2; Yonetoku et al., 2001). Photoionization, e.g. by X-ray flash, could be another possible mechanism to produce a recombining plasma responsible for the reported iron spectra, though, in this case, fluorescence K-lines would also be expected prior to the recombination K-line.

4. Distribution Function

In the above sections, we consider that the electron distribution function is Maxwellian and the electron temperature is well defined. However, this may not be always true of the rarefied hot interstellar medium. The energy distribution function of particles $f(\boldsymbol{r}, \boldsymbol{p}, t)$ in the phase space follows the Boltzmann equation. When its collision term is given by a probability density function of Markov processes, the equation can be expressed approximately by the Fokker–Planck equation.

Assuming that $\nabla_r f = 0$ and $f(\boldsymbol{p})d^3\boldsymbol{p} \propto p^2 f(p)dp$, we have the Fokker–Planck equation

$$\frac{\partial f}{\partial t} = \frac{1}{\tilde{p}^2}\frac{\partial}{\partial \tilde{p}}\left[A(\tilde{p})\sqrt{p}\frac{\partial f}{\partial \tilde{p}} + B(\tilde{p})\tilde{p}^2 f\right], \tag{8}$$

i.e., continuity equation in the momentum space. Here $\tilde{p} \equiv p/\sqrt{2mkT_b}$ for the temperature T_b of background particles, and the coefficients

$$A(\tilde{p}) \sim \frac{1}{2}\frac{\langle \Delta\tilde{p} \cdot \Delta\tilde{p}\rangle}{\Delta t} \quad \text{and} \quad B(\tilde{p}) \sim \frac{\langle \Delta\tilde{p}\rangle}{\Delta t} \tag{9}$$

represent the diffusive and advective effects, respectively, and depend on the interaction between particles. In an equilibrium or without acceleration, there is no net flux and $f(\tilde{p})$ should be Maxwellian.

When some acceleration works on electrons, the distribution function is being altered from the Maxwellian. Since the Coulomb collision frequency $\propto E^{-3/2}$, electrons that get large momenta can stay in the acceleration process without significant collisions with the bulk thermal electrons. Such collisionless electrons are being accelerated more and more to form a power-law, while a fraction of accelerated electrons undergoes collisions to form a quasi-thermal component between thermal (Maxwellian) and nonthermal (power-law) components.

Since the energies of quasi-thermal electrons are high compared to T_z, i.e. ionization degree of the bulk ions, the plasma becomes partially ionizing through the interaction. A fraction of ions are ionized further by quasi-thermal electrons and capture *slow* electrons of the bulk thermal component, i.e. $T_z > T_e (= T_b)$ for such ions, and thereby the plasma becomes partially recombining. Consequently, the plasma exhibits a complex radiation spectrum, reflecting partially ionizing/recombining as well as equilibrium at the bulk temperature. Masai et al. (2002) calculate spectra of radiation by non-Maxwellian electrons to explain the Galactic ridge X-ray emission, taking interaction of the quasi-thermal electrons with the bulk ions into account.

References

Itoh, H. and Masai, K.: 1989, *MNRAS* **236**, 885.
Masai, K.: 1984, *Ap&SS* **106**, 391.
Masai, K.: 1994a, *JQSRT* **51**, 221.
Masai, K.: 1994b, *ApJ* **437**, 770.
Masai, K., Dogiel, V.A., Inoue, H., Schönfelder, V. and Strong, A.W.: 2002, *ApJ* **581**, 1071.
Masai, K. and Ishida, M.: 2004, *ApJ* **607**, 76.
Nakayama, M. and Masai, K.: 2001, *A&A* **375**, 328.
Tarter, C.B., Tucker, W.H. and Salpeter, E.E.: 1969, *ApJ* **156**, 943.
Yonetoku, D., Murakami, T., Masai, K., Yoshida, A., Kawai, N. and Namiki, M.: 2001, *ApJ* **557**, L23.

PRELIMINARY RESULTS FROM AN ASTROPHYSICALLY RELEVANT RADIATION TRANSFER EXPERIMENT

PAUL A. KEITER, GEORGE A. KYRALA, ROBERT G. WATT, GEORGE C. IDZOREK, ROBERT R. PETERSON, BLAKE WOOD, PETER ADAMS, ROBERT E. CHRIEN, DARRELL PETERSON and MERRI WOOD-SCHULTZ

Los Alamos National Laboratory, Los Alamos, New Mexico;
E-mail: pkeiter@lanl.gov

(Received 30 April 2004; accepted 7 July 2004)

Abstract. The results of a diffusive radiation transport experiment in a simple geometry are presented. The experiment depends primarily on two variables, the target density and the temperature drive, which are characterized well. The experiment is designed to verify and validate radiation transport in codes. The codes can then be used to model astrophysical systems. The results of the experiments are found to be in good agreement with simulation results.

Keywords: diffusive, radiation transport, astrophysical scaling

Introduction

Radiation transport is an important process in many different systems. The density and the temperature of the medium determine how radiation is absorbed and emitted. If the radiation mean free path (MFP) is much less than the system scale length then the material is optically thick and the radiation is absorbed and re-emitted many times during passage through the system. If the radiation MFP is larger than the system, then the system is optically thin and only a fraction of the radiation is absorbed and re-emitted during passage through the system. Both of these regimes can be encountered in astrophysical systems and in high energy density physics (HEDP) experiments. Through scaling relations, data from HEDP and astrophysical systems can be compared using analytic methods (Hammer and Rosen, 2003) and radiation transport codes. By using the results of HEDP experiments to verify and validate radiation transport in these codes, we hope to advance our understanding of radiation transfer in astrophysical systems.

Astrophysical systems in which radiation transport plays a major role include stellar atmospheres, supernova and young hot stars interacting with the local interstellar medium (ISM) or molecular clouds (Marsh, 1970). Models and simulations of SN 1987A, for example, indicate that a burst of ionizing UV radiation accompanied the shock breakout (Raga, 1987; Ensman and Burrows, 1992). The radiation generated ionization fronts, which expanded into the ISM around SN 1987A.

Astrophysics and Space Science **298:** 163–170, 2005.

Eventually the supersonic ionization front slowed down until the shock wave caught up with it.

The same general phenomena can be studied in the laboratory. Laboratory radiation transport experiments used either gas (Bozier et al., 1986; Grun et al., 1998; Koenig et al., 2001; Fleury et al., 2002; Reighard et al., 2004) or low-density foams (Massen et al., 1994; Hoarty et al., 1999; Back et al., 2000a,b; Keiter et al., 2002) as the propagation medium. We concentrate on the low-density foam work since it is more directly comparable to the experiment presented here. Many of these experiments have drawbacks that complicate the understanding of the results. In most of the low-density foam work, target characterization is not explicitly addressed in the papers. It is important to characterize the spatial uniformity of the foam because it can affect the spatial structure of the radiation and shock fronts. The experiment presented here employs static radiography of the targets and these measurements show a non-uniform density profile for the targets (Keiter and Kyrala, 2004).

Many previous experiments used either an X-ray converter foil or a laser driven hohlraum to produce a source of X-rays that drives the shocks. Radiation from X-ray converter foils typically cannot be treated as blackbody radiation. Furthermore, foils often produce high energy M-band radiation (Kania et al., 1992). At late times, the stagnation pressure of the gold in a laser-driven hohlraum can provide an additional impulse to the experiment and affect the results. The Z-pinch (Z) at Sandia National Laboratories, used for this experiment, produces a nearly-Planckian, large-area radiation source over a long period of time. The temperature drive of the vacuum hohlraum has been well characterized in previous work (Cuneo et al., 2001).

The main goal of the experiment presented here is to develop a radiation transport test bed that has a reduced set of parameter dependency and is well characterized to validate diffusive radiation transport in codes. The experiment depends primarily on two variables: the target density and the temperature drive. Both of these variables are measured and quantified to compare the results of the experiment to the results of LASNEX (Zimmerman et al., 1975) code simulations. The mean free path of the radiation is very small compared to the dimensions of the target in both the unshocked foam ($\sim$30 μm) and the shocked foam ($\sim$200 μm), which implies diffusive radiation transport.

Experimental Setup

The experimental set-up is shown in Figure 1. The experiment is performed in a very simple geometry – a cylindrical target with no high-Z material walls. The targets, typically 7 mm in diameter and 3–4 mm long SiO_2 aerogel foam, are mounted to the side of the hohlraum. The X-rays are generated in the middle of the hohlraum from the collapse of a tungsten wire array on axis and these X-rays heat the hohlraum. This provides the X-ray source to drive the radiation and shock front in the targets.

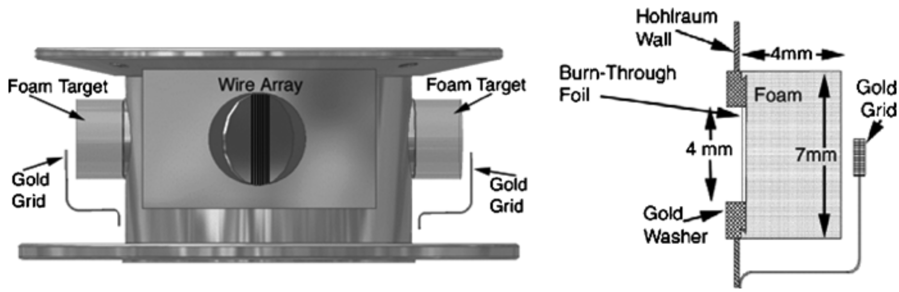

Figure 1. A side-view of the experimental set-up. The foam targets are mounted to a primary hohlraum. A cross-sectional side view of the target mounted to the hohlraum. X-rays are generated to the left and propagate towards the right, through the 4 mm aperture in the gold washer and irradiate the foam target.

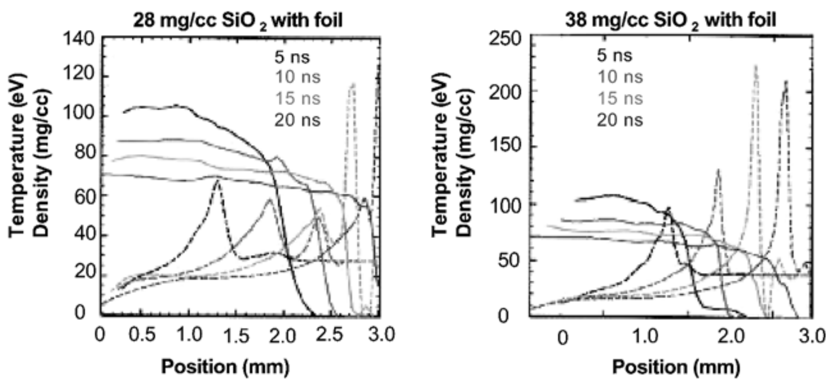

Figure 2. Simulated density (dashed) and temperature (solid) profiles at 5 ns (far left), 10 ns, 15 ns and 20 ns (far right) after the peak of the pinch radiation for a 28 mg/cc and a 38 mg/cc density foam target.

Initially the radiation flow is supersonic (simulation results shown in Figure 2), however later in time, the flow becomes subsonic.

A cross-sectional side-view of the target is shown in Figure 1. The foam targets are mounted to a gold washer with a 4 mm inner diameter (ID) and a 7 mm outer diameter (OD). The washer is mounted to the hohlraum. A 19.2-μm thick plastic (CH) burn-through foil mounted between the target and the washer aperture. This foil limits the amount of target preheat from the low energy component of the radiation temperature drive.

The primary diagnostics for the experiment are two sets of filtered silicon diodes and X-ray radiography. One set of silicon diodes observes the radiation breakout temperature from the target at an angle (typically 30 degrees with respect to the normal) to ensure the diagnostic is not looking into the center of the pinch. The other set observes the hohlraum temperature through a hole in the hohlraum. An X-ray framing camera also observes along the same line-of-sight and measures the hole size over time. Assuming a Planckian radiation source, a brightness temperature is calculated from the measured flux after correcting for aperture closure (Chrien et al., 1999). An X-ray diode is used to observe the pinch directly and provides the timing for the peak of the pinch. For a detailed description of all the diagnostics available for Z, refer to Nash et al. (2001).

X-ray radiography provides a single snapshot of the hydrodynamics in the experiment. The X-rays are generated when a focused beam from the Z-beamlet laser strikes a Fe foil. For this experiment, the laser has a pulse length of 600 ps, a spot size of 60–70 μm and between 600 and 700 J of energy. This creates 6.7 keV He-α Fe X-rays, which pass through the target and are recorded on film. Assuming an average shock velocity of 2×10^7 cm/s, there will be roughly 120 μm of motional blur, which is the limiting factor to the resolution.

Simulation Results

LASNEX simulations for two different target densities are shown in Figure 2. In each of the figures, the solid line represents the temperature profile and the dashed line represents the density profile. Simulated profiles of each are shown at 5, 10, 15 and 20 ns after the peak of the pinch radiation. In the low density, 28 mg/cc, case at 5 ns, the radiation front is ahead of the shock front by roughly 1 mm. This is a clear indication of the supersonic propagation of the radiation front. At 10 ns, the radiation front is still ahead of the original shock (at 2 mm) but the radiation has caused another shock to form at the position of the radiation front. By 20 ns, the radiation front is only barely ahead of the shock front.

For the high-density case (38 mg/cc), the radiation front is ahead of the shock front, indicating it is propagating supersonically. However, by 10 ns, the radiation and shock fronts are co-propagating. At 15 ns and 20 ns, the radiation front is lagging behind the shock front, indicating the radiation is traveling subsonically compared to the shock front.

Experimental Results

In these experiments, there is little ($<5\%$) variation measured in the peak hohlraum temperature drive from shot to shot (Figure 3). The time history of the radiation temperature drive is very repeatable from shot to shot as well. The temperature drive consists of a long (60 ns) 20–50 eV foot, which is not depicted because it is below the instruments sensitivity level, followed by a sharp rise (5 ns) to $\sim$130 eV and then a gradual decrease over many tens of ns. Therefore, varying the target density will vary the shock velocity and the radiation wave velocity. This allows us to control whether the radiation front is subsonic or supersonic in the shocked medium.

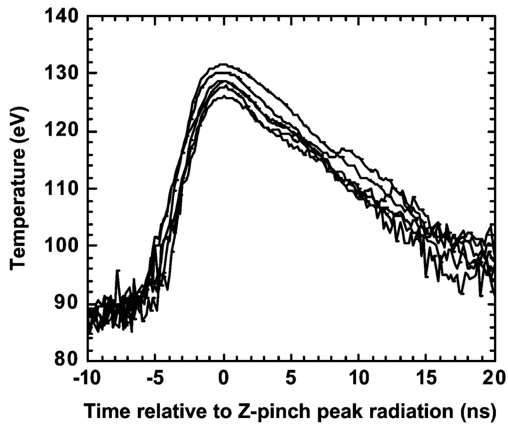

Figure 3. A comparison of the shot-to-shot reproducibility of the Z-pinch hohlraum temperature drive. The comparison includes a group of 2 shots taken 2 months before the other 4 shots. The peaks of the temperature profiles agree to within 5%. The low energy foot is not shown in this figure as the temperature is below the threshold for the instrument.

Figure 4a shows a radiograph for a 31 mg/cc density foam taken 10.7 ns after the peak of the pinch radiation. The shock has traveled a distance of roughly 2.4 mm, implying an average shock velocity of 2.24×10^7 cm/s. The instantaneous velocity is likely lower than this value, but is not measured in these experiments. The shock front has an approximate thickness of about 200 μm. A horizontal lineout down the approximate center of the target is shown in Figure 3b. The shock compresses the foam by a factor of 2 from the unshocked value. The density value decays in the shocked material due to the rarefaction.

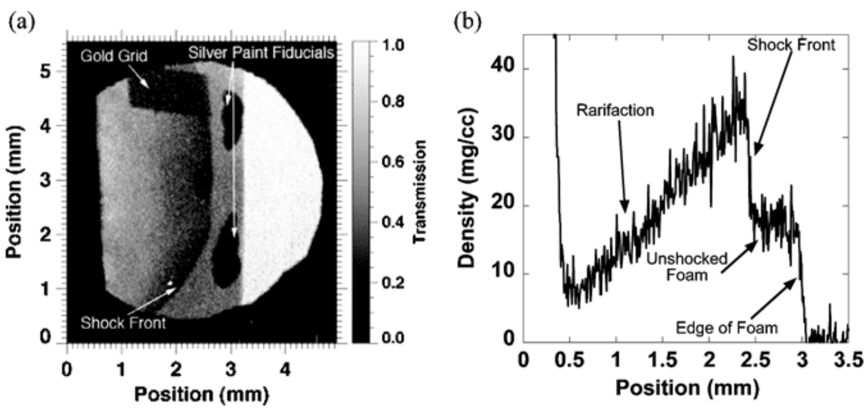

Figure 4. (a) An X-ray radiograph of a 31 mg/cc density aerogel target taken 10.7 ns after the peak of the pinch radiation. Spatial fiducials on the target have been labeled. Although the radiation initially irradiates a 4 mm diameter area of the foam, the shock is only flat over about a 2.5 mm section. (b) A horizontal lineout through the center of the radiograph. Labeled on the lineout are the edge of the foam target, the region of unshocked foam and the position of the shock front.

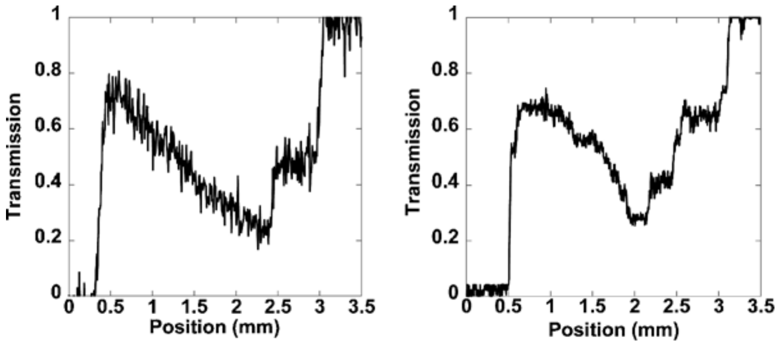

Figure 5. A comparison of the experimentally determined transmission (left) and the transmission calculated by LASNEX (right). The simulation results agree well with the experiment.

Figure 5 compares the experimentally determined transmission of the foam and the post-processed results of a LASNEX simulation. The simulation matches the experimental results well over the first 2 mm of the target. The simulation shows two regions ahead of the shock based on transmission values, whereas the experiment only has a single value of transmission ahead of the shock. This difference may result from the use of a uniform density profile used in the LASNEX simulations when the actual density profile is non-uniform. Density non-uniformities may spread out the shock front while opacity non-uniformities may spread out the radiation front. The experimental resolution of $\sim$100 μm may wash out some features in the radiograph as well.

Supersonic radiation propagation is observed at early times with a 28 mg/cc density target. The target designed for this shot was referred to as a wedge target because the rear surface of the target is sloped. The target has a length of 3.375 mm

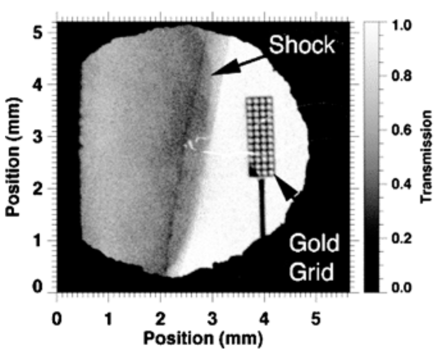

(a)

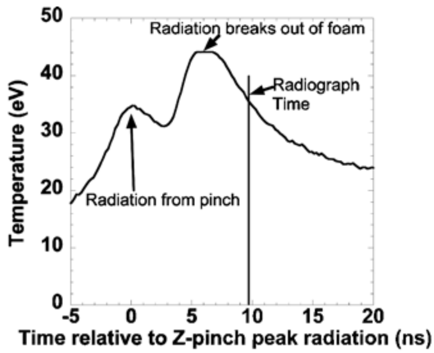

(b)

Figure 6. (a) A radiograph of the target taken 9.7 ns after the peak of the pinch radiation showing the shock still in the foam target. (b) Silicon diode data showing breakout at about 7 ns after the peak pinch.

on the long side and 1.675 mm on the short side. Figure 6a shows the experimental radiograph taken at a time of 9.7 ns after the peak of the pinch radiations. The shock front has traveled roughly 2.4 mm in the foam. Figure 6b shows the time history of the radiation. There are two peaks in the radiation time history. The first peak denotes the peak pinch time whereas the second peak denotes when the radiation is breaking out of the target. This occurs roughly 6 ns after the peak pinch and 3.7 ns before the time of the radiograph in which the shock is observed to be in the foam target. This implies the radiation front is moving faster than the shock front, and is supersonic.

Conclusion

Preliminary experimental results from a radiation transport experiment have been presented. The experiment is designed to minimize the parameter dependency. In this experiment, the target density, which is well characterized before the experiment and the hohlraum temperature, which is characterized during the experiment, affect the experiment the most. LASNEX simulation results agree with the measured on-axis shock position and the transmission profile for the experiment. The slight difference between the experiment and LASNEX may be due to the non-uniform density profile and opacity non-uniformities that are present in the experiment but not present in the simulations. Simulations are underway using a measured density profile.

Acknowledgements

We would like to thank Scott Evans, Bernie Carpenter, Peter Walsh, Tim Pierce, John Poco, the LLNL target fab team, the LANL target fab team, the Sandia Z-machine personnel for their contributions in making these experiments possible. This work was performed under the auspices of the NNSA/DOE by the Los Alamos National Laboratory under contract W-7405-ENG-336.

References

Back, C.A., et al.: 2000a, *Phys. Plasmas* **7**, 2126.
Back, C.A., et al.: 2000b, *Phys. Rev. Lett.* **84**, 274.
Bozier, J.C., Thiel, G., Le Breton, J.P., Azra, S., Decroisette, M. and Schirmann, D.: 1986, *Phys. Rev. Lett.* **57**, 1304.
Chrien, R.E., et al.: 1999, *Rev. Sci. Instrum.* **70**.
Cuneo, M., et al.: 2001, *Phys. Plasma* **8**, 2257.
Ensman, L. and Burrows, A.: 1992, *The Astrophysical Journal* **393**, 742.
Fluery, X., et al.: 2002, *Laser and Particle Beams* **20**, 263.
Grun, J., et al.: 1998, *J. Appl. Phys.* **83**, 2420.

Hammer, J.H. and Rosen, M.D.: 2003, *Phys. Plasmas* **10**, 1829.
Hoarty, D., Willi, O., Barringer, L., Vickers, C., Watt, R. and Nazarov, W.: 1999, *Phys. Plasmas* **6**, 2171.
Hoarty, D., Iwase, A., Meyer, C., Edwards, J. and Willi, O.: 1997, *Phys. Rev. Lett*. **78**, 3322.
Kania, D., et al.: 1992, *Phys. Rev. A* **46**, 7853.
Keiter, P.A., et al.: 2002, *Phys. Rev. Lett.* **89**, 165003.
Keiter, P.A. and Kyrala, G.A.: 2004, *Rev. Sci. Instrum.* **75**, 4057.
Koenig, M., et al.: 2001, *Shock Compression of Condensed Matter* 1367.
Marsh, M.C.: 1970, *Mon. Not. R. Astr. Soc.* **147**, 95.
Massen, J., et al.: 1994, *Phys. Rev. E* **50**, 5130.
Nash, et al.: 2001, *Rev. Sci. Instrum.* **72**, 1167.
Raga, A.C.: 1987, *AJ* **94**, 1578.
Reighard, A.: 2004, private communication.
Sigel, et al.: 1990, *Phys. Rev. Lett.* **65**, 587.
Zimmerman, G.B. and Kruer, W.L.: 1975, *Comments on Plasma Physics and Controlled Fusion* **2**, 51.

X-RAY LINE TRANSFER IN PLASMAS WITH LARGE VELOCITY GRADIENTS

F.M. KERR[1], A. GOUVEIA[1], R.W. LEE[3], P.K. PATEL[3], O. RENNER[2], S.J. ROSE[1], H.A. SCOTT[3] and J.S. WARK[1]

[1]*Department of Physics, Clarendon Laboratory, University of Oxford, Parks Road, Oxford OX1 3PU, UK; E-mail: fraser.kerr@physics.ox.ac.uk*

[2]*Institute of Physics, Czech Academy of Sciences, 18211 Prague, Czech Republic*

[3]*Lawrence Livermore National Laboratories, Livermore, CA 94550, USA*

(Received 30 April 2004; accepted 1 June 2004)

Abstract. An astrophysically relevant experiment is compared to the output of a multidimensional radiation transfer code in which populations and radiation are self-consistently treated. Experimental Al Ly α spectra obtained with a very high-resolution spectrometer are presented as quantitative evidence of dot plasma non-planar expansion. Analysis of these spectra using the code is performed, in particular examining the effects of velocity gradients in directions other than that of the primary expansion. These calculations are found to be in good agreement with the experimental results. Usage of the Ly α doublet as a planarity diagnostic is discussed.

Keywords: plasmas, radiation transport, high-power lasers

1. Introduction

In order to assess the validity of modelling distant astrophysical phenomena via the application of complex radiation transfer computer codes, astrophysically relevant laboratory experiments must be undertaken to provide 'up close' and externally controllable comparisons to this theoretical output. A common facet of an astrophysical plasma, and hence a key area for any code to correctly treat, is the propagation of optically thick line radiation through large velocity gradients internal to the plasma. Previous work by us in this area has used an escape factor methodology in both cylindrical (Patel et al., 1997a,b) and planar (Chambers et al., 2001) geometries. In this paper we move away from such a probabilistic approach, and examine the application of a full linearisation treatment to a specific experimental example.

Over the past 20 years dot target experiments have been used extensively as a tool to investigate laser-produced plasmas, and many examples may be found in the literature (Chambers et al., 2001; Herbst and Grun, 1981; Herbst et al., 1982; Gauthier et al., 1983; Burkhalter et al., 1983). In these experiments, small, thin dots are embedded into, or placed on top of, a lower Z material. A powerful laser is then co-axially focused with the dot centre, with the laser spot diameter

Astrophysics and Space Science **298:** 171–176, 2005.

being much larger than the dot size. Use of a dot target has the advantages that (Herbst et al., 1982): the effects of source broadening are minimised allowing for better spectral resolution; and, through the combination of a relatively large laser spot size, small target, and a confining boundary plasma, the expansion of the dot can be taken to a first approximation as slab one-dimensional (1-D).

In this paper we seek to experimentally question and quantify this assumed planarity of dot plasma expansion, thus simultaneously putting error bars on theoretical analysis undertaken assuming a purely 1-D solution, and testing the ability of a computer code to correctly treat line radiation propagating through a complex region of multidirectionally interacting velocity gradients. In particular, we examine the transverse Ly α spectrum emitted during an Al dot target experiment, recorded using a very high-resolution spectrometer (Renner et al., 1997). We choose Ly α because, while it is theoretically complicated to analyse due to its doublet structure, the complexity leaves it very rich in features, and combining this with its strength we note that it is particularly useful as a diagnostic. These experimental spectra are then compared to theoretical predictions, achieved by artificially applying transverse velocity gradients to MED103 (Christiansen et al., 1974; Djaoui and Rose, 1992) hydrodynamic simulations of the plasma, using a state of the art radiative transfer code CRETIN (Scott, 2001).

2. Theory

We treat a non-planar dot plasma, where velocity gradients exist in directions both parallel and perpendicular to the primary expansion. As we experimentally observe the plasma in a side on geometry, it is the perpendicular gradients which are of key spectroscopic interest, and it is their magnitude that will give the measure of non 1-D expansion.

If the velocity of the primary expansion at a given distance from the target surface is v, then we take the maximal lateral velocity $u_{\max} = x \times v$, where x is a parameterisation of the non-planarity, and is altered to provide agreement with experiment. Hence if the lateral positional coordinate is r, then we assume:

$$u(r) = \frac{u_{\max}}{r_{\max}} r. \tag{1}$$

This linear dependence follows other self-similar solution strategies, e.g. (Pert, 1980). Consequently, the Doppler effect causes the complete redistribution (CRD) equivalent emission and absorption line profiles $\psi(\nu)$ to become spatially variant in a direction perpendicular to the primary expansion:

$$\psi(\nu) \to \psi\left(\nu - \frac{u(r)}{c}\nu_0\right). \tag{2}$$

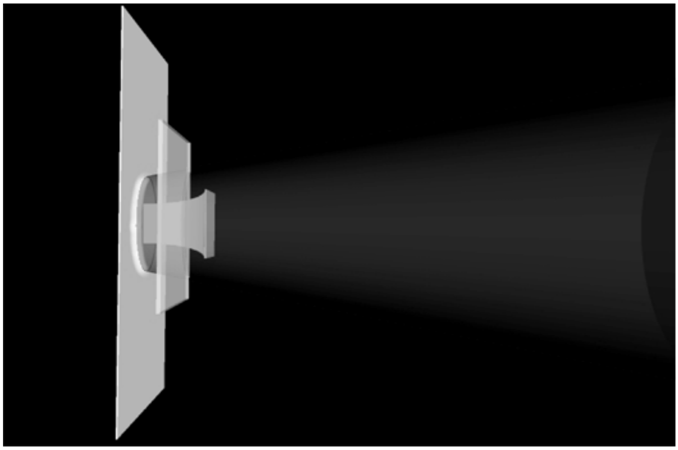

Figure 1. Visualisation of the plasma expansion including non-planar effects. The thin cuboidal region shows the spatial integration region of the spectrometer.

The spectroscopic output hence becomes dependent on, and thus a diagnostic of, the effects of non-planar plasma expansion (Irons, 1975). Figure 1 schematically shows an interpretation of the plasma expansion, including retroaxial and lateral velocity gradients.

We use CRETIN to solve the radiation transfer problem (Mihalas, 1978) for this case. This code utilises a refinement of the Accelerated Lambda Iteration technique (Scott, 2001; Scott and Mayle, 1994) to provide fast and robust convergence. Through the full linearisation procedure overlapping and interacting lines are fully accounted for, along with the continuum; that is, the values for the radiation field and population distribution throughout the plasma are entirely self-consistent.

In addition to the lateral velocities there is a further multidimensional effect, which comes about as a direct response to the source function self-consistency. Radiation into the surrounding vacuum causes a decrease in the upper level populations of the Ly α lines, as we move normally from the axis of primary expansion to the edges of the plasma. This directly leads to a decrease of plasma emissivity η towards the edges, and, since the source function S is given by η/χ (the opacity χ being almost constant), a falling source function. Any strong, optically thick, line propagating through a region where the source function is falling will undergo self-reabsorption – it is the non-symmetric position of the centre of this reabsorption which gives the diagnosis of non-planarity.

3. Experimental Work and Results

The experiment was undertaken on the Janus laser at Lawrence Livermore National Laboratories (LLNL), combining a dot target with the highly sensitive Vertical

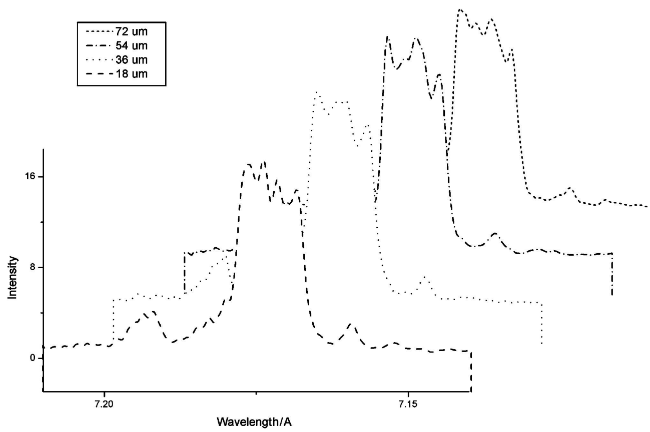

Figure 2. Experimental spectra taken between 18 and 72 μm from the initial target surface. The data has been smoothed using a 2-point FFT algorithm.

Johann Spectrometer (VJS) (Renner et al., 1997). The experimental setup was as that in Figure 1; the spatial resolution of the VJS was approximately 10 μm. Experimental data from this spectrometer is shown in Figure 2. Data at distances of 20–70 μm from the initial target surface of a single shot is presented. The target in this case was a 200 μm square Al dot with an original thickness of 0.75 μm; 65.6 J of laser energy at 532 nm was delivered to a 500 μm diameter spot in 1.5 ns, leading to a maximum intensity on target of $\sim 3 \times 10^{13}$ W cm^{-2}. The theoretical effects on the Ly α lines, of applying increasing magnitudes of transverse velocity gradients across the plasma are shown in Figure 3. Simulations of the spectra relate

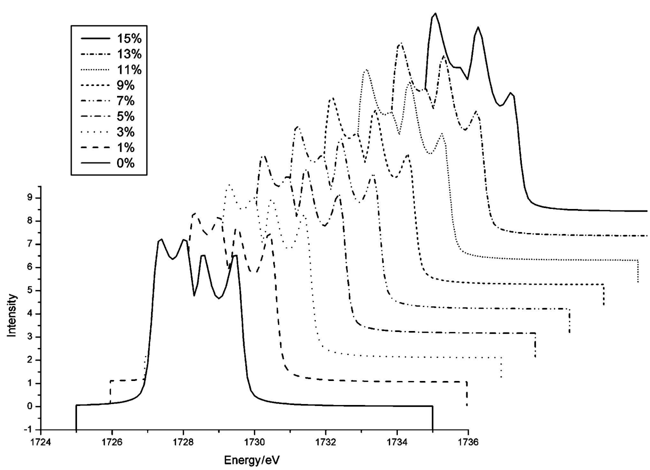

Figure 3. Theoretical spectra showing alterations caused by variation of the maximal lateral velocity, as a percentage of the forward velocities.

to regions of plasma modelled to be similar to a point 50−60 μm from the target surface in the Janus experiment i.e. constrained hydrodynamically to have the same linewidth at this point.

With no velocity gradient applied, we see as expected a doublet, both peaks of which are self-reversed. The unexpected strength of the theoretically weaker $2p_{1/2}-1s_{1/2}$ is due to a complicated collection of effects, and will be fully explained in a later paper. As the lateral velocity gradient steepens, the spectral region of maximal reabsorption shifts to higher energy, causing the red sides of the reabsorbed features to become stronger. Comparison between the theoretical and experimental data is complicated by both the VJS instrumental function, and the data smoothing process, both of which cause slight suppression of the tops of the spectral features in the experimental data. However, by examination of the 54 μm experimental spectrum and comparison with theory, we can assess that the dot plasma is expanding with a lateral velocity gradient whose maximum is somewhere between 7 and 13% of the velocity in the direction of the primary expansion. To our knowledge this is the first time a measurement such as this has been performed.

4. Conclusion

We have shown that high-resolution spectroscopy of one of the strongest lines in the spectrum can yield interesting information about the quality of one-dimensionality present in laser-produced plasma dot target experiments. Furthermore, we have quantified this effect in a given experiment by comparison with a sophisticated radiation transport code, and found the agreement between experiment and theory to be good. We propose future work in this area as examining the differences between a full linearisation treatment and probabilistic escape factor methods as applied to multidimensional laser plasma analysis. We will also be seeking to show that further information regarding plasma diagnosis may be obtained from experiments such as these.

Acknowledgements

FMK acknowledges support from both the EPSRC and AWE, Aldermaston. SJR is grateful to AWE for the award of a William Penney Fellowship. The experimental work in Livermore was fully funded by the US DoE, under contract No. W-7405-ENG-48.

References

Burkhalter, P.G., Herbst, M.J., Duston, D., Gardner, J., Emery, M., Whitlock, R.R., Grun, J., Apruzese, J.P. and Davis, J.: 1983, *Phys. Fluids* **26**(12), 3650.

Chambers, D.M., Glenzer, S.H., Hawreliak, J., Wolfrum, E., Gouveia, A., Lee, R.W., Marjoribanks, R.S., Renner, O., Sondhauss, P., Topping, S., Young, P.E., Pinto, P.A. and Wark, J.S.: 2001, *J. Quant. Spectrosc. Radiat. Transfer* **71**(2–6), 237.

Christiansen, J.P., Ashby, D.E.T.F. and Roberts, K.V.: 1974, *Comput. Phys. Commun.* **7**(5), 271.

Djaoui, A. and Rose, S.J.: 1992, *J. Phys. B: At. Mol. Opt. Phys.* **25**(11), 2745.

Gauthier, J.C., Geindre, J.P., Najmabadi, K., Popovics, C., Poquerusse, A. and Weinfeld, M.: 1983, *J. Phys. D: Appl. Phys.* **16**(10), 1929.

Herbst, M.J., Burkhalter, P.G., Grun, J., Whitlock, R.R. and Fink, M.: 1982, *Rev. Sci. Inst.* **53**(9), 1418.

Herbst, M.J. and Grun, J.: 1981, *Phys. Fluids* **24**(10), 1917.

Irons, F.E.: 1975, *J. Phys. B: At. Mol. Phys.* **8**(18), 3044.

Mihalas, D.: 1975, *Stellar Atmospheres* (2nd edn.), Freeman, San Francisco.

Patel, P.K., Wark, J.S., Heading, D.J., Djaoui, A., Rose, S.J., Renner, O. and Hauer, A.: 1997a, *J. Quant. Spectrosc. Radiat. Transfer* **57**(5), 683.

Patel, P.K., Wark, J.S., Renner, O., Djaoui, A., Rose, S.J., Heading, D.J. and Hauer, A.: 1997b, *J. Quant. Spectrosc. Radiat. Transfer* **58**(4–6), 835.

Pert, G.J.: 1980, *J. Fluid Mech.* **100**(Pt. 2), 257.

Renner, O., Missalla, T., Sondhauss, P., Krousky, E., Forster, E., Chenais-Popovics, C. and Rancu, O.: 1997, *Rev. Sci. Inst.* **68**(6), 2393.

Scott, H.A.: 2001, *J. Quant. Spectrosc. Radiat. Transfer* **71**(2–6), 689.

Scott, H.A. and Mayle, R.W.: 1994, *Appl. Phys. B: Las. Opt.* **B58**(1), 35.

EAGLE NEBULA PILLARS: FROM MODELS TO OBSERVATIONS

MARC W. POUND[1], JAVE O. KANE[2], BRUCE A. REMINGTON[2], DMITRI D. RYUTOV[2], AKIRA MIZUTA[3] and HIDEAKI TAKABE[3]

[1]*Astronomy Department, University of Maryland, College Park, MD, USA; E-mail: mpound@umd.edu*

[2]*Lawrence Livermore National Laboratory, University of California, Livermore, CA, USA*

[3]*Institute of Laser Engineering, Osaka University, Osaka, Japan*

(Received 29 April 2004; accepted 24 May 2004)

Abstract. Over the past few years, our group has been developing hydrodynamic models to simulate formation of the Eagle Nebula pillars. The true test of any model is, of course, how well it can reproduce the observations. Here, we discuss how we go about testing our models against observations. We describe the process by which we "observe" the model data to create synthetic maps. We show an example of this technique using one of our model runs and compare the resultant synthetic map to the real one.

Keywords: Eagle Nebula, radio astronomy, hydrodynamic models, aperture synthesis

1. Introduction

The pillars of the Eagle Nebula are the most spectacular example of a phenomenon that is commonly seen wherever molecular clouds are situated near O stars. Proposed formation mechanisms for such pillars generally fall into two broad categories: (i) instabilities at the boundary between the cloud and the ionized region, which grow with time (e.g., Spitzer, 1954; Frieman, 1954; Williams, 1999; Williams et al., 2001) and (ii) pre-existing density enhancements (i.e., clumps) that locally retard the ionization front creating "cometary globules" (Reipurth, 1983; Bertoldi and McKee, 1990).

We have developed a comprehensive 2-D hydrodynamic model of pillar formation (see Mizuta et al. in this volume) that includes energy deposition and release due to the absorption of UV radiation, recombination of hydrogen, radiative molecular cooling, and magnetostatic pressure (Ryutov et al., 2002); and geometry/initial conditions based on Eagle observations. An example model result is shown in Figure la.

The CO (J = 1–0) observations taken with the Berkeley-Illinois-Maryland interferometer are those of Pound (1998), with the addition of more recent higher spatial resolution data. The map consists of a mosaic of seven fields, each with a Gaussian field of view with 100″ FWHM (see Figure 1b).

To facilitate comparison between model and observations, we can create "synthetic observations" from the model by filtering it through the known telescope

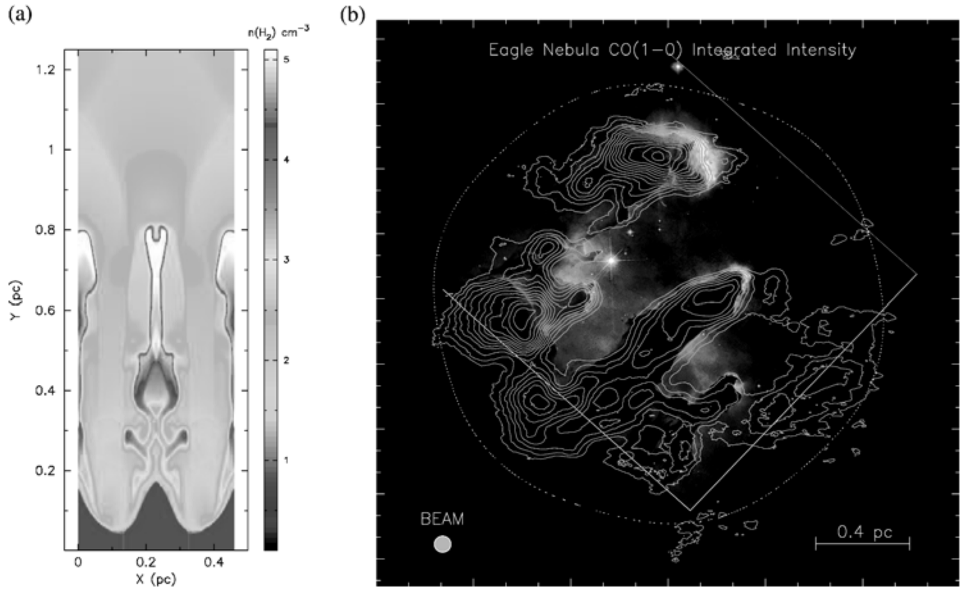

Figure 1. (a) Example model result showing pillar growth after 400,000 years; color intensity represents molecular hydrogen number density $n(H_2)$ in cm^{-3} in logarithmic units. (b) Contours of CO ($J = 1$–0) integrated intensity as measured with BIMA overlaid on the Hubble Space Telescope image.

response function and processing the resultant data *using identical methods as for the observations* to produce maps.

2. Synthetic Observations

The steps to create synthetic observations are

1. Orient the model properly on the sky. This consists of both a rotation in the plane of the sky, θ, and an inclination, i. For the Eagle, we know $\theta = 39^\circ$ and an educated guess for Pillar II is $i = 10^\circ$. We also place the model at the correct distance of 1900 pc.
2. Taper the model brightness according to the field-of-view response function and the mosaic pattern.
3. Sample with actual UV coverage of observations to create Fourier domain visibilities.
4. Add noise due to receivers and atmosphere. Note that this is done in the Fourier domain.
5. Grid the visibilities and Fast Fourier Transform back to image domain.
6. Deconvolve the image with "dirty" beam (Airy pattern). This is the well-known CLEAN algorithm (Högbom, 1974).

7. Reconvolve CLEAN components with "clean" Gaussian beam, add back in residuals.

Note there is no radiative transfer included in this technique. We assume the integrated brightness is proportional to the mass in each pixel. As a first approximation, this is correct because a well-established relationship between CO ($J = 1$–0) integrated intensity and total molecular hydrogen mass exists (e.g., Bloemen et al., 1984).

3. Results

We can see from Figure 2 that the denser regions of the model, with $n(H_2) \sim 10^3\ cm^{-3}$, are recovered by interferometer. This density is about the critical density for excitation of the CO ($J = 1$–0) line, indicating that the synthetic observations can indeed be compared to the actual observations. By comparing the central synthetic pillar to Eagle Pillar II we see that the basic morphology – a dense head with a less dense tail—is reproduced. Furthermore, the synthetic velocity gradient (not shown) $V_y \sin(i) \sim 3\ km\,s^{-1}\,pc^{-1}$ is comparable to that measured in Pillar II ($2.2\ km\,s^{-1}\,pc^{-1}$). However, it is apparent that the synthetic pillar is not large enough by about a factor of 2. Thus, much of the detail in the synthetic pillar is smoothed out due to the spatial resolution of the telescope.

To compare the substructure in the synthetic pillar, we can "cheat" by putting the model twice as close ($d = 950$ pc) before creating the synthetic observations. The resulting map is shown in Figure 3. The similarity between the central synthetic

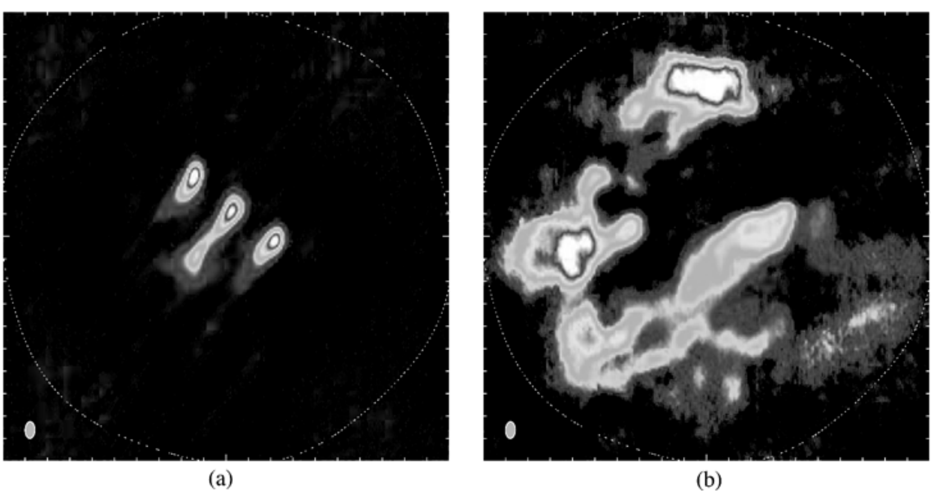

Figure 2. (a) The synthetic integrated intensity map derived from processing the model in Figure 1. Color represents CO ($J = 1$–0) integrated intensity. (b) The actual integrated intensity map from BIMA. Color represents CO ($J = 1$–0) integrated intensity.

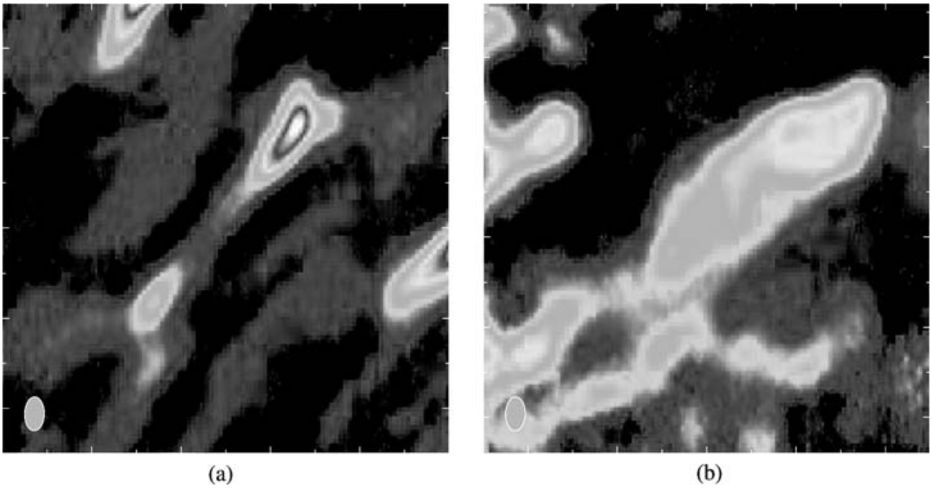

Figure 3. (a) The synthetic integrated intensity map after placing the model twice as close. Here we show only the central pillar. (b) As in Figure 2(b), the integrated intensity map, showing a close-up of Eagle Pillar II.

pillar and Eagle Pillar II is intriguing – in both, the dense head tapers off then bifurcates at the tail.

4. Conclusions

Our model can adequately represent much of the real input astrophysics of the Eagle and the basic physical properties its pillars reproduced. We have a good technique for creating realistic synthetic observations from model data. This technique is equally applicable to full 3-D models, which will allow us to compare velocity fields in addition to morphology. We also have "cometary" models ready to be subjected to the same technique. We can use synthetic observations to identify the best models, which can in turn be used to design an appropriate laser experiment. Both the models and the synthetic observation technique are applicable to many astronomical objects; we have good data already for Eagle, Horsehead (Pound et al., 2003), and Pelican nebulae.

Acknowledgments

This work is supported by NASA Astrophysics Theory Program grant NRA-00-01-ATP-059.

References

Bertoldi, F. and McKee, C.F.: 1990, *A&J* **354**, 529.
Bloemen, J.B.G.M., Caraveo, P.A., Hermsen, W., Lebrun, F., Maddalena, R.J., Strong, A.W. and Thaddeus, P.: 1984, *A&A* **139**, 37.
Frieman, E.A.: 1954, *A&J* **120**, 18.
Högbom, J.A.: 1974, *A&A Suppl.* **15**, 417.
Pound, M.W.: 1998, *A&J* **493**, LI13.
Pound, M.W., Reipurth, B. and Bally, J.: 2003, *A&J* **125**, 2108.
Reipurth, B.: 1983, *A&A* **117**, 183.
Ryutov, D., Kane, J., Mizuta, A., Pound, M. and Remington, B.: 2002, APS Meeting Abstracts, 1004P.
Spitzer, L.: 1954, *A&J* **120**, 1.
Williams, R.J.R.: 1999, *MNRAS* **310**, 789.
Williams, R.J.R., Ward-Thompson, D. and Whitworth, A.P.: 2001, *MNRAS* **327**, 788.

TWO MODELS OF MAGNETIC SUPPORT FOR PHOTOEVAPORATED MOLECULAR CLOUDS

D.D. RYUTOV[1], J.O. KANE[1], A. MIZUTA[2], M.W. POUND[3] and B.A. REMINGTON[1]

[1]*Lawrence Livermore National Laboratory, Livermore, CA, USA;*
E-mail: ryutov1@llnl.gov
[2]*Institute of Laser Engineering, Osaka University, Osaka, Japan*
[3]*Astronomy Department, University of Maryland, College Park, MD, USA*

(Received 5 May 2004; accepted 28 June 2004)

Abstract. The thermal pressure inside molecular clouds is insufficient for maintaining the pressure balance at an ablation front at the cloud surface illuminated by nearby UV stars. Most probably, the required stiffness is provided by the magnetic pressure. After surveying existing models of this type, we concentrate on two of them: the model of a quasi-homogeneous magnetic field and the recently proposed model of a "magnetostatic turbulence". We discuss observational consequences of the two models, in particular, the structure and the strength of the magnetic field inside the cloud and in the ionized outflow. We comment on the possible role of reconnection events and their observational signatures. We mention laboratory experiments where the most significant features of the models can be tested.

Keywords: molecular clouds, photoevaporation, MHD turbulence, reconnection

1. Introduction

The complex shapes of photoevaporated molecular clouds (e.g., the Eagle Nebula and the Horsehead Nebula) are thought to be created by the ablation pressure of the ionized outflows (e.g., Spitzer, 1978). [The ablation is caused by the ionizing radiation of the nearby young stars.] The material inside the clouds is very cold, with the temperature of order of 10–30 K. So low a temperature is explained by that, at the temperature exceeding, roughly, 50 K, the radiation in molecular transitions (Neufeld et al., 2000) becomes so intense that the cooling time reaches a very small value $\sim$100 years, whereas the dynamical time of the typical molecular cloud exceeds 10^5 years. The ablation pressure drives compression waves into the cloud interior. However, the shock and compressional heating cannot compete with the cooling and the cloud interior stays at low temperatures, in the range 10–30 K.

We will make all the numerical estimates for the case of the Eagle Nebula, which is relatively well characterized compared to other similar objects (interesting data pertaining to the Horsehead Nebula can be found in Pound et al., 2003). The most important parameters are presented in Table I, compiled on the basis of Spitzer (1978); Hester et al. (1996); Pound, (1998); Levenson et al. (2000); see also a

TABLE I
Parameters of the Eagle Nebula

Parameter[a]	L (cm)	τ (s)	v' (s^{-1})	n_{H_2} (cm^{-3})	T_0 (K)	x
Numerical value	10^{18}	3×10^{12}	3×10^{-13}	5×10^{4}	30	10^{-8}

[a]Notation: L – characteristic spatial scale (the diameter of a pillar II, Pound, 1998); τ – characteristic temporal scale; v' characteristic velocity gradient, n_{H_2} – average density of the molecular hydrogen; T_0 initial cloud temperature, x – characteristic ionization degree.

TABLE II
Parameters of the ionized outflow

Parameter[a]	v_a (cm/s)	T_a (K)	n_a (cm^{-3})	P_a, CGS (Kelvins/cm^3)
Numerical value	3×10^{6}	10^{4}	10^{3}	1.6×10^{-8} (10^{8})

[a]v_a, T_a, n_a are the velocity, the temperature, and the electron density in the ablation outflow; p_a is the ablation pressure. The quantities related to the ablation outflow bear a subscript "a."

summary in Ryutov et al. (2004). The ionization degree of the cloud is $\sim 10^{-8}$ and is determined by the ionization by cosmic rays and photoemission from the dust grains (Elmegreen, 1998). [The cloud consists predominantly of the molecular hydrogen, with some admixture of molecules like CO and water, as well as dust particles, made of carbon and silicates, e.g., Spitzer, 1978].

Despite so low an ionization degree, the skin time for the cloud is much longer than the dynamical time (see Section 3). In other words, the line-tying of the magnetic field is a reasonable concept, at least at the level of the first rough models.

The amount of ionized gas evaporated from the surface per unit time is determined by the intensity of the ionizing continuum reaching the cloud surface. The resulting outflow has a temperature of order of 10^4 K and the density $\sim 10^3$ cm^{-3} (Hester et al., 1996; Pound, 1998; Levenson et al., 2000).

From Tables I and II, one sees that the ablation pressure is almost two orders of magnitude higher than the gaseous pressure inside the cloud. This means that the cloud should have collapsed to much higher densities than those actually observed. The emerging problem can be called the problem of "missing stiffness" (Ryutov et al., 2004). Here we discuss two possible models that may explain the paradox: the model of a quasi-uniform magnetic field, and the model of magnetostatic turbulence. The main focus of our paper is the identification of the observational consequences that may help in determining the validity of the models. We also briefly discuss possible laboratory experiments.

2. The Model of a Quasi-Homogeneous Magnetic Field

This model is based on the assumption that there is a large-scale primordial magnetic field permeating the cloud. In the past, this assumption was analyzed mainly in

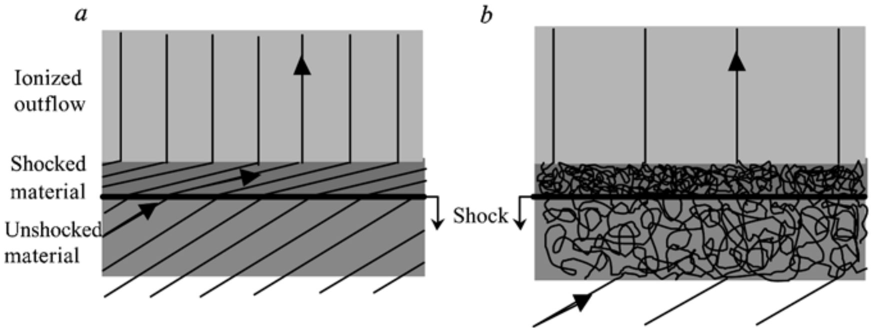

Figure 1. Two models of magnetic support for a slab model of the could illuminated from above: (a) A homogeneous magnetic field is initially tilted with respect to the cloud surface; when the ionizing radiation "turns on," an ablation outflow is formed; the tangential component is compressed in the shocked material; the lowest slab represents the unsocked material with initial magnetic fields. (b) A random small-scale magnetic fields. In this model, the net magnetif flux permeating the cloud is very small; the magnetic field in the ionized outflow is weak and does not have any dynamical significance. It may have a more complex structure than shown.

terms of its effect on the star formation (e.g., McKee et al., 1993, and references therein). We will consider the consequences of this assumption in terms of the effect of the magnetic field on the formation of the observed large-scale structures (the pillars). To make some preliminary estimates, we consider a slab model shown in Figure 1. In order to provide stiffness with respect to the compression by the ablation pressure, the initial magnetic field has to have a substantial component parallel to the surface. On the other hand, there is no reason to believe that the magnetic field would be perfectly aligned with the surface. So, we make a natural assumption that it initially intersects the cloud surface at an angle of order 1, i.e., that the normal and tangential components are initially comparable, $B_{n0} \sim B_{t0}$ (Figure 1a). When the ablation pressure "turns on," the tangential component of the magnetic field inside the cloud is compressed to some value B_t to provide the balance with the ablation pressure; in other words, the condition $B_t^2/8\pi \sim p_\mathrm{a}$ is reached. Here we neglect the contribution of the gaseous pressure, which is small (see Introduction). Assuming the density compression ratio to be $\sim$3 (compatible with the observations, Pound, 1998), one finds, using the value of p_a from Table II, that the initial tangential magnetic field, $B_{t0} \sim (1/3)B_t \sim (1/3)\sqrt{8\pi p_\mathrm{a}}$, should be $\sim$150 μG. For $B_{n0} \sim B_{t0}$, this mean that the total initial magnetic field, $B_0 = \sqrt{B_{n0}^2 + B_{t0}^2}$, should be $\sim$200 μG. Unfortunately, there are no direct measurements of the magnetic field for the Eagle Nebula. Judging from Crutcher's (1999) survey of the magnetic field measurements for analogous objects, this value is somewhat high, but not so high as to rule it out.

Consider now the magnetic field in the ionized outflow, just beyond the ionization front. The normal component of the magnetic field does not change when the gas passes through the ionization front and expands, i.e., $B_{n\mathrm{a}} \sim B_{n0}$ (as before, the

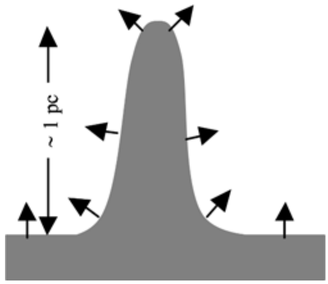

Figure 2. In the quasi-homogeneous model, the magnetic field just outside the cloud must be directed along the normal to the could surface.

subscript a designates the field in the ablation flow). Conversely, the tangential component varies in proportion to the density, $B_{t\text{a}} \sim (n_\text{a}/n_{\text{H}_2})B_{t0}$. Taking the densities from Tables I and II, one finds that the tangential component decreases by a factor of 50 compared to its initial value. Therefore, the magnetic field lines in the ionized outflow will be directed almost normally with respect to the surface of the ablation front. This conclusion, obviously, holds also in the case of a non-planar surface of the column. In other words, if the model of a quasi-homogeneous magnetic field is correct, it predicts that the magnetic field in the ablation outflow near the cloud surface must be essentially normal to the surface. This conclusion is illustrated by Figure 2.

As we have already mentioned, direct measurements of the magnetic field around the Eagle Nebula are not available. As an indirect indication of a possible presence of the perpendicular magnetic field one may consider the presence of fine non-uniformities in the outflow visible at high-resolution images: these non-uniformities are indeed almost perpendicular to the surface.

The $B_{n\text{a}}$ value in the case of the Eagle Nebula must be approximately 150 μG. The corresponding magnetic pressure is significantly less than the ablation pressure, so that the magnetic field does not have any significant dynamical effect on the outflow. The field lines down the stream are shaped according to the line-tying constraint, i.e., they are stretched along the streamlines.

The difficulty with the model of the quasi-uniform magnetic field is that such a field would favor development of 2D structures of the type of ridges, not the 3D column-like structures present in the Eagle Nebula (Figure 3). This is due to the anisotropic nature of the Maxwell stress tensor: The field lines of the magnetic field frozen into conducting medium would be pulled out together with the pillar material as shown in Figure 3b and create a strong tension that would force the column to fall back. Conversely, in the case of a ridge-like structure aligned with the direction of the magnetic field (Figure 3a) such a tension is absent.

This apparent contradiction can be solved by allowing for the magnetic reconnection. Indeed, if such a process near the base of the column occurs (Figure 4a and b), the overall returning force acting on the column significantly decreases.

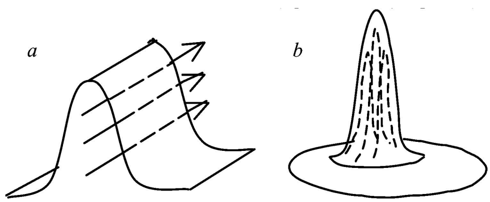

Figure 3. Formation of a ridge aligned with the magnetic field (panel a) does not cause generation of the returning force, whereas formation of a column (panel b) does. The normal component of the magnetic field is not shown, because it plays a relatively minor dynamical role.

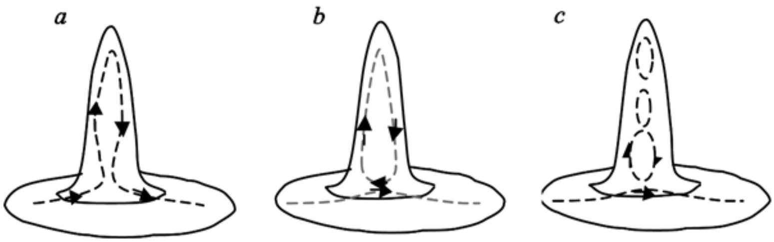

Figure 4. Reconnections near the base of the column may disconnect the field lines. In the lower and the upper parts of the column, thereby reducing the returining force; the force reduction is especially strong if multiple reconnections occur (c).

Reconnection events may occur several times in the course of the pillar growth, generating a structure shown in Figure 4c.

The reconnection time $\tau_{\rm rec}$ must be at least a few times less than the dynamical time τ. The magnetic flux annihilated in each reconnection event is of order of $L^2 B_{t0}$. The loop voltage that develops during the reconnection is $V_{\rm loop} \sim L^2 B_{t0}/c\tau_{\rm rec}$. Assuming that $\tau_{\rm rec} \sim 0.3\tau$, $B_{t0} \sim 150\,\mu$G and taking the other numbers from Table I, one finds that the loop voltage is very large, $\sim 5 \times 10^9$ CGS$\sim 1.5 \times 10^{12}$ V. In other words, reconnections may lead to generation of the cosmic rays. Evaluation of the relative significance of this source with respect to the other known sources of cosmic ray would require collecting the statistics of photoevaporated molecular clouds.

The electric field $E \sim V_{\rm loop}/L$ that develops during the reconnection is large enough to cause a breakdown of the molecular hydrogen. The possibility of gas breakdown in reconnection events was discussed in Birk et al. (2004), in conjunction with low-density diffuse clouds as a mechanism for sustaining the observed ionization degree of such clouds. We note that, because of the higher density of photoevaporated molecular clouds, the breakdown will be accompanied by intense X-ray radiation. The part beyond a few keV would be only weakly absorbed by the cloud material and could, in principle, be detected by the external observer. As is known, e.g., from observation of reconnections in the Solar atmosphere (Title, 2004), the reconnection often leads to formation of significant current concentrations of the type of filaments and knots. If our model is correct, the X-ray radiation will manifest such features.

3. The Model of Magnetostatic Turbulence

We now consider a model in which the magnetic field inside the cloud is random, with the r.m.s. value of this random field being much greater than the value of any possibly present quasi-homogeneous component, $(\langle B^2 \rangle)^{1/2} \gg |\langle B \rangle|$, Figure 1b, and the scale-length l of the random field being much less than the global scale L. In order to be relevant in the problem of "missing stiffness," the magnetic pressure of the random magnetic field has to be comparable to the ablation pressure and, therefore, much higher than the gaseous pressure (see Section 1). This causes a problem: the MHD turbulence driven by so strong a magnetic field is necessarily supersonic and, as shown in McLow et al. (1998), Stone et al. (1998), Ostriker et al. (2001) decays very rapidly, within one turn-over time of the eddies, l/v_{A}, with $v_{\mathrm{A}}^2 = \langle B^2 \rangle / 4\pi\rho$. In our problem, the strong radiative cooling of the gas keeps its sound speed at a deeply sub-Alfvenic level, thereby not allowing the turbulence to reach a weakly compressible state (where one might expect a transition to long-lasting turbulence). Therefore, the MHD turbulence would survive for only a very short time $\sim l/v_{\mathrm{A}} \ll \tau$ and wouldn't provide a lasting support for the cloud.

It was pointed out by Ryutov and Remington (2002), that this difficulty can be circumvented if one assumes that the tangled magnetic field is a *force-free field*, i.e., that the current is everywhere (almost) parallel to the magnetic field, $\mathbf{j} \parallel \mathbf{B}$. In such a case, the presence of a tangled magnetic field does not induce strong small-scale motions, in particular, does not generate shocks, and the tangled structure can exist for the times determined by resistive dissipation of the magnetic field (which time is very long). As the presence of a random "turbulent" magnetic field in this case is not associated with rapid turbulent motions of the gas, this state was called in Ryutov and Remington (2002) the state of "*magnetostatic turbulence*."

Although the magnetostatic turbulence is force-free at small spatial scales, it acts analogously to a gaseous pressure when the compression at a large-scale occurs. For an isotropic turbulence, it acts as a gas with the adiabatic index $\gamma = 4/3$ (Ryutov and Remington, 2002). The numerical analysis of such a system is presented in Mizuta et al., this issue.

In the magnetic field measurements, an integration over the line of sight is carried out; in addition, the finite spatial resolution causes a smearing over a finite area in the plane of the sky. In the case of small-scale random magnetic field, this causes a significant averaging-out. Therefore, if the model of magnetostatic turbulence works, the measured magnetic field strength should be substantially less than $\sim 200\,\mu\mathrm{G}$ required in the model of a quasi-homogeneous field. The weaker field seems to be in a better agreement with Crutcher (1999).

As the current sustaining magnetostatic turbulence flows predominantly along the magnetic field lines, the resistivity η responsible for the dissipation of this state is the parallel resistivity $\eta_{||}$. For the parameters given in Table I, this resistivity (we use CGS units) is certainly lower than (in CGS units) 10^{-6} s (the latter number corresponds to the improbable case where all the electrons are attached to the dust grains and the current in the rest-frame of the fluid is carried solely by the ions; there are all reasons to expect that the resistivity is much lower). Accordingly, the magnetic diffusivity $D_{\mathrm{m}} = c^2\eta_{||}/4\pi$ is lower than 10^{14}. Assuming that the scale l of the magnetic structures is 1/30 of L, one finds that the resistive dissipation time is many orders of magnitude longer than the dynamic time τ.

The magnetostatic turbulence may be dissipated by the reconnection process. However, the fact that the initial state is almost force-free may slow-down the reconnection rate. Additional "longevity" can appear in the turbulent state in which the parameter λ that enters the force-free equation $\nabla \times \boldsymbol{B} = \lambda \boldsymbol{B}$ varies in space slowly, $|\nabla\lambda| \ll \lambda^2$: in this case, the magnetic field is locally in the so-called Taylor state (Taylor, 1974), and reconnection is inhibited. The absolute value of λ is $\sim l^{-1}$.

Reconnection events will serve as sources of X-ray radiation, very much like in the case considered in Section 2. However, these events will now occur in the numerous vortices of the scale $l \ll L$. Therefore, one can expect that the external observer will see only diffuse radiation produced by simultaneously occurring small-scale reconnections distributed over the whole volume of the pillars and averaged due to the finite spatial resolution.

4. Discussion

Two models of magnetic support that we have discussed in this paper seem both to be compatible with the observed general structure of the Eagle Nebula. However, the predictions regarding the properties of the magnetic field are quite different and may, in principle, be used for discrimination between the models. The models differ also in the predictions related to the 1–10 keV-range X-ray radiation from the clouds: the model of a quasi-homogeneous field predicts the presence of a few bright knots and filaments, whereas the model of magnetostatic turbulence predicts the domination of the diffuse radiation.

Laboratory experiments may help to address key physics issues. In the case of a quasi-homogeneous field model, the most interesting issue is that of reconnections occurring during the pillar growth. The corresponding experiment can be performed in the general setting of the experiment described in Yamada et al. (2000). In the case of the model of the magnetostatic turbulence (which predicts that the gas with embedded random force-free magnetic field will behave as a polytropic gas with $\gamma = 4/3$), one can study the hydrodynamics of the ablation front in the setting of the high-energy-density laser experiment (Remington et al., 1993).

Acknowledgments

Work performed for the U.S. DoE by UC LLNL under contract W-7405-Eng-48 and partly supported by the NASA grant NRA-00-01-ATP-059.

References

Birk, G.T., Lesch, H. and Neukirch, T.: 2004, *A&SS* **289**, 359.

Crutcher, R.M.: 1999, *ApJ* **520**, 706.

Elmegreen, B.G.: 1998, in: C.E. Woodward, J.M. Shull and H.A. Thronson, Jr. (eds.), Astronomical Society of Pacifics Conference Series, "*Origins*," Proceedings of the International Conference held at Estes Park, Colorado, May 19–23 1997, v. 148, p. 150.

Hester, J.J., Scowen, P.A., Sankrit, R. et al.: 1996, *AJ* **111**, 2349.

Levenson, N., Graham, J.R., McLean, I.S., Becklin, E.E., Figer, D.F., Gilbert, A.M., Larkin, J.E., Teplitz, H.J. and Wilcox, M.K.: 2000, *ApJ* **533**, L53.

McKee, C.F., Zweibel, E.G., Goodman, A.A. and Heiles, C.: 1993, in: E.H. Levy and J.L. Lunine (eds.), *Protostars and Planets III*, University of Arizona Press, Tucson, p. 327.

Mac Low, M.-M., Klessen, R.S., Burkert, A. and Smith, M.D.: 1998, *Phys. Rev. Lett.* **80**, 2754.

Mizuta, A., Kane, J.O., Pound, M.W., Remington, B.A., Ryutov, D.D. and Takabe, H.: this issue.

Neufeld, D.A., Lepp, S. and Melnick, G.J.: 2000, *ApJS* **100**, 132.

Pound, M.W.: 1998, *ApJ* **493**, L113.

Pound, M.W., Reipurth, B. and Bally, J.: 2003, *AJ* **125**, 2108.

Remington, B.A., Weber, S.V., Haan, S.W., Kilkenny, J.D., Glendinning, S.G., Wallace, R.J., Goldstein, W.H., Wilson, B.G. and Nash, J.K.: 1993, *Phys. Fluids* **B5**, 2588.

Ryutov, D.D. and Remington, B.A.: 2002, *Plasma Phys. Contr. Fus*. **44**, B407.

Ryutov, D.D., Kane, J.O., Mizuta, A., et al.: 2004, Plasmas in the Laboratory and in the Universe, AIP Conference Proceedings, Vol. 703, Melville, NY, p. 415.

Spitzer, L.: 1978, *Physical Processes in the Interstellar Medium*, Wiley, New York.

Stone, J.M., Ostriker, E.C. and Gammie, C.F.: 1998, *ApJ* **508**, L99.

Ostriker, E.C., Stone, J.M. and Gammie, C.F.: 2001, *ApJ* **546**, 980.

Taylor, J.B.: 1974, *Phys. Rev. Lett.* **33**, 1139.

Title, A., 2004, Plasmas in the Laboratory and in the Universe, AIP Conference Proceedings, Vol. 703, Melville, NY, p. 163.

Yamada, M., Ji, H., Hsu, S., Carter, T., Kulsrud, R. and Trintchouk, F.: 2000, *Phys. Plasmas* **7**, 1781.

SHOCK PROPAGATION THROUGH MULTIPHASE MEDIA*

R.J.R. WILLIAMS and D.L. YOUNGS
AWE plc, Aldermaston, RG7 4PR, UK; E-mail: robin.williams@awe.co.uk

(Received 30 April 2004; accepted 17 June 2004)

Abstract. This paper presents two and three dimensional simulations of the interaction of shocks with media with large numbers of dense inclusions. An approximate model of the interaction of a starburst wind with the surrounding galactic ISM illustrates issues which must be addressed in global models of ISM dynamics. As a step towards developing the sub-grid model of multiphase turbulence, we define and study a form of 'multiphase Riemann problem'. This allows us to develop macroscopic characteristics of the flows which may be compared to such subgrid models.

Keywords: hydrodynamics, shock waves, ISM: clouds

1. Introduction

Multiphase flows are widespread in astrophysics. In particular, the interstellar medium has components close to pressure equilibrium,which are at a wide range of temperatures. These multiple phases were shown to result from the form of the cooling curve for interstellar gas in the influential early work of Field et al. (1969). McKee and Ostriker (1977) treated the stochastic input of energy by supernovae in a statistical fashion, developing a multiphase model which included not just molecular and atomic components, but a hot diffuse medium. It is important to study the dynamics of such multiphase flows to understand in detail both how the structure of the interstellar medium is maintained, and the manner in which it controls the process of star formation (e.g. Klein, 2005; van Breugel, 2005).

There have been numerous studies of both microphysics and global dynamics. Continuum multiphase models for the dynamic response of the medium have been developed (e.g. Shu et al., 1972; Scalo and Struck-Marcell, 1984; Pistinner and Shaviv 1993). In many circumstances the condensed phase may be treated simply as a source of distributed mass loading into the flow (Hartquist et al., 1986). Work on the local dynamics has generally concentrated on the properties of shock interactions with individual spherical cores (Woodward, 1976; Nittman et al., 1982; Klein et al., 1994). This work has always been strongly related to experimental work on aerodynamic shattering of droplets in shock tubes (Ranger and Nicholls, 1969; Haas and Sturtevant, 1987) and more recently driven by lasers (Robey et al., 2002; Klein et al., 2003); on both these platforms, experiments are starting to address circumstances in which multiple ablating cores can interact (e.g. Poludnenko et al. 2004).

It is often not possible to resolve fine scale structures in global simulations, for example around starburst nuclei. However, the observed properties of the flows may be dominated by components with small filling fractions. It is now becoming possible to directly study the development of meso-scale regions, with substantial numbers of dense included clouds (Jun et al., 1996; Steffen et al., 1997; Poludnenko et al., 2002). Here, we present results for a simplified two-dimensional model of a starburst galaxy core, which illustrates the importance of multiphase effects in the flow dynamics. We then present a more generic model which we are using to calibrate multiphase turbulence models which may then be applied to the global dynamics of multiphase astrophysical flows and experimental analogues.

2. Multiphase Effects Around Starburst Nuclei

To illustrate the influence of multiphase flows in astrophysics flow, we have calculated a simple model of the flows around a starburst nucleus, based on the parameters used by Strickland and Stevens (2000) in their study of M82. These calculation were of perfect gas flows in 2D slab symmetry, made using the two-dimensional AMR code aqualung (Williams, 2000). While the simplified physics means that the results are not fully realistic, it is nevertheless possible to study the general effects of the dispersed phase by comparing the results for clumpy flows with simulations including only the diffuse phase and where the mean density of clump material is spread smoothly through the loaded region.

We assume that the starburst injects material uniformly in a region of radius 150 pc. For M82, the supernova rate is roughly 0.1 SN yr^{-1} in the central 150 pc, so we take the mass injection rate to be $2 \times 10^{-6}\,\mathrm{m_H\,cm^{-3}\,yr^{-1}}$, and the energy injection rate to be $6 \times 10^{16}\,\mathrm{erg\,g^{-1}}$ times greater. Following Strickland and Stevens, we take the smooth ISM to be the superposition of two phases, one with an initial density in the midplane of $20\,\mathrm{cm^{-3}}$ and sound speed of $30\,\mathrm{km\,s^{-1}}$ and the other with a midplane density of $2 \times 10^{-3}\,\mathrm{cm^{-3}}$ and sound speed of $300\,\mathrm{km\,s^{-1}}$. Each phase satisfies the hydrostatic support equation $dP/dz = -\rho g$, as does the resulting mixed phase when densities and pressures are added. We use a plane parallel form for the gravitational acceleration, $g = 3.3 \times 10^{-8} \tanh(z/500\,\mathrm{pc})\,\mathrm{cm\,s^{-2}}$, corresponding to a surface density of $350\,M_\odot\,pc^{-2}$.

In the clumped simulations, we replace the warm phase gas with dense clouds with 100 times the local warm phase density but with the same pressure, at positions distributed randomly within a region $|z| < 500\,\mathrm{pc}$. We have chosen the cloud radius to be 10 pc so that the hydrodynamics of the cloud interaction can be resolved. The filling factor of the clouds is 3×10^{-2}, a high value which is required so that a reasonable number of clouds can be included in these 2D simulations. Together, these assumptions imply a clump temperature of around 600 K and a mass of $2 \times 10^5 M_\odot$

for ‘spherized’ clumps in the midplane. For comparison, individual cloud masses in the ISM are $\sim 400\, M_\odot$; while the properties we assume were made necessary by computational requirements, they might be taken as more characteristic of cloud complexes (note that these parameters mean that they are close to the Jeans limit).

In Figure 1, we show the results of these simulations 2×10^6 yr after the burst has started. It is clear that when the cloud material is distributed uniformly, the

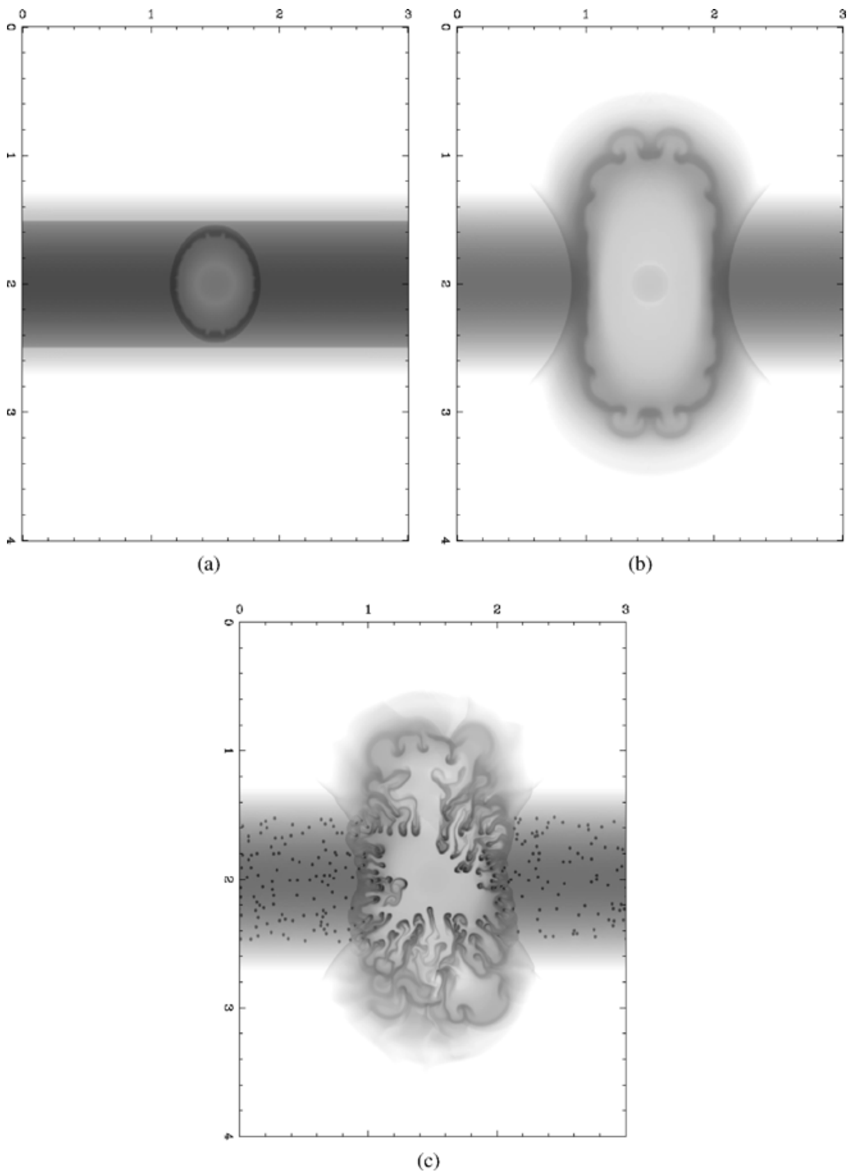

Figure 1. Simulation results for multiphase model of a starburst nucleus. (a) Smoothed dense phase; (b) No dense phase; (c) Explicit multiphase.

bubble driven by the starburst wind is far smaller than for the structured medium. The shocked region is at a considerably higher pressure than the other models, as the forward shock is propagating into a denser medium. When the density of the clumped gas is neglected the results appear more like the clumpy case. However, the wind from the central starburst is starting to become supersonic, and the bubble will soon develop a strong internal standoff shock, while the wind in the clumpy case remains subsonic. In the clumpy case, the gas escaping into the halo develops strong plumes, driven by transonic flow through nozzles between clumps, while retaining its multiphase structure at radii close to the central starburst, where both other cases have smooth flow. The turbulent flow driven by the clumps will remain important for more realistic cloud sizes; the effects of this turbulence would not be captured by simple models of mass loading.

3. A Multiphase Riemann Problem

We have seen that realistic scenarios for the interaction of shocks with clumpy media lead to complex interactions between the phases. Simulating these situations in exhaustive detail is often not feasible. Instead, one can attempt to include a model for turbulent multiphase structures at subgrid scales in a macro-scale continuum simulation. Various models of this nature have been discussed in the astrophysical literature, as well as in other fields such as the modeling of diesel engines. Often the model coefficients have been set by comparison with numerical and experimental data on the interaction of shocks with non-interacting clumps. It would be very difficult to extract systematic results from the heterogeneous conditions which occur in simulations related to specific global systems. Hence, in this section, we investigate the structures which result when a strong shock enters a uniformly seeded multiphase region, in effect a type of multiphase Riemann problem.

We will present full results in a forthcoming paper (Williams and Youngs, in preparation). Here, we show results for the flow when a Mach 10 shock is incident on a dispersion of clouds with a factor 100 overdensity. The two and three-dimensional runs both have a filling fraction of 0.057. The width of the simulation is 1 computational unit for the 2D run and 0.5 for 3D, while we take the adiabatic sound speed of the undisturbed diffuse gas to be unity. In Figure 2, we show the density field at time 0.35 units after the shock reaches the edge of the loaded region for 2D and 3D simulations (performed using Aqualung and TURMOIL3D (Youngs, 1994)), and the average velocity of the clump material and diffuse gas for the 2D case.

When averaged onto a line, the leading shock in 2D appears broadened due to surface fluctuations; this is less of an effect in 3D, perhaps because of the reduced long wavelength power in a random scatter in higher dimensions. The clump gas drags up to the same velocity fairly rapidly, with the structure reaching a

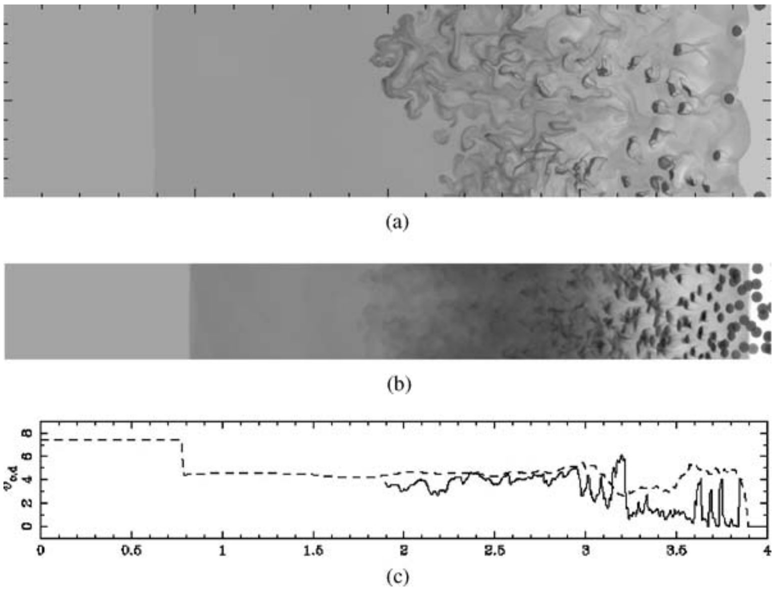

Figure 2. Multiphase Riemann problem solutions, the plots show log column density 0.35 time units after first shock contact for (a) 2D; (b) 3D, The grey scales are not the same, as otherwise it would be difficult to see the dense structures clearly in one or other case. (c) Velocity of the diffuse (dashed) and clump (solid) material (the steep rise at the right hand edge corresponds to a very small amount of material).

statistically steady form and the shock speeds tending to those given by the well-mixed Rankine–Hugoniot conditions. While mixing behind this structure is quite efficient (particularly so when seen in projection from the 3D run), significant density structure and turbulent motions remain, which could seed stable multiphase structure to re-form in a more physically detailed simulation. At the rear edge of the multiphase region, long-wavelength fluctuations appear which engulf diffuse material. The passage of the shock across this interface has led to a multiphase Richtmyer–Meshkov instability with amplitude seeded by the initial density field. In both cases, the reverse shock is almost perfectly plane.

4. Conclusion

Multiphase structures are widespread in astrophysics, and important in determining the evolution of structures on interstellar and galactic scales. Experimental and computational facilities are becoming available to study the detailed evolution of these flows, but it will be necessary to use modeling approaches to include multiphase effects in global simulations for the forseeable future.

References

Field, G.B., Goldsmith, D.W. and Habing, H.J.: 1969, *ApJ* **155**, L149.
Haas, J.-F. and Sturtevant, B.: 1987, *JFM* **181**, 41.
Hartquist, T.W., Dyson, J.E., Pettini, M. and Smith, L.J.: 1986, *MNRAS* **221**, 715.
Jun, B.-I., Jones, T.W. and Norman, M.L.: 1996, *ApJ* **468**, L59.
Klein, R.I., Budil, K.S., Perry, T.S. and Bach, D.R.: 2003, *ApJ* **583**, 245.
Klein, R.I., McKee, C.F. and Collela, P.: 1994, *ApJ* **420**, 213.
McKee, C.F. and Ostriker, J.P.: 1994, *ApJ* **218**, 148.
Nittman, J., Falle, S.A.E.G. and Gaskell, P.H.: 1982, *MNRAS* **201**, 833.
Pistinner, S. and Shaviv, G.: 1993, *ApJ* **414**, 612.
Poludnenko, A.Y., Dannenberg, K., Drake, R.P., Frank, A., Knauer, J., Meyerhofer, D.D., Furnish, M. and Asay, J.: 2004, *ApJ* **604**, 213.
Poludnenko, A.Y., Frank, A. and Blackman, E.G.: 2002, *ApJ* **576**, 832.
Ranger, A.A. and Nicholls, J.A.: 1969, *AIAA J.* **7**, 285.
Robey, H.F., Perry, T.S., Klein, R.I., Kane, J.O., Greenough, J.A. and Boehly, T.R.: 2002, *Phys. Rev. Lett.* **89**, 085001.
Scalo, J.M. and Struck-Marcell, C.: 1984, *ApJ* **276**, 60.
Steffen, W., Gómez, J.L., Raga, A.C. and Williams, R.J.R.: 1997, *ApJ* **491**, L73.
Shu, F.H., Milione, V., Gebel, W., Yuan, C., Goldsmith, D.W. and Roberts, W.W.: 1972, *ApJ* **173**, 557.
Strickland, D.K. and Stevens, I.R.: 2000, *MNRAS* **314**, 511.
Williams, R.J.R.: 2000, *MNRAS* **316**, 803.
Williams, R.J.R. and Dyson, J.E.: 2002, *MNRAS* **333**, 1.
Woodward, P.R.: 1976, *ApJ* **207**, 484.
Youngs, D.L.: 1994, *Laser Particle Beams* **12**, 725.

HYDRODYNAMIC INSTABILITY OF IONIZATION FRONT IN HII REGIONS: FROM LINEAR TO NONLINEAR EVOLUTION

AKIRA MIZUTA[1], HIDEAKI TAKABE[1], JAVE O. KANE[2],
BRUCE A. REMINGTON[2], DMITRI D. RYUTOV[2] and MARC W. POUND[3]

[1]*Institute of Laser Engineering, Osaka University, Osaka, Japan;*
E-mail: mizuta@yukawa.kyoto-u.ac.jp
[2]*Lawrence Livermore National Laboratory, CA*
[3]*Department of Astronomy, University of Maryland, MD*

(Received 30 April 2004; accepted 19 June 2004)

Abstract. We investigate hydrodynamic instabilities at an ionization front in a radiatively driven molecular cloud, using two-dimensional hydrodynamic simulations, including absorption of UV radiation from OB stars, recombination in HII gas, and radiative molecular cooling. We find a strong stabilization mechanism, if the initial perturbation is small, whereas column like structures can emerge, if the perturbation is large. Recombination plays a key role in the observed stabilization mechanism. When recombination is turned off in the simulations, the stabilization disappears, and the perturbation grows at a growth rate consistent with the classical Rayleigh–Taylor instability.

Keywords: HII region, molecular cloud, hydrodynamic instability, numerically

1. Introduction

Columns such as those in the Eagle Nebula, often referred to as elephant trunks (Hester et al., 1996; Pound, 1998), are a common occurrence in radiatively driven molecular clouds. The physical mechanism behind the formation of such columns or pillars is still under debate. There are two broad models widely discussed in the literature for their formation, namely, (1) growth from small initial perturbations, due to hydrodynamic instabilities versus (2) shadowing from pre-existencing dense localized clumps in the molecular cloud. Theoretically studies of ionization front instabilities have been done by Vandervoort (1962) (without recombination in the HII gas), and Axford (1964) (with recombination). Recently Williams (2002) has found an unstable mode with radiation at finite inclination angle at all perturbation wavelengths even if recombination is included. Ryutov et al. (2003) also discussed an unstable mode when the incident radiation is tilted relative to the molecular cloud surface normal. Most work done so far has addressed a non-accelerating surface of a semi-infinite cloud.

In this paper, we investigate the hydrodynamic instability of a finite thickness cloud at an accelerating surface. In Section 2, we describe the basic equations and assumptions of our model. Results and discussions are presented in Section 3, and in Section 4, we conclude with a short summary.

2. Basic Equations and Our Model

We begin by writing conservation of mass, momentum, and energy,

$$\frac{\partial \rho}{\partial t} + \nabla \cdot (\rho \boldsymbol{u}) = 0, \tag{1}$$

$$\frac{\partial (\rho \boldsymbol{u})}{\partial t} + \nabla \cdot (\rho \boldsymbol{u}\boldsymbol{u} + \boldsymbol{P}) = 0, \tag{2}$$

$$\frac{\partial}{\partial t}\left(\rho\left(\frac{1}{2}\boldsymbol{u}^2 + \epsilon\right)\right) + \nabla \cdot \left(\left(\rho\left(\frac{1}{2}\boldsymbol{u}^2 + \epsilon\right) + p\right)\boldsymbol{u}\right) = -q_{\mathrm{re}} + q_{\mathrm{uv}} - q_{\mathrm{mol}}. \tag{3}$$

Here ρ is mass density, **P** is pressure, **u** is velocity vector, ϵ is specific internal energy, and n is volume density of total hydrogen, respectively. The terms on the right hand side of Eq. (3) are energy source terms due to recombination in the ionized region (q_{re}), absorption of UV radiation from OB stars (q_{uv}), and radiative cooling in the molecular gas (q_{mol}), respectively. The transport of UV radiation from OB stars and time evolution of the fraction of ionized hydrogen are considered in the following equations,

$$n\frac{\partial f}{\partial t} + n\boldsymbol{u} \cdot \nabla f = an(1-f)J - \alpha_B n^2 f^2, \tag{4}$$

$$\frac{\partial J}{\partial y} = -an(1-f)J, \tag{5}$$

where $f = n_{\mathrm{i}}/n$ is ionization fraction (note: $f = 0$ or 1 correspond to neutral or fully ionized gas, respectively), n_{i} is ionized hydrogen volume density, $a = 6 \times 10^{-18}\mathrm{cm}^2$ is the photoionization cross-section of hydrogen, and J is the number flux of photons whose energy exceeds the critical energy for the ionization of atomic hydrogen (13.6 eV). It is assumed that the incident photons are parallel to the y axis. We do not include recombination to the ground state, and assume that diffuse radiation and its absorption are balanced locally (known as the "on the spot approximation"). In other words, the emitted photon is absorbed to another neutral hydrogen atom in the same zone. Only the so-called "case B" recombination ($\alpha_{\mathrm{B}} = 2.6 \times 10^{-13}\,\mathrm{cm}^3\mathrm{s}^{-1}$ at $T = 10^4$ K; (Hummer and Seaton, 1963)) is considered in this study, where α_{B} is the summation of the recombination coefficients to all hydrogen states except to the ground state. Energy sources are written as:

$q_{\rm re} = (nf)^2\beta_{\rm B}k_{\rm B}T$, $q_{\rm uv} = Wna(1-f)J$, and $q_{\rm mol} = n_{\rm mol}^2 \times 10^{-29}$ erg cm^{-3}s^{-1}. Here $T = (m_{\rm p}/k_{\rm b})(4\epsilon/(7f+5))$ is temperature in Kelvin ($\rho\epsilon = 2\times 1.5(nf)k_{\rm B}T + 2.5n_{\rm mol}k_{\rm B}T$), $m_{\rm p}$ is proton mass, $n_{\rm mol} = n(1-f)/2$ is volume number density of molecular hydrogen, and $k_{\rm b}$ is the Boltzmann constant. We use $(nf)^2\beta_{\rm B}k_{\rm b}T$ instead of $(3/2)(nf)^2\alpha_{\rm B}k_{\rm b}T$ for the recombination cooling term to include the effects of the thermal velocity dependence for the recombination and free–free collisional cooling. $\beta_{\rm B} = 1.25\alpha_{\rm B}$ at $T = 10^4$ K (Hummer and Seaton, 1963). It is assumed that the averaged energy of the incident photon is $(13.6 + W)$ eV per photon from OB stars. The energy W is deposited to internal energy of the gas when a neutral hydrogen atom absorbs an incident photon. The ionized region becomes isothermal quickly due to the energy balance between these cooling and heating effects. We take $W = 1.73 \times 10^{-12}$ in erg so that the isothermal temperature becomes $T = 10^4$ K. The cooling term $q_{\rm mol}$ is effective when $40\,{\rm K} < T < 3000\,{\rm K}$.

The equation of state consists of two parts, corresponding to thermal pressure and magnetic pressure,

$$p = \frac{2(3f+1)}{7f+5}\rho\epsilon + p_{\rm M}\left(\frac{\rho}{\rho_{\rm M}}\right)^{\gamma_{\rm M}}. \tag{6}$$

The first term in the right hand side is thermal pressure (f = 0 or 1 give $(2/5)\rho\epsilon$ or $(2/3)\rho\epsilon$ corresponding to diatomic or monoatomic adiabatic gas) and the second one is magnetic pressure. $p_{\rm M}$ and $\rho_{\rm M}$ are constant values (we set these values to the initial cloud density and thermal pressure in this study). The index is also constant $\gamma_{\rm M} = 4/3$ (magnetic turbulence) or 2 (initially uniform magnetic field). We studied the case of $\gamma_{\rm M} = 4/3$ in this paper. The magnetic pressure is introduced to prevent radiative collapse due to molecular cooling, when shock heating occurs (Ryutov and Remington (2002)). When the gas is compressed, the second term acts as stiffness, preventing collapse. The numerical calculation is done in the $x-y$ plane using the 2D code used in (Mizuta et al., 2002) but extended to include a real gas equation of state. A uniform grid size $\Delta x = \Delta y = 2.5 \times 10^{-3}$ pc is used.

Then we get the sound speed,

$$c_{\rm s}^2 = \frac{2(3f+1)}{7f+5}\left(\frac{p}{\rho} + \epsilon\right) + \frac{\gamma_{\rm M}p_{\rm M}}{\rho}\left(\frac{\rho}{\rho_{\rm M}}\right)^{\gamma_{\rm M}}. \tag{7}$$

In this paper, the hydrodynamic instability of an ionization front with effective acceleration is studied. A finite cloud, which has an initial width of 0.25 pc and initially located 0.5 pc from the computational boundary, is driven by the radiation from OB stars. The intensity of incident radiation at the boundary is 2.6×10^9 cm^{-2}s^{-1}(without recombination) and 5×10^{11} cm^{-2}s^{-1} (with recombination). When radiation is incident on the cloud surface, a strong shock appears in the cloud. Then, the shock breaks out, a rarefaction moves back through the compressed cloud. Finally, the acceleration phase begins. A perturbation is imposed by a sinusoidal radiation intensity profile, which has 10% amplitude, for the first 10 ky of this acceleration phase.

3. Results and Discussion

At first, we discuss the case of a small imposed perturbation. Figure 1a shows the time evolution of the amplitude of the perturbation for three wavelengths, $\lambda = 0.46$, 0.6, and 0.92 pc, but the recombination coefficient is set to be 0. The perturbation grows in all cases and the growth rate is in good agreement with classical Rayleigh–Taylor (RT) theory.

When the recombination coefficient is turned on in the same problem, the dynamics change dramatically. Figure 1b is the same as Figure 1a, but with recombination turned on. The perturbation oscillates but does not grow. To understand this, consider an initial, small perturbation, as shown in Figure 2a. Ablated plasma from the cloud surface tends to accumulate on or near the axis of the perturbation, i.e., near the normal to the cloud surface from the deepest part of the concave perturbation, as illustrated by the density contours (Figure 2a). This causes a local modification of the radiative flux incident at the surface, as shown by the radiative intensity contour (Figure 2b). Most photons in the central ray are absorbed before they reach the molecular surface, whereas photons near the computational edges deposit their energy closer to the ablation front, yielding locally enhanced pressures at the cloud surface. This effectively flattens out ("heals") the initial, small perturbation. This is the reason why the perturbation does not grow in the recombination-on case.

On the contrary, a large imposed perturbation leads to different dynamics. In this case, the perturbation is put on the surface in density initially, and about 30% larger

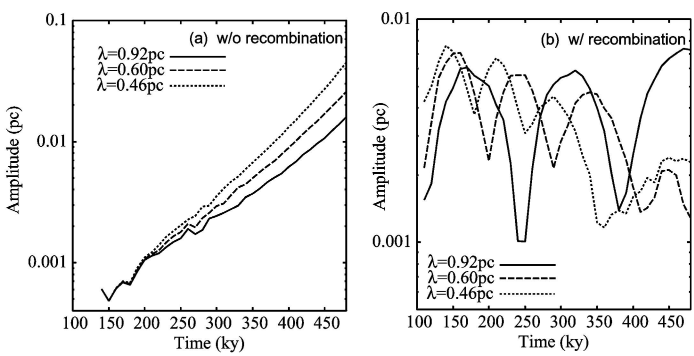

Figure 1. The amplitude of the perturbation in time (without recombination (left: a), with recombination (right: b)). Three wavelength cases ($\lambda = 0.92, 0.6, 0.46$ pc) are shown. The perturbation grows without recombination with classical RT growth rate. The perturbation does not grow with recombination turned on, but just oscillates.

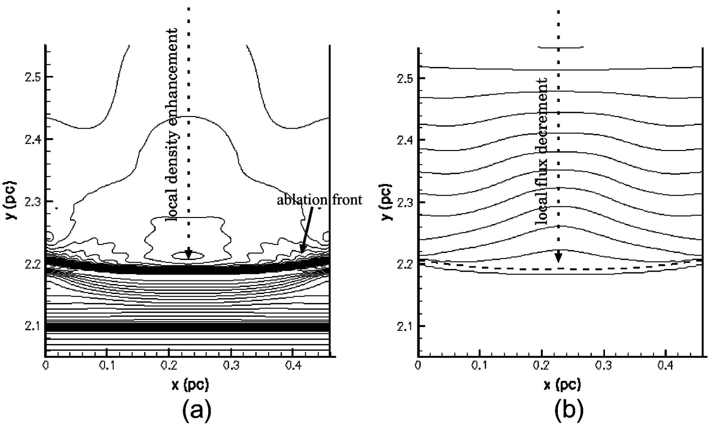

Figure 2. The photon flux (left: a) and number density (right: b) contour (solid lines) with recombination case. The higher density around the bubble caused strong distinction. The radiative intensity at the surface weakens. This works to smooth the surface.

than that of the previous case when the acceleration phase begins. A very curved surface can have a strong effect on the local density structure as discussed above. Then, in some rays of the radiation, all photons are absorbed before they reach the molecular surface. If such regions appear at the cloud surface, this means that some of region is shadowed for a while. If the initial perturbation is large enough that the surface has sufficient curvature, then in the "side walls" of the perturbation, the incident radiation intensity is reduced. This means that the "filling in" effect by the ablated plasma, which led to self-healing of the small perturbation case, is reduced, or even turned off, allowing the perturbation to grow. This leads also to a transition from single mode to a multi-mode perturbation (Figure 3).

In the later phase of this problem we observed a two-column like structure. Their width is about 0.2 pc which is a little shorter than that of observed pillar in the Eagle Nebula. But the velocity gradient along the y axis in the center column, dv_y/dy, is $\sim$7.5 km s^{-1}pc^{-1}, is very similar to the observed velocity gradient in the Eagle Nebula (Pound, 1998).

4. Summary

Hydrodynamic instability of ionization fronts is investigated numerically, including detailed accounting of radiative processes. Without recombination, the perturbation grows at the classical RT growth rate. We observed a stabilization mechanism when recombination is included in the HII gas. If the imposed perturbation is small, the perturbation does not grow due to local modification of the radiation flux at the ablation front, leading to a "self-healing" effect. If the imposed perturbation is large, the perturbation curvature can be sufficient to reduce the linear regime

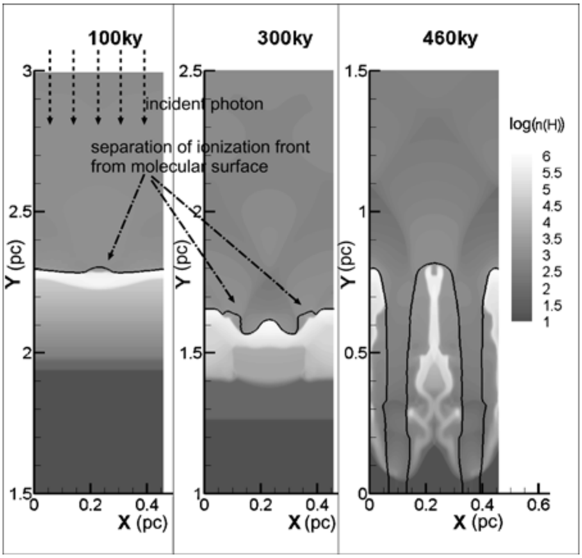

Figure 3. Time evolution of number density contour (gray scale). The separation of ionization front from molecular cloud surface occurs in some regions at $t = 100$ ky (left). A multimode appears at $t = 300$ ky (center). Finally two columns can be seen at $t = 460$ ky (right). The solid line is the counter of hydrogen fraction $f = 0.5$.

stabilization effect, and the perturbation grows. This leads to nonlinear dynamics. In this situation a pillar like structure appears.

Acknowledgements

This work is performed under the auspices of the U.S. Department of Energy by the Lawrence Livermore National Laboratory under Contract No. W-7405-ENG-48 and NASA Grant NRA 00-01-ATP-059.

References

Axford, W.I.: 1964, *Astrophys. J.* **140**, 112.
Hester, J.J., et al.: 1996, *Astron. J.* **111**, 2349.
Hummer, D.G. and Seaton, M.J.: 1963, *MNRAS* **125**, 437.
Mizuta, A., Yamada, S. and Takabe, H.: 2002, *Astrophys. J.* **567**, 635.
Pound, M.W.: 1998, *Astronophys. J.* **493**, L113.
Ryutov, D.D., Kane, J.O., Pound, M.W. and Remington, B.A.: 2003, *Plasma Phys. Control. Fusion* **45**, 769.
Ryutov, D.D. and Remington, B.A: 2002, *Plasma Phys. Control. Fusion* **44**(12B), 407.
Vandervoort, P.O.: 1962, *MNRAS* **135**, 212.
Williams, R.J.R.: 2002, *MNRAS* **331**, 693.

SIMULATING ASTROPHYSICAL JETS IN LABORATORY EXPERIMENTS

PAUL M. BELLAN[1], SETTHIVOINE YOU[1] and SCOTT C. HSU[1,2]
[1]*Caltech 128-95, Pasadena, CA 91125, USA; E-mail: pbellan@its.caltech.edu*
[2]*Current address: LANL*

(Received 23 April 2004; accepted 9 June 2004)

Abstract. Pulsed-power technology and appropriate boundary conditions have been used to create simulations of magnetically driven astrophysical jets in a laboratory experiment. The experiments are quite reproducible and involve a distinct sequence. Eight initial flux tubes, corresponding to eight gas injection locations, merge to form the jet, which lengthens, collimates, and eventually kinks. A model developed to explain the collimation process predicts that collimation is intimately related to convection and pile-up of frozen-in toroidal flux convected with the jet. The pile-up occurs when there is an axial non-uniformity in the jet velocity so that in the frame of the jet there appears to be a converging flow of plasma carrying frozen-in toroidal magnetic flux. The pile-up of convected flux at this "stagnation region" amplifies the toroidal magnetic field and increases the pinch force, thereby collimating the jet.

Keywords: astrophysical jet, collimation, kink, MHD, pinch, stagnation

1. Experiment Motivation and Design

A magnetically driven astrophysical jet is characterized by having a high Lundquist number and boundary conditions that typically consist of azimuthal symmetry, a mass source in the $z = 0$ plane and a poloidal magnetic field linking a rotating accretion disk in the $z = 0$ plane. Figure 1 sketches these boundary conditions and shows how the rotation of the accretion disk causes a radial electric field $E_{\rm r}$ which drives a poloidal current with associated toroidal magnetic field B_ϕ.

We have constructed an experimental configuration that simulates magnetically driven astrophysical jets. The experiment exploits technology previously developed for spheromaks, a magnetohydrodynamic (MHD) configuration relevant to magnetically confined, controlled thermonuclear fusion research (Bellan, 2000). As shown in Figure 2, the experimental boundary conditions are very similar to the astrophysical jet boundary conditions shown in Figure 1. Rotating the annulus would provide an exact replica of the astrophysical jet boundary conditions, but the required rotation velocity would be impractically large. Instead of rotating the annulus, a high-energy capacitor bank is discharged across the gap separating the disk from the annulus. This alternative but equivalent way for producing the radial electric field $E_{\rm r}$ drives a current nearly along the poloidal field lines and similarly

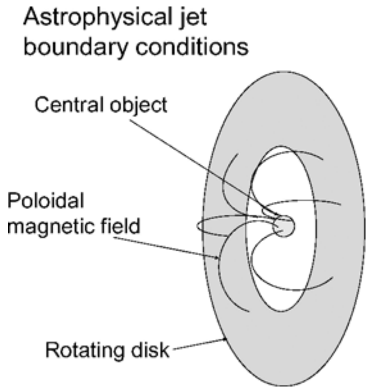

Figure 1. The accretion disk rotating with velocity U_ϕ cuts the poloidal magnetic field leading to a lab frame electric field $E_\mathrm{r} = -U_\phi B_\mathrm{pol}$. This radial electric field drives a poloidal current that flows in a direction approximately along the poloidal magnetic field and so generates a toroidal magnetic field B_ϕ.

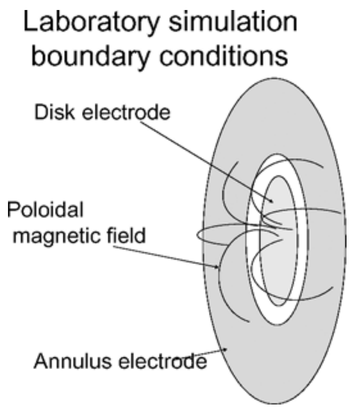

Figure 2. A capacitor bank connected between the central disk and the annulus creates a radial electric field E_r which drives current nearly along the poloidal field lines in analogy to the astrophysical situation.

creates a toroidal magnetic field B_ϕ. Because MHD has no intrinsic scale, simulation of the dimensionless numbers and of the boundary conditions suffices to establish the conditions for creating a lab-scale version of an astrophysical jet. The nominal parameters of the lab experiment are duration $\sim 10\,\mu$s, $B \sim 0.01$–0.1 T, potential drop $\sim$1–6 kV, poloidal current $I \sim 50$–150 kA, density $n \sim 10^{19}$–$10^{20}\ \mathrm{m}^{-3}$, typical $B \ll 1$, and Lundquist number $\sim 10^3$. Various types of gas species are used to observe the effect of changing the ion mass.

Figure 3 shows typical photographs in visible light (Hsu and Bellan, 2002) of a hydrogen plasma produced in these lab simulations of astrophysical jets. The central disk (20 cm diameter) is surrounded by a co-planar, coaxial annulus (51 cm

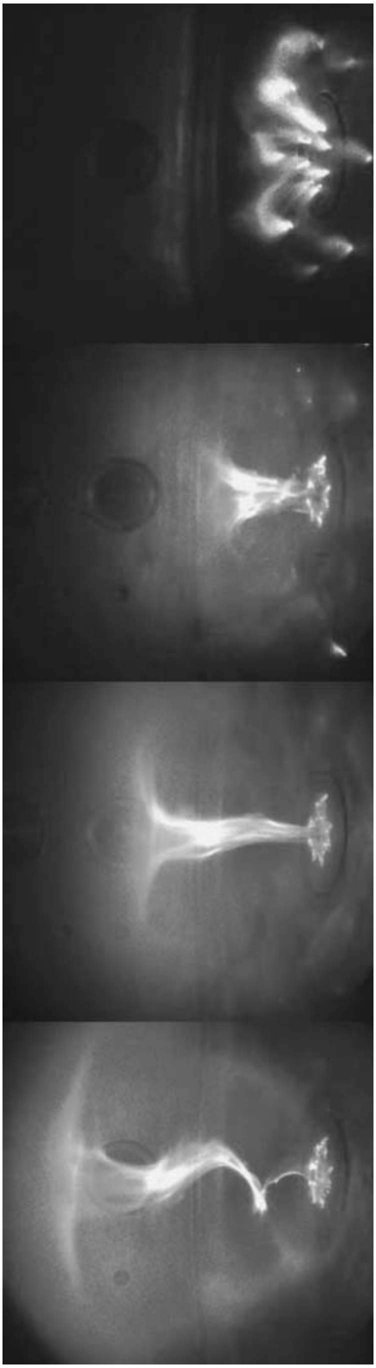

Figure 3. Photos showing experimental sequence from top to bottom: (i) eight plasma-filled loops form and span from gas ports on cathode to gas ports on anode, (ii) the loops merge to form a central column jet, (iii) the jet lengthens and is collimated, (iv) the jet becomes kink unstable.

diameter). Circular arrays of eight gas feed ports are located on both the disk and annulus; the disk is the cathode and the annulus, held at ground, is the anode. A magnetic field coil located just behind the disk provides a poloidal magnetic field simulating the field produced by a central object such as a star. There is a 6 mm gap insulating the disk from the annulus; high voltage is applied across this gap to drive the poloidal current between the disk and the annulus. The disk/annulus configuration is mounted on the end dome of a large cylindrical vacuum chamber the dimensions of which are so large (1.4 m diameter, 2 m length) that there is ample room for the plasma to move without interacting with the walls. The large ratio of vacuum chamber dimensions to plasma dimensions thus approximates the unbounded space into which an actual astrophysical jet propagates.

The plasma evolves through a well-defined and reproducible sequence as follows:

1. Eight distinct, bright arched filamentary plasma loops form as shown in Figure 3 (top). These loops each span from a gas feed port on the cathode to a corresponding gas feed port on the anode. This configuration resembles the eight legs of a spider.
2. The portions of the 'spider legs' near the geometric axis (z-axis) merge to form a single central column as shown in Figure 3 (second image from top) and the outer portions of the spider legs merge to form a mushroom-shaped return current. The central column constitutes the plasma jet.
3. The jet-like central column lengthens in the z-direction as shown in Figure 3 (third image from top). The cocoon-like return current also lengthens. The central column is very bright and collimated, whereas the return current is dim and diffuse.
4. Upon reaching a critical length, the central column undergoes a kink instability (Hsu and Bellan, 2002, 2003) as shown in Figure 3 (bottom image). The conditions for kink instability are in agreement with the Kruskal-Shafranov $q = 1$ instability condition for a cylindrical pinch where $q = 2\pi r B_\phi / B_z L$.

These results and the results from a related solar coronal loop simulation experiment have motivated a model (Bellan, 2003) for jet acceleration and collimation. This model shows that jet acceleration results from the non-conservative nature of the $\mathbf{J} \times \mathbf{B}$ MHD force and collimation results from compressibility of the jet and its embedded toroidal magnetic field. The model is discussed in detail in (Bellan, 2003) and a brief summary will now be given here.

The process is governed by ideal MHD and the relevant equations are the MHD equation of motion, the ideal MHD induction equation, and the equation of mass conservation, i.e.,

$$\rho \frac{d\mathbf{U}}{dt} = \mathbf{J} \times \mathbf{B} - \nabla P, \quad \frac{\partial \mathbf{B}}{\partial t} = \nabla \times (\mathbf{U} \times \mathbf{B}), \quad \frac{\partial \rho}{\partial t} = -\nabla \cdot (\rho \mathbf{U}). \tag{1}$$

The model is first worked out in a geometry simpler than an astrophysical jet but then extended to the astrophysical jet geometry. Cylindrical geometry $\{r, \phi, z\}$ is used; the ϕ direction is called toroidal and poloidal denotes the r or z directions. The configuration is imagined to start as a finite-length, toroidally symmetric, current-free magnetic flux tube that is axially non-uniform as in Figure 4 so that the initial magnetic field is purely poloidal and stronger at the two ends $z = \pm h$ than at the axial midpoint $z = 0$. The two flux tube ends intercept electrodes that can drive a current I along the flux tube (see green arrows in Figure 4). The decreased magnetic field strength at the axial midpoint means that the flux tube radius is larger at $z = 0$ than at $z = \pm h$. A bulged flux tube of this sort could be produced by two coaxial coils located at axial positions somewhat larger than $z = \pm h$. The dynamics is identified (Bellan, 2003) as consisting of three distinct stages.

The first stage, called the twisting stage, consists of the ramping up of the poloidal current I, which is driven by an external electromotive force applied across the two end electrodes (this is topologically equivalent to the electromotive force applied across the disk and annulus electrodes in the astrophysical jet experiment). Because Ampere's law gives $B_\phi(r, z, t) = \mu_0 I(r, z, t)/2\pi r$ and because finite B_ϕ causes the flux tube to be twisted, the flux tube twists up in proportion to I. Thus, the twisting of the flux tube can be considered as being instantaneous upon the application of the current I. The amount of twisting is evaluated using the toroidal component of the induction equation,

$$\frac{\partial B_\phi}{\partial t} = r\mathbf{B}_{\rm pol} \cdot \nabla \left(\frac{U_\phi}{r} \right) - r\mathbf{U}_{\rm pol} \cdot \nabla \left(\frac{B_\phi}{r} \right) - B_\phi \nabla \cdot \mathbf{U}_{\rm pol}. \tag{2}$$

The poloidal velocity $\mathbf{U}_{\rm pol}$ is zero at this stage and also $\boldsymbol{B}_{\rm pol} \cdot \nabla = B_{\rm pol}\partial/\partial s$, where s is the distance along the flux tube from the $z = 0$ midplane. By symmetry $U_\phi = 0$

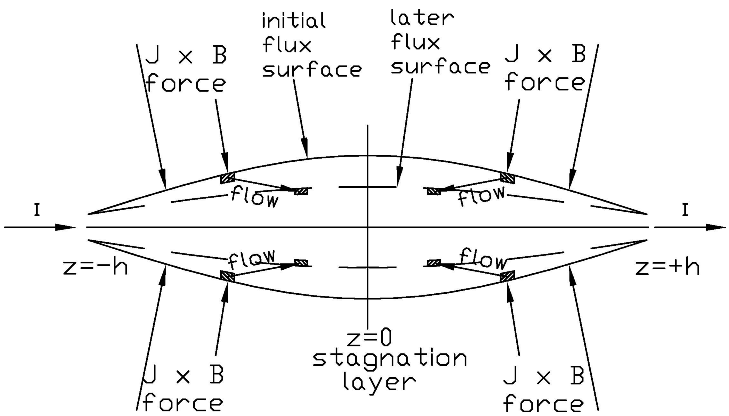

Figure 4. Sketch showing how convergence of flows from $z = \pm h$ towards $z = 0$ cause initially bulged flux tube to become collimated.

on the $z = 0$ plane, and so integrating Eq. (2) with respect to s and then invoking Ampere's law gives

$$U_\phi \approx \frac{\mu_0 s}{2\pi r B_{\mathrm{pol}}} \frac{\partial I}{\partial t}, \tag{3}$$

which shows that a non-zero twist velocity requires a time-changing I.

The second stage occurs when the current has reached its steady-state value so that $\partial I/\partial t = 0$, but the system is not yet in dynamic equilibrium. In this stage, poloidal plasma flows (magenta arrows in Figure 4) are accelerated by the $\mathbf{J} \times \mathbf{B}$ force (blue arrows in Figure 4). These flows are not instantaneous, but rather take time to develop. An approximate interpretation of these flows is to say that they are driven by axial gradients in the toroidal field energy $B_\phi^2/2\mu_0$. This is because the axial component of the $\mathbf{J} \times \mathbf{B}$ force can be expressed as $(\mathbf{J} \times \mathbf{B})_z = J_{\mathrm{r}} B_\phi - J_\phi B_{\mathrm{r}}$ and initially $J_\phi = 0$ because at initial times the flux tube retains its vacuum shape and J_ϕ is a function of the deviation of the flux tube from its vacuum shape. Using Ampere's law, the axial component of the $\mathbf{J} \times \mathbf{B}$ force is

$$(\mathbf{J} \times \mathbf{B})_z = -\frac{\partial}{\partial z}\left(\frac{B_\phi^2}{2\mu_0}\right), \tag{4}$$

showing there exists an axial acceleration from regions where B_ϕ^2 is large to where it is small, i.e., from $z = \pm h$ towards $z = 0$ because $B_\phi^2 = (\mu_0 I/2\pi r)^2$ is weaker at $z = 0$ than at $z = \pm h$.

The third stage involves convergence at the axial midpoint $z = 0$ of the oppositely directed flows coming from $z = \pm h$. This convergence leads to an axial compression of the plasma (shown as red in Figure 4). Because the current is in steady state, $U_\phi = 0$. At $z = 0$ where $\mathbf{U}_{\mathrm{pol}} = 0$, Eq. (2) reduces to

$$\frac{\partial B_\phi}{\partial t} = -B_\phi \nabla \cdot \mathbf{U}_{\mathrm{pol}}; \tag{5}$$

showing that flow convergence causes amplification of B_ϕ. Amplification occurs because compression of toroidal field lines frozen into the plasma, shown as red in Figure 4, occurs when the plasma itself becomes compressed; the plasma compression results as the oppositely directed flows collide at $z = 0$. Because I is fixed, amplification of $B_\phi = \mu_0 I/2\pi r$ requires r to become smaller. Thus, the flow stagnation and resultant axial plasma compression causes the flux tube to become collimated.

These ideas can be generalized to the more complex geometry of an astrophysical jet by writing Eq. (2) as

$$\frac{d}{dt}\left(\frac{B_\phi}{r}\right) = \mathbf{B}_{\mathrm{pol}} \cdot \nabla\left(\frac{U_\phi}{r}\right) - \frac{B_\phi}{r}\nabla \cdot \mathbf{U}_{\mathrm{pol}}. \tag{6}$$

If I is constant in time, then there is no toroidal acceleration because toroidal acceleration requires existence of a current density normal to the poloidal flux surfaces. A steady current normal to flux surfaces is not possible because symmetry constrains the plasma particles to stay within a poloidal Larmor radius of a poloidal flux surface. This constrains any current normal to flux surfaces to be a transient alternating current and consideration of microscopic particle motions shows that this current is the polarization current and is proportional to $\partial^2 I/\partial t^2$. Thus, if the plasma initially has $U_\phi = 0$, U_ϕ will revert to being zero when the current is in steady state. Equation (6) therefore reduces to

$$\frac{d}{dt}\left(\frac{B_\phi}{r}\right) = -\frac{B_\phi}{r}\nabla \cdot \mathbf{U}_{\text{pol}}, \tag{7}$$

which, after being combined with the continuity equation, becomes

$$\left(\frac{B_\phi}{r}\right)^{-1} \frac{d}{dt}\left(\frac{B_\phi}{r}\right) = \frac{1}{\rho}\frac{d\rho}{dt}. \tag{8}$$

This shows that in the frame of the convecting plasma, B_ϕ increases in proportion to the compression of a fluid element. Hence, if an astrophysical jet has $\nabla \cdot \mathbf{U}_{\text{pol}} < 0$ then B_ϕ in convecting fluid elements will increase as these elements becomes axially squeezed. The increase in B_ϕ will cause the outer radius of the fluid elements to decrease because I is constant and $B_\phi = \mu_0 I/2\pi r$. Hence, any MHD poloidal flow with $\nabla \cdot \mathbf{U}_{\text{pol}} < 0$ and finite I will become collimated.

Acknowledgments

This work was supported by DOE.

References

Bellan, P.M.: 2000, *Spheromaks* (Imperial College Press).
Bellan, P.M.: 2003, *Phys. Plasmas* **10**(5), 1999, Part 2.
Hsu, S.C. and Bellan, P.M.: 2002, *MNRAS* **334**(2), 257.
Hsu, S.C. and Bellan, P.M.: 2003, *Phys. Rev. Lett.* **90**(21), art. no. 215002.

PARTICLE ACCELERATION IN RELATIVISTIC MAGNETIZED PLASMAS

EDISON LIANG
Rice University, Houston, TX 77005-1892, USA; E-mail: liang@spaceibm.rice.edu

(Received 6 April 2004; accepted 31 May 2004)

Abstract. We review the particle-in-cell simulation results related to the recently discovered particle acceleration mechanism called the Diamagnetic Relativistic Pulse Accelerator, or DRPA. This mechanism may be relevant to the prompt gamma-ray emission of gamma-ray bursts. It may also be testable with future laboratory experiments using ultra-intense lasers.

Keywords: plasmas, particle acceleration, gamma-ray bursts

1. Introduction

An outstanding problem in astrophysics is the acceleration of high energy particles. The challenge is to find natural mechanisms, which efficiently convert bulk energy (rotational, electromagnetic, bulk motion, thermal, or gravitational), into the relativistic energy of a small fraction of nonthermal particles. During the past 2 years, we used multi-dimensional particle-in-cell (PIC) codes (Birdsall and Langdon, 1991) developed at Los Alamos National Laboratory (LANL) and Lawrence Livermore National Laboratory (LLNL) to pioneer large-scale PIC simulations of the expansion and interaction of relativistic strongly magnetized, collisionless (coulomb mean free path > plasma size) plasmas (RMPs) to search for viable particle acceleration and radiation mechanisms relevant to astrophysics. Using 2.5D (dimensional) PIC simulations of the relativistic expansion of an electromagnetic-dominated plasma, we recently discovered a new robust particle-energization mechanism called the diamagnetic relativistic pulse accelerator (DRPA), which efficiently converts the initial magnetic energy into the ultra-relativistic directed kinetic energy of a fraction of the *surface* particles (Liang et al., 2003). In the case of an e^+e^- plasma, when the simulation is carried to >150 light-crossing times of the initial plasma, the simulated plasma pulse exhibits many of the signatures of cosmic gamma-ray bursts (Liang and Nishimura, 2004).

When a collisionless plasma with a large *transverse* magnetic energy per particle ($\Omega_e/\omega_{pe} > 1$) is deconfined, the cross-field particle drifts generate a strong transverse current, which slows and reshapes the expanding electromagnetic (EM) pulse. The EM pulse can then trap and accelerate the surface particles via the $J \times B$ and

Astrophysics and Space Science **298:** 211–218, 2005.

ponderomotive (Weibel, 1958) force, efficiently converting EM energy into directed particle energy near the surface. However, the trap is leaky. As slow particles fall behind, the EM pulse focuses its acceleration on fewer and fewer fast particles – those that can keep pace. As a result both the EM pulse and remaining trapped surface particles become more and more relativistic with time. We have simulated both electron–positron ($m_{\rm i} = m_{\rm e}$) and electron–ion ($m_{\rm i}/m_{\rm e} = 100$) plasmas. In the e^+e^- case both species are energized equally. But in the electron–ion case most of the energy gain goes to the ions due to charge separation. We have studied both slab and cylindrical geometries with qualitatively similar results (Figure 1).

Figures 2–5 illustrate the slab DRPA at early times (Liang et al., 2003). By $t\Omega_{\rm e} = 1000$, 60% of the initial magnetic energy is converted to directed particle energy in the e^+e^- case, and ~40% is converted to ion energy in the electron–ion case. At least in 2.5D simulations, we find no sign of any plasma instability, including the lower-hybrid-drift instability (LHDI) in the electron–ion case (Winske, 1988; Sgro et al., 1989). They are likely suppressed by the strong transverse EM fields and relativistic motion.

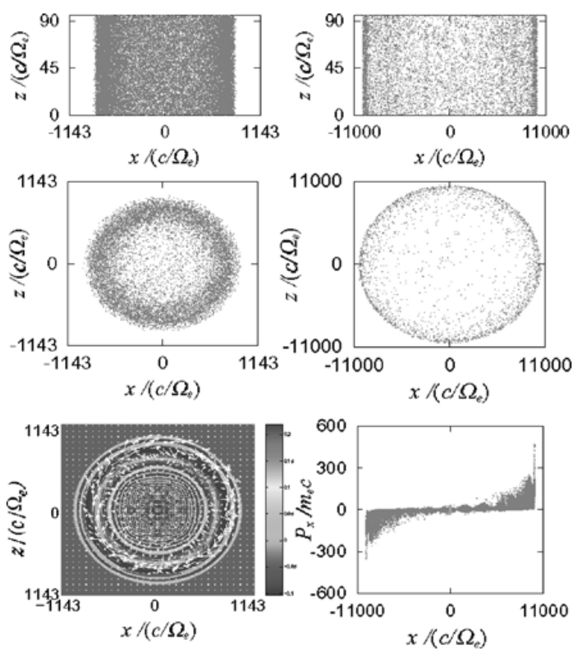

Figure 1. The 2.5-D PIC simulations of slab and cylindrical e^+e^- RMP expansion with initial plasma temperature $kT = 5\,$MeV, $\Omega_{\rm e}/\omega_{\rm pe} = 10$, initial slab width $L_0 = 120c/\Omega_{\rm e}$, and uniform internal $\mathbf{B} = (0, B_0, 0)$. We show snapshots of particle distribution (top and middle), axial magnetic field and current density (white arrows) for the cylindrical case (bottom left), and phase plot for the slab case (bottom right). $\Omega_{\rm e}t = 800$ for all left panels and $\Omega_{\rm e}t = 10^4$ for all right panels. The green dot in the phase plot denotes the initial phase volume (Liang and Nishimura, 2004).

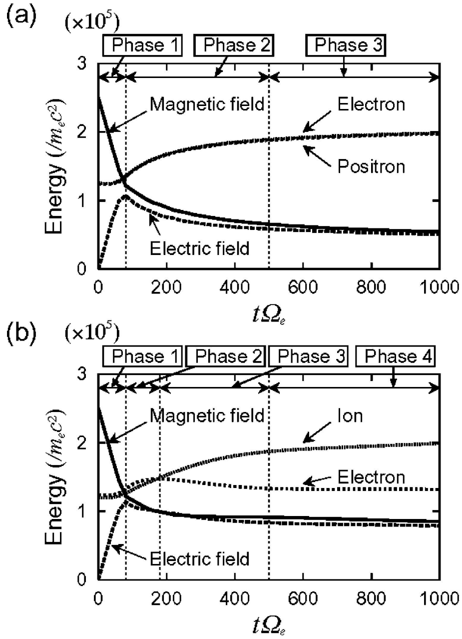

Figure 2. (Left) Evolution of the magnetic field, electric field, and particle energies for (a) the electron positron case and (b) the electron–ion case (from Liang et al., 2003).

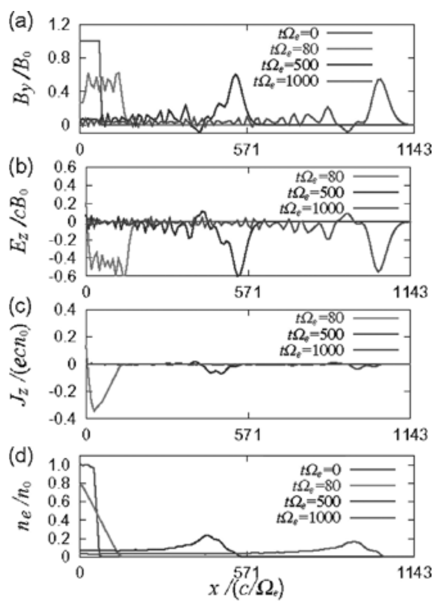

Figure 3. (Right) Results for the electron–positron case. Shown are (a) the magnetic field B_y, (b) electric field E_z, (c) current density J_z, and (d) electron density profiles at $t\Omega_e = 0$, 80, 500, and 1000 for x $>$ 0. Results for x $<$ 0 are identical. The values of E_z and J_z are zero at $t\Omega_e = 0$ (from Liang et al., 2003).

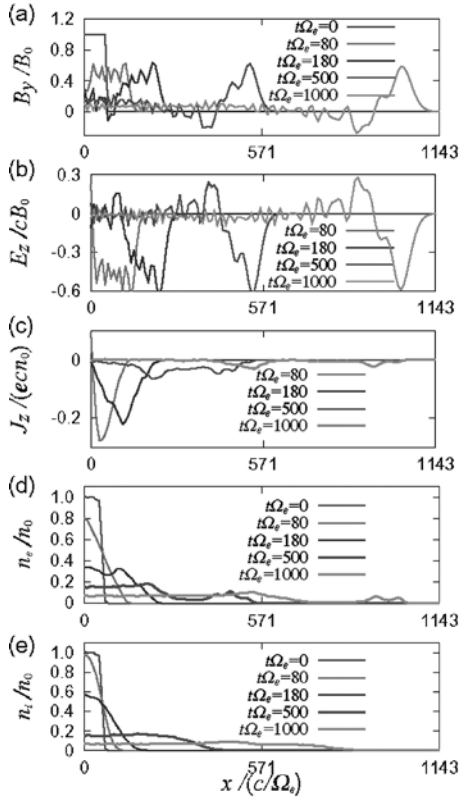

Figure 4. (Left) Results for the electron–ion case. Shown are (a) the magnetic field B_y, (b) electric field E_z, (c) current density J_z, (d) electron density n_e, and (e) ion density n_i profiles at $t\Omega_e = 0$, 80, 180, 500, and 1000 for x >0. The values of E_z, and J_z, are zero at $t\Omega_e = 0$ (from Liang et al., 2003).

2. Bifurcation and Lorentz Factor Scaling

When the above PIC simulations are continued to >150 light-crossing times of the initial plasma, the plasma pulse exhibits many remarkable features that resemble the observed properties of cosmic gamma-ray bursts (GRBs) (Fishman and Meegan, 1995a,b; Preece et al., 2000). These include the repeated bifurcation of the pulse profile (Figure 6) and formation of a power-law momentum spectrum with low-energy cut-off (Figure 7, see Liang and Nishimura, 2004, for details). We also find that the maximum attainable Lorentz factor (i.e., upper cutoff of the power law) scales with the initial plasma size. The most remarkable and important property of DRPA is that the group Lorentz factor of the EM pulse increases asymptotically as the square root of the number of the gyroperiods: $\gamma_m \sim (f\Omega_e(t)t)^{1/2}$ (Figure 8). Preliminary results show that the coefficient $f \sim (\Omega_e/\omega_{pe})^k$, where $k \sim 1$. Such simple scaling laws suggest that the DRPA mechanism may be realizable under

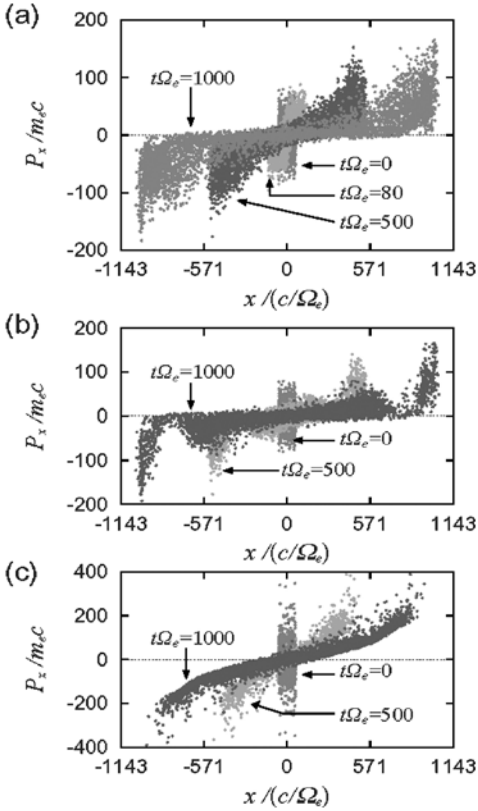

Figure 5. (Right) (a) Phase plots for the e^+e^- case: we plot the electron distribution in phase space x–p_x at $t\Omega_e = 0, 80, 500$, and 1000; (b, c) phase plots for the electron–ion case: shown are the electron (b) and ion (c) distributions in phase space x–p_x at $t\Omega_e = 0, 500$, and 1000 (from Liang et al., 2003).

laboratory conditions that can mimic the astrophysical conditions leading to DRPA (see Section 4).

Figure 9 shows that the DRPA mechanism depends on the initial Ω_e/ω_{pe} but is insensitive to the initial temperature. We find that effective particle acceleration occurs only when $\Omega_e/\omega_{pe} > 3$. We have also studied DRPA with B_z fields and DRPA interaction with ambient plasma. We find that B_z fields enhance the particle acceleration. Although much of the EM pulse energy is eventually absorbed by the ambient cold plasma, the EM pulse still manages to accelerate a small fraction of the particles to high Lorentz factors, with the maximum Lorentz factor comparable to the vacuum case. At least in 2.5D, we find no evidence of plasma instabilities. We speculate that two-stream, Weibel and other 3D instabilities will eventually develop and dissipate the DRPA momentum anisotropy, but only after the transverse EM pulse field has dropped below a certain threshold, say comparable to the

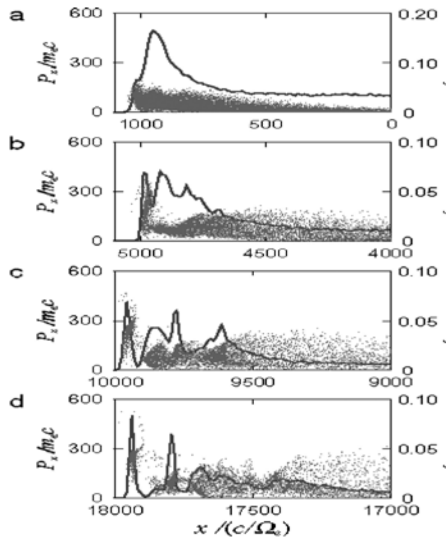

Figure 6. (left) Particle density profiles (blue curves, right scales) and phase plots (red dots, left scales) for the slab run of Figure 1 at (a) $\Omega_e t = 1000$, (b) 5000, (c) 10000 and (d) 18000. Note the repeated bifurcation of the density peak (from Liang and Nishimura, 2004).

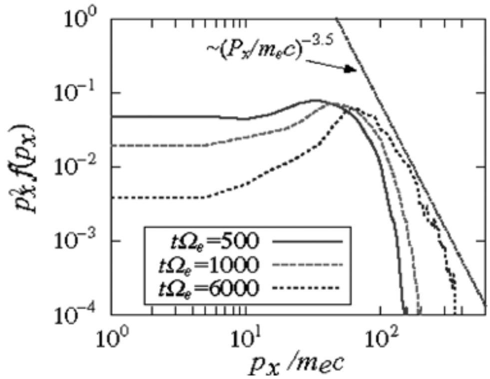

Figure 7. (Right) Evolution of the x-momentum distribution for all surface particles in the slab pulse of Figure 6, showing the peak Lorentz factor $\gamma_m (= p_{x,\max}/m_e c)$ increasing with time, and a power law of slope at about 3.5 at $\Omega_e t = 6000$ (from Liang and Nishimura, 2004).

saturation level of the Weibel instability (few percent of equipartition). Thus, we believe that the DRPA mechanism will prevail even in non-vacuum situations as long as the initial Ω_e/ω_{pe} is sufficiently large, so that the longitudinal acceleration rate is greater than the instability growth rate. Testing this hypothesis with 3D simulations is a priority of future research. Similarly, preliminary results of DRPA running into ambient magnetic fields suggest that the DRPA prevails for as long

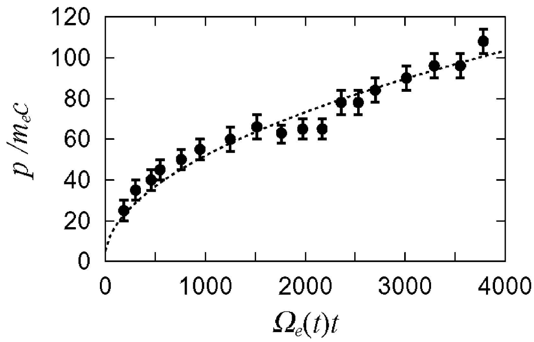

Figure 8. (Left) The peak Lorentz factor γ_m versus time for the slab pulse, compared to the square-root law (text). The best-fit curve (dotted) gives $f = 1.33$. Note that $\Omega_e(t)t = 3800$ is equivalent to $\Omega_e t = 18000$. This result shows that for $t > L_0/c$, γ_m scales as the square root of the number of gyroperiods (from Liang and Nishimura, 2004).

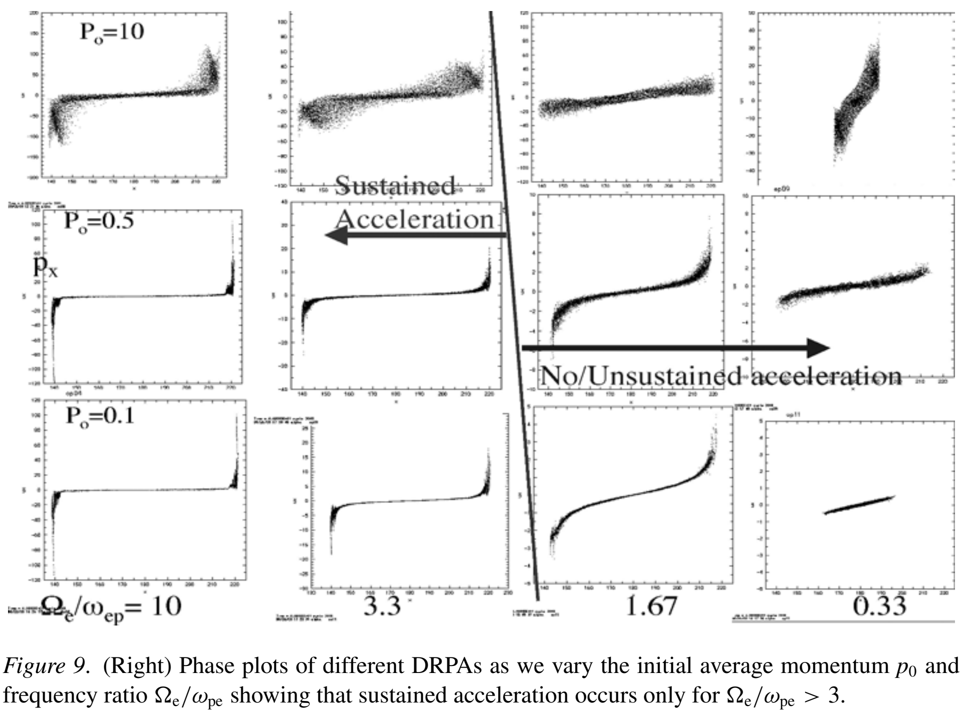

Figure 9. (Right) Phase plots of different DRPAs as we vary the initial average momentum p_0 and frequency ratio Ω_e/ω_{pe} showing that sustained acceleration occurs only for $\Omega_e/\omega_{pe} > 3$.

as the ambient field is much weaker than the expanding EM pulse. More details of DRPA, its interaction and its scaling properties can be found in Liang et al. (2003), Liang and Nishimura (2004), Nishimura and Liang (2004), and Nishimura et al. (2003).

3. Summary

In summary, through large-scale 2.5D PIC simulations, we have discovered a new robust acceleration mechanism unique to electromagnetic-dominated plasmas. DRPA has major implications for particle acceleration both in the universe and laboratory. Future ultra-intense laser experiments may be used to test this mechanism.

References

Birdsall, C.K. and Langdon, A. B.: 1991, *Plasma Physics via Computer Simulation*, Institute of Physics Publishing, Bristol.
Fishman, G. and Meegan, C.A.: 1995a, *Ann. Rev. Ast. Astrophys*. **33**, 415.
Fishman, G. and Meegan, C.A.: 1995b, in: M. Friedlander et al. (eds.), *Proceedings of the American Institute of Physics*, Compton Gamma-Ray Observatory, Vol. 280, p. 669, New York, 1993.
Gallant, Y., Hoshino, M., Langdon, A.B., Arons, J. and Max, C.E.: 1992, *ApJ*. **391**, 73.
Gisler, G.: 1989, *IEEE Trans. Plasma Sci.* **17**, 210.
Hoshino, M. et al.: 1992, *ApJ* **390**, 454.
Liang, E. et al.: 2003, *PRL* **90**, 085001.
Liang, E. and Nishimura, K.: 2004, *PRL* **92**, 175005.
Nishimura, K., Gary, S.P. and Li, H.: 2002, *J. Geophys. Res.*. **107**, 1375.
Nishimura, K., Liang, E. and Gary, P.: 2003, *Phys. Plasmas.* **10**(11), 4559.
Nishimura, K. and Liang, E.: 2004, *Phys. Plasmas* **11**(10), 4753.
Preece, R.D. et al.: 2000, *ApJS*. **126**, 19.
Sgro, A.G., Gary, S.P. and Lemons, D.S.: 1989, *Phys Fluids*. **B1**, 1890.
Sydora, R.D., Wagner, J.S., Lee, L.C., Wescott, E.M. and Tajima, T.: 1983, *Phys. Fluids* **26**, 2986.
Weibel, E.S.:1958, *J. Electr. Contr.* **5**, 435.
Winske, D.: 1988, *J. Geophys. Res.* **93**, 2539.

MAGNETIC RECONNECTION, TURBULENCE, AND COLLISIONLESS SHOCK

HANTAO JI, RUSSELL KULSRUD and MASAAKI YAMADA

Center for Magnetic Self-Organization in Laboratory and Astrophysical Plasmas, Princeton Plasma Physics Laboratory, Princeton, NJ, U.S.A.; E-mail: hji@pppl.gov

(Received 3 May 2004; accepted 28 May 2004)

Abstract. A short summary of recent progress in measuring and understanding turbulence during magnetic reconnection in laboratory plasmas is given. Magnetic reconnection is considered as a primary process to dissipate magnetic energy in laboratory and astrophysical plasmas. A central question concerns why the observed reconnection rates are much faster than predictions made by classical theories, such as the Sweet–Parker model based on MHD with classical Spitzer resistivity. Often, the local resistivity is conjectured to be enhanced by turbulence to accelerate reconnection rates either in the context of the Sweet–Parker model or by facilitating setup of the Pestchek model. Measurements at a dedicated laboratory experiment, called MRX or Magnetic Reconnection Experiment, have indicated existence of strong electromagnetic turbulence in current sheets undergoing fast reconnection. The origin of the turbulence has been identified as right-hand polarized whistler waves, propagating obliquely to the reconnecting field, with a phase velocity comparable to the relative drift velocity. These waves are consistent with an obliquely propagating electromagnetic lower-hybrid drift instability driven by drift speeds large compared to the Alfven speed in high-beta plasmas. Interestingly, this instability may explain electromagnetic turbulence also observed in collisionless shocks, which are common in energetic astrophysical phenomena.

Keywords: magnetic reconnection, plasma instability, turbulence, collisionless shock, laboratory experiment

1. Introduction

Magnetic reconnection (e.g. Biskamp, 2000) plays an important role during evolution of magnetic topology in relaxation processes in high-temperature laboratory plasmas, magnetospheric substorms, solar flares, and more distant astrophysical plasmas. Magnetic reconnection is also invoked to explain the observed rapid release of magnetic energy in these highly conducting plasmas. A local illustration of magnetic reconnection is shown in Figure 1, where dynamics in the dissipation region are of crucial importance. Despite its long history, a central unresolved question concerns why the observed reconnection rates are much faster than predictions by the Sweet–Parker model (Sweet, 1958; Parker, 1957) based on magnetohydrodynamics (MHD) with the classical Spitzer resistivity. In this two-dimensional (2D) model, the extremely small resistivity causes the magnetic field to dissipate only in very thin current sheets, which impede the outflow of mass leading to significantly slow reconnection rates. The subsequently proposed Petschek model (Petschek,

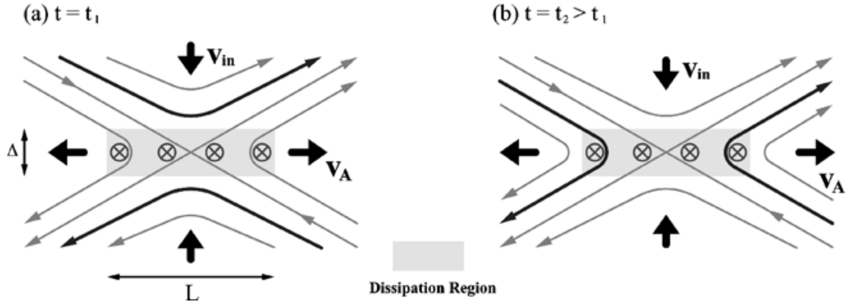

Figure 1. Illustration of local dissipation region (current sheet) of magnetic reconnection. Oppositely directed magnetic field lines, coming in from the top and the bottom, undergo reconnection in the dissipation region (current sheet) and move out sideways.

1964) is based on standing slow shocks that open up the outflow channel allowing larger mass flows and thus the faster reconnection rates. However, it was shown later (Biskamp, 1986; Uzdensky, 2000) that the Petschek solution is not compatible with uniform or smooth resistivity profiles. Currently, there are two leading models to explain the observed fast reconnection rates. The first one is based on anomalous resistivity caused by turbulence driven by instabilities local to the dissipation region, where plenty of free energy exists in the form of a large relative drift between ions and electrons and large inhomogeneities in pressure and magnetic field. This anomalous resistivity not only broadens the current sheet to increase the mass flow and the reconnection rate but also its localization opens up the outflow channel for the fast reconnection (Ugai and Tsuda, 1977; Scholer, 1989; Kulsrud, 2001; Biskamp and Schwarz, 2001). Alternatively, a recent theory (Birn et al., 2001) attempts to explain fast reconnection rates based on non-dissipative terms, notably the Hall term, in the generalized Ohm's law in a 2D and laminar fashion.

Despite its popularity and long history, however, direct identifications of turbulence in the dissipation region, either in laboratory plasmas or space astrophysical plasmas, have been lacking until recently. In this paper, a short summary of recent progress in direct measuring turbulence in reconnecting current sheets of a laboratory plasma is given. It was found that electromagnetic turbulence, in contrast to electrostatic turbulence, does positively correlate with resistivity enhancement, and thus the reconnection rate. The observed electromagnetic turbulence may exhibit similarities with *in situ* satellite measurements at bow shocks in Earth's or other solar planets' magnetosphere. This suggests that electromagnetic turbulence may play an important role not only for reconnection but also for collisionless shocks, which are more common in energetic astrophysical phenomena.

2. Measurements of Turbulence in Reconnecting Current Sheets

The Magnetic Reconnection Experiment (MRX) (Yamada et al., 1997) is a laboratory experiment dedicated for the study of basic physics of magnetic reconnection.

Oppositely directed field lines are brought together by externally controlled electric circuits in a globally two-dimensional geometry. The resulting magnetic reconnection takes place at a rate determined primarily by plasma dynamics in the dissipation region, whose parameters can be largely controlled. An extensive set of diagnostics measure spatial profiles of almost every important quantifies including magnetic field, electric field, plasma density and temperatures. Thus, quantitative determination of reconnection rates and their comparisons with theoretical models were possible. It was found (Ji et al., 1998) that the measured rates can be explained by a modified Sweet–Parker model, which uses the experimentally determined resistivity, η^*. In highly collisional plasmas, η^* is very close to the classical Spitzer perpendicular resistivity η_{Spitzer} while $\eta^* \gg \eta_{\text{Sptizer}}$ when the collisionality is reduced (Ji et al., 1998). Therefore, if resistivity is enhanced by turbulence, the turbulence needs to be active in the dissipation region and its amplitude should correlate positively with resistivity enhancement.

The candidate instabilities (Biskamp, 2000) for the resistivity enhancement have been considered to be predominantly electrostatic in nature due to their effectiveness in wave–particle interactions. The primary candidate is the electrostatic lower-hybrid drift instability (LHDI) (Krall and Liewer, 1971), which has been frequently observed in space plasmas (Gurnett et al., 1976). Direct measurements at MRX showed (Carter et al., 2002) that the observed turbulence is indeed consistent with characteristics predicted by this LHDI. However, the measured electrostatic turbulence is active only in the low-β edge region of current sheet, but *not* in the high-β central region, where the resistivity needs to be enhanced for fast reconnection. This conclusion is consistent with an earlier theory (Davidson et al., 1977) which showed stabilization of LHDI by finite plasma β, and also with more recent numerical simulations (Horiuchi and Sato, 1999; Lapenta and Brackbill, 2002). Furthermore, the measured electrostatic turbulence level does not correlate with collisionality and thus the resistivity enhancement.

By contrast, the measured electromagnetic turbulence exhibits characteristics consistent with requirements for the resistivity enhancement (Ji et al., 2004). Example raw signals are shown in Figure 2 during a single discharge. High-frequency fluctuations appear in all three components of magnetic field when the current sheet moves closer to the probe. Spectrograms, which display the fluctuation power in the time–frequency domain, are shown in the right panels of Figure 2. It is seen that multiple peaks exist in the range of the lower-hybrid frequency $f_{\text{LH}} \equiv \sqrt{f_{\text{ce}} f_{\text{ci}}}$ (shown as black lines) using the upstream reconnecting magnetic field, B_{up}. The spatial profiles of the fluctuation amplitude were determined by repeating measurements at various location in similar plasma discharges. It was found (Ji et al., 2004) that the turbulence amplitude peaks at the center of the dissipation region, in sharp contrast with the electrostatic turbulence which resides only at the edge (Carter et al., 2002).

Propagation characteristics of the observed electromagnetic turbulence have been measured in detail. The direction of the wavenumber vector was determined by the hodogram technique while the wavelength was determined by phase shift

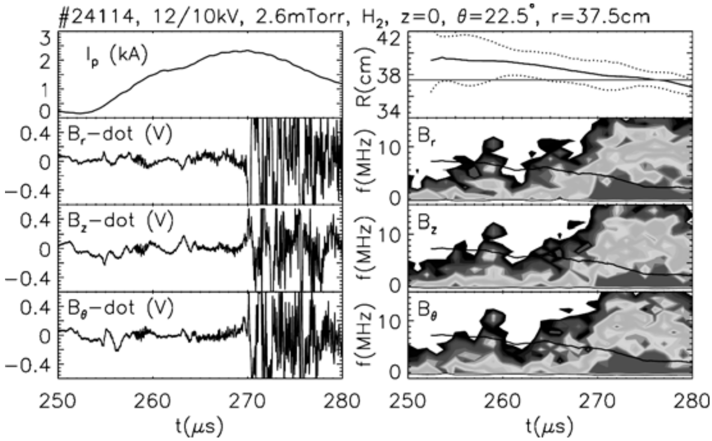

Figure 2. Traces of typical raw signals during reconnection represented by plasma current (top left panel). Spectrograms of each signal are shown on the middle panels where fluctuation powers are color-coded (decreasing power by order of red, yellow, green, blue and white) in the time–frequency domain. The black lines indicate local f_{LH} at the probe. The top right panel displays locations of the probe (red line) and the current sheet (center as black solid line and edges as dashed lines). When the current sheet center moves close to the probe, high-frequency magnetic fluctuations are detected.

measurements at two spatial locations. It is found that most waves propagate within a 90° angle of the background magnetic field direction (∼30 to ∼60° with varying spreads depending on frequency), consistent with right-hand polarized fast (whistler) waves when $f > f_{\mathrm{ci}}$ (Stix, 1992). The phase velocity points in the electron drift direction with amplitudes comparable to the relative drift velocity. Therefore, the observed electromagnetic turbulence was identified as right-hand polarized whistler waves propagating obliquely to the magnetic field.

In order to study the relationship of the observed electromagnetic turbulence with the fast reconnection, a series of experiments were conducted varying the plasma density, and thus the collisionality. It is found that the amplitude of magnetic turbulence is sensitive to collisionality. When the density is reduced from $\sim 5 \times 10^{19}\,\mathrm{m}^{-3}$ to $\sim 2 \times 10^{18}\,\mathrm{m}^{-3}$, $|\tilde{B}_Z|$ increases from 0.1 G (close to the noise level for the measurements) to ∼1 G. Since the resistivity enhancement also strongly depends on the plasma collisionality (Ji et al., 1998), a clear positive correlation between magnetic turbulence and resistivity enhancement is established, as shown in Figure 3. In addition, there is experimental evidence for local non-classical electron heating (Ji et al., 2004).

3. Theoretical Insight into Magnetic Turbulence

Given the experimental data described above, it is clear that the observed electromagnetic turbulence is produced by instabilities driven by large V_{d} and/or large

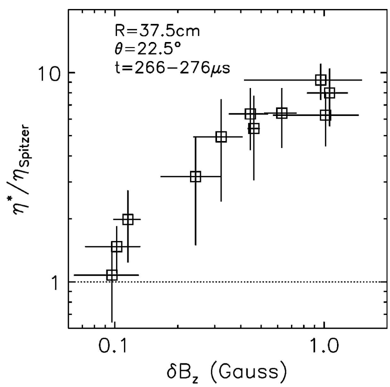

Figure 3. $\tilde{B}_Z$ amplitude versus resistivity enhancement at the current sheet center.

inhomogeneities. The most likely candidate among the known instability seem to be an electromagnetic version of the modified two-stream instability (MTSI) in the high-β limit (Ross, 1970; Krall and Liewer, 1971; Wu et al., 1983; Basu and Coppi, 1992; Yoon and Lui, 1993). When β is large (>1), LHDI is stabilized (Davidson et al., 1977) while MTSI remains unstable but with the Alfvén speed V_A replacing the ion sound (or thermal) speed as the critical drift speed. The resultant waves are largely electromagnetic and right-hand polarized whistler-like waves propagating obliquely to the field with $V_{ph} \sim V_d$ (Ross, 1970). Under the conditions $\beta > 1$ and $V_d/V_A > 5$ as in MRX, the waves are unstable only at certain propagation angles to the field (Wu et al., 1983; Basu and Coppi, 1992). Many basic features from the measurements, such as the multiple peaks in the frequency spectra (Figure 2), are consistent with more recent global eigenmode calculations (Yoon et al., 2002; Daughton, 2003).

In order to gain physical insight into these instabilities, a local two-fluid model (Ji et al., 2005, submitted) with finite relative drifts has been constructed using unmagnetized ions and magnetized electrons. Unlike in the typical treatment of MTSI, finite pressure and magnetic field gradients are taken into account self-consistently. This model describes four waves above the ion cyclotron frequency: two fast or whistler waves associated with the electron fluid and two slow or sound waves associated with the ion fluid. Each wave has one forward propagating and another backward propagating branch with regard to the magnetic field. With no relative drifts, these waves are separated in the (ω, k) space, and thus are stable. However, a finite cross-field drift between ions and electrons can cause two of branches (backward propagating whistler waves and forward propagating sound waves) to couple, resulting in an instability as shown in Figure 4. Thus characteristics of the unstable waves are mixture of both fast and slow waves including their polarizations and they typically possess significant electromagnetic components. This instability is only unstable in certain ranges for wavenumber. Their propagation angles lye in a range different from the electrostatic, perpendicular LHDI, consistent with experiments

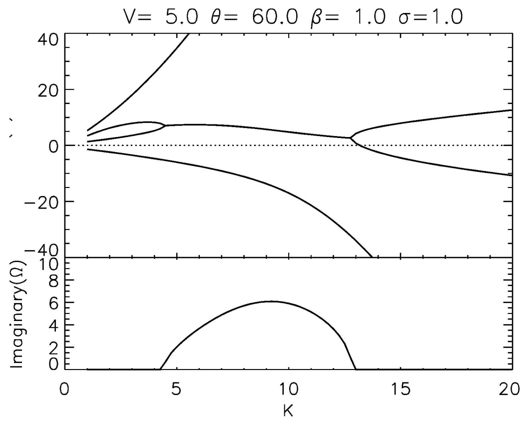

Figure 4. Dispersion relation of an unstable mode due to interception of slow and fast waves by large drafts between ions and electrons in a simple two-fluid model. Real frequency (top, normalized by the ion cyclotron frequency) and growth rate (bottom) are plotted versus wavenumber, k (normalized by the ion skin depth). Other parameters are: $V_d = 5V_A$, $\beta_e = 1$, $T_i = T_e$, and the angle between $\mathbf{k}$ and $\mathbf{B}$, $\theta = 60°$.

(Ji et al., 2004). Furthermore, quasi-linear theory (Kulsrud et al., 2005, submitted) shows that this instability can be important in producing the needed resistivity to explain the fast-reconnection in the MRX.

4. Magnetic Turbulence in Collisionless Shocks

The role of turbulence is also considered to be important in another class of phenomena in astrophysical plasmas: collisionless shocks (e.g. Tidman and Krall, 1971). Large scale structures are considerably different from those of magnetic reconnection, as illustrated in Figure 5, since the main process in a shock is to convert flow energy into heat while magnetic reconnection converts energies in large-scale magnetic field to the flow energy and eventually to heat. However, there is a similarity between all of these processes: existence of large magnetic field gradients, or

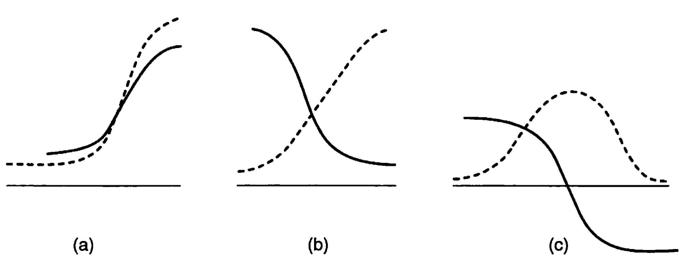

Figure 5. Illustration of differences and similarities of magnetic reconnection and magnetic shocks. Magnetic field (solid line) and pressure (dotted line) both increase in fast shocks (a) while pressure increases with decreasing magnetic field in slow shocks (b) or magnetic reconnection (c).

large electric currents and thus the large relative drifts. In the case of fast shocks, compression transfers flow energy to magnetic energy which can dissipate into heat if there is turbulence supported by efficient current-driven instabilities. In fact, the aforementioned electromagnetic MTSI was largely investigated in search for dissipation mechanisms in collisionless shocks (Ross, 1970; Wu et al., 1983; Basu and Coppi, 1992), motivated by the observations (Gurnett, 1985) of magnetic turbulence at the bow shock region of the Earth and other solar planets. Understanding physics and role of the underlying electromagnetic turbulence in magnetic reconnection may help to solve problems of collisionless shocks, which are common in energetic astrophysical phenomena.

5. Summary

Measurements and the physical understanding of turbulence in the dissipation region of magnetic reconnection in a dedicated laboratory experiment are summarized. A clear and positive correlation between high-frequency electromagnetic turbulence and fast reconnection has been established. The waves have been identified as right-hand polarized whistler waves, propagating obliquely to the reconnecting field, with a phase velocity comparable to the relative drift velocity. These waves are consistent with an obliquely propagating electromagnetic lower-hybrid drift instability, which results from the coupling of fast and slow waves and is driven by large drift speeds between ions and electrons. The observed turbulence may produce the needed resistivity (Kulsrud et al., 2005, submitted) and may share commonalities with magnetic turbulence in collisionless shocks.

Acknowledgments

The authors are grateful to Dr. S. Bale for useful discusions. This work was jointly supported by DOE, NASA, and NSF.

References

Basu, B. and Coppi, B.: 1992, *J. Geophys. Res.* **97**, 17033.

Birn, J., Drake, J., Shay, M., Rogers, B., Denton, R., Hesse, M., Kuznetsova, M., Ma, Z., Bhattachargee, A., Otto, A. and Pritchett, P.: 2001, *J. Geophys. Res.* **106**, 3715.

Biskamp, D.: 1986, *Phys. Fluids* **29**, 1520.

Biskamp, D.: 2000, *Magnetic Reconnection in Plasmas*, Cambridge University Press, Cambridge.

Biskamp, D. and Schwarz, E.: 2001, *Phys. Plasmas* **8**, 4729.

Carter, T, Ji, H., Trintchouk, F., Yamada, M. and Kulsrud, R.: 2002, *Phys. Rev. Lett.* **88**, 015001.

Daughton, W.: 2003, *Phys. Plasmas* **10**, 3103.

Davidson, R., Gladd, N., Wu, C. and Huba, J.: 1977, *Phys. Fluids* **20**, 301.

Gurnett, D.: 1985, in: B. Tsurutani and R. Stone (eds.), *Collisionless Shocks in the Heliosphere: Review of Current Research*, American Geophysics Union, Washington, p. 207.
Gurnett, D., Frank, L. and Lepping, R.: 1976, *J. Geophys. Res.* **81**, 6059.
Horiuchi, R. and Sato, T.: 1999, *Phys. Plasmas* **6**, 4565.
Ji, H., Yamada, M., Hsu, S. and Kulsrud, R.: 1998, *Phys. Rev. Lett.* **80**, 3256.
Ji, H., Terry, S., Yamada, M., Kulsrud, R., Kuritsyn, A. and Ren, Y.: 2004, *Phys. Rev. Lett.* **92**, 115001.
Ji, H., Kulsrud, R. and Yamada, M.: 2005, submitted to *J. Geophys. Res.*
Krall, N. and Liewer, P.: 1971, *Phys. Rev. A* **4**, 2094.
Kulsrud, R.: 2001, *Earth Planets Space* **53**, 417.
Kulsrud, R., Ji, H., Fox, W. and Yamada, M.: 2005, submitted to *Phys. Plasmas*.
Lapenta, G. and Brackbill, J.: 2002, *Phys. Plasmas* **9**, 1544.
Parker, E.: 1957, *J. Geophys. Res.* **62**, 509.
Petschek, H.: 1964, *NASA Spec. Pub.* **50**, 425.
Ross, D.W.: 1970, *Phys. Fluids* **13**, 746.
Scholer, M.: 1989, *J. Geophys. Res.* **94**, 8805.
Stix, T.: 1992, *Waves in Plasmas*, American Institute of Physics, New York.
Sweet, P.: 1958, in: B. Lehnert (ed.), *Electromagnetic Phenomena in Cosmical Physics*, Cambridge University Press, New York, p. 123.
Tidman, D. and Krall, N.: 1971, *Shock Waves in Collisionless Plasmas*, Wiley, New York.
Ugai, M. and Tsuda, T.: 1977, *J. Plasma Phys.* **17**, 337.
Uzdensky, D. and Kulsrud, R.: 2000, *Phys. Plasmas* **7**, 4018.
Wu, C., Zhou, Y, Tsai, S. and Guo, S.: 1983, *Phys. Fluids* **26**, 1259.
Yamada, M., Ji, H., Hsu, S., Carter, T, Kulsrud, R., Bretz, N., Jobes, F., Ono, Y and Perkins, F.: 1997, *Phys. Plasmas* **4**, 1936.
Yoon, P. and Lui, A.: 1993, *Phys. Fluids B* **5**, 1993.
Yoon, P., Lui, A. and Sitnov, M.: 2002, *Phys. Plasmas* **9**, 1526.

DIRECT-DRIVE INERTIAL CONFINEMENT FUSION IMPLOSIONS ON OMEGA

S.P. REGAN[1], T.C. SANGSTER[1], D.D. MEYERHOFER[1], K. ANDERSON[1], R. BETTI[1], T.R. BOEHLY[1], T.J.B. COLLINS[1], R.S. CRAXTON[1], J.A. DELETTREZ[1], R. EPSTEIN[1], O.V. GOTCHEV[1], V.YU. GLEBOV[1], V.N. GONCHAROV[1], D.R. HARDING[1], P.A. JAANIMAGI[1], J.P. KNAUER[1], S.J. LOUCKS[1], L.D. LUND[1], J.A. MAROZAS[1], F.J. MARSHALL[1], R.L. MCCRORY[1], P.W. MCKENTY[1], S.F.B. MORSE[1], P.B. RADHA[1], W. SEKA[1], S. SKUPSKY[1], H. SAWADA[1], V.A. SMALYUK[1], J.M. SOURES[1], C. STOECKL[1], B. YAAKOBI[1], J.A. FRENJE[2], C.K. LI[2], R.D. PETRASSO[2] and F.H. SÉGUIN[2]

[1]*Laboratory for Laser Energetics, University of Rochester, 250 East River Road, Rochester, New York; E-mail: sreg@lle.rochester.edu*

[2]*Plasma Science and Fusion Center, MIT, MA*

(Received 28 April 2004; accepted 19 July 2004)

Abstract. Direct-drive inertial confinement fusion (ICF) creates extreme states of matter. In current direct-drive cryogenic target implosions on the 60-beam OMEGA laser system, the compressed target has a measured pressure of 5 Gbar. These targets are hydrodynamically scaled from ignition targets for the National Ignition Facility. The ignition targets are predicted to have peak pressures of 3 Tbar after the target ignites. ICF target acceleration and deceleration are realized when hot, low-density plasma pushes against cold, high-density plasma, making the target implosion inherently susceptible to the Rayleigh–Taylor hydrodynamic instability (RTI). The unstable RTI growth causes mixing of cold, high-density shell plasma with the low-density, hot-spot plasma and reduces the primary neutron yield of the implosion. The strategy to control the RTI growth is to reduce the seeds (e.g., laser imprint and target-surface roughness) and the growth rates of the dominant modes. This paper reports on our recent experiments, progress in validating the hydrodynamics codes that are used to design future high-gain cryogenic DT targets, and techniques to improve target performance. A brief description is given of a new high energy petawatt laser – OMEGA EP (extended performance) – that is being added to the OMEGA compression facility.

1. Introduction

Extreme states of matter are created with direct-drive inertial confinement fusion (ICF), whereby a spherical shell target containing thermonuclear fuel is imploded (Lindl, 1998; McKenty, 2001). In current direct-drive cryogenic D_2 target implosions on the 60-beam, 30-kJ, 351-nm OMEGA laser system (Boehly et al., 1997), the compressed target has a measured pressure $\sim$5 Gbar (Smalyuk et al., 2004). Implosions of cryogenic-surrogate, D_2-gas-filled plastic shells generate slightly higher pressures of $\sim$10 Gbar (Regan et al., 2002a). These targets are hydrodynamically scaled from ignition targets for the 1.8-MJ National Ignition

Astrophysics and Space Science **298:** 227–233, 2005.

Facility (NIF) (McKenty et al., 2001). One of the primary missions of the NIF is to demonstrate ignition and energy gain using ICF targets (Campbell and Hogan, 1999). The "all-DT" direct-drive ignition target design for the NIF is predicted to generate a peak pressure of $\sim$3 Tbar in the laboratory after the target ignites and a gain of 30 or more (McKenty et al., 2001). To put these numbers in perspective, pressures of $\sim$1 Tbar are characteristic of stellar interiors.

Thermonuclear ignition in the laboratory requires a physical understanding of the entire implosion process, especially the effects of the Rayleigh–Taylor instability (RTI) (Betti et al., 1998; Bodner, 1998; Lindl, 1998, Goncharov et al., 2003). A general description of direct-drive ICF is given in Section 2. The main purpose of the direct-drive-implosion experiments on OMEGA is to validate the hydrodynamics codes that are used to design future high-gain, cryogenic DT targets. In Section 3 the "all-DT" direct-drive ICF ignition target design planned for the NIF is presented. The implosions of scaled cryogenic and warm surrogate targets are discussed in Section 4. Finally, in Section 5, a brief description of the new high-energy petawatt laser – OMEGA EP (extended performance) – that is being added to the OMEGA compression facility for experiments beginning in 2007 is given. OMEGA EP will expand research capabilities in high-energy-density physics (HEDP) (NRC report, 2003) at the Laboratory for Laser Energetics (LLE).

2. Direct-Drive ICF Implosions

A direct-drive implosion is initiated by the ablation of material from the outer surface of a spherical shell containing thermonuclear fuel with intense laser beams (McKenty et al., 2001). The ablated shell mass forms a coronal plasma that surrounds the target and accelerates the shell inward via the rocket effect (Lindl, 1998). Since ICF target acceleration and subsequent deceleration are realized when hot, low-density plasma pushes against cold, high-density plasma, the target implosion is inherently unstable to the RTI (Bodner, 1998; Lindl, 1998; McKenty et al., 2001). The implosion can be divided into four stages: early time, acceleration phase, deceleration phase, and peak compression. Perturbation seeds early in the implosion from laser imprint, laser drive asymmetry, and the outer/inner shell surface roughness determine the final capsule performance. As the shell accelerates inward, perturbations at the ablation surface are amplified by the ablative RTI. These perturbations feed through the shell during the acceleration phase and seed the RTI of the deceleration phase at the inner shell surface (Marinak, 1996). When the higher-density shell converges toward the target center and is decelerated by the lower-density fuel (hot spot), the classical RTI causes mixing of the shell material or pusher with the fuel in the outer regions of the hot spot (i.e., mix region) (Regan et al., 2002a). Modulations also grow due to Bell–Plesset convergent effects throughout the implosion (Bell, 1951; Plesset, 1954). The thermonuclear fusion rate in the resulting central hot spot, which is confined by the inertia of the cold, dense shell, reaches its maximum value just before peak compression, when the fuel temperature peaks. The target performance is diagnosed with neutronics (Meyerhofer, 2001), charged-particle spectroscopy (Li, 2002; Séguin, 2003), X-ray spectroscopy (Regan, 2002b), and X-ray imaging (Smalyuk, 2001). Ultimately, the RTI can disrupt the central hot-spot formation and reduce the yield by mixing cold, high-density shell plasma with hot, low-density, hot-spot plasma. An understanding of the RTI-induced mix and developing ways to control it are of great importance to ICF and the ultimate goal of thermonuclear ignition in the laboratory.

The unstable RTI growth is controlled by reducing the seeds (e.g., laser imprint and target surface roughness) and the growth rates of the dominant modes. The growth rates have been characterized in planar (Glendinning, 1997; Smalyuk, 1998; Pawley, 1999), cylindrical (Hsing, 1997; Dimonte, 1999), and spherical (Glendinning, 2000; Smalyuk, 2001) target-experiments. Laser imprint is substantially reduced with 1-THz, 2-D smoothing by spectral dispersion (Skupsky, 1989; Skupsky and Craxton, 1999) and polarization smoothing (Boehly, 1999; Regan et al., 2004). In a cryogenic target, perturbations of the inner ice surface also seed the RTI. Extensive research and development has produced ice-layer finishes (Meyerhofer, 2003) approaching the 1-μm NIF requirement for ignition targets (McKenty et al., 2004).

The RTI growth rate is expressed as $\gamma = \alpha_{\mathrm{RT}}\sqrt{kg} - \beta_{\mathrm{RT}} k V_{\mathrm{a}}$, where $\alpha_{\mathrm{RT}} = 0.94$ and $\beta_{\mathrm{RT}} = 2.6$ for a DT ablator, k is the perturbation wave number, g is the acceleration, and the ablation velocity V_{a} is proportional to $\alpha^{3/5}$, where the adiabat α or isentrope parameter of the shell is defined as the ratio of the shell pressure to the Fermi-degenerate pressure (Betti et al., 1998). Clearly, increasing α at the ablation surface stabilizes the target by reducing γ. However, α at the inner portion of the shell determines the minimum energy required for ignition $E_{\mathrm{min}} \sim \alpha^{1.88}$ (Herrmann et al., 2001; Betti et al., 2002). If one considers a uniform α, there is a trade-off between target gain and stability. This trade off can be avoided by tailoring the adiabat of the shell to optimize γ and E_{min}. By shaping the adiabat α of the shell, the value of α is raised at the ablation surface to increase the ablation velocity V_{a} and reduce the RTI growth rate γ during the acceleration phase and is kept low in the shell to maintain the compressibility of the target and maximize the yield (Goncharov et al., 2003). Adiabat shaping is initiated by irradiating the target with a short ($\sim$100-ps), intense Gaussian laser pulse (picket) just prior to the foot of the main laser drive pulse (Goncharov et al., 2003).

3. Ignition Target Design

The "all-DT," $\alpha = 3$, direct-drive ICF ignition target design developed at LLE for the NIF is based on the principle of hot-spot ignition, whereby a cryogenic target with a spherical DT-ice layer enclosed by a thin plastic shell is directly irradiated with $\sim$1.5 MJ of laser energy (McKenty et al., 2001). A schematic of

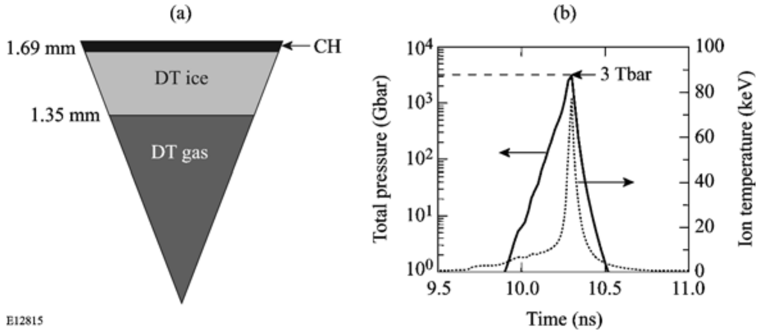

Figure 1. (a) Schematic of the NIF baseline direct-drive "all DT" target and (b) direct-drive-ignition conditions predicted with 1-D hydrodynamics code for this target design.

the target is presented in Figure 1(a). During the implosion the main fuel layer will compress the DT gas, forming a central hot spot. A thermonuclear burn wave is predicted to propagate through the main fuel layer when the fuel areal density and temperature of the central hot spot reach ~0.3 g/cm^2 and ~10 keV, respectively (Lindl, 1998). The ignition conditions predicted with a 1-D hydrodynamics code are plotted in Figure 1(b) for the "all-DT," direct-drive point design. This design has a 1-D predicted gain of 42. It ignites just after $t = 10.2$ ns and generates a peak pressure of 3 Tbar with a peak ion temperature of ~80 keV. The extreme state of matter predicted for the "all-DT," direct-drive ignition target for the NIF is plotted in Figure 2 for comparison with other plasmas in our universe. Therefore, in the next decade it will be possible to create plasmas on the NIF with pressures comparable to stellar interiors.

Adiabat shaping is being investigated for the "all-DT," direct-drive point design (McKenty et al., 2004). Recently, a 200-ps picket pulse was added to the design and simulated with the 2-D hydrodynamics code *DRACO*. When the 2-D effects of the anticipated levels of laser and target nonuniformities are included, the predicted gain was reduced to 30 without the picket. Adiabat shaping boosts the stability of this design and increases the 2-D predicted gain to 35.

4. Ignition-Scaled Implosions on OMEGA

Ignition target designs are being validated with scaled implosions on OMEGA. Cryogenic and plastic/foam (surrogate-cryogenic) targets that are hydrodynamically scaled from ignition target designs (laser energy ~ target radius^3, laser power ~ target radius^2, and time ~ target radius) are being imploded on OMEGA to investigate the key target physics issues of energy coupling, hydrodynamic instabilities, and implosion symmetry (Meyerhofer, 2001; Stoeckl, 2002; Sangster, 2003). The performance of imploded cryogenic D_2 capsules on OMEGA has been found to be

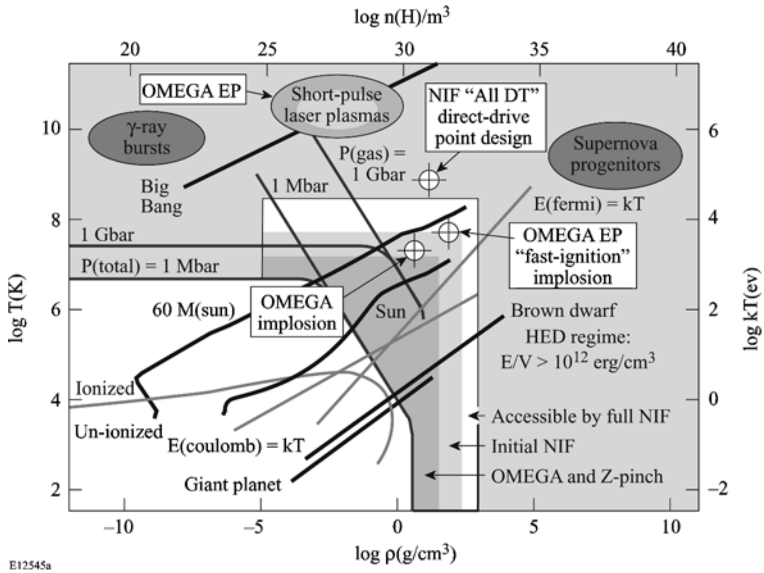

Figure 2. Extreme states of matter created with direct-drive ICF on OMEGA and the NIF plotted on the published density–temperature graph (NRC Report, 2003). *Figure courtesy of The National Academies Press* (*Washington, DC*).

close to the predictions of the 2-D hydrodynamics code *DRACO* (Sangster, 2003; McKenty et al., 2004). The hot-spot n_e and T_e profiles of an imploded cryogenic D_2 target were inferred with gated X-ray core images and secondary neutron measurements and are close to 1-D predictions (Smalyuk et al., 2004). The inferred isobaric core pressure is $\sim$5 Gbar.

The mixing of the cold, high-density shell plasma with the low-density, hot-spot plasma by the deceleration-phase RTI has been studied for implosions of gas-filled, plastic-shell targets. This instability causes a mix region to develop between the shell and the central hot spot. Many shell-mix diagnostics have been developed at LLE (Meyerhofer, 2001; Radha et al., 2002; Regan et al., 2002a; Li et al., 2002). In particular, a novel diagnostic technique that combines time-resolved X-ray spectroscopy, charged-particle spectroscopy, and X-ray imaging was used to quantify the density of plastic shell material in the mix region (Regan et al., 2002a). At the time of peak neutron production, the average electron density in the mix region was determined from the time-resolved, Ar *K*-shell spectroscopy, and the average fuel density in the core was determined from charged-particle spectroscopy. Only $\sim$50% of the measured electron density that was averaged over the neutron-burn width could be accounted for by the fuel. It was therefore concluded that the remaining electrons must come from the CH shell material that had mixed into the core (Regan et al., 2002a). Consequently, in addition to compression, the density in the core is increased by shell mix. This is consistent with the observation that the measured electron density was found to be higher than 1-D predictions (Regan et al., 2002b). The extreme state of matter generated in the core of OMEGA direct-drive implosions is highlighted in Figure 2 with peak pressures $\sim$10 Gbar.

5. OMEGA EP

A two-beam high-energy petawatt (HEPW) laser system is being constructed at the LLE. This two-beam (2.6-kJ per beam) laser will expand research capabilities in HEDP at LLE. The HEPW beams will be integrated into the OMEGA compression facility for experiments beginning in 2007. The beams will be available for experiments in either the OMEGA compression facility or a separate OMEGA EP target chamber. Many extreme states of matter will be created with OMEGA EP. Experiments designed to validate "fast ignition" (Tabak, 1994) will be performed with scaled cryogenic capsules. A high-density fuel configuration will be assembled with the OMEGA compression facility, and the OMEGA EP will produce suprathermal electrons via high-intensity laser–plasma interaction to heat the core. OMEGA EP will extend the diagnostic capability within the existing OMEGA target chamber and complement the significant progress that has been made toward "hot-spot" ignition. Radiographic diagnostic capability will be developed with OMEGA EP for implosions with high fuel areal densities, and for HEDP relevant experiments on the NIF. The relativistic particle generation and acceleration associated with the laser plasmas produced with the ultrahigh intensities will be investigated. The regions of the density–temperature plane that will be explored with the short-pulse laser plasmas and fast-ignition implosions created with OMEGA EP are plotted in Figure 2.

6. Conclusions

Direct-drive inertial confinement fusion creates extreme states of matter. Thermonuclear ignition in the laboratory requires a physical understanding of the entire implosion process, especially the effects of Rayleigh–Taylor instability. Direct-drive-implosion experiments on OMEGA are performed to validate the hydrodynamics codes that are used to design future high-gain cryogenic DT targets on the NIF. The "all-DT" direct-drive ignition target design for the NIF is predicted to generate a peak pressure of $\sim$3 Tbar in the laboratory after the target ignites and a gain of 30 or more. A new high-energy petawatt laser – OMEGA EP – will expand the research capabilities in high-energy-density physics at LLE.

Acknowledgements

The authors are extremely grateful to the staff of the Laboratory for Laser Energetics for their dedicated efforts in developing and providing the high-performance

OMEGA laser system and the cryogenic implosion program. This work was supported by the U.S. Department of Energy Office of Inertial Confinement Fusion under Cooperative Agreement No. DE-FC03-92SF19460.

References

Bell, G.I.: 1951, Los Alamos National Laboratory, Los Alamos, CA, Report LA-1321.
Betti, R. et al.: 1998, *Phys. Plasmas* **5**, 1446.
Betti, R. et al.: 2002, *Phys. Plasmas* **9**, 2277.
Bodner, S.E. et al.: 1998, *Phys. Plasmas* **5**, 1901.
Boehly, T.R. et al.: 1997, *Opt. Commun.* **133**, 495.
Boehly, T.R. et al.: 1999, *J. Appl. Phys.* **85**, 3444.
Campbell, M.D. and Hogan, W.J.: 1999, *Plasma Phys. Control. Fusion* **41**, B39; Dimonte G.: 1999, *Phys. Plasmas* **6**, 2009.
Glendinning, S.G. et al.: 1997, *Phys. Rev. Lett.* **78**, 3318.
Glendinning, S.G. et al.: 2000, *Phys. Plasmas* **7**, 2033.
Goncharov, V.N. et al.: 2003, *Phys. Plasmas* **10**, 1906.
Herrmann, M.C., Tabak, M. and Lindl, J.D.: 2001, *Phys. Plasmas* **8**, 2296.
Hsing, W.W. et al.: 1997, *Phys. Plasmas* **4**, 1832.
Li, C.K. et al.: 2002, *Phys. Rev. Lett.* **89**, 165002.
Lindl, J.D.: 1998, *Inertial Confinement Fusion: The Quest for Ignition and Energy Gain using Indirect Drive*, New York, Springer-Verlag.
Marinak, M.M. et al.: 1996, *Phys. Plasmas* **3**, 2070.
McKenty, P.W. et al.: 2001, *Phys. Plasmas* **8**, 2315.
McKenty, P.W. et al.: "Direct-drive cryogenic target implosion performance on OMEGA," *Phys. Plasmas* (to be published).
Meyerhofer, D.D. et al.: 2001, *Phys. Plasmas* **8**, 2251.
Meyerhofer, D.D. et al.: 2003, *Bull. Am. Phys. Soc.* **48**, 55.
National Research Council (U.S.) Committee on High Energy Density Plasma Physics, *Frontiers in High Energy Density Physics: The X-Games of Contemporary Science*, 2003, National Academies Press, Washington, DC.
Pawley, C.J. et al.: 1999, *Phys. Plasmas* **6**, 565.
Plesset, M.S.: 1954, *J. Appl. Phys.* **25**, 96.
Radha, P.B. et al.: 2002, *Phys. Plasmas* **9**, 2208.
Regan, S.P. et al.: 'Performance of 1-THz-bandwidth, 2-D smoothing by spectral dispersion and polarization smoothing of high-power, solid-state laser beams', *J. Opt. Soc. Am. B* (submitted).
Regan, S.P. et al.: 2002a, *Phys. Rev. Lett.* **89**, 085003.
Regan, S.P. et al.: 2002b, *Phys. Plasmas* **9**, 1357.
Sangster, T.C. et al.: 2003, *Phys. Plasmas* **10**, 1937.
Stoeckl, C. et al.: 2002, *Phys. Plasmas* **9**, 2195.
Séguin, F.H. et al.: 2003, *Rev. Sci. Instrum.* **74**, 975.
Skupsky, S. et al.: 1989, *J. Appl. Phys.* **66**, 3456.
Skupsky, S. and Craxton R.S.: 1999, *Phys. Plasmas* **6**, 2157.
Smalyuk, V.A. et al.: 'Hot-core characterization of the cryogenic D_2 target at peak neutron production in direct-drive spherical implosion', *Phys. Rev. Lett.* (submitted).
Smalyuk, V.A. et al.: 1998, *Phys. Rev. Lett.* **81**, 5342.
Smalyuk, V.A. et al.: 2001, *Phys. Rev. Lett.* **87**, 155002.
Tabak, M. et al.: 1994, *Phys. Plasmas* **1**, 1626.

ACCESSING HIGH PRESSURE STATES RELEVANT TO CORE CONDITIONS IN THE GIANT PLANETS

B.A. REMINGTON, R.M. CAVALLO, M.J. EDWARDS, D.D.-M. HO, B.F. LASINSKI, K.T. LORENZ, H.E. LORENZANA, J.M. MCNANEY, S.M. POLLAINE and R.F. SMITH

Lawrence Livermore National Laboratory, Livermore, CA 94550

(Received 30 April 2004; accepted 13 June 2004)

Abstract. We have designed an experimental technique to use on the National Ignition Facility (NIF) laser to achieve very high pressure ($P_{\max} > 10\,\text{Mbar} = 1000\,\text{GPa}$), dense states of matter at moderate temperatures ($T < 0.5\,\text{eV} = 6000\,\text{K}$), relevant to the core conditions of the giant planets. A discussion of the conditions in the interiors of the giant planets is given, and an experimental design that can approach those conditions is described.

Keywords: laboratory astrophysics, giant planets, planetary core conditions, isentropic compression, National Ignition Facility

The interior structure of the giant planets, Jupiter, Saturn, Uranus, and Neptune, (Guillot, 1999) and the newly discovered extrasolar planets (Lissauer, 2002), is determined by the compressibility of their constituent matter under the very high pressures due to the inwardly directed force of gravity. In laboratory terms, this compressibility is determined by the equation of state (EOS) of the constituent matter along an isentrope (Saumon, 2004). The EOS and other properties of matter at the extreme pressures and densities found in the interiors of the giant planets, however, are quite uncertain. The pressures of interest along an isentrope range from 1–8 Mbar in Uranus and Neptune, 1–10 Mbar or more in Saturn, to 1–40 Mbar or more in Jupiter, as shown in Figure 1 (Guillot, 1999). Under these conditions, dense plasmas are both strongly coupled and Fermi degenerate (Van Horn, 1991). Characteristic isentropes for the giant planets indicate that the plasma in their interiors is both strongly coupled [$\Gamma = (Ze)^2/aT > 1$, where Z, e, a, and T correspond to ionization state, electron charge, average atomic spacing, and temperature (in units of energy)] and degenerate ($T/\varepsilon_F < 1$, where ε_F is the Fermi energy). Hence, the internal structure, $\rho(r)$, $T(r)$, of the giant planets is determined by the EOS of dense, degenerate plasma mixtures at very high pressures, $P = 1$ to 40 Mbar, and moderate temperatures, $T \leq 1$ eV.

Different theories of the EOS of dense, high pressure matter lead to different predictions about the interior conditions of the giant planets, (Saumon and Guillot, 2004) and more generally, may differentiate between different planetary formation

Astrophysics and Space Science **298:** 235–240, 2005.

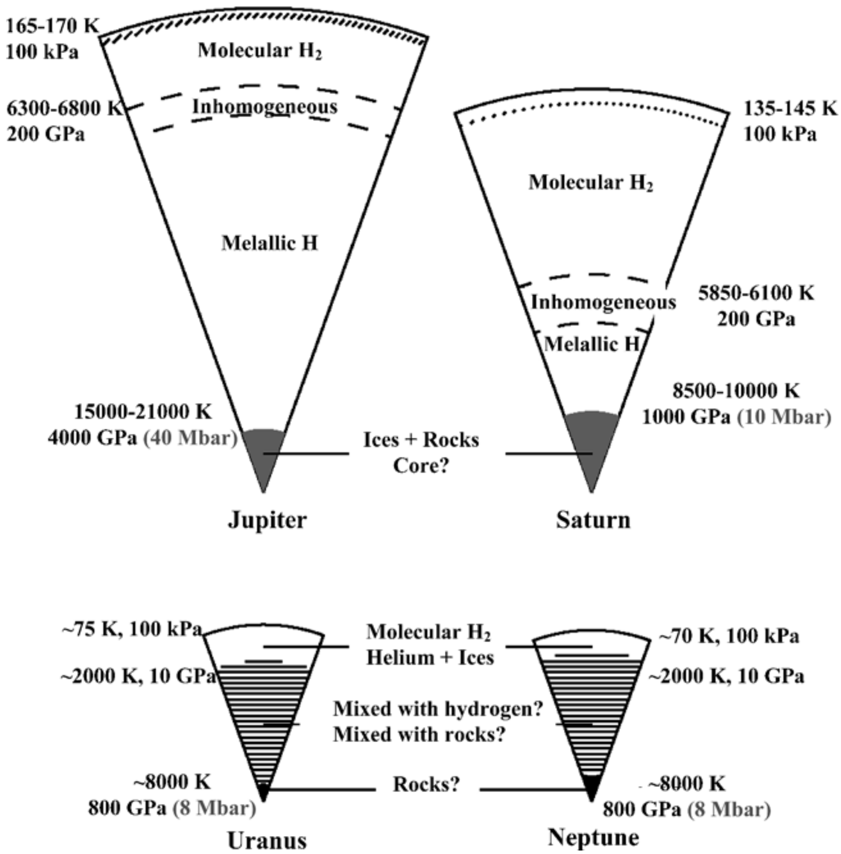

Figure 1. Schematic representation of the interiors of Jupiter, Saturn, Uranus, and Neptune. The range of temperatures for Jupiter and Saturn is taken from models neglecting the presence of the inhomogeneous region. The size of the central rock and ice cores of Jupiter and Saturn is very uncertain. Two representative models of Uranus and Neptune are shown, but their actual interior structure may be significantly different. The figure is reproduced from (Guillot, 1999). Reprinted with permission from Guillot, T.: 1999, Science 286, 72. Copyright 1992, AAAS.

models (Guillot et al, 1997). The EOS of dense, strongly coupled, degenerate plasma is notoriously difficult to calculate from first-principles theories, however, and many uncertainties remain. One of the open questions about the interiors of Jupiter and Saturn, for example, is whether there is a first order plasma phase transition (PPT) between a molecular, dielectric hydrogen mantle and a monatomic, ionized (conducting) hydrogen core over the pressure range of 0.5–5 Mbar. Another open question is whether the He and other higher-Z elements in solution with H condense out (become immiscible) into droplets at sufficiently high pressures and densities. These condensation droplets would sink radially inwards like rain, releasing gravitational potential energy, and serve as an internal heat source for the planet. In the case of the "ice giants" Uranus and Neptune, the uncertainties are even larger. These planets contain much larger fractions of heavier elements and compounds, such as CH_4, NH_3, and H_2O, largely in the form of ice, whose properties and EOS at very high pressures and densities are even more uncertain.

Experiments are vital to improve our understanding of the interior structures of the giant planets. The most widely used experimental technique for determining high-pressure EOS are through the use of shock waves to determine the principle Hugoniot of materials, (Collins et al., 1998; Knudson et al., 2001; Boehly, 2004) or diamond anvil cells (DAC) to determine isothermal compression (Henley and Mao, 2002). The difficulty with strong shocks is that the compressed states are produced at too high a temperature. The difficulty with DAC experiments is the relatively low pressures achieved. What is needed is an experimental technique to produce high-pressure compression at lower temperatures, closer to an isentrope.

We report here on our designs to use the National Ignition Facility (NIF) laser (Hogan et al., 2001) to create a very high pressure ($P > 10\,\mathrm{Mbar} = 10^3\,\mathrm{GPa}$), nearly isentropic "drive" to access high density, modest temperature ($kT <\sim 0.5\,\mathrm{eV}$) conditions similar to those at the cores of the giant planets. The planar target in this design, shown in the inset of Figure 2, was assumed to be a 1.6 mm thick carbon "reservoir" with a density of $1.0\,\mathrm{g/cm^3}$ followed by a 2 mm vacuum gap, then the "payload". The payload consists of a thin CH (2% Br) heat shield at density of $1.2\,\mathrm{g/cm^3}$, followed by the sample under study, then a tamper material. For the purposes of roughing out a design to determine the approximate laser and target parameters required, the sample was assumed to be 100 μm thick Ta, backed by a thick ($\sim$500 μm) Mo tamper. The laser was assumed to be incident on the front face of the reservoir (i.e., the side facing away from the payload) at an intensity of $6.5 \times 10^{13}\,\mathrm{W/cm^2}$ in a 78 ns square pulse in a 3.5 mm diameter flat spot. This would require 0.6–0.9 MJ of laser energy using half of NIF in single-sided illumination

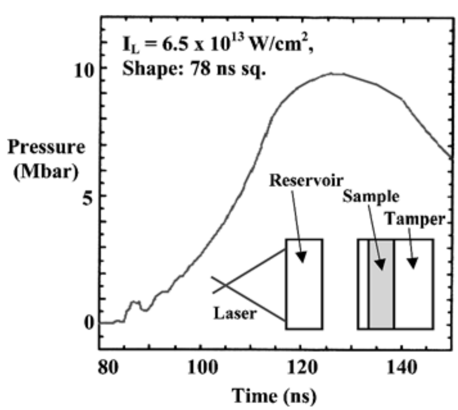

Figure 2. Theoretical design for a ramped pressure pulse drive for the NIF laser, utilizing about 0.6–0.9 MJ of laser energy. Pressure in the leading zones of the Ta sample vs. time, showing a peak pressure of $\sim$10 Mbar with a rise time of 25–30 ns. The inset shows the target configuration.

to drive the compression wave, which just fits within the predicted performance specifications of NIF. This leaves the other half of NIF to drive backlighters, that is, separate synchronized sources of hard X-rays for diagnosis.

The ensuing dynamics from the target configuration (shown in the inset of Figure 2) is described as follows. The laser pulse ablatively drives a strong shock through the low-Z reservoir. When the shock reaches the backside of the reservoir (the side opposite from where the laser was incident), the reservoir unloads into vacuum as plasma “ejecta”. The pressure that is applied to the sample results from the increasing ram pressure, $P_{\mathrm{ram}} = \rho_{\mathrm{ejecta}}\, v_{\mathrm{ejecta}}^2$, as the ejecta plasma stagnates and accumulates on the payload. This pressure increases smoothly with time as the reservoir unloads, until the reservoir material is depleted. We have successfully demonstrated this laser-based technique for generating a high pressure ramped load at the Omega laser over a range of pressures spanning $P_{\max} = 0.1$–2 Mbar (Edwards et al., 2004; Lorenz et al., 2004; Smith, 2004). This laser-based technique for generating a ramped pressure wave was motivated by the early work of Barnes using high-explosives as the energy source for driving the shock through the reservoir (Barnes et al., 1974, 1980). More recently, a technique using the high current pulse at the Z magnetic pinch facility at SNLA has also demonstrated the ability to generate high pressures with a shockless, quasi-isentropic drive (Reisman et al., 2001; Hall et al., 2001; Cauble et al., 2002).

The pressure versus time at the CH(Br)-Ta interface is given in Figure 2, showing that a peak pressure of $\sim$10 Mbar (10^3 GPa) is reached, with a 25–30 ns rise time in the pressure pulse. The temperature at peak pressure was $kT = 0.3$–0.5 eV. To achieve this “gentle” rise time, we assumed 0.5 eV of volumetric preheat in the reservoir, so that the back side started to release into the gap, creating a decreasing density ramp, prior to the arrival of the reservoir shock. Subsequent designs have replaced the preheat with a graded density profile in the reservoir on the side facing the gap, with equivalent results. These peak pressure and temperature conditions are similar to those in the cores of Saturn, Uranus, and Neptune, but fall short of the pressures at the core of Jupiter.

The final point to consider is whether this experimental design proposed for NIF approaches the isentropic conditions of planetary interiors. We examine this by plotting temperature, T (eV), versus compression, ρ/ρ_0, in Figure 3a at locations of 10 μm, 25 μm, 50 μm, and 75 μm into the Ta sample, compared to the isentrope. The dashed curves correspond to simulations that include material strength via the Steinberg-Guinan constitutive model (Steinberg et al., 1980), whereas the solid curves represent simulations with strength turned off. First consider the dashed curves, that is, the simulations including material strength. Starting with the dashed curves G and H, corresponding to the locations deepest into the sample (50 μm and 75 μm, resp.), these profiles are the closest to the isentrope (bottom solid curve). The $\sim$0.04 eV of heating above the isentrope early during the compression phase ($\rho/\rho_0 \sim 1.2$) is likely caused by the ramped pressure pulse steepening into a slight shock at this depth, 50–75 μm into the sample. The peak temperature of $T \sim 0.3$ eV

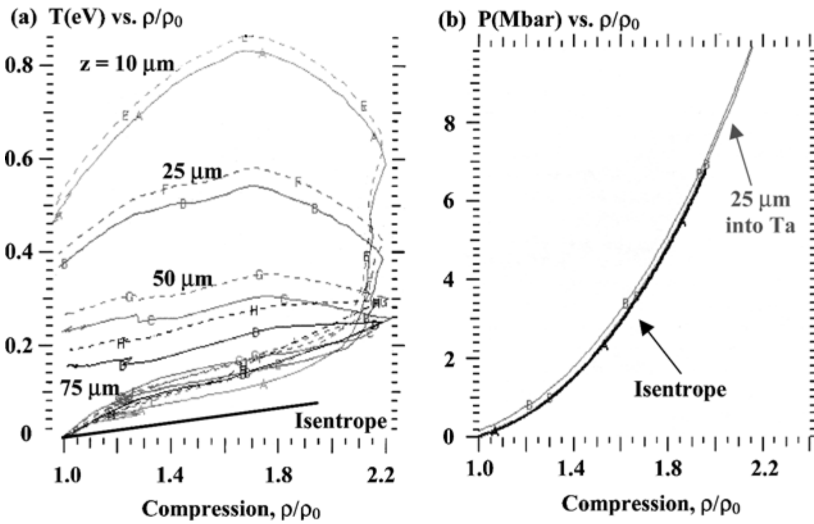

Figure 3. (a) Temperature versus compression, ρ/ρ_0, for the experimental design discussed in Figure 2, for locations of 10 μm (curves A and E), 25 μm (curves B and F), 50 μm (curves C and G), and 75 μm (curves D and H) into the Ta sample. The bottom black curve is the isentrope. The solid curves assume no material strength, whereas the dashed curves correspond to simulations including material strength through the Steinberg-Guinan constitutive model. (b) Pressure (Mbar) versus compression, ρ/ρ_0, for the same design shown in (a). The black curve is the isentrope, and the red curve the trajectory corresponding to a location 25 μm into the Ta.

at peak compression for curve H is about a factor of $\sim$5 below the predicted melt temperature, based on a Lindemann law estimate (Steinberg et al., 1980). The curves E and F in Figure 3 correspond to locations in the Ta that are closer to the CH(Br) heat shield. These curves display a distinctly different behavior. Up to compressions of $\rho/\rho_0 \sim 2$, their trajectories follow curves G and H rather closely. During the subsequent final compression to 2.2 and throughout the release phase, however, these two curves show a distinct increase in temperature. This is due to a conductive heat wave advancing inwards from the hot stagnating plasma impacting the CH(Br) heat shield. Subsequent designs should utilize thicker heat shields, to reduce this source of heating. We note that at peak compression, $\rho/\rho_0 = 2.2$, the Lindemann law implies a melt temperature for Ta of 1.4 eV, which is considerably higher than any of the curves shown in Figure 3a. In this design, the Ta sample is thus predicted to remain in the solid state while under compression, thus retaining its material strength. This strength will become a source of viscous heating as work is done against the strength of the sample during the plastic deformation (compression). By comparing the solid versus dashed curves in Figure 3a, which correspond to identical simulations other than strength being turned on or off, the heating due to work done against material strength is shown to be a small effect, a 10–15% increase in temperature. If, instead of temperature, we had plotted pressure vs. compression, the differences between these curves would have been very small, as illustrated in Figure 3b. At these high densities and low to moderate temperatures, pressure is dominated by degeneracy effects and the interatomic potentials, and is not very sensitive to thermal effects.

In conclusion, we are developing an experimental design for the NIF laser to create conditions relevant to the interiors of Saturn, Uranus, and Neptune all the way to their cores and over much of Jupiter. A NIF design reaching 10 Mbar peak pressure has been described. More recent NIF designs show that such a ramped drive can achieve peak pressures well over 20 Mbar, and possibly even greater than $\sim$30 Mbar, which is approaching the core conditions of Jupiter. We hope in the future that such very high pressure, ramped-pulse drives can be developed and utilized for investigating the properties of matter under conditions relevant to the high pressure interiors of the giant planets and extrasolar planets.

References

Barnes, J.F., Blewett, P.J., McQueen, R.G., Meyer, K.A. and Venable, D.: 1974, *J. Appl. Phys.* **45**, 727.

Barnes, J.F., Janney, D.H., London, R.K., Meyer, K.A. and Sharp, D.H.: 1980, *J. Appl. Phys.* **51**, 4678.

Cauble, R., Reisman, D.B., Asay, J.R., Hall, C.A., Knudson, M.D., Hemsing, W.F., Goforth, J.H. and Tasker, D.G.: 2002, *J. Phys.-Condens. Mat.* **14**, 10821.

Collins, G.W., Da Silva, L.B., Celliers, P., Gold, D.M., Foord, M.E., Wallace, R.J., Ng, A., Weber, S.V., Budil, K.S. and Cauble, R.: 1998, *Science* **281**, 1178.

Edwards, J., Lorenz, K.T., Remington, B.A., Pollaine, S., Colvin, J., Braun, D., Lasinski, B.F., Reisman, D., McNaney, J., Greenough, J.A., Wallace, R., Louis, H. and Kalantar, D.: 2004, *Phys. Rev. Lett.* **92**, 075002.

Guillot, T.: 1999, *Science* **286**, 72.

Guillot, T., Gautier, D. and Hubbard, W.B.: 1997/2004, *Icarus* **130**, 534.

Hall, C.A., Asay, J.R., Knudson, M.D., Stygar, W.A., Spielman, R.B., Pointon, T.D., Reisman, D.B., Toor, A. and Cauble, R.C.: 2001, *Rev. Sci. Instrum.* **72**, 3587.

Henley, R.J. and Mao, H.K.: 2002, *Mineralogical Magazine* **66**, 791.

Hogan, W.J., Moses, E.I., Warner, B.E., Sorem, M.S. and Soures, J.M.: 2001, *Nucl. Fusion* **41**, 567.

Knudson, M.D., Hanson, D.L., Bailey, J.E., Hall, C.A., Asay, J.R. and Anderson, W.W.: 2001, *Phys. Rev. Lett.* **87**, 225501.

Lissauer, J.J.: 2002, *Nature* **419**, 355.

Lorenz, K.T., Edwards, M.J., Jankowski, A.F., Pollaine, S.M., Smith, R.F. and Remington, B.A.: 2004, *J. Appl. Phys.*, submitted.

Reisman, D.B., Toor, A., Cauble, R.C., Hall, C.A., Asay, J.R., Knudson, M.D. and Furnish, M.D.: 2001, *J. Appl. Phys.* **89**, 1625.

Remington, B.A., Bazan, G., Belak, J., Bringa, E., Caturla, M., Colvin, Edwards, M.J., Glendinning, S.G., Kad, B., Kalantar, D.H., Kumar, M., Lasinski, B.F., Lorenz, K.T., McNaney, J., Meyers, M.A., Polaine, S.M., Rowley, D., Schneider, M.S., Stolken, J., Wark, J., Weber, S.V., Wolfer, W.G. and Yaakobi, B.: 2004, *Metallurgical and Materials Transactions* **35A**, 2587.

Saumon, D. and Guillot, T.: 2004, *ApJ* **609**, 1170.

Smith, Ray, private communication.

Steinberg, D.J., Cochran, S.G. and Guinan, M.W.: 1980, *J. Appl. Phys.* **51**, 1496.

Van Horn, H.M.: 1991, Science 252, 384.

FORMATION OF WORKING SURFACES IN RADIATIVELY COOLED LABORATORY JETS

D.J. AMPLEFORD, S.V. LEBEDEV, A. CIARDI, S.N. BLAND, S.C. BOTT, J.P. CHITTENDEN, G. HALL, C.A. JENNINGS, J. ARMITAGE, G. BLYTH, S. CHRISTIE and L. RUTLAND

The Blackett Laboratory, Imperial College, London SW7 2BW, UK;
E-mail: david.ampleford@imperial.ac.uk

(Received 7 May 2004; accepted 7 July 2004)

Abstract. Whilst observations provide many examples of collimated outflows or jets from astrophysical bodies, there remain unresolved questions relating to their formation, propagation and stability. The ability to form scaled jets in the laboratory has provided many useful insights. Experiments (Lebedev et al.: 2002, *ApJ* **564**, 113) using conical arrays of fine metallic wires on the MAGPIE generator (1MA in 240 ns) have produced radiatively cooled collimated jets in vacuum using the redirection of convergent flows by a conical shock. Here we present results of a jet produced by this method propagating through a photo-ionized, quasi-stationary gas cloud. A working surface is observed at the head of the jet. The velocity of this working surface is lower than the velocity of a jet tip in vacuum.

Keywords: jets, outflows, laboratory plasmas

1. Introduction

Collimated outflows or jets are produced by accretion processes in young stars. The Interstellar Medium surrounding jets from young stars has a significant effect on both the jet behaviour and observational properties (e.g., Reipurth and Bally, 2001). The behavior of radiatively cooled jets can be characterized by (Blondin et al., 1990): the jet internal Mach number M, the cooling parameter χ (jet cooling length/jet radius), and the density contrast η (ratio of jet density to ambient density). The presence of an ambient medium has two effects. Firstly, depending on the density contrast, the pressure from the surrounding medium can match the pressure in the jet, and hence enhance the jet collimation. Secondly, a terminal working surface is produced at the head of the jet and a bow-shock is formed ahead of the working surface in the ambient medium. The jet is surrounded by a cocoon of shocked jet material. For a low density contrast η the velocity of the bow shock v_{bs} (and also the working surface) is given as a function of jet velocity v_{j} (Blondin et al., 1990).

$$v_{\mathrm{bs}} \approx \frac{v_{\mathrm{j}}}{(1 + \eta^{-1/2})} \tag{1}$$

Astrophysics and Space Science **298:** 241–246, 2005.

In this paper we describe an experiment for the scaled reproduction of astrophysical jet-plasma interactions. For laboratory jet experiments to be relevant to astrophysics the dimensionless parameters must be similar to those of the astrophysical jets. In addition dissipation due to viscosity, thermal conduction and ohmic heating should be minimal (Ryutov et al., 2000), hence setting limits on hydrodynamic parameters (large Peclet and Reynolds numbers) and MHD parameters (large magnetic Reynolds number).

2. Experimental Setup for Jet Interaction with Gas Cloud

The experimental setup is similar to that described in Lebedev et al. (2002, 2004). The jet is formed using a conical array of 16 fine metallic wires, with a 30° opening angle, 4 mm small radius and 1cm length driven by a 1 mega-ampere, 240 ns current pulse on the MAGPIE generator. The wires act as an ablating mass source and the J×B force acting on the ablated plasma surrounding each wire produces a stream towards the axis. These streams are perpendicular to the wires, and hence have an axial component momentum. Collision of the flows on axis results in the formation of a conical shock (similar to that described by Canto et al., 1988), which recollimates the streams into an axial flow. Radiative cooling enhances the collimation of the flow, producing a highly supersonic jet (Mach number 20–30). A tungsten jet has a cooling parameter $\chi \leq 1$. Changing the wire material (e.g., to stainless steel) can be used as a tool to alter the cooling parameter $-\chi_{SS} > \chi_{W}$. Jet production continues for ~200 ns (many sound transit times), although the parameters of the outflow vary in time. Schlieren imaging of the tip of a tungsten jet has shown it travels at 200–220 km/s (Lebedev et al., 2002). Numerical simulations show that there is differential stretching of the jet along its length; the velocity decreases by a factor of ~2 in the body of the jet compared to the jet tip (Ciardi et al., 2002). The jet density varies from $\rho_{\rm tip} \sim 10^{-5}$ g/cm^3 at the tip to $\rho_{\rm body} \sim 10^{-4}$ g/cm^3 in the main flow. Experiments and simulations both suggest that the collimated jet exiting the array is surrounded by a halo with comparable velocity to the jet but lower density (by a factor of ~10 to the jet tip, ~100 to the jet body).

The scaling parameters that characterize the jets from conical tungsten arrays are similar to those found in young stars; the main exception is the density contrast since the laboratory jets propagate in vacuum. To achieve a density contrast more appropriate to jets from young stars an ambient gas was introduced into the jet propagation region prior to jet formation, as shown in Figure 1a. The gas (Argon in these experiments) is injected using a supersonic nozzle (Mach number 5.5). Reference measurements (i.e., with no jet and not exposed to radiation) have shown that the gas is divergent from the nozzle with a mass density at the exit of the nozzle ~10^{-4} g/cm^3 and in the vicinity of the jet ~10^{-5} g/cm^3. Hence we expect a density contrast $\eta \sim 1$ at the jet tip and $\eta \sim 10$ for the plasma jet body.

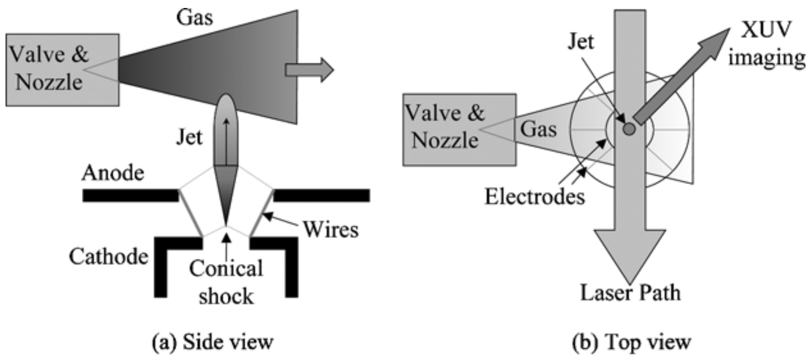

Figure 1. Experimental setup (a) for jet interaction with a quasi-stationary gas cloud, viewed along the laser path. The layout of the diagnostics with respect to the gas nozzle is also shown by an end on view of the apparatus (b).

After the start of formation of the plasma jet, the wires and conical shock radiate at a temperature $T \sim 30$–50 eV. The intensity of this radiation at the surface of the gas cloud is $\sim 10^7$–10^8 W/cm^2. Calculations show that this energy flux will ionize a layer $\sim$10 mm at the base of the gas cloud before the jet reaches it. In the more dense gas closer to the nozzle the thickness of this ionization layer will be less ($\sim$1 mm).

Diagnostics used to monitor the jet-cloud interaction include time resolved laser interferometry and gated imaging of X-UV (Extreme-Ultraviolet) emission. The distribution for the electron line density (n_e integrated along the laser path) is extracted from the laser interferometer images using a fringe analysis package (FRAN, described by Burnett and Judge, 1996). The gated X-UV imaging system (Bland et al., 2004) provides snapshots of the system during its evolution. These images can be used to determine relative velocities of different features of the jet and gas. This is similar to imaging different epochs of a system in astrophysical observations. The laser beam passes perpendicular to the direction of the gas flow (seeing the perspective in Figure 1a). The X-UV imaging system is positioned at 45° to this (see Figure 1b for the layout of these diagnostics).

3. Experimental Results

Figure 2 shows various images of the interaction of a radiatively cooled jet with a gas cloud. Figure 2a is an image of X-UV emission taken 212 ns after the start of current. Figure 2b is a laser interferometer image (for a different setup, but at an equivalent time); from the interferometer image a density map has been obtained (Figure 2c). Both diagnostics show a jet that has propagated along the z-axis from the array (at the base of the image) towards the gas. The decrease in intensity along the z-axis of the X-UV image represents a combination of the cooling of the jet and the drop in density along the jet (as seen on the density map).

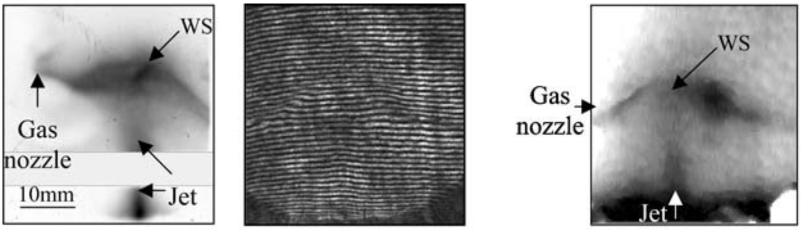

(a) Emission (b) Laser interferometer (c) Density distribution

Figure 2. A tungsten jet interacting with an argon gas cloud. (a) X-UV emission from a tungsten jet interacting with an argon gas cloud taken 212 ns after start of current. The hashed stripe on image is a dead area between frames on the camera (b) Laser interferometer image of the interaction taken 177 ns (for a different setup) and (c) the density map derived from (b). In the density map, white represents sparse areas (no fringe shift) and black represents a line density of $\int n_e dl \approx 4.2 \times 10^{17}\ \mathrm{cm}^{-3}$ (1 fringe shift). The point marked WS is the working surface at the head of the jet.

The gas is seen emerging from the nozzle on the left of each image. The oval ring of emission on the left of every image is re-emission from the gas nozzle housing. The lower edge of the gas is imaged by the X-UV camera, and hence must be emitting radiation with a temperature above the Micro-Channel Plate threshold of 7 eV (corresponding to a minimum temperature of a few eV). The base of the gas cloud is perturbed from the original approximately conical profile by interacting with the plasma jet. Numerical simulations suggest that the width of this shock is caused by the collision of the low density halo with the gas. Closer to the gas nozzle there is a very sharp, more intense line of emission. If the photon energy of this emission was lower than ~50 eV this feature would be smeared by diffraction (Bland, 2004).

At the jet tip there is a significant increase in emission however there is only a slight increase in density. This implies that the presence of the gas has caused the jet material to be shocked at this point, producing a terminal working surface similar to those found in astrophysical jets. Again, as this working surface is well resolved by the X-UV imaging system, it is hotter than ~50 eV. The bow shock in the gas (caused by the main jet) and the cocoon surrounding the jet might not be seen due to either the resolution of the diagnostics used or are indistiquishable from the broader shock in the gas (due to the halo) and the main jet.

Figure 3 shows the evolution of this jet-cloud interaction. Both the bow shock in the ambient medium and the jet working surface move axially. Comparison of the images gives a velocity for the working surface of ~130 km/s, significantly slower than the jet tip velocity in vacuum (220 km/s). For these velocities a density contrast $\eta = 2.1$ is given by equation (1). This is similar to the expected value of $\eta \sim 1$.

Figure 4 shows the evolution with the gas cloud positioned such that the jet travels less distance before interacting with the gas. Due to the differential expansion of the jet, the density near the tip is greater in this case (see Figure 2 in Ciardi et al., 2002). Although the interaction in Figure 4 is morphologically similar to that in Figure 3, measurements indicate that the working surface now has a velocity of

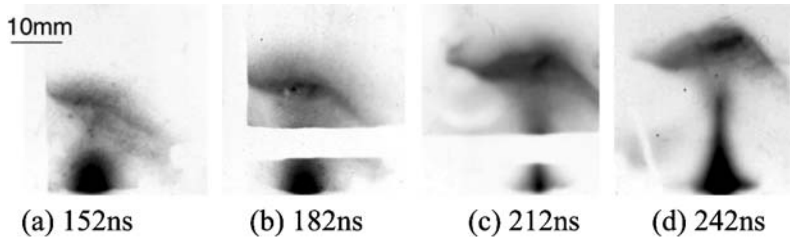

Figure 3. Evolution of emission from tungsten jet interacting with an argon gas cloud at the times shown after the start of current.

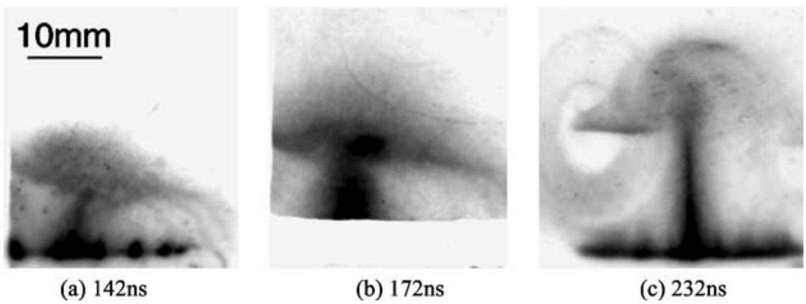

Figure 4. X-UV emission from a jet interacting with a gas cloud that is now positioned closer to the jet formation region.

200–220 km/s. This is comparable to the jet tip velocity in vacuum and consistent with a large density contrast.

Figure 5 shows a stainless steel jet (i.e., with a larger cooling parameter χ) interacting with the gas cloud. The setup is similar to the first experiment described above. In the first two frames of this figure a jet working surface forms and moves both in the direction of jet injection and also in the transverse direction. The transverse motion is probably due to a transverse pressure gradient after photoionisation, leading to a small side wind in the gas. In the second frame (Figure 5b)

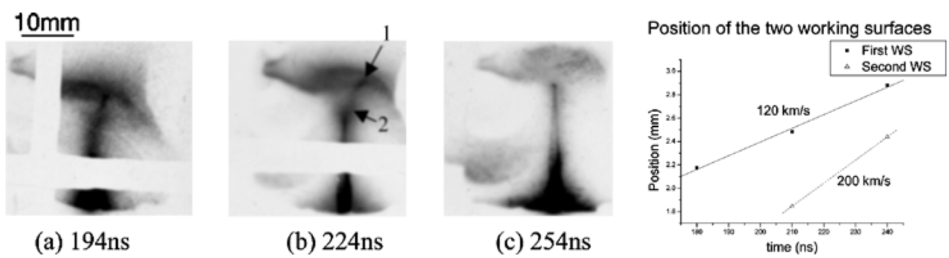

Figure 5. Emission from a stainless steel jet interacting with the argon gas cloud. A second working surface is seen in (b) and (c). The two working surfaces are labelled in (b). The motion of these two working surfaces is graphed in (d).

another working surface has begun to form at the head of the main jet body, which in Figure 5c has also propagated upwards. Figure 5d shows the positions of these working surfaces in time. The second working surface is travelling at 200 km/s compared to 120 km/s for the first working surface. Using Eq. (1) this change in velocity may be due to either the increase in jet density along the beam or the first working surface snow-plowing away the ambient gas.

4. Conclusions and Future Work

We have performed experiments on the propagation of radiatively cooled plasma jets through an ambient medium that are scalable to astrophysical jets, particularly those from young stars. A working surface is observed at the head of the jet, and a bow shock is seen in the ambient gas. The velocity of the working surface is affected by the density contrast between the jet and ambient medium. We plan to modify the setup to minimize the uncollimated low density flow from the wire array reaching the ambient cloud. This will help determine the nature of the bow shock seen in the gas. Experiments are also planned with a less collimated jet to investigate the effects of the ambient cloud on the jet. Also further simulations are underway to compliment the experiments.

References

Bland, S.N., Ampleford, D.J., Bott, S.C. and Lebedev, S.V., 2004, to be published *Rev. Sci. Inst.*

Blondin, J.M., Fryxell, B.A. and Knigl, A.: 1990, *ApJ* **360**, 370.

Burnett, M. and Judge, T.R.: 1996, *The Automatic Analysis of Interferometric Data-FRAN,* Warwick University

Canto, J., Tenorio-Tagle, G. and Rozyczka, M.: 1988, *A&A* **192**, 287.

Ciardi, A., Lebedev, S.V., Chittenden, J.P. and Bland, S.N.: 2002, *Laser and Particles Beams* **20**, 255.

Lebedev, S.V., Chittenden, J. P., Beg, F.N., Bland, S.N., Ciardi, A., Ampleford, D., Hughes, S., Haines, M.G., Frank, A., Blackman, E.G. and Gardiner, T.A.: 2002, *ApJ* **564**, 113.

Lebedev, S.V., Ampleford, D.J., Ciardi, A., Bland, S.N., Chittenden, J.P., Haines, M.G., Frank, A., Blackman, E.G. and Cunningham, A.: 2004, to be published *ApJ.*

Reipurth, B. and Bally, J.: 2001, *An. Rev. Astron. Astrophys.* **39**, 403.

Ryutov, D.D., Drake, R.P. and Remington, B.A.: 2000, *ApJ* **127**, 465.

BOLTZMANN EQUILIBRIUM OF ENDOTHERMIC HEAVY NUCLEAR SYNTHESIS IN THE UNIVERSE AND A QUARK RELATION TO THE MAGIC NUMBERS

HEINRICH HORA[1], GEORGE H. MILEY[2] and FREDERICK OSMAN[3]

[1]*Department of Theoretical Physics, University of New South Wales, Sydney, Australia*
[2]*Fusion Studies Laboratory, University of Illinois, Urbana, USA*
[3]*School of Quantitative Methods and Mathematical Sciences, University of Western Sydney, Penrith, Australia; E-mail: f.osman@uws.edu.au*

(Received 12 April 2004; accepted 3 August 2004)

Abstract. As laser–plasma interactions access ever-increasing ranges of plasma temperatures and densities, it is interesting to consider whether they will some day shed light on questions concerning nuclear synthesis. One such open question is the process of endothermic nuclear synthesis for elements with $A > 60$, thought to have taken place at a point in time during the big bang, or currently in supernovae. We present an explanation based on a Boltzmann equilibrium condition, in combination with the change of the Fermi-statistics from the relativistic branch for hadrons from higher than nuclear densities to the lower density subrelativistic branch. The Debye length confinement of nuclei breaks down at the relativistic change, thus leading to the impossibility of nucleation of the quark-gluon state at higher than nuclear densities. Taking the increment for the proton number Z as $Z' = 10$ of the measured standard abundance distribution (SAD) of the elements for a Boltzmann probability for heavy element synthesis, a sequence 3^n was found with the exponent n for the sequence of the magic numbers. The jump between the magic numbers 20 and 28 does not need then the usual spin-orbit explanation.

Keywords: laser produced plasmas, degenerate electrons, theory of nuclei and nucleation, endothermic element synthesis, quark gluon plasma, magic numbers

1. Introduction

Studies of very high energy density laser–plasma interactions could lead to experiments where violent particle acceleration may produce Hawking-Unruh radiation, similar to that obtained in black holes (Hora et al., 2002). A further consideration of Debye-layer mechanisms of plasma theory may lead to further understanding of a quark-gluon state at higher than nuclear density as will be presented in the this manuscript. The problem we will address is to understand how endothermic syntheses of nuclei heavier than iron can be produced in the universe, while the synthesis up to iron by fusion reactions is exothermic and well understood from the reactions in stars. If a Boltzmann statistics for an unspecified nuclear-chemical process is assumed in the stellar plasmas for creation of the heavy nuclei, we find that the exponential increment fits with the measured standard abundance distribution of

Astrophysics and Space Science **298:** 247–253, 2005.

the elements. This may have the importance of some consistency only if we follow up a relation with the magic numbers of nuclei. Bagge (1948) derived the magic numbers by a purely numerological speculation, where a first connection with the experimental facts was given by a consideration of spin and spin-orbit properties of nuclei (Haxel et al., 1950). We discuss the relation of the magic numbers with the exponent of the mentioned Boltzmann statistics and subsequently find an explanation for the jump between the two Bagge series (Bagge, 1948) without needing the spin and spin-orbit relation. The crucial mechanism for the equilibrium-type generation of all known nuclei in the universe is based on the result that there is a change of the Fermi–Dirac statistics for the nucleons from the relativistic branch at the densities above the nuclear density to the subrelativistic density leading to the nucleation at the well known nuclear densities. This mechanism, due to the surface energy of the nuclei, is combined with the results of the empirically derived Boltzmann increment and then fit together with the magic numbers.

2. Surface Energy and Quark-Gluon Plasma

Surface tension of dielectric materials is explained by the dipole property of molecules. The fact that highly ionized plasmas without any molecules do have a surface tension was derived from the electric fields within the Debye length at a plasma surface due to the gradient of the electrostatic energy density (Hora, 1991a,b, 1992; Hora et al., 1984; Eliezer and Hora, 1989). Extending this to the degenerate electrons in a metal, the surface tension can immediately explain measurements (Hora et al., 1989) where the double layer at the metal surface is produced by a swimming electron layer that is expressed by an exponentially decaying Schrödinger function. In addition, this argument also explains the work function for the emission of electrons. Extending this further to the surface of a nucleus (Hora, 1991a, 1992), the gradient of the energy density leads to a similar Debye length λ_d and a surface energy for compensating the internal energy of the compressed hadrons in a nucleus. This energy is not so much due to the Coulomb repulsion of the protons at the well-known nuclear density n_n but is mostly determined by the Fermi–Dirac energy E_F. In the following argument, we are comparing the surface energy with this internal energy by neglecting the minor contribution by the Coulomb and other effects (Hora, 1991). The surface tension for the nuclei is then

$$\sigma_e = 0.27\, E_F^2 \big/ (8\pi\varepsilon^2\lambda_d) \tag{1}$$

The Fermi energy can be expressed generally (Eliezer et al., 2002)

$$E_F = [(3/\pi)^{2/3}/4][h^2 n^{2/3}/(2m)](\lambda_C/2)^{-1}[n + 1/(\lambda_C/2)^3]^{-1/3} \tag{2}$$

where n is the nucleon density, and m is the nucleon mass. This splits into the branches

$$E_{\mathrm{F}} = \{[(3/\pi)^{2/3}/4]h^2n^{2/3}/(2m)\} \quad \text{(subrelativistic)} \tag{2a}$$
$$E_{\mathrm{F}} = \{[(3/\pi)^{2/3}/4]hcn^{1/3}\} \quad \text{(relativistic)} \tag{2b}$$

where λ_{C} is the Compton wave length $h/(mc)$. The surface energy of the nucleus (Hora, 1991a, 1992) is then

$$E_{\mathrm{surf}} = 0.27[3A(4\pi)^{1/2}]^{2/3}3^{1/3}E_{\mathrm{F}}^{3/2}/(\pi^{1/2}2^{5/2}n^{1/6}e) \tag{3}$$

For comparison between the surface energy and the internal energy we have

$$E_{\mathrm{surf}}/(AE_{\mathrm{F}}) = \{0.27(3^{3/2}/2^{10/3})hn^{1/6}/(em^{1/2}A^{1/3})\} \quad \text{(subrelativistic)} \tag{4a}$$
$$E_{\mathrm{surf}}/(AE_{\mathrm{F}}) = \{0.27[3^{8/3}/(2^{7/3}\alpha^{1/2}A^{1/3})]\} \quad \text{(relativistic)} \tag{4b}$$

using the fine structure constant $\alpha = 2\pi e^2/hc$. From (4a) we see that the nucleus cannot be confined for too low densities. The nucleus is stable only when the density reaches a value of the density n_{n} where the ratio (4a) is equal to one. This is the case for the well-known value of the nuclear density as checked e.g. for bismuth (Hora, 1991a, 1992). The surface "Debye"-layer has a thickness of about 2–3 fm, which is just at the measured Hofstadter decay of the surface charge of heavy nuclei. At relativistic densities just above that of the subrelativistic case reproducing the well-known density of nuclei, we see that the value

$$E_{\mathrm{surf}}/(AE_{\mathrm{F}}) = 6.28/A^{1/3} \tag{5}$$

no longer depends on the nucleon mass or density. We then have no nucleation by the surface energy and the result is a soup of matter. The fact that there is no dependence of this ratio on the mass implies that it holds equally well for either hadrons (as assumed in neutron stars) or quark-gluon plasmas. Only when this dense matter is expanding (as at the big bang or from a neutron star in a supernova, when reaching the nuclear density) will the surface energy produce nucleation. The numerical factor in Eq. (5) may mean that values higher than 247 for A are not possible; otherwise a nucleation or surface effect would appear. This just may explain the fact that the nucleation, by expansion of the matter from the relativistic branch to the lower nuclear density, can produce elements only up to uranium (or up to curium at most) within such equilibrium processes.

3. Cosmic Heavy Nuclear Generation

It is well known from nuclear astrophysics (Audouze and Vauclair, 1980; Rauscher et al., 1994) that there is a standard abundance distribution (SAD) of the elements in the Universe (Hora and Miley, 2000). One interesting feature of the SAD is that for nucleon numbers $A > 60$ (above about iron), a nearly exponential decay of the structure of maxima which are close to the magic numbers can be seen. Element synthesis for heavier nuclides with $A > 60$ cannot be due to fusion because these reactions would be endothermic. There are well known reaction chains in which high density background neutrons may produce reactions for greater than $A = 60$ element synthesis. Some examples are the reactions in supernovae and in white dwarfs known as the r-, s- or p- (rapid, slow or by-pass) processes. Also, for these a rather similar abundance for the elements is gained (Audouze and Vauclair, 1980). Indeed, there is a discussion as to whether these heavy elements can be produced only in the later development of the universe and not before the early development of galaxies (Rauscher et al., 1994; Hora and Miley, 2000; Sneden et al., 1994; McWilliam, 1994; Lefebvre et al., 1997). Nevertheless, there are compelling theories put forth that the heavy elements may have been produced in the state of the big bang when the cosmos had a density close to the nuclear density (Rauscher et al., 1994) and where inhomogeneities provided the conditions for the heavy element generation. This is all related to the conditions by which surface energy of nuclei due to inhomogeneity fields results in stable nuclei of the well known nuclear density, whereas at six times higher density, the Fermi energy of the nucleons changes in the relativistic branch forbidding any nuclear structure and permitting only uniform nucleon or quark-gluon plasmas (Hora, 1991a, 1992). The fact that there is a universally equal distribution of the heavy elements – due to a big-bang or later processes – suggests that without the well known detailed single reactions being taken into account, there seems to be a global reaction equilibrium defined by a Boltzmann-like exponential distribution into which all the heavy nuclei within the background of neutrons may emerge. This is a Boltzmann-like equilibrium process that changes any distribution of nuclides into the well observed standard abundance having the exponentially decaying probability for higher A or proton number Z of nuclei. A distribution of this abundance $N(Z)$ depending on the proton number Z of the form

$$N(Z) = N' \exp(Z/Z') \tag{6}$$

can be written down for the maxima of the SAD (Hora and Miley, 2000) for heavy nuclides. This is therefore rather trivial. Statistically, there is an up and down in nuclei until the exponential distribution has been achieved. One may assume that if this occurs at an early stage of the big bang when all nuclei are some femtometers (Fermi) in distance, then the reaction times may be between femtoseconds and attoseconds or even less. For lower densities, such as those found in supernovae or in white dwarfs, the endothermic element synthesis by the s-, the r- or the p-processes results in a similar Boltzmann equilibrium. This can be seen in Eq. (6), as well as in Fig. VI.1 of Audouze and Vauclair (1980), or Fig. 10a in Rauscher et al. (1994). (Note however, the reaction times in these other cases are up to 10^4 seconds due to the larger distances of the reacting nuclei.) Similar conditions may exist in astrophysical ensembles of nuclei at similar distances and time scales if there is a proton background (Rauscher et al., 1994) where the Coulomb repulsion is compensated thermally and/or there are sufficiently high densities. Following the Boltzmann equilibrium idea further, we evaluate the ratios of the creation probabilities $N(n)$ depending on the numbers n of the sequence of the magic numbers with the only fitting $Z' = 10$:

$$\text{Magic numbers:} M_1 \in 2,\ 8,\ 20,\ 28,\ 50,\ 82,\ 126 \tag{7}$$

These are for protons Z in nuclides as well as for neutrons $N = A - Z$ with the measured well-known maxima of binding energies (see Fig. 2 of Wilets, 1987). We now calculate the ratios $R(n)$ for the astrophysical (Audouze and Vauclair, 1980) SAD-Boltzmann probabilities from Eq. (6) by taking into account the jump between 20 and 28 of the Bagge sequences (Bagge, 1948).

$$R(n) = [N(Z_{n+1})/N(Z_n)] - 1 = \exp[(Z_{n+1} - Z_n)/Z'] \tag{8}$$

where the magic numbers Z_n of the protons are taken with the following indices n (0, 1, 2, 3, ...)

$$Z_0 = 2,\ Z_1 = 8,\ Z_2 = 20, \quad \text{for relation up to the magic number 20} \tag{9}$$

$$Z_2 = 28,\ Z_3 = 50,\ Z_4 = 82,\ Z_5 = 126 \quad \text{for the magic numbers above 20} \tag{10}$$

As seen in Table I, for $Z' = 10$ in Eq. (6), the ratios R given by Eq. (8) result in values very close to

$$R(n) = 3^n \tag{11}$$

showing the best fit for $Z' = 10$ (Hora and Miley, 2000).

TABLE I

Sequence $n = 0, 1, 2, \ldots$ of magic numbers with the values $\exp(Z_n/Z')$ and $R(n) = \exp[(Z_{n+1} - Z_n)/Z']$ of Eq. (3) with $Z' = 10$ from Eq. (6) as measured

n	Magic number	$\exp(Z/Z')$	$R(n)$	$3n$
0	2	1.221	1.822	1
1	8	2.2225	3.321	3
2 ($n + 1$ in (8))	20	7.389	–	–
2 (as n in (8))	28	12.1824	9.025	9
3	50	148.413	24.53	27
4	82	3640.95	81.45	81
5	126	296558.5		

4. Quark and Hadron Structure of Nuclei

The combination of two research topics: “From quarks to the cosmos” and “How were the elements from iron to uranium made?” was the focus of a recent panel of astronomers and physicists that were asked to come up with a list of the key questions in astronomy and physics today (Turner, 2001). We hope that the considerations in this paper may provide insight into the answers of some of those questions. The Boltzmann equilibrium process of nucleation that occurs when matter of higher density than that of the nuclei is expanding, but bound to the surface energy mechanisms, may well explain why nuclei not much larger than that of uranium may be possible. For the properties of the generated nuclei, it is interesting to note that both conflicting properties are present; the hadron structure of the nuclei which determined the Fermi–Dirac statistics and its transition into the relativistic branch by the mass of the hadrons, while the relation for the shell structure for the magic numbers, Eq. (11) indicated the quark property by the threefold multiplicity. Hofstadter’s theoretically predicted decay for large nuclear surfaces of 2–3 fm thickness may also indicate the range of the Yukawa potentials of about 2 fm as tangling bonds at the surface, and not mutually saturated as is the case within the nucleus by mutual hadron interaction (Hora, 1991). It should be mentioned that the motivation to study the Boltzmann plots from Eq. (6) from the empirically given maxima of the standard abundance distribution, was initially motivated by similar measurements of element distribution observed in a fully reproducible way by low energy nuclear reactions of high density protons in palladium, nickel and zirconium (Hora and Miley, 2000).

Acknowledgements

Valuable discussions and support for the final formulations are most gratefully acknowledged to Scott C. Wilks, LLNL Livermore, further discussions with Edward Shuryak, SUNY Stony Brook, I. Krypokluk, Budker Inst. Novosibirsk and N. Ghahramany, Univ. Shiraz.

References

Audouze, J. and Vauclair, S.: 1980, *An Introduction to Nuclear Astrophysics*, D. Reidel, Dordrecht.

Bagge, E.: 1948, *Naturwissenschaften* **35**, 376.

Eliezer, S. and Hora, H.: 1989, *Phys. Rep.* **172**, 339.

Eliezer, S., Ghatak, A.J., Hora, H. and Teller, E.: 2002, *Fundamentals of Equations of State*, World Scientific, Singapore.

Haxel, O., Jensen, J.H.D. and Suess, H.E.: 1950, *Z. Physik* **128**, 295.

Hora, H.: 1991a, *Plasma Model for Surface Tension of Nuclei and the Phase Transition to the Quark Plasma*, Report CERN-PS/DL-Note-91/05.

Hora, H.: 1991b, *Plasmas at High Temperature and Density,* Springer, Heidelberg.

Hora, H.: 1992, *Laser Interaction and Related Plasma Phenomena,* Vol. 10, Plenum, New York, p. 19.
Hora, H., Lalousis, P. and Eliezer, S.: 1984, *Phys. Rev. Lett.* **53**, 1650.
Hora, H. and Miley, G.H.: 2000, *Czech. J. Phys.* **50**, 433.
Hora, H., Min Gu, Eliezer, S., Lalousis, P., Pease, R.S. and Szichman, H.: 1989, *IEEE Trans. Plasma Sci.* **PS-17**, 284.
Hora, H., Osman, F., Castillo, R., Collins, M., et al.: 2002, *Laser Particle Beams* **20**, 79.
Lefebvre, A., Vouzoukas, S., Agner, P., Bogaert, G., Coc, A., Denker, A., de Olivera, F., Forier, A., Görres, J., Kiener, J., Maison, J.M., Porquet, M.G., Rosier, L., Tatischeff, V., Thibaud, J.P. and Wiescher, M.: 1997, *Nucl. Phys. A* **621**, 199.
McWilliam, A.: 1994, *Annu. Rev. Astron. Astrophys.* **35**, 503.
Rauscher, T., Applegate, J.H., Cowan, J.J., Thielemann, F.-K. and Wiescher, M.: 1994, *Astrophys. J.* **429**, 499.
Sneden, Ch., Preston, G.W., McWilliam, A. and Searle, L.: 1994, *Astrophys. J.* **431**, L27.
Turner M.: 2001, *Phys. World* **14**(2), 6.
Wilets, L.: 1987, in: R.A. Meyers (ed.), *Encyclopedia of Physical Sciences and Technology*, Vol. 9, Academic Press, New York, p. 300.

RICHTMYER-MESHKOV EXPERIMENTS ON THE OMEGA LASER

R.M. HUECKSTAEDT[1], S.H. BATHA[1], M.M. BALKEY[1], N.D. DELAMATER[1], J.R. FINCKE[1], R.L. HOLMES[1], N.E. LANIER[1], G.R. MAGELSSEN[1], J.M. SCOTT[1], J.M. TACCETTI[1], C.J. HORSFIELD[2], K.W. PARKER[2] and S.D. ROTHMAN[2]

[1]*Los Alamos National Laboratory, Los Alamos, NM, USA; E-mail: rmhx@lanl.gov*
[2]*Atomic Weapons Establishment, Aldermaston, UK*

(Received 30 April 2004; accepted 23 June 2004)

Abstract. Observations of the interstellar medium reveal a dynamic realm permeated by shocks. These shocks are generated on a large range of scales by galactic rotation, supernovae, stellar winds, and other processes. Whenever a shock encounters a density interface, Richtmyer-Meshkov instabilities may develop. Perturbations along the interface grow, leading to structure formation and material mixing. An understanding of the evolution of Richtmyer-Meshkov instabilities is essential for understanding galactic structure, molecular cloud morphology, and the early stages of star formation. An ongoing experimental campaign studies Richtmyer-Meshkov mixing in a convergent, compressible, miscible plasma at the Omega laser facility. Cylindrical targets, consisting of a low density foam core and an aluminum shell covered by an epoxy ablator, are directly driven by fifty laser beams. The aluminum shell is machined to produce different perturbation spectra. Surface types include unperturbed (smooth), single-mode sinusoids, multi-mode (rough), and multi-mode with particular modes accentuated (specified-rough). Experimental results are compared to theory and numerical simulations.

Keywords: HEDLA, hydrodynamics, instabilities

1. Introduction

Hydrodynamic instabilities play a key role in many astrophysical processes, including star formation, galactic dynamics, and supernova explosions. Two important examples are the Rayleigh-Taylor and Richtmyer-Meshkov (RM) instabilities across a density interface. The Rayleigh-Taylor instability occurs when pressure and density gradients across an interface act in opposite directions (Rayleigh, 1883; Taylor, 1950). The role of Rayleigh-Taylor instabilities in supernovae and other systems has been extensively studied. Less attention has been paid to the RM instability. The RM instability is driven by a shock passing through a density interface. Perturbations are amplified as the shock refracts through the interface (Richtmyer, 1960; Meshkov, 1969).

2. Experiment

A series of experiments was conducted at the OMEGA laser facility at the Laboratory for Laser Energetics of the University of Rochester to study RM mixing in convergent geometry (Lanier et al., 2003). Cylindrical targets consist of a foam inner core and an outer layer of epoxy, with a thin (nominally 8 μm) aluminum marker layer in between. The targets measure about 2 mm in length and 1mm in diameter. An iron backlighter is used to generate radiographs along the cylindrical axis in which the denser aluminum layer appears as a region of minimum transmission. The width of the marker as a function of time is derived from the radiographs and used as the primary diagnostic. A more detailed description of the experimental diagnostics and analysis (as well as an additional set of experiments utilizing a double shell configuration) is given by Taccetti et al. (2004).

Different types of perturbation spectra are machined onto the outer surface of the aluminum marker to seed mix. Spectra types include smooth (unperturbed), single mode, rough (multi-mode), and specified-rough (multi-mode with a high power single mode component). Rough markers with large amplitudes are termed super-rough. For this communication, we place emphasis on a specified-rough case and a super-rough case. As shown in Figure 1, the specified-rough case has a large peak in the power spectrum at $\lambda = 9.38\,\mu$m, but the super-rough contains more overall power.

Prior to the experiment, expectations were that all perturbed markers would show additional marker growth when compared to the evolution of a smooth marker. Additional growth is observed for short wavelength ($\lambda \leq 25\,\mu$m) single mode perturbations for amplitude/wavelength ratios as large as five; whereas, saturation is expected in planar geometry for a ratio of 0.03 (Fincke et al., 2004). Among multi-mode spectra, additional growth is observed for the specified-rough case but not for the super-rough case. Explaining this result is a major goal of our computational efforts.

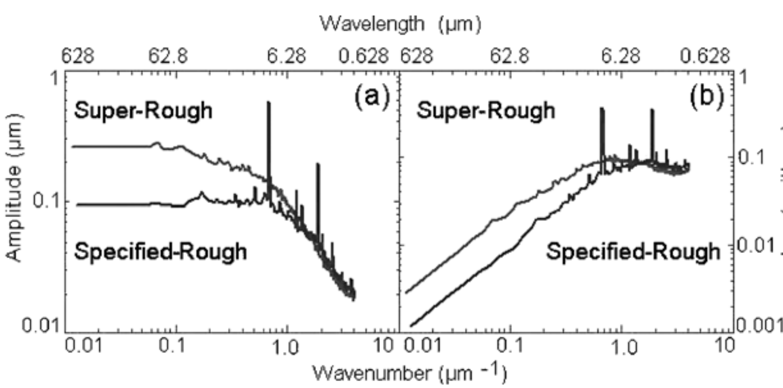

Figure 1. Specified-rough and super-rough perturbation spectra on the outer aluminum surface. Amplitude (a) and amplitude times wave number (b) are plotted as a function of wavelength (top scale) and wavenumber (bottom scale).

3. Simulations

Simulations are performed using the RAGE (Radiation Adaptive Grid Eulerian) code. RAGE is an Eulerian hydrocode which uses a second order Godunov scheme and continuous adaptive mesh refinement. Laser energy deposition and preheats are implemented through time dependent internal energy sources. For 2-d simulations, perturbations are imposed as a combination of cosines. For 3-d simulations, target surface measurements are mapped onto the computational grid. Simulated output does not include the effects of imaging and motion blur that go into generating experimental data, so direct comparisons to experimental results are not made at this time. Instead, we attempt to explain the qualitative experimental result that single-mode and specified-rough markers grow more than smooth markers while super-rough markers do not.

The amount of additional marker growth predicted by 2-d cylindrical RAGE calculations is large for all types of perturbed surfaces. A possible reason for this discrepancy with experimental results is the lack of heating in the simulated marker prior to shock arrival. Figure 2 shows the marker width evolution for examples of smooth, single-mode, and rough markers with and without preheat. When preheats are added to smooth marker simulations, the pre-shock expansion results in a slightly thicker marker throughout its evolution. Perturbed surfaces lose some of their definition due to this expansion, resulting in a somewhat smoother interface at

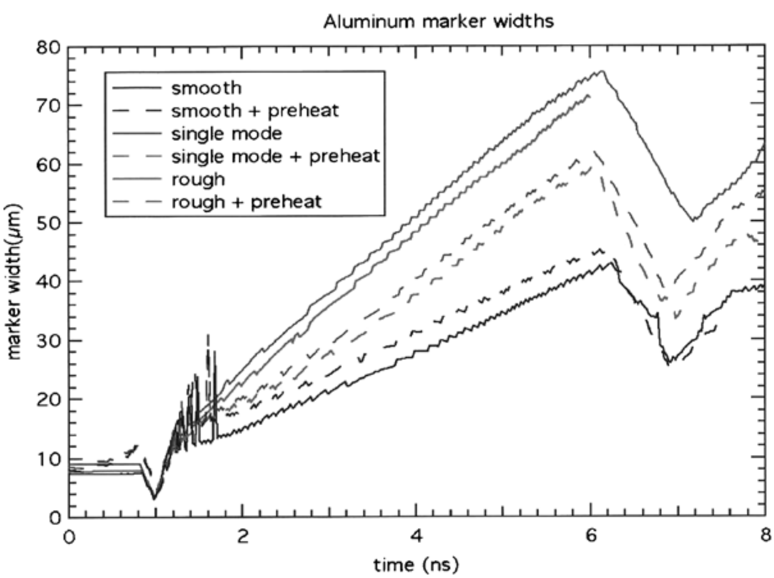

Figure 2. Marker width evolution from 2-d cylindrical simulations for smooth (black), single mode $\lambda = 9.38\ \mu$m (red), and rough (blue) markers. The solid lines correspond to simulations done without preheats, and the dashed lines those done with preheats.

shock arrival and less RM growth. The decrease in overall growth due to preheat in perturbed markers is significant, but not enough to bring simulations into agreement with the experiments. Furthermore, the rough and single mode simulations show similar drops in marker growth, indicating that preheat alone cannot explain the lack of observed growth in the super-rough experiment.

Another possible explanation for the discrepancy between simulations and experiments is that 2-d RAGE simulations do not adequately model the 3-d behavior of the experiments. Rough surfaces are three dimensional, but they must be approximated as 2-d surfaces in R-Z calculations. Theories hold that the dominant mode of energy transfer in complex flows is different in 2-d and 3-d. In 2-d, the dominant mode is from small scale to large scale; whereas, energy preferentially flows from large to small scales in 3-d (Kraichnan and Montgomery, 1980). The specified-rough marker has a strong 2-d component that may aid in the formation of large structures observable as a thicker marker at late times. The super-rough marker lacks this 2-d component.

Three-dimensional RAGE simulations are used to investigate these issues. The cylindrical setup is reduced to a Cartesian shock tube configuration to decrease run time. Target surface measurements are transformed into planar geometry and cut into 96 μm $\times$ 96 μm sections to represent the super-rough and specified-rough markers. The Cartesian geometry removes growth due to convergence, but any differences due solely to the perturbation spectra should still be evident. Each case was run to about 5 ns. The results for the marker width evolution is shown in Figure 3. The 3-d specified-rough and super-rough cases are plotted along with

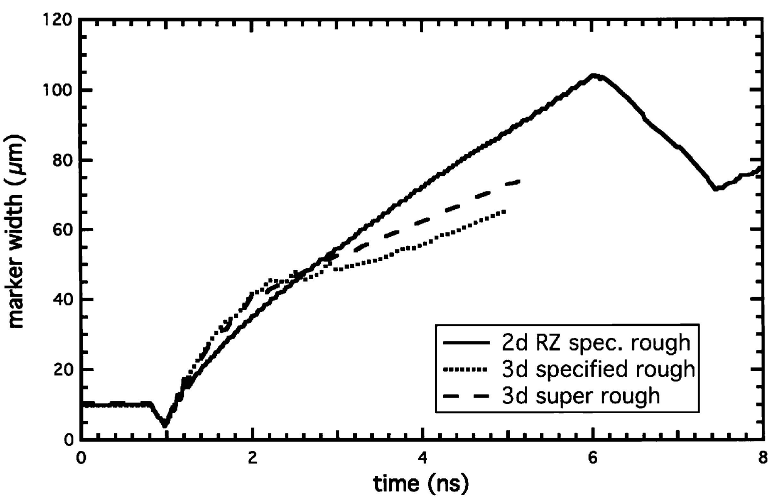

Figure 3. Simulated marker width evolution. The 3-d planar specified-rough (dotted line) and super-rough (dashed line) markers grow in similar fashions. The solid line shows a 2-d cylindrical specified-rough result.

an example of a 2-d cylindrical specified-rough case. Growth slows more at late times for the 3-d cases due to a lack of convergence. Unfortunately, the specified-rough and super-rough markers show similar growth in 3-d simulations. Again, the simulations do not reproduce the experimental differences.

4. Conclusions

Understanding how hydrodynamic instabilities evolve is crucial for understanding the interstellar medium and star formation. We are performing experiments on the Omega laser and running two and three dimensional simulations with RAGE in order to help understand the growth of Richtmyer-Meshkov instabilities. We find that including preheats in the simulations reduces marker growth by about 20%, but does not explain the experimental results. Our initial 3-d simulations have likewise failed to match experimental results. Either planar RM mixing is not quenched by allowing an additional degree of freedom for vortex formation, or these simulations do not adequately show the differences between 2-d and 3-d behavior. Possible shortcomings in the simulations are insufficient numerical resolution, insufficient k-space coverage within the 96 μm $\times$ 96 μm computational domain, and incomplete coverage of the relevant physics. Improved 3-d simulations are under development.

Acknowledgements

This work was performed under the auspices of the U.S. Department of Energy by the University of California at Los Alamos National Laboratory under contract No. W-7405-Eng-36.

References

Fincke, J.R., Lamer, N.E., Batha, S.H., Hueckstaedt, R.M., Magelssen, G.R., Rothman, S.D., Parker, K.W. and Horsfleld, C.J.: 2004, *Phys. Rev. Lett.*, submitted.

Kraichnan, R.H. and Montgomery, D.: 1980, *Rep. Prog. Phys.* **43**, 547.

Lanier, N.E., Barnes, C.W., Batha, S.H., Day, R.D., Magelssen, G.R., Scott, J.M., Dunne, A.M., Parker, K.W. and Rothman, S.D.: 2003, *Phys. Plasmas* **10**, 1816.

Rayleigh, L.: 1883, *Proc. Roy. Math. Soc.* **14**, 170.

Meshkov, E.E.: 1969, *Fluid Dynamics* **43**, 101.

Richtmyer, R,.D.: 1960, *Comm. Pure and Appl. Math.* **13**, 297.

Taccetti, J.M., Batha, S.H., Fincke, J.R., Delamater, N.D., Lanier, N.E., Magelssen, G.R., Hueckstaedt, R.M., Rothman, S.D., Horsfield, C.J. and Parker, K.W.: 2004, *these proceedings*.

Taylor, G.I.: 1950, *Proc. Roy. Soc. London A* **201**, 192.

MOLECULAR CLOUDS: OBSERVATION TO EXPERIMENT

J.O. KANE[1], A. MIZUTA[2], M.W. POUND[3], B.A. REMINGTON[1] and D.D. RYUTOV[1]

[1]*Lawrence Livermore National Laboratory, Livermore, CA 94551, USA;*
E-mail: kane7@unl.gov

[2]*Institute of Laser Engineering, Osaka University, Osaka, 565-0871, Japan*

[3]*Astronomy Department, University of Maryland, College Park, MD 20742, USA*

(Received 24 May 2004; accepted 1 July 2004)

Abstract. Our ongoing investigation of how 'Pillars' and other structure form in molecular clouds irradiated by ultraviolet (UV) stars has revealed that the Rayleigh–Taylor instability is strongly suppressed by recombination in the photoevaporated outflow, that clumps and filaments may be key, that the evolution of structure is well-modeled by compressible hydrodynamics, and that directionality of the UV radiation may have significant effects. We discuss a generic, flexible set of laboratory experiments that can test these results.

1. Introduction

The Eagle Nebula is a molecular cloud irradiated by ultraviolet (UV) stars, and like other molecular clouds (Brandner, 2000) displays remarkable evolving structure, in particular its famous 'Pillars' and smaller 'EGGS' (Hester, 1996; Pound, 1998). Our ongoing investigation of the formation of such structures (Ryutov et al., 2002) involves a combination of theory, computer simulations, and laboratory experiments that mock up key aspects of the relevant physics. Our investigation to date suggests clear directions for such experiments.

Among the results of our work to date are the following: (1) recombination of ionized H in the tenuous outflowing photoevaporated (ablated) material suppresses Rayleigh Taylor growth (A. Mizuta, this issue); this suggests a key role for the pre-existing clumpy, filamentary structure typical of molecular clouds. (2) Direct drive laser experiments at currently available energies allow experiments that address the clump/filament model, and also address observations of the Pillars. (3) Some structure formation may be due to effects of the directionality of the UV radiation – the tilted radiation instability (TR; D. Rytuov et al., 2003) and general directed radiation (DR) effects. (4) Experiments at higher energy lasers or pulsed-power machines may allow us to study such directionality effects, using a 'flashlight' drive from a radiation cavity (hohlraum). Experiments using direct laser illumination (direct drive) may allow directionality experiments at currently available facilities, if the distance between the absorption (critical) surface and the ablation front remains small enough to preserve the directional character of the incoming radiation.

Astrophysics and Space Science **298:** 261–265, 2005.

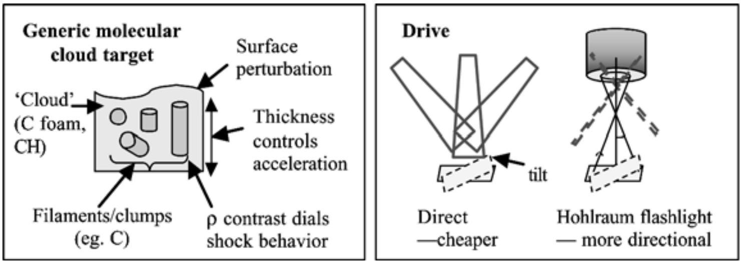

Figure 1.

2. A Generic, Flexible Set of Laser Experiments

We can select from a generic, flexible set of laser experiments to address critical issues in the formation of structures in molecular clouds. Figure 1 shows a generic target and two choices for drive – direct laser illumination and indirect illumination via a hohlraum. In experiments, we represent the molecular cloud by a uniform background material such as C foam, within which we embed rods (filaments) or spheres (clumps) of a denser material such as C (graphite). Initial surface (facing the drive) or other perturbations can be added to trigger Rayleigh–Taylor or Richtmyer–Meshkov hydrodynamic instabilities. Varying the density contrast between the cloud and the embedded material can be used to produce differential dynamic response of the target, in particular to shocks. At laser facilities, compared to indirect drive, direct drive generally allows a simpler target, a longer pulse (permitting more evolution of structure), and higher total energy delivered to the target, which may permit testing aspects of the experiments at smaller lasers.

The surface of the target can be tilted with respect to the average normal direction of the drive, allowing investigation of TR and DR. Directionality experiments may be possible with direct drive if the standoff distance L_c (the distance from the critical surface to the ablation front, between which the drive energy is transported by electron conduction) remains small enough that the ablation front still sees directional effects. Finally, a hohlraum flashlight drive possible at a higher energy facility may allow greater directionality without the complicating issue of the standoff distance.

As illustrated in Figure 2, preliminary simulations and other design work suggests a set of five experiments. A single embedded filament or clump may produce a final structure with a number of diagnosable features. In particular, a filament may produce a structure similar in appearance to a Pillar. Such experiments allow a two-step comparison of embedded filament/clump models to detailed velocity and density data for the Pillars of the Eagle Nebula (Pound, 1998). First, we confirm that simulations reproduce diagnosable features. Second, having validated our simulations, we then compare the detailed density and velocity information in these

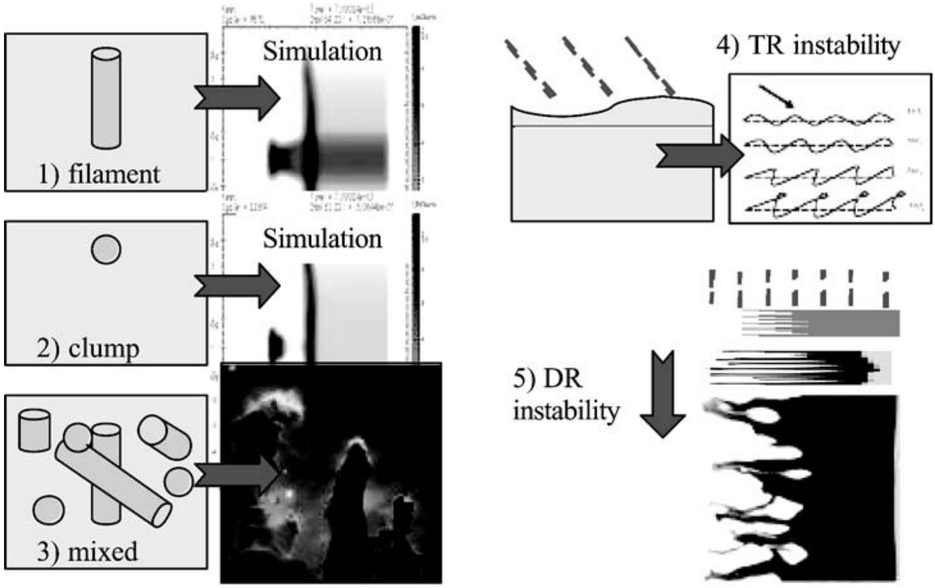

Figure 2.

simulations to the astrophysical data. In this way, we may evaluate Rayleigh–Taylor and other models of structure formation with controlled experiments. With higher energy facilities, we may be able to drive and diagnose larger targets with multiple embedded structures, allowing us to investigate the complicated response of a more realistically structured cloud.

Experimental techniques suitable for TR exist (Azechi et al., 1997; Knauer et al., 2000). Meanwhile, simulations by our group and others (Williams, 2002) have shown what we call the directed radiation (DR) instabilities, short wavelength instability of an ablating surface occurring in the absence of acceleration or a shock. It appears that DR may seed extensive structure formation due to shadowing effects, and may be mitigated by recombination. Theoretical and numerical work have yet to show whether DR has significant physical effects or should be regarded as feature of the energy depositions models commonly used in simulations of molecular clouds. Flashlight drives may help us address this question experimentally.

3. Design of a Clump/Filament Experiment

We have designed a first experiment in which we embed a C rod in C foam parallel to the drive (Figure 3). Our goal is to produce a shocked, ablating pillar-like structure as the lighter foam is compressed past the rod. We wish to produce several diagnosable features we can use to validate our hydrodynamic simulations of the

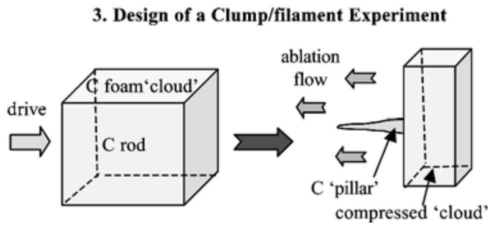

Figure 3.

experiments, then compare the detailed velocity and density profiles in the simulations to observations of Column II of the Eagle Nebula (Pound, 1998.) As a first step, we simulate the C rod-C foam experiment using the LLNL hydrodyamics code CALE. We simulate a 200 μm diameter C rod embedded in a block of 0.25 g/cm^3 C foam. We approximate the drive with a single beam at normal incidence, at laser wavelength $\lambda_L = 0.35\,\mu$m. The drive pulse is 2100 J in a 7 ns square pulse. We assume half the energy is absorbed at the surface of critical electron density $\rho_e(\lambda_L)$, the rest reflected out of the problem. The laser spot size has intensity profile

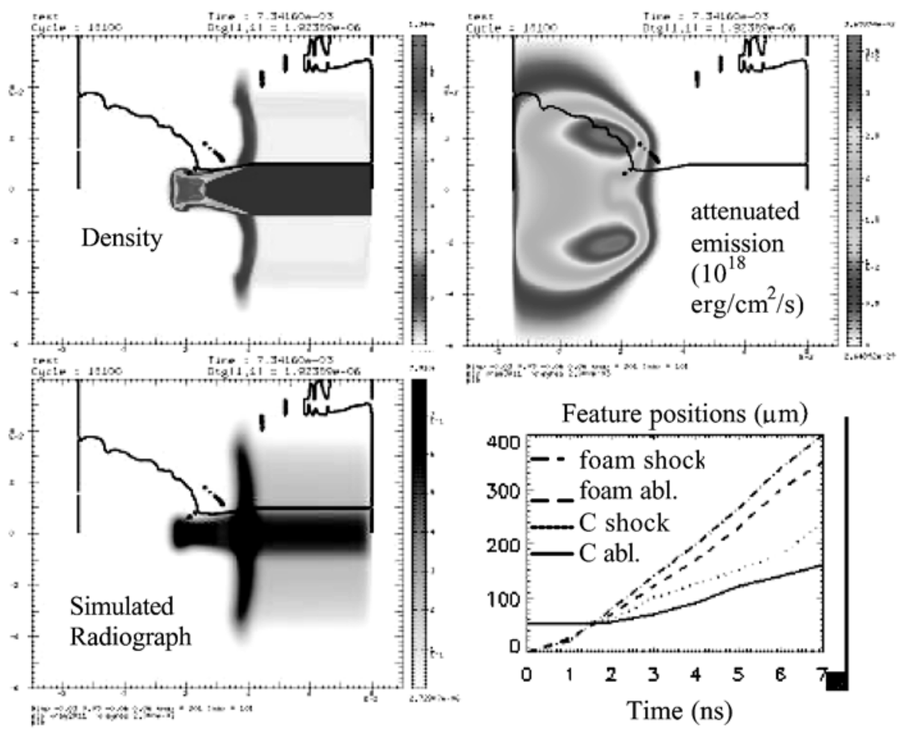

Figure 4.

$I \sim \exp[-(r/411\,\mu\mathrm{m})^{4.6}]$. We assume a backlighter in the 5–6 keV range will be used to produce side-on radiographs; because directly-driven carbon may self-emit in this range, we use multigroup radiation transport including a (5, 6) keV bin. Assuming that to mitigate self-emission we may want to wait until after the drive ends before taking data, we examine how self-emission drops after the drive ends, and whether there is significant attendant hydrodynamic expansion of the target. For simulated radiographs, we assume a diagnostic blurring characterized by a 20 μm Gaussian.

The results are shown in Figure 4. The conclusions are as follows. (1) Radiograph quality and features: the ablation front and the shock are observable in both the C and the C foam, allowing validation of simulations. (2) Self-emission drops rapidly after drive ends. (3) Hydrodynamic expansion is insignificant for 300 ps after drive ends, so self-emission can be mitigated if needed simply by waiting.

References

Azechi et al.: 1997, *Phys. Plasmas* **4**(11).

Brandner, W. et al.: 2000, *AJ*, **119**, 292.

Hester, J.J., Scowen, P.A., Sankrit, R. et al: 1996, *AJ*. **111**, 2349.

Knauer, J.P., Betti, R., Bradley, D.K. et al.: 2000, *Phys. Plasma* **7**, 338.

Levenson, N., Graham, J.R., McLean, I.S. et al.: 2000, *ApJ* **533**, L53.

Mizuta, A. et al.: 2005, *A&SS*.

Pound, M.W.: 1998, *ApJ*, **493**, L113.

Pound, M.W. et al.: 2005, *A&SS*.

Ryutov, D.D. and Remington, B.A.: 2002, *Plasma Phys. Contr. Fusion* **44**, B407.

Ryutov, D.D., Kane, J.O., Pound, M. and Remington, B.A.: 2003, *Plasma Phys. Contr. Fusion* **45**, 769.

Ryutov, D.D., Kane, J.O., Mizuta, A. et al.: 2004, Plasmas in the Laboratory and in the Universe, in: *AIP Conference Proceedings*, Melville, New York, Vol. 703, p. 415.

Ryutov, D.D. et al.: 2005, *A&SS*.

Williams, R.J.R.: 2002, *MNRAS* **331**, 693.

Woodward, C.E., Shull, J.M., Thronson, H.A. Jr. (Eds.): Proceedings of the International Conference, Estes Park, Colorado, May 19–23, 1997, v. 148, p. 150.

PREHEAT ISSUES IN HYDRODYNAMIC HEDLA EXPERIMENTS

C.C. KURANZ[1], R.P. DRAKE[1], K.K. DANNENBERG[1], P.J. SUSALLA[1], D.J. KREMER[1], T. BOEHLY[2] and J. KNAUER[2]

[1]*University of Michigan; E-mail: ckuranz@umich.edu*
[2]*Laboratory for Laser Energetics*

(Received 30 April 2004; accepted 9 June 2004)

Abstract. Hydrodynamic experiments have become a very active area within High Energy Density Laboratory Astrophysics. In such experiments, preheat of an interior surface due to heating prior to shock arrival can alter the initial conditions for further evolution and can change the nature of the experiment (Olson et al., 2003). Unfortunately, preheat cannot typically be detected without undertaking dedicated experiments for this purpose. We have designed such experiments, relevant to hydrodynamic instability experiments using Omega Laser at intensities of $\sim 10^{15}$ W/cm^2. Simulations using the HYADES code suggest that radiative preheat alone causes the interface to move approximately 2 μm before the blast wave reaches it. Hot-electron preheat could cause much larger motions. These experiments will use VISAR to examine the motion of an aluminum sample layer at the rear interface of a standard hydrodynamic target during the period before the shock reaches it (Allen and Burton, 1993).

1. Introduction and Target Design

One of the major areas for experiments of interest to astrophysics using high-energy-density facilities is hydrodynamics. This is a natural connection, in that many astrophysical systems, and many high-energy-density ones, can be accurately described by the Euler equations (Ryutov et al., 1999). Experiments of this type have been done or are planned at numerous laser facilities (and at Z pinches). A partial list includes Nova (Drake et al., 2000; Kane et al., 2000; Remington et al., 1997), Omega (Drake et al., 2002; Robey et al., 2001), Gekko (Kang et al., 2001) and the National Ignition Facility. Such experiments typically seek to produce strong decelerations or strong shear flows, leading one to seek to produce the highest feasible velocities. The desire for strong acceleration leads one in turn to use the highest-feasible laser irradiance and to employ low-density materials. (Plastics have been common; foams have been discussed). Both of these directions lead one toward the regime in which preheat of the experimental system will have significant effects. Some exploration of this issue is the goal of the experiments discussed here.

Preheat occurs when energy is transported, either by radiation or by particles, deep into an experimental system from a region of large energy deposition. In the cases of interest here, a laser-irradiated surface can be a source both of

Astrophysics and Space Science **298:** 267–271, 2005.

X-rays, produced in the hot ($\sim$ keV) coronal plasma, and of "hot" electrons, having suprathermal energies of tens of keV and produced in consequence of laser-plasma instabilities. Some of the hydrodynamic experiments produce a blast wave and use it to create Rayleigh-Taylor instabilities by shocking then decelerating an interface where the density drops. The interface is typically prepared by imposing a very specific initial condition. In such experiments, which are our specific concern here, preheat can modify the initial conditions before the blast wave arrives at the interface. Thus, an accurate understanding of such experiments must include an assessment of the preheat that is present.

This problem is complicated because such an assessment cannot be entirely computational. Current simulation codes, using multigroup diffusive radiation transport, are believed to accurately calculate the radiation preheat. However, they make no attempt to evaluate the hot-electron preheat. What is known is that the laser irradiances used in the experiments of interest, of order 10^{15} W/cm^2 at laser wavelengths of 0.35 μm, can correspond to significant production of hot electrons (Wolf Seka, Laboratory for Laser Energetics, private communication). This motivates the current experiments, the design of which is discussed here.

Figure 1 shows one of the target designs to be used for the preheat experiments. Ten beams of the Omega laser (Boehly et al., 1995) are incident from the left onto the polyimide surface. These produce a laser intensity of approximately 10^{15} W/cm^2 at laser wavelengths of 0.35 μm, using 1 ns flat-topped pulses, on a spot of 800 μm FWHM. This configuration is identical to that used in numerous planar hydrodynamic experiments (Miles et al., 2003a,b; Robey et al., 2001, 2003). The 150-μm thick polyimide (C22H10O5N2) layer would normally be followed by a lower-density material. In this case it is followed by an Al layer, 10 μm thick here but 0.2 μm in other cases. The 10 μm thickness was chosen to absorb and respond to the anticipated preheat as is discussed below. Behind the Al layer is a window of SiO_2, through which a Velocity Interferometer System for Any Reflector (VISAR) (Barker and Hollenback, 1972; Sheffield et al., 1986) can use a laser of 532 nm wavelength to interrogate the surface to see the motion induced by the preheat. The SiO_2 layer was intended to tamp the aluminum surface, so that it would remain reflective even if heated to some degree. This approach has been used successfully

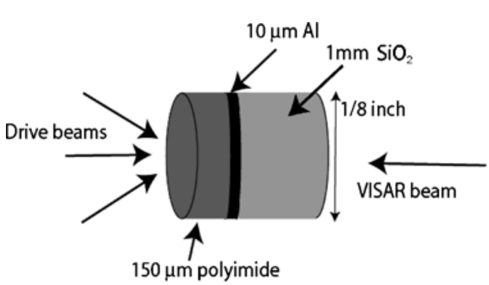

Figure 1. Schematic of one of the preheat targets.

in experiments at Sandia National Laboratories. If there were so much preheat that the SiO_2 became conductive, then the VISAR diagnostic would prove unable to make a measurement because of absorption. Part of the experiment is to see whether this occurs. If the preheat were radiative only and as predicted by the simulations, then the temperature in the SiO_2 would remain below 0.3 eV and one could hope to see the Al layer until the shock arrived. In addition, an optical pyrometer will be used to observe heating of the Al material by detecting the thermal emission from the target. The interior surface of the SiO_2 window is coated by 0.2 μm of Al to assure a high-quality signal for these diagnostics.

2. Predictions from Simulations and Calculations

The experimental system for the preheat experiment was simulated using HYADES (Larsen and Lane, 1994), a one-dimensional, Lagrangian, radiation-hydrodynamics code that is widely used for experimental scoping. It uses multigroup radiation transport, allowing it to predict the effects of the X-ray photons at the interface before the shock arrives. It is possible that hot-electron preheat will greatly increase the movement of the interface, as is discussed further below.

Hyades runs were performed with a 150 μm layer of polyimide, 10 μm of Al, and 1 mm of SiO_2. The output from these runs can be seen in Figures 2 and 3, where different lines indicate different times throughout the run. Figure 2 shows the velocity of the interface to be $\sim$1 μm/ ns and the shock arriving at the interface at $\sim$2.2 ns. Thus the interface moves $\sim$2.2 μm before the shock. Figure 3a and b show the temperature of the interface to be $\sim$1 eV and a change in the density, respectively, prior to shock arrival.

Since HYADES cannot account for hot electrons, calculations of the energy flux of hot electrons through the interface were made. The total energy deposited in the preheated material, on the assumption that the temperature is increased uniformly,

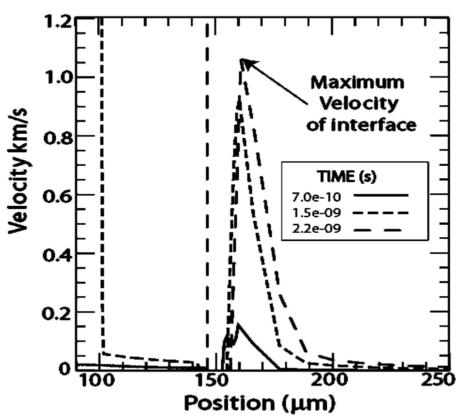

Figure 2. Velocity due to radiation preheat.

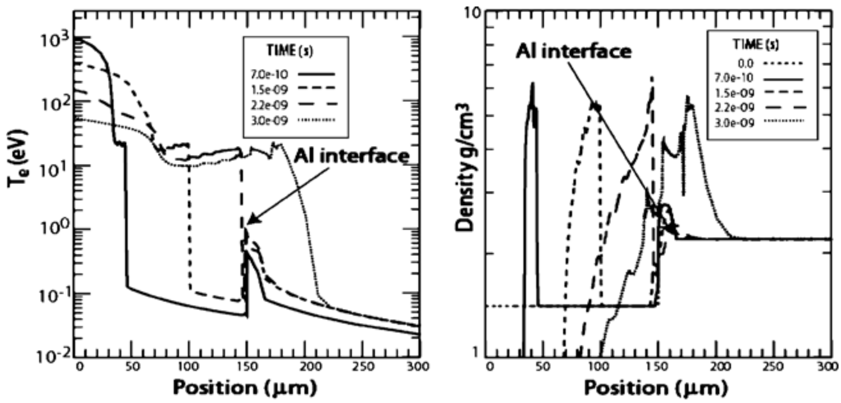

Figure 3. Temperature and density changes due to radiation preheat.

is given by $[\rho k_B T/(Am_p)]da$, where ρ is the density, T is the temperature, A is the atomic mass, m_p is the mass of the proton, d is the thickness, a is the area of the laser spot, and k_B is the Boltzmann constant. To estimate a preheat temperature, we assume that approximately 0.1% of the laser energy (4 J) goes into hot electrons that are deposited in the polyimide underneath the laser spot. (The total energy of the hot electrons produced would be a large multiple of this number, probably more than ten times larger but well within the range of plausibility for this experiment.) Then using $\rho = 1.4$ g/cm^3 for polyimide, $d = 150\,\mu$m, and $a = 0.5$ mm^2, one finds the preheat temperature to be approximately 5 eV. It is thus possible that the hot electrons cause a much larger motion than the radiative preheat alone. This motion would be expected to alter the structure on the surface and to affect the subsequent instability evolution.

3. Conclusions

Through simulations and calculations we have found that X-ray photons and hot electrons from the laser in a hydrodynamic experiment may cause preheat at an interface. This heats the interface and causes it to move prior to the arrival of the shock, changing the initial conditions of the experiment. We have designed an experiment to detect such preheat and to assess its magnitude. These experiments will soon be carried out in order to find out how much energy actually reaches the interface.

Acknowledgments

This work is supported by the U. S. Department of Energy under grants DE-FG03–99DP00284 and DE-FG03-00SF22021.

References

Allen, D.A. and Burton, M.G.: 1993, *Nature* **363**, 54.

Barker, L.M. and Hollenback, R.E.: 1972, *J. Appl. Phys.* **43**, 1669.

Boehly, T.R. et al.: 1995, *Rev. Sci. Intsr.* **66**, 508.

Drake, R.P. et al.: 2000, *Phys. Plasmas* **7**, 2142.

Drake, R.P. et al.: 2002, *Astrophys. J.* **564**, 896.

Kane, J., Arnett, D., Remington, B.A., Glendinning, S.G., Bazan, G., Drake, R.P. and Fryxell, B.A.: 2000, *Ap. J. Suppl.* **127**, 365.

Kang, Y.G. et al.: 2001, *Plasma Phys. Rep.* **27**, 843.

Larsen, J.T. and Lane, S.M.: 1994, *J. Quant. Spectrosc. Radiat. Transfer* **51**, 179.

Miles, A.R., Braun, D.G., Edwards, M.J., Robey, H.F., Drake, R.P. and Leibrandt, D.R.: 2003a, Phys. Plasmas, submitted.

Miles, A.R., Edwards, M.J. and Robey, H.F.: 2003b, in Inertial Fusion and Science Applications, The effect of a short-wavelength mode on the nonlinear evolution of a long-wavelength perturbation driven by a strong blast wave (Monterey, CA), submitted.

Olson, R.E., Leeper, R.J., Nobile, A. and Oertel, J.A.: 2003, *Phys. Rev. Lett.* 91.

Remington, B.A. et al.: 1997, *Phys. Plasmas* **4**, 1994.

Robey, H.F. et al.: 2001, *Phys. Plasmas* **8**, 2446.

Robey, H.F., Zhou, Y., Buckingham, A.C., Keiter, P., Remington, B.A. and Drake, R.P.: 2003, *Phys. Plasmas* **10**, 614.

Ryutov, D.D., Drake, R.P., Kane, J., Liang, E., Remington, B.A. and Wood-Vasey, M.: 1999, *Ap. J.* **518**, 821.

Sheffield, S.A., Rogers, J.W., Castaneda, J.N. and Gupta, V.M.: 1986, in Shock Waves in Condensed Matter (New York: Plenum), p. 541.

ZEUS-2D SIMULATIONS OF LASER-DRIVEN RADIATIVE SHOCK EXPERIMENTS

D.R. LEIBRANDT[1], R.P. DRAKE[1] and J.M. STONE[2]

[1]*Department of Atmospheric, Oceanic, and Space Sciences, University of Michigan; E-mail: dleibran@umich.edu*

[2]*Department of Astrophysical Sciences, Princeton University*

(Received 20 April 2004; accepted 1 June 2004)

Abstract. A series of experiments is underway using the Omega laser to examine radiative shocks of astrophysical relevance. In these experiments, the laser accelerates a thin layer of low-Z material, which drives a strong shock into xenon gas. One-dimensional numerical simulations using the HYADES radiation hydrodynamics code predict that radiation cooling will cause the shocked xenon to collapse spatially, producing a thin layer of high density (i.e., a collapsed shock). Preliminary experimental results show a less opaque layer of shocked xenon than would be expected assuming that all the xenon accumulates in the layer and that the X-ray source is a pure Kα source. However, neither of these assumptions is strictly correct. Here we explore whether radial mass and/or energy transport may be significant to the dynamics of the system. We report the results of two-dimensional numerical simulations using the ZEUS-2D astrophysical fluid dynamics code. Particular attention is given to the simulation method.

Keywords: radiation hydrodynamics, methods: numerical

1. Introduction

This work uses the ZEUS-2D astrophysical fluid dynamics code (Stone and Norman, 1992) with a flux-limited diffusion radiation module (Turner and Stone, 2001) to model a set of laser-driven radiative shock experiments. While several target designs have been used in experiments, this work assumes the target design shown schematically in Figure 1. The target is cylindrically symmetric. The drive disk is 72 μm thick polystyrene with a density of 1.05 g/cm^3. The tube is 4 mm long, has an inner diameter of 600 μm and an outer diameter of 800 μm, and is also 1.05 g/cm^3 polystyrene. The xenon gas has a density of 0.006 g/cm^3. The target is driven by a 1 ns full width at half maximum laser pulse with an irradiance of 1.7×10^{15} W/cm^2 at the center of the drive disk. The irradiance falls off by 45% at the outer diameter of the tube. As ZEUS-2D does not have a laser module, the initial conditions are linearly interpolated from a set of one-dimensional axial simulations of different radial coordinates at 1 ns (i.e., immediately after the drive laser turns off) generated by HYADES. HYADES is a one-dimensional, Lagrangian, single-fluid, three-temperature code with multigroup flux-limited diffusion radiation transport

Astrophysics and Space Science **298:** 273–276, 2005.

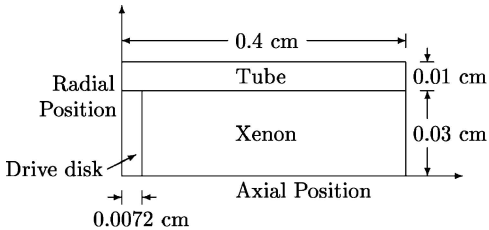

Figure 1. Target schematic. The drive disk and tube are 1.05 g/cm^3 polystyrene and the xenon is 0.006 g/cm^3. The target is driven from the left by a 1 ns laser pulse with an average irradiance of 1.4×10^{15} W/cm^2.

(Larsen and Lane, 1994). The HYADES laser irradiance profile is scaled to 25% of the experimental irradiance to account for lateral heat transport, which is determined by matching simulated and experimental interface and shock motions in previous experiments. The heating of the xenon gas by radiation from the shock is so large that preheat by suprathermal electrons is unlikely to affect the dynamics.

2. Simulation Method

ZEUS-2D is a two-dimensional, Eulerian, single-fluid, two-temperature code with gray radiation transport (Stone and Norman, 1992; Stone et al., 1992). We replaced the original discrete ordinate radiation module with a flux-limited diffusion radiation module based on the work of Turner and Stone (2001) for computational efficiency. The equations solved are

$$\frac{D\rho}{Dt} + \rho\nabla\cdot\mathbf{v} = 0, \tag{1}$$

$$\rho\frac{D\mathbf{v}}{Dt} = -\nabla p + \frac{1}{c}\rho\kappa_{\mathrm{R}}\mathbf{F}, \tag{2}$$

$$\rho\frac{D}{Dt}\left(\frac{E}{\rho}\right) = -\nabla\cdot\mathbf{F} - \nabla\mathbf{v} : \mathbf{P} + 4\pi\rho\kappa_{\mathrm{P}}B - c\rho\kappa_{\mathrm{P}}E, \tag{3}$$

and

$$\rho\frac{D}{Dt}\left(\frac{e}{\rho}\right) = -p\nabla\cdot\mathbf{v} - 4\pi\rho\kappa_{\mathrm{P}}B + c\rho\kappa_{\mathrm{P}}E \tag{4}$$

where $D/Dt \equiv \partial/\partial t + \mathbf{v}\cdot\nabla$ is the convective derivative; ρ, e, $\mathbf{v}$, and p are the material mass density, energy density, velocity, and pressure; E, $\mathbf{F}$, and $\mathbf{P}$ are the radiation energy density, flux, and pressure tensor; κ_{R} and κ_{P} are the Rosseland and Planck mean specific opacities; B is the Planck function; c is the speed of light; and t is time. Note that this work uses the Rosseland mean specific opacity for the radiation flux terms and the Planck mean specific opacity for the heating and cooling terms. These equations are closed by the addition of an equation of state, constitutive relations for the Planck function and opacities, and a flux limiter.

This work uses the ideal gas equation of state $p = (\gamma - 1)e$ where γ is the ratio of specific heats. $\gamma = 5/3$ for polystyrene and $11/9$ for xenon. The latter is determined by the strong shock jump condition, $\rho_2/\rho_1 = (\gamma + 1)/(\gamma - 1)$, using densities from a HYADES simulation with radiation transport suppressed. The Planck function $B = (\sigma/\pi)T^4$ is computed using the implicitly defined material temperature $T = (\gamma - 1)\mu e/(\mathcal{R}\rho(1 + Z))$ with an average ionization $Z = 20\sqrt{T_{keV}}$ (Drake, in preparation) where σ is the Stefan-Boltzmann constant, $\mathcal{R}$ is the gas constant, μ is the dimensionless mean particle mass, and T_{keV} is the material temperature in keV. $\mu = 6.5$ for polystyrene and 131.3 for xenon. The opacities used are least squares fits to the LANL SESAME tables #17593 (polystyrene) and #15190 (xenon). The (Minerbo, 1978) flux limiter is used for this work, but there is little difference when the (Levermore and Pomraning, 1981) flux limiter is used instead.

It is found that the alternating direction-implicit (ADI) matrix solver used to evolve the radiation flux divergence term does not converge when the optical depth per zone is too small; these simulations have an optical depth per zone of order 0.1 in the xenon region. This work replaces the ADI matrix solver with a band matrix lower upper factorization matrix solver from the LAPACK numerical linear algebra package (Anderson et al., 1999).

3. Results

Figure 2 shows the simulation results. Note that the detailed structure of the polystyrene/xenon interface, including the peculiar behavior on axis, is the unphysical result of using a two-dimensional code to model three-dimensional

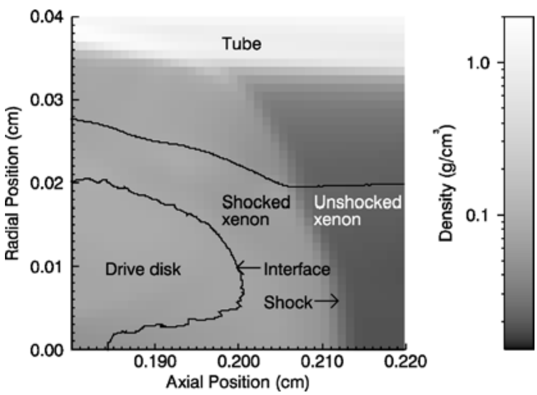

Figure 2. ZEUS-2D simulation results. The density is plotted in false color as a function of position at 20 ns.

hydrodynamic instabilities. There is a significant accumulation of shocked xenon between the drive disk and the tube. In addition, the shock has a large curvature. These results suggest a mechanism for shocked xenon loss that might explain the low opacity of the shocked xenon layer.

4. Conclusions

This work reports the results of ZEUS-2D simulations that suggest an explanation of the low opacity of the shocked xenon layer. Future directions include validation and quantitative comparison with experiment.

Acknowledgements

This work is supported at the University of Michigan by the U.S. Department of Energy under grants DE-FG03-99DP00284, DE-FG03-00SF22021, and other grants and contracts.

References

Anderson, E., Bai, Z., Bischof, C., Blackford, S., Demmel, J., Dongarra, J., Du Croz, J., Greenbaum, A., Hammarling, S., McKenney, A. and Sorensen, D.: 1999, *LAPACK Users' Guide*, SIAM, Philadelphia, PA.

Drake, R.P.: in preparation, *High Energy Density Physics: From Inertial Fusion to Experimental Astrophysics*, Springer-Verlag, New York, NY.

Larsen, J.T. and Lane, S.M.: 1994, *J. Quant. Spectrosc. Radiat. Transfer* **51**, 179.

Levermore, C.D. and Pomraning, G.C.: 1981, *ApJ* **248**, 321.

Minerbo, G.N.: 1978, *J. Quant. Spectrosc. Radiat. Transfer* **31**, 149.

Stone, J.M., Mihalas, D. and Norman, M.L.: 1992, *ApJS* **80**, 819.

Stone, J.M. and Norman, M.L.: 1992, *ApJS* **80**, 753.

Turner, N.J. and Stone, J.M.: 2001, *ApJS* **135**, 95.

MODELING MAGNETIC TOWER JETS IN THE LABORATORY

A. CIARDI, S.V. LEBEDEV, J.P. CHITTENDEN, D.J. AMPLEFORD, S.N. BLAND, B. S. BOTT and J. RAPLEY

The Blackett Laboratory, Plasma Physics Group, Imperial College, Prince Consort Road, London SW7 2BW, U.K.; E-mail: a.ciardi@imperial.ac.uk

(Received 4 May 2004; accepted 17 June 2004)

Abstract. The twisting of magnetic fields threading an accretion system can lead to the generation on axis of toroidal field loops. As the magnetic pressure increases, the toroidal field inflates, producing a flow. Collimation is due to a background corona, which radially confines this axially growing "magnetic tower". We investigate the possibility of studying in the laboratory the dynamics, confinement and stability of magnetic tower jets. We present two-dimensional resistive magnetohydrodynamic simulations of radial arrays, which consist of two concentric electrodes connected radially by thin metallic wires. In the laboratory, a radial wire array is driven by a 1 MA current which produces a hot, low density background plasma. During the current discharge a low plasma beta ($\beta < 1$), magnetic cavity develops in the background plasma (β is the ratio of thermal to magnetic pressure). This laboratory magnetic tower is driven by the magnetic pressure of the toroidal field and it is surrounded by a shock envelope. On axis, a high density column is produced by the pinch effect. The background plasma has $\gtrsim$1, and in the radial direction the magnetic tower is confined mostly by the thermal pressure. In contrast, in the axial direction the pressure rapidly decays and an elongated, well collimated magnetic-jet develops. This is later disrupted by the development of $m = 0$ instabilities arising in the axial column.

Keywords: jets and outflows, laboratory astrophysics, wire array Z-pinches

1. Introduction

Jets are commonly associated with accretion flow phenomena and are found in a variety of astrophysical environments, ranging from the kilo-parsec scale extragalactic jets, to the parsec and sub-parsec jets associated with newly forming stars. Magnetohydrodynamic models of jet formation from accretion disks (see Lovelace et al. (1999) and references therein for a review) require the presence of magnetic fields which remove energy, angular momentum and matter from the accreting system, and collimate at least part of the resulting flow into a jet. In magnetic tower jets (Lynden-Bell, 1996, 2003), accumulation of toroidal loops on axis increases the magnetic pressure. Vertical inflation of the magnetic loops then drives a jet which is collimated by the external pressure of the background corona (Kato et al., 2004a,b). If the Poynting flux dominates the bulk energy flux of the jet then the magnetic tower jet can be thought of as a Poynting jet (Lovelace et al., 2002; Kato et al., 2004a).

Astrophysics and Space Science **298:** 277–286, 2005.

The possibility of reproducing in the laboratory some of the phenomena related with the evolution of a magnetic tower jet is the subject of the present paper. A schematic of the experimental configuration is shown in Figure 1. A radial wire array consists of thin metallic wires (*W*) radially connecting two concentric electrodes. The array forms the load of a pulsed power generator which delivers a fast rising, mega Ampere current. The current ablates the wires and a vertical plasma flow, driven by the $j \times B_{\mathrm{global}}$ force, fills the region above the electrodes. Later in the current discharge, a magnetic pressure-driven cavity develops in the background plasma producing a jet. We present two-dimensional, axisymmetric, resistive magnetohydrodynamic simulations of radial wire arrays and study the evolution of the magnetic tower produced. Section 2 introduces the model used in the simulations. In Section 3 we discuss the initial background flow production and the subsequent formation of a magnetic tower jet. Finally we conclude in Section 4 with a summary and discussion of the results.

2. Model

The model used is based on the 2D(r,z) resistive magnetohydrodynamic code described by Chittenden et al. (1997). Explicit hydrodynamics is performed on an Eulerian grid using second order Van Leer advection. Reflective boundary conditions are used at the axis of symmetry, with free flow conditions at the other boundaries. The thermal and magnetic-field diffusion are backwards differenced and solved implicitly by quin-diagonal matrix solution using iterative conjugate gradient methods. The model is two temperatures with the ion and electron energy equations coupled by an equilibration term. The different ionisation stages are calculated assuming local thermodynamic equilibrium (LTE). Material with a density below $10^{-7}\,\mathrm{g\,cm^{-3}}$ is identified as vacuum and it is given an artificially high resistivity and thermal conductivity, ensuring that it is isothermal and current

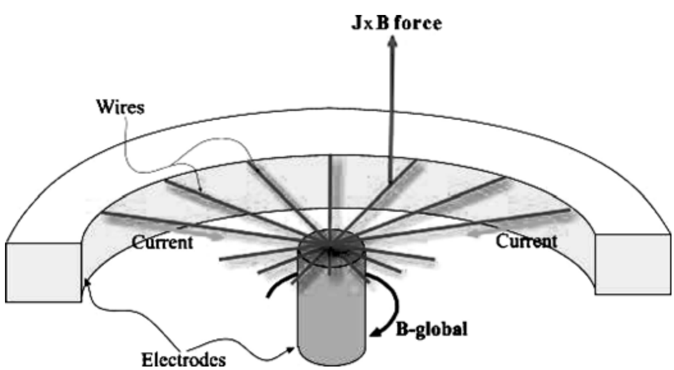

Figure 1. Schematic of a radial wire array. Current-ablated plasma is accelerated by the Lorentz force and expands in the region above the electrodes.

free. Injection of plasma onto the computational grid was implemented according to a phenomenological model of ablation rate presented by Lebedev et al. (2001). The electrodes are modelled as static high density regions, with high electrical conductivity. The array is driven on the Imperial College MAGPIE generator, which is capable of delivering a 1 MA current with a 240 ns rise-time. The current I can be closely approximated by $I \sim \sin^2(t)$. A purely toroidal magnetic field, consistent with the $I(t)$, is imposed on the outermost radial boundary up to the height of the electrode. Simulations were performed for radial arrays with varying central electrode diameter, and composed of 16 tungsten wires with diameters 7.5 and 13 μm. In the radiative efficient regime, the radiative effects are modelled by simple optically thin recombination radiation losses modified to include a probability of escape, which allows a smooth transition to black-body emission in the dense regions. A radiative inefficient regime was also studied, where radiation losses were turned off.

3. Plasma Dynamics in Radial Arrays

In wire array Z-pinches the ablation of the wires produces a distinct two-component structure consisting of a cold, dense, resistive wire core embedded in a high temperature, low density and highly conductive coronal plasma. Because of the lower resistivity present in the outer regions of this structure, currents flow preferentially in the coronal plasma, which is accelerated by the Lorentz $j \times B_{\mathrm{global}}$ force in a direction normal to the wires. The "private" magnetic field associated with each wire cannot confine the high-β coronal plasma that is produced during the discharge and it is therefore the global magnetic field which is dynamically important. Because resistive diffusion dominates over the hydrodynamic advection of the global field ($Re_{\mathrm{m}} \lesssim 1$, with Re_{m} the magnetic Reynolds), the magnetic field remains mostly confined to a region near the wires. Away from the wires there is relatively little toroidal field and the plasma is high-β. Thermal conduction, ohmic and radiative heating continuously deposit energy into the stationary wire cores, which ablate and act as continuous sources of plasma, sustaining the quasi-steady two-component structure just described. Clearly, if all the mass in a wire core is ablated ("wire breakage"), then the whole of the plasma in that region can undergo acceleration. It is worth noting that mass ablation is proportional to $I(t)^2/r^{-1}$, where r is the radius of the mass source (Lebedev et al., 2001). As a result during the current discharge, wire breakage can occur at different times and in different parts of the array; depending on array parameters such as wire thickness, array geometry, etc.

Snapshots of the evolution of a radial wire array are shown in Figure 2. The plots are for the mass density in the case of a radiatively efficient flow. Initial collision of the plasma on axis produces a shock, and since the density of the flow is still low, radiative cooling is not efficient in reducing the thermal energy in the shock. Later

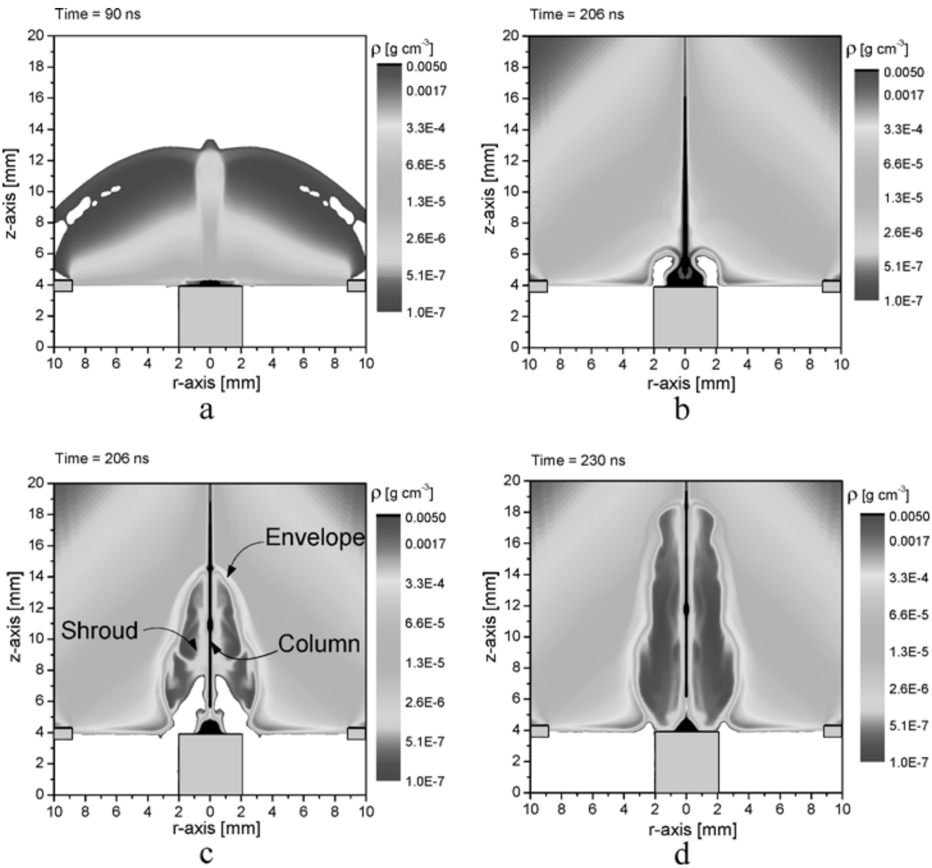

Figure 2. Time series of mass density contour plots in the radiatively efficient regime. Densities are in kg m^{-3} and the contours are on a logarithmic scale. The indicated times are with respect to the start of the current pulse. The grey boxes mark the position of the electrodes.

in time, as the density of the ablated flow and consequently the radiation losses increase, a high density jet-like structure develops on axis. At $\sim$190 ns from the start of the current pulse, breakage of the wires allows a magnetic cavity or tower (in the astrophysical language) to form. The magnetic field pressure drives a shock in the background plasma and the magnetic tower inflates. While radial expansion is slowed by the external pressure, the magnetic tower can easily expand in the axial direction. The toroidal magnetic field also confines a high density plasma column on axis by its pinch effect. This is the basic picture of the magnetic-jet formation in radial wire arrays. By magnetic-jet we will signify the whole structure which develops with the emergence of the magnetic tower. We will now look in more detail first at the initial collimation of the flow and then at the formation and propagation of the magnetic-jet.

3.1. Initial flow evolution

In radial wire arrays, the accelerating Lorentz force is mostly directed in the axial direction. Pressure gradients present in the plasma produce further axial and radial acceleration. Figure 3 shows a plot of the current density vectors overlaid on a mass density contour plot for the radiatively inefficient regime simulations. Advection of the global field with the ablated flow produces axial current components in the expanding flow which accelerate it radially. This acceleration occurs mostly in regions close to the wires where a relatively large magnetic field is present. The converging plasma undergoes a shock on axis which redirects the flow in the vertical direction. Figure 4 shows the velocity vectors overlaid on a mass density plot for a radiatively inefficient simulation. The collimation of the flow into a jet can be clearly seen by following the radially converging velocity vectors. This mechanism was observed in conical wire arrays and was shown to be very effective in re-collimating converging conical flow (Ciardi et al., 2002; Lebedev et al., 2002). Collimation depends on the radiative cooling efficiency of the plasma, with highly collimated jets formed when radiation losses are significant. In this case, the kinetic energy that is thermalized at the shock is rapidly lost to radiation; the shocked plasma remains cool and the ram pressure of the unshocked plasma can confine the jet to a small opening angle. In the radiatively inefficient regimes the resulting lower density collimated flow is confined to a larger opening angle conical shock. In general, along the axis of the jet $\beta > 1$ and the jet is confined by the ram and thermal pressure of the plasma. The magnetic field only dominates near the base of the jet, where $\beta \lesssim 1$. After the initial collision of the ablated plasma, a quasi-steady

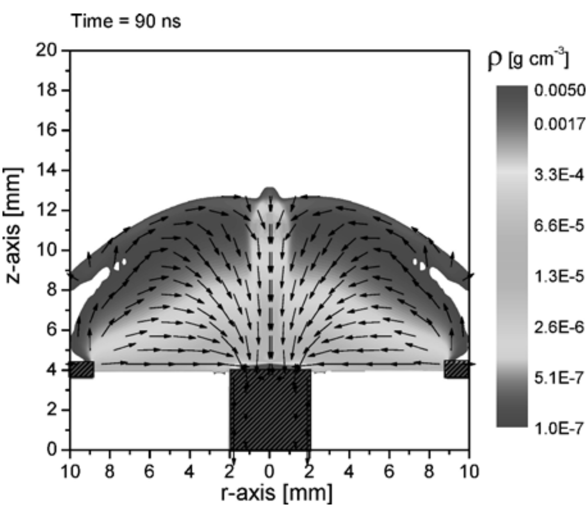

Figure 3. Logarithmic contour plot of mass density in the radiatively inefficient regime. Current density vectors are overlaid on the contours. Shaded regions indicate the electrode position.

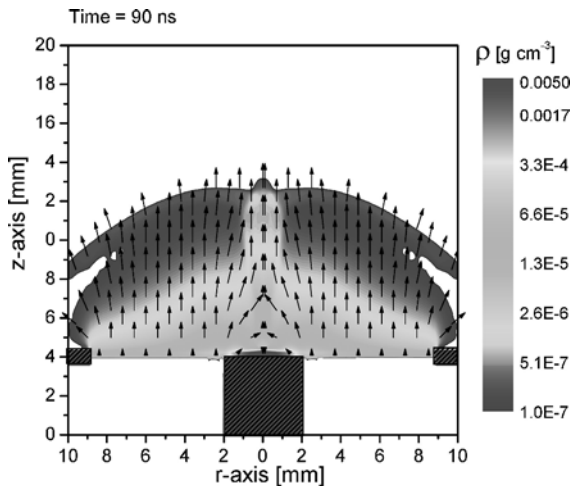

Figure 4. Logarithmic contour plot of mass density in the radiatively inefficient regime. Flow velocity vectors are overlaid on the contours. Shaded regions indicate the electrode position.

configuration ensues, consisting of a poorly collimated, high plasma beta ($\beta > 1$) flow, with low density and high Mach number ($M \sim 10$) surrounding a high density, jet-like flow with Mach number $M \sim 3$.

3.2. Magnetic-jet launching

The flow conditions described in the previous section persist until wire breakage, which occurs first at the smallest radius where wire ablation is highest. In the simulations, sourcing of the plasma onto the grid takes place until all wire mass, at a given radius, has been ablated. At wire breakage, the magnetic pressure is able to push the plasma upward and side-ways forming a magnetic cavity. This is the beginning of the development of a jet driven by rising magnetic loops. As the magnetic tower grows, it produces strong axial and radial flows of matter and drives a shock in the surrounding medium. Typical shock velocities and Mach number in the axial direction are of the order $\sim$500–1500 km s^{-1} and $M \sim 40$ respectively, depending on the array geometry and radiative cooling properties of the plasma. Eruption of the magnetic tower produces a three-component structure (the magnetic-jet), which comprises a high density column pinched on axis by the magnetic field, a shroud of hot, low density plasma embedded in the magnetic tower and a shock envelope driven by the magnetic piston and surrounding the magnetic tower (see Figure 2c).

Currents associated with the toroidal magnetic field are shown in Figure 5. These currents flow up along the shock envelope and down the central part of the magnetic-jet, with only a small fraction of the total current flowing in the low density plasma shroud. In the magnetic tower the field has small axial gradients with

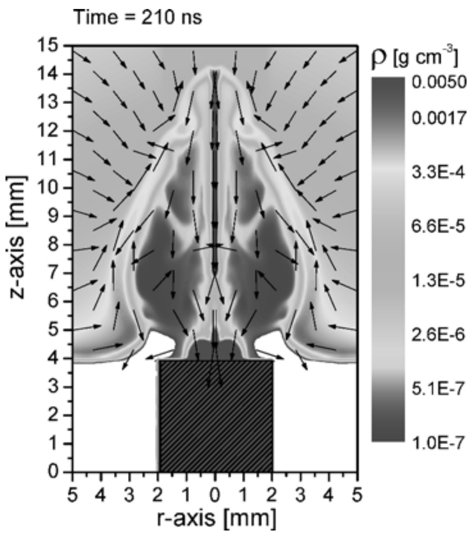

Figure 5. Logarithmic contour plot of mass density in the radiatively inefficient regime. Current density vectors are overlaid on the contours. Shaded regions indicate the electrode position. Only the central part of the computational box is shown.

currents flowing predominantly in the axial direction. Radial currents may, from time to time, reconnect across the plasma shroud between the shock envelope and the central column. Since the plasma in this region is highly magnetized ($\beta < 1$) the axial gradients in the magnetic field can quickly relax, leading to strong axial acceleration of the shroud plasma. The low density of this plasma means that its kinetic energy and ram pressure are negligible. A plot of the velocity vector field, overlaid onto a mass density contour is shown in Figure 6. The somewhat complex velocity field present in the low density plasma shroud is clearly visible. Overall, the magnetic tower drives a well-collimated outflow, with an increasing length to width ratio. The axial velocity profile of the plasma column rapidly increases with height above the electrode, $v_z \sim 100$–$1000\,\mathrm{km\,s^{-1}}$. Velocities in the column are higher than those seen in the jet-like flow present prior to the development of the magnetic tower, thus indicating that it is not just the shock envelope which is accelerated by the inflation of the magnetic tower but also the plasma column on axis.

We now turn our attention to the collimation of the whole magnetic-jet. As the shock envelope grows laterally, the magnetic field driving the expansion decreases in strength as $\sim 1/r$. Lateral expansion is halted when the magnetic pressure in the cavity equals the external pressure of the background matter. Therefore we expect the pressure distribution in the ambient plasma to be fundamental in determining the overall collimation of the magnetic-jet. Because in the background medium the temperature is approximately constant ($\sim 15\,\mathrm{eV}$), it is the density distribution that determines to a larger degree the collimation. This dependence is important in the

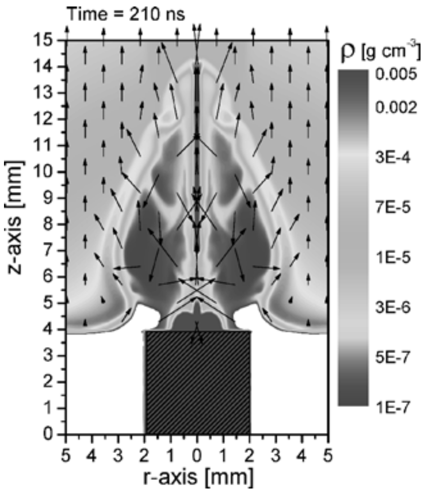

Figure 6. Logarithmic contour plot of mass density in the radiatively inefficient regime. Flow velocity vectors are overlaid on the contours. Shaded regions indicate the electrode position. Only the central part of the computational box is shown.

experiments, since by changing the initial properties of the radial array we can in principle change the density distribution of the background plasma and influence the collimation of the magnetic-jet. Some of the effects on the collimation of the magnetic-jet are visible by comparing Figures 2c and 5. The two simulations are for arrays of different total mass. Wire breakage and the initial formation of the magnetic tower occur at different times, when different background density distributions are present. Furthermore, in the radiatively inefficient simulation, the density above the magnetic tower is lower and axial expansion occurs faster. As discussed previously, the magnetic pressure in the background plasma is generally negligible with respect to the thermal pressure. Only at the base of the shock envelope the confinement is also due to the magnetic field. Comparing the panels c and d of Figure 2, we can see there is very little lateral expansion of the shock envelope for axial positions below $\sim$12 mm. While radial expansion is slowed down by the background pressure, in the axial direction the pressure gradients rapidly decay and the magnetic tower can easily grow. During the experiment energy is supplied to the magnetic field and the axial growth does not decrease as the magnetic tower elongates.

The plasma column which develops on axis is confined by the toroidal field and it is prone to the typical magnetohydrodynamic Z-pinch instabilities. The axis-symmetry imposed in the simulations limits the development of the instabilities to the $m = 0$ mode. Growth of this mode leads to break up of the plasma column and the set up of large electric fields which can drive electron beams across the gaps left behind. At this point the MHD model employed breaks down and the simulations have to be stopped.

4. Summary and Discussion

We carried out simulations of the dynamical evolution of radial wire arrays in the context of astrophysical models of magnetic-jet launching. In these models, a toroidal field is generated on axis by the differential rotation of a central object and its accretion disk. Accumulation on axis of toroidal magnetic field loops is then responsible for driving an outward flow and the formation of a magnetic tower. The global structure consists of a low-β magnetic tower where a poloidal magnetic field on axis is surrounded by a dominant toroidal magnetic field. The magnetic tower forms a cavity and drives a jet in the high-β background plasma which provides the collimating pressure (Kato et al., 2004b).

In the simulations of radial wire arrays, the formation of a magnetic tower begins after wire breakage, which corresponds to a stage when the magnetic pressure is large enough to inflate and expand through the background plasma. The impulsive release of magnetic energy in the background plasma produces a shock, which envelopes the magnetic tower as it inflates vertically and radially. While the radial expansion is halted, the magnetic tower accelerates in the axial direction and elongates until the jet is disrupted. There are no poloidal magnetic fields in the system which may help prevent the formation of a dense plasma column on axis. Furthermore, pinching of the axial column leads to the development of an $m = 0$ instability which later destroys the jet. It is expected and experiments indicate that the column is also kink unstable; three-dimensional simulations are needed to ascertain whether this is the case and what are the conditions for jet disruption. An axial magnetic field could in principle be introduced in the experiments and may increase the stability of the central column. Global collimation of the jet is determined, like in the astrophysical models, by the external pressure. In the experiments we expect a pressure profile which roughly decrease as $\sim 1/r$ in the radial direction and an exponentially decreasing profile in the axial direction. Furthermore, these profiles can be modified by changing, for example, the inclination angle of the wires. Different radiation efficiency regimes can also be investigated by using different wire materials, low atomic number material being less efficient radiators.

The results obtained indicate that radial arrays may provide an interesting platform to study the dynamics of certain classes of magnetically launched jets. Further analysis and three-dimensional simulations are underway to fully establish the similarity, scalability and thus the relevance of the experiments to the astrophysical models.

References

Chittenden, J.P., Aliaga-Rossel, R., Lebedev, S.V., Mitchell, I.H., Tatarakis, M., Bell, A.R. and Haines, M.G.: 1997, *Phys. Plasmas* **4**, 4309.

Ciardi, A., Lebedev, S.V., Chittenden, J.P. and Bland, S.N.: 2002, *Laser Part. Beams* **20**, 255.

Kato, Y., Hayashy, M.R. and Matsumoto, R.: 2004, *ApJ* **600**, 338.
Kato, Y., Mineshige, S. and Shibata, K.: 2004, *ApJ* **605**, 307.
Lebedev, S.V, Beg, F.N., Bland, S.N., Chittenden, J.P., Danger, A.E., Haines, M.G., Kwek, K.H., Pikuz, S.A. and Shelkovenko, T.A.: 2001, *Phys. Plasmas* **8**, 3734.
Lebedev, S.V, Chittenden, J.P., Beg, F.N., Bland, S.N., Ciardi, A., Ampleford, D., Hughes, S., Haines, M.G., Frank, A., Blackman, E.G. and Gardiner, T.: 2002, *ApJ* **564**, 113.
Lovelace, R.V.E., Li, H., Koldoba, A.V., Ustyugova, G.V. and Romanova, M.M.: 2002, *ApJ* **572**, 445.
Lovelace, R.V.E., Ustyugova, G.V. and Koldoba, A.V.: 1999, in: Y. Terzian, E. Khachikian and D. Weedman (eds.) Proceedings of IAU Syposium 194 on Active Galactic Nuclei and Related Phenomena, Astronomical Society of the Pacific, San Francisco, p. 208.
Lynden-Bell, D.: 1996, *MNRAS* **279**, 389.
Lynden-Bell, D.: 2003, *MNRAS* **341**, 1360.

TAILORED BLAST WAVE PRODUCTION PERTAINING TO SUPERNOVA REMNANTS

A.S. MOORE[1], D.R. SYMES[1,2] and R.A. SMITH[1]

[1]*The Blackett Laboratory, Imperial College of Science, Technology and Medicine, London SW7 2BZ, United Kingdom; E-mail: alastair.moore@imperial.ac.uk*

[2]*Present address: University of Texas at Austin, Fusion Research Center, 1 University Station C1510, Austin, TX, USA*

(Received 26 April 2004; accepted 5 August 2004)

Abstract. We report on the first production of "tailored" blast waves in cluster media using a 1 ps laser pulse focused to 2×10^{16} W/cm^2. This new technique allows cylindrical blast waves to be produced with a strong axial modulation of variable spatial frequency, as a seed for instability growth. Energy deposition is modified by changing the cluster density whilst keeping the atomic density of the target constant. Electron density maps show the production of strongly modulated blast waves and the development of a thin shell structure in H at late times, and the trajectories show blast waves forming in H, and Ar. In Xe, a blast wave does not form on the timescales studied. Analysis of astrophysical similarity parameters suggests that a hydrodynamically similar situation is created in H, and that further evolution would create a regime where radiative effects may be influential in Ar and Xe.

Keywords: laser-cluster interactions, laser-driven shocks and discontinuities, hydrodynamic and radiative plasma instabilities

The blast wave from an "idealized" supernova remnant (SNR) will become adiabatic during its evolution. Analytically this is a self-similar, Sedov-Taylor (ST) solution, and is characterised by the formation of a thin shell behind the smooth shock front. However, the shocks of actual SNR's are rarely smooth, and typically appear irregular due to a host of instabilities. The self-similar analysis yields a power law dependence of the shock front radius, R, on time which is appropriate once the initial gas pressure is small compared to the pressure behind the shock front. When the blast wave cannot be treated as adiabatic, two analytical, radiative or snowplow solutions are obtained assuming a constant fraction of energy is lost across the evolving shock front: the pressure driven snowplow (PDS) and the momentum conserving snowplow (MCS). The PDS regime occurs if radiative cooling only occurs in the thin shell, whereas the MCS regime occurs later when radiation cooling is prevalent in the thin shell and the core. In the transition to both radiative phases, numerical modeling has predicted that hydrodynamic instabilities are likely to occur (Blondin et al., 1998) and experiments by (Grun et al., 1991) have shown some evidence of this. Overstabilities (Vishniac, 1983) are also thought to be found when radiation becomes significant and the wavelength of the perturbation is large compared to the shell thickness.

In cylindrical geometry, the situation here, the blast wave will follow a different trajectory to the spherical case causing α to increase. For a cylindrical ST blast wave the shock front evolves as: $R(t) = \beta(\gamma)(E_l/\rho_0)^{1/4}t^{1/2}$ being dependent on E_l, the initial energy per unit length, ρ_0 the density of the unperturbed medium, and γ the adiabacity. A cylindrical blast wave in the PDS and MCS regimes will follow a trajectory with $\alpha = 3/8$ and $1/3$ respectively (Edwards et al., 2001).

The use of high power, sub-picosecond lasers to produce blast waves in the laboratory is an area of growing interest (Dunne et al., 1994; Remington et al., 1999; Ditmire et al., 2000). These lasers allow energy deposition to be de-coupled from the later ns-timescale hydrodynamic motion of the plasma. Used in conjunction with a new target medium composed of atomic clusters (Hagena and Obert, 1972), extremely high energy deposition efficiencies (near 100%) can be realized, compared to $\approx$1% absorption for atomic gas targets of comparable average density (Glover et al., 1994). Resultant energy densities have been measured to be as high as 10^4–10^5 J/cm^3 (Zweiback and Ditmire, 2001).

In high Z, Xe targets, radiative processes will be predominant so precursors and instabilities might be observed. Previous work (Ditmire et al., 2000; Edwards et al., 2001) involving blast waves in cluster media show strong evidence of a precursor, but no instability growth has yet been observed. We present here a new technique allowing a strong, variable scale length spatial modulation to be imprinted on the blast wave to act as a seed for the growth of instabilities. In Symes et al. (2002) a "laser-machining" technique was used to shape the cluster medium. By destroying clusters in specific regions the average atomic density is unchanged, but the cluster density is modified. The large difference in efficiency of laser absorption between clusters and the monatomic gas then results in a strong variation in the energy deposition of a second, high-power, heating beam, tailoring the blast wave radius in a controlled and repeatable fashion (Smith and Ditmire, 2001).

Our experiment was performed using a Nd:glass laser delivering pulses of duration 1 ps with an energy of up to 1 J at a wavelength of 1.054 μm and is illustrated in Figure 1. Clusters of a range of species (H_2, Ar and Xe) were produced with backing pressures of up to 50 bar, and temperature between 293 K and 97 K (to control cluster size) (Smith et al., 1998). The main laser beam was split into three beamlets, with half the energy focused into an extended cluster medium to provide a heating beam with vacuum intensity of 2×10^{16} W/cm^2. The second beamlet was frequency doubled producing a probe pulse at 527 nm, which interferometrically imaged the plasma with a wide (>3 mm) field of view (Ditmire and Smith, 1998). This could be delayed to arrive up to 6 ns after the heating beam. FFT processing (Takeda et al., 1982) and Abel inversion of the images allowed the calculation of electron density. The remaining beamlet was used to machine the cluster medium, and was split further into two synchronous but spatially separated beams that were loosely focused into the cluster medium 1.4 ns prior to, and transverse to, the heating beam,

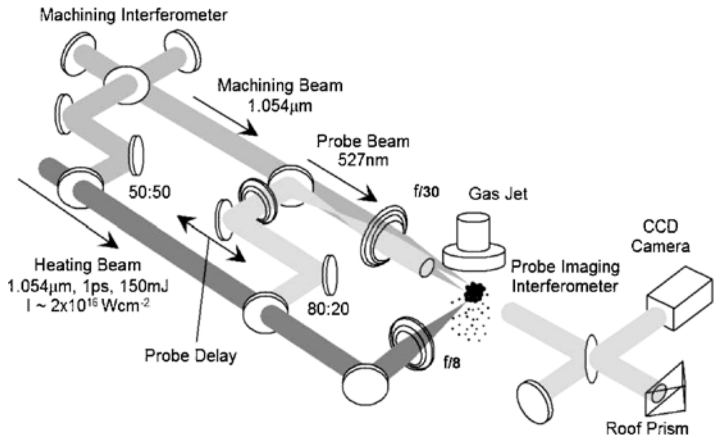

Figure 1. Experimental layout for producing tailored blast waves in an atomic cluster medium.

ensuring the clusters had fully disintegrated before the arrival of the heating beam. Each machining beam contained $\approx$100 mJ that was defocused to produce two low intensity spots in the plane of the heating beam.

The interaction of the heating beam with the unmodified cluster spray formed a cylindrical plasma filament 2 mm below the gas jet nozzle, $\approx$2 mm long, with an initial radius of $\approx$50 μm. A shock front developed and the electron density, which was initially Gaussian shaped, peaked on the laser axis, typically evolved towards a more "thin-shell" structure.

Interferometric images show that when no machining beam is present a smooth, uniform shock front parallel to the laser axis is formed. The time evolution of this showed no indication of any sizeable changes in the radius along the plasma filament. In contrast the "tailored" blast wave has a maximum radius comparable to that of the unmachined target, but it is greatly reduced in the locations where the machining beams have destroyed clusters. All the self-similar solutions denote that the blast wave radius is proportional to deposited energy, so there is negligible deposition in the regions where clusters have previously been destroyed. A spatial cross-section of the electron density of a machined blast wave in H is shown in Figure 2(a), illustrating the tailoring of the blast wave.

Studying the late-time (post 2 ns) behavior of H, a strong shock forms with velocity $V_{H_2} = 3.0(\pm 0.3) \times 10^6$ cm/s, corresponding to Mach 45. In Ar the blast wave forms later in the evolution at $\approx$4.5 ns, and has a slower velocity of $1.5(\pm 0.3) \times 10^6$ cm/s. In Xe it is less clear whether the shock has formed by the latest time in the data set, and the front velocity was found to be lower again at $1.3(\pm 0.5) \times 10^6$ cm/s. For each cluster element the deposited energy is the same. Assuming a ST trajectory, the blast wave velocity will be $\propto \rho_0^{0.25}$. The ratio of this quantity for the different cluster elements used shows that shock velocities in Ar and Xe should be 0.4 V_{H_2} and 0.3 V_{H_2} respectively, in good agreement with the velocities measured.

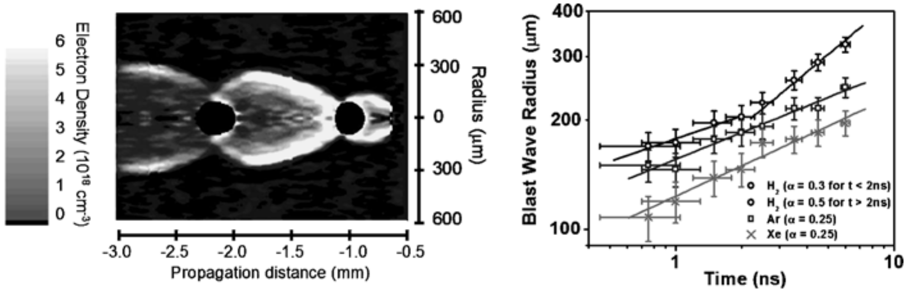

Figure 2. (a) Electron density map of a strongly modulated blast wave in an extended H cluster medium at 6 ns after the heating pulse, (b) Measured blast wave trajectories for H (o), Ar (□) and Xe (×) cluster media. Solid lines represent the best fit to the data points for each cluster gas.

Figure 2(b) shows that the trajectories of the unmodulated blast waves for each gas are initially very similar. In H the shock evolves as $t^{0.30(\pm 0.05)}$ and for Ar and Xe the deceleration parameter is, $\alpha = 0.25(\pm 0.07)$. However, after 2 ns, the H trajectory changes to $\alpha \approx 0.5$ corresponding to a ST blast wave. No change is observed in Ar or Xe.

It is clear that the blast waves in each gas are at different stages of development. In H the thin shell is present and the blast wave radius is large compared to $r_{\mathrm{initial}} \approx 50\,\mu$m from about 2 ns onwards. At 2 ns the radius is $\approx$200 μm, which corresponds to a change in mass per unit length from the initial energy deposition by a factor of 16, sufficient to assume self-similarity. In Ar the thin shell is only clear at $\approx$4.5 ns, when the radius reaches 200 μm, but a considerable density of gas remains at the core of the plasma filament, suggesting it is becoming self-similar. Most noticeably, in Xe the density is still peaked on axis, and the radius does not grow to 200 μm implying the shock front does not propagate a sufficient distance to appropriate a self-similar analysis.

The deceleration parameters in Ar and Xe are considerably lower than 0.5, expected from a ST solution, which is most likely due to the blast wave being underdeveloped, but notably different other results (Shigemori et al., 2000; Edwards et al., 2001). Energy transport at this early time is due to electrons, so whilst the trajectories we observe correspond well to the MCS or PDS trajectories, the timescales are not that of the electron-ion collision ($\approx$10's ns), when radiation effects are expected. The most likely explanation for the trajectories we observe is electron thermal conduction that transports energy ahead of the forming shock front. This drives a radial ionization wave, due to the high initial temperature ($T_e \approx 1.5$ keV), which quickly thermalizes on the electron – electron collision timescale ($\approx$100's ps) and forms a thermal heat wave (Zeldovich and Raizer, 1966). On a longer timescale (up to a few ns) the ion-shock propagates into the preheated plasma, accumulating mass, until the shock combines with the electron thermal front and the dynamics become self-similar.

We have demonstrated a method of tailoring blast waves within a laboratory environment in low and high Z gases. The blast wave trajectories we observe are in good agreement with that expected during formation. Radiative effects are not observed, but are calculated to occur on a longer timescale than was studied. Further investigations of the blast wave evolution over longer timescales to verify this are in preparation. Tremendous potential exists for using this laser-machining technique to create shaped blast waves of relevance to astrophysics. The reproducibility with which modulations can be imprinted upon the cluster medium and the ease with which the seeded perturbation can be altered makes this desirable for studying instabilities, and early analysis indicates that the H results are hydrodynamically scalable. The extension of which, to study late-time evolution of blast waves in high Z clusters, will probe the dynamics of radiative shock instabilities and over-stabilities. In addition this work presents huge possibilities for creating spherical or custom-shaped blast waves, and for studying collisions between multiple shocks, or shocks and cold gas or solid targets.

Acknowledgements

We would like to thank John Tisch, Mike Dunne, Ed Gumbrell and Aaron Edens for a number of very useful discussions, and Peter Ruthven and Andy Gregory for technical assistance. This work was supported by the EPSRC and MoD UK.

References

Blondin, J.M. et al.: 1998, *ApJ* **500**, 342.
Ditmire, T. and Smith, R.A.: 1998, *Optics Lett.* **23**, 618.
Ditmire, T. et al.: 2000, *ApJSS* **127**, 299.
Dunne, M. et al.: 1994, *Phys. Rev. Lett.* **72**, 1024.
Edwards, M.J., et al: 2001, *Phys. Rev. Lett.* **87**, 085004.
Glover, T.E. et al.: 1994, *Phys. Rev. Lett.* **73**, 78.
Grun, J. et al.: 1991, *Phys. Rev. Lett.* **66**, 2738.
Hagena. O.F. and Obert. W.: 1972, *J. Chem. Phys.* **56**, 1793.
Remington, B.A., Arnett, D., Drake, R.P. and Takabe, H.: 1999, *Science* **284**, 1488.
Ryutov, D. et al.: 1999, *ApJ* **518**, 821.
Shigemori, K. et al.: 2000, *ApJ* **533**, L159.
Smith, R.A. and Ditmire, T.: 2001, in: J. Posthumus (ed.), Molecules and Clusters in Intense Laser Fields, Cambridge University Press, p. 216.
Smith, R.A., Ditmire, T. and Tisch, J.W.G.: 1998, *Rev. Sci. Inst.* **69**, 3798.
Symes, D.R., Comley. A.J., Tisch. J.W.G. and Smith, R.A.: 2002, *Appl. Phys. Lett.* **80**, 4112.
Takeda, M., Ina, H. and Kobayashi, S.: 1982, *J. Opt. Soc. Am.* **72**, 156.
Vishniac, E.T.: 1983, *ApJ* **274**, 152.
Zeldovich, Y.B. and Raizer, Y.P., 1966, in: W.D. Hayes and R.F. Probstein (eds.), Physics of Shock Waves and High Temperature Hydrodynamic Phenomena, Vol. 1, Academic, New York.
Zweiback. J. and Ditmire. T.: 2001, *Phys. Plasmas* **8**, 4545.

A NEUTRON STAR ATMOSPHERE IN THE LABORATORY WITH PETAWATT LASERS

S.J. MOON[1], S.C. WILKS[1], R.I. KLEIN[1,2], B.A. REMINGTON[1], D.D. RYUTOV[1], A.J. MACKINNON[1], P.K. PATEL[1] and A. SPITKOVSKY[3]

[1]*Lawrence Livermore National Laboratory, Livermore, CA; E-mail: moonl@lln1.gov*
[2]*UC Berkeley, Dept of Astronomy, Berkeley, CA*
[3]*Stanford Linear Accelerator Center, Stanford University, Stanford, CA*

(Received 6 May 2004; accepted 14 June 2004)

Abstract. We discuss the preliminary estimates to create Neutron Star atmospheric conditions in the laboratory and the possibility of generating photon bubbles. The minimal requirements for photon-bubble instability could potentially be met with a properly configured 10 ps petawatt laser experiment. The high energy (multi-MeV) electrons generated by an ultra-intense laser interacting with a foil are coupled to the electrons in the solid to heat the entire solid generating high thermal temperatures. Small amounts of matter could potentially be heated to ∼1 keV temperatures with large radiation temperature. Additionally, 2-D PIC simulations show large B-fields on both the front and back of these targets with B fields consistent with experiments using the petawatt at Rutherford Appleton Laboratory (Tatarakis, M. et al.: 2002c, *Nature* **415**, 280).

Keywords: petawatt laser, neutron star atmosphere

1. Introduction

Accretion-powered pulsars shine because fully ionized plasma falls onto the polar caps of a strongly magnetized, rotating neutron star. For the brightest sources ($L_x > 10^{36}$ ergs/s, $B \sim 10^{10\text{–}12}$ gauss) the radiation pressure becomes locally super-Eddington, resulting in a strong deceleration of the inflowing plasma. Since radiation escapes from the sides of the accretion column, the inhomogeneous pressure distribution creates strong inhomogeneities throughout the accretion column. Below a radiation dominated accretion shock, the plasma settles with approximate hydrostatic balance maintained between radiation pressure and gravity. Such support suggests the possibility of strong time variability in the flow, since a heavy fluid (plasma) gains its support against gravity from a light fluid (photons). Stability investigations of such phenomena suggest the possibility of variability occurring on the surfaces of neutrons stars on millisecond timescales resulting in photon bubble instabilities. In a series of papers Richard Klein and collaborators (Klein et al., 1989, 1991, 1996a,b; Hsu et al., 1997) have investigated such effects by solving the self-consistent multi-dimensional time dependent equations of magneto-radiation-hydrodynamics governing the accretion of matter onto the polar caps. These calculations have shown that the settling mound on the surface

Astrophysics and Space Science **298:** 293–298, 2005.

of a neutron star does indeed develop a new form of "turbulence" in which photon bubbles form in the medium and transport energy to the surface of the accretion column. Recent work by Blaes and Socrates (2003) has shown photon bubbles in accretion disks around black holes. When the photon bubble instability occurs in concert with continued accretion onto the polar caps, the numerical calculations show clear evidence for a substantial coalescence of the photon bubbles to become relatively large, rising, optically thin pockets within the settling mound filled with hot ($T \sim 10\,\mathrm{keV}$) radiation, embedded in optically thick, settling plasma. The discovery of such photon bubble instabilities in the accretion mound of X-ray pulsars has important consequences for probing the physics of the accretion column of a neutron star. Low-mass X-ray binaries could potentially exhibit similar phenomena. Here, the magnetic field strengths in the neutron star atmosphere are 10^8–10^9 gauss.

With the recent advent of the Rossi X-Ray Timing Explorer (XTE), a time-resolved X-ray satellite, the dynamics occurring near the surface of a neutron star on time-scales less than a millisecond have been diagnosed, and have discovered a new phenomena, photon bubble instabilities, in an accreting X-ray pulsar Centaurus X-3 (Jernigan et al., 2000) predicted by the multi-dimensional calculations.

It is important to study these phenomena and one methodology is to develop an appropriate laboratory experiment. Scaling astrophysical experiments to laboratory parameters is important to further our understanding of astrophysical phenomena (Robey et al., 2002; Klein et al., 2003; Remington et al., 1999, 2000; Ryutov and Remington, 2002). The length scales and energy content in stellar atmospheres is one area that high power and high-intensity lasers can begin to approach. As an example we can consider the low-lying atmosphere of a magnetized neutron star. The thermal temperature of the dense plasma 10^{-1}–$10^{-3}\,\mathrm{g/cm^3}$ is 10 keV with similar radiation temperatures and magnetic fields of order 10^{12} Gaus for X-ray pulsars. Generating these intense magnetic fields and radiation-dominated environments in these dense plasmas is not currently possible. However, using a petawatt laser magnetic fields greater than 100 Megagauss (Tatarakis et al., 2002a,b) and temperatures on the order of 1 KeV could potentially be achieved.

We have investigated achieving these conditions using a hybrid code. Shown in Figure 1 is both the hot electron particle temperature and the thermal temperature of an Al plasma at 4 ps after the peak of the interaction with a high intensity laser, $I = 2 \times 10^{19}\,\mathrm{W/cm^2}$, with a pulse width of 1 ps FWHM and a spot of $10\,\mu\mathrm{m}$, diameter. The simulation injected a stream of hot, $T = 750\,\mathrm{keV}$, electrons generated from the high intensity laser into the plasma with a profile similar to the measured laser spot. The results demonstrate ultra-strong magnetic fields with ultra-intense lasers and have made the first approximate calculations of the laboratory conditions needed to simulate the radiation dominated flow regime necessary to achieve neutron star atmosphere conditions on large laser system with a petawatt laser platforms. Figure 1(a) shows a contour of the hot electron temperature (hots). The on-axis electrons stream through the solid and interact with the thermals. The initial population of hots has had their temperature reduced from collisions and

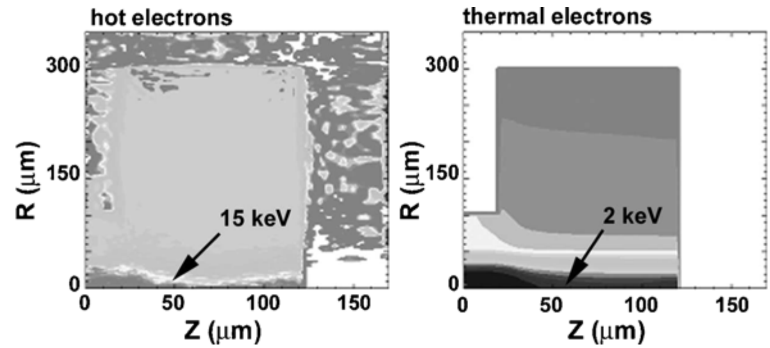

Figure 1. Simulations show a beam of hot electrons interacting with the solid target – heating the matter to high thermal temperatures.

field effects. Their temperature is reduced to 15 keV on-axis and the electrons dump a large amount of energy into the thermal electrons. Figure 1(b) shows the thermal temperature of the solid. The on-axis temperature is seen to be 2 keV in a 10 μm radius. This thermal temperature does not include some important energy loss mechanisms such as ionization and may result in a reduction of as much as half the energy or a final thermal temperature of 1 keV. In further simulations this effect will be included.

Petawatt lasers, coupled with large laser systems, will open the door to laboratory studies of extreme conditions of density and temperature including those found in neutron star atmospheres. This capability will seed a new era in the study of physics generated by strongly radiative flows and laser-plasma interactions for the laboratory study of both distant astrophysical phenomena, and the physics of extreme conditions of density and temperature.

2. Bringing the Star to the Lab

Ultra-intense laser pulses from a new generation of petawatt lasers can potentially generate the conditions appropriate to the atmospheres of magnetized neutron stars in an earth-based laboratory. Development of a plasma under such conditions would enable a breakthrough in our ability to study highly dynamical phenomena such as photon bubble instabilities (Klein et al., 1996b), thought to be present in the low altitude atmosphere above the surface of magnetized neutron stars.

Photon bubble instabilities need conditions such that a super strong magnetic field of order several 10^9 gauss threading an optically thick flow that is radiation pressure dominated, with radiation temperatures of order 1 keV, confines the flow in the direction of accelerations of order 10^{14} cm/s^2. Laboratory measurement of self-generated magnetic fields during an ultra-high intensity ($> 10^{19}$ W/cm^2) short pulse (0.7–1 ps) laser-plasma interactions have reported fields in excess of 340 Megagauss (Tatarakis et al., 2002a,b).

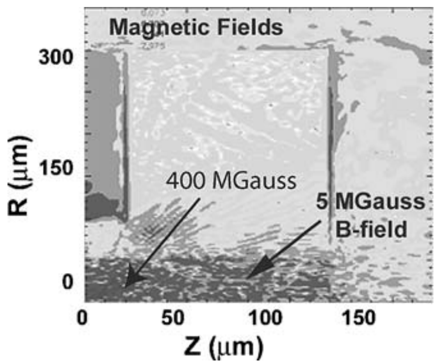

Figure 2. The generation of strong magnetic fields is shown in a thin foil.

To achieve neutron star atmospheric conditions in a laboratory setting, we need radiation temperatures of order 1 keV to achieve radiation pressure dominance, densities of order $n_e \sim 10^{22}$ in a mid-Z material like Cu to obtain appropriate optical depths >1 and accelerations $>10^{14}$ cm/s^2 to provide an effective gravity and magnetic field strengths $\sim 10^8$ gauss that can confine the plasma to move in one direction. A stability analysis (Arons, 1992) showed that the photon bubbles form when radiation conduction destabilizes the g-modes in the column, provided the magnetic field is strong enough to suppress the stabilizing expansion of the modes and this occurs when the vertical magnetic field is $B \sim 10^9$ G.

Our initial estimates show that relevant densities, accelerations and magnetic field strengths may be achievable on a petawatt class lasers coupled to a large laser system. Simulations using a hybrid PIC/fluid code show that thermal temperatures of order ~ 1 keV are generated, see Figure 1. Figure 2 shows a 400 Megagauss magnetic field inside the overdense plasma can be created, and fields $\sim 10^9$ G can be transported well into a solid target. The challenge for the design of this experiment will be to obtain radiation temperatures of the order of 1 keV and an optical depth great enough in the plasma to achieve optically thick conditions. Radiation temperatures of ~ 1 keV may be achievable using a large laser system plus petawatt lasers.

3. PW Laser Physics and Plasmas Created

The electron temperature in ultra-intense laser interactions can be very high. The ultra-high intensity laser interacts with the electrons in the solid to produce multi-MeV electrons. The characteristic kinetic energy of electrons generated by an ultra-intense laser interacting with a foil is roughly given by (Wilks and Kruer, 1997),

$$E_{\mathrm{hot}} \sim m_e c^2 \left[\sqrt{1 + \frac{I\lambda^2}{2.7 \times 10^{18}}} - 1 \right] \tag{1}$$

These multi-MeV electron energies are generated when petawatt laser pulses interact with solids. These hot electrons couple to the electrons in the solid, and heat the entire solid. Electrons 'reflux' through thin walls. Hybrid codes that model finite conduction and collisions must then be used.

What radiation temperature can we get? The trapped electrons led to a high thermal electron temperature which in turn creates a high radiation temperature. In addition to heating the solid these hot electrons create a current and generate a strong magnetic field. We have used a hybrid code to propagate these hot electrons and have investigated a simple experiment of an ultra-short pulse laser heating a foil, shown in Figure 2. The simulation showed small amounts of matter heated to high thermal temperatures $\sim$1 keV.

4. Conclusions

An investigation into the possibility of using petawatt lasers to generate the photon-bubble instability was presented. These extreme plasma conditions could potentially be met with a properly configured 10 ps petawatt laser experiment. High energy (multi-MeV) electrons generated by an ultra-intense laser interacting with a thin ($\sim$10's of μm) solid target efficiently couple to the electrons in the solid, resulting in high thermal temperatures for the solid. Preliminary simulations show that these small amounts of matter could potentially be heated to $\sim$1 keV temperatures with large radiation temperature. Additionally, 2-D PIC simulations show large B-fields of 400 MGauss on the front and 5 MGauss on the back of these targets. The combination of a radiation-dominated environment in a large magnetic field is fundamental to create Neutron Star atmospheric conditions and the possibility of generating photon-bubbles in the laboratory.

Acknowledgements

The authors would like to thank H. Chen, J. Kuba, R. Town and R. Shepherd for their valuable input to this work. We gratefully acknowledge partial support from LLNL Laboratory Directed Research and Development (LDRD) grant number 04-ERD-28. This work was performed under the auspices of the U.S. Department of Energy by University of California, Lawrence Livermore National Laboratory under Contract W-7405-Eng-48.

References

Arons, J.: 1992, *ApJ* **388**, 561.
Blaes, O. and Socrates, A.: 2003, *ApJ* **596**, 509.
Hsu, J.J.L., Arons, J. and Klein, R.I.: 1997, *ApJ* **478**, 663.

Jernigan, J.G., Klein, R.I. and Arons, J.: 2000, *ApJ* **530**, 875.
Klein, R.I. et al.: 1996a, *ApJ* **469**, L119.
Klein, R.I., Arons, J., Jernigan, G. and Hsu, J.J.L.: 1996b, *ApJ* **457**, L85.
Klein, R.I. and Arons, J.: 1989, in N.E. White and T.D. Guyenne, Proceedings of 23rd ESLAB Symposium on Two Topics in X-ray Astronomy, ESA SP-296, ESA, Paris.
Klein, R.I. and Arons, J.: 1991, in Stellar Atmospheres: Beyond Classical Models, L. Crivillari (ed.), Kluwer, Boston, p. 205.
Klein, R.I., Budil, K.S., Perry, T.S. and Bach, D.R.: 2003, *ApJ* **583**, 245.
Remington, B.A., Arnett, D., Drake, R.P. and Takabe, H.: 1999, *Science* **284**(5419), 1488.
Remington, B.A. et al.: 2000, *Phys. Plasmas* **7**(5), 1641.
Robey, H.F. et al.: 2002, *Phys. Rev. Lett.* **8908**(8), 5001.
Ryutov, D.D. and Remington, B.A.: 2002, *Plasma Phys. Control. Fussion* **44**(12B), B407.
Tatarakis, M. et al.: 2002a, *Phys. Plasmas* **9**(8), 3642.
Tatarakis, M. et al.: 2002b, *Phys. Plasmas* **9**(5), 2244.
Tatarakis, M. et al.: 2002c, *Nature* **415**, 280.
Wilks, S.C. and Kruer, W.L.: 1997, *IEEE J. Quantum Elect.* **33**(11), 1954.

LABORATORY SIMULATION OF MAGNETOSPHERIC PLASMA SHOCKS

R. PRESURA[1], V.V. IVANOV[1], Y. SENTOKU[1], V.I. SOTNIKOV[1], P.J. LACA[1], N. LE GALLOUDEC[1], A. KEMP[1], R. MANCINI[1], H. RUHL[1], A.L. ASTANOVITSKIY[1], T.E. COWAN[1], T. DITMIRE[2], C. CHIU[2], W. HORTON[2], P. VALANJU[2] and S. KEELY[2]

[1]*University of Nevada, Reno; presura@physics.unr.edu*
[2]*University of Texas, Austin*

(Received 30 April 2004; accepted 30 May 2004)

Abstract. An experimental simulation of planetary magnetospheres is being developed to investigate the formation of collisionless shocks and their effects. Two experimental situations are considered. In both, the solar wind is simulated by laser ablation plasmas. In one case, the "solar wind" flows across the magnetic field of a high-current discharge. In the other, a transverse magnetic field is embedded in the plasma flow, which interacts with a conductive obstacle. The ablation plasma is created using the "Tomcat" laser, currently emitting 5 J in a 6 ns pulse at 1 μm wavelength and irradiance above 10^{13} W/cm^2. The "Zebra" z-pinch generator, with load current up to 1 MA and voltage up to 3.5 MV produces the magnetic fields. Hydrodynamic modeling is used to estimate the plasma parameters achievable at the front of the plasma flow and to optimize the experiment design. Particle-in-cell simulations reveal details of the interaction of the "solar wind" with an external magnetic field, including flow collimation and heating effects at the stopping point. Hybrid simulations show the formation of a bow shock at the interaction of a magnetized plasma flow with a conductor. The plasma density and the embedded field have characteristic spatial modulations in the shock region, with abrupt jumps and fine structure on the skin depth scale.

Keywords: collisionless bow shock, magnetosphere, laboratory simulation

1. Introduction

Laboratory simulations have been considered for decades a source of information complementary to observational data and computer simulations for understanding physical phenomena related to collisionless shocks in extraterrestrial plasmas (Baranov, 1969; Podgorny and Sagdeev, 1969; Drake, 2004; Horton and Chiu, 2004; and references therein). In this paper we present the development of an experiment planned to simulate the interaction of the solar wind with a planetary magnetosphere, namely to investigate the formation of collisionless bow shocks and magnetospheres from magnetic obstacles.

The surrogate solar wind is generated by laser ablation and it interacts with a magnetic field powered by a z-pinch generator. This approach, based on higher energy density "solar wind" and stronger magnetic fields leads to interaction regions

Astrophysics and Space Science **298:** 299–303, 2005.

smaller and time scales shorter than in previous experiments and is advantageous from the point of view of diagnostics. For example, the z-pinch can generate magnetic fields up to megagauss values and this makes possible the measurement of the magnetic field distribution in the dense plasma using non-perturbative diagnostics such as Faraday rotation and Zeeman splitting.

2. Experiment Design

To evolve into relevant physical states, the experimental system must have similar characteristics to the natural system it attempts to model. A few of these constraints are detailed here. To form a shock, the plasma flow velocity (u) has to exceed both the sound velocity ($M > 1$) and the Alfvén velocity ($M_A > 1$). Also, collisions have to be prevented from perturbing the formation of the shock, which means that the mean free path for ion-ion collisions (λ_{ii}) has to be much larger than the space scale of the shock which is given by the ion Larmor radius (r_{Li}). Practical matters have to be considered as well. For example, the magnetic field strength must be adequate to stop the plasma flow in the original direction (to form a "magnetopause") before reaching the magnetic field source. Additional constraints are imposed by the sensitivity of diagnostics.

All these requirements are satisfied by an expanding Hydrogen plasma with flow velocity $u = 4 \times 10^7$ cm/s, density $n_e = n_i = 10^{17}\,\mathrm{cm}^{-3}$, temperature $T_e = T_i = 400$ eV, and magnetic field strength $B = 30$ kG. In this case $M = 1.4$, $M_A = 2.1$, $\lambda_{ii} = 4.8$ cm, $r_{Li} = 0.14$ cm, $c/\omega_{pi} = 0.07$ cm, $\beta = 1.8$, $\omega_{ci} = 3 \times 10^8$ rad/s. To obtain further insight in the details of the experiment, necessary for the experimental design, particle-in-cell (PIC) and hybrid simulations were performed with these parameters.

A 1D (x) PIC simulation of the collisionless interaction of a plasma flow across a magnetic field in the direction of a positive gradient of the field strength showed that the ions are stopped and reflected, and that they transfer half of their directed kinetic energy to the electrons (Sentoku, 2004). A 2D PIC simulation in the plane (x, z) perpendicular to the magnetic field lines was performed with scaled parameters (Sentoku, 2004). When flowing in the magnetic field, the plasma does not expand in the z direction and the flow continues beyond the stopping point predicted by pressure balance. This simulation confirmed that the ions are stopped when half their directed kinetic energy is imparted to electrons, resulting in significant electron heating and the population of a non-Maxwellian high-energy tail. Due to the geometry adopted, these predictions do not take into account the plasma flow along the magnetic field lines (y).

A 2D hybrid simulation (Sotnikov, 2005) performed in the (x, y) plane determined by the plasma velocity and the magnetic field, predicted the formation of a collisionless bow shock at the interaction of a magnetized plasma flow with a conductive obstacle, in a regime relevant to the formation of cometary bow shocks.

The collisionless shock forms after several times the inverse of the ion cyclotron frequency (ω_{ci}).

3. Experiment Set-Up

In the present experiment the solar wind is simulated by an expanding laser ablation plasma and the magnetosphere by the azimuthal magnetic field produced by a z-pinch generator. This gives to some extent independent control on the parameters of the simulated "solar wind" and "magnetosphere".

The plasma flow is created by the "Tomcat" laser with pulse energy up to 5 J at 1 μm wavelength and 6 ns pulse width. Focused to a spot diameter less than 100 μm, the laser irradiance on target is higher than 10^{13} W/cm^2. The laser beam is incident at 45° on a thick plastic target. The "Zebra" z-pinch generates up to 1 MA load current with rise-time of about 100 ns. Depending on the load geometry, it can produce magnetic fields up to megagauss values. In the present experiment "Zebra" is used in the long pulse regime with maximum current 0.6 MA and rise time 200 ns. At the target position the typical magnetic field is 7 T and has a positive gradient along the normal to the target surface. The main components of the experimental set-up are shown in Figure 1. The vacuum magnetic field is measured with differential B-dot probes in the location indicated and in the top plate. The laser is typically synchronized with the z-pinch such that the ablation plasma is produced and evolves during a constant magnetic field period at the current peak. The experiment is optimized for high repetition rate by using a rotatable

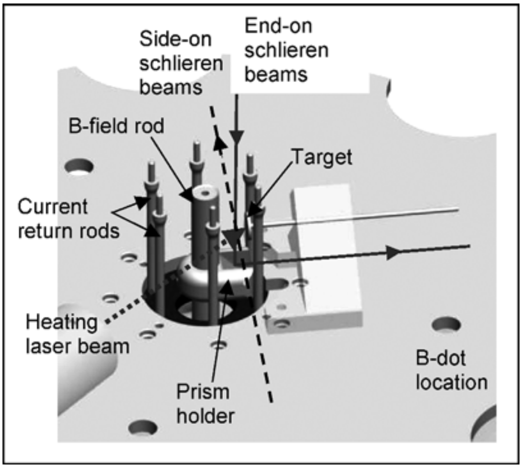

Figure 1. The main components of the experimental set-up are the target heated by a laser pulse (dotted arrow) and the current-carrying load with a center rod and current-return rods (the top of the structure is hidden for clarity). The laser beam paths used for schlieren imaging are also shown.

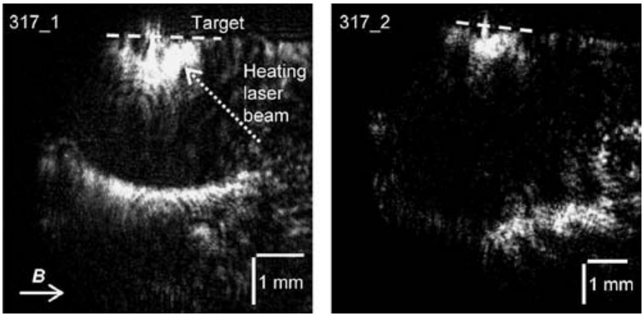

Figure 2. Top-view two-frame schlieren images. The position of the target, the direction of the heating laser beam, and the orientation of the magnetic field are shown.

target and an oversized field generating rod. In the current experiment, the vacuum is maintained lower than 10^{-5} Torr to avoid any influence of the background gas.

Two-frame schlieren imaging is used to probe the plasma density gradients. A laser with 0.2 ns pulse width and 532 nm wavelength is used. The laser beam is split in two beams that follow the same path with 8 ns delay. The field of view is approximately 6 mm and is centered 2 mm in front of the target. The dark field image is created with a knife edge. The overall space resolution is better than 10 μm.

An example of schlieren images obtained with the current set-up (end-on) is shown in Figure 2. In the plane containing the normal to the target and the magnetic field vector (x, y), the two frames show a plasma front with steep density gradient. This structure propagates perpendicular to the magnetic field and expands along the magnetic field lines at about the same rate. The front decelerates as it propagates towards stronger field regions. The formation of the steep gradient structure at the front of the plasma flow and its deceleration are similar to the predictions of the PIC simulations.

Upgrades are planned for all components of the experiment. The laser energy and the magnetic field strength will be increased, and a 2D dipole configuration will be implemented. To investigate the effects predicted by simulations, several diagnostics will be added including time-gated interferometry to measure the actual density distribution and time-gated space-resolved spectroscopy to detect the temperature increase expected at the stopping point.

Acknowledgements

The authors thank the NTF technical team and to C. Plechaty, and R.J. Hall. This work was supported by DOE (NNSA under UNR grant DE-FC08-01NV14050.

References

Baranov, V.B.: 1969, *Cosmic Res.* **7**, 98.

Drake, R.P.: 2000, *Phys. Plasmas* **7**, 4690.

Horton, W. and Chiu, C.: 2004, *Phys. Plasmas* **11**, 1645.

Podgorny, I.M. and Sagdeev, R.Z.: 1969, *Sov. Phys. Uspekhi* **98,** 409–440 Russian; (1970) 445–462 English.

Sentoku, Y. et al.: 2004, 5th HEDLA Int. Conf., March 10–13, 2004, Tucson, AZ.

Sotnikov, V.I. et al.: 2005, *Ap&SS* **298**, 369.

STUDYING HYDRODYNAMIC INSTABILITY USING SHOCK-TUBE EXPERIMENTS

O. SADOT[1,2], K. LEVY[1,2], A. YOSEF-HAI[1,2], D. CARTOON[1,2], Y. ELBAZ[2], Y. SREBRO[1,2], G. BEN-DOR[2] and D. SHVARTS[1,2]

[1]*Physics Department, Nuclear Research Center Negev, BEER-SHEVA, Israel*
[2]*Ben-Gurion University of the Negev, BEER-SHEVA, Israel; E-mail: sorens@bgumail.bgu.ac.il*

(Received 4 May 2004; accepted 13 June 2004)

Abstract. The hydrodynamic instability, which develops on the contact surface between two fluids, has great importance in astrophysical phenomena such as the inhomogeneous density distribution following a supernova event. In this event acceleration waves pass across a material interface and initiate and enhance unstable conditions in which small perturbations grow dramatically.

In the present study, an experimental technique aimed at investigating the above-mentioned hydrodynamic instability is presented. The experimental investigation is based on a shock-tube apparatus by which a shock wave is generated and initiates the instability that develops on the contact surface between two gases. The flexibility of the system enables one to vary the initial shape of the contact surface, the shock-wave Mach number, and the density ratio across the contact surface.

Three selected sets of shock-tube experiments are presented in order to demonstrate the system capabilities: (1) large-initial amplitudes with low-Mach-number incident shock waves; (2) small-initial amplitudes with moderate-Mach-number incident shock waves; and (3) shock bubble interaction.

In the large-amplitude experiments a reduction of the initial velocity with respect to the linear growth prediction was measured. The results were compared to those predicted by a vorticity-deposition model and to previous experiments with moderate- and high-Mach number incident shock waves that were conducted by others. In this case, a reduction of the initial velocity was noted. However, at late times the growth rate had a $1/t$ behavior as in the small-amplitude low-Mach number case. In the small-amplitude moderate-Mach number shock experiments a reduction from the impulsive theory was noted at the late stages.

The passage of a shock wave through a spherical bubble results in the formation of a vortex ring. Simple dimensional analysis shows that the circulation depends linearly on the speed of sound of the surrounding material and on the initial bubble radius.

Keywords: Richtmyer-Meshkov instability, turbulent mixing, shock-tube experiments

1. Introduction

The instability mechanism, which appears at an interface between two fluids of different densities when it is impulsively accelerated by a shock wave, i.e., the Richtmyer-Meshkov (RM) instability, can give rise to turbulent mixing. Recent theoretical studies have predicted the evolution of a single mode perturbation through the linear (Richtmyer, 1960; Meshkov, 1969), early nonlinear (Zhang and Sohn, 1997; Sadot et al., 1998) and late nonlinear stages (Hecht et al., 1994; Alon et al., 1995; Sadot et al., 1998). In those models, after the shock passes through the interface the penetration of light gas to the heavy gas (bubbles) and heavy gas to the light gas (spikes) can be described by an incompressible evolution of the flow field. In the linear stage the bubble and spike tip velocities are: $U_{\mathrm{RM}} = A^* \, ka^* \, \Delta u_{1D}$ where k is the wave number $(2\pi/\lambda)$, A^* and a^* are the post-shock Atwood number and amplitude, respectively, and $\Delta u_{1\mathrm{D}}$ is the one-dimensional post-shock interface velocity. The linear stage is followed by a nonlinear stage during which the growth velocity reaches an asymptotic $C(A^*)\lambda/t$ behavior where $C(A^*)$ is a constant that depends on the Atwood number and the dimensionality (for more details see Hecht et al., 1994; Rikanati et al., 2000). Those nonlinear classical models are applicable when the initial perturbation wavelength is much smaller than the initial amplitude ($a_0 k \ll 1$) and incompressible flow.

In recent years, efforts have been made to study the evolution of the Richtmyer-Meshkov instability in the case of high-Mach numbers. Shock-tube experiments were conducted by Aleshin's research group (Aleshin et al., 1990, 1997) using moderate-Mach numbers (2.5–3.5), various initial conditions and different test gas combinations (He-Xe, Ar-Kr, He-Xe in *heavy to light* and *light to heavy* arrangements). In their study, an effort was made to map the behavior of the instability and to quantify the differences between the various regimes.

Dimonte et al. (1996) conducted experiments with higher Mach numbers. The experiments were conducted on the NOVA laser at Lawrence Livermore National Laboratory (LLNL). The focusing of the laser beams into a radiation enclosure (indirect drive configuration) generated shock waves with Mach numbers of $M \sim 15$ in Be ($\rho = 1.7\,\mathrm{g/cm^3}$) to foam ($\rho = 0.12\,\mathrm{g/cm^3}$) configuration. The initial amplitudes ranged in these experiments from $a_0 k \sim 0.2$ to $a_0 k \sim 4$, which is well above the applicability limit of the linear models. In some of these experiments with $a_0 k > 4$, large reductions of the initial instability growth velocities from those predicted by the linear classical model were observed, while in others with $a_0 k \leq 4$ the agreement was good. It is commonly assumed that the reduction was due to high-Mach number effects (see e.g., Aleshin et al., 1997; Holmes et al., 1999).

In our theoretical complementary study (Rikanati et al., 2003) the reduction of the initial instability growth velocity as compared to the predictions of a new nonlinear classical model was presented and two models were introduced and supported by 2D-simulations. The models, which described correctly the reduction, accounted for the effect of the high-initial amplitude (geometrical effect) – the "vorticity deposition" model and the shock-interface proximity effect (high-Mach number effect) – the "wall" model. It was found that the geometric effect was dominant only at the initial stage. At the late stages the effect was diminished and the bubble front floated in its asymptotic velocity. The Mach number effect reduced the initial velocity.

The phenomenon of shock-bubble interaction is of importance in several differently scaled situations, from fragmentation of gallstones or kidney stones (lithotripsy) by shock waves (Gracewski et al., 1993) to the interaction of supernovae shock waves with interstellar clouds (Klein et al., 2000). Therefore the scalability of the interaction is important.

The passage of a shock wave through a spherical bubble results in the formation of a vortex ring. It is shown that the velocities characterizing the flow field are linearly dependent on the speed of sound, and are independent of the initial bubble radius. The dependence of the circulation on the shock wave Mach number, M, was derived by Samtaney and Zabusky (1994) as: $(1 + 1/M + 2/M^2)(M - 1)$. The validity of this scaling was tested.

In the following section the experimental setup will be described. Following, experimental result and discussion of three selected studies, which were conducted in the past two years.

2. Experimental Apparatus

The experiments were performed in a 5.5-m long horizontal double-diaphragm shock tube with an 8 cm × 8 cm cross section. A thin membrane separated the two gases (note that the effect of the membrane is negligible: Erez et al., 2000). The evolution of the shock-wave-induced mixing zone was measured by recording a series of schlieren photographs using a Nd:YAG frequency doubled laser pulsed at intervals of about 20 to 200 μs and a shutterless rotating-prism camera. The photographs were analyzed using a computerized image analysis. In order to generate a shock wave having a Mach number in the range $1.2 \div 2.0$, the driver section was first filled with air or He until it reached the pressure that was required to rupture a 0.14-mm thick diaphragm consisting of one or two layers of mylar sheet.

An extremely thin membrane was placed between the two investigated gases in the test section. Upon the rupture of this membrane by the shock wave, the mixing process began. To create the spherical bubbles soap solution was filled with He or SF_6 to create the heavy to light and light to heavy configuration.

In order to investigate the high-initial amplitude effect a set of experiments with varied a_0k was performed. All the experiments were done with air/SF_6 gas combination (light to heavy combination, Atwood number $A = 0.67$) and a Mach number of $M = 1.2$. The higher-Mach number study was done using air/SF_6 gas combination with $M = 2$.

For the bubble shock interaction, the bubble was created with a thin soap membrane and then inflated using a special needle. This needle was then used to suspend it from the upper side of the tube. The effect of the needle on the large-scale flow was found to be negligible.

3. Experimental Results and Discussion

3.1. High initial amplitude with small Mach numbers

An experimental verification of the high-initial amplitude dominance in the above experiments was obtained using shock-tube experiments at low-Mach numbers

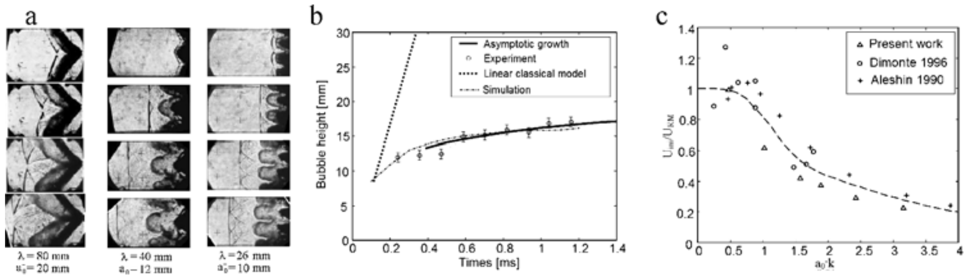

Figure 1. (a) Three sets of schlieren photographs with different initial conditions. The shock travels from right to left. All the experiments were conducted with air/SF_6 gases. (b) Bubble height in the high-initial amplitude shock-tube experiments. (c) Comparison of the reduction factor between the vorticity deposition model and the shock-tube experiment at $M = 1.2$.

($M = 1.2$) with saw-tooth initial perturbations of low- and high-initial amplitudes ($a_0k = 0.5$–3). A set of schlieren photographs taken from the shock-tube experiment is shown in Figure 1a. The comparison between the experimental results and our 2D-simulation is presented in Figure 1b.

LEEOR2D, which is a homemade two dimensional ALE (Arbitrary Lagrangian Eulerian) code, was used. Details about the code can be found in Ofer et al., 1996.

Owing to the good agreement between the simulation and the experimental results that is evident in Figure 1b, the initial bubble velocity for the experimental results (which was not measured due to technical limitations) was assumed to be equal to that predicted by the simulation. It is also evident from Figure 1b the linear classical model (Richtmyer, 1960) fails to correctly predict the velocity growth at the early stages. Note that there is a very good agreement between the experimental results and the predictions of the classical nonlinear model (Alon et al., 1995; Sadot et al., 1998) of the asymptotic evolution (note that the theoretical predictions were shifted vertically to fit the experimental results).

A comparison of the reduction factor of the initial velocity with predictions of the vorticity deposition model was also made and very good agreement was achieved (for more details see Rekanati, 2003). Our results together with those of Aleshin et al. (1990, 1998) and Dimonte et al. (1996) for moderate- and high-Mach number experiments are presented in Figure 1c. As can be seen, the reductions in all of the experiments fit a single curve. (It should be noted that a calculation using the vorticity deposition model produced a similar curve, see Rekanati et al., 2003). The result suggests that the main reduction in those experiments is due to the high a_0/λ ratio and not the shock wave Mach number.

3.2. Small initial amplitude with moderate Mach number

Experiments with air/SF_6 gas combination and shock-wave Mach number $M = 2$ were conducted in order to investigate the Mach number effect. Schlieren

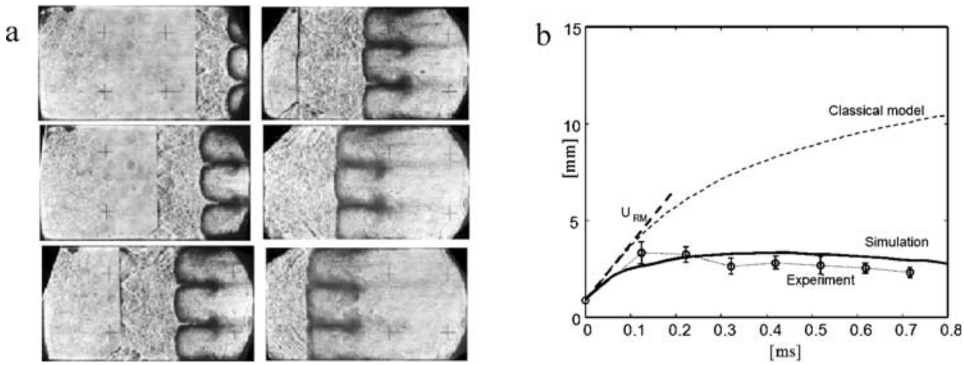

Figure 2. (a) Schlieren photographs from the shock-tube experiment with $M = 2$ air/SF_6 $\lambda = 26$ mm, $a_0 = 3$ mm. (b) Comparison between the nonlinear model-thin dashed line (Sadot et al., 1998) and the high-Mach number experiment. full 2D-numerical simulation-solid line and the linear theory – thick dashed line (Richtmyer, 1960).

photographs from one of those experiments are presented in Figure 2a. It is seen clearly that the shock wave is in the vicinity of the perturbed interface during a longer time and that the shock reverberation is traveling in a direction tangential to the interface propagation. Due to the tangential traveling of the shock reverberation, the shocks collide and create regions of high and low pressure in front of the bubbles and the spikes alternately. While the high-pressure in front of the spike increases the spike growth, the high-pressure in front of the bubble reduces the bubble growth and can even cause the bubble tip to drift downstream as is evident in Figure 2b. The experimental results were compared to a full 2D-numerical simulation and the same pressure pattern and bubble behavior were observed. This effect does not occur in the low-Mach number case. When the shock is weak the interface travels much slower than the shock and small pressure fluctuation dissolve quickly. In this case the evolution of the perturbation is dominated by the inertia and drag. In Figure 2b, initially the bubble rises as predicted by the nonlinear classical theory (Hecht et al., 1994; Sadot et al., 1998) but later on the bubble is decelerated and is washed downstream due to the pressure, which evolves in front of it. The deceleration and negative velocity effect flattened the tip of the bubble and increased the bubble radius of curvature. Due to the moderate-Mach number and to the linear initial conditions the perturbation evolved initially as predicted by the nonlinear classical model. To the best of the authors' knowledge a model that predicts the late time bubble evolution in the high-Mach number situations does not yet exist.

3.3. Interaction of Spherical Bubble with Shock Wave

Experiments were conducted using slow/fast configuration (air/He bubble). In the experiment a He bubble was inflated in air at ambient conditions. A set of schlieren

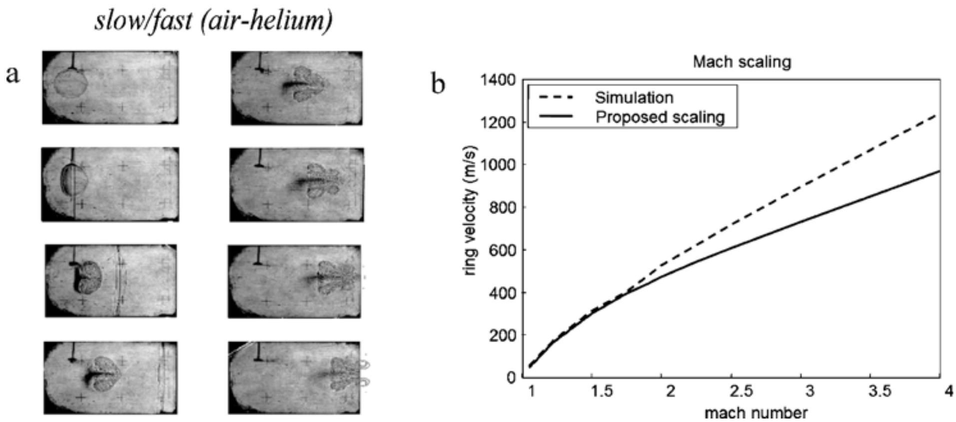

Figure 3. (a) A set of schlieren photographs from the shock tube experiment on which the simulation results are superimposed. (b) Mach number scaling: comparison between the vorticity deposition model and 2D-simulations.

photographs in which the shock-bubble interaction is seen together with a 2D-simulation using cylindrical symmetry is presented in Figure 3. In the shock wave Mach number was $M = 1.2$. The agreement between the experimental and simulation results is very good. The deformation of the bubble and the creation of two vortex rings is clearly seen in the photographs. The results strengthen our confidence in the simulation, which in turn enables us to push the simulation a little further to higher Mach numbers.

Using the simulation results the Mach scaling together with other scaling parameters where tested. The ring velocity with respect to the Mach number together with the prediction of the ring velocity from the velocity deposition model by Samtaney and Zabusky (1994) are presented in Figure 3b. It is seen that for Mach numbers smaller the 1.8 the agreement is very good. However, for higher Mach numbers the discrepancy increases significantly.

The origin of this change is in the derivation of the scaling factor in the model of Samtaney and Zabusky (1994). The model assumes that the deposition of vorticity is performed by the passage of the shock wave over the entire sphere. This is the case for Mach numbers lower than $M = 1.5$. However, this is not the case for higher Mach numbers. When a shock wave having a Mach number $M > 1.8$ passes the bubble the upstream section of the He bubble travels faster than the shock wave in the surrounding air. That morphology of interaction is more complex than the model assumption and must be accounted for. The shock wave interacts with different interface geometries. As the Mach number increases, the morphology is more complex and the validity of the model loses ground.

Finally, it is noted that investigations of other scaling parameters are present in Levy et al. (2004).

4. Summary

An attempt was made to understand the effects of the high-initial amplitudes and high-Mach numbers on the evolution of the Richtmyer-Meshkov instability. Recent theoretical and experimental studies by Aleshin et al. (1990, 1997), Dimonte et al. (1996) showed that in some cases there is a reduction in the initial growth velocity with respect to the predictions of the linear model (and likewise the nonlinear classical model). In the present investigation combined experimental and theoretical studies reveal two different effects that dominate the instability evolution, the geometric effect and the high-Mach number effect. Two sets of shock-tube experiments were conducted to validate these effects by using low-Mach number and high-initial amplitude and moderate-Mach number and linear initial conditions. The reduction factors that were obtained in the high-initial amplitude experiments were compared to experimental results of others and good agreement was found. The results suggested that even at high-Mach numbers the geometric effect is the dominant one. It is also shown that at late stages the asymptotic velocity in the high-initial amplitude experiments is the same as that predicted by the nonlinear classical models. For the case of moderate-Mach number experiments with linear initial conditions, no significant reduction was observed since the Mach number was not high enough. However, an irregular asymptotic behavior, namely a negative growth rate, was observed experimentally and numerically. Pressure fluctuations in front of the bubble due to shock reverberation, suppress the bubble growth and can even cause a negative growth velocity.

The phenomenon of a shock wave bubble interaction was investigated using shock tube experiments and simulations. A comparison of the bubble interface and vortex ring position shows very good agreement. The velocities in the interaction were found to be independent of the initial bubble radius. For slow/fast interactions (air/He) the Mach scaling factor was found to be valid for $M < 2$. It is shown that the scaling is invalid for $M > 2$ due to a change in the topology of the ring evolution.

References

Aleshin, A.N., Lazareva, E.V., Chebotareva, E.I., Sergeev, S.V. and Zaytsev, S.G.: 1997, *6th IWCTM Conf.,* **1** *Marseille, France*.

Aleshin, A.N., Lazareva, E.V., Zaitsev, S.G, Rozanov, V.B., Gamali, E.G. and Lebo, I.G.: 1990, *Sov. Phys. Dokl.* **35**, 159.

Alon, U., Hecht, J., Ofer, D. and Shvarts, D.: 1995, *Phys. Rev. Lett.* **74**, 534.

Dimonte, G., Frerking, C.E., Schneider, M. and Remington, B.: 1996, *Phys. Plasmas*, **3**, 614.

Erez, L., Sadot, O., Levin, L.A., Shvarts, D. and Ben-Dor, G.: 2000, *Shock Waves J.* **4**. 241.

Hecht, J., Alon, U. and Shvarts, D.: 1994, *Phys. Fluids* **6**, 4019.

Holmes, R.L., Dimonte, G., Fryxell, B., Gittings, M.L., Grove, J.W., Schneider, M., Sharp, D.H., Velikovich, A.L., Weaver, R.P. and Zhang, Q.: 1999, *J. Fluid Mech.* **389**, 55.

Lindl, J.D.: 1995, *Phys. Plasmas* **2**, 3933.
Levy, K., Sadot, O., Rikanati, A., Katroon, D., Srebro, Y., Yosef-Hai, A., Ben-Dor, G. and Shvarts, D.: 2004, *L&PB*. **21**, 335.
Meshkov, E.E.: 1969, *Fluid Dyn.* **4**, 101.
Meyer, K.M. and Blewett, P.J.: 1972, *Phys. Fluids* **15**, 753.
Richtmyer, R.D.: 1960, *Comm. Pure Appl. Math*. **13**, 297.
Rikanayi, A., Alon, U. and Shvarts, D.: 1998, *Phys. Rev. E*. **58**(6), 7410.
Rikanati, A., Sadot, O., Oron, D. and Shvarts, D.: 2003, *Phys. Rev. E*. **67**, 26307.
Sadot, O., Yosef-Hai, A., Rikanati, A., Kartoon, D., Oron, D., Arazi, L., Levin, L.A., Sarid, E., Ben-Dor, G. and Shvarts, D.: 2001, *Proc. 24th ICHSP&P Conf.*, 798, Sendai, Japan.
Sadot, O., Erez, L., Alon, U., Oron, D., Levin, L.A., Erez, G., Ben-Dor, G. and Shvarts, D.: 1998, *Phys. Rev. Lett*. **80**, 1654.
Samtaney, R. and Zabusky, N.J.: 1994, *J. Fluid Mech.* **269**, 45.
Zhang, Q. and Sohn, S.-I.: 1997, *Appl. Math.s Lett.* **10**, 121.

NOVEL DIAGNOSTIC OF SHOCK FRONTS IN LOW-Z DENSE PLASMAS

S. LE PAPE[1], M. KOENIG[1], T. VINCI[1], E. MARTINOLLI[1], D. HICKS[2], A. MACKINNON[2], P. PATEL[2], M. BORGHESI[3], L. ROMAGNANI[3] and T. BOEHLY[4]

[1] *UMR7605-LULI, École Polytechnique, France; E-mail: sebastien.lepape@polytechnique.fr*
[2] *Lawrence Livermore National Laboratory, Livermore, CA 94550, USA*
[3] *Queen's University of Belfast, UK*
[4] *Laboratory for Laser Energetics, University of Rochester, USA*

(Received 21 April 2004; accepted 10 June 2004)

Abstract. We performed an experiment using high-energy protons to characterize *in situ* the spatial and temporal evolution of a laser-driven shock propagating through a low-Z material. Radiography of the shock propagating through the low-Z transparent material (Lexan, quartz, diamond) enabled estimation of density under compression. In order to discriminate the influence of the shocked matter on the protons trajectory, a Monte-Carlo simulation was developed. This code describes the protons trajectory through the matter, calculating the scattering angle and the loss of energy.

Keywords: laser driven shocks, proton radiography, shortpulses

1. Experimental Setup

The determination of material density compressed by a shock wave is an important issue in EOS physics (Koenig et al., 1995). An experiment was therefore conducted using high-energy protons to characterize *in situ* the spatial and temporal evolution of a laser-driven shock propagating through a low-Z material.

The experiment was conducted on the terawatt (100 TW) facility at the LULI (Figure 1). The shock was created by focusing a 60 J–550 ps Gaussian shape -1053 nm on a multilayer target. It was composed of a pusher (4–6 μm CH and 25 μm of aluminium), leading to a shock pressure about 5 Mbar. A low-Z material sliver (Lexan, quartz, diamond, LiF) was glued on this foil. The characteristics of the shock (velocity and spatial extension) were deduced from the VISAR diagnostic (Celliers et al., 1998).

The proton beam was generated with an ultra high intensity short pulse 30 J–350 fs -3×10^{19} W cm^{-2} irradiating a thin (15 μm) aluminium foil (Clark et al., 2000; Roth et al., 2002). The produced proton burst has an extremely good emittance and a short duration ($\sim$ps), determining an excellent spatial and temporal resolution when used as a particle probe in a point-projection scheme (Borghesi et al., 2003). Protons with energy from a 3 to 10 MeV were detected on a radiochromic film (RCF) placed at 5 cm from the proton's target (Figure 2).

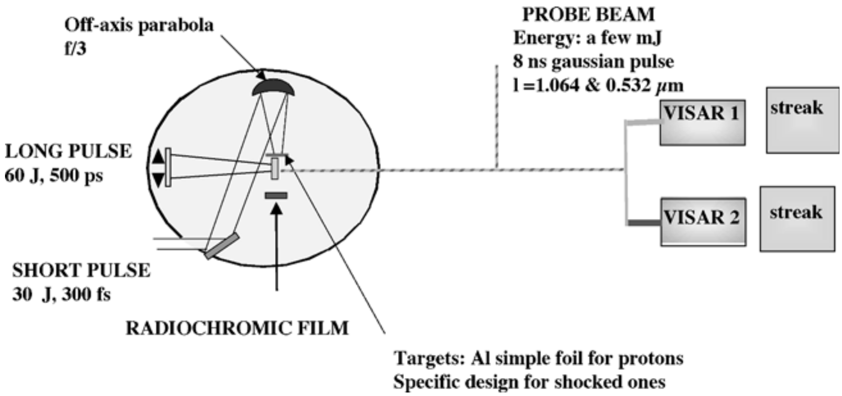

Figure 1. Experimental setup.

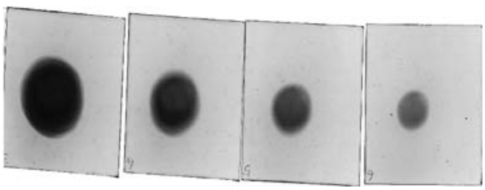

Figure 2. Tracks of the proton beam on an RC film from 3 MeV (*left*) to 10 MeV (*right*), the beam divergence decreases with the increase of the proton energy.

2. Shock Data

In order to compare the experimental results to 1D hydro simulations, shots were made on aluminium step targets. Shots are realized to associate the laser energy to the numerical intensity used in hydro code. From this code calibration, the state of the probe material is deduced in real shots from simulations. For instance shots were made on step target (2.5 μm CH, 8.5 μm Al, 3.7 μm Al step), the delay observed in the shock release is $\delta t = 150\,\text{ps}$ resulting in a shock velocity about $D = 23$ km/s which corresponds to a intensity of 6×10^{13} W cm^{-2}. The release of a single aluminium foil (15 μm), i.e. without the sliver, was probed 7 ns after the rear side breakout (Figure 3). A very bright frontier between the void and the expanding plasma at the back of the foil is observed. From Figure 3, the shift of the foil was determined by considering that the edge of the image denotes its initial position. We found a value equal to 100 μm, which corresponds to a mean velocity of $\sim$14 km/s. These experimental results was compared to simulations both 1D hydro code and Monte Carlo (MC) simulation of the proton propagation in the shocked matter (Figure 4). The large scale spatial dimensions observed on the proton image were consistent with the results of the 1D hydro code. The density foil decreases from 2.7 g/cc to about 0.5 g/cc and its width expands from 20 to 80 μm.

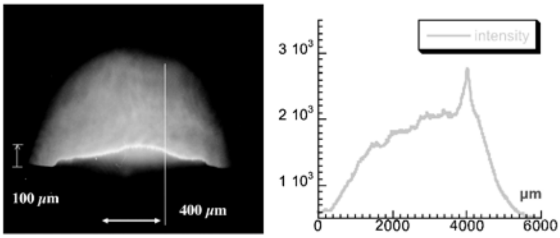

Figure 3. (*Left*) Proton image of an aluminium foil 7 ns after the long pulse beam, (*right*) distribution of the protons along the axis shown on the right figure. The pile up of the protons corresponds to the position of the foil taken 7 ns after the long pulse interaction.

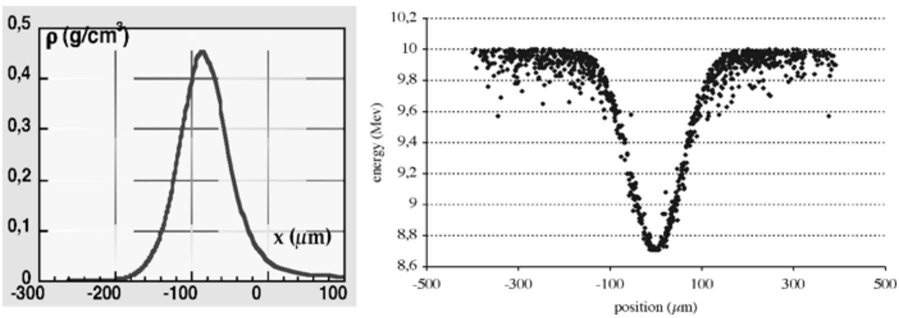

Figure 4. (*Left*) Density profile 7 ns after the long pulse laser, (*Right*) energy distribution of the proton at 2.3 cm from the shock target.

The foil position after 7 ns (100 μm) is also consistent with the hydro calculations. Nevertheless the MC calculations cannot reproduce the observed proton pile up. The results (Figure 4) shows a strong absorption in the proton beam due to the overdensity. The scaterring is then too low to explain the experimentally observed proton pileup. But this simulation does not reproduce any field effect and depends on the density profile given by the hydro code.

3. Propagation of the Shock in Quartz

The density of the shock was sampled during its propagation through the quartz sliver. As shown in Figure 5, the overdensity induced by the shock wave is not visible on the proton image whatever the protons energy is. This could be explained by the scattering of the protons in the sliver. MC simulations were made using 1D density profil of the shock in quartz (Figure 5). On the right of Figure 5, the plain curve presents the proton profile just at the end of the target, i.e without any free propagation of the protons. The shape of the profile is mainly induced by the absorption in the overdensity. It clearly shows a decrease in the profile located at

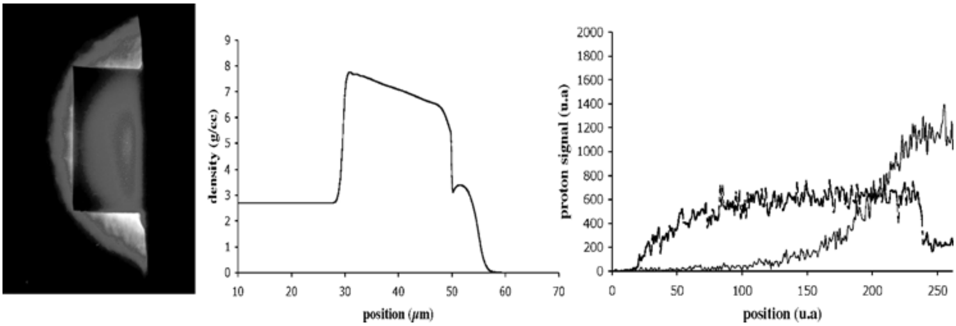

Figure 5. (*Left*) 10 MeV proton's image of the shock in the quartz sliver, (*Center*) corresponding simulated density profile in quartz, (*Right*) calculated proton's profile at the end of the target (plain curve), and after free propagation (dashed curve). The protons position was normalized.

the overdensity position and having a width (20 μm) corresponding to the width of the overdensity (see center figure). The dashed curve corresponds to the protons profile after a free propagation of 2.3 cm which is the distance between the shocked target and the RCF. The decrease in the proton's signal is then masked, protons are spread out because of the scattering in the sliver. The resolution is then strongly altered by the propagation in the sliver.

4. Conclusion

Laser driven shock experiments are now able to bring quantitative data to the high pressure physics community. A laser driven proton beam was used on shocked material showing a highly contrasted image of an aluminium foil release state in vacuum.

References

Borghesi.: 2003, *Appl. Phys. Lett.* **82**, 1529.
Celliers.: 1998, *Appl. Phys. Lett.* **73**, 1320.
Clark.: 2000, *Phys. Rev. Lett.* **85**, 1654.
Koenig.: 1995, *Phys. Rev. Lett.* **74**, 2260.
Roth.: 2002, *Plasma Phys. Control. Fusion* **44**, B99+.

EVOLUTION AND FRAGMENTATION OF WIDE-ANGLE WIND DRIVEN MOLECULAR OUTFLOWS

ANDREW CUNNINGHAM[1], ADAM FRANK[1], PEGGY VARNIÈRE[1], ALEXEI POLUDNENKO[1], SORIN MITRAN[2] and LEE HARTMANN[3]

[1]*University of Rochester, Department of Physics and Astronomy, Rochester*
[2]*University of North Carolina, Chapel Hill*
[3]*Harvard-Smithsonian Center for Astrophysics, Cambridge*

(Received 10 May 2004; accepted 8 June 2004)

Abstract. We present two dimensional cylindrically symmetric hydrodynamic simulations and synthetic emission maps of a stellar wind propagating into an infalling, rotating environment. The resulting outflow morphology, collimation and stability observed in these simulations have relevance to the study of young stellar objects, Herbig-Haro jets and molecular outflows. Our code follows hydrogen gas with molecular, atomic and ionic components tracking the associated time dependent molecular chemistry and ionization dynamics with radiative cooling appropriate for a dense molecular gas. We present tests of the code as well as new simulations which indicate the presence of instabilities in the wind-blown bubble's swept-up shell.

Keywords: protostellar outflow, HH object, molecular outflow, wide-angle wind, fragmentation

1. Introduction

Bipolar Jets and wide angle molecular outflows are recognized as a ubiquitous phenomena associated with star formation. It is expected that most if not all low mass stars produce such outflows during their formation through the gravitational collapse of gas from the parent molecular cloud. A molecular outflow is formed when molecular gas is displaced from the cavity evacuated by a fast stellar wind. This results in the formation of irregular lobes and thin shells of swept up shocked molecular gas along the walls of the cavity. The strong radiative energy loss from the shock heated molecular gas can result in the onset of several instabilities in the molecular outflow (Vishniac, 1994), (Vishniac and Ryu, 1989). We present some preliminary results of our work employing multidimensional numerical models including molecular chemistry and associated radiative losses to explore the fragmentation and stability properties of these outflows.

Simulations of protostellar outflows in the presence of a collapsing molecular core have been carried out using the AstroBEAR adaptive mesh refinement muti-physics code (Poludnenko et al., 2004), (Varnie et al., 2004). The AstroBEAR code employs an exact hydrodynamic Riemann solver and a conservative integration scheme in an Eulerian frame of reference to advance the solution of the source

Astrophysics and Space Science **298:** 317–322, 2005.

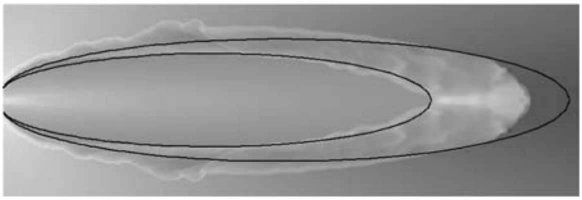

Figure 1. X-wind outflow at $t = 304$ year. The outer curve represents the analytically predicted shell morphology at this time. The inner curve follows the shape of the analytical model at an earlier time and whose morphology matches the shape of the inner shock in our simulations.

free Euler equations. The geometric and microphysical source terms are split from the hydrodynamic integration using an implicit fourth-order Rosenbrock source term integration scheme for stiff ODE's. The use of adaptive mesh code has been essential to achieve the necessary resolution in the neighborhood of thin shock bounded high density slabs that are prevalent in these simulations.

2. Isothermal X-Wind Model Simulation

We first compare our code with results of previous calculations. In Figure 1 we show a simulation of an isothermal outflow with conditions similar to the X-wind model of (Shu et al., 1995) driving into a toroidal ambient medium. This simulation uses a velocity and density pattern similar to the X-wind but no magnetic field is included. We compare Figure 1 with the results of the same calculation performed by (Lee et al., 2001) at 1/4 the resolution of the current work. Of particular interest is the extent to which the late-time flow morphology depicted in Figure 1 agrees with the analytically predicted result of (Lee et al., 2001) delineated by the black curve in the figures as a verification of our code in these regimes.

The higher resolution in our simulation allows us to track the internal dynamics of the swept-up shell. Our simulations reveals fine scale features generated as the material flows along the shell walls something not possible with the lower resolution study. Note that the analytic shell morphology model assumes a thin shell. The violation of this conditions is likely responsible for the deviation from the analytically predicted morphology given by the outer curve. The general form of the outflow morphology is, however, well approximated by the analytic model.

3. Protostellar Wind-Infall Model with Non-Equilibrium Ionization, H_2 Chemistry and Cooling

We have also performed simulations including the effects of non-equilibrium HI ionization (Arnaud and Rothenflug, 1985), (Hollenbach and McKee, 1977), (Mazzotta et al., 1998), H2 dissociation and cooling (Dove and Mandy, 1986),

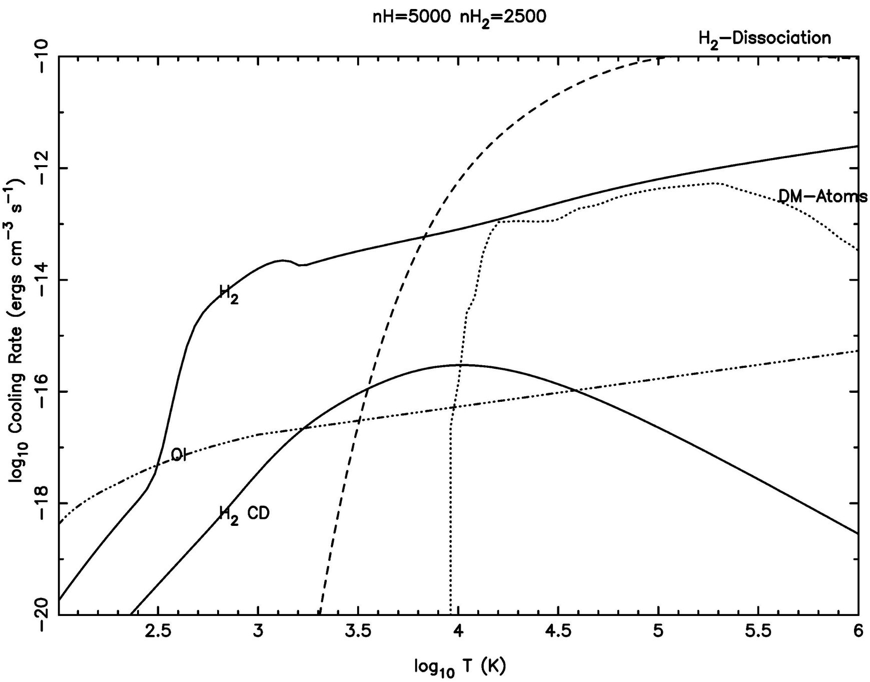

Figure 2. Cooling rates for typical ISM abundances, $n_{H_2} = 2500$, $n_{HI} = 5000$. H_2 is the molecular hydrogen cooling function for a tenuous gas, H_2 CD is the molecular cooling function valid for $n \gg n_{\text{critical}}$, $H_2 - \textit{Dissociation}$ is the thermal energy loss due to the dissociation of H_2 molecules, OI is the singly ionized oxygen line cooling and DM-*Atoms* is the atomic line and recombination cooling function of Dalgarno & McCray.

(Lepp and Schull, 1983), (Lim et al., 2002), (Mandy and Martin, 1993), (Martin et al., 1998). OI line cooling, a dominant cooling agent at temperatures below 1000 K has also been included (Launay and Roueff, 1977). Atomic line and recombination cooling has been included using the cooling rates of a coronal gas (Dalgarno and McCray, 1972). The volumetric cooling rates for the case of a partially ionized gas are plotted in Figure 2. We have also performed tests of our chemistry routines. We show one of these tests where we find the shock speeds which produce 90% molecular dissociation. Figure 3 shows our code produces results consistent with those of previous authors (Smith, 1994), (Hollenbach and McKee, 1977).

Figure 4 shows the interaction of a tenuous, initially ionized protostellar wind with a cold, slowly rotating molecular environment in the presence of the central gravitational potential of .21 $M_{\odot}$ protostar (not resolved in these simulations). The model for the molecular environment is that of a collapsing of non-magnetic, self-gravitating sheet of (Hartmann et al., 1996) as implemented by (Delamarter et al., 2000). The initial outflow takes the form of a sphere ejecting gas at a uniform velocity with an azimuthal density gradient varying as $\cos(\theta)$ and an equator to pole density contrast of 50. Thus our inflow condition creates a wide angle wind in

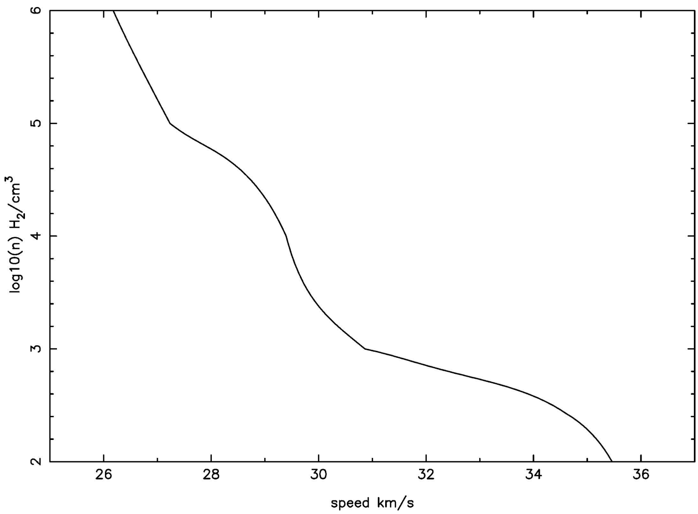

Figure 3. Preshock density vs. shock speed for a steady shock resulting in 90% downstream H_2 dissociation.

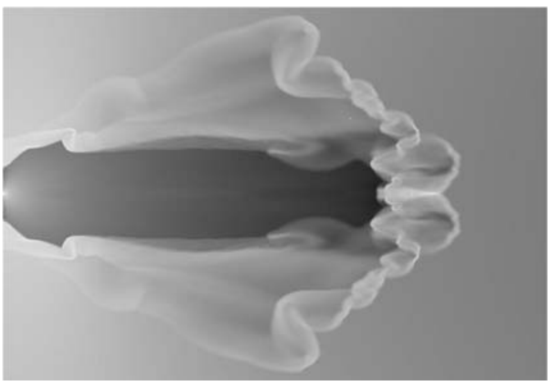

Figure 4. Collapsing sheet outflow, low speed case, logarithm of density at t = 97 year.

which the momentum input to the environment by the protostar is aspherical with the bulk of the thrust being directed along the poles.

The outflow speed in the simulation is maintained at 100 km s^{-1} with the inflow injected through a "wind sphere" of radius of 33 AU, an outflow rate of $10^{-8} M_{\odot}$year^{-1} and an initial infall rate of $10^{-9} M_{\odot}$year^{-1} from the collapsing environment. The equatorial outflow ram pressure is overcome by the gravitational infall of the shocked ambient gas resulting in appreciable shock focusing of the outflow. This leads to very efficient collimation of the ejected wind material.

The resolution achieved in these simulations is sufficient to resolve the swept up shells to 6 to 10 pixels. This is enough to track the onset of what appear to be thin

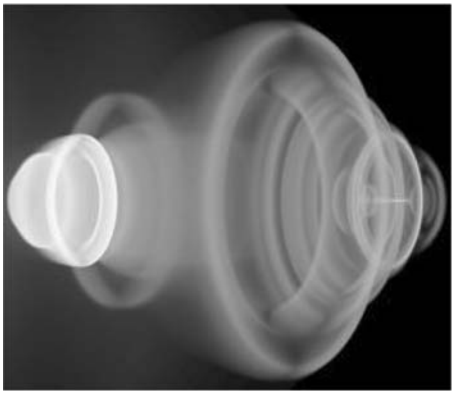

Figure 5. Collapsing sheet outflow, low speed case, synthetic H_2 emission projection at t = 97 year.

shell instabilities. The shell fragmentation process resulting from such instabilities may have a significant effect on the efficiency with which the outflow is able to entrain and disperse its momentum in support of the collapsing environment and on the morphological signatures of the outflow.

Figure 5 shows the 3D H_2 emissivity of the outflow projected onto a plane tilted 30° from the symmetry axis of the outflow. Note that the brightest emission emanates from the dissociation region immediately behind the outer bowshock. Of course the stability properties of the wind collimation mechanism as well as the three dimensional nature of the fragmentation of the thin shell of swept up molecular gas cannot be fully addressed using the 2D cylindrically symmetric approach taken here. Future work will focus on the three dimensional stability of the flow collimation mechanisms as well as on the effect that the outflow geometry has on the fragmentation of protostellar accretion shells, morphology and momentum dissipation efficiency.

4. Conclusions

We have presented first results of simulations of molecular outflows using a new Adaptive Mesh Refinement code which tracks both ionzation and chemistry. These simulations focus on the early time evolution of a wide angle wind expanding into collapsing rotating sheet. Our simulations are able to marginally resolve the internal dynamics of the swept-up and with this resolution we find the leading sections of the outflow lobe to be unstable to what appear to be Thin Shell modes. Future work will focus on exploring the dynamics of the outflows in greater detail providing links between the early evolution of the outflow and the late-time large scale appearence. In particular we are interested to see if the fragmentation of the shell changes the global dynamics of the outflow in significant ways by generating a “clumpy” lobe which expands and sweeps up ambient material.

References

Arnaud, M. and Rothenflug, R.: 1985, *A&AS* **60**, 425.
Dalgarno, A. and McCray, R.A.: 1972, *ARA&A* **10**, 375.
Delamarter, G., Frank, A. and Hartmann, L.: 2000, *ApJ* **530**, 923.
Dove, J.E. and Mandy, M.E.: 1986, *ApJL* **311**, L93.
Hartmann, L., Calvet, N. and Boss, A.: 1996, *ApJ* **464**, 387.
Hollenbach, D. and McKee, C.F.: 1979, *ApJS* **41**, 555.
Hollenbach, D. and McKee, C.F.: 1980, *ApJL* **241**, L47.
Launay, J.M. and Roueff, E.: 1977, *A&A* **56**, 289.
Lee, C., Stone, J.M., Ostriker, E.C., Mundy, L.: 2001, *ApJ* **557**, 429.
Lim, A.J., Raga, A.C., Rawlings, J.M.C. and Williams, D.A.: 2002, *MNRAS* **335**, 817.
Lepp, S. and Shull, J.M.: 1983, *ApJ* **270**, 578.
Mandy, M.E. and Martin, P.G.: 1993, *ApJS* **86**, 199.
Martin, P.G., Keogh, W.J. and Mandy, M.E.: 1998, *ApJ* **499**, 793.
Mazzotta, P., Mazzitelli, G., Colafrancesco, S. and Vittorio, N.: 1998, *A&AS* **133**, 403.
Poludnenko, A., Varniere, P., Frank, A. and Mitran, S.: 2004, to appear in Springer's Lecture Notes in Computational Sciences and Engineering (LNCSE) Series.
Smith, M.D.: 1994, *MNRAS* **266**, 238.
Shu, F.H., Najita, J., Ostriker, E.C. and Shang, H.: 1995, *ApJ* **455**, 155.
Varniere, P., Poludnenko, A., Cunningham, A., Frank, A. and Mitran, S.: 2004, to appear in Springer's Lecture Notes in Computational Sciences and Engineering (LNCSE) series.
Vishniac, E.T.: 1994, *ApJ* **428**, 186.
Vishniac, E.T. and Ryu, D.: 1989, *ApJ* **337**, 917.

X-RAY LINE AND RECOMBINATION EMISSION IN THE AFTERGLOW OF GRB

S. SUGIYAMA[1], S. YAMADA[2] and H. TAKABE[1]

[1] *Institute of Laser Engineering, Osaka University, 2-6 Yamada-oka, Suita, Osaka, Japan; E-mail: ssugiyam@ile.osaka-u.ac.jp*

[2] *Department of Physics, Waseda University, Okubo 3-4-1, Shinjuku-ku, Tokyo, Japan*

(Received 29 April 2004; accepted 5 August 2004)

Abstract. We calculate the time-dependent line and recombination spectrum of nonequilibrium plasma heated by the strong radiation as the test model of X-ray line emission of GRB afterglows. Our calculation shows that the non-equilibrium effect of plasma is complex and important to the time evolution of the spectrum. The origin of these lines puzzles us, but is essential to understand the nature of GRBs and their circumstellar matter.

Keywords: X-ray line, GRB, afterglow

Introduction

Recently, it was strongly suggested that GRBs are connected with supernova (Hjorth et al., 2003), and they release γ-ray energy as not spherical but conical jet-like at a relatively narrow angle (Frail et al., 2001). The collapsar model (Woosley, 1993) can explain many features of long GRBs. However, the model cannot explain some observations such as detections of line emission and absorption in the spectrum of early X-ray afterglow. For example, the emission lines of GRB 970508 (Piro et al., 1999), 970828 (Yoshida et al., 2001), 991216 (Piro et al., 2000) and 000214 (Antonelli et al., 2000) were interpreted as the $K\alpha$ iron line and recombination. The lines of GRB 020813 (Bulter et al., 2003) and 030227 (Watson et al., 2003) had very little iron and had large abundance of other hydrogen like ions.

Especially, GRB 011211 (Reeves et al., 2002) in which afterglow was detected by the XMM-Newton satellite 11 h after the burst is very interesting. The emission lines were interpreted as the Kα lines of several ions as Mg(XI), Si(XIV), S(XVI), Ar(XVIII), Ca(XX), and no iron. Significant line emissions were observed during the initial 10^4 s observation and decayed after the duration. Its temperature was about 4.5 keV from the background thermal continuum. Because of the difference of line redshift between these X-ray lines and optical absorption lines of afterglow, it was interpreted that the emission lines came from the matter blueshifted relative to the source's frame at a velocity of $\sim$0.1 c (Reeves et al., 2002). This interpretation

Astrophysics and Space Science **298:** 323–326, 2005.

however has serious problem. As Kosenko et al. pointed out (Kosenko et al., 2003), it is hard to explain the large emission measure and absence of iron lines. Emission measure, which is estimated by the flux of photons, describes the relation of volume size and density of emitting region i.e. $EM = n_e^2 V = 10^{69}\,\mathrm{cm}^3$ (in this case).

Then Kosenko et al. (2003) propose different interpretation of the origin of the lines and their time evolution of the spectrum of GRB011211. They identify that the observed decay time of line is the thermal relaxation time of the hot plasma heated by GRB i.e. $n_e \sim 10^{11}$–$10^{12}\,\mathrm{cm}^{-3}$. From the estimation of the heating energy per nucleon by the γ-ray, the upper limit of distance of the matter from the GRB central source is derived $d \simeq 2 \times 10^{17}\,\mathrm{cm}$. Using this limit and required large volume of emission region, the cone opening angle can be estimated $\theta \simeq 3^\circ$. This large distance and small angle is consistent with the large emission measure and angle $3.4 \pm 0.1^\circ$ estimated by other restriction (Jakobsson, 2003).

In the present paper, we solve the rate equation for the circumsteller matter under such situation that γ-ray emission from the central engine heat up, and consequently, the matter sustains the line or recombination emission of X-ray over a typical time scale of 10^4 s. In this case, the time scale of plasma becomes longer than that of incident irradiation. Therefore, we must solve the ionization and recombination processes with time evolution. We discuss how such time-dependent atomic processes affect the line and recombination spectrum.

Test Calculation and Result

We assume that the circumstellar matter lies at a distance $10^{17}\,\mathrm{cm} \simeq 0.1\,\mathrm{pc}$ from central engine. Gamma-ray of the burst heat up the circumstellar matter at a stretch, and the matter radiate the X-ray line and recombination emission with cooling down. Its electron density and temperature are $n_e \sim 10^{12}\,\mathrm{cm}^{-3}$ and $T_e = 1\,\mathrm{keV} \simeq 10^7\,\mathrm{K}$ respectively. The irradiation time of incident γ-ray is 10 s. In this condition, the cooling time (order of 10^4 s) is much longer than the irradiation time scale. Therefore, the populations of each quantum state in each ionization state of accounting ion vary at every moment. We cannot deal with the plasma as the corona equilibrium or collisional radiative equilibrium (CRE) state. Thus, we must calculate the rate equation of an element,

$$\frac{dN_{\zeta,m}}{dt} = \sum N_{\zeta',m'} R(\zeta', m' \to \zeta, m) - \sum N_{\zeta,m} R(\zeta, m \to \zeta', m'), \tag{1}$$

where $N_{\zeta,m}$ is the population of ionization state ζ, quantum state m, and $R(\zeta', m' \to \zeta, m)$ is a transition rate $(\zeta', m' \to \zeta, m)$. Summation must be performed for all the important transition rates, i.e. excitation, de-excitation, ionization and recombination rates of atomic process.

As the test case, we calculate that the plasma is one-zone and has only helium gas considering the photoionizaton, photorecombination and bound-bound transition processes. The quantum state is considered up to principal quantum number 6. Bound–bound transition and photoionization rate coefficients are calculated by the atomic code using More's method (More et al., 1991). This method is based on the appropriate semiclassical approximation of the wave function. It can calculate any quantum state, any ionization sate, any atom up to $Z \leq 29$, and dramatically reduce the calculation time with good accuracy. Radiative recombination rate coefficients are calculated approximately (Salzmann, 1998).

Time evolution of the spectrum is shown Figure 1 at 1 s (*upper left*), 10 s (*upper right*), 10^2 s (*lower left*), 10^3 s (*lower right*) after the beginning of the irradiation. Helium atom is quickly ionized and all bound electrons are teared off to be free as soon as strong irradiation. After the end of irradiation, the plasma cools down slowly. At the time of 10–10^2 s, many lines come from He(II) and strong recombination edges as the transition from He(III) to He(II) are dominant. At the time $>10^2$ s, lines from He(I) and recombination edges from He(II) to He(I) are dominant, but its energy and emissivity are much weaker than the previous time range. At the case of high Z metal or realistic mixing case, variation of the population and spectrum will be more complicated.

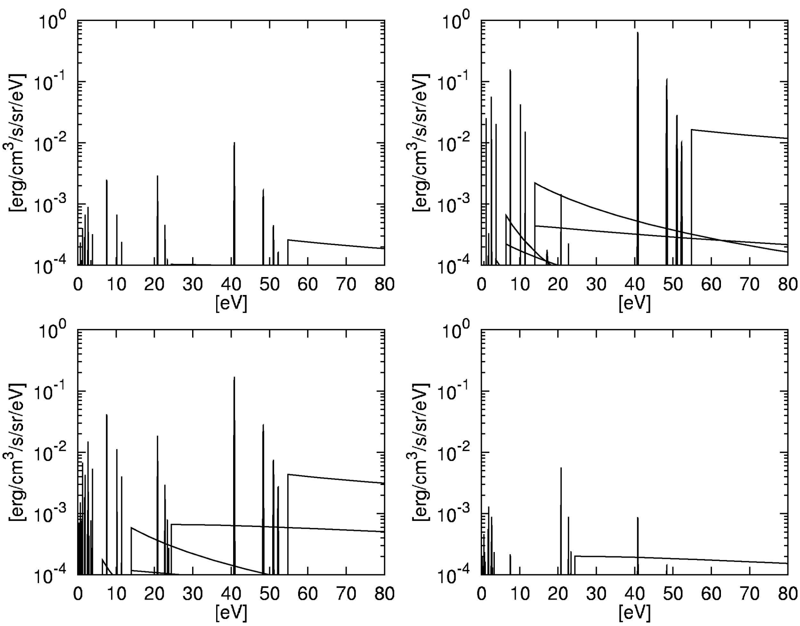

Figure 1. Time evolution of the spectra of helium ions and atom. Upper left spectrum is the 1 s after the irradiation, upper right is the 10 s, lower left is the 10^2 s, lower right is the 10^3 s.

Conclusion

We calculate the time dependent line and recombination spectrum of nonequilibrium plasma heated by the strong radiation as the test model of X-ray line emission of GRB afterglow. Our conclusions are: (i) Strong irradiation make the circumstellar matter ionized immediately, and it cools down slowly over 10^4 s, (ii) The ionization state and spectrum are highly fluctuating with time, (iii) Nonequilibrium effect will be more complicated and important especially in the case of high Z metal.

We will develop the calculation code solving the rate equation to calculate the bound–bound process, free-free process, auger effect, high Z case, so that we will solve the puzzle of X-ray afterglow line emission.

References

Antonelli, L.A., Piro, L., Vietri, M., et al.: 2000, *ApJ* **545**, L39.
Butler, N.R., Marshall, H.L., Ricker, G.R., et al.: 2003, *ApJ* **597**, 1010.
Salzmann, D.: 1998, *Atomic Physics in Hot Plasmas*, Oxford University Press.
Frail, D.A., et al.: 2001, *ApJ* **562**, L55.
Hjorth, J., et al.: 2003, *Nature* **423**, 847.
Jakobsson, et al.: 2003, *Aap.* **408**, 941.
Kosenko, D.I., Blinnikov, S.I., Postnov, K.A., et al.: 2003, *Astron. Lett.* **29**, 205.
More, R.M. and Warren, K.H.: 1991, *Ann. Phys.* **207**, 282.
Piro, L., Costa, E., Feroci, M., et al.: 1999, *ApJ* **514**, L73.
Piro, L., Garmire, G., Garcia, M., et al.: 2000, *Science* **290**, 955.
Reeves, J.N., Watson, D., Osborne, J.P., et al.: 2002, *Nature* **416**, 512.
Watson, D., Reeves, J.N., Hjorth, J., et al.: 2003, *ApJ* **595**, L29.
Woosley, S.E.: 1993, *ApJ* **405**, 273.
Yoshida, A., Namiki, M., Yonetoku, D., et al.: 2001, *ApJ* **557**, L27.

RICHTMYER–MESHKOV INSTABILITY RESHOCK EXPERIMENTS USING LASER-DRIVEN DOUBLE-CYLINDER IMPLOSIONS

J.M. TACCETTI[1], S.H. BATHA[1], J.R. FINCKE[1], N.D. DELAMATER[1], N.E. LANIER[1], G.R. MAGELSSEN[1], R.M. HUECKSTAEDT[1], S.D. ROTHMAN[2], C.J. HORSFIELD[2] and K.W. PARKER[2]

[1]*Los Alamos National Laboratory, Los Alamos, USA; E-mail: taccetti@lanl.gov*
[2]*Atomic Weapons Establishment Plc, Aldermaston, UK*

(Received 22 April 2004; accepted 31 May 2004)

Abstract. As a shock travels through the interface between substances of different densities, existing perturbations can grow via the Richtmyer–Meshkov (RM) instability. The study of the RM instability in a convergent geometry leads to a better understanding of implosions applicable to inertial confinement fusion and various astrophysical events, such as core-collapse supernovae. We present results of laser-driven double-cylinder implosions performed at the Omega laser facility with an emphasis on sending a second shock through an already shocked RM unstable interface. The uniform reshock of a cylindrical interface is achieved by inserting a second cylinder inside the first that reflects the inwardly traveling shock and causes it to interact a second time with the unstable interface. We present an analysis of the instability growth as a function of shock strength and zero-order perturbation behavior during reshock.

Keywords: Richtmyer–Meshkov, cylindrical implosion, experiment, simulation

1. Richtmyer–Meshkov Instability Reshock and Astrophysical Processes

The Richtmyer–Meshkov instability (RMI) drives the growth of perturbations at the interface between different substances when a shock travels through it, regardless of whether the shock is traveling from a heavier to a lighter medium or vice versa. It promotes turbulence and mixing of the materials at either side of this interface. The RMI has relevance for a broad range of topics, including many astrophysical processes, such as RMI-induced mixing during the explosion phase of core-collapse (Type II) SNe, shock waves generated by SNe interacting with compressed ISM or denser molecular clouds, vortex formation in ISM (which may affect evolution scenarios of stars and structure formation in nebulae), morphology of SNe remnants (e.g. Cygnus Loop), and shock-clump interaction (Takabe, 2001). Any of these processes could experience reshock as well. Reshock occurs when a second shock travels through an already shocked interface.

We study RMI reshock in cylindrical geometry, which includes convergent effects such as those seen in many astrophysical systems, but is still 2D and therefore simpler to diagnose, model, and interpret than fully 3D spherical geometry. This

Astrophysics and Space Science **298:** 327–331, 2005.

work is a subset of a larger campaign to study mix in cylindrical geometry, which includes work with singly shocked surfaces, both smooth and perturbed (Barnes et al., 2002, Lanier et al., 2003, Hueckstaedt et al., 2005; Balkey et al., in preparation; Fincke et al., 2004). The principal aim of this experiment is to measure the RMI growth and mix during shock and reshock in a convergent geometry, and to use this knowledge to validate existing simulation codes (Parker et al., 2004).

2. Experimental Method

The experiment implodes cylinders (or 'targets') composed of concentric shells of different materials, using multiple laser beams to drive the implosion. The laser energy deposited on the outer surface of the target ablates material, causing the target to implode, and drives a cylindrically symmetric shock through the shells embedded in the target. The experiments are performed at the OMEGA laser facility at the University of Rochester (Boehly et al., 1997).

The basic – 'single-shell' – target to study growth is a foam core inside a cylindrical epoxy shell (ablator) with a radiographically opaque Al tracer layer at the interface. The Al layer in the target is shocked twice: first by the inward-traveling shock and then again by an outward-traveling reflected one. A solid inner cylinder is added in the 'double-shell' design, developed to study mixing due to reshock in a controlled manner. The added inner core makes the reflected shock more uniform than if reflected from the origin. It also shortens the time between shock and reshock, allowing more of the dynamics to be captured in our short diagnostic time window.

The target (Figure 1) is approximately 2 mm long and 1 mm in diameter. The outer Al shell, or 'marker layer', is 500 μm long, centered on the target. The inner core extends $\sim$100 μm beyond either end of the marker layer. All the results presented in this paper were obtained using targets such as the one described, and all were shot during a single 2-day experimental run. No perturbations were added to the Al marker surfaces, and a sample surface was metrologized to be smooth

material	thickness
epoxy	55 μm
Al	8 μm
CH 90 mg/cc foam	310 μm
Cu	5 μm
acrylic	115 μm

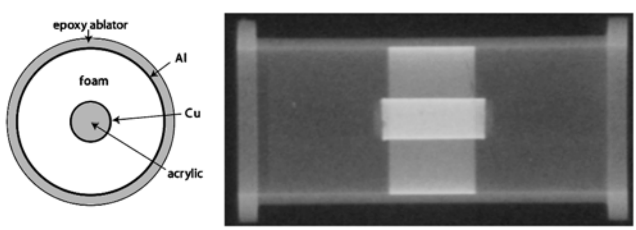

Figure 1. Cylindrical target nominal layer thicknesses, cross-section, and side-on radiograph.

to within 100 nm RMS. Follow-up reshock experiments will investigate growth of surfaces with prescribed perturbations.

It is instructive to follow the sequence of events that occur during a double-cylinder implosion. As explained in more detail by Graham et al. (2000), a shock traveling from a lighter to a heavier fluid results in a transmitted shock (TS) and a reflected shock (RS), and a shock traveling from a heavier to a lighter fluid results in a TS and a reflected rarefaction wave. The laser beams drive a cylindrical shock inwards from the epoxy. This shock traverses the epoxy/Al (light to heavy) interface, resulting in a RS and a TS. The TS next traverses the Al/foam interface (heavy to light), resulting in a TS traveling inwards and a rarefaction wave traveling outwards. The TS travels through the foam until it crosses the foam/Cu interface (light to heavy), resulting in a RS and a TS. This reflected shock is the one that will reshock the marker layer. The TS entering the core rattles around resulting in multiple reflected and transmitted shocks.

A simplified *r–t* diagram can be used to explain two observed dynamic effects (Figure 2). The laser beams are on for 1 ns, and $t = 0$ is defined as the 2% rise point of the pulse. The Al and Cu layer thicknesses are ignored and shocks are followed. The shock velocities shown are estimated by using initial layer radii and approximate shock-interface interactions observed in our data, and by requiring that shocks travel faster in lighter media. The post-shock Al marker velocity is $\sim 70\ \mu$m/ns. The principal dynamic effects observed are:

1. Multiple shocks between the Al and Cu slow down, stop, and reverse the implosion of the inner surface of the Al marker, and
2. A rarefaction wave propagating inward from the epoxy/vacuum interface causes the outer surface of the marker to expand.

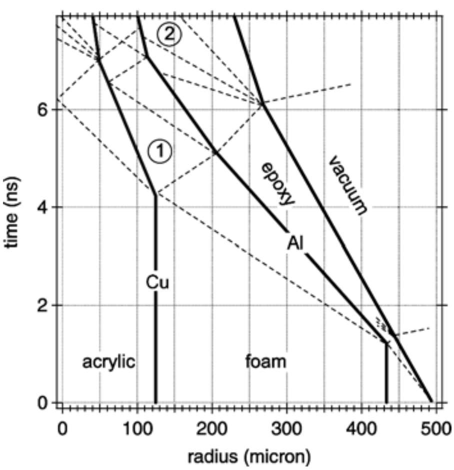

Figure 2. Simplified *r–t* diagram. Solid lines represent material interfaces (Al and Cu layer thicknesses are ignored); dashed lines represent shocks. Effects at 1 and 2 are explained in the text.

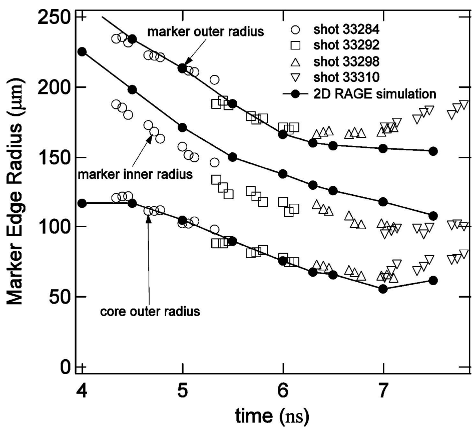

Figure 3. Comparison of experimental results and 2D RAGE simulation results.

3. Data Analysis and Comparison with RAGE Simulations

The primary diagnostic is an X-ray framing camera viewing the target axially. The camera uses a 4-strip microchannel plate and a 4 $\times$ 4 pinhole array with 15 μm diameter pinholes (Lanier et al., 2003). The Fe backlighter, mounted on the opposite end of the target, is heated by five OMEGA laser beams (1 ns pulse time-delayed relative to the driving pulse) and produces 6.7 keV X-rays. The strength of the signal recorded on film depends on the transmission through the target, which in turn depends on the materials and density in the target. Each of the 16 frames is recorded for a duration of 60 ps. The entire observational window is 1.2 ns.

The principal measurements are the marker layer outer edge and inner edge, and the outer edge of copper coating on the acrylic core. A lineout of the angle-averaged transmission is obtained, and each edge is defined as the 50% intensity point between the local maximum and minimum intensity near that edge. Parallax errors are taken into account and removed numerically (as in Lanier et al., 2003). The result of the analysis of four targets shot is shown in Figure 3.

Marker and core trajectories show implosion and re-expansion. The marker layer reaches a minimum width at $\sim$5.2 ns, when the shock reflected from the core strikes the inner surface of the marker layer. The marker width then remains approximately constant for $\sim$1 ns during shock transit through the Al layer. Maximum compression (minimum inner edge) of the marker layer occurs at $\sim$6.8 ns. At this point, the outer edge of the marker layer begins to expand. As stated earlier, this may be the result of a rarefaction wave traveling inwards from the epoxy/vacuum interface.

The experiments were modeled with the RAGE code (Baltrusaitis et al., 1996). RAGE is a 3D multi-material Eulerian radiation-hydrodynamics code developed by LANL and Science Applications International Corporation It features a continuous adaptive mesh refinement algorithm for following shocks and contact discontinuities with a very fine grid while using a coarse grid in smooth regions. It uses a second-order Godunov-type scheme. Laser deposition is not yet fully integrated into the code; it is calculated with LASNEX and implemented as an energy source in RAGE.

The calculations shown were performed in 2D, with a 200 nm periodic perturbation applied on the outer edge of the Al marker layer, and don't include instrumental blurring effects, which would add about 15 μm to the marker width. The calculated thickness of the marker layer shows reasonable agreement with the data up to the start of re-expansion of the outer surface of the marker layer (from 6–7 ns). This discrepancy is still under investigation, including whether other as of yet unaccounted for possible sources of blurring exist. RAGE does better with the timing: the shock strikes the core between 4 and 4.5 ns, reshock of the marker layer occurs at $\sim$5.5 ns (exact time is not as clear from the data since event is bracketed by two shots), and expansion of the core begins at $\sim$7 ns.

Results obtained thus far indicate that the cylindrical target design is a very useful testbed for gaining a more fundamental understanding of both shock and reshock induced mixing in a convergent geometry.

Acknowledgments

We would like to acknowledge the target fabrication team at LANL, including people from the MST-7, MST-6, and ESA groups, for their high-quality cylindrical targets and support. This work was performed under the auspices of the U.S. DOE by the University of California at LANL under contract No. W-7405-Eng-36.

References

Balkey, M.M., Batha, S.H., Lanier, N.E. et al.: in preparation.
Baltrusaitis, R.M., Gittings, M.L., Weaver, R.P. et al.: 1996, *Phys. Fluids* **8**, 2471.
Barnes, C.W., Batha, S.H., Dunne, A.M. et al.: 2002, *Phys. Plasmas* **9**, 4431.
Boehly, T.R., Brown, D.L., Craxton, R.S. et al.: 1997, *Opt. Commun.* **133**, 495.
Fincke, J.R., Lanier, N.E., Batha, S.H. et al.: 2004, *Phys. Rev. Lett.* **93**, 115003.
Graham, M.J. and Zhang, Q.: 2000, *Astrophys. J. Suppl. Ser.* **127**, 339.
Hueckstaedt, R.M., Batha, S.H. Balkey, M.M. et al.: 2005, *Ap&SS* **298**, 255.
Lanier, N.E., Barnes, C.W., Batha, S.H., et al.: 2003, *Phys. Plasmas* **10**, 1816.
Parker, K., Rothman, S.D., Horsfield, C.J. et al.: 2004, *Phys. Plasmas* **11**, 2696.
Takabe, H.: 2001, *Prog. Theor. Phys. Suppl. (Japan)* **143**, 202.

DENSITY AND TEMPERATURE MEASUREMENTS ON LASER GENERATED RADIATIVE SHOCKS

T. VINCI[1], M. KŒNIG[1], A. BENUZZI-MOUNAIX[1], L. BOIREAU[2,3], S. BOUQUET[2], S. LEYGNAC[3], C. MICHAUT[3], C. STEHLÉ[3], O. PEYRUSSE[4] and D. BATANI[5]

[1]*LULI, École Polytechnique, France; E-mail: tommaso.vinci@polytechnique.fr*
[2]*Commissariat à l'Énergie Atomique, Centre DAM/Ile-de-France, France*
[3]*LUTH, Observatoire de Paris, Meudon, France*
[4]*Célia, Université de Bordeaux, Talence, France*
[5]*Università degli Studi di Milano Bicocca, Italy*

(Received 12 May 2004; accepted 14 June 2004)

Abstract. This paper presents some recent measurements on radiative shocks generated in a xenon gas cell using high power laser. We show new results on temperature and electronic density, and on radial expansion of the shock at various initial conditions (laser energy and gas pressure). The data obtained are compared with one-dimensional and two-dimensional hydro simulations.

Keywords: laser, radiative shock, temperature, interferometry

1. Introduction

Supercritical radiative shocks regime can be achieved using high power lasers (Bozier et al., 1986; Bouquet et al., 2004). These experiments can be a key point for astrophysics applications (Remington et al., 2000).

The results presented here have been obtained at LULI (100 J – 1 ns Gaussian shape – 527 nm – 400 μm FWHM). The laser was focused on an ablator–pusher foil (2 μm CH + 3 μm Ti). A strong shock wave is generated and pushes the piston insider a 1 mm^3 quartz cell filled with xenon at different pressures (0.1–0.2 bar). Piston velocity can be changed by varying laser intensity.

Rear side Self-Emission is collected onto a strek camera while a probe beam (low power – 8 ns – 532 nm) diagnoses the cell in the transversal direction through Mach–Zehnder interferometry (for more details see Kœnig et al., 2004).

2. Emission Diagnostic

2.1. Temperature measurement

At a given time we collect on the streak camera a number of photons emitted from the plasma in the cell. In order to relate this number to an "Equivalent Temperature"

Astrophysics and Space Science **298:** 333–336, 2005.

we performed an absolute calibration (spectrum and energy) of the optical system. Since we collect photons emitted inside the cell on the back side, we need to understand which part contributes to our signal: Ti foil, shocked xenon and/or precursor.

To understand this key point, we determine the temperature and the electronic density (T_e and N_e) profiles with 1D simulations and calculate the radiative transfer of visible emission along the whole cell (Zel'Dovich and Raizer, 1967). To know the total amount of photons that will reach our diagnostic, we integrate the emission contribution of each slice of xenon, using opacities given by a simple Free–Free model (Celliers and Ng, 1993). In order to ensure that our model is not opacity-model dependent, we also used detailed opacity data for xenon (Peyrusse, 2000).

In Figure 1a, we present the results obtained on a high laser energy and low initial xenon pure shot corresponding to the image 2a. The experimental data (•) are in a very good agreement with the model (· · ·). We observe also that the shock front temperature (♦) given by the 1D code is higher: this implies that some of the emitted light is probably absorbed in the shock front.

To understand this point, we plot in Figure 1b a snapshot of the calculated emission contribution (—) along with the corresponding temperature (· · ·). We can recognize the typical "spike" of the shock temperature, and the shape of the precursor (shock is moving from left to right). The first important point is that we observe no emission behind the shock front which means that the Ti pusher doesn't contribute to the emission. The second point is that the emission due to the precursor is very weak compared to the total one. Therefore we can be sure that the equivalent temperature we determined corresponds to the shock temperature.

2.2. Radial expansion

The radial expansion of the emissive zone can be deduced from the self emission diagnostic (Figure 2a). We suppose here that it is primarily due to thermal wave

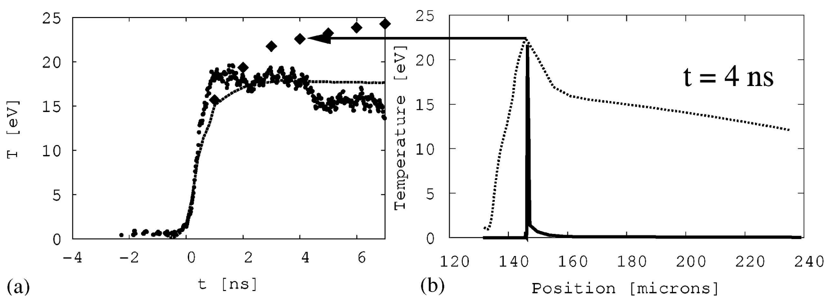

Figure 1. Shot 307: $E = 85$ J, $P_0 = 0.1$ bar. (a) emission of the central zone vs. time: (•) experimental data, (· · ·) model, (♦) shock temperature given by 1D simulations. (b) along the cell: (· · ·) 1D simulated temperature, (—) emission contribution.

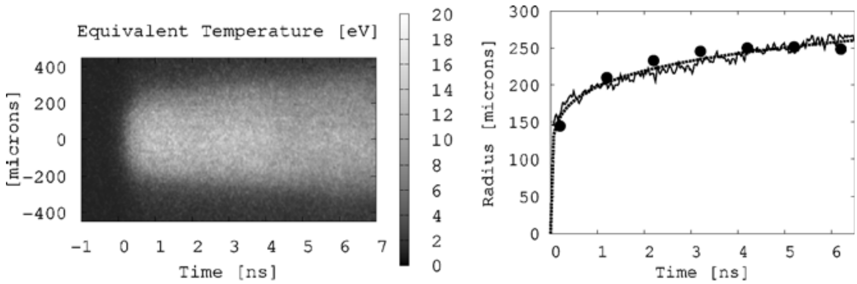

(a) (b)

Figure 2. Shot 0307: $E = 85$ J, $P_{\mathrm{Xe}} = 0.1$ bar. (a) experimental data converted in eV. (b) radial expansion of the emissive zone: (—) experimental data, $(\cdots)$ fit via $r(t) = a\,t^{1/b}$, (•) 2D code simulation.

expansion. The self similar solutions in the non linear case and in the cylindrical geometry, gives a scaling law for the radius given by $r(t) \propto t^{1/7}$ (Zel'Dovich and Raizer, 1967).

We observe (Figure 2b) a quick rise (few ps) of the radius to 150 μm which corresponds to the flat–top part of the laser spot. A fit to our results (Figure 2b $\cdots$) using such a law $r(t) = a\,t^{1/b}$, gives $a = 197$ and $b = 6.8$ in good agreement with the model ($b = 7$). Finally, we also compared with fully 2D radiative simulations (Figure 2b •) and found good agreement.

3. Transverse Optical Probing

3.1. Electronic density measurement

Probing along shock propagation has been done coupling a Mach–Zehnder interferometer to a streak camera. From the fringes shift, we can determine the electronic density: $N_{\mathrm{e}}(x, t) = n_{\mathrm{c}} F(x, t) \frac{\lambda}{r(t)}$, where n_{c} is the critical density, $F(x, t)$ is the fringes shift number, λ the wavelength of the probe beam and $r(t)$ is the radial plasma thickness as given by scaling law seen in previous section (the evolution of $r(t)$ has been taken into account).

In Figure 3 we present a series of shots with different initial conditions: Figure 3(a) and (b) are for an initial pressure of 0.2 bar while (c) and (d) are at 0.1 bar; in addition (a) and (c) are at lower energy (around 55 J on target) while (b) and (d) are at higher energy (85 J). We observe the different shapes of the precursor: for shots at lower energies (a) and (c) it is not yet formed, while for shots at higher energy (b) and (d) precursor length is much more important as predicted by calculations. The initial gas pressure influence the precursor shape: for lower pressure (a) and (b) the precursor is well formed with the typical step (Bouquet et al., 2004).

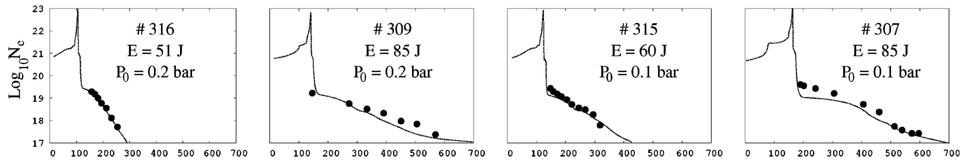

Figure 3. Precursor electronic density for different laser energy and initial gas pressure vs. position (μm) at $t = 4.5$ ns. (•) experimental data, (—) 1D simulations.

4. Conclusions

We have presented here the evidence of a radiative precursor in laser generated shocks. We have been able to observe and measure important parameters simultaneously (temperature, radial expansion and electronic density) and they are well represented by simulations and models.

References

Bouquet, S., Romain, T. and Chieze, J.P.: 2000, *ApJS* **127**, 245.
Bouquet, S. et al.: 2004, *Phys. Rev. Lett.* **22**, 5001.
Bozier, J.C., Thiell, G., Le Breton, J.P., Azra, S. and Decroisett, M.: 1986, *Phys. Rev. Lett.* **57**, 1304.
Celliers, P. and Ng, A.: 1993, *Phys. Rev. E* **47**, 3547.
Kœnig, M. et al.: 2004, 'Radiative shock experiments at LULI', in: *5th HEDLA Meeting*, Tucson.
Peyrusse, O.: 2000, *J. Phys. B Atomic Mol. Phys.* **33**, 4303.
Remington, B.A., Drake, R.P., Takabe, H. and Arnett, D.: 2000, *Phys. Plasmas* **7**, 1641.
Zel'Dovich, Y.B. and Raizer, Y.P.: 1967, *Physics of Shock Waves and High-Temperature Hydrodynamic Phenomena*, New York: Academic Press, 1966/1967.

LINEAR ANALYSIS OF AXIAL SHEARED FLOW IN ASTROPHYSICAL JETS

LUCAS F. WANEX
University of Nevada, Reno; E-mail: lucas@physics.unr.edu

(Received 7 April 2004; accepted 1 June 2004)

Abstract. A linear analysis of axial sheared flow in magnetohydrodynamic (MHD) jets with helical magnetic fields is presented. A linearized set of ideal MHD equations allows the investigation of plasmas with both magnetic shear and flow shear included in the equilibrium profile. These equations are integrated numerically by following the linear development in time of an initial seed perturbation. Global instability growth rates are obtained after the numerical solution converges to the fastest growing mode. It is shown that axial sheared flow reduces the growth of current-driven instabilities in plasma jets with constant magnetic pitch $P = rB_z/B_\theta$.

Keywords: astrophysical jets, linear analysis, axial sheared flow

1. Collimation of Astrophysical Jets

Astrophysical jets occur in a wide range of celestial objects including young stellar objects, supernova, black holes, radiogalaxies, quasars, and active galactic nuclei. Some of these outflows are collimated to 1° or less for distances covering hundreds of kiloparsecs. The stabilizing mechanism for such narrow, elongated objects is to this date still in question. Many simulations of these jets are based on magnetohydrodynamic (MHD) models, in which magnetic fields either pre-existing in the ambient medium or as part of the central object and accompanying accretion disk cause a pinching effect similar to that present in laboratory Z-pinch experiments.

Jets consisting of MHD outflows are subject to instabilities, which may deter their propagation, or even destroy it. Observed features such as wiggles, knots, and filamentary structures in astrophysical jets may be manifestations of these instabilities. The focus of this paper will be restricted to current-driven instabilities (CDI). The most important of these is the so-called sausage and kink instabilities in Z-pinch plasmas.

It has been shown that axial sheared flow is a stabilizing mechanism in Z-pinch plasmas (Sotnikov et al., 2002; Wanex et al., 2004). Sheared flow with speed that decreases with increasing distance from the jet axis has been observed in the HH 1/2 astrophysical jet system in Orion (Bally et al., 2002). Axial sheared flow has been modeled with hydrodynamic simulations (Völker et al., 1999). Here we ask the

Astrophysics and Space Science **298:** 337–340, 2005.

question; can axial sheared flow reduce the growth of current-driven instabilities in astrophysical jets? We will attempt to answer this question by performing a global linear analysis with ideal MHD simulations.

2. MHD Model of an Astrophysical Jet

The jet model adopted here was first published by Appl et al., 2000 (without axial sheared flow). The MHD jet is simulated as an infinitely long cylinder surrounding a perfectly conducting plasma. The boundary between the jet and the ambient medium is modeled as a metal cylinder because the outflow's high speed limits the transmission of information from the interior of the jet to the ambient medium (Appl et al., 2000). The jet is then considered as a region in space wherein supermagnetosonic plasma and an electric current flow. The electric current I is balanced by a return current I_r of equal size. This current can be modeled as a diffuse flow in the ambient medium or as a sheet on the jet surface.

3. Stability Analysis

The stability of supermagnetosonic current-carrying jets is examined with ideal MHD. The MHD equations are linearized by breaking each plasma variable into an equilibrium part and a small perturbation (see Wanex et al., 2004 for the equations). Plasma perturbations are represented mathematically as Fourier components with functional form (in cylindrical coordinates) $\xi(r,\ t)e^{i(m\theta+k_z z)}$. This method has been used in cylindrical plasmas (Bateman et al., 1974), and Z-pinches (Coppins et al., 1984; Sotnikov et al., 2002).

The linearized equations are solved numerically with a generic two-step predictor-corrector, second-order accurate space and time-centered advancement scheme. The problem is treated by introducing perturbations into the plasma equilibrium state and following their linear development in time. Initially the growth rates of the plasma variables (magnetic field, density, pressure, and velocity) are uncorrelated. After several growth times the solution converges to the fastest growing unstable mode.

The equilibrium state of the plasma can be obtained by solving the radial force balance equation in cylindrical coordinates. This equation is

$$\frac{\partial}{\partial r}\left(P_0 + \frac{B_{0\theta}^2}{2} + \frac{B_{0z}^2}{2}\right) + \frac{B_{0\theta}^2}{r} = \frac{P_0 v_{0\theta}}{r}.$$

Here we consider non-rotating jets with constant magnetic pitch $P_0/R = 1/3$, constant density, and negligible thermal pressure. These restrictions are applied in order to compare results with Appl et al., 2000. Their solution to the force balance equation is

$$B_{0\theta} = \frac{r/P_0}{1 + r^2/P_0^2}, \qquad B_{0z} = \frac{1}{1 + r^2/P_0^2}.$$

Since CDIs occur in the rest frame of the jet and are transported along with the plasma flow, axial sheared flow will be modeled as $-v_{0z}\ r^2$. Here v_{0z} is given in multiples of the Alfvén velocity. Thus the sheared flow occurs in the axial (z) direction only and the flow appears to be swept away in a direction opposite to the outflow as one moves from the center of the jet radially outward to the edge at $r = R$.

4. Axial Sheared Flow

In the absence of axial sheared flow the plasma will evolve from equilibrium to a state that is dominated by the fastest growing unstable mode. When this occurs each plasma variable can be written in the form $\xi(r)e^{\gamma t}e^{i(\omega t + m\theta + k_z z)}$, where γ is the growth rate and ω is the angular frequency of the dominate unstable mode. Notice that the phase of this Fourier component is independent of r. The introduction of axial sheared flow will cause an increasing phase shift with increasing r. The phase shift per unit time per unit radial distance is given by $k_z \partial v_{0z}/\partial r$. This phase shift disrupts the unstable mode and prevents it from growing as it does in the absence of axial shear.

5. Results

Figure 1 shows the effect of axial sheared flow on the $m = -1$ to -4 azimuthal modes for axial wave numbers ranging from $k_z R = 1$ to 14. The instability growth

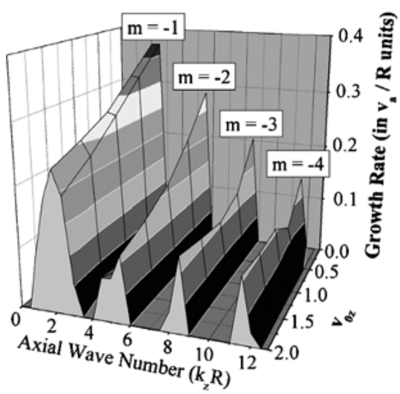

Figure 1. Instability growth rates for the $m = -1$ to -4 azimuthal modes for axial wave numbers ranging from $k_z R = 1$ to 14 and v_{0z} ranging from 0 to 2.

rates are cut by nearly a factor of 2 for $m = -1$ and -2 when $v_{0z} = 2$. The $m = -3$ and -4 azimuthal mode instabilities are reduced less efficiently but these are shorter wavelengths and are less significant in disrupting the jet than the longer wavelengths.

6. Conclusion

For $v_{0z} = 2$ the kink instability growth rates are a factor of two smaller than without axial sheared flow. The distance a jet can travel before current-driven instabilities become important is vt_e, where t_e is the e-folding time. Axial sheared flow increases this time by a factor of two. This means the jet can travel twice as far as predicted by models without axial sheared flow before suffering any disruptive effects caused by current-driven instabilities.

References

Appl, S., Lery, T. and Baty, H.: 2000, *Astron. Astrophys.* **355**, 818.
Bally, J., Heathcote, S., Reipurth, Bo., Morse, J., Hartigan, P. and Schwartz, R.: 2002, *ApJ* **123**, 2627.
Bateman, G., Schneider, W. and Grossman, W.: 1974, *Nucl. Fusion* **14**, 669.
Coppins, M., Bond, D.J. and Haines, M.G.: 1984, *Phys. Fluids* **27**, 2886.
Sotnikov, V.I., Paraschiv, I., Makhin, V., Bauer, B.S., Leboeuf, J.N. and Dawson, J.M.: 2002, *Phys. Plasmas* **9**, 913.
Völker, R., Smith, M.D., Suttner, G. and Yorke, H.W.: 1999, *Astron. Astrophys.* **343**, 953.
Wanex, L.F., Sotnikov, V.I., Bauer, B.S. and Leboeuf, J.N.: 2004, *Phys. Plasmas* **11**, 1372.

VALIDATING THE FLASH CODE: VORTEX-DOMINATED FLOWS

GREG WEIRS[1], VIKRAM DWARKADAS[1], TOMEK PLEWA[1], CHRIS TOMKINS[2] and MARK MARR-LYON[2]

[1]*ASCI FLASH Center, University of Chicago, Chicago, IL, USA;*
E-mail: weirs@flash.uchicago.edu
[2]*Los Alamos National Laboratory, USA*

(Received 4 May 2004; accepted 1 June 2004)

Abstract. As a component of the Flash Center's validation program, we compare FLASH simulation results with experimental results from Los Alamos National Laboratory. The flow of interest involves the lateral interaction between a planar $M_a = 1.2$ shock wave with a cylinder of gaseous sulfur hexafluoride (SF_6) in air, and in particular the development of primary and secondary instabilities after the passage of the shock. While the overall evolution of the flow is comparable in the simulations and experiments, small-scale features are difficult to match. We focus on the sensitivity of numerical results to simulation parameters.

Keywords: Richtmyer-Meshkov instability, numerical simulation

1. Introduction

The impulsive acceleration of a material interface can lead to complex fluid motions due to the Richtmyer–Meshkov (RM) instability. Here, the misalignment of pressure and density gradients deposits vorticity along the interface, which drives the flow and distorts the interface. At later times the flow may be receptive to secondary instabilities, most prominently the Kelvin–Helmholtz instability, which further increase the flow complexity and may trigger transition to turbulence.

Verification and validation are critical in the development of any simulation code, without which one can have little confidence that the code's results are meaningful. FLASH is a multi-species, multi-dimensional, parallel, adaptive-mesh-refinement, fluid dynamics code for applications in astrophysics (Fryxell et al., 2000). Calder et al. discuss initial validation tests of the FLASH code (Calder et al., 2002). Herein we continue our validation effort by comparing FLASH simulations to an RM experiment performed at Los Alamos National Laboratory (Tomkins et al., 2003; Zoldi, 2002).

2. Experimental Facility and Data

The experimental apparatus is a shock-tube with a 7.5 cm square cross-section, as shown in Figure 1. Gaseous SF_6 flows from an 8 mm diameter nozzle in the top

Astrophysics and Space Science **298:** 341–346, 2005.

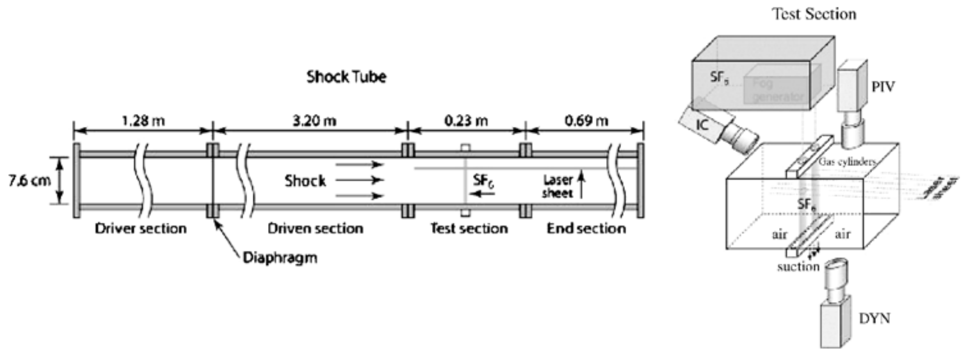

Figure 1. LANL shock tube dimensions with test section detail.

wall of the shock-tube, forming a cylinder of dense gas in the otherwise air-filled test section. A $M_a = 1.2$ Shock wave travels through the shock-tube and passes through the cylinder. Our interest is in the resulting evolution of the SF_6. All the experimental data is obtained in a plane normal to the cylinder axis, 2 cm below the top wall of the test section. The experiment is nominally two-dimensional; however, air diffuses into the SF_6 column as it flows downward, thickening the interface and reducing the peak concentration of the heavy gas.

The initial SF_6 distribution (before the shock impact) is visualized directly by Rayleigh-scattering from the SF_6 molecules (Tomkins et al., 2003). The pixel intensity in the experimental image gives only the mole fraction of SF_6 relative to the peak mole fraction, X_{SF_6}, which must be assumed. The distribution of SF_6 is only approximately radially symmetric, and the signal is dominated by noise at the level of about 5–10%. Smooth initial conditions for our simulations are obtained by fitting a radially symmetric function to the experimental data.

During the experiment the SF_6 distribution is indirectly visualized by visible light scattering off water/glycol droplets, which are seeded in the SF_6. A sequence of experimental images is shown in Figure 2. The shock traverses the cylinder in less than 25 μs. The vortex Reynolds number of the flow, as measured experimentally, is $Re = \Gamma/\nu \approx 5 \times 10^4$, where Γ is the circulation and ν is the kinematic viscosity. Each image is taken from a different experimental run. The water/glycol droplets can also be used to construct two-dimensional velocity vectors in the image plane

Figure 2. Experimental time series of the distribution of SF_6. The first image corresponds to 50 μs after shock impact; following images are at 190, 330, 470, 610, and 750 μs. Intensity corresponds to the mole fraction of SF_6.

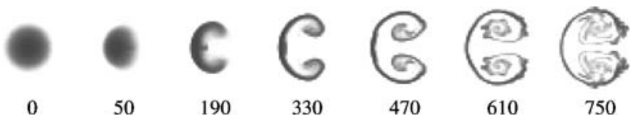

Figure 3. Evolution of the SF_6, with time elapsed after shock impact listed in μs. The mass fraction of SF_6 is shown from a simulation in which $X_{SF_6} = 0.6$ and CFL $= 0.8$.

using particle image velocimetry (PIV) (Prestridge et al., 2000), but the entire test section must be seeded, so simultaneous velocity and composition measurements cannot be obtained.

3. Flowfield Evolution

As the shock traverses the cylinder, vorticity is deposited along the interface due to the misalignment of the pressure gradient (normal to the shock) and the density gradient (normal to the interface.) The density gradient arises from the gas composition; SF_6 is about five times as dense as air. Once the shock has passed through the SF_6, the flow is dominated by a counter-rotating vortex pair, as shown in Figure 2. Instabilities develop along the distorted interface at the edge of the primary vortices. The development and evolution of the vortex pair and subsequent instabilities at the interface proceed in a weakly compressible regime. More precise descriptions can be found in the references (Jacobs, 1993; Quirk and Karni, 1996; Zoldi, 2002).

The flowfield evolution is driven by flow instabilities and vortex dynamics, which are sensitive to the initial conditions and noise in the system. For validation, this sensitivity is desireable because it provides a severe test for the FLASH code. Figure 3 shows a sequence of images from our baseline simulation. The minimum grid resolution is 78 microns, the initial peak mole fraction of SF_6 is 0.6, and the Courant (CFL) number is 0.8. Overall the flow features in the simulation results are similar to those in the experimentally obtained images. Next we describe the effects of several simulation parameters on the computed results. The amount and location of small-scale structure, relative to the experimental data at 750 μs, will be used as a qualitative metric.

4. Results

In our initial investigations we have focused on the sensitivity of the computed solutions to several simulation parameters. We have considered the dependence on the initial maximum mole fraction of SF_6, the mesh resolution, the mesh refinement pattern, and the Courant number. We have also compared velocity data, and are beginning to consider three-dimensional effects. Here we show results only for different mesh refinement patterns and Courant numbers. More thorough discussion of the results can be found in (Dwarkadas et al., 2004).

Regarding the initial maximum mole fraction of SF_6, we find that simulations where $X_{SF_6} = 0.6$ seem to match the experimental results better than when $X_{SF_6} = 0.8$. At a higher value, the initial density gradient is larger; this leads to greater vorticity deposition, faster instability growth, and consequently, excessive small scale structure. However, the time sequences match better for $X_{SF_6} = 0.8$.

It is known that unavoidable discretization errors at discontinuous jumps in grid resolution can act as sources of spurious small-scale structure (Quirk, 1991). To test this possibility we have run simulations in which a predetermined area around the vortices is uniformly refined to the highest resolution. Compared to fully adaptive refinement (the default) this approach significantly reduces the amount of perturbations introduced by the grid adaption process but increases the computational cost of the simulations.

In Figure 4 we compare the results from a fully adaptive grid and grids with maximally refined rectangles of 3×3 cm, 4×4 cm, and 4×8 cm. The vortex structure is always less than 2 cm across. For the different grids the large scale morphology remains the same, but the shape of the cross-section visibly differs depending on the grid, as does the amount and location of small-scale structures. In particular, differences are noticeable in the small-scale instabilities present on the vortex rolls. Since all other simulation aspects are the same, the differences must originate with perturbations at jumps in refinement.

We then repeated the simulations on the different grids, but at a limiting Courant number of CFL = 0.2. The results are shown in Figure 5. We observe much less variation between solutions on adaptive and locally uniform grids at CFL = 0.2 than at CFL = 0.8. One explanation for these results is that the errors at the fine-coarse

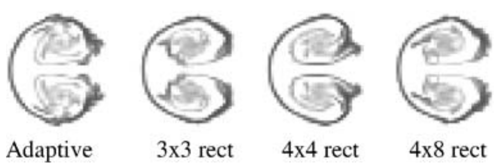

Figure 4. Solutions on different grids, 750 μs after shock impact at CFL = 0.8. Left to right: fully adaptive grid; 3×3 cm refined rectangle; 4×4 cm refined rectangle; 4×8 cm refined rectangle. In the rightmost image, the refined rectangle covers the entire spanwise extent of the test section.

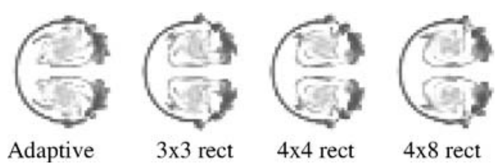

Figure 5. Solutions on different grids for CFL = 0.2; for other details see Figure 4.

boundaries are larger and lead to stronger perturbations at higher CFL numbers. An alternative explanation might be that at higher Courant numbers, PPM does not adequately compute solutions at these conditions. Our simulations indicate that for FLASH, a lower CFL number leads to more consistent results on different grids.

In addition to the SF_6 distribution, experimental measurements of the velocity field in the vicinity of the vortex pair are available. The particle image velocimetry technique provides two-dimensional velocity vectors in the image plane. We find that in the frame of reference of the vortices, the velocity magnitude and large scale structure of our simulations match those measured. The greatest discrepancies are at smaller scales at the outside edges of the vortices.

Finally, we executed a speculative three-dimensional simulation. Our extension of the initial conditions in the third (cylinder axis) dimension is purely ad hoc, because we have no corresponding experimental data. For this reason this simulation cannot be used as a validation test for the FLASH code, but we hope it will open a new line of investigation and discussion. In the cylinder-axis dimension, we varied the maximum mole fraction from $X_{SF_6} = 0.64$ at the top wall of the test section to $X_{SF_6} = 0.47$ at the bottom, and in the same direction the radius of the cylinder increases slightly. These changes result in greater vorticity deposition at the top wall, and the vortex pair and instabilities evolve more quickly there. This behavior is expected based on the two-dimensional simulations; more interesting is that the maximum flow velocity in the axial direction is greater than half that in the spanwise direction by the end of the simulation ($750\,\mu$s). The stronger vortices have lower core pressures, and the pressure gradient in the vortex cores accelerates the flow from the bottom wall toward the top wall. The air is preferentially accelerated because of its lower molecular weight and confinement by the SF_6, which acts like the wall of a tube. For the initial conditions we have assumed, the axial velocities suggest the three-dimensional effects are present.

5. Concluding Remarks

To date we have made a large number of two-dimensional simulations to validate the FLASH code for problems dominated by vortex dynamics. So far, we have gained a better understanding of the sensitivity of the computed solutions to simulation parameters such as resolution, CFL number, and mesh adaption. While we can recover the overall morphology, the approximate amount and location of small scale structure, and velocity field, we must make assumptions (though reasonable) about the initial conditions to do so.

We continue to work on several fronts. We lack quantitative, physically meaningful metrics for comparing simulation and experimental data. These metrics are difficult to develop and are rarely given the attention they deserve. FLASH simulations do not currently include a physical model for viscosity, but resolution-dependent numerical viscosity is present. Simulations with a minimum grid spacing of $78\,\mu$m exhibit approximately the same amount of small scale structure as seen in the experimental data, while results on coarser grids show too little and on finer grids too much. We will soon begin simulations with models for physical diffusion; all the results presented here will then be reviewed. Our three-dimensional simulation, despite issues with the initial conditions, suggests that three-dimensional effects might be important for this experiment. We are performing a systematic study of three-dimensional effects, and hope that experimental data will become available for comparison.

References

Fryxell, B., Olson, K., Ricker, P., Timmes, F.X., Zingale, M., Lamb, D.Q., MacNeice, P., Rosner, R., Truran, J.W. and Tufo, H.: 2000, *ApJS* **131**, 273.

Calder, A.C., Fryxell, B., Plewa, T., Rosner, R., Dursi, L.J., Weirs, V.G., Dupont, T., Robey, H.F., Kane, J.O., Remington, B.A., Drake, R.P., Dimonte, G., Zingale, M., Timmes, F.X., Olson, K., Ricker, P., MacNeice, P. and Tufo, H.M.: 2002, *ApJSS* **143**, 201.

Tomkins, C., Prestridge, K., Rightley, P., Marr-Lyon, M., Vorobieff, P. and Benjamin, R.: 2003, *Phys. Fluids* **15**(4), 986.

Zoldi, C.A.: 2002, PhD Thesis, State University of New York at Stony Brook.

Prestridge, K., Vorobieff, P., Rightley, P.M. and Benjamin, R.: 2000, *Phys. Rev. Lett.* **84**(19), 4353.

Jacobs, J.W.: 1993, *Phys. Fluids A* **5**(9), 2239.

Quirk, J.J. and Karni, S.: 1996, *J. Fluid Mech.* **318**, 129.

Dwarkadas, V., Plewa, T., Weirs, G., Tomkins, C. and Marr-Lyon, M.: 2004, in: T. Plewa, T. Linde, and V.G. Weirs (eds.), *Adaptive Mesh Refinemen – Theory and Applications,* Springer LNCSE Series. Springer-Verlag, Berlin.

Quirk, J.J.: 1991, PhD Thesis, Cranfield Institute of Technology, UK.

ELECTRON-POSITRON PLASMAS CREATED BY ULTRA-INTENSE LASER PULSES INTERACTING WITH SOLID TARGETS

S.C. WILKS, H. CHEN, E. LIANG, P. PATEL, D. PRICE, B. REMINGTON, R. SHEPHERD, M. TABAK and W.L. KRUER

Lawrence Livermore National Laboratory, L-473, Livermore, CA 94550, USA; E-mail: wilks1@llnl.gov

(Received 19 April 2004; accepted 23 April 2004)

Abstract. We discuss the necessary requirements to create dense electron-positron plasmas in the laboratory and the possibility of using them to investigate certain aspects of various astrophysical phenomena, such as gamma ray burst engines. Earth-based electron-positron plasmas are created during the interaction of ultra-intense laser pulses impinging on a solid density target. The fact that positrons can be generated during this interaction has already been demonstrated by Cowan et al. (2000). However, several questions concerning the number, energy, and dynamics of these positrons have yet to be answered. Through insight gathered from PIC simulations, we postulate that the e^+e^- plasma leaves the creation region in dense jets, with relativistic energies. In order to estimate the number density of the positrons created, we begin by first experimentally measuring the hot electron temperatures and densities of such interactions using a compact electron spectrometer. Once the electron distribution is known, the positron creation rate, Γ, can be estimated. This same experimental diagnostic can also, with minor modification, measure the energy distribution of positrons. Initial estimates are that, with proper target and laser configurations, we could potentially create one of the densest arraignments of positrons ever assembled on earth. This experimental configuration would only last for a few femtoseconds, but would eventually evolve into astrophysically relevant pure electron-positron jets, possibly relevant to e^+e^- outflow from black holes.

Keywords: positron plasma, ultra-intense lasers, laboratory astrophysics

It was predicted several years ago that the large electric fields present in Ultraintense laser solid interactions can generate a large number of energetic electrons whose effective temperatures are in the keV to several MeV range (Wilks et al., 1992; Wilks and Kruer, 1997). As is well known, if an electron has a kinetic energy of at least twice the energy associated with the rest mass of itself, it has a finite probability of creating a pair (we will give actual estimates of cross sections in the next section.) With the continued increase in laser energy and intensities, the realization of what seemed at the time "far out" ideas (Liang et al., 1998) proposed only 6 years ago concerning the possibility of generating significant numbers of positrons (and hence dense electron-positron plasmas) is quickly becoming a reality. Although thought to be common in many astrophysical objects, this peculiar state of matter is not typically present on earth, due to the relatively fast annihilation rate (on the order of

Astrophysics and Space Science **298:** 347–355, 2005.

a nanosecond) of positrons in solid density matter. Although low density electron positron plasmas have been studied for some time, very little is known about dense electron positron plasmas, in particular about jets. This manuscript will consider the near term prospects for creating substantial electron-positron plasmas and jets in the laboratory.

We begin with estimating the number and effective temperature of the hot electron component that is thought to be generated in Ultraintense laser matter interactions. The theoretical maximum effective electron temperature that can be achieved with a linearly polarized laser pulse of intensity I (W/cm^2) and wavelength λ (μm) for intensities ($I\lambda^2$) greater than about 10^{18} W/cm^2 (assuming normal incidence) is given by Wilks et al. (1992) and Wilks and Kruer (1997)

$$kT_{\text{hot}} = \left[\sqrt{\left(1 + \frac{I\lambda^2}{2.8 \times 10^{18}}\right)} - 1\right] 511\,\text{keV} \tag{1}$$

The actual effective temperature attained in any given experiment is usually below this value, and is actually a function of many specific details of the laser used, such as the laser pulse length, spot size, energy, target thickness (Mackinnon et al., 2002; Chen and Wilks, to be submitted), target material, amount of prepulse, and/or Amplified Spontaneous Emission (ASE) present on the laser, to name only a few. An example energy spectra, obtained from a 1-D PIC simulation of a thin (~1 micron Au foil) is shown in Figure 1. For the parameters of this simulation, Eq. (1) would predict 180 keV, the measured is approximately 200 keV, and experiment gives about 160 keV. (Typically, 1-D PIC overestimates temperatures, unless colllisional effects are explicitly included.) Similarly, the number of hot electrons can also vary

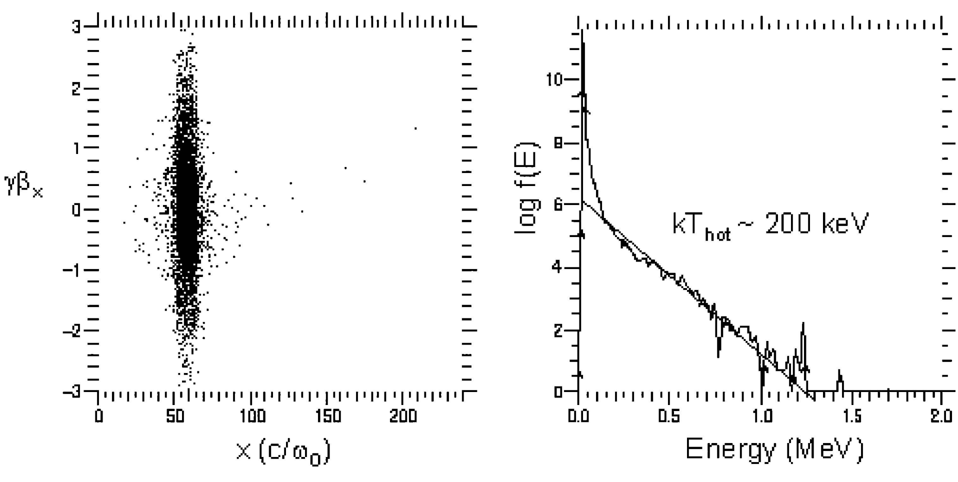

Figure 1. Electron phase space and energy distribution at $t = 200$ fsec, for a thin (1 micron) foil with a 100 fsec, $I\lambda^2 = 2 \times 10^{18}$ W μm/cm^2 laser.

considerably from laser to laser, but it has been found generally to fall in the 20–60% range (Wharton et al., 1998), although virtually every experiment done in this regime is typically reliant on assumptions from various computer codes, and hence have inherent large uncertainties. Thus, we will consider the entire range of possible absorption fractions of hot electrons. In fact, it may be that the precise measurement of the number of positrons, coupled with the actual electron and positron energy spectra, may provide one of the better (more direct) measurements of fraction of hot electrons that can be achieved.

The first, and most obvious, result of pair production is the generation of positrons. In fact, Cowan et al. (2000) first confirmed the existence of positrons in ultra-intense laser solid interactions using the LLNL Petawatt laser in 1999. Since that time, others have confirmed this using other short pulse laser facilities (Norreys et al., 2003; Gahn et al., 2000). Usually in the laboratory, positrons are created by using electron acceletors that generate buncheees of electrons that are directed toward thick slabs of high Z materials, called converters. The resulting positrons are then collected in a particular static electric and magnetic field configuration, known as a "Penning-Malmberg trap" (Greaves and Surko, 2000). Typical numbers of positrons found in these traps are around $N_{e+} \sim 8 \times 10^7$, with maximum densities reaching roughly $n_{e+} \sim 4 \times 10^9\,\mathrm{cm}^{-3}$. Another potential source of earth-based positrons is thought to be Tokamaks, where the runaway current can reach several MeV (Helander and Ward, 2003). Although this has yet to be experimentally confirmed, theoretical estimates of the number of positrons potentially could reach $N_{e+} \sim 8 \times 10^{14}$, but the large volume ($\sim$2.7 $\times$ $10^7\,\mathrm{cm}^{-3}$) only allow for low densities of roughly $n_{e+} \sim 3 \times 10^7\,\mathrm{cm}^{-3}$. Lasers are very good at delivering a relatively large amount of in energy ($\sim$1 kJ), in a relatively short amount of time ($\sim$ picoseconds), in a very small spot ($\sim$ microns). We will present calculations below suggesting that 200 Joule class ultraintense lasers could potentially create a large number of positrons $N_{e+} \sim 10^{10}$ in a very small volume ($\sim$100 micron cube), which would result in a maximum density of roughly $n_{e+} \sim 10^{16}\,\mathrm{cm}^{-3}$. Although only at this density for a fraction of a second, this would be the densest positron source possible in a controlled laboratory setting. Further, as the positrons and electrons expand, a dense electron positron "jet" will be formed that could be studied and measured to determine if it is astrophysically relevant. In the remainder of this manuscript, we will provide detailed calculations that give estimates for current and nearly completed laser systems and specific target designs that optimize the electron temperature. In addition, we will consider the possibility of diagnosing these plasmas (Chen et al., 2003).

The next step in the calculation of the number of positrons created in an ultraintense laser pulse solid interaction is to look at the cross section for pair production, given the electron energy distribution described by Eq. (1). As pointed out in the original pair paper, the dominant creation mechanism for pair creation in thin slab targets is electron ion collisions, and this can be maximized by choosing high Z

material (Liang et al., 1998). The pair density growth is then given by

$$\frac{dn_{e+}}{dt} = \frac{dn_{ei}}{dt} + \frac{dn_{\gamma i}}{dt} \tag{2}$$

In fact, as pointed out by Nakashima and Takabe (2002), it may be possible to include bremsstrahlung if the target is thick. Here, we add further, that if one considers electrons to reflux through a think target, then even a thin slab is, in effect, acting as a thick target, in the sense that electrons are continuously interacting with solid density, and thus the same electron can generate many pairs, and become accelerated to high energy again, as it is reaccelerated by the laser at the vacuum-solid interface. Next, we consider the cross section for these two terms, as given by Evans (1995)

$$\sigma_{ei} = \frac{28(Z\alpha r_e)^2 \ln^3 \gamma}{27\pi} \tag{3}$$

where $\alpha = 1/137$ (fine structure constant) and γ is the relativistic Lorentz factor for the hot electrons, and r_e is the classical electron radius. Putting into Eq. (2) and integrating, yields

$$n_{e+} = \frac{Zn_i[e^{\Gamma t} - 1]}{2} \tag{4}$$

where the pair growth rate is given by

$$\Gamma = 2n_i C \int d\gamma \sigma_{ei} f(1-\gamma^{-2})^{1/2} \tag{5}$$

where *f*(*E*) is taken to be given by the distribution function resulting from the electron energy spectra as obtained according to Eq. (1). In addition, it is found empirically, via simulations, that the maximum electron energy is approximately 6 times the effective temperature of the electrons, by this heating mechanism. Thus, one might be tempted to use this as the high energy cut-off for the integral. However, there are could be other accelerating mechanisms present that could easily produce much higher energy electrons (forward Raman, for example) and hence the factor of 6 is not a hard and fast rule, but the real cut-off is probably not much different than this. As noted in the original paper (Liang et al., 1998), the pair production rate is sensitive to this cut-off, as it can easily vary by a factor of 10, depending on where the cut-off is taken.

We are now in a position to estimate the number of pairs achievable, as a function of laser parameters. The total number of hot electrons can be estimated from the above arguments as

$$N_{\text{hots}} = \frac{\eta E_{\text{laser}}}{kT_{\text{hot}}} \tag{6}$$

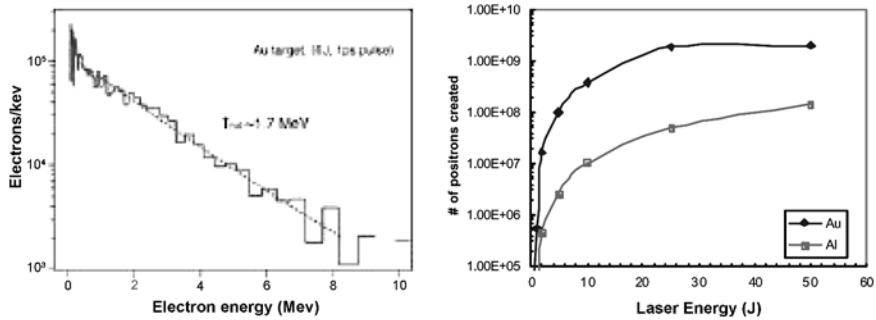

Figure 2. (a) Experimental electron spectra obtained from 5×10^{19} W/cm^2 laser incident onto a thin Au foil. (b) A plot of the number of positrons as a function of laser energy for a 100 fsec laser pulse. The number of positrons thought to be generated for shot in 2(a) would be about 10^8.

where η is the coupling efficiency of laser energy into hot electrons. An actual experimental electron energy spectrum from the JanUSP laser at 6 Joules best focus is shown in Figure 2 using the electron spectrometer. If we use the conservative estimate that the pair production will happen only when the laser pulse is on, then we can use the laser pulse length, τ_{pulse}, for the time in Eq. (4). Thus, the number of pairs is given by

$$N_{e+} = \frac{N_{\text{hots}}\,\Gamma\tau_{\text{pulse}}}{2} \tag{7}$$

For example, we can now estimate the number of pairs for various laser systems. Take a 100 fsec, 10 J laser system (the JanUSP laser at LLNL.) In this case, a plot of the number of pairs as a function of laser intensity can be calculated using the results above. A plot of this is shown in Figure 2a.

It is also instructive to plot the number of positrons generated for this laser system, as shown in Figure 2b. It is interesting to note that for fixed laser pulse duration, the pair rate eventually saturates. Here, we have assumed 30% conversion of laser light into hot electrons, and a cut-off of $3T_{\text{hot}}$. For comparison, we plot the same quantities for both gold and aluminum, just for comparison, and to note that it is clearly beneficial to shoot as high a Z as possible, for a given laser intensity. In addition, by comparing experimental results from the two materials, it will be an easy test to determine whether the measured signal is actually positrons, or low energy protons that make it through the thin Al filter on the front of the spectrometer.

In the next few years, several lasers will be running at the 100–200 J level, at around 1 pSec. The number of pairs that might be generated with proper target design can also be found from the equations above. The results, for both 1 psec and 1/2 psec laser pulses, is shown in Figure 3. This time, we take a realistic cut-off of about $6kT_{\text{hot}}$. It is obvious that the number of positrons generated can be quite

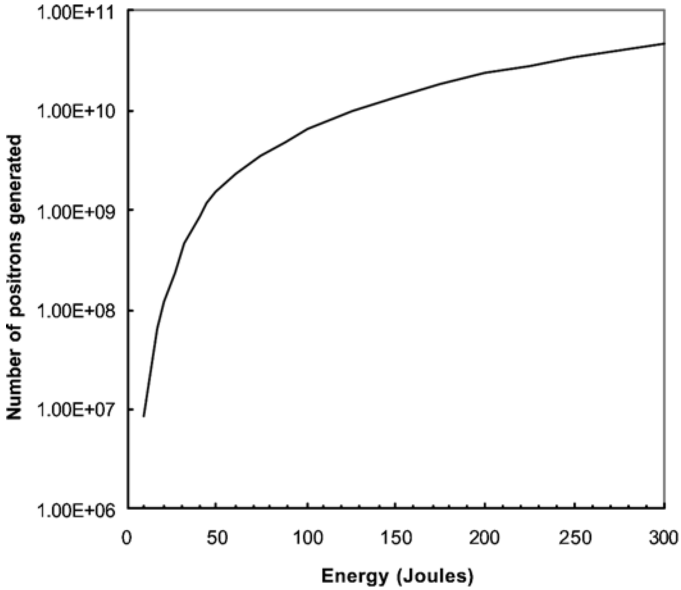

Figure 3. Number of positrons generated as a function of laser energy for a 1 psec laser pulse incident on a thin gold foil.

large, and during the peak pair production stage, near the peak of the laser pulse. Even a relativistic positron can only move 120 microns in 400 femtoseconds, so that one can easily imagine positron densities approaching $10^{15}\,\mathrm{cm}^{-3}$ in the gold slab just around the laser spot. In fact, Nakashima and Takabe (2002) have shown that for thicker targets, one can even include the contribution of the bremsstrahlung to creating pairs (it is non-negligible in this target limit) and hence even more pairs (of order a factor of 2 more) could potentially be generated.

Although somewhat interesting from a theoretical standpoint, it is a completely different question to ask whether enough positrons are created to make for an interesting experiment. To begin with, one must be able to measure positrons, if one is to consider positrons from this source as being useful in a laboratory experiment, one must estimate the number of electrons that would be observed using an actual spectrometer. Our spectrometer has been described elsewhere, but it is instructive to go through the calculation as to how many CCD counts will be generated given a particular set of laser parameters.

Up to this point, we have mainly been concerned with calculating the number of positrons. Suffice it to say; although the precise number of positrons is dependent on a number of assumptions, there will be some large number present. We will now consider that they are in fact present, and we will attempt to gain some insight into their motion and interaction with the slab during and after the laser pulse interaction. To do this, we resort to PIC simulations. Figure 4 shows the geometry of the PIC simulation that we will use. The box is 20 microns by 20 microns, and the incident

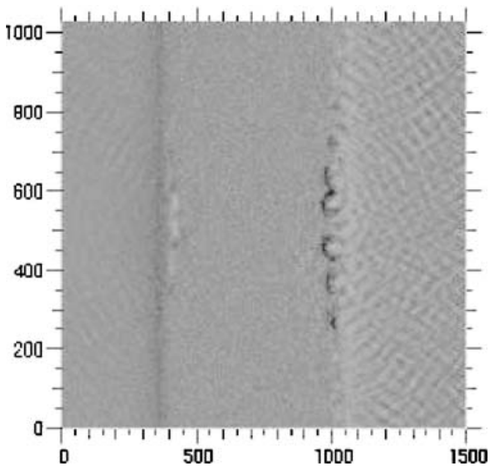

Figure 4. Basic simulation set up for a 2-D positron run.

laser is 4 micron radius, and 100 fsec long. A small density ($n_{e+} \sim 10^{15}\,\mathrm{cm}^{-3}$) is present in the simulation at $t = 0$, spread evenly throughout the box. Although the actual dynamics will most likely be different than what we present, to zeroth order, the results should be qualitatively correct.

As the simulation is run, one thing is clear. The positrons leave from the back of the target. There are very few positrons leaving from the front of the target. It is quite interesting to consider the effect of the accelerating sheath to the target normal at the rear surface. This can easily be done in 1-D, and the phase space of the positrons is shown in Figure 5.

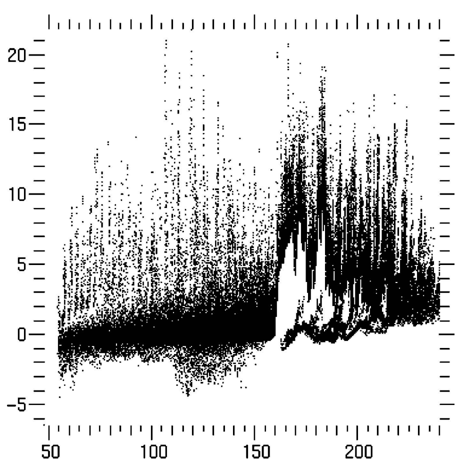

Figure 5. Positrons leaving the thin slab (here ending at $x = 160\ \mathrm{c}/\omega_0$) completely out the rear of the target.

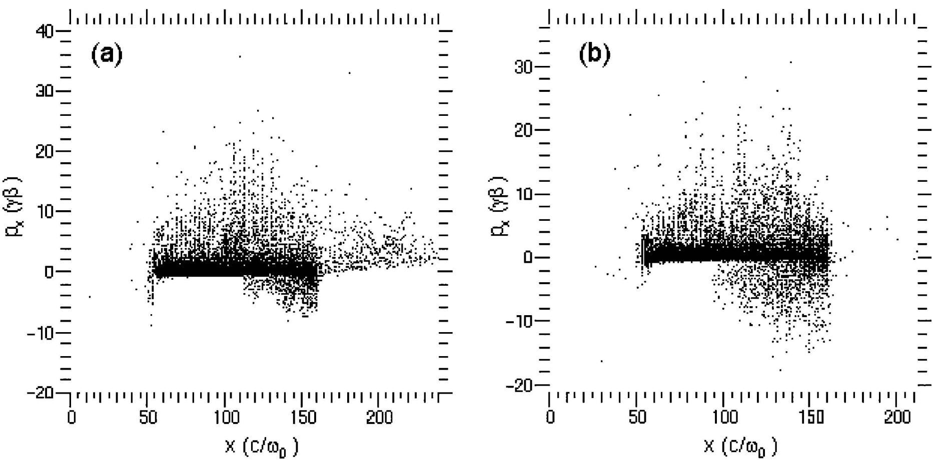

Figure 6. Electron phase space (a) with and (b) without positrons present in the simulation. In (a), the electrons from 150 to 240 c/ω_0 are associated with a relativistic ($\gamma \sim 2$–10) electron positron jet ejected from the back of the target.

A natural next question to ask is this: how does the presence of positrons influence the electron dynamics of the laser-solid interaction? In light of Figure 5, consider the dynamics of the rear surface of the target. As discussed earlier, the electrons typically only get so far from the back of the target, and then are forced by space charge to return. However, if relativistic positrons are present as well (as in the simulations discussed here) some fraction of electrons are free to stream out, as long as they are shielded by the positrons. This behavior is shown in Figure 6, where the electron phase space is shown and it is clear that the some fraction of electrons are streaming out the rear of the target (a), just as the positrons do, but they do not if there are no positrons present Figure 6b. Depending on 2 and 3-D effects, this could result in an extremely dense jet of electron-positron plasma exiting the rear of the target surface. The more massive ions will lag behind, thus allowing the energetic jet to approximate a pure pair plasma moving at relativistic speeds.

Depending on the intensity, this could maximize pair production in several ways. The first is that the ion density will increase, due to the opposing "snowplow" shocks that form on each side of the foil. In addition, it stalls the ion expansion of the solid. Finally, it allows for a thicker foil to be heated to the T_{hot} given in Eq. (1). All these factors will result in a larger number of pairs. To show how the energy maximizes at the peak, we have done a number of 1-D simulations of double-sided illumination. It is clear from the plots that even as the laser energy is increased by lengthening the pulse, the electron energy does not get any hotter. In this case (using PIC codes) the energy simply gets reflected back out of the plasma.

In conclusion, the potential for using ultra-intense lasers as sources of electron positron plasmas of interest for laboratory astrophysics is sufficiently interesting that more work towards understanding this rare and exciting new form of matter.

Although in its infancy, this could very easily become a fundamental proving ground for such diverse astrophysical speculations as electron positron outflow from black holes to possible gamma ray burst engines.

References

Chen, H., Patel, P.K., Price, D.F., Young, B.K., Springer, P.T., Berry, R., Booth, R., Bruns, C. and Nelson, D.: 2003, *Rev. Sci. Instrum.* **74**, 1551.

Cowan, T.E., Roth, M., Allen, M.M., Johnson, J., Hatchett, S.P., LeSage, G.P. and Wilks, S.C.: 2000, Lawrence Livermore National Lab. Reprint, UCRL-JC-138049: Cowan, T., Hunt, A.W., Johnson, J., Perry, M.D., Fountain, W., Hatchett, S., Key, M.H., Kuehl, T., Parnelli, T., Pennington, D.M., Phillips, T.W., Roth, M., Takahashi, Y. and Wilks, S.C. in *High Field Science*, Tajima, T., Mima, K. and Baldis, H. (eds.), Kluwer (Academic/Plenum), New York, 2000 pp. 145–156.

Evans, R.B.: 1955, *The Atomic Nucleus,* McGraw-Hill, New York pp. 695–710.

Gahn, C., Tsakiris, G.D., Pretzler, G., Witte, K.J., Delfin, C., Wahlström, C.-G. and Habs, D.: 2000, *Appl. Phys. Lett.* **77**, 2622.

Greaves, R.G. and Surko, C.M.: 2000, *Phys. Rev. Lett.* **85**, 1883.

Helander, P. and Ward, D.J.: 2003, *Phys. Rev. Lett.* **90**, 135004.

Liang, E., Wilks, S.C. and Tabak, M.: 1998, *Phys. Rev. Lett.* **81**, 4887.

Mackinnon, A., Sentoku, Y., Patel, P.K., Price, D.W., Hatchett, S., Key, M., Anderson, C., Snavely, R. and Freeman, R.R.: 2002, *Phys. Rev. Lett.*, **88**, 215006.

Nakashima, K. and Takabe, H.: 2002, *Phys. Plasmas* **9**, 1505.

Norreys, P.: 2003, *RAL Annual Report.*

Wharton, K.B., Hatchett, S.P., Wilks, S.C., Key, M.H., Moody, J.D., Yanovsky, V., Offenberger, A.A., Hammel, B.A., Perry, M.D. and Joshi, C.: 1998, *Phys. Rev. Lett*. **81**, 822.

Wilks, S.C. and Chen, H.: 2005, accepted Laser and Particle Beams.

Wilks, S.C. and Kruer, W.L.: 1997, *IEEE J. Quantum Electronics* **33**, 1954.

Wilks, S.C., Kruer, W.L., Tabak, M. and Langdon, A.B.: 1992, *Phys. Rev. Lett.* **69**, 1383.

NUMERICAL TREATMENT OF RADIATIVE TRANSFER

MATTHIAS GONZÁLEZ and EDOUARD AUDIT
CEA-Saclay, DSM/DAPNIA/Service d'Astrophysique, F91191 Gif-sur-Yvette Cedex, France;
E-mails: mgonzale@cea.fr, edouard.audit@cea.fr

(Received 4 May 2004; accepted 24 June 2004)

Abstract. We present a numerical treatment of radiative transfer in three dimensions. The radiation is modeled by the grey moment M_1 system. The introduced scheme is able to compute accurate numerical solutions over a broad class of regimes from the transport to the diffusive limit. We discuss numerical issues concerning the resolution and the parallelization of this scheme for multi-dimensional simulations. Several numerical results are then presented, which show that this approach is robust and have the correct behavior in both the diffusive and free-streaming limits. We also present a comparison in two dimensions of our code with a Monte-Carlo transfer code.

Keywords: radiative transfer, diffusion limit, transport, hyperbolic system, Godunov-type methods

1. Introduction

Radiation hydrodynamics play an important role in topics as different as astrophysics, laser fusion and plasma physics. Much efforts are therefore underway to have a proper description both theoretical and numerical of this phenomenon.

Different physical approximations have been developed to model radiative transfer in particular cases. For large values of material opacities, the equation leads to parabolic systems referred to as the diffusion limit (Mihalas and Mihalas, 1984; Dai and Woodward, 1998; Stone et al., 1992). On the other hand, for small values of the opacity, the transport limit is reached. Particular methods have been implemented to describe this regime (Hayes and Norman, 2003; Dai and Woodward, 2000).

However, in many problems of physical interest, regions of large opacities run along transparent regions, and coupling different models on various zones introduces large drawbacks due to the domain partition and some loss of accuracy in the transition zone. Moreover, semi-transparent regions would not be well described by any of these two models. Monte-Carlo codes which solve directly the transfer equation (Mihalas and Mihalas, 1984) can describe both regimes, however they are difficult to couple to hydrodynamical codes and are very costly especially in the diffusion regime.

Astrophysics and Space Science **298:** 357–362, 2005.

We present in this paper a method to tackle radiation hydrodynamics problems in multi-dimensions whatever the opacity. This method will be used to describe situations where radiation plays an important dynamical role, such as laser experiments or the interstellar medium.

2. Model

For most problems and for the foreseeable future, solving the full transfer equation is too much costly both in time and memory. This problem is even greater if one wants to couple the radiative transfer with hydrodynamics to study multi-dimensional time-dependent problems. For this reason, we have decided to use a moment model which is much less expensive than the full transfer equation and couples naturally to hydrodynamics.

Moment models differ from each other by their closure relation. This relation could be computed by solving locally the transfer equation (Gehmeyr and Mihalas, 1993; Hayes and Norman, 2003) or by an analytical formulation (Levermore, 1994; Dai and Woodward, 2000).

As far as we are concerned, we have chosen a moment model with the analytical M_1 *closure* based on a minimum entropy principle (Dubroca and Feugeas, 1999). The M_1 scheme has above all the great advantage of being valid from the transport to the diffusion limit. Therefore, it is well suited to model situations where regions with different regimes coexist.

Noting down E_r and F_r the frequency integrated radiative energy density and flux, P_r the radiative pressure tensor and κ the mean grey opacity, the equations of the grey M_1 model are:

$$\begin{cases} \partial_t E_\mathrm{r} + \nabla \cdot \mathbf{F}_\mathrm{r} = \kappa\rho c(a_\mathrm{r} T^4 - E_\mathrm{r}) \\ \partial_t \mathbf{F}_\mathrm{r} + c^2 \nabla \cdot \mathbf{P}_\mathrm{r} = -\kappa\rho c \mathbf{F}_\mathrm{r} \end{cases} \quad \text{with} \quad \mathbf{P}_\mathrm{r} = \mathbf{D} E_\mathrm{r} \tag{1}$$

where the Eddington tensor $\mathbf{D}$ is defined by

$$\mathbf{D} = \frac{1-\chi}{2}\mathbf{I} + \frac{3\chi - 1}{2}\mathbf{n} \otimes \mathbf{n} \quad \text{and} \quad \chi = \frac{3 + 4\|\mathbf{f}\|^2}{5 + 2\sqrt{4 - 3\|\mathbf{f}\|^2}} \tag{2}$$

$\mathbf{I}$ is the identity matrix, χ the Eddington factor, $\mathbf{f} = \frac{\mathbf{F}_\mathrm{r}}{cE_\mathrm{r}}$ the reduced flux and $\mathbf{n} = \frac{\mathbf{f}}{\|\mathbf{f}\|}$ a unit vector aligned with the radiative flux.

We can notice that this closure well describes the two limits. When $\|f\| = 0$, we recover the proper diffusion limit ($P_\mathrm{r} = E_\mathrm{r}/3$) and when $\|f\| = 1$, we recover the proper transport limit ($P_\mathrm{r} = E_\mathrm{r}$ and correct propagation speed).

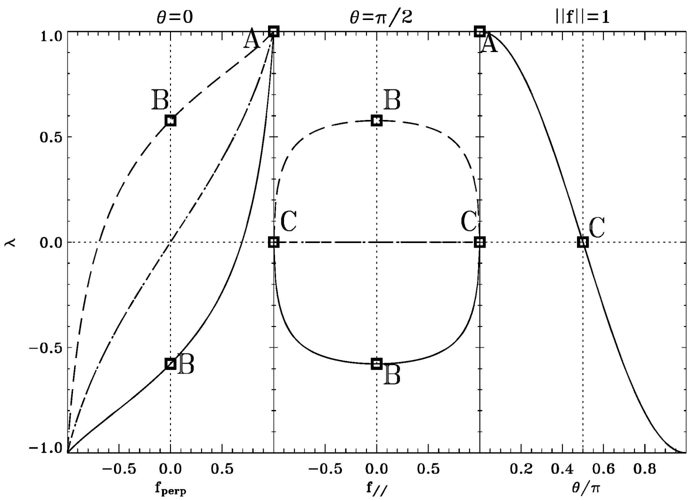

Figure 1. Eigenvalues of the Jacobian matrix normalized by c.

3. Numerical Scheme

To solve numerically the hyperbolic grey model M_1 (Eqs. (1)), we use a second order *Godunov*-type algorithm.We compute the fluxes at each interface of the mesh and then update the variables. The intercell fluxes are computed with a *HLLE (Harten-Lax-van Leer-Einfeldt) scheme* (Einfeldt et al., 1991).

To compute these fluxes, we need to know the eigenvalues of the 4×4 Jacobian matrix of system (1). It is worth noticing that these eigenvalues depend only on the reduced flux f and the angle θ of this flux with the considered interface. Figure 1 illustrates the behavior of the eigenvalues normalized by c for some characteristic values of θ and f.

The left plot corresponds to a flux perpendicular to the interface which is similar to the mono-dimensional problem (cf. Figure 1 of Audit et al. (in press)). In particular, for a unit reduced flux (points A), the four eigenvalues are equal to c so the transport limit is well described. The middle plot represents the case where the flux is parallel to the interface. In that particular case, two eigenvalues are always equal to zero and the two others are equal in norms but of opposite sign. The two null eigenvalues correspond to the transport of the radiative energy and the component of radiative flux perpendicular to the interface. We can also notice that, when the reduced flux is unity (points C), the four eigenvalues are null. This is particularly interesting because it inhibits numerical diffusion (cf. shadow test below). In all cases, we find that for $\|f\| = 0$ (points B), the eigenvalues are $\{-c/\sqrt{3}, 0, 0, c/\sqrt{3}\}$ which are the proper propagation speeds in the diffusion limit. We see that the M_1 model well describes both the diffusion and the transport limit.

The computation of these eigenvalues is rather time consuming however, since they depend only on two parameters (i.e., f and θ) they can easily be tabulated. We have therefore decided to compute them once for a set of θ and f and to interpolate the value needed. This method performs well because the eigenvalues have a smooth behavior. The maximum difference obtained between the exact eigenvalues and the interpolated ones never exceeds 1% using a 100×100 interpolation grid.

4. Implementation

Because the explicit time step limitation by CFL number is very restrictive for radiation, one must use an implicit scheme. The non-linear M_1 equations are solved using an iterative solver which is used as a preconditioner for a GMRES algorithm. Moreover, in order to minimize the computational time, the code has been parallelized with the MPI library and runs on the CEA supercomputer.

5. Tests

5.1. Shadow test

We have performed a 2D test using the shadow test (Hayes and Norman, 2003). This test consists in lighting an oblate spheroid clump. Initially, the medium is at equilibrium $T = T_r = 290$ K, with homogeneous density except for an oblate spheroid region with density one thousand times greater located at the center of the box width. At time $t = 0$, a uniform source is lighted on at the left boundary with $T_r = 1740$ K. The mean free path of the photon being much smaller in the clump (by a factor thousand), a shadow develops behind it. Until the light has crossed the clump, the shadow should remain stable.

Figure 2 shows the radiative temperature for two runs performed on a 280×80 grid. These two runs differ only by the method of computing the eigenvalues of M_1 model. In the first case (upper figure), we chose not to compute these eigenvalues and to set them arbitrarily equal to $\pm c$ whereas in the second run (lower figure), the eigenvalues were interpolated.

The two figures agree each other in way of time propagation. But, as could be expected, the first method is much more diffusive than the second one. It is worth noticing that the classical diffusion approximation is even more diffusive than this first scheme. Using the diffusion approximation, the shadow would disappear in a few light crossing time. The improvement obtained with the second method is easy to understand when looking at the real eigenvalues (cf. Section 3). The proper treatment of the propagation speed in the HLLE scheme is enough to inhibit large numerical diffusion between the shadowed and enlightened regions.

Figure 2. Radiative temperature in the shadow test with fixed eigenvalues (upper panel) or calculated ones (lower).

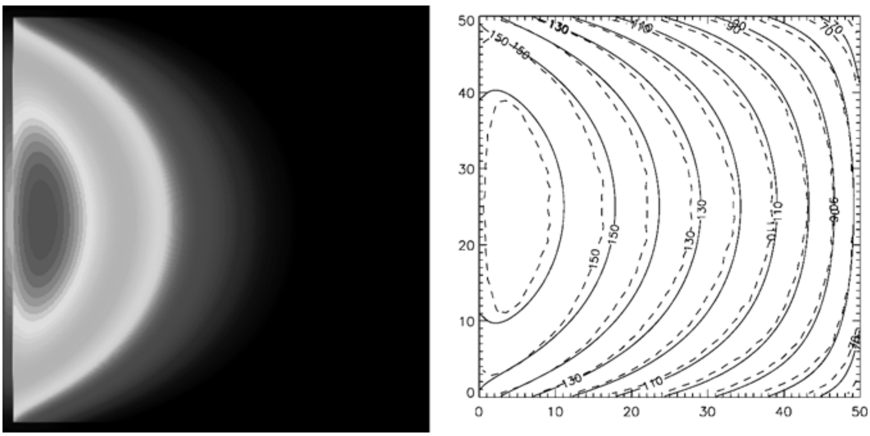

Figure 3. Temperature for our code (solid lines) and a Monte-Carlo one (dashed lines).

5.2. Comparison with a Monte-Carlo code

We have compared our code with a Monte-Carlo one. To do so, we chose a test where the simulation box is at equilibrium and at $t = 0$ an incoming horizontal radiative flux is set. Outside the box, there is vacuum and transparent medium. Figure 3 shows the isotherms obtained at equilibrium by the two methods. The width of the box corresponds to seven mean free paths and is sampled over 50 cells. This box is therefore a semi-transparent region.

The two results agree with a good precision. The differences could be due to the M_1 model itself or to the slightly different treatment of the boundary conditions. It is important to note that the Monte-Carlo code solves exactly the transfer equation and therefore, the agreement between these two approaches is a very good test to validate our model.

6. Conclusion

We have developed a 3D radiative scheme based upon the grey M_1 model equations which are valid in both the diffusive and free-streaming limits. This scheme solves these equations using a second order Godunov-type method and a HLLE scheme to compute the flux at each interface of the mesh. This method implies to know the system's eigenvalues. The proper treatment of the propagation speed allows to keep numerical diffusion under control at a reasonable cost. Moreover, comparisons have been carried between our code and a Monte-Carlo one which show a good agreement. Coupling this numerical scheme with an hydrodynamics solver is in progress and show good performances. Therefore, this tool will be used to model laser experiments involving radiative shocks, accretion flows in star formation, interstellar medium fragmentation or interaction between supernovæ remnants and the ambient medium.

References

Audit, E., Charrier, P., Chièze, J.P. and Dubroca, B.: in press, *AA*.

Dai, W. and Woodward, P.: 1998, *JCP* **142**, 182.

Dai, W. and Woodward, P.: 2000, *JCP* **157**, 199.

Dubroca, B. and Feugeas, J.L.: 1999, *CRAS* **329**, 915.

Einfeldt, B., Munz, C.D., Roe, P.L. and Sjgreen, B.: 1991, *JCP* **92**, 273.

Gehmeyr, M. and Mihalas, D.: 1993, *AAS* **25**, 1366.

Hayes, J.C. and Norman, M.L.: 2003, *ApJS* **147**, 197.

Levermore, C.D.: 1984, *JQSRT* **31**, 149.

Mihalas, D. and Weibel-Mihalas, B.: 1984, *Foundation of Radiation Hydrodynamics*, Oxford University Press, Oxford.

Stone, J.M., Mihalas, D. and Norman, M.L.: 1992, *ApJS* **80**, 819.

3D SIMULATIONS OF RAYLEIGH–TAYLOR INSTABILITY USING "VULCAN/3D"

SHIMON M. ASIDA, ELI LIVNE, JOSEF STEIN and LIOR METZKER
Racah Ins. of Physics, Hebrew University, Jerusalem, Israel; E-mail: sasida@phys.huji.ac.il

(Received 29 April 2004; accepted 17 May 2004)

Abstract. The growth rate of the turbulent mixing zone, which develops from random perturbations under Rayleigh–Taylor instability, has been studied using the 3D version of the hydrodynamical code VULCAN. Previous studies show large differences between the α parameter of different codes. In its Eulerian mode VULCAN/3D employs Van–Leer scheme for the advection of all variables, and can also use interface tracking for multi-phase flows. Simulations using parallel version of VULCAN/3D give α of about 0.06, a value which agrees very well with experiments and some other simulations.

Keywords: hydrodynamics, simulation, instability

1. Problem

Simulations of hydrodynamical instabilities present a difficult challenge for numerical codes. In particular, estimating the growth rate of a turbulent mixing zone which develops from random multi-mode perturbations under Rayleigh–Taylor instability – known as the α parameter – has been proven to be problematic. For that reason it is a good test for code validation (Calder et al., 2002). We used this test with a three-dimansional (3D) version of the hydro-code VULCAN.

2. Code

VULCAN uses the Arbitrary Lagrangian Eulerian (ALE) scheme (Kurzweil et al., 2003). It has a two-dimensional (2D) version, which was used for a variety of astrophysical and hydrodynamical problems (Livne, 1993; Asida, 2000). In its Eulerian mode, VULCAN/3D employs Van–Leer scheme for the advection of all variables, and also uses interface tracking (IT) for multi-phase flows. It was parallelized using domain decomposition and message passing, and may be used on a small cluster of Linux servers.

3. Simulations

The computational box is 1cm $\times$ 1 cm $\times$ 2 cm (cm^3) with $128 \times 128 \times 256$ cells. We use ideal gas with $\gamma = 1.4$, the densities are 3 and 1 (g/cm^3) i.e. Atwood no. (A) of

0.5, the gravity is $f_z = -0.2$ (cm/s^2). The initial state is perturbed by a divergence free velocity field that correspond to k-modes 15–30 with random amplitudes. The compressibility value M^2 is $\sim$0.01. The simulations end at time $t = 10$ s. Boundary conditions are reflective.

4. Results

As the simulation evolves, bubbles and spikes develop and then bubbles are merged (Figures 1 and 3). As a result, the Mixing Zone (MZ) gets wider (Figures 2 and 4). The scaling law of the MZ boundaries evolution should be $\alpha \times g \times A \times t^2$, as indeed can be seen in (Figures 4 and 5). A fit of a straight line yields $\alpha = 0.058$ (where bubbles' boundary is defined by a volume fraction of 0.95).

5. Numerical Sensitivity

Several simulations were performed to test some numerical aspects. It was claimed that IT is essential to get the experimental value of α. As a test we see that a simulation without IT gives $\alpha = 0.048$ (Figure 5). Several simulations have a lower resolution of $64 \times 64 \times 128$ cells. In these simulations we check the importance of the initial perturbation. In the standard simulation the amplitude of each 2D mode

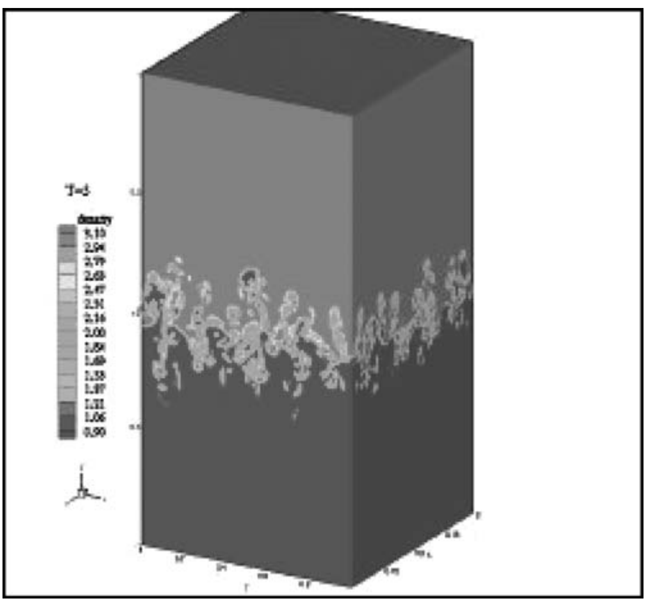

Figure 1. Density colormap at $T = 5$ s.

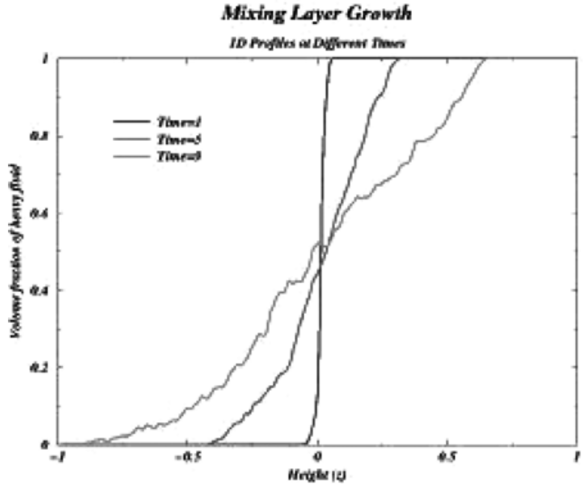

Figure 2. 1D Volume fraction of heavy fluid.

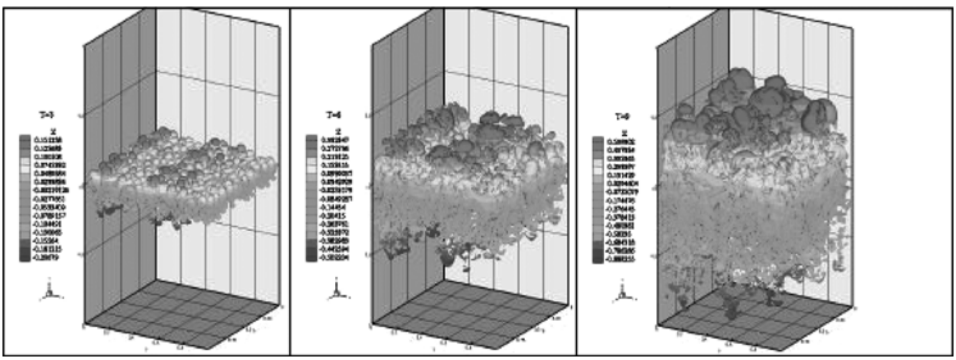

Figure 3. Interface at time 3, 6 and 9 s. colors represent height (z).

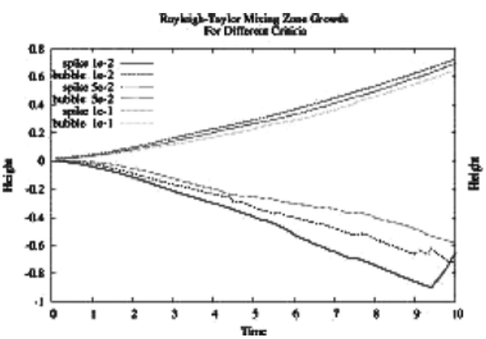

Figure 4. Evolution of mixing zone boundaries for different boundary definition.

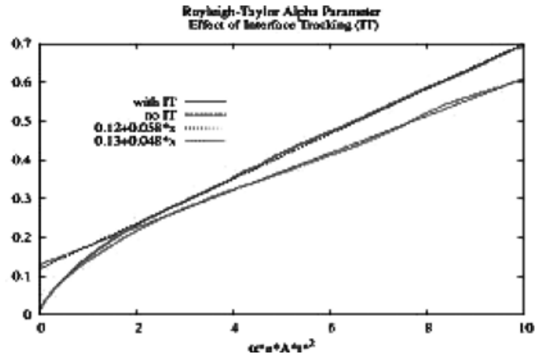

Figure 5. Bubbles' boundary evolution Red – simulation with Interface Tracking, Green – simulation without Interface Tracking.

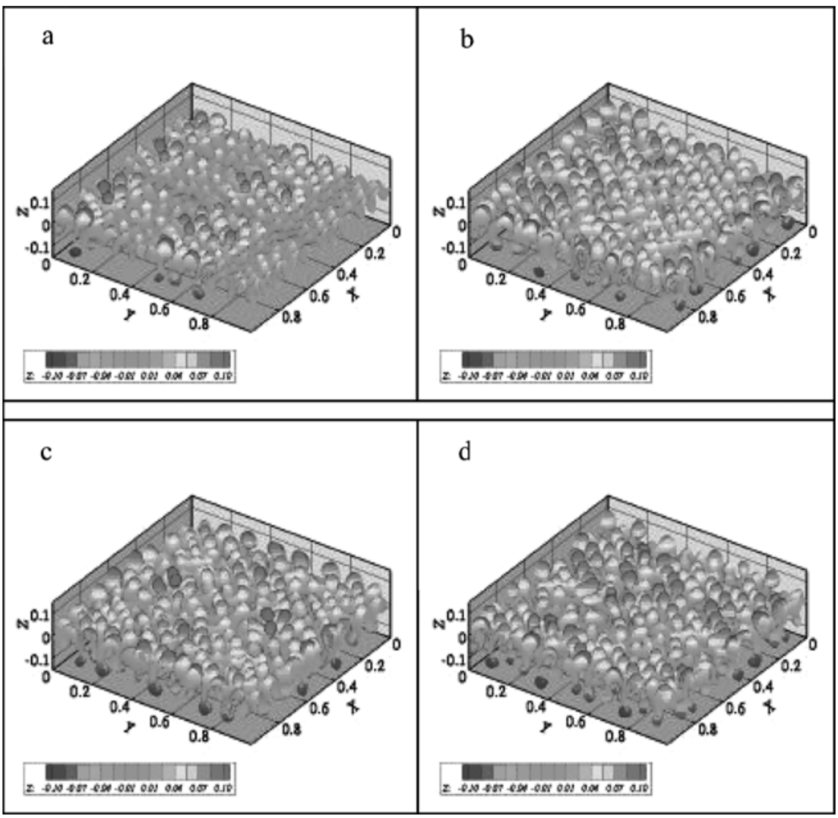

Figure 6. Interface at time 3 s for four low-resolution simulations with diferent initial perturbations (see text): (a) 1D-1, (b) 2D-1, (c) 2D-2, (d) 2D-3. Colors represent height (z).

is the product of a random amplitude in the x direction and a random amplitude in the y direction, and all modes in the range 15–30 are present (we will name this option as "1D-1"). As a result, the initial perturbations are ordered and might have a long wavelength features (Figure 3). In several simulations the amplitude of each 2D mode is random, and only each second (or third) mode in the range are present (2D-2 or 2D-3). As can be seen (Figuer 6), we present four such simulations: (a) 1D-1 perturbation (checking the effect of resolution), (b) 2D-1, (c) 2D-2, (d) 2D-3. In all of these simulations, as in another simulation with a different range of modes (10–20), $\alpha = 0.058 \pm 0.004$.

6. Summary

Simulations with VULCAN/3D are consistent with a value of 0.058 for the growth rate α.This result seems not to be significantly dependent on initial perturbation or resolution. Indeed, a simulation without interface tracing gives a lower value, though the difference is not large. This value agrees well with experiments (Dimonte and Schneider, 2000) theoretical models (Kartoon et al., 2003) and some other simulations (Kartoon et al., 2003).

References

Asida, S.M.: 2000, *ApJ* **528**, 896.
Calder, A., et al.: 2002, *ApJS* **143**, 201.
Dimonte, G. and Schneider, M.: 2000, *Phys. Fluid* **V12**(2), 304.
Kartoon, D., Oron, D., Arazi, L. and Shvarts, D.: 2003, *Laser Particle Beans* **21**, 327.
Kurzweil, Y., Livne, E. and Meerson, B.: 2003, *Phys. Fluid* **V15**(3), 752.
Livne, E.: 1993, *ApJ* **412**, 634.

HYBRID SIMULATION OF COLLISIONLESS SHOCK FORMATION IN SUPPORT OF LABORATORY EXPERIMENTS AT UNR

V.I. SOTNIKOV[1], H. RUHL[1], R. PRESURA[1], T. COWAN[1], J.N. LEBOEUF[2], P. HELLINGER[3] and P. TRAVNICEK[3]

[1] *UNR, Department of Physics, Reno, NV*
[2] *UCLA, Department of Physics, Los Angeles, CA*
[3] *IAP, Prague 4, Czech Republic*

(Received April 2004; accepted June 2004)

Abstract. The problem of producing collisionless shocks in the laboratory is of great interest for space and astrophysical plasmas. One approach is based on the idea of combining strong magnetic field (up to 100 Tesla) created during a Z-pinch discharge with a plasma flow produced in the process of the interaction of a laser pulse with a solid target. In support of laboratory experiments we present hybrid simulations of the interaction of the plasma flow with frozen in it magnetic field, with the spherical obstacle. Parameters of the flow correspond to a laser plasma ablation produced in the laboratory during irradiation of the target by a 3 J laser. Magnetic fields in the plasma flow and around the obstacle are created by the currents produced by the pulse power ZEBRA voltage generator. With the appropriate set of initial conditions imposed on the flow collisionless shocks can be created in such a system. Using independent generators for plasma flow and magnetic field allows for the exploration of a wide range of shock parameters. We present simulations of the formation of supercritical collisionless shock relevant to the experiment, performed with the 2D version of the hybrid code based on the CAM-CL algorithm [Planet. Space Sci. 51, 649, 2003].

Keywords: collisionless shock, laser plasma ablation, hybrid code

1. Introduction

To investigate the possibility of forming a bow shock during the interaction of a laser ablation plasma flow, having an embedded magnetic field, with a conducting target we carried out 2D hybrid simulations with the plasma flow and magnetic field parameters produced in the NTF (Nevada Terawatt Facility) laboratory. Laser ablation of a solid target will be used to create the plasma flow. The "Tomcat" laser, currently emitting 5 J in a 6 ns pulse at 1 μm wavelength and irradiance above $10^{13}\,\mathrm{W\,cm^{-2}}$ will be used for this purpose. For example, 30 ns into the expansion of the plasma plume, the simulations predict a plasma density about $1.25 \times 10^{16}\,\mathrm{cm^{-3}}$, temperature 100 eV, and expansion velocity $6.6 \times 10^{7}\,\mathrm{cm\,s^{-1}}$. With these parameters, the skin depth results in 0.2 cm, and the mean free path for electron-ion collisions is 3.5 cm. For a magnetic field 10^4 G, the ion gyrofrequency is about $10^8\,\mathrm{rad\,s^{-1}}$, the Mach number is 3 and β is 0.5. To embed this magnetic

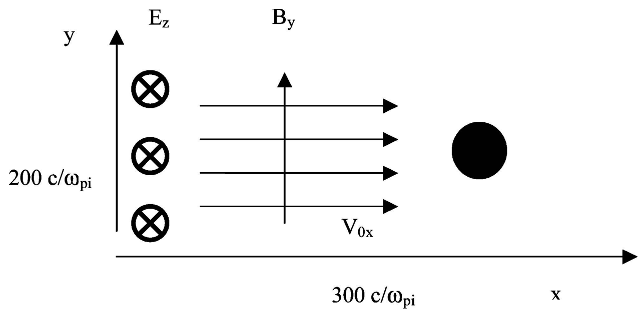

Figure 1. Plasma flow created by the laser ablation is coming from the left boundary. Electric field E_z is perpendicular to the simulation plan. Magnetic field B_y is frozen into the plasma flow. V_{0x} is the speed of the plasma flow.

field into the plasma flow, an electric field 6.3×10^3 V cm^{-1} is necessary in the flow injection region (Figure 1). Such field can be generated with the Zebra pulsed-power generator.

2D hybrid simulations show that the plasma density and the magnetic field have characteristic space distributions in the region of the bow shock, showing abrupt jumps and fine structure with space scale of the order of the ion skin depth. The diagnostics will focus on detecting these features.

2. Hybrid Model and Numerics

We use the 2D version of the hybrid simulation model based on the CAM-CL algorithm (Matthews, 1994). In this model, the plasma is described by a combination of kinetic ions and fluid electrons. This set of equations is sufficient to investigate ion kinetic effects. In the hybrid simulations, the magnetic field is scaled to B_0 and the density to n_0. The units of space, time, and velocity are collisionless skin depth c/ω_{pi}, inverse of the ion cyclotron frequency $1/\Omega_{\mathrm{i}}$, and Alfven speed v_{A} respectively. These quantities are also defined through B_0 and n_0. The fields and particle moments are determined on a 2D grid with $(N_x = L_x/\Delta x = 300) \times (N_y = L_y/\Delta y = 200)$ points or cells. There is a maximum of 128 particles per cell for a scaled peak density of $n_0 = 1$ and the total number of particles is 1 920 000 for the simulation box size used.

In the hybrid model electrons act as a massless, charge-neutralizing fluid ($m_{\mathrm{e}} = 0$) and the electric field can then be written as

$$\vec{E} = -\frac{\vec{J}_i \times \vec{B}}{\rho_{\mathrm{e}}} + \frac{(\vec{\nabla} \times \vec{B}) \times \vec{B}}{\mu_0 \rho_{\mathrm{e}}} - \frac{\vec{\nabla} p_{\mathrm{e}}}{\rho_{\mathrm{e}}}$$

Therefore, the equation for the magnetic field becomes

$$\frac{\partial \vec{B}}{\partial t} = \vec{\nabla} \times \frac{\vec{J}_i \times \vec{B}}{\rho_e} - \vec{\nabla} \times \frac{(\vec{\nabla} \times \vec{B}) \times \vec{B}}{\mu_0 \rho_e} + \eta \Delta \vec{B}$$

where η is plasma resistivity.

Our aim is to demonstrate that with the initial parameters of the plasma flow, which can be produced during the experiment it is possible to form a collisionless shock, when the plasma flow interacts with the nonmagnetized target (cometary type bow shock).

Below are the initial parameters of the flow with embedded in it magnetic field:

$$\begin{array}{llll}
n = 1.25 \times 10^{16}\,\mathrm{cm}^{-3} & V_A = 2.2 \times 10^7\,\mathrm{cm\,s}^{-1} \quad M_\mathrm{A} = 3 \quad B = 10^4\,\mathrm{G} \\
V_0 = 6.6 \times 10^7\,\mathrm{cm\,s}^{-1} & E \sim V_0 \times B/c = 6.6 \times 10^3\,\mathrm{V\,cm}^{-1} \\
T = 100\,\mathrm{eV} & r_\mathrm{Li} = 0.1\,\mathrm{cm} \\
\omega_\mathrm{pi} = 1.63 \times 10^{11}\,\mathrm{s}^{-1} & \omega_\mathrm{ci} = 9.58 \times 10^7\,s^{-1} \quad \mathrm{c}/\omega_\mathrm{pi} \sim 0.2\,\mathrm{cm} \quad L_\mathrm{ei} \sim 3.5\,\mathrm{cm} \\
\sigma \sim 1.3 \times 10^{16}\,\mathrm{s}^{-1} & \eta = c^2/4\pi\sigma \sim 5.5 \times 10^3\,\mathrm{cm}^2\,\mathrm{s}^{-1} \quad \beta_\mathrm{i} = 0.5
\end{array}$$

We also wanted to demonstrate how a magnetic field created on the left boundary of a simulation box propagates with the plasma flow towards the target, because it is frozen into a plasma flow.

In simulations the plasma flow is coming from the left boundary (Figure 1). On the left boundary electric field E_z directed perpendicular to simulation plane, so the plasma flow will contain an induction magnetic field $\mathrm{B}_{y,}$ that satisfies the equation $E_z = -V_{0x} B_y / c$.

At initial moment $t = 0$ the simulation box is filled with plasma with initial velocity V_{0x}, but there is no magnetic field inside. When the plasma flow starts to come from the left boundary it brings into the system magnetic field which is frozen into the flow. The flow with embedded in it magnetic field will interact with the obstacle, placed in the middle of the simulation box.

3. Simulation Results

In this section we present results of 2D hybrid simulation with the setup described in the Section 2. Figure 2a corresponds to the magnetic field along the slice $y = 100$ at the moment $t = 2$. In Figure 2b is shown the distribution of a magnetic field in the simulation plane.

It is clearly seen that magnetic field is moving together with the plasma flow from the left boundary.

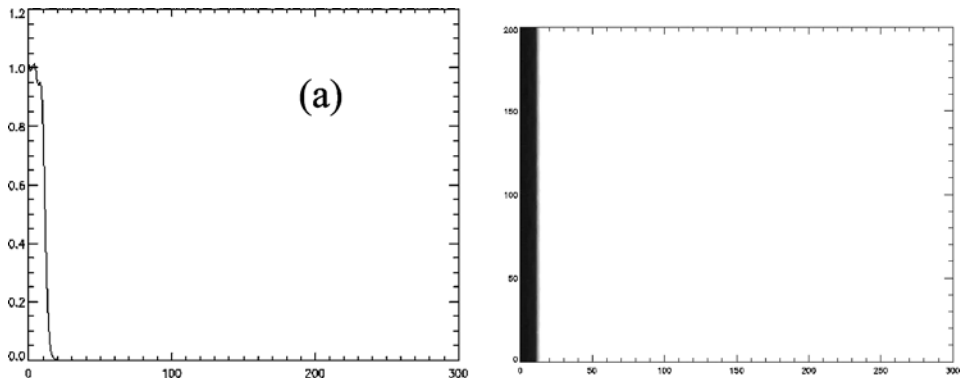

Figure 2. (a) Magnetic field profile along the line $y = 100$. (b) Distribution of magnetic field inside the simulation box.

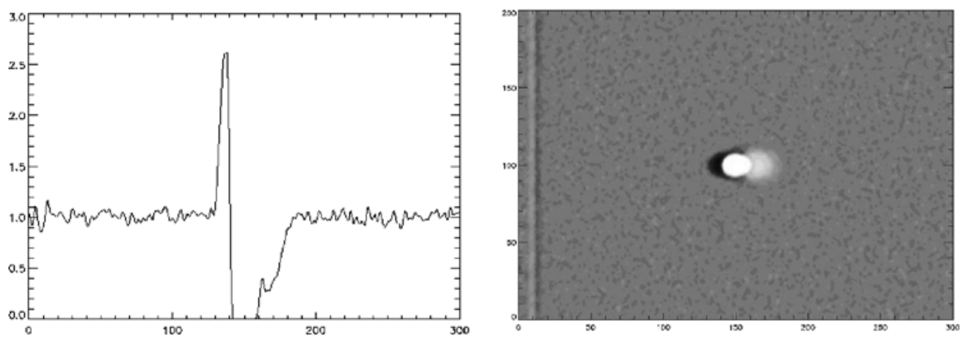

Figure 3. (a) Density profiles along the line $y = 100$. (b) Distribution of plasma density in the simulation plane.

In Figure 3a the plasma density along the slice $y = 100$ at the moment $t = 2$ is presented. Distribution of a plasma density inside the simulation box is presented in Figure 3b.

Although the plasma as a whole is moving with the speed V_{0x} towards the obstacle, without the magnetic field in the plasma flow formation of the collisionless magnetosonic shock wave does not take place.

As the plasma flow with magnetic field starts to approach the obstacle, collisionless magnetosonic type shock structure tends to form. This can be seen in the Figure 4, where the slice of magnetic filed at $y = 100$ and distribution of magnetic field in the simulation plane are presented at tim $t = 30$.

At time $t = 62$ we already have the well formed bow shock. Plots for the magnetic field and density are presented in Figures 5 and 6.

In Figures 5 and 6 it is clearly seen that the supercritical quasi-perpendicular shock (Winske and Quest, 1988; Hellinger, 2003) is formed in the plasma flow in

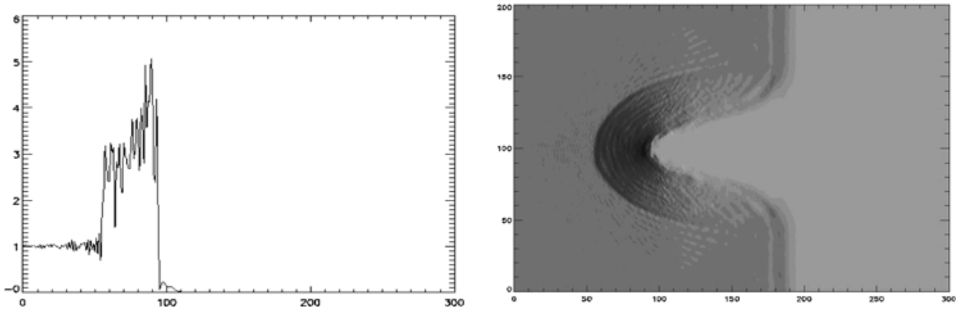

Figure 4. (a) Magnetic field profile along the line $(x,\ y = 100)$. (b) Distribution of magnetic field inside the simulation box.

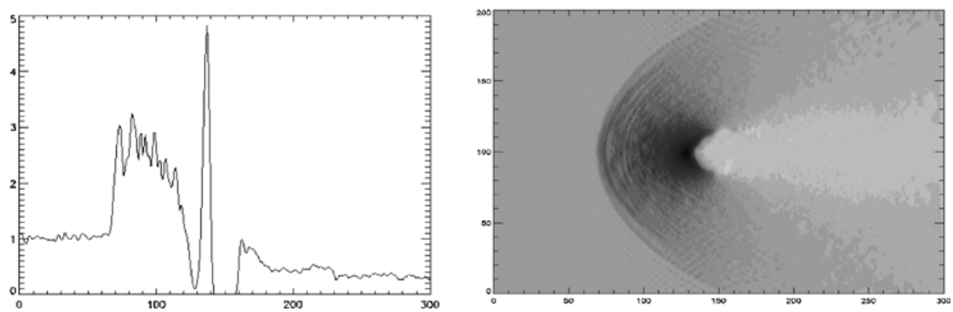

Figure 5. (a) Magnetic field profile along the line $(x,\ y = 100)$. (b) Distribution of magnetic field inside the simulation box.

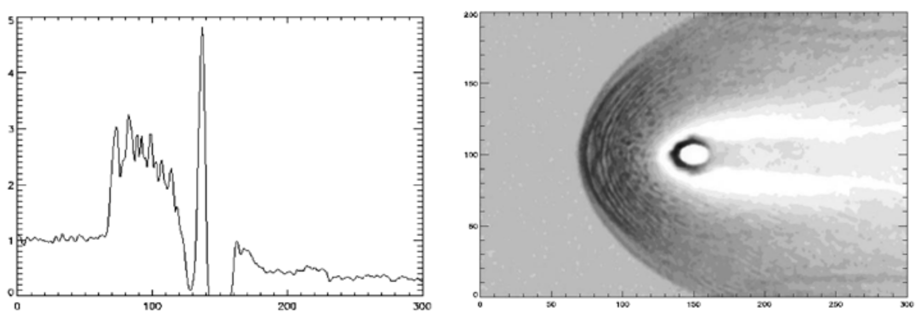

Figure 6. (a) Density profiles along the line $(x,\ y = 100)$. (b) Distribution of plasma density in the simulation plane.

front of the obstacle. Structure of such shock wave is connected with the proton reflection from the shock front. As a result of reflection protons experience strong heating, but electrons mainly stay adiabatic. The shock structure depends on the proton beta, but its dependence on the electron beta is negligible.

4. Conclusion

In support of the planned experiment to produce a collisionless supercritical shock in the NTF laboratory, 2D hybrid simulations with the plasma flow and magnetic field parameters close to that in the experiment were carried out. In the experiment, the plasma flow will be created by laser ablation of a solid target. The "Tomcat" laser projected to emit up to 25 J in 6 ns at 1 μm wavelength and irradiance up to 10^{14} W cm^{-2} and a thin plastic target will be used for this purpose. For example, 30 ns into the expansion of the plasma plume, one-dimensional hydrodynamic simulations predict plasma density about 10^{17} cm^{-3}, temperature 150 eV, and expansion velocity 2.5×10^8 cm s^{-1}. The front of the plasma plume is expected to consist mainly of Hydrogen. The super-alfvenic plasma flow creates conditions for shock formation. To embed a magnetic field into a plasma flow, an electric field 6.6×10^3 V cm s^{-1} is necessary in the flow injection region (Figure 1). Such field can be easily generated with the "Zebra" pulsed-power generator. Plasma diagnostics will focus on the interaction region between the plasma flow and a conductive obstacle.

2D hybrid simulation results confirm that supercritical collisionless shock can be formed in a plasma flow with parameters corresponding to the laser ablation experiment.

Acknowledgements

This work was supported by the United States Department of Energy under Grant No. DE-FC08–01NV14050 at the University of Nevada Reno, Grant No. DE-FG03-01ER54617 at the University of California at Los Angeles and Grant B 3042106/01 of the Czech Academy of Science at the Institute of Atmospheric Physics in Prague.

References

Hellinger, P.: 2003, *Planet. Space Sci.* **51**, 649.
Matthews, A.P.: 1994, *Journ. Comp. Physics* **112**, 102.
Winske, D. and Quest, K.B.: 1988, *J. Geophys. Res.* **93**, 9681.

VIRTUAL MHD JETS ON GRIDS

THIBAUT LERY[1], CÉLINE COMBET[1,2], GARETH MURPHY[1] and LUKE O.C. DRURY[1]

[1]*Dublin Institute for Advanced Studies, 5 Merrion Square, Dublin 2, Ireland; E-mail: lery@cp.dias.ie*

[2]*Laboratoire de l'Univers et de ses Théories, Pl. J. Janssen, Meudon, France*

(Received 30 April 2004; accepted 25 May 2004)

Abstract. As network performance has outpaced computational power and storage capacity, a new paradigm has evolved to enable the sharing of geographically distributed resources. This paradigm is known as Grid computing and aims to offer access to distributed resource irrespective of their physical location. Many national, European and international projects have been launched during the last years trying to explore the Grid and to change the way we are doing our everyday work. In Ireland, we have started the CosmoGrid project that is a collaborative project aimed to provide high performance supercomputing environments. This will help to address complex problems such as magnetohydrodynamic outflows and jets in order to model and numerically simulate them. Indeed, the numerical modeling of plasma jets requires massive computations, due to the wide range of spatial-temporal scales involved. We present here the first jet simulations and their corresponding models that could help to understand results from laboratory experiments.

Keywords: Grid technology, jets, outflows

1. Grid Technology and Jet Simulation

Computer speed doubles every 18 months, while network speed doubles every 9 months. This makes a difference of an order of magnitude per 5 years. Indeed from 1986 to 2000, the computers performance has been multiplied by 500 while the network has increased by 340,000. During the present decade up to 2010, this effect should slow down with a factor of 60 for computer performance and 4000 for networks. This shows that networking will not be the biggest obstacle to bring together machines geographically distributed. A new paradigm, also known as Grid computing, aims to offer access to distributed resource irrespective of their physical location. Grid computing enables the clustering of a wide variety of geographically distributed resources, such as supercomputers, storage systems, or data sources, that can then be used as a unified resource. The real and specific problem that underlies the Grid concept is coordinated resource sharing and problem solving in dynamic, multi-institutional virtual organizations. The emerging standardization for sharing resources, along with the availability of higher bandwidth, are driving a possibly equally large evolutionary step in grid computing. Because of their focus

Astrophysics and Space Science **298:** 375–378, 2005.

on dynamic, cross-organizational sharing, Grid technologies complement rather than compete with existing distributed computing technologies.

Many national and international projects have been launched during the last years trying to explore the Grid and to change the way we are doing our everyday work. In Ireland, we have started the CosmoGrid project that is a collaborative project aimed to provide high performance super-computing environments. CosmoGrid is a collaborative project entitled Grid-enabled computational physics of natural phenomena. It is aimed at providing high performance super-computing environments for dealing with sciences more challenging problems, and to act as a technology transfer. Researchers in this Irish project are able to access and use High Performance Computing systems from any location as easily and securely as they use their own workstation. Using the Grid for computational science, however, presents a huge number of challenges that must be solved for this vision to become reality.

This will help to address complex problems such as magnetohydrodynamic outflows and jets in order to model and numerically simulate them. Indeed, the numerical modeling of jets requires massive computations, due to the wide range of spatial-temporal scales involved. The main objective of this ongoing work is to compare jet simulations with laboratory experiments to reproduce, in a scaled manner, key aspects of the dynamics of astrophysical jets, relevant to their formation, collimation and interaction with the interstellar medium. Our main interest is the study of radiative shocks indifferent geometries. Such experiments can be carried out with different large-scale laser systems. The data from these experiments will be used for direct comparison with astronomical observations and for the validation of computer codes. For this purpose the experiments are modeled by the codes developed for both laboratory plasma physics and for astrophysics. Let us now present the first results of jet simulations from forming stars (Figure 1).

2. Models of Jets During Star Formation

We have developed a model to study the first stages of star formation (Fiege and Henriksen, 1996; Lery et al., 2002). The principal characteristics of the model is that it produces a heated pressure-driven outflow with magneto-centrifugal acceleration and collimation. An evacuated region exists near the axis of rotation where the high speed outflow is produced. This outflow decreases in speed and increases in mass systematically with angle from the axis. Near the equatorial plane a thick rotating extended disk forms naturally when sufficient heating is provided to produce a high-speed axial outflow. The most rapidly outflowing gas is always near the symmetry axis because these streamlines pass closest to the star, deeper into the gravitational potential well. Also, the material on these streamlines is heated the most vigorously by the star. As the gas gets closer to the source, it rotates faster. Gas streamlines make a spiraling approach to the axis and then emerge in the form of an helix wrapped about the axis of symmetry. The infalling plasma therefore has a larger

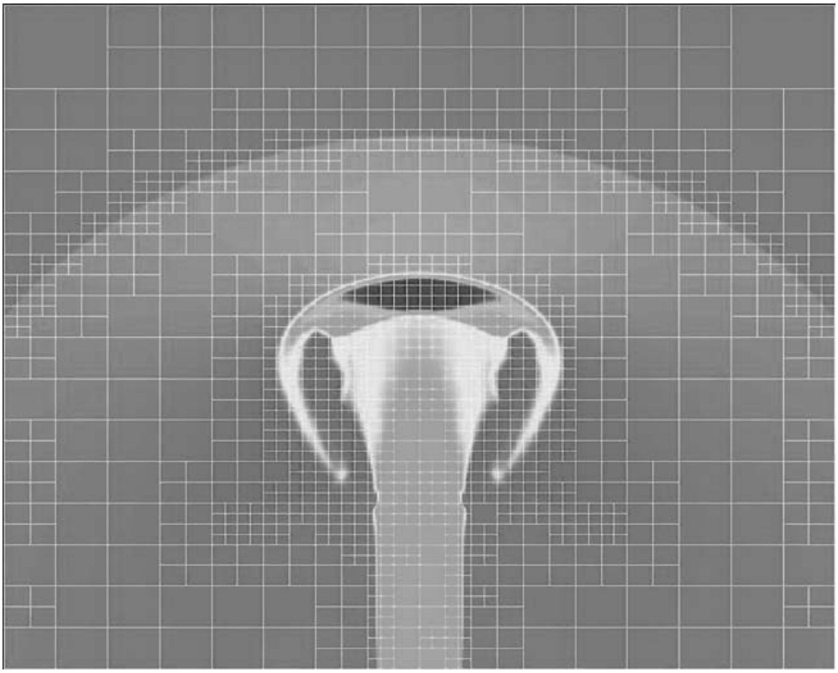

Figure 1. Jet simulation using adaptive mesh refinement.

electric current driven by the rotational motion. This increases the magnetic energy at the expense of gravity and rotation, which is eventually converted into kinetic energy as the gas is redirected outwards (Lery et al., 2002). The magnetic field acts to collimate and accelerate the gas towards the polar regions. There the flow presents a strong poloidal velocity and a low magnetic energy. The Poynting flux included in the model increases both the velocity and collimation of the outflows by helping to transport mass and energy from the equatorial to the axial regions.

The last but central element around protostars is the fast jet. A consensus seems to prevail on the magneto-centrifugal origin of jets, either launched from the accretion disk (*disk wind*) or from the location of the interaction of the protostar's magnetosphere with the disk (*X-wind*). Indeed, accretion disks play a key role in the physics of the fast jets from young stellar objects. Infalling, rotating matter is stored in these disks until dissipation allows material to spiral inward and feed the central, gravitating object. Such disks are believed to support strong, well ordered magnetic fields. The current consensus holds that these fields are the agents for producing jets in a process known as magneto-centrifugal launching. In this mechanism, plasma in the disk is loaded on to corotating field lines. If conditions in the disk are favorable the plasma is centrifugally flung outward along open field lines, which form a certain angle with the disk's surface. The ensuing plasma flow properties must then be determined by solving for the equilibrium of forces parallel and perpendicular to the magnetic surfaces, the former described by using the Bernoulli equation and the latter is solved via the Grad–Shafranov equation.

By using the jet model, it is possible to obtain jet equilibria whose properties directly depend on the source (Lery and Frank, 2000). These equilibria have been used to model numerically the propagation of MHD jets into the interstellar medium. The present work differed from previous studies in that the cross-sectional distributions of state variables are derived from an analytical model for magneto-centrifugal launching from a source rotator. The jets in these simulations are considerably more complex than the usually used 'top-hat' profiles. Many features of the simulation are in good agreement with observations, such as the molecular cavities, the location and shape of the shocks, as well as the variation with distance of the ionization fraction and of the density along the jet. By varying the properties of the source, it is also possible to vary the properties of the jet itself. This introduce non-ad-hoc variations of the jet and gives rise to more complex behaviors of the propagating jet but also of the interaction with the ambient medium. This opens the possibility that the physics of the jet source may be read off the jets themselves. Our results suggest that one might ideally be able to distinguish between different classes of MHD launching models via consideration of the way the jets from these models would appear on the sky.

References

Fiege, J.D. and Henriksen, R.N.: 1996, *MNRAS* **281**, 1038.
Lery, T. and Frank, A.: 2000, *ApJ* **533**, 897.
Lery, T. et al.: 2002, *A&A* **387**, 187.

NON-LINEAR DYNAMICS OF THE RICHTMYER–MESHKOV INSTABILITY IN SUPERNOVAE

SNEZHANA I. ABARZHI and MARCUS HERRMANN

Center for Turbulence Research, Stanford University, USA;
E-mail: snezha@stanford.edu, marcus.herrmann@stanford.edu

(Received 30 April 2004; accepted 2 June 2004)

Abstract. We report analytical and numerical solutions describing the evolution of the coherent structure of bubbles and spikes in the Richtmyer–Meshkov instability in supernovae. It is shown that the dynamics of the flow is essentially non-local, and the nonlinear Richtmyer–Meshkov bubble flattens and decelerates.

Keywords: Richtmyer–Meshkov, supernovae, singularities, non-local

1. Turbulent Mixing in Supernovae

The Richtmyer–Meshkov instability (RMI) develops when a shock wave passes an interface between two fluids with different values of the acoustic impedance (Dimonte et al., 1996; Ye et al., 2003; Meshkov, 1969; Richtmyer, 1960). The instability results in a growth of the interface perturbations and produces with time the turbulent mixing of the fluids (Dimonte, 2000). The RM mixing plays an important role in many astrophysical phenomena (Kull, 1991). In particular, in supernova type II, the observations indicate an extensive mixing of the inner and outer layers of the progenitor star, and suggest RMI followed by the Rayleigh–Taylor instability as a plausible mechanism (Chevalier, 1992). This astrophysical system can be replicated with proper scaling in high energy density laboratory experiments (Robey et al., 2001; Ryutov et al., 2001) and modeled numerically (Calder et al., 2002).

Laboratory observations report the following evolution of the RMI. Initially, the light fluid accelerates the heavy fluid "impulsively" and the acceleration value is determined by the shock–interface interaction. With time a coherent structure of bubbles and spikes appears, the light (heavy) fluid penetrates the heavy (light) fluid in bubbles (spikes), and eventually a mixing zone develops (Dimonte, 2000). The dynamics of RMI is far from being completely understood. Only recently, an adequate description of the linear regime of compressible RMI was found (Holmes et al., 1999; Wouchuk, 2001), while the nonlinear motion yet remains a puzzle (Dimonte, 2000). Singular aspects of the interface evolution (such as secondary instabilities, vorticity generation, direct and inverse cascades of the fluid energy) cause theoretical and numerical difficulties and preclude elementary methods of

Astrophysics and Space Science **298:** 379–383, 2005.

solution (Abarzhi et al., 2003; Abarzhi and Herrmann, 2003). Here, we suggest analytical and numerical solutions describing the nonlinear coherent dynamics of the two-dimensional Richtmyer–Meshkov instability for fluids with a finite density ratio. Our results report new properties of the interface evolution in RMI, explain existing experiments, and identify sensitive diagnostic parameters for observations.

2. Nonlinear Evolution

To describe the RMI dynamics, we consider the compressible two-dimensional Navier–Stokes equations for the heavy (light) fluid with density $\rho_{h(l)}$ and velocity $\boldsymbol{v}_{h(l)}$. The flow has no mass sources. The normal component of velocity and the pressure are continuous at the fluid interface. Initially, the interface is slightly disturbed with a small amplitude co-sinusoidal perturbation. The development of secondary instabilities in the flow and therefore the formations of singularities in the governing equations are controlled by the density ratio, i.e. the Atwood number $A = (\rho_h - \rho_l)/(\rho_h + \rho_l)$.

The shock–interface interactions result in the baroclinic production of vorticity at the fluid interface and in the growth of the perturbation amplitude at a constant rate (Dimonte et al., 1996; Ye et al., 2003; Wouchuk, 2001). The coherent structure appears, and the dynamics of RMI becomes nonlinear. The bubbles and spikes decelerate and the fluid motion is nearly incompressible. To study the effect of the density ratio on the evolution of the coherent structure analytically, we separate scales and divide the fluid interface into active regions (small scales) with intensive vorticity and passive regions (large scales), which are simply advected. The large-scale coherent motion is potential and one can apply group theory and a spectral approach. We expand the velocity potential as the Fourier series, re-expand then the governing equations in a vicinity of a highly symmetric point of the interface (the tip of the bubble or spike), and derive in this way dynamical system of ordinary differential equations in terms of surface variables and correlation functions. Yet, due to singularities the interface dynamics is essentially non-local, and the dynamical system meets with a closure problem. To resolve this issue, we apply symmetry arguments, and find a continuous family of regular asymptotic solutions. The family involves all local solutions allowed by the symmetry of the global flow. We perform the stability analysis and choose the fastest stable solution as the physically significant one.

This analysis suggests the following dynamics of the bubble front in the Richtmyer–Meshkov instability. The shock–interface interaction causes the growth of the small perturbation at the fluid interface (Wouchuk, 2001), and the structure of bubbles and spikes is formed. The bubble velocity v reaches its maximum value and starts to decay afterwards. First, v decreases linearly with time t, while the absolute value of the bubble curvature $|\zeta|$ increases linearly with t. Then, the bubble curvature reaches an extreme value, dependent on the initial conditions and the Atwood number. Asymptotically, the bubble flattens, $\zeta \to 0$, and decelerates, $v \to 0$, with power-law time dependencies. The flattening of the bubble front is a distinct feature of RMI universal for all A. It follows from the fact that RM bubbles decelerate, and indicates a non-local character of the interface dynamics (Abarzhi et al., 2003).

In our numerical simulations, we solve the governing equations using a finite volume hybrid capturing–tracking scheme (Smiljanovski et al., 1997; Schmidt and Klein, 2003). All shocks and expansion fans are captured whereas the contact discontinuity at the interface is tracked by a level set scalar. Within this scheme, the boundary conditions at the interface are used to reconstruct the exact states on each side of the interface, so the interface remains a discontinuity. Details concerning the scheme can be found in (Abarzhi and Herrmann, 2003).

We perform the numerical simulations for a weak shock, Mach number of Ma $=$ 1.2, and two different Atwood and Reynolds numbers. In the first case, the Atwood number is typical for supernova explosions $A = 0.55$ and Re $= 13140$, whereas in the second case $A = 0.9$ and Re $= 6980$. The initial interface with spatial period $\lambda = 0.0375$ m and amplitude $a_0 = 0.0024$ m is located at $z = 0$ m. All simulations are performed in a $[-0.475\text{ m}, 0.05\text{ m}] \times [0.0\text{ m}, 0.01875\text{ m}]$ box resolved by 1792×64 equidistant cartesian grid cells.

Figure 1 depicts the temporal evolution of the interface for $A = 0.55$ and $A = 0.9$. In both cases, a mushroom shaped spike of heavy gas is formed and penetrates into the light gas. Figure 2 presents the dimensionless bubble velocity as a function of the absolute value of the bubble curvature, with v_∞ being the post-shock velocity of a flat interface.

Initially, the bubble exhibits an abrupt acceleration that is due to the interaction with the passing shock, whereas the curvature remains roughly unchanged. This result is consistent with the linear theory (Wouchuk, 2001) and with experiments (Dimonte et al., 1996; Ye et al., 2003). Then, the absolute value of the bubble curvature increases with only gradual changes in the bubble velocity. As the instability evolves, the bubble curvature reaches a local maximum and then starts to decrease. Eventually, the bubble curvature asymptotically approaches zero while the bubble continues to decelerate, as predicted by our non-local theory. A slight flattening of the bubble shape can be discerned in Figure 1, and it is clearly visible in Figure 2. Our simulations are stopped, once the refelected shock wave rehits the interface.

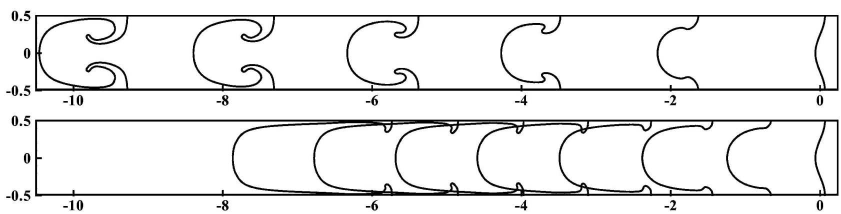

Figure 1. Interface shape for $A = 0.55$ (top) and $A = 0.9$ (bottom) every $\Delta t = 1$ m s.

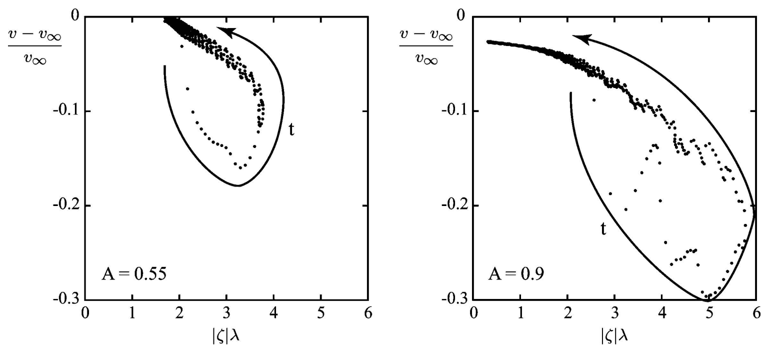

Figure 2. Bubble velocity v as function of absolute bubble curvature $|\zeta|$ for $A = 0.55$ (left) and $A = 0.9$ (right).

3. Discussion and Conclusion

We performed systematic theoretical and numerical studies of the large-scale coherent dynamics in the Richtmyer–Meshkov instability for fluids with finite values of the density ratio. The analysis and simulations validate each other and describe the new properties of the interface evolution in RMI. We found that flattening of the bubble front is a distinct property of nonlinear RMI, universal for all values of the density ratio. The obtained dependencies of the bubble curvature and velocity differ qualitatively and quantitatively from those suggested by the heuristic models of Oron et al. (Oron et al., 2001), which disregarded the conservation of mass in the flow (Abarzhi et al., 2003; Abarzhi and Herrmann, 2003). Yet, our conclusions agree qualitatively with the observations of Jacobs and Glendinning (private communication) and indicate that the interface dynamics in RMI is essentially non-local. Our results may serve as a benchmark for high energy density laboratory experiments (Drake et al., 2002; Robey et al., 2001; Ye et al., 2003) and for modeling supernova explosions.

References

Abarzhi, S.I. and Herrmann, M.: 2003, in: *Annual Research Briefs-2003*, Stanford, CA: Center for Turbulence Research.

Abarzhi, S.I., Nishihara, K. and Glimm, J.: 2003, *Phys. Letters A* **317**, 470.

Calder, A., Fryxell, B. and T.P.: 2002, *Astrophys. J. Suppl. S* **143**(1), 201.

Chevalier, R.A.: 1992, *Nature* **355**(6361), 617.

Dimonte, G., Schneider, M. and Remingon, B.: 1996, *Phys. Plasmas* **3**(2), 614.

Dimonte, G.: 2000, *Phys. Plasmas* **7**, 2255.

Drake, R.P., Robey, H.F. and O.A.H.: 2002, *Astrophys. J.* **564**(2), 896.

Holmes, R.L., Dimonte, G., Fryxell, B., Gittings, M.L., Grove, J.W., Schneider, M., Sharp, D.H., Velkovitch, A.L., Weaver, R.P. and Zhang, Q.: 1999, *J. Fluid Mech.* **389**, 55.

Jacobs, J. and Sheeley, J.: 1996, *Phys. Fluids* **8**, 405.
Kull, H.F.: 1991, *Phys. Rep.* **206**, 197.
Meshkov, E.: 1969, *Sov. Fluid Dyn.* **4**, 101.
Oron, D., Alon, U., Offer, D. and Shvarts, D.: 2001, *Phys. Plasmas* **8**, 2883.
Richtmyer, R.: 1960, *Commun. Pure Appl. Math.* **13**, 297.
Robey, H.F., Kane, J.O. and B.A.R.: 2001, *Phys. Plasmas* **8**(5), 2446.
Ryutov, D.D., Remington, B.A., Robey, H.F. and Drake, R.P.: 2001, *Phys. Plasmas* **8**, 1804.
Schmidt, H. and Klein, R.: 2003, *Combust. Theory Model.* **7**, 243.
Smiljanovski, V., Moser, V. and Klein, R.: 1997, *Combust. Theory Modelling* **1**, 183.
Wouchuk, J.: 2001, *Phys. Rev. E* **63**(056303), 1.
Ye Zhou, Remington, B.A., Robey, H.F., Cook, A.W., Glendinning, S.G., Dimits, A., Buckingham, A.C., Zimmerman, G.B., Burke, W.W., Peyser, T.A., Cabot, W. and Eliason, A.: 2003, *Phys. Plasmas* **10**(5), 1883.

LOWER HYBRID WAVE ELECTRON HEATING IN THE FAST SOLAR WIND

J. MARTIN LAMING
Naval Research Laboratory, Code 7674L, Washington, DC 20375;
E-mail: jlaming@ssds.nrl.navy.mil

(Received 30 April 2004; accepted 8 July 2004)

Abstract. We discuss electron–ion equilibration by lower hybrid waves in the fast solar wind, and its observed effects upon element charge state distributions.

Keywords: solar wind, ionization balance, electron heating

The solar wind is the plasma medium upon which the various manifestations of solar activity act to cause the phenomena collectively referred to as "Space Weather". It is also an attractive "laboratory" for the more collisionless aspects of plasma physics that can be studied in a variety of ways; by *in situ* measurements of particles, wave activity and fields, and by remotely sensed imaging and spectroscopy of both the wind itself and its source regions in the solar corona. One may study processes in the solar wind, that while potentially important in the search for the solar wind acceleration mechanism, are known now to be crucial in other astrophysical settings. Important examples are the anomalous electron thermal conductivity in cooling flows in clusters of galaxies, and the means by which electrons and ions may (or may not) equilibrate their temperatures in two temperature black hole accretion flows or behind collisionless shock waves in supernova remnants.

The *fast* solar wind is known to emanate from solar coronal holes where the electron temperature is $\sim 8 \times 10^5$ K. At this temperature the ionization balance of Fe is dominated by the Ar-like charge state, Fe^{8+}. However in the fast solar wind observed at 1 AU, Fe is observed to be mainly in charge states Fe^{11+} or Fe^{12+} (Geiss et al., 1995; Ko et al., 1997), requiring the existence of an electron heating mechanism that causes a sufficient increase in electron temperature within about 3 solar radii heliocentric distance to further ionize Fe before charge states freeze in the expanding solar wind. Further, the fact that essentially none of this heat deposited in the electrons seems to conduct back to the coronal hole base also requires an anomalous conductivity.

A recent paper, (Laming, 2004) proposed that electrons in the fast solar could be heated beginning at heliocentric distances 1.5–2.0 solar radii. At these distances ions begin to be strongly heated by resonance with ion cyclotron waves. This causes a dramatic increase in the ion temperature perpendicular to the magnetic field, and a corresponding increase in the ion gyroradii. Under such conditions in a cross-field density gradient of length scale similar to the ion gyroradii (see Figure 1), lower hybrid waves may be excited by the resulting anisotropy in the ion velocity distribution function.[1] These waves damp by heating electrons as well as ions, leading to a collisionless energy transfer from the hot ions to the cooler electrons. Such a scheme bears most relation to an instability previously discussed for two temperature accretion flows by (Begelman and Chiueh, 1988), but similar electron heating mechanisms have also been invoked elsewhere for supernova remnants and cometary X-ray emission (Laming, 2001a,b; Bingham et al., 1997; McClements et al., 1997).

We model the evolution of the ionization balance of the various elements observed in the fast solar wind using an implementation of time-dependent ionization balance within an analytic approximation for the magnetohydrodynamical flow. The new ideas about electron heating have proven a little controversial, despite a long history of study of density inhomogeneities in the solar wind, so we use a code called BLASPHEMER,[2] described at more length in (Laming and Grun, 2002, 2003; Laming and Hwang, 2003; Hwang and Laming, 2003). The electron heating by the lower hybrid instability is implemented by evaluating the ion–electron energy transfer rate in quasi-linear theory, taking this to be two times the wave growth rate times the wave energy density (Karney, 1978). A typical run for the element Fe is shown in Figure 2. At low altitudes Fe^{8+} dominates. At distances beyond 1.5 solar radii heliocentric distance, ion cyclotron heating becomes strong, and some of the energy from the ion heating is able to find its way to the electrons by the instability discussed above. The result is an increase in the average charge state of Fe, consistent with observations, which occurs out to be about 3 solar radii, where charge states freeze in (i.e. the solar wind expansion rate is faster than typical ionization and recombination rates). Results for other elements (C, O, Mg, and Si) show similar behavior (Laming, 2004).

The anomalous thermal conductivity associated with lower hybrid turbulence at the level predicted (Karney, 1978) is also sufficient to inhibit electron heat

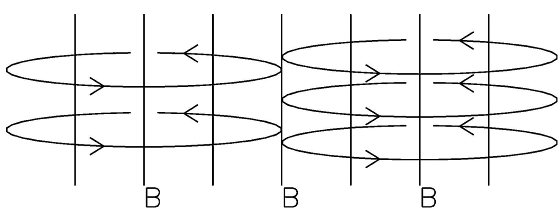

Figure 1. Schematic diagram of lower hybrid wave generation in the density gradient by gyrating ions. The density increases from left to right. In the center of the figure, more ions are moving out of the page than into it, leading to a two-stream instability.

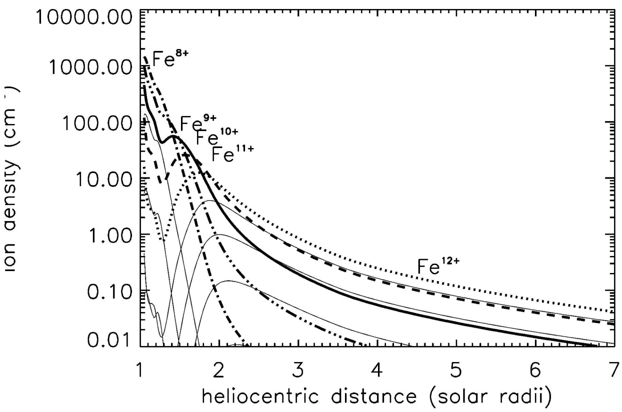

Figure 2. Evolution of Fe ionization balance with heliocentric distance.

conduction back to the sun to the degree required. It is likely that this estimate is in fact an underestimate of the turbulence level, and so similar electron heating could be maintained with lower growth rates for the lower hybrid waves, which are probably consistent with the density inhomogeneities observed in the fast solar wind by interplanetary scintillation. Thus several aspects of the microphysics of collisionless electron–ion equilibration of wide importance elsewhere in astrophysics may be studied by careful observation and modeling of the solar wind. The anomalous conductivity also places constraints on mechanisms by which the ion cyclotron wave necessary for the solar wind acceleration may be excited. To date we have only considered spatial inhomogeneities in solar wind plasmas. Temporal inhomogeneities such as recently invoked for the generation of ion cyclotron waves (Markovskii and Hollweg, 2004) may also play a role, which will be interesting and fun to explore.

Acknowledgments

This work was supported by NASA contract S13783G and by the NRL/ONR Solar Magnetism and the Earth's Environment 6.1 Research Option.

Notes

1. Lower hybrid waves are an electrostatic oscillation of the ions, with wavevector close to the perpendicular to the magnetic field, and with wavelength $\gg$ electron gyroradius. Under these conditions, the electrons are pinned on magnetic field lines and may only damp the wave by motions along the magnetic field direction.
2. BLASt Propagation in Highly EMitting EnviRonment.

References

Begelman, M.C. and Chiueh, T.: 1988, *Astrophys. J.* **332**, 872.
Bingham, R., Dawson, J.M., Shapiro, V.D., Mendis, D.A. and Kellett, B.J.: 1997, *Science* **275**, 49.
Geiss, J et al.: 1995, *Southern High-Speed Stream: Results from the SWICS Instrument on Ulysses Science*, Vol. 268, 1033.
Hwang, U. and Laming, J.M.: 2003, *ApJ* **597**, 362.
Karney, C.F.F.: 1978, *Phys. Fluids* **21**, 1584.
Ko, Y.-K., Fisk, L.A., Geiss, J., Gloeckler, G. and Guhathakurta, M.: 1997, *Solar Phys.* **171**, 345.
Laming, J.M.: 2001a, *Astrophys. J.* **546**, 1149.
Laming, J.M.: 2001b, *Astrophys. J.* **563**, 828.
Laming, J.M.: 2004, *Astrophys. J.* **604**, 155.
Laming, J.M. and Grun, J.: 2002, *Phys. Rev. Lett.* **89**, 125002.
Laming, J.M. and Grun, J.: 2003, *Phys. Plasmas* **10**, 1614.
Laming, J.M. and Hwang, U.: 2003, *Astrophys. J.* **597**, 346.
Markovskii, S.A. and Hollweg, J.V.: 2004, *Astrophys. J.*, in press.
McClements, K.G., Bendy, R.O., Bingham, R., Kirk, J.G. and Drury, L.: 1997, *MNRAS* **291**, 241.

INTERFEROMETRIC MEASUREMENTS OF THE INTERACTION OF TWO PLASMAS IN A TRANSVERSE MAGNETIC FIELD

C.D. GREGORY, A.D. ASH, D.M. CHAMBERS[1], C. COURTOIS, R.A.D. GRUNDY and N.C. WOOLSEY

Department of Physics, University of York, York, YO10 5DD, United Kingdom; E-mail: cdg104@york.ac.uk

[1]*Current address: AWE, Aldermaston, Reading, RG7 4PR, United Kingdom*

(Received 30 April 2004; accepted 5 July 2004)

Abstract. Presented are interferometric results of the interaction of two plasmas without and with a magnetic field. This study is based on the collision-free interaction of two millimetre-scale, counter-streaming plasmas – a proposed experimental simulation of shock production in a supernova remnant. This collision-free interaction is compared with a separate set of experiments with an external 7.5 T magnetic field applied. The interaction dynamics are inferred from spatially and temporally resolved electron density measurements, and the effect of the magnetic field on the plasma interaction is discussed.

Keywords: collisonless shocks, supernova remnants, laboratory experiments

1. Introduction

High-power laser experiments are playing an increasingly important role in our understanding of astrophysical phenomena (Remington, 1999; Takabe, 1999). The relevance of these studies relies on scaling analysis (Ryutov, 2001) where dimensionless parameters are matched between the experiment and the astrophysical object of interest. A previous publication (Woolsey, 2001, 2002; Drake, 2002) described a laser-plasma experiment designed to create a scaled snapshot of a young supernova remnant (SNR) approximately 100 years after the supernova explosion. Two supersonically expanding counter-streaming plasmas were allowed to interact both with and without the presence of a strong magnetic field. The aim was to introduce new, shorter scale lengths – namely the ion and electron gyro-radii. This may give rise to an effective collisionality *if* the plasma is magnetised, and while the ions are sufficiently cold. We present results from a similar experiment, which scaling analysis (Courtois, 2004a,b) suggests can be used to simulate aspects of collisionless shocks in SNR.

2. Experiment

The experimental setup is shown in Figure 1(a). Two C_8H_8 foils of thickness 0.1 μm ($\pm 10\%$) are mounted face-parallel a distance of 1 mm apart. The non-opposing faces

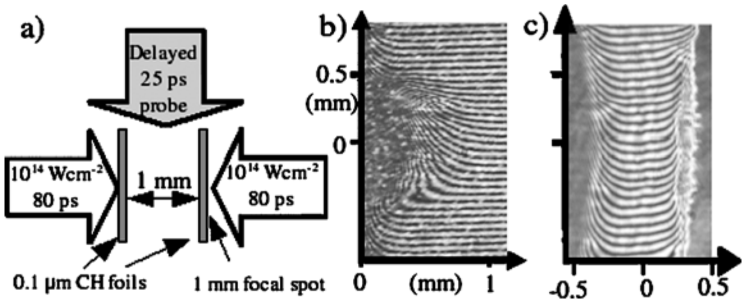

Figure 1. (a) Experimental setup. The probe is delayed relative to the peak of the drive laser pulses by between 250–750 ps. The magnetic field is oriented parallel to the probe, and perpendicular to the plasma flow. (b) An interferogram from a single foil experiment. (c) An interferogram from a two-foil experiment, with a 7.5 T magnetic field applied.

of the foils are simultaneously irradiated with an 80 ps drive laser pulse at 1.053 μm wavelength, with a peak intensity of 6×10^{13} W cm^{-2} ($\pm 10\%$).

For shots with a magnetic field, the foils are placed at the centre of a pulsed electromagnet, which gives a uniform 7.5 T field for a duration of 1 ms. The field is oriented perpendicular to the direction of plasma flow. The magnetic field strength is chosen so that the plasma pressure is greater than the magnetic field pressure (plasma $\beta > 1$), and so the field is not expected to affect the expansion of the plasma. In addition, the field is large enough to localise the ions and electrons on gyroradii smaller than the 1 mm size of the system (Courtois, 2004a,b).

The plasma expansion is characterised with an interferometry diagnostic, using a 25 ps probe laser pulse, frequency doubled to 0.53 μm. The delay of the probe beam with respect to the drive beams can be changed, giving a series of snapshots of the temporal evolution of the plasma expansion. From the fringe shifts in the resulting interferograms, the electron density, n_e, is inferred across a 1 mm cord in the plasma.

3. Experimental Results

In this section interferometric data are presented from experiments both with and without magnetic field. Each interferogram is a 25 ps snapshot, and these snapshots are taken between 250–750 ps after the peak of the drive laser pulse. From these data, n_e profiles are inferred along a 1 mm cord through the centre of the plasma.

By using thin plastic foil targets, the production of a rapidly expanding, low density, low atomic number plasma is achieved. This is important in order to achieve a collision-free interaction in the counter-streaming experiments. Figure 1(b) shows an example of interferometric data from a single-foil experiment. This image was recorded at a probe delay of 750 ps with respect to the peak of the drive pulse. The initial foil position is at 0 on the horizontal axis, and the drive laser is incident from the left and centred on the position 0 on the vertical axis. The dark region, which

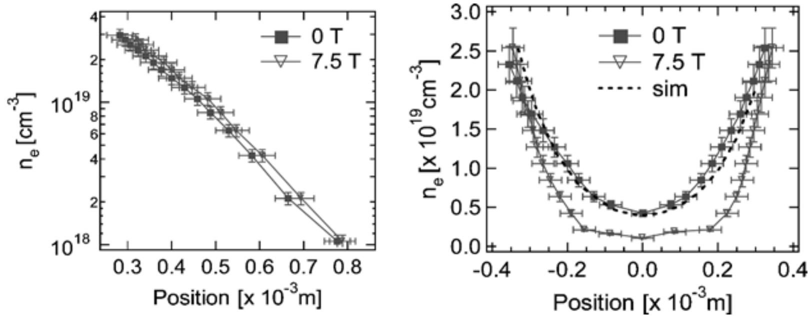

Figure 2. (a) Single foil and (b) two-foil inferred n_e profiles with and without a 7.5 T magnetic field. The dashed line in (b) is discussed in Section 4.

can be seen immediately to the right of the initial foil position, is below critical density for the probe, but the density gradients in this region are high enough to refract the probe beam out of the collection angle of the imaging system. From similar measurements of n_e taken at a probe delay of 500 ps, the expansion speed, V_{exp}, of the leading edge of the plasma is estimated. At 6×10^{13} W cm^{-2}, after 500 ps, $V_{exp} = 1.1 \times 10^8$ cm s^{-1}.

Figure 2(a) shows inferred horizontal n_e measurements along the centre of the plasma expansion at 750 ps after the peak of the drive pulse, taken from data similar to that shown in Figure 1(b). The solid blue squares represent the field-free expansion of the exploded foil, and the open red triangles show data taken in the presence of a 7.5 T transverse magnetic field. The intensities on target are 6×10^{13} W cm^{-2}. The n_e profiles are identical, indicating that up to relatively long times (750 ps), and distances comparable to the initial foil separation in the two-foil experiments ($\sim$1 mm), the presence of the magnetic field *does not* affect the hydrodynamics of the expansion of the plasma.

Figure 1(c) shows an interferogram taken from a counter-streaming plasma experiment. In these experiments two face-parallel foils are placed 1 mm apart, and simultaneously exploded. The initial foil positions are at -0.5 mm and $+0.5$ mm on the horizontal axis. The drive laser beams are incident from the left and the right, and centred at the position 0 on the vertical axis. Figure 2(b) shows inferred n_e profiles from an experiment with an applied 7.5 T magnetic field (red triangles), from Figure 1(c), and a similar experiment with no applied field (blue squares). The field-free n_e profile is parabolic in shape, and is consistent with the density profiles from the free expansion of a single foil, suggesting that the plasmas interpenetrate. The n_e profile when the magnetic field is applied is characterised by a steepened density gradient close to initial foil positions, and an extended density plateau around 350 μm in width. This plateau is centred on the interaction point of the two plasmas. In contrast to the results in the single foil case, the magnetic field affects the evolution of the n_e profiles of two counter-streaming plasmas.

4. Discussion

From experimentally inferred n_e and V_{exp} at 500 ps, the ion-ion mean free path is found to be larger than the system size (Courtois, 2004a,b), therefore coulomb collisions are not believed to be important at the time of the interaction. This is reinforced by the data in Figure 2(b). Here the inferred n_e profile for the two counter-streaming plasmas, at a time of 500 ps and with no magnetic field present, is represented by the blue squares. The dashed line represents an n_e profile taken from a simulation (Courtois, 2004a,b) in which the plasma interaction is collision-free, and the plasmas interpenetrate. The simulation fits the experimental results relatively well, and it is suggested that the two plasmas interpenetrate in the experiment.

As shown in Figure 2(b), the n_e profile changes notably in the presence of an applied 7.5 T magnetic field transverse to the plasma flow. The density profile is steepened, and exhibits a density plateau around 350 μm wide. It is difficult to explain these features in terms of the magnetic field directly retarding the plasma flow, since single-foil measurements show that at the interaction time the hydrodynamic expansion of the plasmas is not affected by the presence of the field. Compressing the magnetic field between two pistons (for example two expanding plasmas) would increase the magnetic pressure. In this experiment the magnetic pressure would dominate the plasma ram pressure if the field is compressed by more than a factor of 10. This implies that the compressed magnetic field should occupy a region of around 100 μm between the two plasmas. Although this is similar to the size of the observed density plateau, it is unlikely to occur due to the two-dimensional nature of the experiment. The approximate 1 mm lateral extent of the experiment probably allows the magnetic field to escape during the collision of the two plasmas. An alternative explanation is that the magnetic field reduces the fundamental scale length from the particle mean free path, to the Larmor radius, which could lead to an increase in the effective collisionality of the system. This could occur if the magnetic field penetrates the plasma, and the Larmor radius is smaller than the system size. A simple model (Courtois, 2004a,b) suggests that at 500 ps, the field could penetrate the plasma and localise the ions up to a distance of 150 μm from the experimental mid-point. This is consistent with the scale of the density plateau seen in Figure 2(b). It should be noted that the plasma n_e profile is sensitive to experimental changes, such as a 10% variation in foil thickness or separation. This means that the inferred values n_e with and without magnetic field cannot be compared absolutely. It can be seen however that there is a qualitative difference between the two cases.

5. Conclusion

The laser driven explosion of one thin plastic foil, and of two thin plastic foils in opposing geometry, has been studied. These experiments were performed both with and without a transverse 7.5 T applied magnetic field, and the plasma expansion was characterised using interferometry. Results show that the magnetic field is not sufficiently strong to affect the expansion of one foil, and suggest that counter-streaming plasmas interpenetrate in the absence of an applied field. When a 7.5 T field is applied to the system in the counter-streaming case, the inferred electron density profiles are modified: The profiles are steepened, and a density plateau is observed. These features cannot be explained by retardation of the plasma by the field, and it has been suggested that the magnetic field introduces new physics by reducing the important scale length, the Larmor radius, below the size of the system. This may lead to an increase of the effective collisionality of the system, and a collisionless interaction.

References

Courtois, C. et al.: 2004a, *Phys. Plasmas* **11**, 3386.
Courtois, C. et al.: 2004b, *Astrophysics Space Science* Proceedings of the 5th HEDLA Conference, 10th–13th March 2004, Tucson, AZ.
Drake, R.P. et al.: 2002, *Phys. Plasmas* **9**, 727.
Remington, B.A. et al.: 1999, *Science* **248**, 1488.
Ryutov, D.D. et al.: 2001, *Phys. Plasmas* **8**, 1804.
Takabe, H. et al.: 1999, *Plasma Phys. Controlled Fusion* **41**, A75.
Woolsey, N.C. et al.: 2001, *Phys. Plasmas* **8**, 2439.
Woolsey, N.C. et al.: 2002, *Phys. Plasmas* **9**, 729.

LABORATORY SIMULATIONS OF BOW SHOCKS AND MAGNETOSPHERES

W. HORTON, C. CHIU and T. DITMIRE

Institute for Fusion Studies, The University of Texas, Austin, TX, U.S.A.;
E-mail: horton@physics.utexas.edu

(Received 13 May 2004; accepted 3 June 2004)

Abstract. Laboratory experiments using a plasma wind generated by laser-target interaction are proposed and analyzed to investigate the creation of a shock in front of the magnetosphere and the dynamo mechanism. The proposed experiments and simulations are thought to be relevant to understanding the electron acceleration mechanisms at work in shock-driven magnetic dipole confined plasma in compact magnetized stars.

Keywords: magnetospheres, bow shocks, compact magnetized stars, laser blow-off plasmas

1. Magnetospheres

Magnetospheres are ubiquitous in space and astrophysics, being formed from plasma winds streaming past magnetic planets and stars. In the solar system we know a great deal about magnetospheres formed by the solar plasma wind interaction with Earth (Fälthammar, 1973) and Jupiter (Dessler, 1983). We will use this knowledge in designing the laboratory astrophysical experiments. The scaling factor from the laboratory to the geophysical space scale is of order 10^9. The scaling factor from the laboratory to a magnetic white dwarf is 10^{12}. In Table I we describe the dimensional and dimensionless parameters for the proposed laser Z-pinch experiments compared with magnetospheres of the Earth, a magnetic white dwarf and a neutron star.

Detailed parameters have been given in Horton and Chiu (2004) for the laser Z-pinch simulation of the Earth. A more challenging question is whether one can extend the design to laboratory experiments for the magnetospheres surrounding magnetic stars. Much theoretical work has been carried out for the magnetospheres of pulsars (Beskin et al., 1993). The difficulty of modeling the pulsar electrodynamics is that there is extremely rapid rotation playing a key role and there is an electron-positron plasma in the auroral region determining the critical electric field for triggering the synchrotron emission.

The astrophysical magnetosphere that is more approachable for laboratory simulations is that inferred to precede the Type Ia supernova. The Type Ia supernova is modeled as the culmination of a plasma wind accreting on a white dwarf.

TABLE I

Magnetospheres R_s, B_s and Plasma Winds n_w, T_w, $M_s = 1.4{-}7$

Plasma	Lab	Earth	White dwarf	Neutron star
n_w (cm^{-3})	10^{17}	10	.01	.01
T_w (eV)	10–100	10	10	10
$B_s^2/8\pi$ (erg/cm^3)	4×10^8	10^{-2}	4×10^{14}	4×10^{22}
R_{mp} (cm)	10	6×10^9	6×10^{12}	6×10^{12}
R_{mp}/R_s	5	10	10^4	10^6
Scaling $R_{\mathrm{mp}}/R_{\mathrm{mp}}^L$	1	10^9	10^{12}	10^9
c/ω_{pi} (cm)	0.1	10^7	10^8	10^8
$R_{\mathrm{mp}}\omega_{pi}/c$	10^2	10^2	10^3	10^2
$c_s(RB)_{\mathrm{mp}}$ (V)	10^3	10^6	10^{16}	10^{14}
$10^3\omega_{p_i}^{-1}$(s)	10^{-10}	10	100	100

1 pars $= 3.1 \times 10^{18}$ cm, $R_E = 6 \times 10^8$ cm, 1 Pa $=$ 10 erg/cm^3 $=$ 10 dyne/cm^2.

White dwarfs typically contain a strong magnetic field $B \sim 10^8$ G produced by the magnetic flux-conserving collapse of stars with typical stellar magnetic fields $B \sim 100$ G.

In Table I we describe the dimensional and dimensionless parameters in the proposed laser Z-pinch experiment and those in nature.

Because the plasma wind is supersonic, the stationary magnetic dipole can be viewed as a piston that drives a shock in the rest frame of the inflowing plasma (Zel'dovich and Raizer, 1966). The electron acceleration mechanisms are not well understood (for example, see Li et al. (1998), Li (2002), and Sarris et al. (2002) compared with Summers et al. (1998, 2003), for two different theoretical models). The same type of phenomenon is also found in the magnetosphere of Jupiter, and similar processes probably account for the electron energy fluxes inferred from synchrotron radiation from magnetic stars (Shapiro and Teukolsky, 1983).

2. Laser Blow-off Plasma Winds

Laser blow-off plasmas (London and Rosen, 1986) and laser-plasma diagnostics require that the plasma wind pressure exceed $P \sim 10^6$ Pa $\sim$ 10 atm for a laboratory simulation experiment. Thus the dipoles need to have magnetic fields above 10 T to stand off the plasma wind. We are carrying out modern, high magnetic field, laser blow-off experiments in the laboratory to create the bowshock and magnetosphere. Both front side and back side plasma ejecta are candidates for different types of plasma winds. The super strong magnetic dipoles are produced by the Z-pinch facility. Key objectives in the experiment are to create a shock from the dipole obstacle, to create a dynamo electric field, and to measure the impact of the electrons on the surface of the sphere surrounding the dipole. Initial results are reported by Presura et al. (2004) in these HEDLA Proceedings.

3. Bow Shocks from Plasma Winds

The forty-year long history of magnetospheric spacecraft that have passed through the bow shock provides a wealth of information about the microscale structure of collisionless bow shocks. This field has taken another large step forward with the detailed correlation measurements from the extensively instrumented ensemble of four Cluster spacecrafts (Escoubet et al., 2004). Cluster is a European Space Agency mission in operation for 3 years which will continue until December 2005. The spacecraft separation distances have been 600, 2000, 100, and 5000 km. An example of the Cluster data for the electron density and magnetic field is shown in Figure 1.

The bow shock (Stasiewicz et al., 2003) is now clearly seen to consist of hundreds to thousands of microshocks that have widths of order of the ion skin depth $\delta_i = c/\omega_{pi}$, which is comparable to the ion gyro-radius $\rho_i = v_i/\omega_{ci}$ for the solar wind plasma since it has $\beta_i = p_i/(B^2/8\pi)$ of order unity. The compression ratio of the magnetic field in the microshocks is observed to be $B/B_0 \sim \rho/\rho_0 \sim 2$–$7$ over the distance of 500 km which is about $3c/\omega_{pi}(3 \times 150\,\text{km})$. The magnetic field increases by a factor of six from 2 to 12 nT. In Section 4 we discuss how the microshock is formed from the Hall-MHD description of the plasma.

The individual pulse shapes are well resolved by the four spacecrafts, and there are hundreds of these nonlinear pulses in the overall shock region, as shown in Figure 1. The shocked plasma streams around the magnetopause with plasma entry in the nightside filling the magnetotail. The spiky, nonlinear nature of the plasma

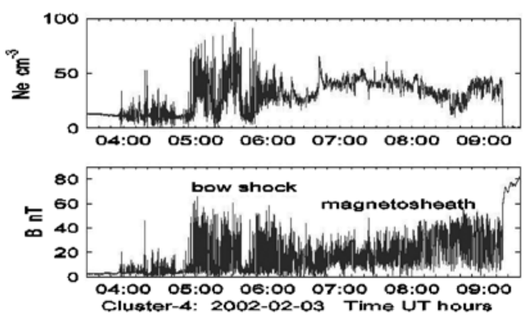

Figure 1. Cluster spacecraft data showing hundreds of microshocks called SLAMS making up the collisionless bow shock. Courtesy of C.P. Escoubet at ESA.

in the bow shock, called short large-amplitude magnetic structures (SLAMS), has been known earlier. SLAMS have a variety of shapes, some with little density variation.

4. Hall-MHD Microshock Structures and Energizations

We take $\hat{\boldsymbol{x}}$ to point upwind into the undisturbed plasma and $\hat{\boldsymbol{z}}$ (north) in the direction of the ambient normal magnetic field $B_z(x)$. We allow a B_x and there is a Hall current sheet $j_y(x)$ in the shock front. The plasma wind of density n_w and electron temperature T_w flows with speed u with respect to the dipole $M = B_s R_s^3$, where s denotes the surface surrounding the dipole. The ion temperature is typically lower than the electron temperature so that the acoustic waves are given by $\omega/k_x = c_s = (T_e/m_i)^{1/2}$ and the Mach number is $M_s = u/c_s > 1$. Here we restrict attention to the regime of $M_s = 1.4-7$ and take $T_e \simeq 5-10\,\text{eV}$. The plasma wind density will vary from $n_e \sim 10\,\text{cm}^{-3}$ for the Earth's magnetosphere to $n_e \sim 10^{-3}-10^{-2}$ cm^{-3} for the interstellar winds and the winds on to compact stars. In the laboratory simulation $n_e \sim 10^{17}\,\text{cm}^{-3}$. We postpone the study of strong shocks $M_s \gg 1$ to a later work.

The magnetic dipole obstacle in the plasma wind turns the positive ions and negative electrons in opposite directions, creating a current layer j_y in the shock front, which we take centered at $x = 0$ in the frame moving with the shock. The electrons are turned promptly over the short distance $\rho_e = v_e/\omega_{ce}$, while the ions penetrate much deeper over the scale $\rho_i = v_i/\omega_{ci} > 43\,\rho_e$. This charge separation creates an electric field E_x pointing upwind that draws the electrons into the shock front for repeated attempts to pass through the shock front. The magnitude of the electric potential is $\Delta\Phi = -\int^x E_x dx = B_0 B_z/(4\pi n_i e)$ as determined by the Hall-MHD description with massless electrons and charge quasi-neutrality. Here B_0 is the field upstream and $B_z > B_0$ is the field in the shock front.

Compressional shock structure. The shock structure is described as Hall physics since the ion and electron have opposite velocities in the shock front that differ strongly from the $\mathbf{E} \times \mathbf{B}$ drift velocity. Thus, the Ohm's law is given by the electron momentum balance equation,

$$\mathbf{E} + \mathbf{u}_e \times \mathbf{B} = \mathbf{E} + \mathbf{u} \times \mathbf{B} - \frac{\mathbf{j} \times \mathbf{B}}{e n_e} = \eta \mathbf{j}, \tag{1}$$

where η is the microscale resistivity produced by wave-particle scattering. A turbulent viscosity $\mu/\rho \sim c_B T_e/eB$ is also included with small $c_B \leq 10^{-2}$.

The ion fluid velocity $\mathbf{u}$ is given by the ion momentum balance equation

$$\frac{d\mathbf{u}}{dt} = \frac{e_i}{m_i}(\mathbf{E} + \mathbf{u} \times \mathbf{B}) + \mu \nabla^2 \mathbf{u} = \frac{1}{m_i n_i} \mathbf{j} \times \mathbf{B} + \mu \nabla^2 \mathbf{u}, \tag{2}$$

where the term $|e\eta j/m_i| \ll |j \times B/m_i n_i|$ is omitted. The ion pressure gradient is small for these shocks. The equations of state are taken as cold ions with negligible T_i/T_e and isothermal electrons with $T_e =$ constant.

Here we summarize the Hall-MHD shock compressional model. The shape of the pulse is determined by the ion viscosity μ. The speed and compression ratio are determined by the Rankine–Huginiont conditions for an oblique magnetic shock. We are motivated by the success of the particle-in-cell simulations of Bessho and Ohsawa (1999, 2002) which are able to accelerate electrons effectively with similar compressional shock structures.

For a compressional disturbance propagating toward the Earth at speed u into undisturbed near-Earth plasma with $v_x = 0, \rho_0, p_0$, and B_{z0} fields, the conservation conditions are $\rho(u - v_x) = \rho_0 u$ and

$$\rho v_x(v_x - u) + p_0\left(\frac{u}{u - v_x}\right)^2 + \frac{B_{z0}^2}{2\mu_0}\left(\frac{u}{u - v_x}\right)^2 - \mu\frac{dv_x}{dx} = p_0 + \frac{B_{z0}^2}{2\mu}. \tag{3}$$

The fixed points ($v_x = v_{x1}$ and $v_x = 0$ where $dv_x/dx = 0$) of Eq. (3) for the two solutions in front and behind the dipolarization pulses are given by the roots of

$$\mu\frac{dv_x}{dx} = -\rho_0 u v_x + \left(p_0 + \frac{B_{z0}^2}{2\mu_0}\right)\left[\left(\frac{u}{u - v_x}\right)^2 - 1\right] = 0. \tag{4}$$

The structure is given by the quadrature from Eq. (4).

The compressional pulse shape is $v_x(x) = v_{x1}[1 + \exp(x/D)]$, where $D = \mu/\rho_0 u$. Now $v_x(x)$ goes from $v_x = 0$ upstream to downstream $x \to -\infty$. The numerical integration of Eq. (4) for the shock structure with the full polynomial in Eq. (4) is straightforward.

The electron motion is a complex with three-dimensional orbits. For nearly normal shocks $B_x = B\ \cos\ \theta \ll B$, the electrons gain large amounts of parallel kinetic energy. The orbits are very different depending on the dimensionless parameter ρ_e/D, where D is the shock thickness of a few c/ω_{pi}. The work done in acceleration charge q along the y-direction is given by $W_y = qE_y\Delta y = q(E_y u B_0)c\Delta\xi/\omega_{pi}$.

While thermal electrons pass through the shock front with a small energy gain, there is a group of higher energy electrons that make repeated reflections from the shock front and drift large distances along the electric field $E_y = uB_z$ interacting repeatedly with the shock front as shown in Figure 2.

The initial energy of the electron must be high enough that the gyroradius ρ_e is comparable to the thickness D of the raising part of the compressed $B_z(x)$.

During the passage through the microstructure there is strong acceleration in the z-direction. The energy gain through $\int qv_y E_y dt$ is mostly transferred to the parallel

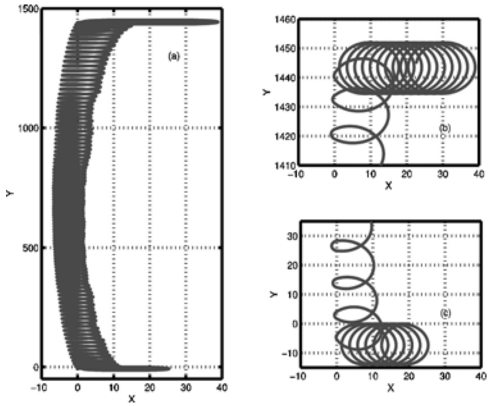

Figure 2. Electron orbits with large energy gain from $eE_y \Delta y$ in the frame of the shock. Frame (a) is the full orbit with $\Delta y = 1400\, c/\omega_{pi}$ while frames (b) and (c) show the exit and entrance motion in detail.

component kinetic energy through the work done by the integral $\int v_y v_z B_x dt$. There is a transfer of energy from the y-component into the parallel component. We have verified that the computer simulations satisfies energy conservation within the accuracy of the truncation error of the integrator.

5. Conclusions

Proof of principle laser Z-pinch experiments are being carried out in collaboration with the University of Nevada Terawatt Facility and The University of Texas Institute for High Intensity Lasers for documenting plasma wind driven magnetospheric physics.

Measurements and theory for the change in the magnetic geometry due to the plasma wind, including the creation of a bow shock, the existence of the magnetic tail and the creation of a magnetopause behind the bow shock. Measurements of the shock front and the change in the magnetic field are being investigated using schlieren imaging and Faraday phase rotation, magnetic probes, and the Zeeman effect. Electron fluxes are predicted.

Acknowledgments

The University of Texas acknowledges support from the National Science Foundation through Grant ATM-0229863 and the U.S. Department of Energy National Nuclear Security Administration Cooperative agreement DE-FC52-03NA00156.

References

Beskin, V.S., Gurevich, A.V. and Ya. N.: 1993, *Istomin*, Cambridge University Press, New York.

Bessho, N. and Ohsawa, Y.: 1999, *Phys. Plasmas* **6**, 3076.

Bessho, N. and Ohsawa, Y.: 2002, *Phys. Plasmas* **9**, 979.

Dessler, A.J. (ed.): 1983, *Physics of the Jovian Magneto Sphere*, Cambridge University Press, Cambridge.

Escoubet, C.P., Laakso, H., Goldstein, M. and Paschmann, G.: 2004, *Proceedings of the Conference on Earth-Sun Connection, Kona, Hawaii*, "Cluster: New Measurements of Plasma Structure in 3D."

Fälthammar, C.G.: 1973, *Space. Sci. Rev.* **15**, 803.

Horton, W. and Chiu, C.: 2004, *Phys. Plasmas* **11**, 1645.

Li, X.: 2002, in: R.M. Winglee (ed.), *Radiation belts and substorm particle injections (PDF), Proceedings of the Sixth International Conference on Substorms*, p. 305.

Li, X., Baker, D.N., Temerin, M., Reeves, G. and Belian, R.: 1998, *Geophys. Res. Lett.* **25**, 3763.

London, R.A. and Rosen, M.D.: 1986, *Phys. Fluids* **29**, 3813.

Presura, R., Cowan, T. et al.: 2004, *Proceedings of the HEDLA Conference*, Tucson, AZ.

Sarris, T.E., Li, X., Tsaggas, N. and Paschalidis, N.: 2002, *J. Geophys. Res.* **107**, 10.1029/2001JA900166.

Shapiro, S.L. and Teukolsky, S.A.: 1983, *Black Holes, White Dwarfs and Neutron Stars. The Physics of Compact Objects*, Wiley, New York.

Stasiewicz, K., Shukla, P.K., Gustafsson, G., Buchert, S., Lavraud, B., Thidé, B. and Klos, Z.: 2003, *Phys. Rev. Lett.* **90**, 085002.

Summers, D. and Thorne, R.M.: 2003, *J. Geophys. Res.* **108**, A4,1143.

Summers, D., Thorne, R.M. and Xiao, F.: 1998, *J. Geophys. Res.* **103**, 20487.

Zel'dovich, Ya.B. and Raizer, Yu.P.: 1996, in: W.D. Hayes and R.F. Probstein (eds.), *Physics of Shock Waves and High-Temperature Hydrodynamics Phenomena*, Academic Press, New York and London, see Chapter VII.